2017

# Defining Multi-Scale Relationships Between Biomechanics & Neuronal Dysfunction In Ligament Pain Using Integrated Experimental & Computational Approaches

Sijia Zhang
*University of Pennsylvania*, sijiaz@seas.upenn.edu

# Defining Multi-Scale Relationships Between Biomechanics & Neuronal Dysfunction In Ligament Pain Using Integrated Experimental & Computational Approaches

**Abstract**
Capsular ligaments can encode the mechanical state of joints owing to their innervation. For example, the spinal facet capsular ligament that encloses the facet joint is innervated by mechanoreceptors and nociceptors, and is a major source of neck and low back pain from aberrant spinal motions. The cervical facet capsule is commonly injured by its excessive stretch during neck trauma. Although supraphysiologic deformation of the facet capsular ligament can activate its afferents and induce pain, the local biomechanical and neuronal mechanisms underlying sensory transduction for pain from mechanical inputs remain unclear. The studies in this thesis use integrated in vitro, in vivo and in silico methods to investigate the interplay between the mechanical and nociceptive functions of the cervical facet capsular ligament. Tissue-level mechanics, collagen network restructuring and neuronal dysfunction are all assessed across length scales using a neuron collagen construct (NCC) system as well as animal and computational modeling. Afferent activation, nociception and dysfunction are found to depend on the macro-scale tissue strains. Yet, relationships between macroscopic stretch and micro-scale pathophysiology in the facet capsule is confounded by its heterogeneous fibrous architecture. Studies in this thesis show that localized collagen disorganization is associated with excessive network-level reorganization and fiber-level stretch using network analysis and finite element-based modeling. Integrated imaging of the extracellular matrix structure and neuronal dysfunction in the NCC system provides evidence for collagen network organization and local fiber kinematics as mediators of pain-related neuronal signaling. Stretch-induced production of nociceptive neuropeptides in NCCs is prevented by inhibiting collagen-binding integrins, supporting a role of cell-matrix adhesion in converting noxious mechanical stimuli in to pain signals. Further, neuronal mechanotransduction that initiates pain is found to involve the intracellular RhoA/Rho kinase ROCK. In vivo studies in the rat suggest that intra-articular ROCK likely contributes to the development of central sensitization and facet joint pain, possibly via neuropeptide-mediated synaptic transmission and spinal microglial activation. Collectively, these findings establish the role of collagen networks and fibers in translating macroscopic ligament stretch in to neuronal pain signals and identify mechanotransductive signaling cascades that have clinical relevance as possible treatment for trauma-induced facet pain.

**Degree Type**
Dissertation

**Degree Name**
Doctor of Philosophy (PhD)

**Graduate Group**
Bioengineering

**First Advisor**
Beth A. Winkelstein

# DEFINING MULTI-SCALE RELATIONSHIPS BETWEEN BIOMECHANICS & NEURONAL DYSFUNCTION IN LIGAMENT PAIN USING INTEGRATED EXPERIMENTAL & COMPUTATIONAL APPROACHES

Sijia Zhang

A DISSERTATION

in

Bioengineering

Presented to the Faculties of the University of Pennsylvania in

Partial Fulfillment of the Requirements for the

Degree of Doctor of Philosophy

2017

Supervisor of Dissertation

_____

Beth A. Winkelstein, Professor of Bioengineering

Graduate Group Chairperson

_____

Ravi Radhakrishnan, Professor of Bioengineering & Chemical and Biomolecular Engineering

Dissertation Committee

Danielle S. Bassett, Associate Professor of Bioengineering & Electrical and Systems Engineering

D. Kacy Cullen, Research Associate Professor of Neurosurgery

Vivek Shenoy, Professor of Materials Science and Engineering, Mechanical Engineering and Applied Mechanics & Bioengineering

William C. Welch, Vice Chair & Professor of Neurosurgery

ACKNOWLEDGEMENT

First and foremost, I am very grateful to my advisor, Dr. Beth Winkesltein, for her help and support over the years. I would like to thank her for offering me the opportunity to pursue my passion and higher education in Bioengineering and her guidance through challenges in research and professional development. She has set an example of excellence as a researcher and educator. Her mentorship will influence me both academically and personally in the years to come.

I would like to thank the members of my thesis committee, Dr. Danielle Bassett, Dr. Kacy Cullen, Dr. Vivek Shenoy and Dr. William Welch, for their invaluable feedback and commitment throughout my training. I highly appreciate their insight and guidance on the development of this work and my professional career. I am also grateful to Dr. David Meany, for his mentorship during my research rotation and generosity in sharing knowledge and experimental resources. I would also like to thank Dr. Victor Barocas for all of his help during our collaboration. He has set a good role model and inspired me with his enthusiasm for research and teaching. I hope to continue to learn from him throughout the rest of my career.

I am grateful to the past and present members of the Spine Pain Research Lab for their friendship, advice and help. In particular, I would like to thank Dr. Nathan Crosby, Dr. Jeffrey Kras, Dr. Kristen Nicholson, Dr. Kyle Quinn, Dr. Sagar Singh and Christine Weisshaar for their contributions to my thesis and other work that I have completed in the past five years. I greatly appreciate the assistance offered by members in the Cullen Lab and the Shenoy Group at the University of Pennsylvania, by Dr. Catalin Picu and his

students at the Rensselaer Polytechnic Institute, and by my friends from the Barocas Group at the University of Minnesota.

Special thanks to Meagan Ita, Sonia Kartha, Megan Sperry, Jenell Smith, Martha Zeeman and Vahhab Zarei for their friendship and encouragement. Their support and company have made me stronger and happier. I want to thank them for standing by my side through thick and thin. Last but not least, I would like to thank my family, especially my parents, for their unconditional love, patience, sacrifices and support as I navigate my way through life. Thank you mom and dad for everything that you have done for me and I love you both from the bottom of my heart.

ABSTRACT

DEFINING MULTI-SCALE RELATIONSHIPS BETWEEN BIOMECHANICS & NEURONAL DYSFUNCTION IN LIGAMENT PAIN USING INTEGRATED EXPERIMENTAL & COMPUTATIONAL APPROACHES

Sijia Zhang

Beth A. Winkelstein

Capsular ligaments can encode the mechanical state of joints owing to their innervation. For example, the spinal facet capsular ligament that encloses the facet joint is innervated by mechanoreceptors and nociceptors, and is a major source of neck and low back pain from aberrant spinal motions. The cervical facet capsule is commonly injured by its excessive stretch during neck trauma. Although supraphysiologic deformation of the facet capsular ligament can activate its afferents and induce pain, the local biomechanical and neuronal mechanisms underlying sensory transduction for pain from mechanical inputs remain unclear. The studies in this thesis use integrated in vitro, in vivo and in silico methods to investigate the interplay between the mechanical and nociceptive functions of the cervical facet capsular ligament. Tissue-level mechanics, collagen network restructuring and neuronal dysfunction are all assessed across length scales using a neuron collagen construct (NCC) system as well as animal and computational modeling. Afferent activation, nociception and dysfunction are found to depend on the macro-scale tissue strains. Yet, relationships between macroscopic stretch and micro-scale pathophysiology in the facet capsule is confounded by its heterogeneous

fibrous architecture. Studies in this thesis show that localized collagen disorganization is associated with excessive network-level reorganization and fiber-level stretch using network analysis and finite element-based modeling. Integrated imaging of the extracellular matrix structure and neuronal dysfunction in the NCC system provides evidence for collagen network organization and local fiber kinematics as mediators of pain-related neuronal signaling. Stretch-induced production of nociceptive neuropeptides in NCCs is prevented by inhibiting collagen-binding integrins, supporting a role of cell-matrix adhesion in converting noxious mechanical stimuli in to pain signals. Further, neuronal mechanotransduction that initiates pain is found to involve the intracellular RhoA/Rho kinase ROCK. In vivo studies in the rat suggest that intra-articular ROCK likely contributes to the development of central sensitization and facet joint pain, possibly via neuropeptide-mediated synaptic transmission and spinal microglial activation. Collectively, these findings establish the role of collagen networks and fibers in translating macroscopic ligament stretch in to neuronal pain signals and identify mechanotransductive signaling cascades that have clinical relevance as possible treatment for trauma-induced facet pain.

## TABLE OF CONTENTS

Page

LIST OF TABLES

Page

LIST OF FIGURES

Page

# Chapter 1

# Introduction & Background

## 1.1. Introduction

Chronic pain is a major healthcare problem affecting over 100 million adults in the United States (Institute of Medicine 2011; Nahin 2015). Annual costs for chronic pain exceed $500 billion, of which treatment for neck and back pain accounted for $86 billion in 2005 (Martin et al. 2008; Manchikanti et al. 2013). Spinal pain has an estimated annual incidence of 14-50% (Côté et al. 2004; Strine and Hootman 2007). Nearly two-thirds of the general population is affected by neck pain at least once in their lifetime and approximately one-half of the chronic neck pain cases are due to cervical spine trauma, such as that which can occur with whiplash (Côté et al. 1998; Côté et al. 2000; Côté et al. 2004; Strine and Hootman 2007).

Motor vehicle collisions are a major cause of neck pain (Freeman et al. 1999; Curatolo et al. 2011). The estimated incidence of whiplash injury is approximately 4 per 1,000 persons and the annual economic cost is nearly $4 billion (Freeman et al. 1999; Eck et al. 2001). Over one-half of the whiplash patients report chronic pain that lasts for at least six months (Kwan and Fiel 2002). Previous biomechanical studies suggest that whiplash injuries are a result of abnormal cervical spine motions (Pettersson et al. 1997; Panjabi et al. 1998b; Eck et al. 2001). After impact is made to a vehicle from the rear, the

passenger's head can undergo rotation, translation and acceleration (Panjabi et al. 1998b; Eck et al. 2001). That aberrant head motion causes the upper cervical spine to undergo flexion while the lower cervical spine is in extension, producing an "S-shaped" spine (Panjabi et al. 1998b; Eck et al. 2001). Abnormal cervical spine motions can potentially injure many structures in the neck, including the intervertebral discs, facet joints, spinal ligaments and muscles, all of which could lead to pain (Pettersson et al. 1997; Jaumard et al. 2011; Curatolo et al. 2011; Hauser et al. 2015).

The cervical facet joint is a major source of neck pain (Lord et al. 1996; Manchikanti et al. 2004; Cavanaugh et al. 2006; Bogduk 2011). The facet joint facilitates articulation between adjacent vertebrae in the spine (Panjabi et al. 1998a; Pearson et al. 2004; Jaumard et al. 2011). Using anesthetic nerve blocks, the facet joint has been identified as the origin of pain in approximately 65% of neck pain patients (Lord et al. 1996; Manchikanti et al. 2004; van Eerd et al. 2010). The bilateral facet joints are each enclosed by a capsular ligament that is primary comprised of dense collagen fibers and is innervated by primary afferents (McLain 1994; Yamashita et al. 1996; Quinn et al. 2007; Jaumard et al. 2011; Kallakuri et al. 2012). During simulations of whiplash exposures using human cadaveric cervical spines, the facet capsular ligament undergoes stretch due to facet joint compression and sliding and sustains supraphysiologic strains that exceed those measured during typical normal neck motions (Panjabi et al. 1998a; Pearson et al. 2004).

Excess elongation of the facet capsule can induce pain because the capsular ligament is innervated by afferents that can be activated by mechanical stimuli (McLain

1994; Lu et al. 2005a; Chen et al. 2006). The cervical facet joint capsule is innervated by different types of mecahanoreceptors and nociceptors (McLain 1994; Chen et al. 2006; Kallakuri et al. 2012). Mechanoreceptors are sensory neurons that are specialized for proprioception and can be activated by a range of tissue strains (McLain 1994; Lu et al. 2005a). Nociceptors, on the other hand, detect and process noxious stimuli for nociception and pain (Basbaum et al. 2009). Supraphysiologic strains can activate sub-populations of the nociceptive C fibers and Aδ fibers (Chen et al. 2006), triggering a complex cascade of electrophysiological and biochemical events that conveys the nociceptive signals from the periphery to the spinal cord and rest of the central nervous system (CNS) (Basbaum et al. 2009; Steeds 2009; Winkelstein 2011; Woolf 2011). Sensory inputs to the spinal cord can cause widespread changes in the CNS, such as increased neuronal excitability and glial activation in the spinal cord, that facilitate and potentiate persistent pain (Woolf and Salter 2000b; Julius and Basbaum 2001; Quinn et al. 2010b). Pain signals can be further transmitted by higher order neural pathways to the brain and can give rise to a host of behavioral pain responses (Basbaum et al. 2009; Steeds 2009).

Although biomechanical, animal and clinical studies indicate the cervical facet joints as the leading source of pain from neck trauma (Panjabi et al. 1998a; Pearson et al. 2004; Cavanaugh et al. 2006; Manchikanti et al. 2008; Bogduk 2011; Dong et al. 2012), the local biomechanical mechanisms by which macroscopic capsule stretch is translated into afferent loading and signaling are not fully defined. Further, limited understanding about the signaling cascades that underlie mechanically-induced neuronal dysfunction

and nociception hampers the identification of drug targets for effectively treating facet pain. From 2000 to 2011, the utilization of all types of facet joint therapies increased substantially at an annual rate of 13.6% (Manchikanti et al. 2013). Specifically, the number of cervical and thoracic facet joint injections and radiofrequency neurotomies increased by 359% and 836%, respectively (Manchikanti et al. 2013). However, current interventions for facet-mediated pain have several drawbacks, including low specificity, low response rates and, if effective, only providing temporary pain relief (Kwan and Fiel 2002; Tibrewal et al. 2007). The inability of existing therapies to completely relive facet pain is partially due to the lack of scientific information fully defining the relationships between the mechanical and nociceptive functions of the facet capsular ligament. Identifying molecular modulators of neuronal mechanotransduction and nociceptive transmission could help reveal new targets for interventional facet pain therapies.

During neck trauma, the human facet capsule can experience large, multi-axial, non-uniform deformations at high accelerations under combined shear, bending and compression loading of the facet joint (Panjabi et al. 1998a; Winkelstein et al. 2000; Siegmund et al. 2000; Siegmund et al. 2001). Previous studies have shown that the magnitude of strain in the facet capsular ligament regulates neuronal responses and pain (Lu et al. 2005a; Kallakuri et al. 2008; Lee and Winkelstein 2009; Dong and Winkelstein 2010). Distraction of the rat C6/C7 facet joint to capsule strain of 6±6% does not induce pain; whereas, a significantly higher strain (19±11%) induces persistent behavioral hypersensitivity in the rat (Quinn and Winkelstein 2009; Dong et al. 2012; Ita et al. 2017a). Both slow quasi-static and high rate dynamic capsule stretch of large magnitudes

of strain can induce pain in the rat that is established as early as day one and lasts for at least 21 days (Lee et al. 2004b; Quinn et al. 2010b; Dong et al. 2012; Crosby et al. 2013; Ita et al. 2017b). In contrast to non-painful or physiologic capsule strains, pain-inducing ligament stretch can activate a subset of afferents innervating the facet capsule (Lu et al. 2005b), leading to a host of neurotransmitter and glutamatergic changes in the dorsal root ganglion (DRG) and spinal cord (Chen et al. 2006; Lee and Winkelstein 2009; Dong et al. 2012; Kras et al. 2013b; Crosby et al. 2014). Despite prior work defining the relationships between ligament strain and pathophysiological responses, the micromechanical environment of neurons may directly mediate their function *and* dysfunction in the facet capsular ligament.

Understanding the micromechanics and neuronal mechanisms of nociception in ligamentous capsular tissue is confounded by the complex architecture of the collagen-based extracellular matrix (ECM). The facet capsular ligament is a heterogeneous and multi-scale tissue, presenting varied structural and mechanical features at different length scales. In this thesis, three different length scales are defined with relevance to the facet capsular ligament: (1) *macro-scale* refers to the entire tissue domain, (2) *meso-scale* applies to sub-regions in the ligaments (approximately one-tenth the size of the tissue domain) within which the collagen fiber alignment remains relatively uniform (Ban et al. 2017) or for which regional strains are calculated based on elemental mesh (Quinn and Winkelstein 2008), and (3) *micro-scale* corresponds to the length scale of the local ECM (approximately two orders of magnitude smaller than the tissue size) that contains single, or a small number of, fibers that are in close contact with the innervating afferents.

The human facet capsular ligament contains sub-regions of collagen fibers with irregular and parallel orientations (Yamashita et al. 1996; Kallakuri et al. 2012; Ban et al. 2017) and exhibit non-homogeneous meso-scale regional strains even during simple uniaxial stretch (Quinn and Winkelstein 2008). Microstructural tissue abnormalities, which can be indicated by local collagen fiber disorganization, occur at macroscopic strains that correspond to no visible tissue rupture (subfailure) but can induce pain in vivo (Quinn et al. 2010a; Dong et al. 2012; Crosby and Winkelstein 2016; Ita et al. 2017b). Yet, the effects of fiber organization and deformation on neuronal transmission have not been fully defined, at least partially due to the multi-scale and heterogeneous nature of the facet capsular ligament and the associated experimental challenges in measuring non-homogeneous changes in the local mechanical environment during capsule stretch. Computational models that complement experimental measurements are helpful to predict and/or quantify mechanical changes in the collagen networks and fibers that transfer tissue-level deformations to load and activate micro-scale neurons.

Neurons respond to changes in their microenvironment and transduce mechanical stimuli into electrical and biochemical signals via receptor-mediated cell-ECM interactions (Martinac 2004; Raoux et al. 2007; Delmas et al. 2011). Collagen fiber motion, elongation and failure that accommodate soft tissue deformations may affect local forces, activating ion channels through conformational changes of those channels and altering cellular stresses via focal adhesions (Cullen et al. 2007a; Quinn and Winkelstein 2009; Sander et al. 2009a; Delmas et al. 2011). Although mechanotransduction pathways have been studied extensively in homeostasis in a wide

variety of cells including neurons (Martinac 2004; Ross et al. 2013), how noxious mechanical stimuli of neurons in ligaments are translated into pain signals is still unknown. In order to understand the non-physiologic mechanotransduction of the afferents in the facet capsular ligament, it is necessary to probe changes in the neuron-ECM adhesion(s) and the related cell signaling pathways that mediate both mechanosensing and nociception.

In this thesis, *pain* refers to "an unpleasant sensory and emotional experience associated with actual or potential tissue damage" (Radu et al. 2013), based on the definition provided by the International Association for the Study of Pain (IASP). Distinctly different, *nociception* is the process by which intense and potentially harmful physical stimuli (*noxious stimuli*), are detected, processed and transmitted by a sub-set of peripheral nerve fibers, called *nociceptors* (Markenson 1996; Basbaum et al. 2009). Quantifiable measures have been developed to assess evoked pain (Chaplan et al. 1994; Winkelstein 2011; Woolf 2011). For example, *mechanical hyperalgesia*, which was used in the in vivo rat studies in this thesis to measure pain, is the increased response to a mechanical stimulus that normally induces pain (Malik-Hall et al. 2005; Scott et al. 2005; Winkelstein 2011).

The next sections of this chapter provide relevant background information about the cervical spine and facet joint anatomy, innervation and microstructure of the facet capsular ligament, ligaments as sensory organs, neural anatomy and mechanisms of pain, biomechanics of facet capsular ligament injury and pain, and cell-ECM interactions and

mechanotransduction. Additional background information is provided at the beginning of each chapter as relevant and to rationalize each specific study.

## 1.2. Background

### 1.2.1. Cervical Spine & Facet Joint Anatomy

The cervical spine consists of seven bony vertebrae (C1-C7) that provide structural support for the neck. C1 and C2 retain specialized functions in facilitating skull movement; C3-C7 are more typical vertebrae made up of a spinous process, transverse process, vertebral body and the bilateral articular facets (Figure 1.1a). Each pair of adjacent vertebrae in the spine is connected by the intervertebral discs anteriorly and the bilateral articulating facet joints posterolaterally, and is stabilized by a variety of soft tissues that include muscles and ligaments (Figure 1.1) (Vasseur et al. 1981; Yoganandan et al. 2003; Blouin et al. 2007; Jaumard et al. 2011). The spinal motion segment is the smallest functional unit in the spine made up of two adjacent vertebrae and their connecting tissues; it captures the biomechanical features of the entire spine, and has been used extensively to define the joint kinematics and kinetics that occur during spinal trauma (Panjabi et al. 1998a; Gudavalli and Triano 1999; Siegmund et al. 2000; Siegmund et al. 2001; Pearson et al. 2004). The facet, or zygapophyseal, joint is a diarthrodial synovial joint that is formed by the contacting inferior and superior articular facets of adjacent vertebrae (Figure 1.1). The opposing surfaces of the boney facet joint are covered by articular cartilage; lubrication of the articular surfaces is maintained by the synovium connective tissue lining and the synovial fluid (Yoganandan et al. 2003;

Jaumard et al. 2011). Each facet joint is enclosed by a collagenous capsular ligament (Figure 1.1) (Vasseur et al. 1981; Ahmed et al. 1990; Yamashita et al. 1996). Overall, the cervical facet joints provide the articulation that supports the mobility and mechanical stability of the cervical spine (Figure 1.1b) (Jaumard et al. 2011).

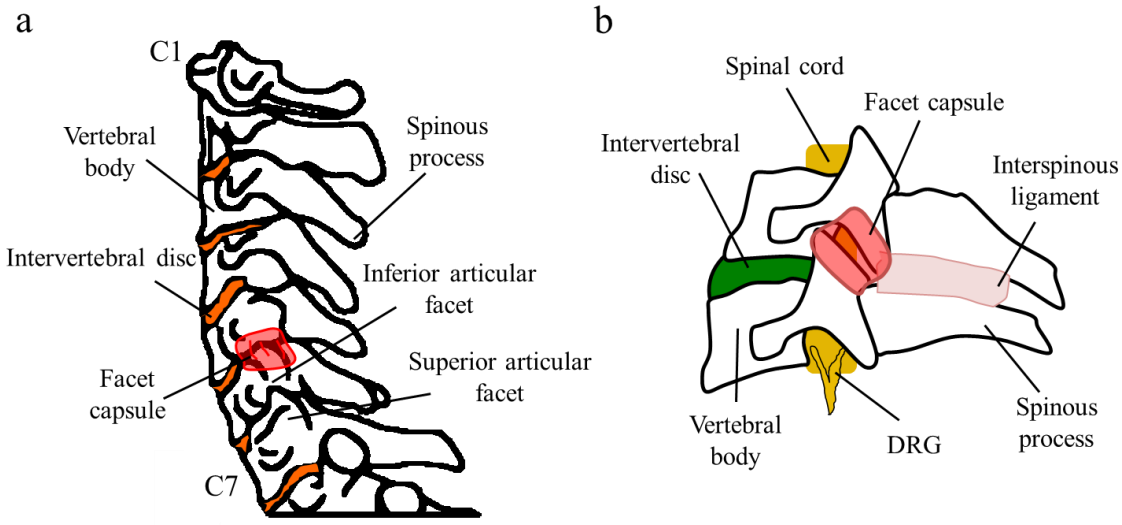


**Figure 1.1.** Lateral view of the human cervical spinal column and a representative motion segment. **(a)** The bilateral facet joints are formed by the contacting inferior and superior articular processes of adjacent vertebrae and located on the postero-lateral aspects of each motion segment. Each facet joint is enclosed by a ligamentous capsule (red). **(b)** A spinal motion segment showing anatomical structures, including the intervertebral disc (green), the spinal cord and DRG (yellow), interspinous ligament (pink) and the facet capsule (red).

### 1.2.2. Neural Innervation & Microstructure of Facet Capsular Ligament

The spinal facet joints are innervated by the medial branches of the dorsal rami (Bogduk 1982; Bogduk et al. 1982; Chua and Bogduk 1995). As such, a medial branch block, which is a local anesthetization of the medial branch, has been established as diagnostic test for facet-mediated neck pain (van Eerd et al. 2010; Bogduk 2011). On a local level, the human cervical facet capsule is innervated by both encapsulated

mechanoreceptors and free-ending nociceptors (McLain 1994; Kallakuri et al. 2012). Nociceptors innervating the cervical facet joint are found in sub-synovial, loose areolar, and dense capsular tissues (McLain 1994). The presence of mechanoreceptors and nociceptors in the normal cervical facet capsule confirm that the facet joint serves as a sensory organ and has the potential for any damage to its capsule to be monitored by the central nervous system.

Nociceptors that innervate the facet capsule include medium-diameter (21-40μm) myelinated Aδ fibers and small-diameter (4-21μm) unmyelinated C fibers (Cavanaugh et al. 2006; Chen et al. 2006; Kallakuri et al. 2012; Kras et al. 2013b). C fiber nociceptors can be further classified as *nonpeptidergic* and *peptidergic*, both of which have been shown to contribute to facet joint pain from its mechanical injury (Kras et al. 2015b; Weisshaar et al. 2017). Nonpeptidergic C fibers express the c-Ret neurotrophin receptor that responds to glial-derived neurotrophic factor, neurturin and artemin; a majority of the c-Ret-positive neurons also bind the isolectin IB4 (Zylka 2005; Basbaum et al. 2009). In contrast, peptidergic C fibers express the TrkA receptor, which is targeted by nerve growth factor, and produce the neuropeptides substance P and calcitonin-gene related peptide (CGRP) (Braz et al. 2005; Basbaum et al. 2009). CGRP-positive and substance P-reactive and nerve fibers are found in the human cervical facet capsule (Jaumard et al. 2011; Kallakuri et al. 2012). The expression of those neuropeptides is increased in the DRG and/or the spinal cord following facet joint distraction that induces sustained pain in the rat (Lee and Winkelstein 2009; Kras et al. 2013b), suggesting that the production and

release of substance P and CGRP from primary afferents plays a role in transmitting pain signals from the facet joint.

The facet capsular ligament is a fibrous tissue that primarily consists of dense collagen fibers linked by proteoglycans, with elastin fibers interspersed (Yamashita et al. 1996; Kallakuri et al. 2012). The structural heterogeneity of this ligament has been shown by scanning electron microscopy images and histological evidence at the nano- and micro-scale (Sato et al. 2002; Kallakuri et al. 2012; Zarei et al. 2017). Further, histological studies demonstrate that nociceptors innervate the facet capsule both in regions sustaining parallel collagen bundles and in areas of irregular connective tissues (Kallakuri et al. 2012). The microstructural variation and the innervation pattern of the facet capsular ligaments suggest that afferents in different sub-regions of the capsule may experience varied mechanical loading during stretch of the facet capsular ligament.

The architecture of collagen in the facet capsular ligament is highly non-uniform across the entire tissue domain, especially in the cervical spinal region. The spatial variation in the cervical and lumbar facet capsule has been characterized by prior studies using quantitative polarized light imaging (QPLI) and polarization-sensitive optical coherence tomography (Quinn and Winkelstein 2008; Ban et al. 2017; Zarei et al. 2017). QPLI, which utilizes the linear birefringence of collagen fibers, is a useful tool to assess the collagen organization in the human cervical facet capsule. A QPLI system has been previously developed in our lab, adapted from the design by Glazer et al. (1996) and Tower et al. (2002). Briefly, light from a fiber-optic illuminator is polarized by a rotating polarizer, travels through the ligament and is received by a circular analyzer mounted on

a high-speed camera (Figure 1.2a) (Quinn and Winkelstein 2008; Quinn 2010). Fiber alignment maps generated by harmonic analysis of the QPLI images reveal non-uniform collagen orientation in the cervical facet capsule, evidenced by the form of curvy patterns formed by collections of collagen fibers or fiber bundles (Figure 1.2b) (Ban et al. 2017). In addition to intra-sample variation, a high degree of inter-sample heterogeneity also exists in human cervical facet capsules, as observed in the diverse collagen organization pattern across all samples examined in a previous study (Figure 1.2c) (Ban et al. 2017).

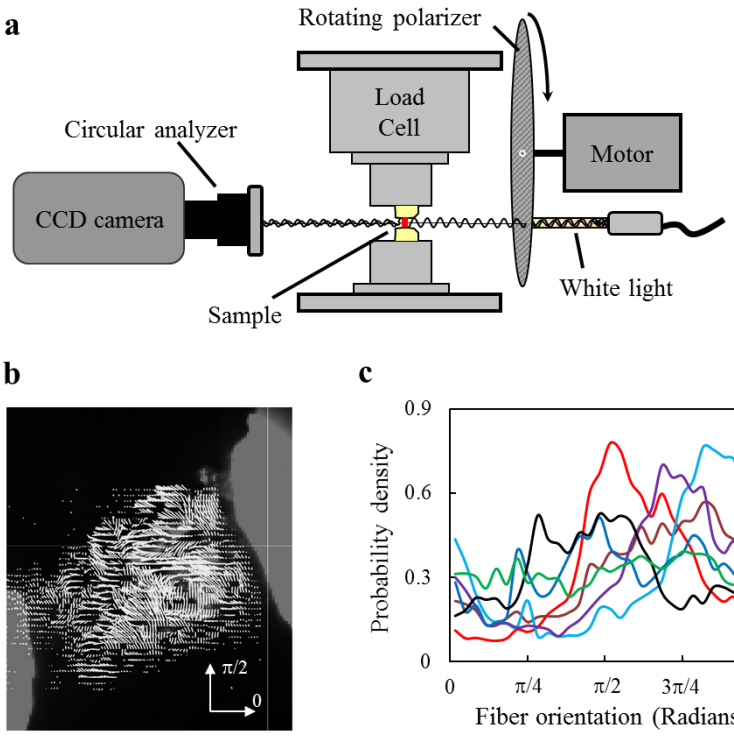


**Figure 1.2.** QPLI system and its application for studying collagen organization in the human facet capsular ligament. **(a)** Schematic of the QPLI system (adapted from Quinn, 2010). White light passes through a rotating polarizer, the birefringent ligament sample, and a circular analyzer mounted on a high speed camera. **(b)** A representative fiber alignment map is overlaid on a corresponding C4/C5 facet capsule sample. **(c)** Fiber orientation distribution from C4/C5 facet capsule samples showing both intra- and inter-sample heterogeneity in collagen structure (adapted from Ban et al. 2017).

### 1.2.3. Ligaments as Sensory Organs

In addition to the facet capsular ligament, many other ligaments contain neural elements and serve as sensory organs for proprioception and nociception. For example, the superior glenohumeral ligament in the shoulder joint, the knee joint capsule, palmar wrist ligaments, elbow ligaments and cruciate ligaments are all innervated by encapsulated mechanoreceptors and free-ending nociceptors (Schultz et al. 1984; Halata et al. 1985; Petrie et al. 1997; Petrie et al. 1998; Guanche et al. 1999). Similar to the facet capsular ligament, those ligamentous tissues are also under the surveillance of the central nervous system for normal and aberrant deformations. The presence of sensory nerve endings in those peripheral tissues suggests that the mechanical functions of the facet capsule and other ligaments could affect, and be mediated by, neuronal signals. Ligaments have been identified as sources of neuromusculoskeletal disorders, like pain, that often result from exposure to traumatic or repetitive loading (Solomonow 2004).

The stretch-sensitive neurons in ligamentous capsules encode the mechanical states of the joints. For instance, neuronal reactivity has been shown to be highly correlated with capsule stress in the knee joint (Khalsa et al. 1996), and afferent activation in the cervical facet capsule depends on the magnitude of capsule strain (Lu et al. 2005a; Chen et al. 2006). Given the similarities in innervation and loading-dependent sensory responses in the facet capsule and other ligaments, understanding the relationships between tissue mechanics and neurological properties of the facet capsular ligament could have a broader impact on defining the mechanical and nociceptive functions of other innervated joint capsules and ligaments.

### 1.2.4. General Neuroanatomy & Mechanisms of Pain

Mechanical stimuli are sensed and translated into electrical and biochemical signals by mechanosensitive neurons. Sensory information is transmitted from the peripheral nervous system to the central nervous system via primary afferents. Primary afferents project axons distally to innervate peripheral targets and centrally to the spinal cord (O'Brien et al. 1989; Steeds 2009; Dubin and Patapoutian 2010). Their cell bodies are contained in the DRG (Figure 1.3); afferent axons extending from the DRG to the spinal cord form the dorsal nerve root and synapse with neurons in the spinal dorsal horn (Figure 1.3) (Markenson 1996).

The spinal cord is organized into laminae consisting of ten layers of grey matter (I-X) (Rexed 1952; Molander et al. 1989). Laminae in the spinal dorsal horn contain second-order neurons that receive input from specific populations of primary afferents (Todd 2010). C and Aδ nociceptors synapse mostly with projection neurons and interneurons in the superficial dorsal horn (laminae I-II), with some Aδ fibers connecting more deeply in lamina V (Basbaum et al. 2009; Todd 2010) (Figure 1.3). In contrast, the myelinated Aβ fibers, which are tactile and hair afferents carrying innocuous inputs, terminate mainly in the deep laminae (III-V), with some extension into the ventral half of the inner lamina II (Figure 1.3) (Basbaum et al. 2009; Todd 2010).

There are three main classes of neurons in the spinal cord that receive input from the primary afferents. Second-order neurons are classified as nociceptive specific (NS), low-threshold mechanoreceptive (LTM), or wide dynamic range (WDR), based on their evoked responses to stimulations (Saito et al. 2008; Quinn et al. 2010b). NS neurons in

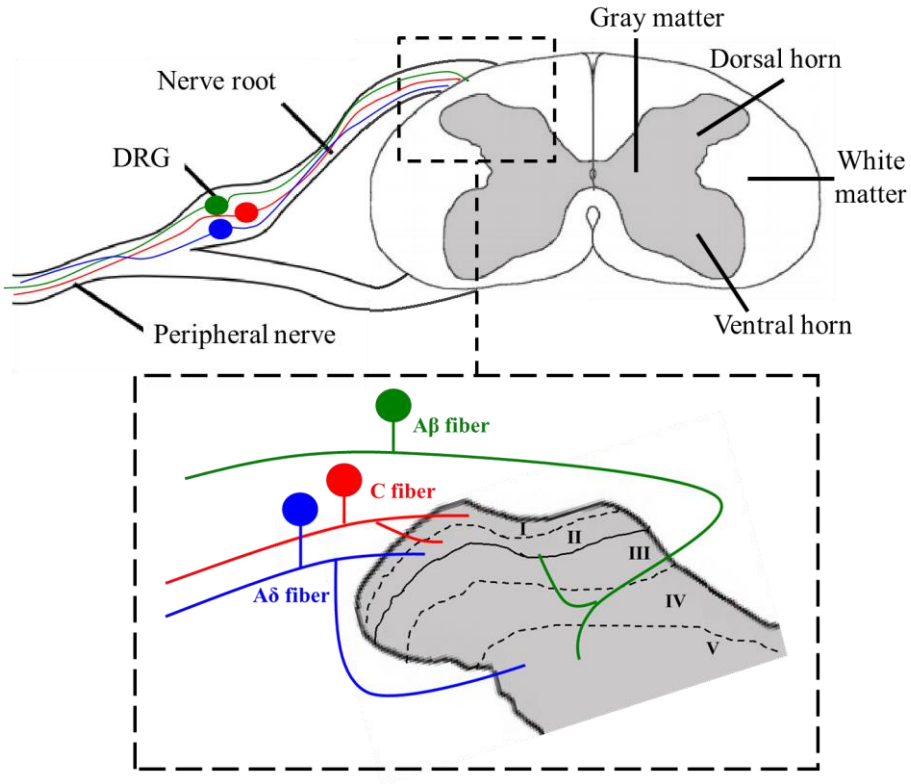


**Figure 1.3.** Neuroanatomy of the dorsal root ganglion (DRG) and the spinal cord. Primary afferents, with their cell bodies in the DRG, transmit sensory information from the periphery to the spinal cord. Afferents terminate in different spinal dorsal horn laminae. The superficial laminae (I-II) receive input mainly from nociceptive C and Aδ fibers; most of the tactile sensory Aβ fibers and some of the Aδ nociceptors synapse in the deep laminae (III-V).

the superficial laminae synapse with C and Aδ nociceptors and are only activated by noxious stimuli (Woolf and Fitzgerald 1983; Saito et al. 2008; Steeds 2009). The deep laminae contain both LTM neurons that respond maximally to light innocuous stimuli and WDR neurons that exhibit a graded response to innocuous and noxious stimuli (Saito et al. 2008; Steeds 2009). Both LTM and WDR neurons receive input from Aδ nociceptors and Aβ light-touch receptors (Woolf and Fitzgerald 1983; Saito et al. 2008; Steeds 2009; Basbaum et al. 2009).

From the spinal dorsal horn, sensory information is conveyed by spinal projection neurons along ascending pathways to higher order structures in the brain (Julius and Basbaum 2001; Steeds 2009). A large number of projection neurons reside in lamina I; a majority of them express the neurokinin 1 (NK1) receptor for substance P that is released by peptidergic C nociceptors (Todd 2002; D'Mello and Dickenson 2008). Those NK1-positive projection neurons transmit nociceptive signals to several brain regions including the parabrachial area and periaqueductal grey (Todd 2002). In addition, they innervate the brainstem and activate descending pathways that modulate spinal processing (Mantyh et al. 1997; Suzuki et al. 2002; D'Mello and Dickenson 2008). Projection neurons in the deep laminae project predominantly to the thalamus, a brain area that relays pain signals to the cerebral cortex for further processing and sensation (D'Mello and Dickenson 2008; Steeds 2009; Yen and Lu 2013).

The generation of pain normally serves as a protective mechanism that signals to the brain of existing or potential tissue injury (Woolf and Salter 2000a; Steeds 2009). Nociception can provide feedback to promote tissue adaptation and/or repair (Woolf and Salter 2000a; Steeds 2009). However, potentiation of nociceptive processing can develop into a chronic neurological disorder, deviating from the protective properties of pain (Dubner and Ruda 1992; Coderre et al. 1993). Aberrant activation of nociceptors can result in sensitization that involves pathologic neuronal responses in the central nervous system, leading to pain (Lee et al. 2004b; Latremoliere and Woolf 2009; Dubin and Patapoutian 2010; Gold and Gebhart 2010; Zhang et al. 2013). Noxious stimuli commonly induce decreased response thresholds to thermal and mechanical stimuli in the

regions that are supplied by the affected nerves; those regions are referred to as *dermatomes*. For instance, the C6 and C7 dermatomes include several anatomical regions that are innervated by the C6 and C7 spinal nerves, like the arms, shoulders, and bilateral C6/C7 facet joints (Dwyer et al. 1990; Hauser et al. 2015). Because of this widespread innervation pattern and the fact that the C6/C7 facet joints are commonly involved in neck trauma from whiplash (Panjabi et al. 1998b; Pearson et al. 2004), whiplash patients routinely report pain and sensitivity in the upper arm and shoulder area (Dwyer et al. 1990; Barnsley et al. 1994; Kasch et al. 2001).

Nociceptors can be activated at their peripheral terminals by external stimuli, such as heat and mechanical loading (Khalsa et al. 1997; Julius and Basbaum 2001; Chen et al. 2006). Noxious stimuli alter the electrophysiological properties of the afferents, which includes lowering their thresholds for firing, increasing their firing rates, and inducing their persistent activation (Cavanaugh et al. 2006; Costigan et al. 2009; Nicholson et al. 2011). In addition, tissue damage can up-regulate the release of inflammatory mediators from the nociceptor, as well as the expression of receptors to inflammatory molecules, like cytokines and neurotrophins (Basbaum et al. 2009; Kras et al. 2013a; Kras et al. 2013c; Kras et al. 2015a). Nociceptive signals are transmitted to the spinal cord via the release of neurotransmitters, such as glutamate and the neuropeptides substance P and CGRP, from the primary afferents (Julius and Basbaum 2001; Basbaum et al. 2009). Together, these nociceptor responses can lead to increased excitability of spinal neurons and their transmission of nociceptive information to the brain (Julius and Basbaum 2001; Costigan et al. 2009; Latremoliere and Woolf 2009). Numerous other complex cellular

mechanisms, such as neuron-glia interactions and glutamatergic neurotransmission, are involved in the generation of a prolonged hyperexcitability state in the central nervous system, a state referred to as *central sensitization* (Basbaum et al. 2009). Central sensitization manifests as mechanical hyperalgesia and is associated with the development of chronic pain.

### 1.2.5. Biomechanics of Facet Capsular Ligament Injury & Facet Pain

Whiplash is a soft-tissue injury in the neck that commonly occurs during rear-impact automobile collisions. Mechanical loading to the facet capsule and other ligaments of the cervical spine during neck trauma has been shown to contribute to the pathomechanisms of the complex symptoms as a result of spinal trauma, including neck pain (Panjabi et al. 1998b; Bogduk and Yoganandan 2001; Siegmund et al. 2001; Cavanaugh et al. 2006; Winkelstein 2011; Ita et al. 2017b). Previous biomechanical and imaging studies using human cadaveric spine specimens demonstrate a bi-phasic response of the cervical spine during whiplash-like loading, which involves an initial sigmoid deformation and a second phase of full extension of the cervical spine (Figure 1.4a) (Panjabi et al. 1998a; Bogduk and Yoganandan 2001; Pearson et al. 2004). In the first phase of that response, between 50ms and 75ms after the rear-end impact, the lower cervical motion segments undergo hyper-extension and the upper levels flex, forming an S-shaped curvature (Panjabi et al. 1998b; Eck et al. 2001) (Figure 1.4). In the second phase, every level in the cervical spine is extended to form a C-shaped curve and the head

reaches its maximum extension at around 100ms (Panjabi et al. 1998b; Bogduk and Yoganandan 2001) (Figure 1.4).

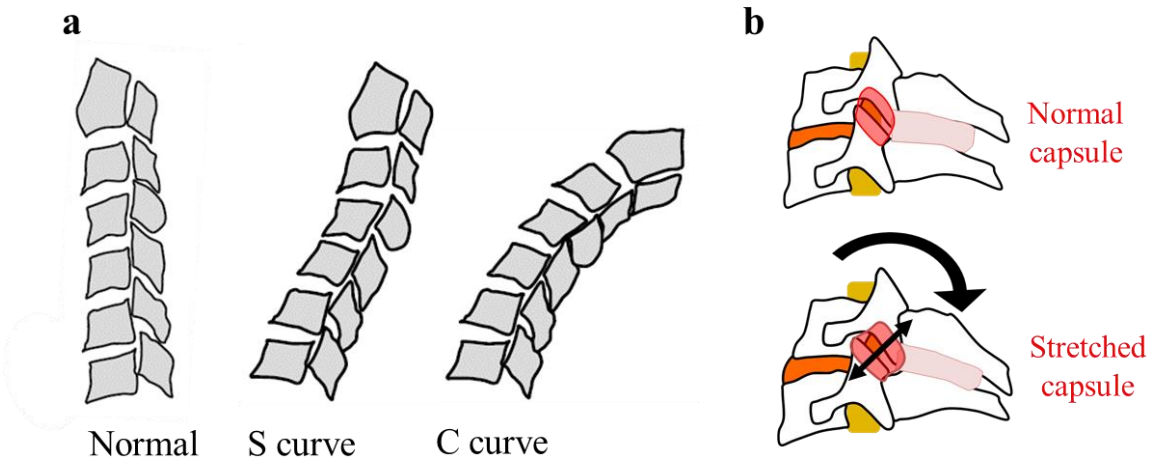


**Figure 1.4.** Cervical spine mechanics during whiplash. **(a)** Abnormal deformation of the cervical spine occurs, forming an early S-shaped curvature and a later C-shaped curvature. **(b)** Corresponding local facet joint kinematics extend the joint and stretch the capsular ligament.

Altered facet joint kinematics have been reported during whiplash simulations. During biomechanical testing of the cadaveric spinal motion segments that simulates whiplash neck trauma, the facet capsular ligament stretches beyond its maximum physiologic range as determined by a standard intact flexibility test (Figure 1.4b) (Panjabi et al. 1998a; Winkelstein et al. 2000). Dynamic flexion/extension of the facet joint that occurs during frontal and rear-end automobile collisions induces the same intervertebral rotations as during slower loading, but can produce significantly higher maximum principal and shear strains in the facet capsule (Winkelstein et al. 1999; Holsgrove et al. 2016). Both high-speed dynamic and quasi-static capsule stretch to similar supraphysiologic capsular strains induce persistent pain in the rat (Lee et al. 2004b;

Quinn et al. 2010b; Dong et al. 2012; Crosby and Winkelstein 2016). The C6/C7 facet capsule undergoes the largest dynamic elongation during hyper-extension of the lower cervical spine in the initial S-shaped phase, reaching a maximum of ~40% strain during an 8g simulation, which is considerably higher than its physiologic strain of ~6% (Panjabi et al. 1998a; Panjabi et al. 1998b; Pearson et al. 2004). The displacement of the upper inferior facet towards the lower superior facet surface during simulated whiplash leads to compression across the joint and is the greatest at C4/C5 (Pearson et al. 2004). Collectively, these biomechanical findings point to the lower cervical spine as prone to hyper-extension in whiplash, with facet joints from C4 to C7 being particularly vulnerable during neck trauma.

Tensile loading of isolated human C4/C5 facet bone-capsule-bone specimens to strains that induce pain in the rodent (Lee and Winkelstein 2009; Quinn et al. 2010b; Dong et al. 2012) does *not* produce any macroscopic tissue failure (Quinn and Winkelstein 2008; Quinn and Winkelstein 2009; Quinn 2010). This lack of visible ligament rupture is consistent with clinical studies using magnetic resonance imaging that show no lesion in the capsule for most whiplash patients with neck pain (Pettersson et al. 1997; Voyvodic et al. 1997; Winkelstein 2011). Using histology and QPLI, microstructural tissue damage, including collagen disorganization in the fibrous ECM, have been observed in the facet capsule due to subfailure ligament loading. Histological evidence shows that subfailure distraction (7.30±3.01% strain) of the rat cervical facet capsule that induces pain in vivo also produces significant angular deviation of collagen fibers relative to unloaded naïve samples (Quinn et al. 2007). Further, a vector correlation

technique analyzing QPLI data detected anomalies in collagen fiber realignment to occur at 74±26% strain during tensile loading of isolated human cervical facet capsules (Quinn and Winkelstein 2009). These microstructural abnormalities indicated by anomalous collagen reorganization have been reported to associate with ligament yield (Quinn and Winkelstein 2008; Quinn and Winkelstein 2009), indicating a role of local collagen organization in modulating tissue-level forces. In addition, most abnormal fiber realignment develops prior to, and in the region of, the eventual production of visible rupture (at a strain of 102±35% strain) (Quinn and Winkelstein 2009). Together, this prior evidence suggests that micro-scale matrix failure likely occurs well before macroscopic ligament tearing and likely contributes to the loss of mechanical strength of the facet capsule, as well as pain. As such, understanding the microstructural abnormalities that develop before visible rupture in the capsular ligament could provide more relevant mechanical thresholds for pain generation from facet joint trauma.

Stretch of the cervical facet capsular ligament beyond its physiologic range can lead to a host of neuronal responses, such as persistent firing, altered expression of nociceptive molecules and glial activation in the spinal cord, all of which relate to pain (Figure 1.5) (Lu et al. 2005a; Lee and Winkelstein 2009; Dong et al. 2013a; Crosby et al. 2014; Ita et al. 2017b; Sperry et al. 2017). Low-threshold and high-threshold mechanoreceptors in the goat C5/C6 facet capsule are activated at subfailure strains of 10-15% and 25-47%, respectively; strains greater than 38±12%, activate high-threshold receptors and induce persistent afterdischarge of low-threshold receptors (Lu et al. 2005a; Chen et al. 2006). These findings not only highlight a need to more fully understand the

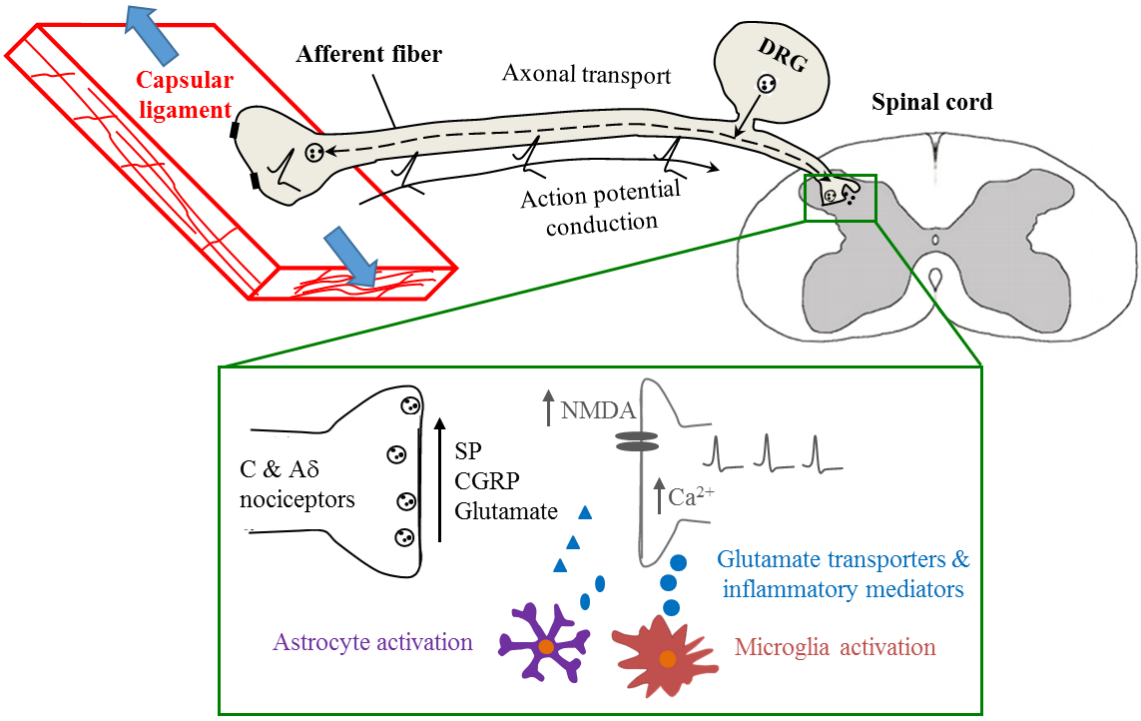


**Figure 1.5.** Schematic illustrating neuronal connections between the facet capsular ligament and the spinal cord and relevant central sensitization mechanisms. Excessive stretch of the facet capsule can induce persistent afferent firing and neurotransmitter release from afferents. Activated C and Aδ nociceptors release different neurotransmitters, including substance P (SP), CGRP and glutamate. Those neurotransmitters can activate the NMDA glutamate receptors on postsynaptic neurons residing in the superficial dorsal horn of the spinal cord. Activated NMDA receptors can increase spinal neuronal excitability via calcium-dependent signaling pathways. Spinal astrocytes and microglia are also activated, which can contribute to nociception by regulating the release of glutamate transports and inflammatory mediators.

complicated subfailure loading regime, but also suggest the importance of joint afferents in *regulating* the production of pain. The functional role of early afferent activity in pain was also supported by the fact that facet pain is prevented after blocking the C6/C7 joint afferent in the rat using intra-articular injection of the anesthetic bupivacaine at the time of facet capsule stretch (Crosby et al. 2014). Further, selective ablation of peptidergic joint afferents before capsule stretch also prevents pain (Kras et al. 2015b). Of note,

unlike subfailure joint distraction (~10-30% strain) that induces persistent pain (Lee et al. 2008; Lee and Winkelstein 2009; Dong et al. 2012), stretching the facet capsule to its failure (41±20% strain) produces transient pain that lasts for only three days (Lee et al. 2008), which may be due to interrupted afferent signaling, since strains at the level for a capsule failure can cause axonal swelling in the capsular ligament (Kallakuri et al. 2008).

Mechanical activation of afferents in the subfailure loading regime can lead to a range of neuronal responses in the DRG and spinal dorsal horn after a facet joint distraction that causes pain (Figure 1.5). For example, increased substance P expression in the DRG and modifications in glutamatergic transmission as evidenced by up-regulation of metabotropic glutamate receptor-5 (mGluR5) in nociceptors, parallel sustained pain after supraphysiologic facet joint distraction in rat (Lee and Winkelstein 2009; Dong et al. 2012). Painful capsular stretch also increases the expression of a marker of the endoplasmic reticulum stress response and up-regulates the activating transcription factor-4 in the DRG (Dong et al. 2008; Dong et al. 2011). Those integrated stress responses in DRG neurons may be associated with neuronal injury and/or neuroinflammation induced by facet joint injury (Dong et al. 2008; Lee et al. 2008; Dong et al. 2011; Kras et al. 2013a; Kras et al. 2015a) and mediate facet pain by altering the ability of primary afferents to sensitize neurons in the spinal cord.

Nociceptive signals from afferents also modulate cellular responses in the spinal dorsal horn, leading to central sensitization after painful facet joint distraction (Figure 1.5). Hyperexcitability of dorsal horn neurons, a hallmark of central sensitization, develops between six hours and one day after capsule stretch and is still evident at seven

days in the rat, paralleling the presence of sustained behavioral hypersensitivity (Quinn et al. 2010b; Crosby et al. 2013; Dong et al. 2013a). The persistently increased spinal neuronal excitability and phosphorylation of extracellular signal-regulated kinases (ERK) is accompanied by up-regulation of substance P and altered glutamatergic neurotransmission in the spinal cord (Lee and Winkelstein 2009; Dong et al. 2012; Kras et al. 2013c; Crosby et al. 2014). Changes in the glutamatergic system include increased neuronal expression of mGluR5, dysregulated glutamate transporters and increased phosphorylation of the glutamate receptor NMDA subunit NR1 in the spinal cord (Dong et al. 2012; Crosby et al. 2014). Activated NMDA receptors on postsynaptic neurons can increase neuronal excitability via calcium-dependent signaling cascades (Basbaum et al. 2009). Painful facet capsule stretch also initiates widespread inflammation (Dong et al. 2013b; Kras et al. 2013c; Kras et al. 2014; Kras et al. 2015a). Recruitment and activation of astrocytes and microglia in the spinal cord following capsular ligament stretch (Dong et al. 2013b; Dong et al. 2013a; Weisshaar and Winkelstein 2014; Crosby et al. 2014) may sensitize nociceptors via the release of inflammatory mediators (Woolf and Salter 2000b; Lee et al. 2008; Kras et al. 2014) leading to aberrant neuronal activity and pain development and maintenance.

Anti-hyperalgesic drugs that attenuate neuronal excitability in the spinal cord and anti-inflammatory drugs that suppress broad inflammation have been shown in recent pre-clinical studies to effectively reduce facet-mediated pain (Dong et al. 2011; Dong et al. 2013b; Dong et al. 2013a). Gabapentin, which is primarily used to treat seizures and neuropathic pain, decreases the frequency of evoked firing of spinal neurons and

attenuates mechanical hyperalgesia when given intrathecally prior to and one day after painful facet joint distraction in the rat (Dong et al. 2013a). Intra-articular injection of a general nonsteroidal anti-inflammatory drug (NSAID), ketorolac, effectively reduces spinal astrocytic activation and alleviates facet-mediated pain (Dong et al. 2011; Dong et al. 2013b). However intrathecal injection is highly invasive and ketorolac is a non-selective NSAID with increased risk of side effects.

Similarly, even radiofrequency neurotomy, the most effective and commonly used clinical treatment for facet pain to date, is invasive and only *temporarily* relieves chronic neck pain in about 70% of the patients (Bogduk 2011; MacVicar et al. 2012). Minimally invasive facet restoration implants have been developed for treating chronic lumbar facet pain (Meisel et al. 2014). Although those implants have been suggested by a clinical study as a promising treatment option, they restore only the mechanical function of the facet joint and reduced back pain only by 41% (Meisel et al. 2014). Since afferent activity at the facet joint within four to eight hours after capsule stretch is required for pain onset (Crosby et al. 2014), therapeutic strategies for facet pain may be improved by information regarding the local afferent signaling cascades that occur during and after injurious facet capsule stretch. Accordingly, continued work is needed in order to discover new drug targets and develop safe and specific pharmacological interventions for facet joint pain.

### 1.2.6. Cell-ECM Interactions & Mechanotransduction

Adhesive cell-ECM interactions have been previously indicated to mediate

mechanoreceptor activation and neuronal injury in response to tissue stretch (Khalsa et al. 2004; Cullen et al. 2007a; Hemphill et al. 2011). Cell adhesion to the ECM is primarily mediated by transmembrane receptors, such as integrins. Integrins are expressed on many types of cells, including primary afferent neurons (Tomaselli et al. 1993; Hynes 2002). Integrin-dependent cell-ECM interactions can trigger the formation of focal adhesions (FAs), which involves the clustering of an array of intracellular components at the sites of integrin binding (Figure 1.6) (Moore et al. 2010; Schwartz 2010; Ross et al. 2013). The FA complex can transmit force from the ECM to the cytoskeleton via interactions with the activated integrin and other intracellular components. Focal adhesion kinase (FAK), as a part of the FA complex, plays a critical role in integrin-mediated signal transduction (Guan 1997; Humphrey et al. 2014). During cell-ECM adhesion, FAK interacts with the cytoplasmic domain of the integrin β subunits and associates with other cytoskeletal proteins, such as talin and Src (Guan 1997; Seong et al. 2011). Aggregation of FAK at the focal contacts leads to activation and autophosphorylation of FAK (Guan 1997), which can regulate a variety of biological processes, including inflammation and neuronal plasticity (Stevens et al. 1996; Lian et al. 2015).

Cell-ECM interactions not only facilitate morphogenesis and migration in developing neurons (Barros et al. 2011; Myers et al. 2011), but also mediate neuronal responses to loading of the surrounding fibrous matrix (Khalsa et al. 2004; Hemphill et al. 2011). In fact, the generation of stretch-induced action potentials in DRG neurons depends on the pattern of axonal outgrowth that is regulated by the local ECM (Lin et al. 2009). Besides the ECM-controlled cell architecture, specific integrin populations can

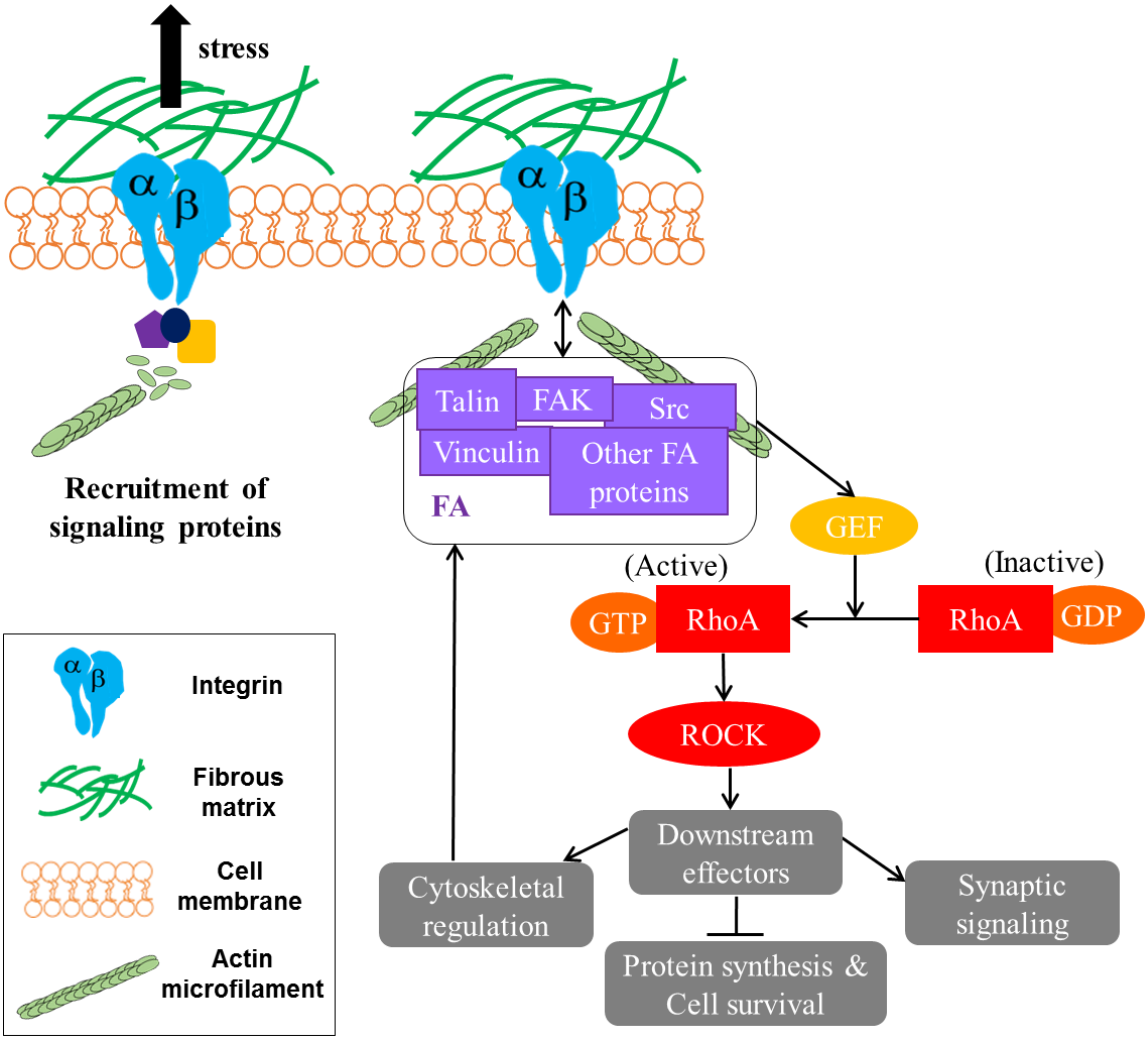


**Figure 1.6.** Schematic of a simplified version of the integrin-mediated RhoA signaling cascades in mechanotransduction. Stress applied to the fibrous extracellular matrix can activate integrins, leading to the assembly of the focal adhesion (FA) complex. FA-mediated regulation of the guanine nucleotide exchange factors (GEF) facilitates the conversion from inactive GDP-bound RhoA to active GTP-bound RhoA. Active RhoA activates the major downstream effector, ROCK, which modulates a variety of cellular functions, like cytoskeletal regulation, neuronal survival and synaptic strength.

also modulate the mechanosensitive responses of sensory neuron terminals. For example, firing of cutaneous mechanoreceptors in response to skin stretch relies on the activation of the α2β1 integrin (Khalsa et al. 2000; Khalsa et al. 2004). Furthermore, integrin-

dependent cell signaling mediates morphological changes of cortical neurons after high-speed stretch of their underlying substrate (Hemphill et al. 2011). The degree of morphological abnormalities in axons depends on the density of FAs (Hemphill et al. 2011), suggesting the involvement of cell adhesion sites in transmitting ECM loading to neurons. The assembly of FAs following external ECM loading is highly regulated and can activate many intracellular signaling cascades, such as pathways that are mediated by the Ras homolog gene family, member A (RhoA) (Bershadsky et al. 2003; Schwartz 2004; Hoffman et al. 2011) (Figure 1.6).

Mechanical stress transmitted through adhesion receptors can convert inactive RhoA (GDP-bound state) to active RhoA (GTP-bound state) via regulation of the guanine nucleotide exchange factors (GEFs) (Figure 1.6) (Schwartz 2004; Marjoram et al. 2014). The Rho-associated protein kinase ROCK is the major downstream effector of RhoA that plays a key role in cytoskeletal regulation (Schwartz 2004; Mueller et al. 2005). The Rho/ROCK-mediated formation of actin stress fibers, in turn, regulates the growth and disassembly of the FAs (Schwartz 2004; Boccafoschi et al. 2010; Oakes and Gardel 2014), suggesting a feedback-controlled mechanosensing mechanism. The RhoA/ROCK pathway not only is involved in mechanotransduction (Guilluy et al. 2011; Lessey et al. 2012; Marjoram et al. 2014), but also modulates specific neuronal responses, including stretch-induced neuronal injury, neuronal survival, axon regeneration, synaptic plasticity and nociceptive transmission (Figure 1.6) (Inoue et al. 2004; Wang et al. 2005; McMullan et al. 2006; Hiraga et al. 2006; Hirata et al. 2008; Ohsawa and Kamei 2010; Hemphill et al. 2011; Tönges et al. 2011).

Both of the integrin and the RhoA/ROCK pathways have been implicated in mediating inflammatory and neuropathic pain (Dina et al. 2004; Tatsumi et al. 2005; Paiva-Lima et al. 2014; Ferrari and Levine 2015). Their involvement in pain may be due to interactions with the cytoskeleton and second messenger cascades, such as ERK-mediated pathways in afferents, which play crucial roles in neuroplasticity and the development of hyperalgesia (Lei et al. 2001; Bhave and Gereau 2003; Dina et al. 2005; Gao and Ji 2009). Although prior evidence supports the involvement of integrin-dependent cell-ECM adhesion and the RhoA signaling in modulating force transmission and nociception in neurons (Khalsa et al. 2004; Dina et al. 2004; Tatsumi et al. 2005; Hemphill et al. 2011), their contributions to mechanically-induced musculoskeletal pain are not understood. Mechanistic studies investigating whether disrupting the neuron-ECM interaction or relevant mechanosensitive intracellular pathways could have effects on nociception following mechanical injury of the innervated facet capsular ligament would be beneficial.

# Chapter 2

# Rationale, Hypotheses & Aims

## 2.1. Rationale & Context

Neck pain is a significant healthcare problem with high prevalence and substantial economic cost (Hoy et al. 2010). It affects nearly two-thirds of the general population (Côté et al. 1998; Côté et al. 2000), with approximately one-half of the chronic neck pain cases resulting from trauma (Ono and Kanno 1996; Côté et al. 2004; Strine and Hootman 2007). The cervical facet joint is the source of pain in over 50% of the reported neck pain cases (van Eerd et al. 2010), and is vulnerable to injury from neck trauma due to the mechanical weakness of its capsular ligament and its neural innervation (Siegmund et al. 2001; Cavanaugh et al. 2006a; Bogduk 2011; Jaumard et al. 2011; Winkelstein 2011). The facet capsular ligament that encloses the facet joint can undergo stretch exceeding its physiologic range during trauma and whiplash-like loading (Panjabi et al. 1998a; Pearson et al. 2004). Since the facet capsular ligament is innervated by pain fibers (Chen et al. 2006; Kallakuri et al. 2008; Kallakuri et al. 2012), its excessive stretch can activate nociceptors, leading to pain (Lee et al. 2004b; Lu et al. 2005a; Dong et al. 2012; Crosby et al. 2014). Although previous clinical, biomechanical and animal studies have identified the facet capsular ligament as a common source of mechanically-induced neck pain (Panjabi et al. 1998b; Kwan and Fiel 2002; Manchikanti et al. 2004; Cavanaugh et al.

2006; Lee et al. 2008; Quinn et al. 2010b; Bogduk 2011; Winkelstein 2011), no study has defined the complex relationships between ligament loading, ECM abnormalities and nociceptor activation in the facet capsular ligament. As a result, the local mechanical stimuli to joint afferents during traumatic ligament loading and the neural mechanisms of mechanically-induced facet joint pain remain not fully understood.

Moreover, current treatment strategies for facet joint pain, including oral pain medications, nerve blocks and radiofrequency ablation, all have relatively low specificity and achieve only temporary pain relief (Lord et al. 1996; Kwan and Fiel 2002; Manchikanti et al. 2008). The inability of current approaches for long-term facet pain relief is likely associated with the lack of mechanistic understanding of the heterogeneous pain conditions that develop after neck trauma. It is not well-understood why some patients experience neck pain that lasts for only a few days or weeks after a rear-end vehicle collision, but facet-mediated pain in approximately one-half of the whiplash patients persists for at least six months, becoming chronic (Bogduk and Yoganandan 2001; Kwan and Fiel 2002; Sterling et al. 2012). Understanding the biomechanical causes of the varied pain symptoms may improve existing facet pain therapies and may inform the discovery of new therapeutic targets. However, defining the mechanical and nociceptive mechanisms that underlie facet capsule injury and pain is confounded by the difficulties in visualizing a ligament lesion and the great heterogeneity of the facet capsule structure.

It is challenging to detect pain-related facet capsule damage partially because pain can accompany joint distraction that does not produce visible rupture of the capsular

ligament (Cavanaugh et al. 2006; Lee et al. 2008; Lee and Winkelstein 2009; Dong et al. 2012). Radiographic evidence suggests there is no lesion in the facet capsular ligament for most neck pain patients after whiplash injury (Pettersson et al. 1997; Voyvodic et al. 1997). In fact, facet joint distraction that produces capsule failure induces *only* transient behavioral hypersensitivity (Lee et al. 2008), likely due to the disruption of axonal transport and nociceptive transmission in the ligament afferents, as suggested by swollen nerve endings in the ruptured capsules (Kallakuri et al. 2008). In contrast, subfailure capsule stretch that exceeds the deformations that occur during normal joint motions can activate nociceptors and lead to sustained mechanical hyperalgesia that last for weeks in animal models (Lu et al. 2005; Cavanaugh et al. 2006a; Lee et al. 2008; Ita et al. 2017a; Ita et al. 2017b). These previous findings in patients and animal models highlight a need to investigate possible microstructural abnormalities in the ligament ECM and their effects on neuronal activation within that tissue matrix in the subfailure loading regime of the facet capsular ligament.

Prior to gross tissue failure, microstructural tissue injury can develop in the cervical facet capsular ligament due to its stretch; local collagen disorganization has been detected by quantitative polarized light imaging (QPLI) (Quinn and Winkelstein 2008; Quinn and Winkelstein 2009). Since anomalous realignment of collagen fibers has been previously found to arise at capsular strains that induce pain in vivo (Quinn et al. 2007; Lee and Winkelstein 2009; Quinn et al. 2010a; Dong et al. 2012), microscopic collagen disorganization presents a possible local mechanism for deforming and activating the neurons embedded in the ligament. The development of anomalous fiber realignment

likely relates to the reconfiguration of the local collagen network and associates with other mechanical events, like elongation and failure of individual fibers and subsequent stress redistribution in the collagen networks. Deformation of, reorganization of, and elevated stresses in the collagen network and individual fibers may transmit tissue loads to the enclosed neurons, leading to their activation and transmission of pain signals.

Identifying injury-prone anatomical regions of the facet capsule where collagen disorganization and/or nociceptor activation may occur is confounded by the non-uniform structure of the facet capsular ligament itself. Human cervical facet capsular ligaments exhibit high inter-subject and intra-subject variability in their fibrous structure (Quinn and Winkelstein 2008; Ban et al. 2017). The heterogeneous collagen architecture in the facet capsule is associated with its non-uniform stress and strain fields even during simple uniaxial tension (Quinn and Winkelstein 2008; Quinn 2010). In addition, the lack of co-localization of peak stresses, peak strains and micro-scale collagen fiber disorganization has been observed previously during subfailure ligament stretch (Quinn and Winkelstein 2008; Quinn and Winkelstein 2009; Quinn 2010). Findings from those prior biomechanical studies highlight the need to understand the multi-scale mechanics of the facet capsular ligament and contributed efforts to identify appropriate mechanical metrics that may describe microstructural abnormalities in the ligament ECM.

Both the initial fibrous architecture and the mechanical restructuring of the ECM in the facet capsular ligament are spatially non-uniform (Yamashita et al. 1996; Quinn and Winkelstein 2008; Quinn and Winkelstein 2009; Kallakuri et al. 2012; Ban et al. 2017). Therefore, depending on their location in the ligament, nociceptive afferents may

receive mechanical inputs with varied magnitudes via cell-ECM interactions during ligament stretch. Since sensory neurons can interact with their surrounding tissue matrix through cell surface receptors (Tomaselli et al. 1993; Khalsa et al. 2000; Wallquist et al. 2004; Ribeiro et al. 2013), they can sense changes in their microenvironment and translate mechanical stimuli into intracellular signaling cascades, including those for pain transmission (Dina et al. 2004; Khalsa et al. 2004; Wallquist et al. 2004). Yet, the molecular pathways that play dual roles in neuronal mechanotransduction and processing of painful or noxious stimuli (nociception) have not been identified in the context of ligament loading or joint pain. Despite evidence that subfailure facet capsular ligament stretch activates nociceptors and induces pain (Lu et al. 2005a; Lee et al. 2008; Crosby et al. 2013), the local biomechanical mechanisms by which afferents in the capsule are sensitized and initiate pain transmission also are unknown. Therefore, the **overall goal** of this thesis was to define the multi-scale biomechanics of the cervical facet capsular ligament and to evaluate the influence of tissue-level mechanical properties and local ECM restructuring under different stretch modalities on neuronal activation and nociception in the facet capsular ligament, which exhibits spatially heterogeneous collagen organization and stress and strain profiles.

In this thesis, *facet joint injury* or *capsule injury* refers to the case in which the facet capsular ligament undergoes excessive or supraphysiologic stretch defined as abnormal capsule deformation exceeding its maximum physiologic strain in normal facet joint motions (Panjabi et al. 1998a; Pearson et al. 2004). The studies under all three aims of this thesis focus on ligament injury from its *subfailure* mechanical loading, meaning

that no visible tearing is observed in the tissue during stretch (Voyvodic et al. 1997; Lee et al. 2006; Quinn et al. 2007). Despite no visible tissue rupture, subfailure deformations of the facet capsular ligament could lead to *microstructural tissue damage*, which is defined in this thesis as abnormalities in the local ECM, such as collagen network disorganization and/or fiber failure (Quinn et al. 2007; Quinn and Winkelstein 2009; Hadi et al. 2012a; Lee and Winkelstein 2012; Voycheck et al. 2014). In addition, supraphysiologic subfailure strains of the cervical facet capsule can introduce noxious stimuli that activate the nociceptors embedded in the capsule (Lu et al. 2005a), leading to neuronal processing and transmission of pain signals, which encompasses *nociception*. Loading of the facet capsule in vivo that does not induce pain or behavioral hypersensitivity is referred to as a *non-painful* condition; whereas, those conditions that induce pain in vivo are produced by *painful* loading. Work presented in this thesis emphasizes the possible interplay between ECM damage and neuronal nociception in the painful subfailure loading regime of the cervical facet capsule.

The studies in Aim 1 of this thesis investigated if structural and mechanical changes are associated with local collagen disorganization before the development of gross tissue failure in the human facet capsular ligament. To date, understanding collagen reorganization during tissue stretch has been hampered by a lack of analytic methods to quantify fiber realignment patterns and to evaluate the existence of coordinated realignment of spatially-distributed fibers. Broadly, studies in Aim 1 utilize different analytical and computational approaches to investigate the stretch-induced changes of the fibrous structure in the human cervical facet capsule and the underlying mechanical basis

of ECM restructuring. Network analysis provides a representational framework to quantify the topological characteristics and dynamics of complex systems and has been used to reveal structural changes in physical materials (Zhu et al. 2007; Bassett et al. 2013a; Bassett et al. 2014). As such, network analysis was implemented to quantitatively describe collagen reorganization patterns in regions of the facet capsular ligament where anomalous fiber realignment occurred and in regions sustaining only normal fiber realignment (Aim 1a). The complex fibrous structure of the cervical facet capsule and limitations with existing imaging tools prohibit the visualization of deformations of local collagen networks or individual fibers in the ligament during its loading. Since it is difficult to measure the microstructural stresses and strains during ligament stretch, finite element-based multi-scale models that incorporate subject-specific collagen organization and ligament geometry were used to predict the mechanics of collagen networks and single fibers (Aim 1b). Possible associations between facet capsular collagen reorganization and multi-scale stresses and strains were assessed by correlation analysis to more fully define the structure-mechanical properties of the cervical facet capsule that may impact its sensory function (Aim 1). Collectively, the computational studies in Aim 1 characterize the local mechanical environment that may directly or indirectly affect the neurons within it during subfailure stretch of the facet capsule.

Although biomechanical tests of the isolated human facet joint or capsular ligament enable real-time assessment of collagen kinematics and provide structural data for computational analysis and modeling (Panjabi et al. 1998a; Pearson et al. 2004; Quinn and Winkelstein 2009; Quinn 2010; Claeson et al. 2015; Zarei et al. 2017), most studies

use cadaveric tissues that do not enable measuring neuronal responses. In order to define the neuronal responses to heterogeneous mechanical inputs due to the non-uniform ECM restructuring under different tissue stretch modalities, an in vitro neuron-collagen construct (NCC) gel system was developed (Aim 2a). That in vitro model both simulates the innervation of collagenous tissue and enables prescribing the collagen fiber orientation, controlling the mechanical stretch to simulate painful capsule strains in vivo, and integrating collagen imaging, mechanical measurements and cellular assessments. The NCC system was used to characterize if, and how, collagen organization and loading conditions modulate neuronal signaling, and to define the relationships between stretch-induced neuronal responses and NCC mechanics, including strains, forces and fiber kinematics (Aims 2b & 2c). In order to more fully define the micromechanical environment of neurons in the NCC, a complementary computational model of collagen networks was used to predict fiber strains that could not be measured experimentally during loading; predictions from that simulated collagen network were compared to the estimated fiber-level stretch in the human cervical facet capsular ligament (Aim 2b). Overall, studies in Aim 2 evaluated the dependency of neuronal responses on the multi-scale mechanical signals from the mechanical restructuring and the stresses developed in the spatially heterogeneous tissue matrix, which are relevant to the facet capsule anatomy and the potential loading it undergoes during painful trauma.

Neurons sense their environment via cell surface receptors, such as integrins (Tomaselli et al. 1993; Khalsa et al. 2004; Hemphill et al. 2011; Ribeiro et al. 2013). Integrins mediate bi-directional cell signaling; specific integrin subunits, such as the

subunit β1, can be activated by external mechanical stimuli and by intracellular signals involved in chemically-induced pain (Hynes 2002; Dina et al. 2004; Dina et al. 2005; Malik-Hall et al. 2005). Mechanical stress can trigger integrin-dependent cell signaling cascades, including the activation of the small GTPase protein RhoA and its major downstream effector Rho kinase ROCK (Marjoram et al. 2014). In addition to mechanotransduction, the RhoA/ROCK pathway is also involved in the pathogenesis of neural injury (Dubreuil et al. 2003; Hemphill et al. 2011; Kopp et al. 2012) and neuropathic and inflammatory pain (Inoue et al. 2004; Mueller et al. 2005; Tatsumi et al. 2005; Paiva-Lima et al. 2014).

To test if integrin signaling and the RhoA/ROCK pathway mediate facet joint pain from facet capsule stretch, integrated in vivo and in vitro models were used in Aim 3. An in vivo rat model enables direct evaluation of the contributions of those molecular pathways to pain; whereas, the in vitro NCC model provides a system to isolate the effects of mechanical loading from the more complex system responses in vivo and enables direct mapping between local afferent regulation and applied regional strains. The involvement of the integrin subunit β1 in facet joint pain was assessed in the rat by first measuring its production in the DRG, with the occurrence of behavioral hypersensitivity; the effects of inhibiting β1 integrins on nociceptive neuropeptide expression was then evaluated after NCC stretch (Aim 3a). Similarly, coordinated in vivo and in vitro studies tested whether excessive stretch of the innervated facet capsular ligament and NCCs activates RhoA in the DRG and if ROCK inhibition modulates afferent signaling in NCCs exposed to stretch, neuropeptide expression in the DRG, and

spinal neuronal excitability and glial activation, in the context of pain in the rat (Aim 3b). Collectively, studies in Aim 3 identify potential molecular pathways that may underlie mechanically-induced facet joint pain and could serve as possible therapeutic targets for pain treatment from facet capsule trauma.

## 2.2. Overall Hypothesis & Specific Aims

The work in this thesis uses complementary computational and experimental methods to define the multi-scale biomechanical and neuronal mechanisms of pain from facet capsular ligament stretch. The **overall hypothesis** of this thesis is that subfailure stretch of the cervical facet capsular ligament that exceeds its physiologic range alters the local biomechanics of the collagen networks and fibers in that ligament, which mediates the responses of the embedded neurons to tissue loading conditions that lead to pain. Owing to indirect neuronal loading that is transmitted through the complex fibrous structure of the ligament, the translation of mechanical stimuli into pain signals depends on the surrounding collagen architecture and cellular signaling cascades that play dual roles in mechanotransduction and nociception. This central hypothesis has three sub-hypotheses that are tested in the following associated specific aims.

**Hypothesis 1.** The establishment of anomalous collagen fiber realignment in the human cervical facet capsular ligament at subfailure strains is associated with the altered coordination of groups of spatially-distributed fibers and excessive network-level and fiber-level stresses and strains. Accordingly, the collagen reorganization pattern and the

local mechanics of networks and fibers differ in the facet capsular ligament between regions where anomalous fiber realignment develops and regions that sustain only normal fiber realignment.

**Aim 1.** Define the multi-scale stresses and strains of the human cervical facet capsular ligament using image-based computational models, with particular emphasis on abnormal collagen realignment. Evaluate the association between fiber-level, network-level and tissue-level mechanics of the facet capsule and the development of local anomalous fiber realignment at subfailure strains that induce neuronal activation and pain in vivo.

**1a.** Measure collagen fiber reorientation patterns in different sub-regions of the human cervical facet capsular ligament that sustains anomalous or normal fiber realignment during stretch, using a novel extension of network science methods.

**1b.** Predict the multi-scale stresses and strains in the isolated human cervical facet capsular ligament during subfailure stretch using a finite element-based model that incorporates sample-specific, spatially-varied collagen organization.

**Hypothesis 2.** The intensity of heterogeneous mechanical signals present in different sub-regions of the facet capsular ligament during its stretch depends on the collagen organization and the loading modality, such as the stretch magnitude, stretch rate and tissue boundary conditions. The magnitude of mechanical stimuli differentially mediates

stretch-induced neuronal activation and nociception via altered microstructural mechanics of the ligament ECM.

**Aim 2.** Assess if, and how, different patterns of collagen organization in the facet capsular ligament and magnitudes of ligament stretch due to the applied strain, rate or boundary conditions affect neuronal activation and nociceptive responses and the mechanical environment of their surrounding ECM, using an in vitro neuron-collagen construct (NCC) system.

**2a.** Develop an in vitro NCC model system that mimics the innervation of the facet capsular ligament and enables fabrication of collagen fibers with prescribed orientation, supports mechanical loading, and enables the integrated assessment of collagen organization, macro-scale mechanics and cell morphology and expression of pain-related signaling proteins.

**2b.** Measure and predict the effects of collagen organization, strain magnitude and rate, and tissue boundary conditions, on the degree of changes in macroscopic and microscopic mechanics during tissue loading, including tissue-level forces and strains, and fiber-level realignment and stretch, using the NCC system and simulated collagen networks.

**2c.** Determine if, and how, collagen organization, stretch magnitude, stretch rate and tissue boundary conditions, regulate neuronal morphology, ERK-mediated activation

and substance P-dependent nociception via changes in the ECM mechanics in response to NCC stretch.

**Hypothesis 3.** The integrin subunit β1 and the Rho/ROCK pathway are involved in pain from facet capsular ligament stretch. Specifically, painful facet capsule stretch increases the integrin subunit β1 in the DRG, and β1 integrin inhibition prior to painful stretch attenuates loading-induced nociceptive signaling in those joint afferents. Painful facet capsule stretch also up-regulates RhoA activity in the DRG; inhibiting ROCK in the facet joint can attenuate pain by reducing nociceptive transmission in the afferents and neuronal firing and glial activation in the spinal cord.

**Aim 3**. Test if, and how, integrin signaling and the RhoA/ROCK pathway are involved in pain from excessive stretch of the facet capsular ligament using integrated in vivo and in vitro methods.

**3a**. Determine the constitutive expression of the integrin subunit β1 in the DRG and its regulation at day seven after painful facet capsule stretch in the rat. Test if inhibiting the β1 integrins in vitro prior to NCC loading simulating painful ligament strains prevents substance P-mediated nociceptive signaling in the DRG axons after NCC stretch.

**3b**. Measure RhoA activation in the DRG at 30 minutes and 6 hours after NCC stretch and one day after painful facet capsule stretch in the rat. Assess whether ROCK

inhibition immediately after NCC stretch prevents loading-induced neuronal substance P expression. Test whether intra-articular ROCK inhibition immediately after cervical facet capsule stretch in the rat prevents the development of behavioral hypersensitivity that is typical within one day after painful facet distraction, and assess pain-related neuronal responses in the DRG and spinal cord at that time, with and without ROCK inhibition.

## 2.3. Overview of Thesis Organization

The aims of this thesis are organized into chapters corresponding to the individual studies. The studies under Aim 2 were performed first to ensure that the mechanical features of the human facet capsular ligament proposed in Aim 1 were indeed relevant to neuronal activation and pain. Work from Aim 2 is presented in Chapters 3 and 4. Both chapters examine the effects of structural factors and loading conditions on neuronal signaling using the NCC system, but Chapter 3 focuses on the effects of initial collagen organization whereas Chapter 4 has a particular emphasis on the stretch-induced collagen reorganization. Work from Aim 1a is presented in Chapter 5; stretch-induced collagen network reconfiguration in human cervical facet capsular ligaments is analyzed in relation to the development of anomalous fiber realignment. Based on that same set of structural data, Chapter 6 summarizes studies under Aim 1b using that human data and a finite element-based model to predict the multi-scale mechanics of the cervical facet capsular ligament as those metrics relate to anomalous fiber realignment. The experimental design and findings related to Aim 3 are presented in Chapters 7 and 8.

Chapter 7 addresses the involvement of integrin signaling in nociception initiated by ligament stretch (Aim 3a); studies probing the role of the RhoA/ROCK pathway in facet joint pain from capsule stretch (Aim 3b) are described in Chapter 8. Lastly, Chapter 9 integrates the main findings of this thesis in the broader context of ligament injury and pain, and also addresses limitations and implications of this work for future research.

# Chapter 3

# Effects of Collagen Organization on Pain-Related Neuronal Responses to Tissue Stretch

*Part of this chapter has been adapted from:*

Zhang S, Singh S, Winkelstein BA. Collagen organization regulates stretch-initiated pain-related neuronal signals in vitro: Implications for structure-function relationships in innervated ligaments. *Journal of Orthopaedic Research,* in press, doi: 10.1002/jor.23657.

## 3.1. Overview

Injury to the innervated spinal facet capsular ligament that has heterogeneous collagen organization produces pain (Yamashita et al. 1996; Cavanaugh et al. 2006; Quinn and Winkelstein 2008; Dong et al. 2012; Kallakuri et al. 2012; Ban et al. 2017). Tensile stretch of that ligament exceeding its physiologic range also induces collagen disorganization, nociceptor activation in the capsule, central sensitization and pain (Lu et al. 2005a; Quinn and Winkelstein 2008; Quinn and Winkelstein 2009; Dong et al. 2012; Crosby et al. 2013; Crosby et al. 2014). Although mechanical trauma to the facet can activate the afferents embedded in it and produce nociception, it is unclear if, and how, the varied local extracellular microstructure of the capsular ligament modulates sensory transduction for pain from mechanical inputs.

Different sub-regions of the facet capsule are known to vary in their fiber architecture (Yamashita et al. 1996; Quinn and Winkelstein 2008; Kallakuri et al. 2012; Ban et al. 2017). Histological evidence shows that some sub-regions of the human facet

capsular ligament are comprised of parallel collagen bundles, while others contain irregular connective tissue (Yamashita et al. 1996; Kallakuri et al. 2012). Afferents, including nociceptors expressing neuropeptide substance P, are found in both types of sub-regions (Kallakuri et al. 2012). In areas with different collagen organization, afferents may experience varied loading and be injured to different degrees during macro-scale tissue deformations.

The human cervical facet capsular ligament is mainly composed of collagen fibers (Quinn 2010; Kallakuri et al. 2012). Its collagen organization has been shown by QPLI to exhibit high inter-sample heterogeneity, which is manifested in the form of curvy patterns formed by collections of collagen fibers (Quinn and Winkelstein 2008; Ban et al. 2017). Anisotropy of the collagen matrix in soft tissues affects the regional and local stresses and strains throughout the tissue (Quinn 2010; Lake and Barocas 2012; Hadi and Barocas 2013), which themselves can modulate the activity of mechanosensitive neurons exposed to that tissue loading (Khalsa et al. 1996; Khalsa and Ge 2004). Further, tensile stretch of heterogeneous fibrous tissues can produce a complex array of mechanical signals at the micro-scale, including non-uniform network reorientation, fiber deformation and fiber forces, as suggested by studies using collagen-based tissue analogues and complementary computational models (Sander et al. 2009a; Nair et al. 2014). Those microstructural changes can also influence the responses of the embedded neurons via cell-ECM interactions. Elucidating the potential interplay between neurons and their matrix environment in the context of mechanically-induced ligament pain is needed in order to

understand how macroscopic tissue deformation is transferred through the fibrous ECM to load and activate neurons.

The studies in this chapter test hypotheses in Aim 2 by evaluating the effects of collagen organization on neuronal dysfunction after stretch with different boundary conditions, using an in vitro neuron-collagen construct (NCC) model. The NCC model was developed to provide a simplified system to study the complex relationships between tissue-level mechanics, ECM structure and neuronal function in an innervated ligament, like the facet capsule. NCCs with either randomly organized or parallel aligned collagen fibers were used to mimic the varied microstructure in the facet capsular ligament. Embryonic rat DRGs were encapsulated in the NCCs to create a three-dimensional (3D) neuronal culture that is suitable for mechanical loading and imaging of collagen and neuronal responses. NCCs underwent separate uniaxial or equibiaxial tension to simulate either simplified stretch or the more complex multi-axial loading that is due to bone-ligament constraints in vivo. The imposed NCC strains that were targeted were consistent with the strains that normally induce nociceptor firing and/or pain in animal models of facet joint injury (Lee et al. 2004b; Lu et al. 2005a; Dong et al. 2012; Crosby and Winkelstein 2016).

This chapter includes summary of three sub-studies. In the first sub-study, NCCs with varied collagen organization were stretched uniaxially, and neuronal expression of the nociceptive neurotransmitter substance P (SP) and phosphorylated ERK (pERK) were evaluated in the associated DRGs to assess if collagen organization has any effect on pain signaling and/or neuronal activation (Section 3.3). In a parallel sub-study, equibiaxial

stretch was applied to NCCs with the same random or aligned collagen organization. In addition to SP and pERK expression, the induction of activating transcription factor 3 (ATF3), a marker of nerve injury (Bráz and Basbaum 2010; Nascimento et al. 2011), was also evaluated after biaxial NCC stretch to investigate whether neuronal dysfunction is induced at different macroscopic strains and if it is mediated by collagen organization (Section 3.4). The results from Section 3.3 and Section 3.4 were integrated in Section 3.5 to directly compare the effects of boundary conditions and alignment together on the stretch-induced pERK and SP expression in the NCC system. Findings presented in this chapter relate collagen organization to pain-related neuronal signaling and support structural heterogeneity of ligament tissue as a potent mediator of sensory function.

## 3.2. Relevant Background

Ligaments are soft collagenous tissues that not only have important mechanical functions, but can also provide sensory feedback due to their proprioceptive and nociceptive afferents (Schultz et al. 1984; McLain and Pickar 1998; Petrie et al. 1998; Kallakuri et al. 2012). They are increasingly recognized as sources of musculoskeletal pain due to abnormal loading (Lee et al. 2004a; Solomonow 2004; Cavanaugh et al. 2006). The spinal facet capsular ligament can induce neck and back pain due to its excessive stretch (Manchikanti et al. 2004; Bogduk 2011; Dong et al. 2012), particularly in the cervical spine as a result of whiplash injury and neck trauma (Tominaga et al. 2006; Bogduk 2011). The capsular ligament encloses the bilateral facet joints, which facilitate articulations between adjacent vertebrae in the spine. The capsular ligament is

primarily comprised of densely packed collagen fibers interspersed with elastin fibers (Yamashita et al. 1996; Kallakuri et al. 2012). Fiber organization in the capsular ligament is highly heterogeneous; fibers in some regions have parallel orientation but are unaligned in others (Yamashita et al. 1996; Quinn and Winkelstein 2008; Ban et al. 2017). Afferent nerve fibers, including pain fibers, innervate both regions with parallel collagen bundles and those with irregular organization (Kallakuri et al. 2012). Accordingly, afferents, even in the same capsule, can experience very different loading conditions and injury risks during macroscopic tissue stretch (Quinn and Winkelstein 2008). Supraphysiological strains of the cervical facet capsular ligament prior to tissue failure are known to activate neurons embedded in it and lead to pain (Lu et al. 2005a; Lee and Winkelstein 2009; Dong et al. 2012; Crosby et al. 2014). Yet, it remains unknown if, and how, the microstructure and organization of the capsular ligament affect the sensory function of the innervating afferents in response to excessive ligament deformation.

Collagen organization of soft collagenous tissues affects macro- and micro-scale mechanical responses of the fibrous matrix (Lake et al. 2009; Lake and Barocas 2012; Hadi and Barocas 2013), which may modulate the activity of the embedded mechanosensitive neurons (Khalsa et al. 1996; Lu et al. 2005a). The collagen organization before loading has been shown in a host of musculoskeletal tissues, collagen-based tissue-equivalents, and computational models to affect tissue-level stress-strain responses, macroscopic failure forces and micro-scale fiber kinematics during loading (Lake et al. 2009; Lake and Barocas 2012; Hadi and Barocas 2013). Abnormal

collagen fiber kinematics, likely resulting from failure of load-bearing fibers and subsequent force redistribution, have been observed in specific regions of the facet capsular ligament where eventual tissue failure develops (Quinn and Winkelstein 2008; Quinn and Winkelstein 2009). Both local collagen disorganization and persistent afferent activation in facet capsules occur at pain-inducing strains in vivo (Lu et al. 2005a; Quinn and Winkelstein 2009; Dong et al. 2012), suggesting possible associations between collagen fiber orientation, neuronal signaling, and macroscopic tissue deformation. Accordingly, collagen organization in innervated ligaments is hypothesized to mediate neuronal activation and pain signaling as a result of excessive tissue stretch.

To better define the relationship between neurons and their matrix environment in the context of ligament pain, an in vitro NCC model was developed to enclose neurons in collagen gels with either random or aligned fiber organization. The NCCs encapsulated embryonic rat DRG containing the cell bodies of sensory neurons that innervate peripheral tissues like the facet capsular ligament (Basbaum et al. 2009; Kras et al. 2013b). By varying the collagen organization of NCCs, and allowing DRGs to grow axons along collagen fibers, the varied innervation of afferents in sub-regions of the facet capsular ligament with different microstructures (Kallakuri et al. 2012) was simulated. Collagen fiber alignment and axon orientation were assessed in un-stretched control gels using polarized light imaging and confocal imaging to characterize the structural differences between the NCCs with random and aligned fiber organization.

NCCs were stretched uniaxially or biaxially to strains that induce pain in vivo (Lee and Winkelstein 2009; Dong et al. 2012). Both uniaxial and biaxial testing have

been performed previously on isolated human facet capsular ligaments to study changes in their mechanical behaviors and collagen fiber alignment in response to loading (Quinn and Winkelstein 2008; Quinn and Winkelstein 2009; Claeson and Barocas 2017). Uniaxial tension is a simple loading modality whose effects on macro-scale and micro-scale mechanics of 3D collagen gels have been well assessed by experiments and modeling (Roeder et al. 2002; Vader et al. 2009; Stein et al. 2011; Nair et al. 2014). It is thus a preferred loading condition over more complicated stretch scenarios to tease apart the effects of tissue mechanics (e.g. forces and strains) and collagen organization on neuronal responses. On the other hand, biaxial stretch can better simulate the complex loading of the facet capsular ligament in vivo that results from ligament-bone attachment and multi-axial loads applied to the facet joint in whiplash (Siegmund et al. 2008; Jaumard et al. 2011).

After NCC stretch, neuronal expression of phosphorylated ERK (pERK) and the nociceptive neuropeptide SP was measured to evaluate the effects of tissue loading, convolved with collagen organization and boundary conditions, on neuronal activation and pain signaling. Phosphorylation of ERK, a signaling second messenger, can be induced by noxious stimuli in nociceptive afferents and spinal neurons and serve as a marker for neuronal activation (Dina et al. 2005; Gao and Ji 2009). The neurotransmitter SP is expressed by peptidergic DRG neruons and modulates nociceptive signal transmission (Basbaum et al. 2009). Both pERK and SP have been shown to be involved in facet join pain (Lee and Winkelstein 2009; Kras et al. 2013c; Crosby et al. 2014; Kras et al. 2015b). In order to test the effects of collagen organization on neuronal activation

and nociception, axonal expression of pERK and SP were measured in separate uniaxial and biaxial stretch experiments of NCCs with random and aligned fiber organization and compared to the levels in the corresponding unloaded controls within each loading scenario (Sections 3.3 & 3.4). The stretch-induced pERK and SP expression in the DRG was then compared between uniaxially and biaxially loaded NCCs to examine the effects of boundary condition (Section 3.5). In addition to pERK and SP expression, ATF3, a neuronal injury marker that can be induced in afferents by noxious stimuli (Bráz and Basbaum 2010; Nascimento et al. 2011), was measured after biaxial NCC stretch in the studies in Section 3.4 to evaluate the degree of neuronal dysfunction at different strains in NCCs with varied collagen organizations. The implications of each of these separate studies is integrated in a larger discussion together in Section 3.6.

## 3.3. Effects of Collagen Organization Under Uniaxial NCC Stretch

### 3.3.1. Methods

#### 3.3.1.1. Neuron-Collagen Construct Model

Studies used an in vitro DRG-collagen model system in which neurons were embedded in collagen with varied fiber alignment. The NCCs were prepared using rat tail Type I collagen (PH 7; 2mg/ml; Corning Inc.; Corning, NY) cast in 12-well tissue culture plates (Figure 3.1). Gels with random fiber organization (random NCCs) were made by incubating the collagen solution at 37°C overnight. NCCs with parallel collagen fibers (aligned NCCs) were produced using magnetic alignment (Tranquillo et al. 1996; Xu et al. 2011), with plates containing the collagen solution placed in a 4.7T 50cm horizontal

bore magnetic resonance system equipped with a 30cm inner diameter 3gauss/cm and a 12cm inner diameter 25gauss/cm gradient tube, interfaced to an Agilent DirectDrive console (Agilent Technologies; Santa Clara, CA) at 37°C for 45 minutes and then incubated at 37°C overnight.

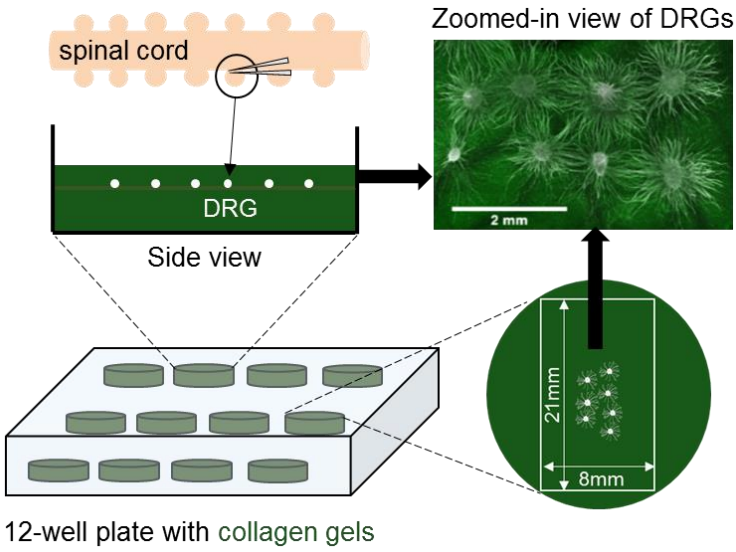


**Figure 3.1.** Generation of 3D NCCs. Embryonic rat DRG explants (white) are embedded in the center of collagen gels (green) cast in a 12-well tissue culture plate. They are allowed to extend axons for seven days before the NCCs are cut into a rectangular shape (white box) for uniaxial tensile loading.

Rat DRGs at all spinal levels were sterilely isolated using fine forceps from embryonic day 18 Sprague-Dawley rats (from the CNS Cell Culture Service Center of the Mahoney Institute of Neuroscience), according to procedures approved by the Institutional Animal Care and Use Committee at the University of Pennsylvania. DRG explants (5-10/gel) were plated in the center of the gels and allowed to attach and grow axons on the surface. NCCs were cultured in neurobasal medium supplemented by 1% GlutaMAX, 2% B-27, 1% Fetal Bovine Serum and 10ng/mL 2.5S nerve growth factor

(all from Thermo Fisher Scientific; Waltham, MA), with addition of 2mg/mL glucose, 10mM FdU and 10mM uridine (all from Sigma-Aldrich; St. Louis, MO) (Cullen et al. 2012). Additional collagen was added three days after the initial plating to encapsulate the DRGs. NCCs were cultured for another four days.

#### 3.3.1.2. Assessment of Collagen Fiber & Axon Orientation

To characterize collagen alignment and axonal orientation, the directions of collagen fibers and axons were measured in NCCs with randomly oriented fibers (n=8) and with magnetically aligned fibers (n=9). At day 7 in vitro, those unloaded control NCCs were fixed with 4% paraformaldehyde. A previously developed polarized light imaging technique (Tower et al. 2002; Quinn 2010) was used to acquire pixel-wise (20 pixels/mm) collagen alignment angles over the entire gel. The code used to compute the fiber angles from QPLI images is provided in Appendix A. Circular variance quantified the spread of fiber orientation angles, with a lower circular variance indicating a tighter clustering and a higher degree of fiber alignment (Miller et al. 2012b). The microstructure of the collagen gel in both aligned and random NCCs also was visualized by immunolabeling of Type I collagen. Gels were blocked in 10% goat serum with 0.1% Triton-X 100 in phosphate-buffered saline (PBS) solution and incubated overnight with a mouse anti-collagen I antibody (1:250; Abcam; Cambridge, MA) followed by incubation with a fluorescent secondary goat anti-mouse Alexa Fluor 488 antibody (1:1000; Invitrogen; Carlsbad, CA). Labeled gels were imaged with a Zeiss 710 confocal microscope (Carl Zeiss Microscopy; Thornwood, NY).

In order to evaluate neuronal morphology, the NCCs were blocked in 1% donkey serum with 0.3% Triton-X 100 in PBS, and fluorescently labeled using a chicken anti-βIII tubulin antibody (1:200; Abcam; Cambridge, MA) and a secondary donkey anti-chicken Alexa Fluor 647 antibody (1:1000; Invitrogen; Carlsbad, CA). A Fourier transform method was used to analyze the confocal images and measure the direction of axon outgrowth by computing the axon orientation distribution in polar coordinates based on image intensity values, as described previously (Sander and Barocas 2009; Susilo et al. 2015). This method defines the degree of fiber alignment along the principal orientation axes, the ratio of which indicates the extent of anisotropy (Sander and Barocas 2009; Susilo et al. 2015). As such, the ratio of the axon alignment strength along the minor orientation axis to that along the major orientation axis was computed. Differences in collagen fiber alignment (circular variance) and axonal direction (minor-to-major-axis ratio) were compared between random and aligned NCCs using Student's t-tests.

#### 3.3.1.3. Mechanical Loading & Data Acquisition

At day 7 in vitro, separate groups of aligned and random NCCs (n=8/organization group) underwent uniaxial stretch using a planar testing machine (574LE2; TestResources; Shakopee, MN) (Figure 3.2a). Circular NCCs cast in 12-well plates were cut into vertical strips (21mm×8mm; Figure 3.1) and a grid of markers was drawn on each gel surface covering the area of the gel containing the DRGs (Figure 3.2b). Together with visible DRGs, the markers were used to designate sub-regions of each gel for measuring local strains during mechanical loading. Gels were clamped in the test system,

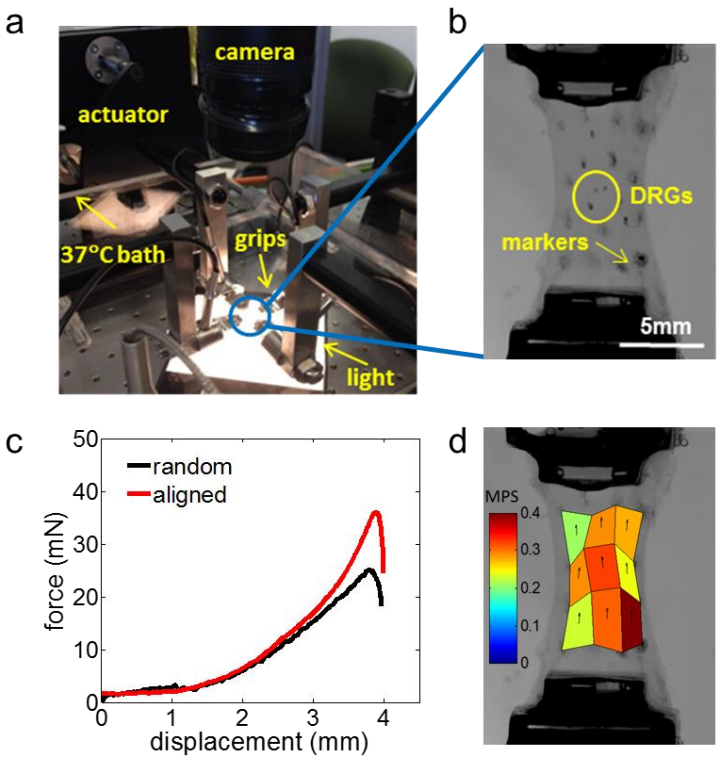


**Figure 3.2.** Overview of the NCC experimental test set-up. It shows **(a)** the mechanical test system, **(b)** the high-speed image of a stretched NCC at maximum stretch of 4mm, **(c)** representative force-displacement responses from a random gel (sample #U-R7) and an aligned gel (sample #U-A8), and **(d)** a representative strain map showing both the magnitude and direction of MPS for the NCC in **(b)** at its maximum stretch.

which was equipped with a bio-bath filled with PBS maintained at 37°C and a high-speed camera (Phantom-v9.1; Vision Research Inc.; Wayne, NJ) to track the movements of the markers and the visible DRGs (Figure 3.2a). Uniaxial stretch was applied to distract the NCCs by 4mm (~25% strain) to simulate the subfailure strains shown to induce pain in vivo (Lee and Winkelstein 2009; Dong et al. 2012). The loading rate was 3.7mm/s, the highest rate that the testing machine could achieve for 4mm displacement. Aligned gels were stretched along the major direction of axonal outgrowth, as determined using a light microscope before the gels were positioned in the test system.

During loading of all gels, acquisition of force and displacement data (200Hz) was synchronized with that of the high-speed images (200 frames/s). Force-displacement data were filtered with a ten-point moving average filter and the peak force was extracted (Figure 3.2c). Based on the positions of fiducial markers and visible DRGs shown in the high-speed images, the maximum principal strain (MPS) in each of the four-node sub-regions of the NCCs was calculated using LS-DYNA (Livermore Software Technology Corp.; Livermore, CA) (Figure 3.2d). Each of the peak force and average MPS across each gel's surface were compared between random and aligned NCCs with separate Student's t-tests. After tension, the gels that were held in their stretched position were immediately released from the testing machine, returning to an unloaded state, and washed with fresh PBS supplemented by 1% Pen-Strep (Thermo Fisher Scientific; Waltham, MA). They were then transferred into pre-warmed culture media supplemented by 1% Pen-Strep and incubated for 24 hours to allow time for transcriptional and/or translational changes before undergoing fixation with 4% paraformaldehyde. Un-stretched NCCs having each of random and aligned collagen organization (n=7/organization group) were included as controls for defining neuronal regulation of activation and nociceptive signals.

#### 3.3.1.4. Immunolabeling & Quantification of Axonal pERK & substance P

Control and stretched NCCs were immunolabeled for βIII tubulin to visualize neuronal morphology, pERK as a marker of neuronal activation and substance P as a measure of neuropeptide-mediated nociception. NCCs were blocked in 1% normal

donkey serum with 0.3% Triton-X PBS for 2 hours at room temperature. Then they were incubated overnight at 4°C with chicken anti-βIII tubulin (1:200; Abcam; Cambridge, MA), rabbit anti-pERK (1:200; Cell Signaling Technology; Danvers, MA) and guinea pig anti-substance P (1:500; Neuromics; Bloomington, MN) primary antibodies. The next day, NCCs were fluorescently labeled with secondary antibodies for donkey anti-chicken Alexa Fluor 647 (1:1000; Invitrogen; Carlsbad, CA), donkey anti-rabbit Alexa Fluor 555 (1:1000, Invitrogen; Carlsbad, CA) and donkey anti-guinea pig Alexa Fluor 488 (1:1000; Jackson ImunoResearch Labs; West Grove, PA). Images were taken using a Zeiss 710 confocal microscope (Carl Zeiss Microscopy; Thornwood, NY) and processed in ImageJ (National Institutes of Health; Bethesda, MD) for background subtraction and intensity measurement. Three regions of interest (ROIs; 1803μm x 1300μm) containing only axons were randomly selected in each gel, in order to measure axonal expression of pERK and SP throughout the gel and corresponding the regions in which strains were quantified. Axons were outlined based on the positive βIII tubulin labeling; the average intensities of each of pERK and SP labeling were measured in those axons and normalized to their respective unloaded control values to ensure appropriate comparison between different experimental runs. The normalized pERK and SP intensity values were compared between groups by separate two-way analysis of variances (ANOVAs) and post-hoc Tukey HSD tests, with the collagen organization and loading group as the two factors.

### 3.3.2. Results

#### 3.3.2.1. Effects of Collagen Organization on Axonal Outgrowth & NCC Forces

Magnetic alignment of collagen produces NCCs with more homogeneous fiber orientation, accompanied by directed axon outgrowth (Figure 3.3). Specifically, the circular variance of fiber angles measured over the entire gel area is significantly lower

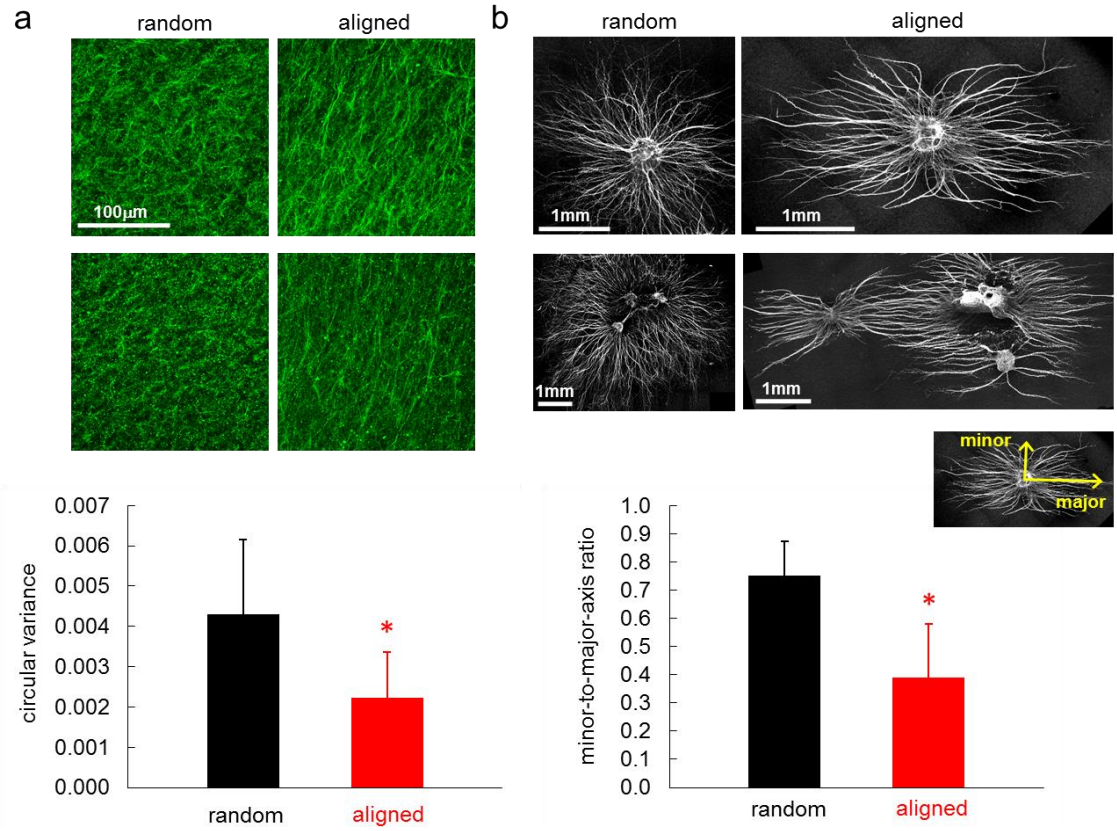


**Figure 3.3.** The orientation of collagen fibers and alignment of axons are more homogeneous in aligned NCCs than in random NCCs. **(a)** Representative confocal images demonstrate that the collagen fibers are oriented more parallel to each other in aligned NCCs as compared to the random NCCs. The scale bar is 100μm and applies to both images. The circular variance obtained using polarized light imaging for the entire gel area is significantly lower (*p=0.007) in the aligned than random NCCs, indicating higher similarity in fiber angles in aligned gels. **(b)** Representative images show the isotropic axon orientation in random NCCs and directed axon outgrowth in aligned NCCs (scare bar=1mm). The ratio of axon alignment strength in the minor and the minor axes (axes of a representative DRG shown in the inset) is significantly lower (*p<0.001) in aligned NCCs than in random NCCs.

(p=0.007) in the aligned NCCs than in the random NCCs (Figure 3.3a). In addition, randomly distributed collagen fibers and parallel fibers are observed in unaligned and aligned NCCs, respectively (Figure 3.3a), demonstrating higher structural anisotropy of the magnetically aligned collagen matrices. Immunolabeling of βIII tubulin indicates that axons in the aligned, but not random, NCCs exhibit a preferred outgrowth direction, which is apparent by visual assessment of the confocal images and is quantified by a significantly lower ratio ($p<0.001$) of alignment strength between the minor and major axon orientation axes; aligned NCCs have a ratio of 0.39±0.19 which is almost ½ that of the random NCCs which have a ratio of 0.71±0.19 (Figure 3.3b). The circular variance of fiber angels and the minor-to-major-axis ratio of axon alignment for individual NCCs are provided in Appendix B.

Varying the collagen organization in an NCC alters the peak force, but not the strain, of the loaded NCCs. The peak force of aligned gels (32.7±13.9mN) is significantly greater (p=0.025) than the peak force sustained by random gels (21.1±6.5mN) at similar displacements (Table 3.1). However, there is no difference (p=0.886) between the average MPS sustained by the NCCs with randomly organized collagen fibers (0.25±0.06) and those with aligned fibers (0.26±0.07) (Table 3.1).

#### 3.3.2.2. Effects of NCC Stretch & Collagen Organization on pERK & substance P Expression

Collagen organization also differentially up-regulates pERK and SP expression at

24 hours after NCC stretch (Table 3.1; Figures 3.4 & 3.5). Immunolabeling of pERK in neuronal axons is greater ($p<0.001$) than control levels after NCC stretch, regardless of whether the collagen fibers are randomly organized or aligned (Table 3.1; Figure 3.4). The normalized intensity of pERK labeling in aligned gels is also greater ($p=0.013$) than the level in random gels after equivalent stretches (Table 3.1; Figure 3.4). Similar to

**Table 3.1.** Summary of mechanics and normalized protein levels for uniaxially stretched NCCs with random or aligned fiber organization.

| **random** | | | | |
|---|---|---|---|---|
| **sample** | **peak force (mN)** | **average MPS[+]** | **pERK[#]** | **SP[#]** |
| U-R1 | 30.8 | 0.313 | 3.09 | 1.22 |
| U-R2 | 14.7 | 0.320 | 2.98 | 3.48 |
| U-R3 | 14.0 | 0.282 | 3.05 | 3.13 |
| U-R4 | 22.8 | 0.180 | 1.11 | 1.01 |
| U-R5 | 23.4 | 0.226 | 0.95 | 1.18 |
| U-R6 | 14.3 | 0.210 | 1.00 | 1.22 |
| U-R7 | 28.2 | 0.189 | 1.36 | 1.67 |
| U-R8 | 20.3 | 0.320 | 1.19 | 1.96 |
| **Mean** | **21.1** | **0.255** | **1.84** | **1.86** |
| **SD** | **6.50** | **0.060** | **1.00** | **0.95** |
| **aligned** | | | | |
| **sample** | **peak force (mN)** | **average MPS** | **pERK** | **SP** |
| U-A1 | 39.9 | 0.213 | 2.59 | 1.59 |
| U-A2 | 22.8 | 0.220 | 3.21 | 2.92 |
| U-A3 | 13.7 | 0.203 | 3.56 | 1.57 |
| U-A4 | 29.3 | 0.216 | 2.43 | 2.02 |
| U-A5 | 54.8 | 0.402 | 1.93 | 2.41 |
| U-A6 | 45.5 | 0.337 | 1.86 | 2.54 |
| U-A7 | 19.5 | 0.258 | 2.33 | 2.38 |
| U-A8 | 36.0 | 0.231 | 2.41 | 1.74 |
| **Mean** | **32.7*** | **0.260** | **2.54*** | **2.15** |
| **SD** | **13.9** | **0.072** | **0.58** | **0.49** |

[+] Average MPS is the mean maximum principal strain across all elements in each NCC.
[#] Normalized intensity of pERK and SP is the mean across the three ROIs in each NCC.
*****The peak force ($p=0.025$) and pERK expression ($p=0.013$) are each significantly greater in the aligned NCCs than in the random NCCs.

pERK, SP labeling is significantly greater in both random and aligned NCCs relative to their respective un-stretched control levels ($p<0.001$) (Table 3.1; Figure 3.5). In contrast to pERK, the normalized expression of SP after stretch is not different between the two collagen organization groups ($p=0.760$), despite the peak force being higher in the aligned gels (Table 3.1; Figure 3.5). Detailed measurements of pERK and SP expression are summarized for each NCC sample in Appendix C.

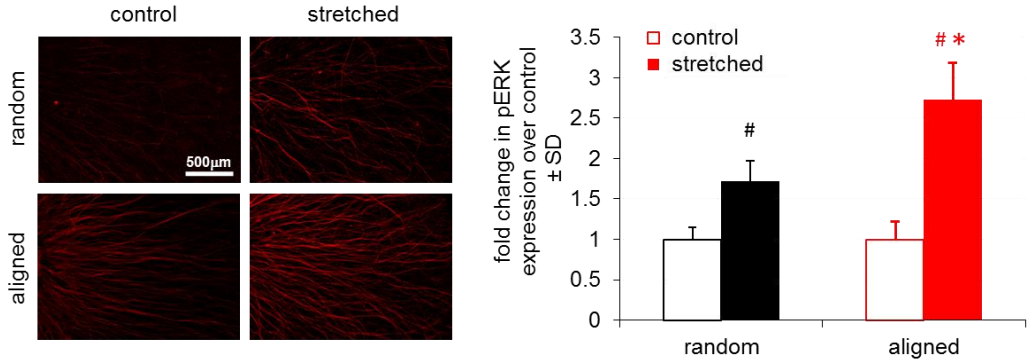


**Figure 3.4.** Uniaxial stretch-induced increases in pERK expression differs between random and aligned NCCs. Representative images and quantification of normalized intensity of pERK exhibit significant increases in axonal pERK after NCC stretch in both random and aligned NCCs (#$p<0.001$). That increase in pERK expression is significantly higher (*$p=0.013$) in aligned gels after stretch than in random NCCs after stretch.

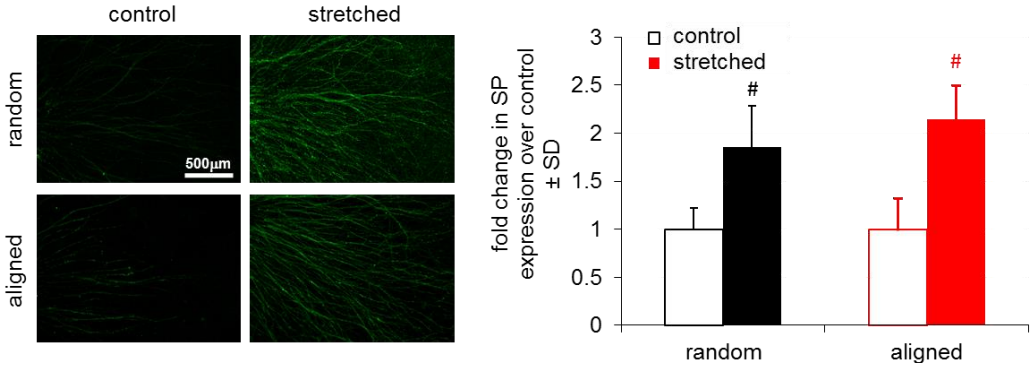


**Figure 3.5.** Expression of substance P increases in both random and aligned NCCs after uniaxial stretch. Representative images and quantification of normalized intensity demonstrate significant increases in axonal SP after NCC stretch in gels with both collagen organizations ($^{\#}p<0.001$) relative to their respective controls.

## 3.4. Effects of Collagen Organization Under Equibiaxial NCC Stretch

### 3.4.1 Methods

#### 3.4.1.1. DRG Explant Culture

Separate sets of random and aligned NCCs (n=8 for each alignment) were prepared as described in Section 3.3.1. At day seven in vitro, NCCs were cut into a cruciform shape for undergoing equibiaxial stretch, with each of the four arms having the dimensions of 6.25mm×8mm (Figure 3.6) (Sander et al. 2011). Using the same planar testing system detailed in Section 3.3.1, NCCs were stretched to 1.5mm for each arm at 3.7mm/s to generate strains that are similar to those painful strains (Dong et al. 2012; Crosby and Winkelstein 2016) imposed during uniaxial stretch in Section 3.3. The applied strains and peak forces were calculated and statistically compared using separate t-tests, as described in Section 3.3.1. After stretch, NCCs were unloaded, fixed at one day and assayed for pERK and SP expression following the same labeling and analysis protocols described in Section 3.3.1. Unloaded NCCs (random, n=5; aligned, n=5) were also included to control for possible differences in baseline pERK and SP expression

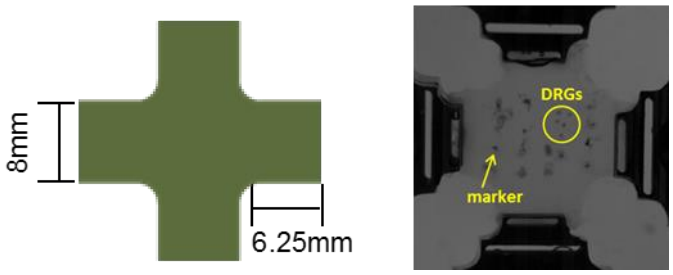


**Figure 3.6.** Cruciform NCCs for biaxial loading. NCCs are cut into a cruciform shape with each arm having the dimensions of 6.25mm×8mm for biaxial stretch. A grid of markers is drawn on the NCC surface to cover the area containing the DRG explants before loading the gel in the testing system.

before stretch due to different experimental materials and conditions between separate runs. The normalized pERK and SP intensities were compared between groups by separate two-way ANOVAs and post-hoc Tukey HSD tests, with the collagen organization (random, aligned) and loading group (loaded, unloaded) as the two factors.

#### 3.4.1.2. Dissociated DRG Culture

Axonal injury can induce the production of ATF3 in cell bodies (Kiryu-Seo et al. 2008; Hunt et al. 2012; Dubový et al. 2013). In order to measure ATF3 expression in the soma of neurons with higher resolution, dissociated DRG neuronal cultures were used instead of the DRG explant culture in which cell bodies are clustered to form the 3D ganglion. To dissociate the embryonic day 18 DRGs, the explants were exposed to pre-warmed trypsin (0.25%) plus EDTA (1mM) for one hour at 37°C (Cullen et al. 2012). Dissociated DRG neurons were embedded in collagen gels to form NCCs and cultured for six days, as described in Section 3.3.1. Similar to the DRG explant culture, NCCs containing dissociated DRG neurons were cut into a cruciform shape at day 7 in vitro. To generate a wide range of strains in the subfailre and failure loading regimes that may or may not lead to neuronal dysfuction, NCCs were equibiaxially stretched to 1.5mm for each arm producing no failure (random NCCs, n=2; aligned NCCs, n=3) or gross failure (n=3 for each NCC alignment). A grid of markers was placed on the NCC surface (Figure 3.6) and tracked during loading to measure the MPS in each four-node strain element, using methods described in Section 3.3.1.

NCCs were fixed with 4% PFA at one day after stretch and immunolabeled using

antibodies against ATF3 (1:200; Sigma-Aldrich; St. Louis, MO) and βIII-tubulin (1:200; Abcam; Cambridge, MA) to assess positive ATF3 signaling in neurons. Unloaded NCCs (n=2 for each alignment) were included to control for protein expression in NCCs with different collagen organization. The strains of unloaded NCCs were taken as having a value of zero. The percentage of pixels labeled positively for ATF3 in neurons after stretch was measured in a uniform-sized region of interest (2100×1800 pixels) in each strain element and normalized to the level in the corresponding unloaded control NCCs. The normalized ATF3 expression in each strain element was mapped to the MPS in the same sub-region and the relationship between ATF3 expression and strain was assessed using correlation analysis. Three separate linear regressions were performed to evaluate the effects of regional strain and collagen organization on ATF3 induction: (1) using all NCCs regardless of collagen organization to simulate the condition of a heterogeneous facet capsular ligament, (2) using only random NCCs, and (3) using only aligned NCCs.

### 3.4.2. Results

Random and aligned NCCs undergoing similar strains to a painful subfailure stretch exhibit different peak forces (Table 3.2). The peak force of aligned gels (28.0±17.3mN) is significantly greater ($p=0.041$) than the peak force sustained by random gels (16.0±5.5mN) at similar displacements (Table 3.2).

Collagen organization differentially up-regulates pERK and SP expression in NCCs after painful biaxial stretch (Table 3.2; Figure 3.7). Immunolabeling of pERK in neuronal axons after stretch is similarly greater ($p<0.032$) than control levels in both

**Table 3.2.** Summary of mechanics and normalized protein levels for NCCs undergoing subfailure painful biaxial stretch with random or aligned fiber organization.

| **random** | | | | |
|---|---|---|---|---|
| **sample** | **peak force (mN)** | **average MPS[+]** | **pERK[#]** | **SP[#]** |
| B-R1 | 15.8 | 0.139 | 2.17 | 2.19 |
| B-R2 | 9.3 | 0.188 | 1.16 | 1.22 |
| B-R3 | 13.6 | 0.159 | 1.04 | 1.17 |
| B-R4 | 10.9 | 0.166 | 1.98 | 1.64 |
| B-R5 | 14.4 | 0.200 | 2.53 | 0.69 |
| B-R6 | 22.5 | 0.202 | 2.42 | 1.94 |
| B-R7 | 16.3 | 0.168 | 2.33 | 1.83 |
| B-R8 | 25.3 | 0.242 | 2.41 | 1.89 |
| **Mean** | **16.0** | **0.183** | **2.00** | **1.57** |
| **SD** | **5.5** | **0.032** | **0.58** | **0.50** |
| **aligned** | | | | |
| **sample** | **peak force (mN)** | **average MPS** | **pERK** | **SP** |
| B-A1 | 18.6 | 0.142 | 3.18 | 1.38 |
| B-A2 | 19.5 | 0.172 | 2.07 | 2.77 |
| B-A3 | 37.9 | 0.297 | 4.21 | 3.16 |
| B-A4 | 15.3 | 0.126 | 4.53 | 2.38 |
| B-A5 | 11.4 | 0.27 | 3.26 | 2.90 |
| B-A6 | 61.8 | 0.244 | 1.29 | 1.53 |
| B-A7 | 41.1 | 0.197 | 2.06 | 1.29 |
| B-A8 | 18.7 | 0.121 | 1.03 | 1.18 |
| **Mean** | **28.0*** | **0.196** | **2.71** | **2.07*** |
| **SD** | **17.3** | **0.068** | **1.30** | **0.81** |

[+] Average MPS is the mean maximum principal strain across all elements in each NCC.
[#] Normalized intensity of pERK and SP is the mean across the three ROIs in each NCC.
*****The peak force ($p=0.041$) and SP expression ($p=0.046$) are each significantly greater in the aligned NCCs than in the random NCCs.

random and aligned NCCs (Table 3.2; Figure 3.7). Although SP labeling appears to increase in both aligned and random NCCs after stretch, that increase is only significant in aligned NCCs over the corresponding un-stretched control level ($p<0.001$), when considering the collective effects of loading and collagen organization on SP expression

(Table 3.2; Figure 3.7). The SP expression in aligned NCCs is also greater than that in random NCCs after stretch (p=0.046) (Table 3.2; Figure 3.7). Detailed measurements of the pERK and SP expression are summarized in Appendix C.

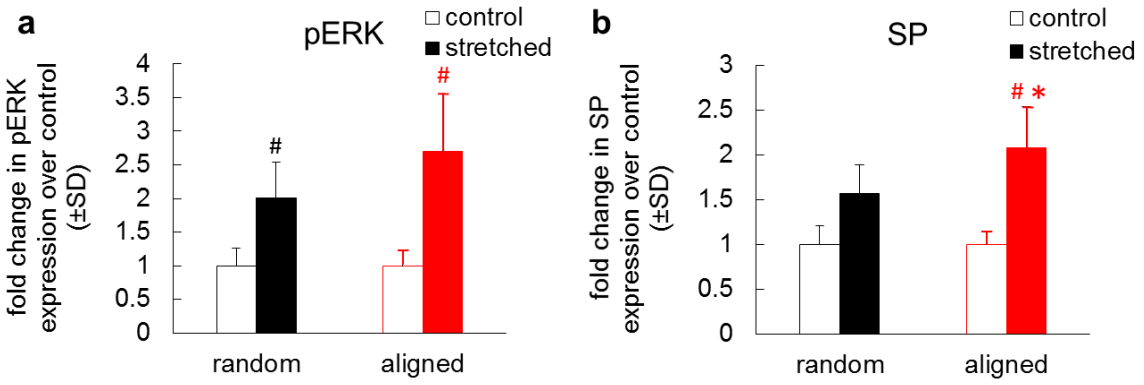


**Figure 3.7.** Collagen organization differentially up-regulates pERK and SP expression after biaxial NCC stretch. **(a)** Expression of pERK increases in both random and aligned NCCs after subfailure painful biaxial stretch (#p<0.032). **(b)** Yet, expression of SP is only significantly increased in aligned NCCs (#p<0.001), but not in random NCCs, by painful biaxial stretch. The stretch-induced SP expression in aligned NCCs is also greater than in random NCCs (*p=0.046).

A wide range of strains is produced in both the random and aligned NCCs by biaxial stretch up to and at failure (Table 3.3). The ATF3 expression is significantly correlated with the applied regional MPS ($R^2$=0.305; p<0.001), regardless of the collagen organization (Figure 3.8a). Significant positive correlations between ATF3 expression and MPS are also separately detected in each of randomly organized NCCs ($R^2$=0.219; p<0.001) and aligned NCCs ($R^2$=0.413; p<0.001), with a slightly stronger correlation identified in the aligned NCCs (Figures 3.9b & 3.9c). Images of the ATF3 labeling in control and stretched NCCs and normalized ATF3 expression in each strain element are detailed in Appendix C.

**Table 3.3**. Summary of strains in random and aligned NCCs undergoing loading to failure which were used to study the relationship between ATF3 expression and strain.

| random | | aligned | |
|---|---|---|---|
| **sample** | **average MPS ±standard deviation** | **sample** | **average MPS ±standard deviation** |
| Subfailure R1 | 0.157±0.058 | Subfailure R1 | 0.186±0.048 |
| Subfailure R2 | 0.190±0.087 | Subfailure R2 | 0.174±0.119 |
| | | Subfailure R3 | 0.227±0.057 |
| Failure R1 | 0.191±0.030 | Failure R1 | 0.498±0.087 |
| Failure R2 | 0.284±0.054 | Failure R2 | 0.288±0.055 |
| Failure R3 | 0.307±0.045 | Failure R3 | 0.416±0.124 |

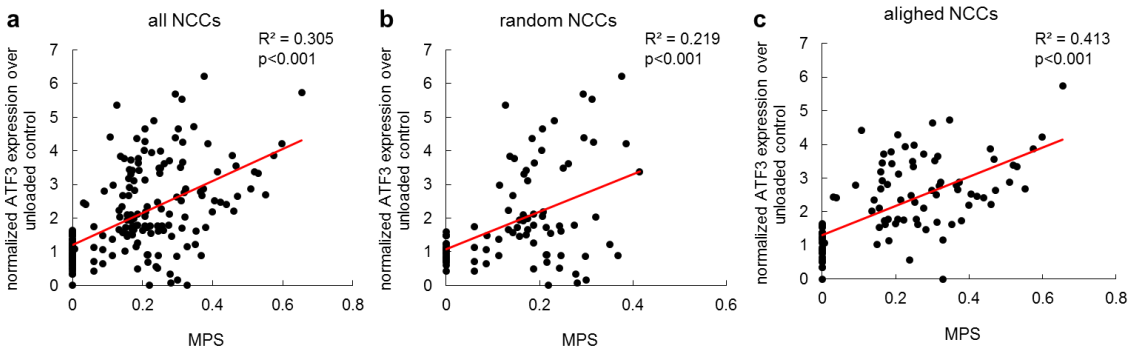


**Figure 3.8.** ATF3 and NCC strain are significantly correlated. The normalized ATF3 expression over unloaded control levels is significantly correlated with the applied regional MPS **(a)** regardless of the collagen organization ($R^2$=0.305; p<0.001), **(b)** in random NCCs ($R^2$=0.219; p<0.001), and **(c)** in aligned NCCs ($R^2$=0.413; p<0.001).

## 3.5. Effects of Boundary Condition on Stretch-Induced pERK & substance P Expression

The expression of pERK and SP after subfailure painful stretch in random and aligned NCCs was separately compared between uniaxial and biaxial loading scenarios to test the effects of loading condition (i.e. uniaxial vs. equibiaxial) on neuronal activation

and nociception. Normalizing the labeling intensity in stretched NCCs to the corresponding protein level in unloaded controls enables comparison between protein expression (i.e. pERK and SP) after uniaxial loading and equibiaxial loading that was performed in separate runs. Separate two-way ANOVAs and post-hoc Tukey HSD tests, with the loading conditions and collagen organization as the two factors, compared the peak force, MPS and expression of pERK and SP between the NCCs with varied fiber alignment and undergoing loading along different directions.

With no difference in the applied strain, the aligned NCCs have higher force than the random NCCs ($p=0.008$) regardless of the boundary condition (Tables 3.1 & 3.2). For both the random and the aligned NCCs, uniaxial and equibiaxial stretch induce similar changes in the expression of pERK and SP (Figure 3.9). No difference is detected by statistical comparison among the loaded NCC groups that have varied collagen organization and boundary conditions (Figure 3.9).

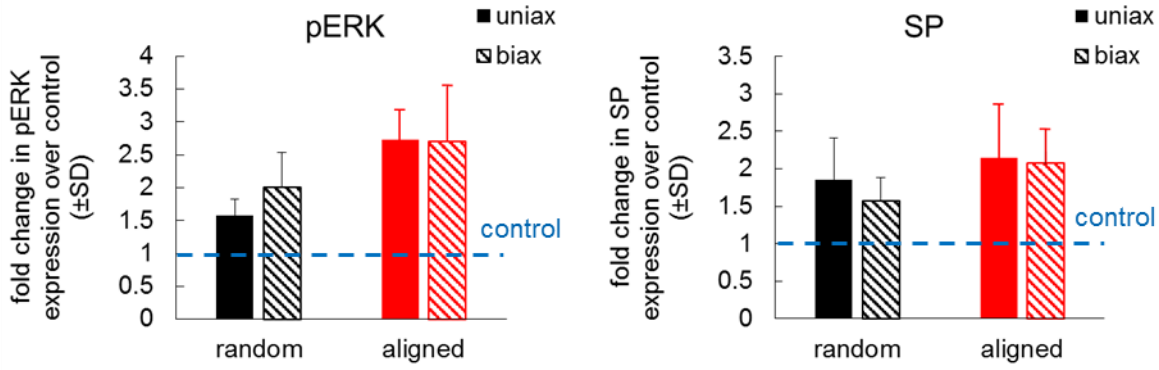


**Figure 3.9.** Comparison of pERK and SP expression between stretched NCCs with varied collagen organization and loading conditions. Neither the expression of **(a)** pERK nor **(b)** SP is different between uniaxially and equibiaxially loaded NCCs with random or aligned fiber organization.

## 3.6. Discussion

Although ligaments, particularly spinal facet capsular ligaments, are increasingly recognized as pain sensors (Lee et al. 2004a; Cavanaugh et al. 2006; Bogduk 2011; Kallakuri et al. 2012; He et al. 2016), the structure-function relationships that underpin mechanically-induced ligament pain are not well defined. This is partially due to the complex hierarchical organization of such tissues and their heterogeneous fibrous structure. Work presented in this chapter shows that collagen organization appears to regulate stretch-induced, pain-related signaling in neurons embedded in an extracellular matrix. Regional differences in collagen organization have been well-documented in the human cervical facet capsular ligament (Quinn and Winkelstein 2008; Ban et al. 2017). Recently, spatial correlation analysis suggests that this ligament contains sub-regions in which collagen fiber orientation is very similar (Ban et al. 2017). Those sub-regions are approximately one-tenth the size of the overall tissue domain and about 400 times larger than the diameter of the nociceptive free nerve endings that innervate the cervical facet capsular ligament (McLain 1994; Ban et al. 2017). The random and aligned DRG-collagen constructs used in this thesis simulate two types of sub-feature domains in the cervical facet capsule – regions with irregularly organized fibers (i.e. random) and regions with parallel collagen fibers (i.e. aligned). The width and gauge length of the stretched NCCs are about two orders of magnitude larger than the diameter of the embedded axon bundles (Figures 3.2, 3.3 & 3.6), which is similar to the in vivo condition and makes this NCC system suitable for investigating the effects of regional (meso-scale)

structural variation in the cervical facet capsule on neuronal activation and dysfunction (McLain 1994; Ban et al. 2017).

By applying a strong magnetic field around the collagen solution during gelation and embedding DRG explants in that gel, NCCs with collagen fibers preferentially oriented in one direction were created (Figure 3.3a). To avoid exposing live DRGs to a strong magnetic field, the top collagen layer that was added later to encapsulate the growing DRGs was not magnetically oriented in the aligned NCCs. However, that collagen layer was ten times thinner than the aligned substrate underneath the DRGs and was added three days after the initial DRG plating. While that top collagen layer does not appear to alter the parallel axonal outgrowth directed by the aligned collagen fibers (Figure 3.3b), it is in direct contact with the axons and may have affected their micromechanical environment of the neurons. Nevertheless, in aligned NCCs, the axonal outgrowth (Figure 3.3) resembles nerve fibers in the facet capsule that run along parallel collagen fibers (Kallakuri et al. 2012). In contrast, random NCCs simulating the irregular fibrous structure in the facet capsule exhibit uniform axonal outgrowth towards all directions (Figure 3.3b). Although the in vitro NCC system used here only includes Type I collagen and no other extracellular components, it does model the innervation of SP-positive afferent nociceptors (Figure 3.5) that have been reported in sub-regions of the human cervical facet capsular ligaments (Kallakuri et al. 2012), with both parallel collagen bundles and irregular connective tissues. By enabling the integrated assessment of macroscopic mechanics and neuronal responses, this work links tissue structural heterogeneity to a varied local mechanical environment and signaling of embedded

neurons in the context of facet joint pain (Lu et al. 2005a; Quinn and Winkelstein 2008; Dong et al. 2012).

In addition to different axonal morphology in the DRG explants, variable collagen organization also produces different NCC mechanics during tensile loading. The higher peak force for the aligned NCCs than the random ones (Tables 3.1 & 3.2) is likely because more fibers are aligned with the loading direction in the aligned gels. Previous studies incorporating fiber- and tissue-level mechanics in simulated collagen networks have shown that during uniaxial tension, fibers that are not initially oriented in the loading direction first rotate and bend under small macroscopic deformations before aligning and elongating along the stretch direction (Stein et al. 2011; Nair et al. 2014). The transition from bending-dominated to stretching-dominated deformation has been implicated in strain hardening of collagen gels (Roeder et al. 2002; Stein et al. 2011; Nair et al. 2014). The fiber stretch-dominated loading likely occurs at a lower stretch magnitude in the aligned gels, exerting high loads on the encapsulated neurons, possibly activating them, and for a longer duration. The potentially lower bending-stretching transition threshold is because a large number of fibers in the aligned NCCs are already pre-oriented in the loading direction and so can be stretched axially to accommodate macroscopic deformation without going through the bending- or rotation-dominated phase of fibers. Despite differences in force, both the random and aligned NCCs experience comparable macroscopic strains (Tables 3.1 & 3.2). The magnitude of tissue-level strain has been shown to affect neuronal excitability and SP expression in innervated joint capsules (Khalsa et al. 1996; Lu et al. 2005a; Lee and Winkelstein 2009).

However, because macroscopic strains were similar across groups (Tables 3.1 & 3.2), any difference in protein expression that is observed here between random and aligned NCCs is taken as not being due to differences in the macroscopic strains, but may be attributed to altered macroscopic forces, axonal orientation and/or the micromechanical environment due to the changing collagen organization (Figure 3.3; Tables 3.1 & 3.2).

Findings reported in this chapter support the role of initial matrix structure in mediating neuronal activation in response to macroscopic stretch. ERK phosphorylation, a marker for cellular activation, can be induced by cellular deformation and is involved in nociception in neurons (Ji et al. 1999; Neary et al. 2003; Samarakoon and Higgins 2003; Dina et al. 2005; Crosby et al. 2014). Although ERK signaling is triggered in both the random and aligned NCCs by stretch (Figures 3.4 & 3.7), the increase is even greater in the aligned gels than in the random gels after uniaxial loading (Figure 3.4). This differential up-regulation of pERK dependent on collagen organization is likely due to the fact that local axonal stretch and forces are greater in the aligned NCCs as a result of directed axon outgrowth in the loading direction and the larger tissue-level forces (Tables 3.1 & 3.2; Figure 3.3). Tissue deformations and stresses in the fiber alignment direction can be borne by the elongation and strength of the collagen fibers in that direction (Korenczuk et al. 2017); the afferents also in that direction can interact with surrounding collagen fibers via cell-collagen adhesion (Tomaselli et al. 1993; Hynes 2002). As such, axons that are oriented in the loading direction in the aligned NCCs may undergo greater deformations due to the higher local collagen fiber strains, leading to more robust ERK activation (Figures 3.3 & 3.4). Further, the axons in aligned NCCs likely sustain greater

forces that may directly affect ERK-mediated neuronal responses via integrin-signaling and cytoskeletal tension (Guilluy et al. 2011; Hirata et al. 2017). Nevertheless, macroscopic force is unlikely the dominant contributor to elevated pERK expression, since pERK levels are similar in random and aligned NCCs after biaxial stretch despite the force being higher in the aligned gels (Figure 3.7). These findings suggest the importance of the microstructural mechanics of the ECM in contributing to the biomechanical mechanisms that underlie neuronal activation in ligaments.

Although pERK can mediate neuroplasticity and neuronal excitability (Cheng and Ji 2008; Gao and Ji 2009; Stamboulian et al. 2010), ERK activation is involved in many different signaling pathways that regulate various cellular cascades in addition to pain transmission (Kim and Choi 2010). In addition, since a variety of cells present ERK signaling, the pERK measured in the current study is not specifically localized to nociceptive neurons. For this reason, it should be noted that the DRG explant culture system used here (and throughout this thesis) contains heterogeneous cell populations, including different neuronal types and glia. The diverse neuronal populations, including mechanoreceptors and nociceptors, make it difficult to isolate those responses that are exclusive to only nociceptive neurons. Since SP is more specifically involved in pain signaling, its expression was used to better evaluate the effects of collagen organization on nociceptors.

SP is produced by peptidergic neurons, which are a subset of primary afferents that are primarily nociceptors and modulate pain after capsular ligament stretch injury (Lee and Winkelstein 2009; Basbaum et al. 2009; Kras et al. 2013b; Kras et al. 2015b).

SP has been previously found to increase in the innervated tissue and/or DRG in models of knee and facet joint pain (Lee and Winkelstein 2009; He et al. 2016). In contrast to pERK, neuronal regulation of SP depends *only* on the applied tissue strain for the uniaxial loading scenario, despite the NCC samples sustaining significantly different forces (Table 3.1; Figure 3.5). The macroscopic strains that increase axonal SP in both types of NCCs (Tables 3.1 & 3.2) directly map to facet capsule strains that induce pain in vivo (Lee and Winkelstein 2009; Dong et al. 2012). This strain-dependent SP modulation is consistent with its differential expression in DRG neurons in vivo graded by magnitude of uniaxial facet capsule stretch and pain severity (Lee and Winkelstein 2009). However, although both uniaxial and biaxial stretch induce higher forces in the aligned NCCs than the random NCCs (Tables 3.1 & 3.2), differential regulation in SP between random and aligned NCCs is *only* evident after biaxial loading (Figures 3.5 & 3.7). Since only macro-scale NCC strains and forces were measured in this study and microstructural mechanics were not assessed, it remains unknown how the same initial collagen organization, which likely leads to different ECM restructuring patterns during uniaxial and biaxial stretch, differentially regulates neuronal signaling in different loading conditions. Defining the *local* (on the order of 10-100μm) biomechanical environment of the neurons during stretch would provide a more specific measure of the direct mechanical cues that the neurons sense. For example, understanding the realignment and deformation of fibers that can directly interact with the neuronal cell surface (Khalsa et al. 2004; Jokinen et al. 2004) could provide a mechanical basis for local neuron deformation, activation and

nociception in tissues with varied collagen organization. However, it is challenging to experimentally measure the microscopic tissue stresses and strains during loading.

ATF3 in neurons, especially in their nuclei, is a mediator of the cellular stress response and is closely associated with neuronal survival and regeneration following axotomy (Kiryu-Seo et al. 2008; Bráz and Basbaum 2010; Hunt et al. 2012; Dubový et al. 2013). The induction of ATF3 in DRG neurons has been observed after peripheral nerve injury and in inflammatory pain from noxious chemical stimulation (Tsujino et al. 2000; Bráz and Basbaum 2010; Lindå et al. 2011; Hunt et al. 2012), suggesting that ATF3 can serve as a marker of axonal injury of sensory neurons. Although failure strains greater than 70% in the cervical facet capsule can induce afferent damage as indicated by morphological abnormalities (Kallakuri et al. 2008), it is still unknown whether less severe ligament strains also injure the innervating axons and if the degree of axonal injury is related to the magnitude of the applied strain. Findings in this chapter, for the first time, shows that local ATF3 expression is significantly correlated with the strain in the surrounding ECM, regardless of the collagen organization (Figure 3.8). At subfailure strains that can induce pain in vivo (10-40%) (Dong et al. 2012; Crosby and Winkelstein 2016), some neurons exhibit higher ATF3 expression than the unloaded control level (Figure 3.8), which suggests that painful subfailure tissue stretch may also lead to neuronal dysfunction although it may be to a lesser degree than the extent induced at higher failure strains. The stronger correlation that is evident between ATF3 expression and strain in the aligned NCCs compared to the random NCCs (Figure 3.8) implies that the neuronal dysfunction may be mediated by the local ECM organization together with

the applied macroscopic strains. The more variable ATF3 expression and the weaker correlation between ATF3 and strain in the random NCCs may be caused by micromechanical changes, such as collagen fiber realignment that is highly heterogeneous in the random NCCs during biaxial stretch (Sander et al. 2009a). In order to fully understand the role of macro- and micro-scale ECM mechanics in modulating neuronal dysfunction, the relationships between ATF3 expression and the local ECM reorganization and deformation require further elucidation.

Although this set of studies used an idealized simplified in vitro model whose structural anisotropy and fiber density are lower than those in sub-regions of the native ligaments exhibiting long parallel collagen bundles, this NCC system enabled assessing the relationships between collagen organization and neuronal responses in the context of facet capsular ligament pain. Indeed, the initial collagen fiber organization was found to not only modulate macroscopic mechanics and axonal outgrowth, but to *directly* and *differentially* regulate stretch-initiated neuronal signals. The differences in neuronal regulation of pERK and SP are possibly due to the fact that those molecules are involved in *different* cell signaling cascades, with SP being more nociceptive-specific (Basbaum et al. 2009; Kras et al. 2013b; Kras et al. 2015b) and pERK playing a role in a host of cellular responses to external stimuli, including regulation of neuronal activity and excitability (Ji et al. 1999; Neary et al. 2003; Samarakoon and Higgins 2003; Dina et al. 2005; Kim and Choi 2010). Fully understanding the local biomechanical factors that trigger the modification of these and other signaling molecules in different structural collagen matrices requires further investigation of both the micromechanical environment

and the intracellular signaling pathways of afferents. Studies evaluating the effects of varied degrees of fiber alignment and density, which are not uniform within and between facet capsular ligaments (Yamashita et al. 1996; Quinn and Winkelstein 2008; Ban et al. 2017), on neuronal responses and pain, would help to understand the responses of the native ligaments and also to provide more physiologically relevant parameters for the NCC system to better simulate that tissue. Nevertheless, these findings show that collagen organization differentially modulates pain-related neuronal responses likely through the macro- and micro-scale mechanics.

## 3.7. Conclusions & Integration

Work presented in this chapter shows that activation and SP-mediated nociception of sensory neurons can result from stretch of their surrounding collagen matrix and is differentially modulated by the ECM structure. The imposed MPS in uniaxial and biaxial loading (0.223±0.067) is supraphysiologic and can induce pain in vivo. The C6/C7 human facet capsule, a common source of injury and pain associated with neck trauma, undergoes a maximum physiologic strain of approximately 6% during normal spine motions and can reach to a strain of 35% in simulated neck trauma (Panjabi et al. 1998a; Pearson et al. 2004). Cervical facet capsule strains of 5-15% are found to activate its nociceptors (Lu et al. 2005a; Lu et al. 2005b) and capsule strains of 8-30% are sufficient for pain generation (Dong et al. 2012). Consistent with prior reports, the studies in this chapter show that macroscopic stretch exceeding the physiologic strains of the facet capsule produces neuronal activation and nociception, as evidenced by increased axonal

pERK and SP expression in the NCCs relative to unloaded control levels, regardless of collagen organization (Figures 3.4, 3.5 & 3.7). No difference in pERK and SP expression is found for either random or aligned NCCs between uniaxial and biaxial stretch imposing similar MPS (Table 3.2; Figure 3.9). These findings suggest that neurons may be more sensitive to strain magnitude of tissues than their anatomy or boundary condition. Yet, the relationships between macroscopic tissue strains and the responses of the innervating fibers are not well-defined in the context of pain. It remains unclear whether physiologic ligament stretch also affects the intracellular signaling cascades of those cells in the ECM and how different strain levels may alter the microenvironment of mechanosensitive neurons.

Although the applied tension used here induces similar tissue-level MPS in both the random and aligned NCCs, the corresponding forces are greater in the aligned NCCs than those with random fiber orientation (Tables 3.1 & 3.2). Macroscopic deformation and tissue forces likely differentially affect the local fiber and network mechanics in the random and aligned NCCs (Sander et al. 2009; Vader et al. 2009), leading to differential modulation of pain-related neuronal responses (Figures 3.4, 3.5 & 3.7). Current findings point to the possible contributions of collagen organization to the regional differences in tissue mechanics (Quinn and Winkelstein 2008; Quinn and Winkelstein 2009; Ban et al. 2017), differential regulation of pain signaling proteins in afferents (Lee and Winkelstein 2009; Dong et al. 2012) and varied pain symptoms (Kwan and Fiel 2002), all of which are observed with facet capsular ligament injury (Kwan and Fiel 2002; Quinn et al. 2007; Bogduk 2011; Dong et al. 2012; Ban et al. 2017). This study also sheds light more

broadly on pain development in other joint ligaments, such as the hip and knee joint capsules.

While findings presented in this chapter suggest that pERK expression indicating neuronal activation (Gao and Ji 2009) may be regulated by tissue deformation and collagen orientation, only macro-scale mechanical measurements were acquired in these studies. Work revealing the local biomechanical mechanisms by which tissue strains and fiber alignment affect neuronal activation and dysfunction will provide insights into how different magnitudes of macroscopic tissue deformations trigger different cascades of local mechanical and cellular events that lead to the presence or absence of pain. The studies in Chapter 4 utilize this same NCC system, QPLI and computational modeling to investigate how tissue stretch with different strain magnitudes and rates affect neuronal deformation, orientation and pERK expression, and how those strains reorganize and deform collagen fibers in random NCCs. Based on the findings presented in this chapter and Chapter 4 suggesting the importance of tissue-level strains and microstructural mechanics of the ECM in modulating neuronal responses, the studies in Chapter 5 and Chapter 6 probe the multi-scale structural and mechanical changes in the human cervical facet capsule during excessive ligament stretch.

# Chapter 4

# Tissue Strain, Collagen Reorganization & Neuronal Activation

*This chapter has been adapted from:*

Zhang S, Cao X, Stablow AM, Shenoy VB, Winkelstein BA. Tissue strain reorganizes collagen with a switchlike response that regulates neuronal extracellular signal-regulated kinase phosphorylation in vitro: Implications for ligamentous injury and mechanotransduction. *Journal of Biomechanical Engineering*, 138(2):021013, 2016.

## 4.1. Overview

Excessive stretch of innervated ligaments is a complex injury that can lead to both disruption of the collagenous matrix and altered neuronal morphology and function (Khalsa et al. 1996; Lu et al. 2005a; Cavanaugh et al. 2006; Kallakuri et al. 2008; Quinn and Winkelstein 2011; Crosby et al. 2014). For example, gross failure of the facet capsular ligament has been shown to induce swelling of the innervating nerve fibers and to produce transient pain behaviors in animal models (Kallakuri et al. 2008). Although supraphysiologic subfailure loading of the cervical facet capsule does not cause visible tissue rupture, it results in local collagen disorganization (Quinn and Winkelstein 2008; Quinn and Winkelstein 2009). Facet stretch to those same subfailure strains also activates neuronal afferents embedded in the fibrous matrix (Lu et al. 2005a; Crosby et al. 2014) and induces persistent pain in vivo (Lee et al. 2004b; Dong et al. 2012; Ita et al. 2017b).

Unlike a direct mechanical insult to neurons, the effects of excessive ligament stretch on neuronal deformation and singling is confounded by the ECM structure and cell-ECM interactions. Tissue strains and stresses are likely transmitted to neurons and mediate their activation via remodeling of the local collagen matrix that surrounds the neurons, as evidenced by the stretch-induced fiber realignment that is observed in capsular ligaments (Quinn et al. 2007; Quinn and Winkelstein 2009; Voycheck et al. 2014). A reorganizing ECM under stress can exert local forces (Sander et al. 2009a) and activate integrin receptors on the surface of cells embedded in it (Katsumi et al. 2005; Cao et al. 2015). Integrin activation can regulate neuronal activity and contribute to the development of pain via interaction with specific second messenger cascades, such as the ERK pathway in afferents (Khalsa et al. 2004; Dina et al. 2005). Collectively, these prior reports suggest an altered local ECM environment as a possible mechanism by which external tissue stretch modulates responses of the enclosed neurons.

Initial collagen organization of neuron-seeded collagen NCC gels has been shown to mediate stretch-induced neuronal ERK phosphorylation, with neuronal pERK increasing more after NCC loading of collagen matrices with more aligned fibers (Chapter 3; Zhang et al, 2017). Because the direction of fiber alignment relative to the direction of loading has been shown to affect the microstructure of fibrous tissues (Korenczuk et al. 2017), it is possible that the fiber kinematics differ in isotropic and anisotropic collagen networks during macroscopic stretch and exerts different loads on the embedded neurons depending on the fiber organization in their surrounding ECM. Fibers in the ECM realign towards the direction of loading and elongate to accommodate

macroscopic deformations in ligaments, tissue analogs and simulated fibrous networks (Tower et al. 2002; Sander et al. 2009a; Vader et al. 2009). Since the macro-scale strain of joint capsular ligaments has been shown also to modulate the activity of the embedded neurons (Khalsa et al. 1996; Lu et al. 2005a), fiber motions and local stresses and strains due to capsule stretch likely dictate the biomechanical pathomechanisms by which neurons are loaded and respond to non-physiologic deformations. Although fiber kinematics in soft tissues and collagen constructs and neuronal activity during facet capsule stretch both have been previously investigated (Tower et al. 2002; Lu et al. 2005a; Vader et al. 2009), no study has assessed the simultaneous collagen fiber reorganization and neuron activation during macro-scale tissue deformation. As such, the relationships between collagen fiber mechanics, neuronal activation and macroscopic tissue strains are not fully defined.

This chapter summarizes a subset of studies under Aim 2, using combined experimental and modeling approaches to define the behaviors of neurons and the collagen fibers that surround them in responses to macroscopic deformation. This work begins to define how tissue strain is translated in to neuronal loading and activation, and begins to test the hypothesis that tissue-level strains mediate neuronal pERK expression likely via changes in the local collagen fiber mechanics. Integration of an in vitro neuron-collagen gel system similar to the NCC model described in Chapter 3 and QPLI (Tower et al. 2002; Quinn 2010) together enables assessment of the neuronal shape, orientation and pERK expression, macroscopic forces and strains, and real-time collagen reorganization during stretch. Besides strain magnitude, the loading rates experienced by

the facet capsular ligament can vary during neck trauma (Pearson et al. 2004; Panjabi et al. 2006) and affect the tissue mechanics and neuronal responses. Ligament and neuronal responses to mechanical loading are dependent on the loading rate due to their viscoelastic properties (Solomonow 2004; Lu et al. 2006; Cullen et al. 2011). Both the applied strain magnitudes and the loading rate can modulate tissue forces, collagen kinematics and neuronal viability and activity (Noyes et al. 1974; Khalsa et al. 1996; Solomonow 2004; Lu et al. 2005a; Vader et al. 2009). Therefore, relationships between tissue mechanics and neuronal responses were evaluated under four different loading conditions with two different strain magnitudes and two different strain rates in this chapter. Although the QPLI system provides methods to measure collagen fiber orientation (Tower et al. 2002; Quinn and Winkelstein 2011), it is difficult to assess the fiber-level strains experimentally during loading. Therefore, a finite element-based discrete fiber network (DFN) model was used to predict fiber strains under macroscopic stretch matching experimental conditions.

The first set of experiments (described in Section 4.3) was performed using NCCs containing dissociated cortical neurons, which is a commonly used in vitro model to study neural mechanobiological phenomena within three-dimensional microenvironments (LaPlaca et al. 2007; Cullen et al. 2007b; Irons et al. 2008; Cullen et al. 2011). Both cortical neurons from the brain and the primary sensory neurons that innervate peripheral tissues have been reported to sustain similar morphological impairments and exhibit electrophysiological changes in response to stretch injury (Lu et al. 2005a; Kallakuri et al. 2008; Tang-Schomer et al. 2010; Hemphill et al. 2011; Jaumard et al. 2011; Magou et

al. 2015). However, those two neuronal phenotypes are functionally different and experience different extracellular environments in vivo (Topp and Boyd 2006; Mietto et al. 2015a). Those local environments can alter the post-injury cellular cascades in neurons, which can induce distinctly different inflammatory responses and regenerative capacity after mechanical stimulation (Siddique and Thakor 2014; Mietto et al. 2015a). Therefore, an additional pilot study was performed using NCCs with DRG explants to better mimic the environment and response of neuronal afferents in innervated ligaments. Similarities and differences between stretch-induced ERK activation were evaluated separately in three-dimensional cortical cultures and DRG cultures. That work is presented in Section 4.4.

## 4.2. Relevant Background

Although ligaments function to primarily stabilize joints, they are increasingly recognized as sensory organs due to their afferent innervation, providing both mechanoreceptive and nociceptive feedback (Schultz et al. 1984; Yahia and Newman 1991; Petrie et al. 1998; Kallakuri et al. 2012). The mechanical and neurological functions of ligaments can produce a variety of musculoskeletal pathologies (Solomonow 2004). For example, excessive facet capsular ligament stretch that produces supraphysiologic strains induces damage to the collagen network, axons of the innervating neurons, persistent afferent firing, spinal neuronal hypersensitivity, and altered neurotransmitter expression, as well as pain (Lu et al. 2005a; Quinn et al. 2007; Kallakuri et al. 2008; Lee et al. 2008; Lee and Winkelstein 2009; Quinn et al. 2010a;

Quinn et al. 2010b; Crosby et al. 2013; Crosby et al. 2014; Kras et al. 2015a). Although injurious ligament loading is known to activate nociceptors for pain signaling (Lu et al. 2005b; Crosby et al. 2014), the local biomechanical mechanisms by which neurons are injured, their biomechanical vulnerability, and the resulting physiological dysfunction are still not fully understood.

Cells respond to changes in the mechanical microenvironment via adhesive interactions with the ECM (Rosso et al. 2004; Barros et al. 2011). Neurons embedded in a collagen matrix have passive mechanical roles due to their lack of contractility and high compliance compared to matrix that surrounds them (Wenger et al. 2007; Lopez-Garcia et al. 2010; Spedden et al. 2012). They may be loaded and reoriented by the surrounding collagenous matrix because of fiber deformation and realignment during tissue loading. Studies using advanced imaging techniques and computational modeling have found that collagen fibers realign and generate fiber forces to accommodate macroscopic deformation in both ligaments and artificial collagen networks (Tower et al. 2002; Quinn and Winkelstein 2009; Sander et al. 2009a). Ligaments can undergo a variety of magnitudes and rates of strains during injury (Panjabi et al. 1998a; Schenck et al. 1999). Strain magnitude correlates with ECM abnormalities and neuronal firing in joint capsules (Khalsa et al. 1996; Lu et al. 2005a; Quinn 2010); strain rate is also found to modulate ligament tension (Noyes et al. 1974; Solomonow 2004), collagen reorganization under cyclic loading (Vader et al. 2009), and cell viability and permeability (Geddes et al. 2003; Cullen et al. 2007b). Therefore, both strain magnitude and rate are hypothesized to regulate the micromechanical environment of the neurons embedded in the ligament and,

thereby, modulate their responses during tissue loading. However, no study has defined the relationships between tissue-level mechanics, collagen micromechanics and neuronal responses under different loading conditions for ligament systems with embedded neurons.

Deformation of neuronal membranes can activate mechanosensitive ion channels and cell surface receptors, which transform the applied mechanical stress into electrical signals and modulate expression of a host of molecules involved in a wide range of cellular functions (Martinac 2004; Raoux et al. 2007; Delmas et al. 2011; Hemphill et al. 2011). Activation of the ERK pathway by phosphorylation can be induced by cellular deformation (Neary et al. 2003; Samarakoon and Higgins 2003; Chaturvedi et al. 2008). Further, phosphorylation of ERK can be induced within one minute by noxious stimuli and has been hypothesized to mediate neuronal plasticity and to increase neuronal excitability by modulating the gating properties of specific sodium channels (Cheng and Ji 2008; Gao and Ji 2009; Stamboulian et al. 2010). As such, expression of phosphorylated ERK has been used as an indicator of neuronal activation in both the peripheral and central nervous systems (Ji et al. 1999; Cheng and Ji 2008; Gao and Ji 2009; Kras et al. 2013c). Investigating neuronal deformation and activation due to external tissue loading is often confounded by the complex mechanics of fibers in the ECM. Integrated assessment of ERK phosphorylation in neurons and the mechanical responses of the surrounding fibrous matrix are required to understand how tissue loading is translated into neuronal signals. Reorganization and deformation of the local collagen networks and fibers during tissue stretch may be important biomechanical cues that

trigger mechanotransduction in the embedded neurons.

The mechanical and sensory functions of ligaments are commonly investigated by biomechanical testing of isolated tissues or using animal models of ligament injury and pain. Although mechanical testing of isolated ligaments enables evaluating tissue mechanics across different length scales, measuring physiological cellular responses is challenging due to complications in maintaining the viability of the innervating afferents. In addition, it is difficult to measure collagen fiber and network biomechanics during ligament loading in vivo because the tissue of interest needs to be positioned in between the light source and the circular analyzer to enable polarized light imaging. Several groups have combined polarized light imaging with mechanical testing in order to define collagen fiber kinematics in real time during loading of isolated ligaments and cell-compacted collagen-based gels (Tower et al. 2002; Quinn and Winkelstein 2009; Sander et al. 2009b; Lake and Barocas 2011). Although those integrated imaging and mechanical studies provide evidence for stretch-induced collagen fiber realignment, they are unable to measure the microscopic fiber stresses and strains because polarized light imaging only provides structural information about the collagenous tissue.

Computational models have been developed to perform parametric studies of the properties of a fibrous matrix with cells embedded in it, and have been used to predict how different levels of macroscopic strains and cell contraction affect collagen fiber deformation and alignment (Evans and Barocas 2009; Sander et al. 2009a; Hadi et al. 2012b; Aghvami et al. 2013; Nair et al. 2014). Previously developed finite element-based DFN models represent 2D fiber networks containing randomly organized linear elastic

fibers (Nair et al. 2014). They provide useful computational approaches to study the mechanical behavior and cell-mediated ECM remodeling in biopolymer networks (Chen et al. 2011; Nair et al. 2014). Among a variety of utilities, a DFN model has been used to predict heterogeneous fiber deformations and realignment due to cell contraction that leads to force transmission in randomly organized networks (Nair et al. 2014), providing a platform to estimate microscopic fiber mechanics. Although that DFN model can predict fiber-level strains that cannot be measured in NCC experiments, experiments are still needed to construct and validate an image-based model that mimics the NCC microstructure. Therefore, a combined experimental and modeling approach is needed to assess both the local collagen mechanics and neuronal responses, as well as to evaluate their relationships.

The goal of the studies in this chapter was to define if, and how, macroscopic tissue deformations modulate neuronal responses via regulation of microstructural collagen mechanics, using complementary experimental and computational methods. In the first study, a 3D in vitro NCC system was used to measure macro-scale tissue mechanics, matrix reorganization and neuronal responses. Separate groups of NCCs were distracted to displacement magnitudes simulating those strains sustained by the facet capsular ligament that are associated with either non-painful (8% strain) or painful (16% strain) states in vivo (Lu et al. 2005a; Dong et al. 2011; Dong et al. 2012). Two separate rates were used – 0.5mm/s (1%/s) and 3.5mm/s (7%/s) – to simulate loading conditions across a seven-fold difference in strain rate. These strain rates are similar to those used in quasi-static testing of isolated ligaments and have been shown to correspond to normal

joint motion and slow-rate injury (Crisco et al. 2002; Bonner et al. 2015). Although a 4mm displacement could not be achieved at a rate greater than 3.5mm/s using the mechanical testing machine that was available for this work, quasi-static loading at comparable rates has been shown to induce facet pain in vivo (Lee et al. 2004b; Quinn et al. 2010b).

Neuron shape and orientation, expression of pERK in neurons, and collagen fiber realignment after NCC loading were each evaluated to define the effects of strain magnitude and loading rate on the neuronal responses and collagen reorganization. The neuronal aspect ratio was measured to define the relationship between neuronal deformation and the applied NCC strain. Furthermore, the orientation of the long-axis of neurons was assessed to investigate the direction of neuronal elongation and reorientation during reorganization of the surrounding collagen networks at different loading rate and strain magnitude. Logistic regression was used to determine if a strain threshold for neuronal activation exists between the physiologic and non-physiologic mechanical loading regimes and if those regimes relate to collagen reorganization. In addition, a DFN model was created using the collagen fiber density, length and orientation distributions of the NCCs and that model was validated by comparing the predicted fiber reorientation to that measured experimentally. Then, that DFN model was used to predict fiber strains in order to begin to understand the local biomechanical mechanisms by which neurons are loaded and respond to physiologic and non-physiologic tissue deformations.

## 4.3. Studies Using 3D Cortical Cultures

### 4.3.1. Methods

#### 4.3.1.1 Neuron-Collagen Construct Model

All animal procedures were approved by the Institutional Animal Care and Use Committee at the University of Pennsylvania. The cells used for the cortical culture were a kind gift from Dr. David F. Meaney at the University of Pennsylvania. Cortical neurons were isolated from embryonic day 18 Sprague-Dawley rats as described previously (Patel et al. 2015). Briefly, timed pregnant rats were anesthetized with 5% $CO_2$ and terminated by cervical dislocation. Embryos were surgically removed and the neocortical tissue was dissected, dissociated in trypsin (1.4mg/ml; Life Technologies; Frederick, MD) and DNase (0.6mg/ml; Roche Applied Science; Indianapolis, IN) for 15 minutes at 37°C, and underwent trituration and filtration through Nitex mesh (Crosswire Cloth; Bellmawr, NJ). Isolated cells were re-suspended in plating medium containing Minimum Essential Media with Earle's salts (Life Technologies; Frederick, MD) and GlutaMAX (Life Technologies; Frederick, MD) supplemented with 0.6% D-glucose (Sigma-Aldrich; St. Louis, MO), 1% Pen-Strep (Life Technologies; Frederick, MD), and 10% horse serum (Life Technologies, Frederick, MD), and plated on poly-D-lysine (0.08mg/ml; Sigma-Aldrich; St. Louis, MO) and laminin-coated (0.001mg/ml; BD Biosciences; San Jose, CA) T75 flasks.

A collagen solution was prepared using rat tail collagen I (2mg/ml; Corning Inc.; Corning, NY) and cast in a dog-bone shaped Teflon mold for gelation at 37°C overnight to form a gel with randomly oriented collagen fibers (Lake and Barocas 2011). The dog-

bone shaped construct is 62.5mm long, 23.5mm wide and 3mm thick with the middle narrow section being 31.5mm long and 7.5mm wide (Figure 4.1). Neurons were then re-plated onto the prepared collagen gels at a density of $10^7$ cells/ml (~4500 cells/$mm^2$) (Figure 4.1) and were allowed to grow in the feeding medium containing Neurobasal Media (Life Technologies, Frederick, MD) supplemented with 2% B-27 (Life Technologies, Frederick, MD), 0.2% GlutaMAX and 1% Pen-Strep for 2 days in vitro (DIV) in a humidified 37°C 5% $CO_2$ incubator. Additional collagen solution was added on DIV4 to encapsulate the neurons in the NCC construct.

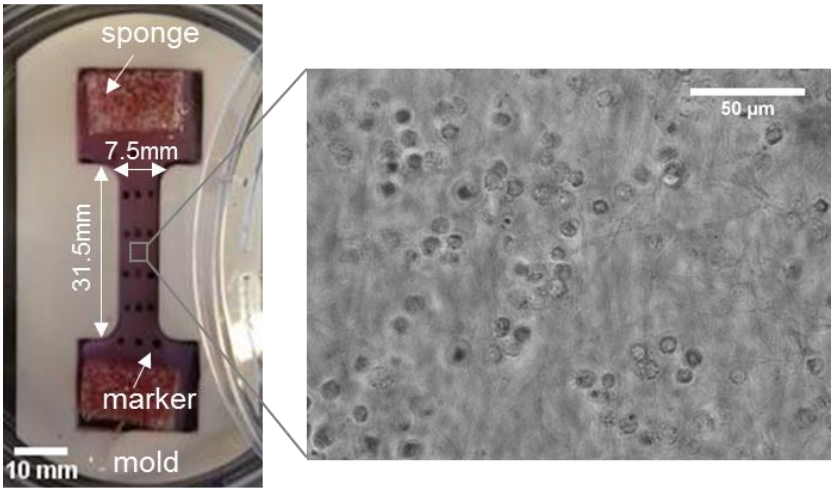


**Figure 4.1.** Dog-bone shaped NCC. The 3D cortical neuron-collagen cultures are created in a dog-bone shaped Teflon mold with sponges placed at the two ends to be gripped in the mechanical testing machine. A representative phase contrast image shows the cortical neurons embedded in the NCC before loading.

#### 4.3.1.2. Mechanical Testing & Polarized Light Imaging

On DIV8, NCCs were distracted at 0.5mm/s or 3.5mm/s to displacements simulating non-painful (4mm; n=8 0.5mm/s, n=7 3.5mm/s) and painful (8mm; n=9 each

of 0.5mm/s or 3.5mm/s) facet capsular ligament loading in vivo (Lu et al. 2005a; Dong et al. 2011; Dong et al. 2012). Unloaded NCCs (n=5) were also included as controls for neuronal shape and ERK phosphorylation in an unloaded resting state. NCCs were immersed in a PBS-filled chamber and loaded by an Instron 5865 (Instron; Norwood, MA) that was integrated with a QPLI system (Figure 4.2). Fiber alignment maps were acquired from the NCCs before, during and after loading using the QPLI system, as described previously (Quinn and Winkelstein 2009; Quinn et al. 2010a).

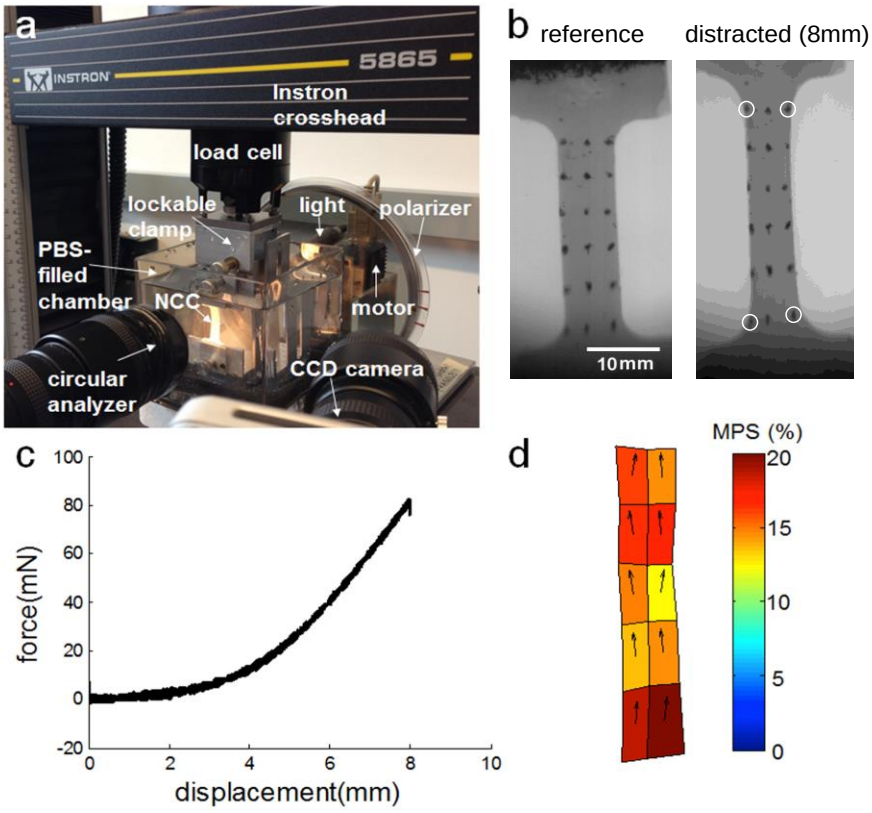


**Figure 4.2.** Experimental test set-up and representative data for dog-bone shaped NCCs. **(a)** The mechanical testing system is integrated with the elements of the QPLI system. Representative images show **(b)** an NCC in an unloaded reference state and at 8mm of distraction with markers used for elemental (black dots) and bulk (white circles) strain measurements, **(c)** the corresponding force-displacement response, and **(d)** strain map showing both the color magnitude and directions of MPS at 8mm displacement in each four-node strain element.

The QPLI system consists of a fiber-optic illuminator (Dolan-Jenner Industries Inc.; Boxborough, MA), a linear polarizer (Edmund Optics; Barrington, NJ) that rotates at 750rpm and a customized circular analyzer attached to a high-speed camera (Phantom-v9.1; Vision Research Inc; Wayne, NJ) (Figure 4.2a). The birefringent NCC sample was placed between the rotating polarizer and the circular analyzer (Figure 4.2a). Images were collected at 500fps with a resolution of 14.5pixel/mm, and pixel-wise fiber alignment maps were created in MATLAB (R2014a, MathWorks Inc.; Natick, MA) based on a harmonic equation using every 20 consecutive images (Tower et al. 2002; Quinn and Winkelstein 2008). Circular variance is a measure of the spread of dihedral angles, with a lower value representing tighter clustering (MacArthur and Thornton 1993; Miller et al. 2012b), and was used to quantify the fiber alignment before, during and after loading for each NCC. In order to quantify the degree of fiber realignment, the circular variance measured at the maximum displacement of each NCC was normalized to the corresponding unloaded reference level, which was measured before any load was applied to the same NCC.

The force and displacement data collected at 1kHz during loading (Figure 4.2c) were used to ensure that no failure occurred and to determine the maximum stiffness and the maximum force during NCC loading. Stiffness was calculated by differentiating the force-displacement data using a centered finite difference approximation at 0.5mm-displacement increments throughout loading, as described previously (Quinn and Winkelstein 2008). In addition, a grid of fiducial markers was placed on each NCC that was used to track the regional deformations of the NCC and to estimate strains in ten

four-node elements on each NCC surface (Figure 4.2). Marker displacements were recorded at 500fps during loading and processed in MATLAB to construct a finite element mesh in LS-DYNA (Livermore Software Technology Corp.; Livermore, CA). That mesh and marker displacement were used to estimate maximum principal strain (MPS) maps (Figure 4.2d) (Lee et al. 2006; Weisshaar et al. 2010). Bulk strain was defined as the overall MPS across the entire gel and was measured by tracking the four markers in the corners of the marker grid and using them to create a single four-node element for each NCC (Figure 4.2b). The MPS estimated in each of the ten four-node elements of each gel was also calculated as the elemental strain; elemental strains were used to relate regional strains to neuronal responses.

At the limit of the applied distraction (either 4mm or 8mm depending on the group) the NCCs were held fixed using customized lockable clamps (Figure 4.2a). together, the clamps and sample were removed from the mechanical test frame and chemically fixed for immunocytochemistry processing, in order to measure neuron deformation and orientation. All NCCs were chemically fixed using 4% paraformaldehyde (Sigma-Aldrich; St. Louis, MO) in PBS for 2 hours at room temperature and stored in 30% sucrose (Sigma-Aldrich, St. Louis, MO) in PBS at 4°C.

#### 4.3.1.3 Assessment of Cellular pERK Expression, Shape & Orientation

Fixed NCCs were blocked using 10% normal goat serum (Vector Laboratories; Burlingame, CA) with 0.3% Triton-X100 (Bio-Rad Laboratories; Hercules, CA) in PBS for 2 hours and treated with rabbit anti-pERK antibody (1:200; Cell Signaling

Technology; Danvers, MA) and chicken anti-βIII-tubulin antibody (1:200; Abcam; Cambridge, MA) for 36 hours at 4°C to label pERK and neurons, respectively. NCCs were then washed with PBS and incubated for 2 hours in the secondary antibodies goat anti-rabbit Alexa Fluor 568 (1:1000; Life Technologies; Frederick, MD) for pERK and goat anti-chicken Alexa Fluor 488 (1:1000; Life Technologies; Frederick, MD) for βIII-tubulin. Three images of each element of each NCC (Figure 4.2), were taken using the 40X objective of a Zeiss LSM510 confocal microscope (1024x1024 pixels; Carl Zeiss Inc.; Thornwood, NY). Automated densitometry quantified labeling of total pERK in each image by measuring the percent of positively labeled pixels (Figure 4.3), as described previously (Zhang et al. 2013; Kras et al. 2014). The MATLAB code used for automated densitometry is provided in Appendix D. Expression of pERK was averaged across images from each element of each NCC sample to define the elemental pERK expression in that element. The elemental pERK expression in loaded gels was normalized to the expression in matching unloaded control NCCs that were similarly

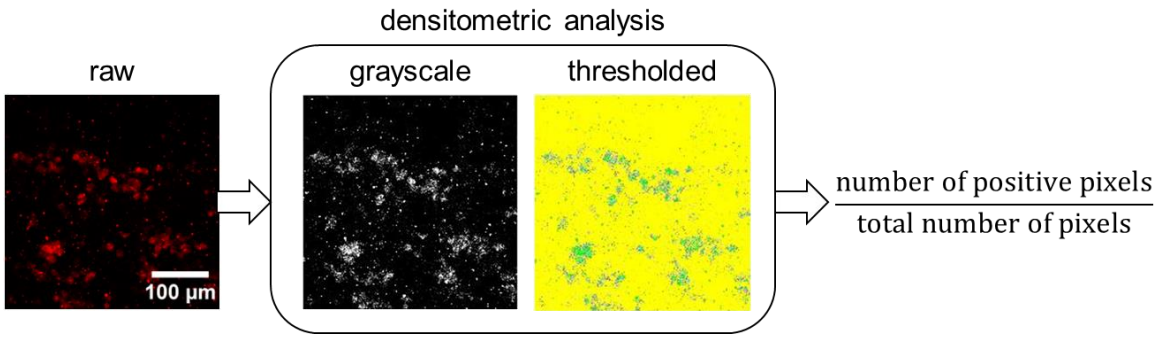


**Figure 4.3.** Overview of automated densitometry for quantification of pERK expression. Raw confocal images of pERK are converted to grayscale images and binarized using a user-specified threshold, determined based on images of unloaded controls. Image processing and calculation of the percent positive pixels over the total number of pixels are performed using a customized MATLAB code.

immunolabeled in order to account for any differences between processing. The mean normalized pERK expression of each loading group was calculated by averaging the values across all elements from all NCCs within each group.

Neuronal structure was also measured using the confocal images. The cellular aspect ratio and cell orientation were measured by an assessor blinded to groups in 30 representative cells sampled throughout each NCC (3 cells/element) using ImageJ (National Institutes of Health, Bethesda, MD). Cellular aspect ratio was defined as the ratio between the cell's long and short axes (Figure 4.4a); cell orientation was defined as the angle difference between the long axis of the neuron and the applied loading direction (Figure 4.4b). To account for differences in the initial cell shape and orientation between NCCs, phase contrast images of neurons were taken prior to mechanical loading to serve as unloaded references and the mean aspect ratio from 30 representative cells was computed for each NCC before loading (Figure 4.1). The normalized aspect ratio after loading was defined as the aspect ratio measured in the confocal image divided by the

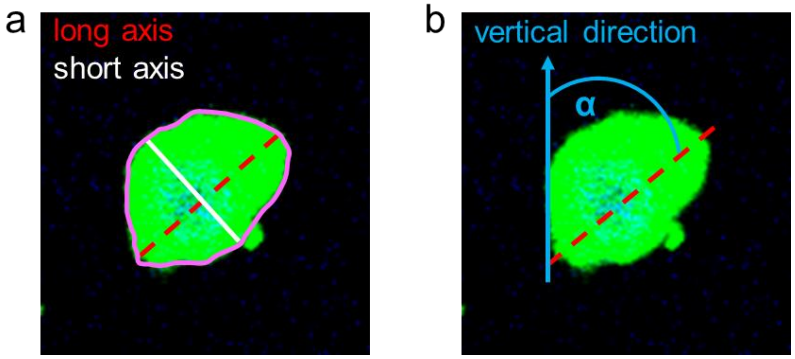


**Figure 4.4.** Neuronal aspect ratio and orientation measurement. **(a)** Aspect ratio, defined as the length ratio of the long axis (dashed red line) to the short axis (solid white line), is measured automatically using ImageJ software by tracking the cell boundary (pink line). **(b)** The orientation of each neuron is captured by the angle ($\alpha$) between the neuron's long-axis and the vertical loading direction (blue arrow).

mean aspect ratio from the unloaded NCCs, and was averaged within each element. Orientation angles were only measured in non-circular cells exhibiting identifiable long-axes among the 30 selected cells from each NCC.

#### 4.3.1.4. Statistical Analyses

All statistical tests were performed in JMP (version 11; SAS Institute; Cary, NC), with significance determined at $p<0.05$. Differences in the maximum force and stiffness, pERK expression, normalized circular variance and cell orientation angles between different groups were evaluated using separate two-way ANOVAs, with distraction magnitude and rate as the two factors. If significant differences were detected due to the interaction effect of strain magnitude and rate, post-hoc Tukey HSD tests were performed.

The relationships between elemental MPS and each of the normalized pERK expression and the normalized aspect ratio were tested by separate correlation analyses using linear regression models for each distraction rate separately. The relationship between elemental MPS and collagen fiber realignment was also examined using a linear regression model. Each of the mean circular variance and the mean MPS were computed separately at the 0.5mm displacement increments during loading, and circular variance was plotted against MPS for regression analysis. A two-phase linear regression model was used to test the correlation between the circular variance and MPS and to estimate the transition strain between the two phases (Koul et al. 2003; Diniz and Brochi 2005; Atanasov 2010), since it can fit the apparent segmented response of fiber realignment

with respect to strain. For each regression, the significance was evaluated using F-tests.

Strain thresholds for elevated ERK phosphorylation were estimated using logistic regressions (Bain et al. 2001; Hubbard and Winkelstein 2008). Normalized pERK expression was binarized based on if ERK phosphorylation was increased due to loading. If the normalized pERK expression in an element was greater than 1 immediately after loading, ERK phosphorylation in that element was considered to be higher than unloaded control levels. If the normalized pERK expression was equal to or slightly less than 1, then no elevation in ERK phosphorylation was detected and the binarized expression level was denoted as 0. Unloaded controls also were included and the associated pERK expression was taken as 0. Binarized pERK expression was plotted against elemental MPS and fitted using logistic regressions. The $50^{th}$- and $95^{th}$-percentile MPS with 95% confidence intervals for elevated ERK phosphorylation were determined for, and compared between, groups undergoing different loading rates.

#### 4.3.1.5. DFN Modeling & Collagen Fiber Mechanics

In order to evaluate collagen micromechanics during NCC loading, an image-based DFN model was constructed based on the NCC collagen structure. The average microstructure of the collagen network in the NCCs was measured by immunolabeling. Four unloaded control gels were immunolabeled for collagen I using a mouse anti-collagen I antibody (1:400; Abcam; Cambridge, MA) and a secondary goat anti-mouse Alexa Fluor 488 antibody (1:1000; Invitrogen; Carlsbad, CA). NCCs were imaged using confocal microscopy as described above in Section 4.3.1.3. The average collagen fiber

density and length measured from confocal images of the control NCCs were used as network parameters to create a comparable fibrous network (Figure 4.5) using previously described methods (Nair et al. 2014). Fiber length and density were measured to be 28.7μm and 9621 fibers/mm$^2$ in the NCC, and fiber diameter was assumed to be 250nm (Nair et al. 2014). The initial fiber orientation distribution was assigned to be uniform, because the NCCs were created with random fiber organization. Collagen fibers were treated as linear elastic materials with rigid cross-links and modeled using shear flexible Timoshenko beam elements in ABAQUS (Version 6; Dassault Systemes; Providence, RI) (Nair et al. 2014). Each fiber section between two crosslinks was meshed into four elements based on prior convergence studies with this DFN model (Nair et al. 2014). Uniaxial tension was applied to the network model with the same boundary conditions as in the NCC experiment (Figure 4.5). The bottom of the network was held fixed and the top boundary edge was distracted along the vertical direction, with the sides allowed to undergo unconstrained movement. Fiber orientation and axial strains were computed throughout the network before loading and at bulk strains of 7% and 16% which correspond to strain magnitudes that are either non-painful or painful in vivo, respectively (Lu et al. 2005a; Dong et al. 2011; Dong et al. 2012). To quantify the changes in the fiber angle distribution after stretch in the DFN model, a Chi-squared goodness-of-fit approach was used to measure the deviation from the initial uniform fiber angle distribution, with a higher Chi-squared value indicating a less uniform distribution (McDonald 2014).

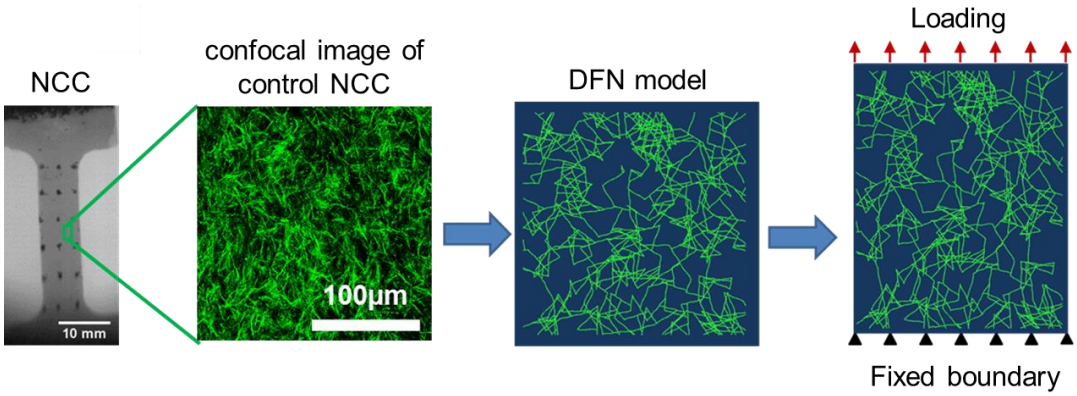


**Figure 4.5.** A schematic overview of the DFN model. The model was constructed using the confocal images of collagen in elements of the unloaded control NCCs, as well as the boundary conditions simulating experimental conditions for the NCCs.

### 4.3.2. Results

#### 4.3.2.1. Strain-Dependent Regulation of pERK Expression

Both distraction magnitude and rate alter the maximum force ($p<0.006$) and maximum stiffness ($p<0.001$) of the loaded NCCs. Not surprisingly, increasing the magnitude of distraction significantly increases both the bulk MPS ($p<0.001$) and the mean elemental MPS ($p<0.001$) (Table 4.1). The strains in the NCC are doubled for corresponding doubling of the applied distraction, regardless of the loading rates used in this study (Table 4.1).

The amount of ERK phosphorylation increases with the extent of loading (Figure 4.6) and is correlated with the local elemental MPS (Figure 4.7). The amount of pERK normalized to control levels is significantly elevated in NCCs distracted to 8mm compared to the levels expressed at 4mm, for both of the 0.5mm/s ($p<0.001$) and 3.5mm/s ($p=0.002$) distraction rates (Figure 4.6). However, pERK expression is not different between the two loading rates at either distraction magnitude (Figure 4.6).

**Table 4.1.** Summary of mechanics, pERK production and fiber alignment for NCCs.

| Displacement (mm) | Rate (mm/s) | Sample | Maximum Force (mN) | Maximum Stiffness (mN/mm) | Average Bulk MPS (%) | Average Elemental MPS (%) | Average Normalized pERK Expression | Average Normalized Circular Variance |
|---|---|---|---|---|---|---|---|---|
| 4 | 0.5 | 1 | 21.6 | 5.7 | 7.88 | 8.55 | 0.75 | NA |
| | | 2 | 16.7 | 6.7 | 7.74 | 8.79 | 0.9 | NA |
| | | 3 | 18.6 | 8.2 | 8.53 | 9.6 | 0.91 | NA |
| | | 4 | 27.4 | 12.7 | 7.54 | 7.49 | 0.96 | 3.93 |
| | | 5 | 7.8 | 5.8 | 6.04 | 6.22 | 0.72 | 1.4 |
| | | 6 | 3.2 | 4.2 | 9.6 | 9.76 | 1.14 | 0.41 |
| | | 7 | 6.5 | 2.9 | 8.55 | 8.98 | 0.75 | 1.83 |
| | | 8 | 13.7 | 5.8 | 7.79 | 7.82 | 1.03 | 0.62 |
| | | **Mean** | **14.4** | **6.5** | **7.96** | **8.4** | **0.9** | **1.64** |
| | | **SD** | **7.7** | **2.8** | **0.96** | **1.1** | **0.14** | **1.4** |
| 4 | 3.5 | 1 | 30.4 | 18.6 | 6.15 | 6.18 | 1.01 | NA |
| | | 2 | 20.6 | 4.7 | 5.5 | 5.9 | 1.02 | NA |
| | | 3 | 26.5 | 9.6 | 6.36 | 7.22 | 0.96 | NA |
| | | 4 | 25.5 | 8.3 | 5.46 | 6.11 | 0.91 | NA |
| | | 5 | 19.6 | 10.8 | 9.23 | 9.12 | 0.96 | 1.23 |
| | | 6 | 29.4 | 15.7 | 8.34 | 9.31 | 1.33 | 1.17 |
| | | 7 | 30.4 | 20.6 | 8.57 | 8.47 | 1.06 | 1.95 |
| | | **Mean** | **26** | **12.6** | **7.09** | **7.48** | **1.04** | **1.45** |
| | | **SD** | **4.2** | **5.4** | **1.46** | **1.37** | **0.13** | **0.43** |
| 8 | 0.5 | 1 | 49 | 12 | 13.37 | 12.44 | 1.18 | NA |
| | | 2 | 59.8 | 11.5 | 15.77 | 15.75 | 0.97 | NA |
| | | 3 | 79.4 | 21.7 | 17.86 | 18.12 | 1.48 | NA |
| | | 4 | 100.9 | 23.9 | 18.96 | 19.5 | 1.44 | NA |
| | | 5 | 97 | 22.7 | 15.57 | 15.47 | 0.74 | 98.5 |
| | | 6 | 112.7 | 29.6 | 16.52 | 16.48 | 1.35 | 259.7 |
| | | 7 | 76.4 | 32.4 | 12.92 | 14.21 | 1.18 | 36.5 |
| | | 8 | 82.3 | 21.9 | 18.35 | 18.95 | 1.53 | 56.2 |
| | | 9 | 78.4 | 24.3 | 18.93 | 19.11 | 1.96 | 155 |
| | | **Mean** | **81.8*** | **22.2*** | **16.47*** | **16.67*** | **1.31*** | **121.2*** |
| | | **SD** | **19.9** | **6.9** | **2.27** | **2.44** | **0.35** | **89.8** |
| 8 | 3.5 | 1 | 123.5 | 38.2 | 15.13 | 14.48 | 1.21 | NA |
| | | 2 | 95.1 | 32.3 | 16.06 | 15.81 | 1.14 | NA |
| | | 3 | 121.5 | 27.4 | 13.86 | 13.33 | 1.21 | NA |
| | | 4 | 73.5 | 28.4 | 12.12 | 11.94 | 1.36 | NA |
| | | 5 | 168.6 | 51 | 14.23 | 14.55 | 1.21 | 48.8 |
| | | 6 | 79.4 | 26.5 | 15.43 | 16.01 | 1.09 | 1.7 |
| | | 7 | 135.2 | 33.3 | 17.18 | 16.85 | 1.04 | 54.3 |
| | | 8 | 104.9 | 30.4 | 17.84 | 17.21 | 1.12 | 15.9 |
| | | 9 | 96 | 31.4 | 17.21 | 17 | 2.84 | 8.9 |
| | | **Mean** | **110.8$^{+\#}$** | **33.2$^{+\#}$** | **15.45$^{+}$** | **15.24$^{+}$** | **1.36$^{+}$** | **25.9$^{\#}$** |
| | | **SD** | **29.8** | **7.5** | **1.85** | **1.81** | **0.56** | **24** |

* Significant difference compared to the 4mm, 0.5mm/s group ($p \leq 0.009$).
$^{+}$ Significant difference compared to the 4mm, 3.5mm/s group ($p \leq 0.002$).
$^{\#}$ Significant difference compared to the 8mm, 0.5mm/s group ($p \leq 0.017$).

Further, normalized pERK expression and elemental MPS are correlated at both rates, with weak, but significant, correlations at both 0.5mm/s ($R=0.447$; $p<0.001$) and 3.5mm/s ($R=0.202$; $p=0.017$) (Figure 4.7a). Of note, although weak, the production of pERK is more strongly correlated with elemental MPS at the slower loading rate (0.5mm/s) than the faster rate (3.5mm/s) (Figure 4.7a). The expression level of pERK for each sample is detailed in Table 4.1.

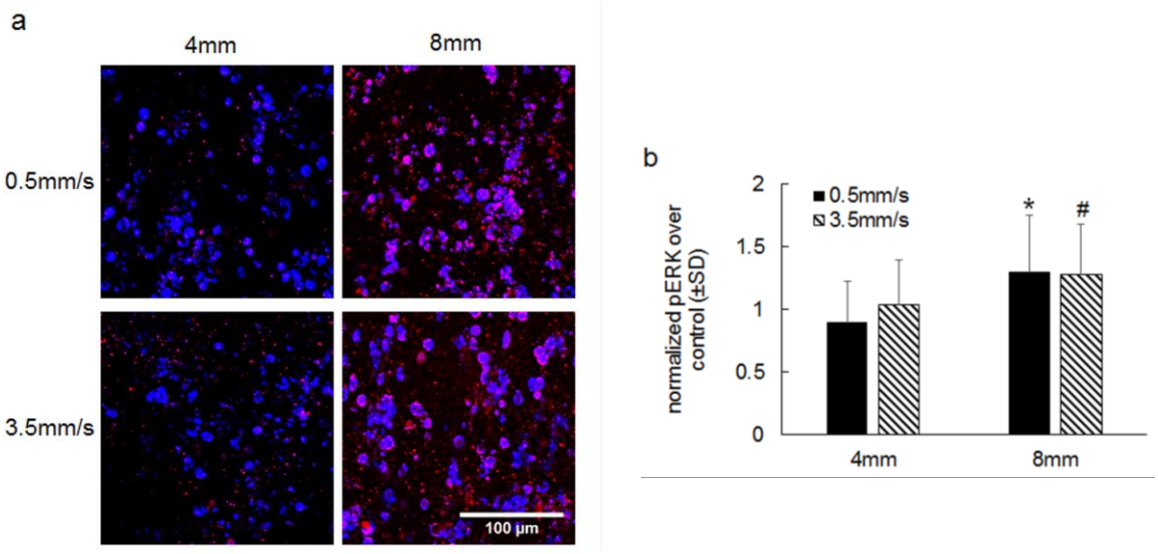


**Figure 4.6.** ERK phosphorylation increases with increasing distraction magnitude. **(a)** Representative confocal images show neuronal structure labeled for βIII-tubulin (blue), pERK expression (red) and their co-localization (pink). These images demonstrate higher pERK expression in NCCs distracted to 8mm than in those distracted to 4mm regardless of the loading rate. The scale bar applies to all panels. **(b)** Quantification of pERK expression in loaded constructs normalized to unloaded controls indicates significant increases in NCCs distracted to 8mm compared to 4mm at both the 0.5mm/s (*$p<0.001$) and 3.5mm/s ($^{\#}p=0.002$) distraction rates.

The strain thresholds for elevated ERK phosphorylation are also similar between the two loading rates, with slightly higher thresholds for slower loading (Figure 4.7b). Logistic regression of the binarized pERK expression against the elemental MPS predicts

a 50th-percentile threshold of 11.7% (95% confidence interval: 10.2-13.4%) for 0.5mm/s loading and a threshold of 10.2% (95% confidence interval: 8.7-12.0%) for tensile loading applied at 3.5mm/s (Figure 4.7b). In addition, the 95th-percentile MPS for increased pERK production is estimated at 24.9% (95% confidence interval: 21.6-30.1%) at 0.5mm/s and 23.7% (95% confidence interval: 20.3-29.6%) at 3.5mm/s. The logistic regressions run separately for each distraction rate are significant ($p<0.001$).

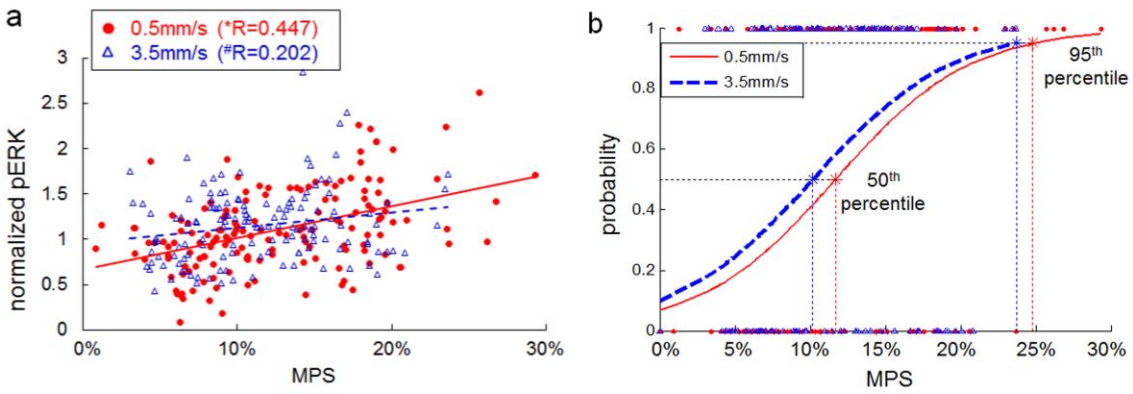


**Figure 4.7.** Elemental pERK expression is positively related to elemental MPS. **(a)** Significant positive correlations exist between normalized elemental pERK expression and elemental MPS at both 0.5mm/s ($R^2=0.200$, *$p<0.001$) and 3.5mm/s ($R^2=0.041$, #$p=0.017$) distraction rates. **(b)** pERK expression is significantly ($p<0.001$) regressed against elemental MPS at both distraction rates. Solid dots (•) represent samples in which elevated pERK expression is detected (probability of 1), and open triangles (Δ) represent those in which it is not detected (probability of 0) at each strain level for 0.5mm/s (red) and 3.5mm/s (blue). The predicted 50th-percentile (horizontal line) thresholds for ERK phosphorylation are 11.7% for 0.5mm/s rate, 10.2% for 3.5mm/s (vertical lines); the corresponding 95th-percentile (horizontal line) thresholds are 24.9% and 23.7% at the 0.5mm/s and 3.5mm/s distraction rates, respectively (vertical lines).

#### 4.3.2.2. Modulation of Neuronal Shape & Orientation by Strain Magnitude & Rate

The neuronal aspect ratio and orientation due to loading are also affected by the loading parameters, but in different ways. For example, the aspect ratio increases with

increasing elemental MPS, but the cell orientation response during loading is different for each rate of loading (Figure 4.8). At the unloaded reference configuration, most neurons are circular and there is no difference detected in cell shape and orientation between any group. After loading, the normalized aspect ratio displays significant positive correlations with elemental MPS at both 0.5mm/s ($R=0.500$, $p<0.001$) and 3.5mm/s ($R=0.742$, $p<0.001$) rates (Figure 4.8a). In addition, the distributions of cell orientation (Figure 4.8b) are significantly different ($p=0.004$) at the slower (0.5mm/s) and faster (3.5mm/s) loading rates after NCC distraction. The long-axes of neurons in NCCs loaded at 0.5mm/s to 8mm are more aligned with the loading direction than those neurons in NCCs distracted

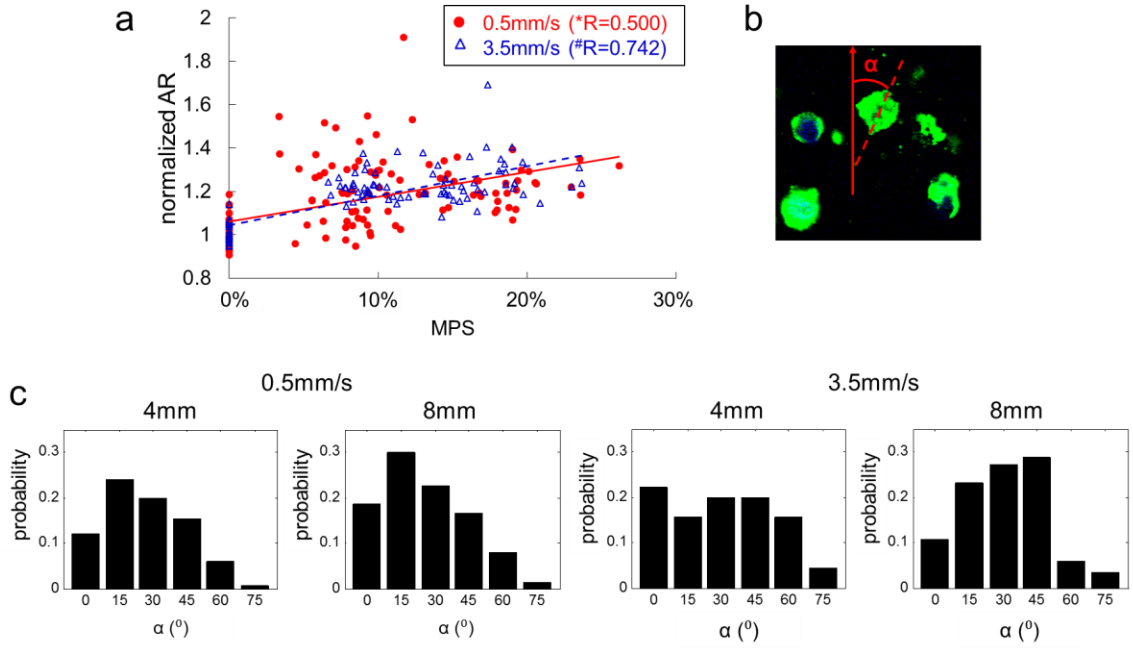


**Figure 4.8.** Neuronal aspect ratio and orientation towards the loading direction depend on the NCC displacement and loading rate. **(a)** Significant correlations are detected between normalized cell aspect ratio (AR) and MPS for both 0.5mm/s (*$p<0.001$) and 3.5mm/s (#$p<0.001$) rates of distraction. **(b)** Cell orientation angle (α) is measured as the angle between cell's long axis (dotted line) and the direction of applied tension (arrow). **(c)** Distributions of cell orientation angles show that cell orientation angle is significantly smaller ($p=0.004$) at the slow distraction rate (0.5mm/s) than at the fast rate (3.5mm/s).

to 8mm at 3.5mm/s (Figure 4.8c). Further, more neurons remain circular with no identifiable long axis in gels loaded only to 4mm compared to neurons in gels loaded to 8mm at the 0.5mm/s. This difference results in a lower probability of aligning neurons towards the loading direction at the non-painful distraction magnitude (Figure 4.8c). The detailed cell shape and orientation data for each sample are summarized in Appendix E.

#### 4.3.2.3. Switch-Like Collagen Reorganization with Increasing Fiber Strains

More collagen fiber realignment is evident with increased distraction magnitude, and is greater for the slower loading rate. In the unloaded reference configuration, the average collagen fiber direction through the gel thickness is approximately 0° (Figure 4.9a), which is consistent with the initial random collagen fiber orientation. With increasing imposed distraction, collagen fiber realignment towards the loading direction occurs in all groups but to different degrees, as indicated by the orientation vectors in the alignment maps (Figure 4.9a). Tensile loading to 8mm induces non-uniform fiber reorganization across the overall NCC, with the most realignment evident along the free boundaries where the lateral contraction is the greatest (Figure 4.9a). As with the orientation of neurons towards the loading direction (Figure 4.9c), the greatest degree of fiber realignment, indicated by a high normalized circular variance, is induced at 8mm under the slower applied tension (0.5mm/s). The degree of fiber realignment in NCCs distracted to 8mm at slower rate is significantly greater than the collagen fiber reorganization in gels distracted to 4mm at the same rate ($p=0.009$) or 8mm at the higher

distraction rate (p=0.040) (Figure 4.9b). The circular variance for each NCC is summarized in Table 4.1.

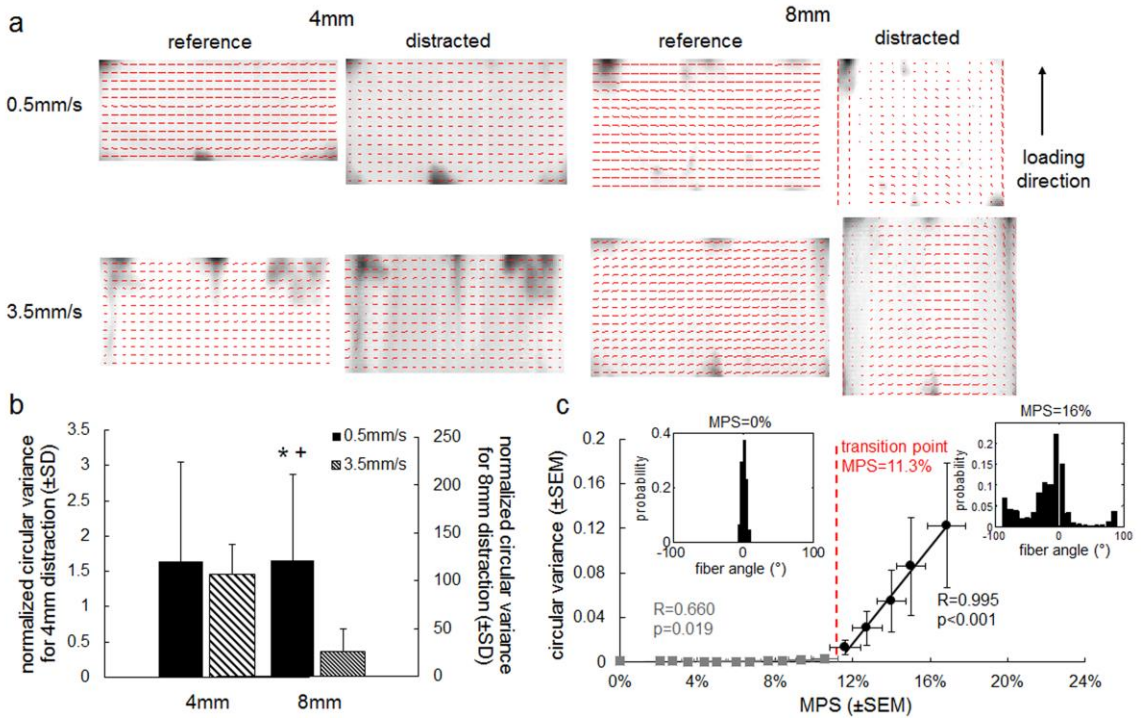


**Figure 4.9.** Strain-dependent fiber realignment exhibits a switch-like response to increasing strain. **(a)** Representative collagen fiber alignment maps in two adjacent elements before (reference) and at maximal distraction (distracted) showing different fiber realignment responses that depend on both the distraction magnitude and rate. The direction of the orientation vector (red line) indicates the average fiber alignment direction measured through the NCC thickness; its length represents the alignment strength in that direction. Fiber reorientation towards the loading direction is apparent by the changes in the length of the orientation vectors and their directions towards the vertical direction, with the most realignment along the lateral edges (indicated by vertically orientated vectors). **(b)** Quantification of the normalized circular variance measures the degree of fiber realignment in the distracted configuration relative to the unloaded reference. The normalized circular variance is significantly higher in NCCs distracted to 8mm at 0.5mm/s than in those distracted to 4mm at the same rate (*p=0.009) or 8mm at the higher distraction rate ($^{+}$p=0.040). **(c)** The mean circular variance of collagen fiber orientation angles during loading at 0.5mm/s exhibits a biphasic response with increasing applied strain (MPS), with a transition point of 11.3% strain estimated. The insets show representative distributions of collagen fiber alignment angles before (MPS=0%) and after (MPS=16%) evident fiber realignment occurs.

The circular variance of fiber orientation exhibits a two-phase response to increasing bulk strain. There is little change initially at small strains followed by a rapid increase in circular variance with increasing strain (Figure 4.9c). A two-phase linear regression model identifies a switch-like transition between isotropic and anisotropic collagen reorganization based on changes in the circular variance. That modeling identifies 11.3% strain as the transition point between the two phases of fiber realignment (Figure 4.9c), a strain value very close to the $50^{th}$-percentile strain threshold (11.7%) identified for elevated pERK production at this rate of applied tension (Figure 4.7b). At strains below that transition point, the average fiber orientation angle of the isotropic collagen matrix remains near 0° (0.47±6.66°), with a small-to-negligible circular variance (0.001±0.001) (Figure 4.9c). Beginning at a mean strain of 11.6±1.8%, the circular variance starts to increase substantially, rising to 0.122±0.056 at 16.8±2.2% strain (Figure 4.9c). This over 100-fold increase in the circular variance induced by NCC loading reflectes a mean fiber realignment of 12.2±11.0° that is averaged across all the NCCs (Figure 4.9). The distribution of fiber orientation angles displays a tight cluster around 0° before loading is applied (at 0% strain) and a high degree of dispersion, with peaks at ±90°, after distraction to 16% strain (Figure 4.9c), which indicates a strong realignment in the direction of loading with increased strain.

Fiber realignment predicted by the DFN model is consistent with the experimental observations and also illustrates the switch-like response of fiber network reorganization (Figure 4.9c & 4.10). For small strains, such as 7%, below the 11.3% transition point, fiber alignment remains similar to the initial uniform distribution (Figure 4.10a).

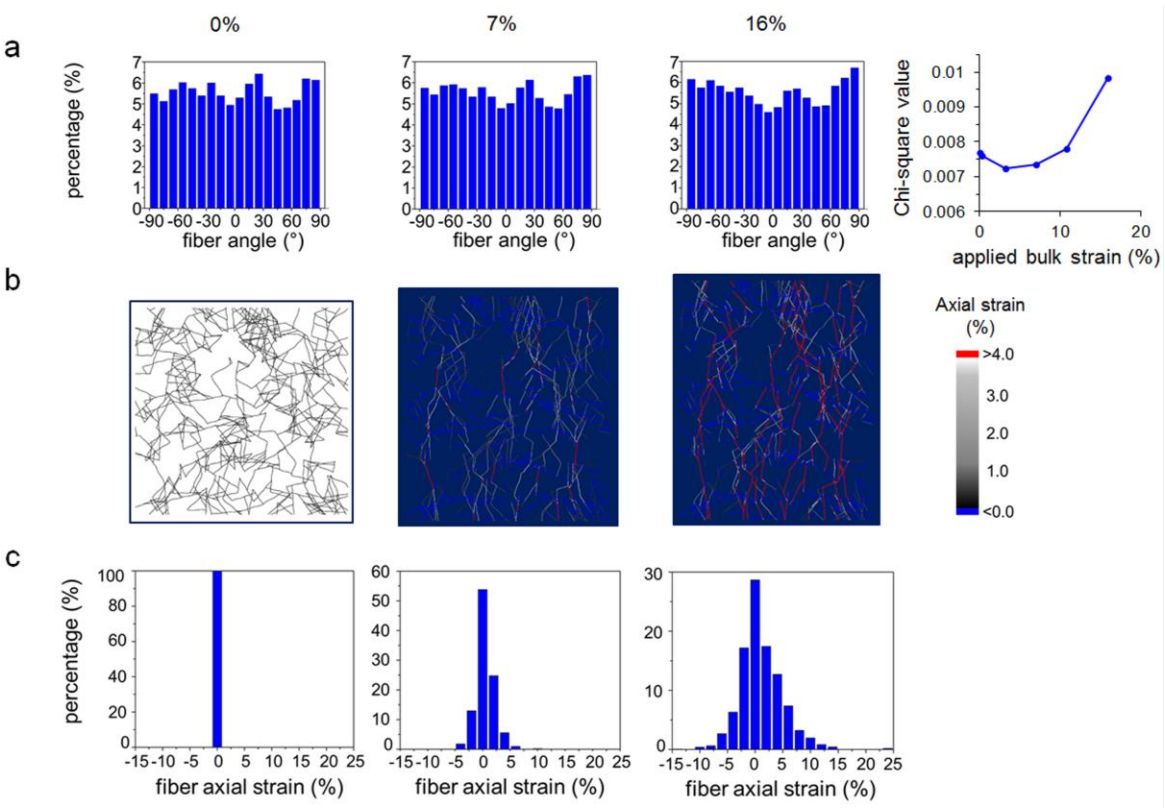


**Figure 4.10.** DFN modeling predicts that collagen fiber realignment and fiber strain increase with bulk strain. **(a)** The distribution of fiber angle indicates more realignment towards the loading direction (±90°) at 16% strain, which is different from the uniform distributions that are observed at 0% and 7% strain. Plotting the Chi-squared statistic against the applied bulk strain shows that the fiber angle distribution becomes less uniform with increasing strain above 10%. **(b)** Visualization of the heterogeneous fiber axial strains during network loading show more fibers under large tensile strain as more fibers realign towards the loading direction at 16% strain compared to 0% and 7% strains. **(c)** Distributions of fiber strains show that most fibers have strains lower than the applied bulk strain and both compressive and tensile fiber strains increase with bulk strain.

However, at a larger strain of 16%, which is greater than the transition point, there is preferable reorientation of fibers in the model towards the loading direction (Figure 4.10a). The DFN model also predicts heterogeneous collagen fiber strains, with fibers undergoing both tension and compression (Figure 4.10). Most fibers undergo axial strains that are less than the applied bulk strain. For example, at a bulk strain of 16%, the

majority of fibers undergo -5% to 10% strain (Figure 4.10c). As more collagen fibers realign towards the direction of loading with increasing bulk strain, the distribution of the fiber axial strains exhibits increased fiber counts and higher dispersion at high fiber strains (Figure 4.10). In fact, a few load-bearing fibers exhibit axial strains that are actually greater than the applied bulk strain (Figure 4.10c).

## 4.4. Studies Using 3D DRG Cultures

### 4.4.1. Methods

DRG explants used in this pilot study were a kind gift from Dr. D. Kacy Cullen at the University of Pennsylvania. Embryonic day 16 DRGs were harvested from Sprague-Dawley rats as described in Section 3.3 of Chapter 3. DRG explants were embedded in dog-bone shaped collagen gels that were identical to those used for the cortical culture (Figure 4.1). The DRG culture was maintained using methods described in Chapter 3 until mechanical testing. Separate groups of NCCs were distracted at 0.5mm/s to either 4mm (n=2 gels, 22 DRGs) or 8mm (n=3 gels, 12 DRGs) to simulate the non-painful or painful facet capsular ligament loading in vivo, respectively (Lu et al. 2005; Dong et al. 2011; Dong et al. 2012). Unloaded NCCs (n=4 gels, 23 DRGs) were also included as controls for pERK expression. MPS was measured from the loaded gels using the same approach applied to the cortical-collagen constructs (Section 4.3.1.2) and is summarized for each NCC in Appendix F. Loaded DRG cultures were removed from the Instron and in so doing returned to an unloaded state immediately after loading; they were chemically fixed and immunolabeled for pERK as described in Sections 4.3.1.2 and 4.3.1.3. Images

were taken using a Zeiss LSM 710 confocal microscope (Carl Zeiss Inc.; Thornwood, NY) and analyzed using Image J software. The average intensity per unit area was measured from each cell body cluster and from five axons for each DRG. The expression of pERK was normalized over unloaded control levels and compared between 4mm and 8mm groups using t-tests for the cell bodies and axons, separately. The relationships between pERK expression and the applied strains in sub-regions where the DRGs reside were evaluated using linear regressions and logistic regressions as described in Section 4.3.1.4.

### 4.4.2. Results

Consistent with results from the cortical culture (Figures 4.6 and 4.7), the expression of pERK in the cell bodies and axons of the DRGs increases with the extent of distraction and is correlated with the elemental MPS (Figure 4.11). The amount of pERK normalized to control levels is significantly increased ($p<0.004$) in NCCs distracted to 8mm compared to the levels expressed at 4mm, for both cell bodies and axons (Figure 4.11a). Furthermore, normalized pERK expression in the cell bodies ($R=0.629$; $p<0.001$) and axons ($R=0.619$; $p<0.001$) are both positively correlated with the regional MPS (Figure 4.11b). The strain thresholds for elevated ERK activation also exhibit similar behavior in the DRG cultures as in the cortical cultures. Logistic regressions of the binarized pERK expression against the elemental MPS detect significant correlations ($p<0.001$) and predict a $50^{th}$-percentile threshold of 11.7% (95% confidence interval: 8.9-15.8%) for the cell bodies and a 9.7% (95% confidence interval: 7.2-12.8%) for the axons.

The 95$^{th}$-percentile MPS for increased pERK production is estimated at 22.5% (95% confidence interval: 17.6-37.4%) for the cell bodies and 19.2% (95% confidence interval: 15.2-30.7%) for the axons. The quantification of pERK expression for each NCC is summarized in Appendix C.

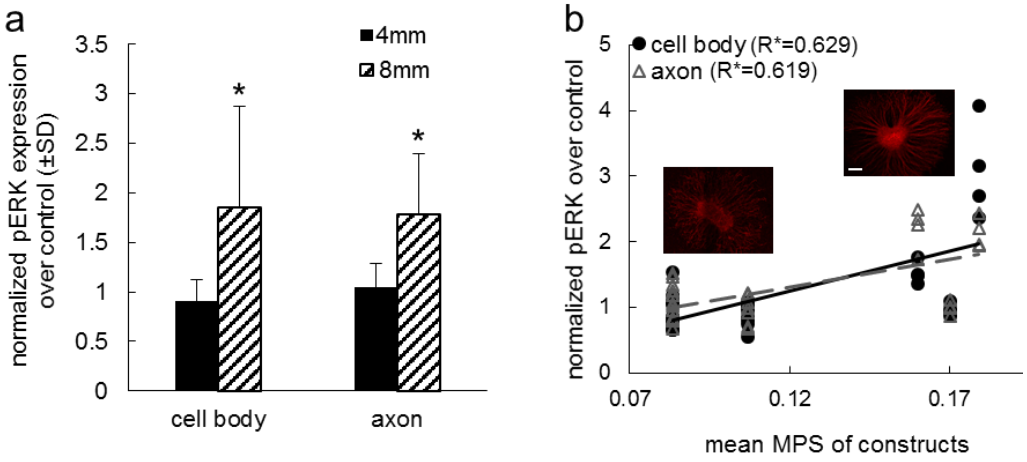


**Figure 4.11.** Expression of pERK in DRG cultures increases with increasing distraction magnitude. **(a)** Quantification of pERK expression in loaded NCCs normalized to unloaded controls indicates significant increases at 8mm compared to 4mm, for both the cell bodies and axons (*p<0.004). **(b)** Significant positive correlations exist between the normalized pERK expression and elemental MPS, for both the cell bodies ($R^2$=0.396, *p<0.001) and axons ($R^2$=0.383, *p<0.001). Insets demonstrate a DRG from the 4mm non-painful group and a DRG from the 8mm painful group. The scale bar is 200μm.

### 4.5. Discussion

This study used integrated in vitro and computational models to understand if, and how, tissue-level loading relates to neuronal deformation and signaling via changes in the micromechanics of the collagen that surrounds the neuronal afferents. Both the applied distraction magnitude and the rate of loading regulate the macro- and micro-scale NCC mechanics (Table 4.1; Figure 4.9) and the resulting neuronal responses in the 3D cortical culture (Figures 4.6-4.8). In fact, pERK expression and the neuronal aspect ratio both

positively correlate with the strains in the local surrounding collagen matrix at both distraction rates tested in this study (Figures 4.6-4.9). The strain-dependent regulation of pERK expression is consistently observed in both the cortical and DRG cultures (Figures 4.6, 4.7 & 4.11), with similar strain thresholds for elevated pERK estimated for both types of in vitro models. For pain initiation from ligament trauma, tissue stretch directly activates the innervating DRG neurons, but this is not the case for cortical neurons. However, the similar strain-dependent ERK phosphorylation in both the DRG and cortical cultures (Figures 4.6, 4.7 & 4.11) suggests that those two neuronal populations may have similar responses to stretch. Thus, findings from the cortical NCCs may have implications on neuronal activation in peripheral tissue due to noxious mechanical stimuli.

The strain thresholds for increased ERK phosphorylation and collagen fiber realignment are the same (Figures 4.7 & 4.9), suggesting that excessive *local* fiber motion may directly influence the neuronal responses, altering both the loading to neurons and the induction of mechanotransduction pathways, like pERK activation. As more collagen fibers reorient towards the loading direction with increasing bulk strain, those fibers also undergo larger strains due to their elongation (Figure 4.10). The increase in fiber realignment and elongation likely presents a mechanism by which the much weaker neurons reorient and deform (Figure 4.8), since they are adherently embedded in the surrounding fibers matrix (Schwartz 2010; Hemphill et al. 2011; Spedden and Staii 2013). Therefore, in order to understand the biomechanical mechanisms underlying neuronal loading and nociception in the context of ligament pain, it is important to define

the fiber-level mechanics in ligaments and investigate neuronal mechanotransduction in non-physiologic conditions.

Under the testing conditions used in these studies, both neuronal orientation and collagen fiber realignment are sensitive to the loading rate, with the greatest degree of reorientation of neurons and collagen fibers towards the loading direction evident at the lower 0.5mm/s rate (Figures 4.8 & 4.9). This finding implies that slowly applied tension across the tissue enables microstructural changes of the collagen matrix that lead to more and greater changes in the microenvironment of neurons that is not evident for similar bulk strains that are applied more quickly (Figure 4.9). Regardless of the imposed NCC strain and loading rate, collagen fiber orientations within the same NCC element vary based on their location in the construct, as are the heterogeneous strains in the local collagen networks (Figures 4.9 & 4.10). These observations, together with variability in pERK production across neurons in the same NCC element (Figure 4.6), suggest that even for simple bulk tissue loading, like uniaxial tension, complicated mechanotransduction signaling may occur in the cells embedded in fibrous tissues due to non-uniform microstructure.

Only strains above the supraphysiologic threshold activate neurons (as evaluated by pERK expression) embedded in this collagenous network (Figures 4.6 & 4.7). Behavioral hypersensitivity (i.e. pain) in the rat has been shown to be significantly correlated with the magnitude of strain to the facet capsular ligament (Dong and Winkelstein 2010). In addition, the strain threshold for the generation of facet joint pain in vivo has been estimated to be 8-12% based on a rat model of facet capsule injury

(Dong et al. 2012). Complementary studies in the goat support excessive tensile stretch of the facet capsular ligament as inducing persistent afferent activity in low-threshold (strains of 10.2±4.6%) and high-threshold (strains of 47.2±9.6%) neurons (Lu et al. 2005a; Chen et al. 2006). The current findings that neuronal aspect ratio and ERK phosphorylation are correlated with applied strain and that a corresponding strain threshold (10-12%) for activation of ERK signaling in the NCCs is similarly evident (Figures 4.6-4.8), provide additional evidence that a relevant pain threshold for facet capsular ligament strain exists between 8-12%. The strain threshold for initiating pain-related changes in neurons may vary slightly depending on the applied loading rate, the choice of neuronal activation marker and/or the cellular signaling cascades of interest.

Altered neuronal responses, here taken as significant increases in ERK phosphorylation, occur under the same loading conditions as those that induce substantial changes in collagen fiber orientation and at bulk strains greater than the physiologic limit of the cervical facet capsular ligament (Figures 4.6 & 4.9). Biomechanical studies using the same QPLI methods for isolated rat and human cervical facet capsular ligaments have detected collagen fiber disorganization at strains (Quinn and Winkelstein 2009; Quinn et al. 2010a) that induce pain in vivo (Lee and Winkelstein 2009; Dong et al. 2012). Such collagen fiber realignment may be due to the redistribution of forces among intact fibers after other load-bearing fibers fail; failure strains of collagen fibers in ligament has been reported at between 6% and 22% (Liao and Belkoff 1999). Indeed, that estimated failure strain for collagen fibers in ligaments is consistent with the fiber strains predicted by the DFN model at bulk strains simulating painful loading conditions (Figure 4.10). However,

the connection between fiber realignment and fiber failure was not tested explicitly since neither the experimental nor the computational approaches used in the current study enable measuring, or modeling, fiber failure. Future studies should simultaneously measure failure, stress and realignment responses of fibers in the local collagen network to examine whether fiber failure indeed results in abnormal fiber reorientation via stress redistribution in the network. Nonetheless, the integrated collagen fiber kinematics and neuronal responses in the current study (Figures 4.7 & 4.9) support the notion that microstructural collagen reorganization in the facet capsular ligament can occur concurrently with altered neuronal responses at supraphysiologic strains and may contribute to the induction of pain from ligament loading (Quinn and Winkelstein 2009; Quinn et al. 2010a).

The transition from isotropic to anisotropic collagen reorganization with increasing applied bulk strain (Figure 4.9) is likely related to the bending-stretching transition of collagen fibers that leads to strain hardening (Nair et al. 2014). A characteristic strain hardening response has been documented with collagen constructs under tension and shear (Roeder et al. 2002; Münster et al. 2013). In fact, a shift from a compliant regime to a stiffening regime has been reported at approximately 10% strain for gels with a collagen density of 2mg/ml (Roeder et al. 2002), which is comparable to the transition point that is evident between the two phases of fiber realignment in our study (Figure 4.9). Those gels have the same collagen concentration as NCCs used in this thesis. Collagen networks under shear exhibit strain hardening that starts around the transition between collagen fiber bending and stretching, with an energy cross-over

slightly above 10% strain from a bending-dominated domain to a stretching-dominated domain, for both single fibers and the network (Nair et al. 2014). Stiffening of the collagen network may substantially increase the loading exerted on the embedded neurons even with small increases in the applied bulk strain. Strains exceeding the strain hardening threshold could lead to substantial changes in neuronal activity likely due to the increased neuronal loading exerted by the strained collagen fibers that are parallel to the stretch direction.

In addition to strain magnitude, the applied loading rate also regulates some, but not all, of the responses of neurons and collagen measured in this study. The greatest degrees of collagen fiber realignment and neuron reorientation that occur at the slower loading rate (0.5mm/s) (Figures 4.8 & 4.9) may be due to the viscoelastic properties of the neurons and their surrounding collagen matrix (Lu et al. 2006; Topp and Boyd 2006; Xu et al. 2013). Viscoelasticity of the collagen fibers may limit the extent of their altered kinematics during rapid NCC stretch because the hydrogen bonds between, and within, the collagen molecules are less likely to break under rapid loading (Silver et al. 2002; in't Veld and Stevens 2008). This resistance to fiber movement and deformation may limit fiber realignment towards the loading direction more in the NCCs loaded at 3.5mm/s than at 0.5mm/s (Figure 4.9), because the hydrogen bonds may stay intact and prevent changes in fiber kinematics at the higher 3.5mm/s rate of loading. Of note, continuous fiber reorientation during loading at 3.5mm/s was not measured in this study due to limitations with the acquisition rate of the QPLI data. Since the circular variances measured at 4mm are not different from each other between the two rates used, nor from the corresponding

baseline circular variance at the unloaded state (Figure 4.9), there is not expected to be different adaptation of collagen to tension at low strain magnitudes. Yet, because there is significantly less fiber realignment at 8mm of distraction at the faster loading rate than at the slower rate (Figure 4.9), the corresponding transition point for fiber realignment at 3.5mm/s is expected to be higher than the threshold at the 0.5mm/s loading rate. Accordingly, that transition point also will be greater than the strain threshold (10.2%) measured for ERK phosphorylation at 3.5mm/s (Figure 4.7), which is comparable to the strain threshold for the biphasic fiber realignment response observed at 0.5mm/s (Figure 4.9). The potential mismatch between the strain thresholds for fiber realignment and ERK activation at 3.5mm/s suggests that collagen microstructure and neuronal activation may not parallel each other for all loading conditions, particularly at higher loading rates. However, further studies are needed to fully understand those relationships between fiber kinematics, neuronal activation and tissue loading.

Since the nonlinear properties of collagen and neurons can induce higher stress and less stress relaxation in the tissues they make up, which undergo more rapid stretch (Solomonow 2004; Laplaca and Prado 2010; Xu et al. 2013), neurons stretched at the faster rate are hypothesized to experience greater loads and to exhibit elevated activity compared to those undergoing the slower loading rate. However, no difference in pERK production was observed between the two rates, regardless of the distraction magnitude (Figure 4.6). This may be due to the fact that there is only a seven-fold difference between the two distraction rates tested in this study, owing to limitations with the mechanical testing device in reliably imposing such relatively small displacement.

Additional loading rates at several orders of magnitude higher than those tested here are needed to meaningfully evaluate the effects of neuronal signaling as a function of loading rate, particularly at rates simulating traumatic loading, which can reach as high as 500%/s (Panjabi et al. 1998a).

Considering previous biomechanical and neurophysiological findings, the results of these in vitro studies can begin to elucidate possible mechanisms by which supraphysiologic ligament deformation modulates responses in the neurons embedded in that collagenous tissue. For bulk tissue strains within the physiologic limit (~8-12%), collagen fibers undergo almost no realignment but may bend and/or uncrimp to accommodate macroscopic deformation (Liao and Belkoff 1999; Sacks 2003; Franchi et al. 2010; Miller et al. 2012a); during that regime, the fibers experience small strains that are lower than the bulk strain of the collagen network (Figures 4.9 & 4.10). Minimal changes in the collagen fiber alignment and axial strains can lead to small-to-negligible changes in the local stresses for increasing tissue strain, corresponding to the initial compliant mechanical response of the collagen network (Roeder et al. 2002; Nair et al. 2014). Neurons may still be loaded during this compliant regime due to collagen fiber motions and the Poisson effect, but at levels within their physiologic tolerance. That notion is supported by the same degree of pERK being evident in NCCs distracted to simulate non-painful strains as in the unloaded control samples (Figures 4.6 & 4.7).

When supraphysiologic bulk strains are reached in the cases for painful facet capsular ligament loading (Dong and Winkelstein 2010; Dong et al. 2012), substantial collagen fiber realignment towards the loading direction occurs (Figures 4.9 & 4.10).

Reorientation of collagen fibers is likely due to the fact that the molecular bonds between collagen fibers may be breaking. As some fibers reorient along the loading direction and others remain unaligned, the collagen network sustains highly inhomogeneous strains (Quinn and Winkelstein 2008; Korenczuk et al. 2017), with a few load-bearing fibers sustaining axial strains that exceed the applied bulk strain (Figure 4.10). Those fibers undergo excessively large local strains along the gel's loading axis to accommodate the applied macroscopic deformation, as the fibers oriented off-axis relative to the loading direction sustain strains that are less than the applied bulk strain. Further, stretching of those aligned fibers is a potential likely mechanism by which strain hardening rapidly increases stress in the collagen network at large bulk strains (Roeder et al. 2002; Nair et al. 2014). Heterogeneous fiber strains predicted by the DFN model indicates that there is a range of tensile and compressive forces in the neurons' microenvironment in this collagen matrix (Figure 4.10). The finding that fiber strains are different from the applied bulk strain (Figure 4.10) suggests the importance of microscopic fibers in the local mechanical environment of neurons because they may directly modulate neuronal stresses and alter mechanotransduction pathways during macroscopic loading.

Supraphysiologic stretch of the facet capsular ligament can activate its nociceptors; both neuronal activity in the facet capsule and pain have been shown to correlate with ligament strain (Lu et al. 2005a; Lee and Winkelstein 2009; Dong and Winkelstein 2010; Quinn et al. 2010b). Soft neurons embedded in the comparatively stiff collagen matrix in the facet capsular ligament can be deformed and reoriented to a degree exceeding their physiologic range due to the excessive collagen fiber motions and stretch

that accommodate the large macroscopic tissue deformation (Figures 4.9 & 4.10). Fiber forces can be transmitted to compress or stretch neurons via direct contact and/or cell surface receptors with stress concentrations at the adhesion sites (Cullen et al. 2007a; Quinn and Winkelstein 2009; Sander et al. 2009a). ERK signaling in neurons has been shown to occur on the order of minutes in response to cellular deformation and/or stress exceeding their mechanical tolerance (Neary et al. 2003; Samarakoon and Higgins 2003; Chaturvedi et al. 2008; Gao and Ji 2009). In this study, pERK was measured immediately after loading, which is at the time when ERK phosphorylation is first induced after tissue injury (Gao and Ji 2009). Activation of ERK signaling can produce persistent changes in neurons, such as increased excitability, altered expression of ion channels and neuromodulators, and nociceptive signaling (Ji et al. 1999; Cheng and Ji 2008; Gao and Ji 2009).

Although significantly less fiber reorientation is induced by the faster rate in this study (Figure 4.9), pERK expression is not different between the two loading rates tested (Figure 4.6), suggesting that *mechanical factors other than collagen fiber kinematics* may also contribute to neuron activation after tissue loading. High stress due to high-rate loading of ligament (Solomonow 2004) induces mechanotransduction in neurons under rapidly applied macro-scale tension. In fact, ligament stress correlates with neuronal activity (Khalsa et al. 1996). As such, tissue strain and fiber kinematics may not provide the complete picture of the mechanical environment of neurons, since other mechanical inputs, like tissue stress or loading rate, may also affect the mechanical state and excitability of neurons (Khalsa et al. 1996; Cullen et al. 2007a). Relating macro- and

micro-scale mechanical factors with neuronal dysfunction would help fully define the biomechanical pathomechanisms for nociception in injured ligaments.

Although the integrated experimental and computational models used here enable measurement of neuronal and collagen responses across length scales, there are several limitations that prevent fully defining the relationships between tissue mechanics and neuronal activation. One limitation of this study is the measurement of total pERK expression, and not the neuron-co-localized pERK. Total pERK was assessed in order to account for the possibility that the plasma membrane of neurons may be disrupted by the applied loading (Cullen et al. 2011) and that pERK might diffuse out of neurons due to mechanically damaged cell membrane from NCC stretch. However, the cell models used here were mixed culture containing both neurons and glia, although the proliferation of glia was suppressed by the culture medium used. Therefore, an additional pilot study was performed to investigate whether pERK localized specifically in neurons shows similar correlation with strain as the total pERK.

For the pilot study, confocal images from a subset of the cortical-collagen constructs (n=4 distracted to 4mm at 0.5mm/s; n=4 distracted to 8mm at 0.5mm/s; n=2 unloaded controls) that were used in the study presented in Section 4.3 were analyzed. Both the total amount of pERK and the amount co-localized with βIII-tubulin labeling (neuronal pERK) in each element defined for strain analysis of those stretched NCCs were quantified using densitometry and normalized to unloaded control levels. Correlation between each of the total pERK and neuronal pERK and the mean MPS across each element of the corresponding NCC was evaluated using linear regression, as

described in Section 4.3.1. Both the normalized total pERK (R=0.536, p<0.001) and the normalized neuronal pERK (R=0.377, p<0.001) were found to be significantly correlated with MPS (Figure 4.12). Findings from this pilot study suggest that total pERK and neuron-localized pERK are similarly regulated by imposed strain. However, separate evaluations of intracellular and extracellular pERK may provide additional insight into the level of neuronal ERK activation and its direct effect on other intracellular events that are related to mechanotransduction and nociception. Further studies directly comparing pERK (and other neuronal mediators) and collagen realignment would provide important insight about these and other regulatory processes in neurons.

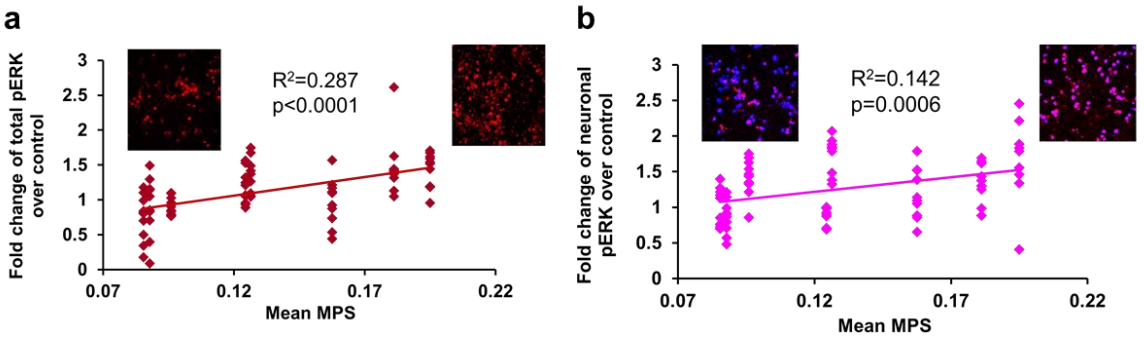


**Figure 4.12.** Both total **(a)** and neuronal **(b)** pERK are positively correlated with NCC strain. Significant correlations are detected between mean elemental maximum principal strain (MPS) and **(a)** total pERK ($R^2$=0.287, p<0.001) and **(b)** neuronal pERK ($R^2$=0.142, p<0.001), both normalized to unloaded control levels. Insets show representative images of total pERK (red) and neuronal pERK (pink).

In addition to the quantitative analysis of pERK expression, there are a few caveats associated with the DFN model used in this work. Long collagen fibers have been reported to uncrimp during tensile loading of ligaments in animal and computational studies (Liao and Belkoff 1999; Franchi et al. 2010). Fiber uncrimping was not included

in the DFN model, but that additional mechanism of fiber deformation may affect the network strain stiffening and reorganization responses under load. The simple fibrous network model used here does not include neurons. Although a computational model only containing fibers is adequate for investigating the matrix and fiber mechanics of the NCCs due to the high compliance and low contractility of neurons (Spedden and Staii 2013; O'Toole et al. 2015), the incorporation of neuronal morphology and surface receptors would better represent the in vivo conditions and enable more explicit measurements of neuronal stresses and strains that can trigger intracellular signaling cascades (Janmey and McCulloch 2007; Hemphill et al. 2011). Moreover, to ensure that quantitative results obtained from the model are relevant and valid, additional parametric studies determining the minimum fiber density required in the simulated network should be performed. Such a convergence study would not only validate the choice of the model parameters, but also assess possible effects of fiber density on fiber kinematics. Nevertheless, the 2D DFN model *does* capture the important mechanical aspects of isotropic collagen networks, including non-affine stiffening and bending-stretching transition (Nair et al. 2014), and does predict a fiber realignment response that mimics the QPLI data from the 3D NCCs (Figures 4.9 & 4.10).

## 4.6. Conclusions & Integration

In summary, the studies in this chapter support the hypothesis that tissue-level strains regulate neuronal ERK phosphorylation likely via changes in the local collagen mechanics, such as fiber realignment and deformation. The distraction magnitude and the

loading rate modulate the macroscopic mechanics of the NCCs (Table 4.1) as well as the degree of collagen fiber realignment (Figure 4.9), which also correspond to altered neuronal shape, orientation and pERK production (Figures 4.7 & 4.8). ERK phosphorylation is *only* significantly increased at supraphysiologic strains, under conditions in which collagen fibers exhibit evident realignment towards the loading direction and high axial strains, pointing to possible effects of the local fiber reorientation and elongation on neuronal activation. Together, these data suggest that there is an association between neuronal activation and the switch-like collagen micromechanical responses that are modulated by the tissue strain and influence the microenvironment of neurons.

The findings from these studies provide insight into why the uniaxial stretch-induced increase in pERK expression is greater in NCCs containing more aligned fibers (Chapter 3). This differential upregulation of pERK by collagen organization is likely related to the degree of collagen realignment during tissue stretch. Fibers aligned along the stretch axis experience higher strains (Figure 4.10), and the afferents that are also oriented in the loading direction can interact with surrounding parallel collagen fibers via cell-collagen adhesion (Tomaselli et al. 1993; Hynes 2002). As a result, axons that are oriented in the loading direction in the aligned NCCs may experience less initial reorientation and undergo greater deformations due to higher local collagen fiber strains, which leads to more robust ERK activation (Chapter 3).

Although the studies in this chapter begins to define potential relationships between aspects of neuronal activation and tissue mechanics across the length scales,

additional work is needed to more fully define the mechanics of collagen networks and fibers in complex tissues, like the facet capsular ligament, in order to understand the interactions between the mechanical and sensory functions of ligaments. Subsequent chapters in this thesis begin to define the multi-scale mechanical responses of the human facet capsular ligament to tensile stretch, providing statistical dependencies between spatially distributed changes in a cell's local biomechanical environment. Work reported in Chapter 5 applies a novel extension of network science methods to investigate how excessive tensile stretch of the human cervical facet capsular ligament affects the meso-scale reorganization of collagen fibers. The studies in Chapter 6 utilize image-based finite element models that capture the structural heterogeneity of human cervical facet capsules to predict the stresses and strains of the collagen networks and fibers in those ligaments.

# Chapter 5

# Network-Level Collagen Reorganization during Cervical Facet Capsular Ligament Stretch

*This chapter has been adapted from:*

Zhang S, Bassett DS, Winkelstein BA. Stretch-induced network reconfiguration of collagen fibers in the human facet capsular ligament. *Journal of the Royal Society Interface*, 13:20150883, 2016.

## 5.1. Overview

Neck trauma and other spinal pathologies can alter the mechanical behavior of the cervical facet capsular ligament and lead to sustained pain (Panjabi et al. 1998a; Cavanaugh et al. 2006; Bogduk 2011). The afferents that innervate the facet capsular ligaments likely have only passive contributions to the mechanics of those ligaments due to their high compliance relative to the surrounding collagen matrix (Wenger et al. 2007; Lopez-Garcia et al. 2010; Spedden et al. 2012). So, they can be oriented, deformed and activated by collagen fiber motions during tissue stretch, as suggested by the findings reported in Chapter 4. Prior studies using collagen-based in vitro constructs and computational modeling suggest that collagen fibers reorient, elongate and generate forces to accommodate macroscopic stretch, altering the microenvironment of the adhered cells (Sander et al. 2009a; Zhang et al. 2016b), and that the micro-scale network alignment and fiber failure affects the macro-scale tissue failure (Hadi et al. 2012a; Hadi

and Barocas 2013). Similar to the responses of simplified artificial collagen constructs, the collagen matrices in the human cervical facet capsular ligaments also exhibit reorganization in response to tissue stretch (Quinn and Winkelstein 2008; Quinn and Winkelstein 2009). However, the reconfiguration process is more complicated in ligaments even during simple uniaxial tension due to the highly heterogeneous fibrous structure that exists within, and across, the native ligament tissue (Quinn and Winkelstein 2008; Ban et al. 2017). Abnormal collagen fiber realignment, which develops prior to ligament rupture and at the site of eventual failure, is localized to certain sub-regions of the cervical facet capsular ligaments and occurs at strains sufficient to induce pain in vivo (Quinn and Winkelstein 2008; Quinn and Winkelstein 2009; Lee and Winkelstein 2009; Dong et al. 2012). However, it is not well understood why some locations in the cervical facet capsular ligament are more prone to structural damage than others during tissue loading. The development of local collagen disorganization at subfailure strains likely depends on, and affects, the motion and coordination of nearby fiber groups (Quinn and Winkelstein 2009; Sander et al. 2009a; Hadi et al. 2012a; Hadi and Barocas 2013). The regional differences in the collagen organization in the cervical facet capsular ligament could result in complex spatial variability in the neuronal responses to tissue deformations and forces, as described in Chapters 3 and 4 (Zhang et al. 2016b; Zhang et al. 2017b). Therefore, understanding the spatially distributed changes in the local biomechanical environment of the neurons in the facet capsular ligament, with a particular focus on the regional differences in collagen reorganization patterns at the

network level, is important for predicting the ligament sub-regions that may be prone to matrix damage and/or nociceptor activation.

Quantification of the temporally coordinated reorganization across spatially-distributed fibers is challenging due to a lack of available analytic tools. Previous methods detecting local collagen fiber reorientation (Quinn et al. 2007; Quinn and Winkelstein 2009; Voycheck et al. 2014) neglect the potential for larger-scale realignment of fiber groups as they adapt to tissue-level deformations. Thus, it is unknown if, and to what extent, local collagen networks display meso-scale organizational changes whose complexity can affect ligament mechanics. Network analysis using graph theory and statistics provides a representational framework to study a system's topological characteristics and dynamics and has revealed important structural and organizational properties in many biological and material systems (Zhu et al. 2007; Blondel et al. 2008; Mucha et al. 2010; Bassett et al. 2014). As such, network analysis was used to resolve the complexity of the coordinated multivariate pattern of collagen fiber realignment in the human cervical facet capsular ligament during tensile loading to failure.

The study reported in this chapter is a subset of the investigations under Aim 1a. Novel network-based techniques were used to investigate how excessive tensile stretch before failure affects collagen reorganization in the human cervical facet capsular ligament. Collagen alignment networks were constructed based on similarity in fiber orientation angles measured by QPLI (Quinn and Winkelstein 2009). Community detection techniques (Jutla et al. 2011; Bassett et al. 2011) were applied to those networks

to identify groups of collagen fibers that display similar alignment angles and to probe their organizational changes due to the development of local collagen disorganization. Dynamic properties of the network architecture were computed based on the temporal changes in fiber alignment. To uncover if there is any possible interplay between time-dependent collagen fiber kinematics and altered tissue-level mechanics, relationships between the dynamic properties of the constructed networks and the ligament forces and stresses were evaluated using linear regressions.

## 5.2. Relevant Background

The structural integrity of ligaments depends on complex interactions between the individual ECM components. At the extreme of the loss of such integrity, the tissue can fail, but the more subtle tissue responses that occur in the macroscopic subfailure regime are also critical in the pathomechanisms of physiological dysfunction. For instance, tissue responses of the cervical facet capsular ligament at strains below tissue failure have important physiological consequences, even in the absence of macrostructural ligament failure. Subfailure stretch of the facet capsular ligament that exceeds its physiologic range can occur during neck trauma and whiplash-like loading (Panjabi et al. 1998a; Siegmund et al. 2000; Bogduk 2011), and has been reported to activate the pain fibers embedded in the collagen matrix of the facet capsular ligament (Chen et al. 2006; Kallakuri et al. 2008; Quinn et al. 2010b; Crosby et al. 2014). The mechanisms by which facet capsular ligament stretch induces pain are believed to depend on the kinematics and kinetics of the local collagen fiber matrix (Zhang et al. 2016b; Zhang et al. 2017b), which

under normal physiological circumstances accommodate macroscopic tissue deformations via local fiber motion and matrix reorganization (Quinn and Winkelstein 2009; Sander et al. 2009a; Quinn et al. 2010a). However, some facet capsular ligament loading conditions can result in local collagen disorganization that may eventually lead to tissue failure (Quinn and Winkelstein 2008; Quinn and Winkelstein 2009; Quinn et al. 2010a; Dong et al. 2012). Despite increasing evidence supporting this notion, collagen fiber kinematics during facet capsular ligament loading and the ability to predict the relationships between those responses and tissue-level mechanics are still not well understood.

The reconfiguration of collagen fibers during facet capsule loading can be characterized as either *normal* or *anomalous*. Anomalous collagen fiber realignment occurs when local fiber directions change significantly more than expected in the majority of the tissue, redistributing the forces after the load-bearing fibers have failed (Quinn and Winkelstein 2009; Quinn et al. 2010a). Anomalous fiber realignment is an important predictor of tissue failure; it has been associated with the occurrence of altered mechanical properties, occurs prior to any visual signs of tissue rupture, and predicts the location of eventual tissue failure (Quinn and Winkelstein 2008; Quinn and Winkelstein 2009; Quinn et al. 2010a).

Fiber realignment during loading has been measured empirically using dynamic quantitative polarized light imaging to generate a sequence of spatial maps of collagen fiber alignment over time (Tower et al. 2002; Quinn and Winkelstein 2008; Quinn et al. 2010a). Prior studies have demonstrated the feasibility of using QPLI to accurately assess

collagen fiber alignment in human cervical facet capsular ligaments (Quinn and Winkelstein 2008; Quinn 2010; Quinn and Winkelstein 2011; Lee and Winkelstein 2012). The correlations between alignment vectors over time have previously been used to define regions of anomalous fiber realignment, which enables accurate quantitative and spatial measurements of changes in collagen fiber orientation (Quinn and Winkelstein 2009). Yet, that detection technique and existing image-based computational models capture tissue damage at the single pixel or fiber level (Quinn and Winkelstein 2008; Quinn and Winkelstein 2009; Sander et al. 2009a). Accordingly, they do not capture the larger-scale collective realignment of fiber *groups* as they adapt to facet capsular ligament loading. As such, it is not known if, and to what extent, the collagen matrix displays spatially extended domains whose changes during macroscopic loading may affect, or relate to, the mechanical behavior of ligamentous tissues. The eventual rupture of collagenous tissue involves damage to collagen fiber bundles and/or a large number of distributed collagen fibers in domains greater than several fibers in the micro-scale (Hayashi et al. 2003; Hodgson et al. 2012; Hadi and Barocas 2013). As such, understanding the changes in meso-scale collagen fiber networks prior to the development of anomalous fiber realignment may improve the detection and prediction of tissue failure.

Understanding collagen realignment has been hampered by the lack of analytic methods to probe the collective *coordination* of realignment across many spatially distributed fibers. The complexity of this coordinated multivariate process is hypothesized to be successfully captured using tools from the field of network science

(Newman 2010). Networks provide a useful representational framework to systematically examine the topological characteristics and the dynamics of complex systems (Zhu et al. 2007; Ganguly et al. 2009; Bassett et al. 2013b). System components are represented as network nodes and their relationships with one another are represented as network edges (Rubinov and Sporns 2010; Kaiser 2011). In many biological (Luscombe et al. 2004; Zhu et al. 2007; Meunier et al. 2009) and material (Bassett et al. 2012; Bassett et al. 2014) systems, this formalism reveals important organizational changes that impact the system's underlying structure and resulting function. For example, network-based tools known as *community detection techniques* can be used to characterize the presence and organization of local geographic domains in non-biological materials (Bassett et al. 2012; Walker and Tordesillas 2014; Bassett et al. 2014) which are referred to as *network communities* or *modules*. Those domains constrain sensitivity to mechanical perturbations in the form of acoustic signals (Bassett et al. 2014) and track alterations in material topology as a function of applied force (pressure) (Bassett et al. 2012), indicating their broad sensitivity to material microstructure.

The study in this chapter investigated the effects of the stretch-induced microscopic fiber movements on the meso-scale organization of local collagen networks in relation to facet capsular ligament mechanics using tools from network science. Collagen networks were defined based on the similarity in fiber alignment directions acquired using QPLI during facet capsular ligament loading, and applied novel community detection techniques (Mucha et al. 2010) to probe the organizational changes that may be due to anomalous realignment of fibers. The temporal evolution of the

network was captured using diagnostics such as modularity, which measures the presence and strength of time-dependent communities, and flexibility, which measures the reconfiguration of communities (Mucha et al. 2010; Bassett et al. 2011). Dynamic properties of the network architecture were compared between regions with anomalous realignment (AR) and regions with normal realignment (NR) in the facet capsular ligament, and their associations with macroscopic tissue mechanics were evaluated. The work reported in this chapter tested the hypothesis that regions with anomalous realignment are associated with greater changes in the collagen network structure than regions with normal realignment, and that network disorganization contributes to the loss of tissue mechanical integrity, both of which are detectable using the community detection technique.

## 5.3. Methods

### 5.3.1. Collagen Alignment & Macromechanics of Facet Capsular Ligaments

The collagen fiber alignment data and mechanical data for the human cervical facet capsular ligaments were obtained previously during loading using a system that integrates QPLI with a tensile testing device in our lab (Quinn and Winkelstein 2009). The studies in this chapter only include those specimens (n=7; age 63±15 years) in which anomalous realignment was detected with sufficient light transmission and in the mid-substance (central region) by a previously-defined vector correlation analysis (Quinn and Winkelstein 2009). The nine specimens that were excluded had either a low signal-to-noise ratio during polarized light imaging, leading to no detection of anomalous fiber

realignment, or the onset of collagen disorganization occurring only along the tissue edges, which could be due to boundary artifacts. Donor information, specimen dimensions and the displacement at the onset of anomalous fiber alignment for the seven human cervical cadaveric facet capsular ligaments used in this analysis are detailed in Appendix G.

Briefly, the C4/C5 human facet joints were dissected with the ligament-bone attachment preserved. The width and thickness of unloaded specimens were measured using a digital caliper, and was used to estimate the cross sectional area. The bone-ligament-bone specimens were cast in aluminum cups that were fixed to the testing machine and underwent uniaxial tensile loading at 0.5mm/s applied by a testing machine (Instron 5385; Instron Corporation, Norwood, MA), with tissue forces and displacements acquired at 1kHz. Prior to testing, the mid-substance of the ligament surface of each human C4/C5 facet capsular ligament sample was labeled with a grid of fiduciary markers dividing it into sub-regions (Figure 5.1). QPLI data were acquired with a 12.5 pixel/mm resolution in the unloaded reference position with the ligament under 5kPa of pre-stress, and also during continuously applied uniaxial tensile distraction until tissue failure. Continuous collagen fiber alignment maps were generated at 0.04s increments during loading until tissue failure. Stress was also estimated for each specimen throughout loading using the recorded force data and that specimen's unloaded cross-sectional area.

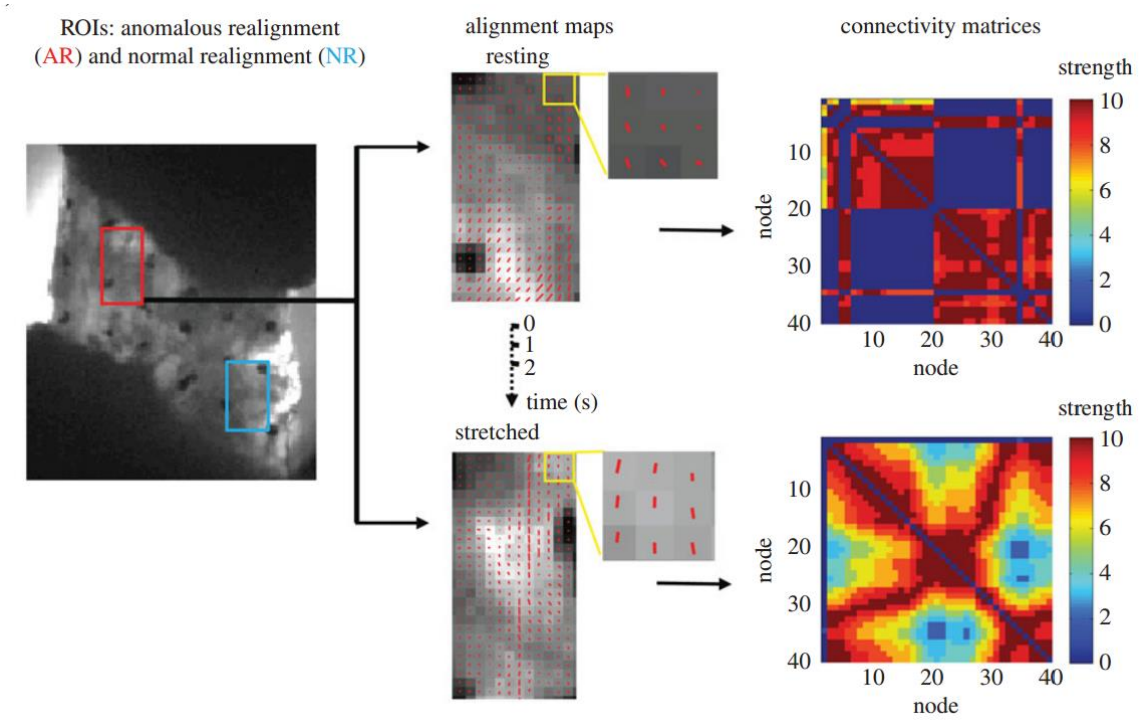


**Figure 5.1.** Network construction using QPLI data from the human cervical facet capsular ligament. QPLI images obtained before and during loading were used to generate pixel-wise collagen alignment maps in the selected ROIs of anomalous realignment (AR; red box) and normal realignment (NR; blue box) at rest, at the onset of anomalous realignment, and in between those two time points at 1s increments. Rectangular ROIs were defined using the upper left and lower right fiduciary markers as the common information between different time points. Network nodes were defined as 3x3 pixel windows in the ROIs at rest. Representative 3x3 pixel windows are shown at the resting and the stretched states, with corresponding demonstration of alignments. Network edges were established based on the difference in alignment angles between nodes. Weighted networks were constructed by thresholding and scoring the connection strength from 1 to 10. Connectivity matrices, with nodes numbered spatially, display the pairwise connectivity strength.

### 5.3.2. Network Construction

For each specimen, two rectangular regions of interest (ROIs) were created, including: (1) a region with anomalous fiber realignment and (2) a region with normal realignment (Figure 5.1) based on previous work using similar regions as mesh elements

for strain field calculations (Quinn and Winkelstein 2008; Quinn and Winkelstein 2009). Tissue strains, such as the principal Lagrangian strains, have been used previously to define mechanical thresholds of soft tissues to loading; for example, strain thresholds have been defined for facet capsular ligament's yield and failure, and for nociception from the facet capsular ligament (Deng et al. 2000; Lee et al. 2004b; Lu et al. 2005b; Gefen et al. 2008; Quinn and Winkelstein 2008; Quinn et al. 2010a). However, most tissue strains measured in those earlier studies are macroscopic and lack the resolution to detect microscopic tissue responses in sub-failure conditions. Therefore, techniques that detect collagen fiber realignment have been developed to identify sub-regions in the facet capsular ligament where excessive collagen disorganization occurs during loading prior to gross tissue failure (Quinn and Winkelstein 2009).

ROIs were selected based on those pre-determined areas of normal and anomalous realignment. The normal realignment ROIs were chosen uniformly at random from the set of all normally realigned regions with sufficient, but not excessive, light transmission. Since fiber reorganization is the only criterion for the selection of ROIs, the group of normal realignment areas includes regions that are both adjacent to, and distant from, the anomalously realigned regions. That group also includes both regions that eventually developed visible rupture and regions that did not rupture. For anomalous realignment, regions that were chosen as ROIs exhibited the most anomalous realignment but did not sustain the maximum principal strain of the ligament in order to represent collagen networks with the most detectable microscopic damage. Among all of the samples that were examined, only one of the 17 regions of anomalous fiber realignment

overlapped with the location of the sample's maximum principal strain, suggesting a disconnect between tissue strain and fiber realignment measures (Quinn and Winkelstein 2009). Therefore, in order to decompose the effects of ligament strain and anomalous fiber realignment on the tissue response to injurious loading, only AR regions that displayed no co-localization with maximum principal strain were evaluated.

Within each ROI, the fiber alignment maps generated from the QPLI data were taken to construct discrete networks at 1s increments from the unloaded pre-stressed resting position to the onset of anomalous fiber realignment (Figure 5.1). The nodes of the collagen networks were defined as non-overlapping 3x3 pixel windows in each ROI at the resting state, in order to decrease the sensitivity of the fiber orientation measurement to the random noise present at single pixels. Eight-pixel connectivity has been used to eliminate random noise when defining the occurrence of anomalous realignment (Quinn and Winkelstein 2009). In ROIs at the stretched positions, network nodes were defined based on the nodal configuration from the resting state. That is, the same number of nodes in each row and each column as in the resting position were used in order to generate networks with identical numbers of nodes before and during loading; this is a feature necessary for a fair comparison of network properties (van Wijk et al. 2010).

The mean alignment direction was defined in each window as the average of the fiber orientation angles within one standard deviation of all angles in that 3x3 pixel window. Using one standard deviation, on average two pixels from the 3x3 pixel window that were farthest from the mean alignment direction were removed. This approach

minimized outliers (Swingler 1996) due to fiber alignment measurement from aberrant pixels, but remained sensitive to the main alignment direction represented by a majority of fibers in each widow. Two nodes were considered "connected" by a network edge if the difference in the mean alignment direction of the two nodes was less than 90°. Integer weights were assigned to each edge from 1 (a difference of up to 100% of the 90°) to 10 (a difference of less than 10% of the 90°), such that smaller differences (greater similarity in mean alignment directions) weighed more (Figure 5.1). For instance, the edge between two nodes whose difference in mean alignment direction was smaller than 9° was given a weight of 10 (i.e. strongest connection), while the edge between two nodes whose difference in mean alignment direction was between 81° and 90° was given a weight of 1 (i.e. weakest connection). This integer weighting scheme is consistent with our confidence in the measured angles produced by the QPLI measurement, where a 9° polarizer step exists between each QPLI image collected during data acquisition (Quinn and Winkelstein 2008; Quinn and Winkelstein 2009; Quinn et al. 2010a).

### 5.3.3. Static Community Detection & Network Visualization

A goal of this study was to understand differences in the stretch-induced network organization in both regions of the facet capsular ligament using networks measured in the unloaded condition in comparison to networks measured at the onset of anomalous fiber realignment. To quantify network organization, static community detection (a form of clustering for networks) was performed by optimizing a modularity quality function (Newman 2006) using a Louvain-like locally greedy algorithm (Blondel et al. 2008). In

this approach, modules are defined as sets of nodes that are more highly inter-connected than expected in an appropriate statistical null model (Blondel et al. 2008; Kaiser 2011) (Figure 5.2a). The modularity index, which is optimized over different configurations that compartmentalize the network into modules, quantifies how well a network is segregated into modules. The mathematical definition for the modularity index is provided in Appendix H.

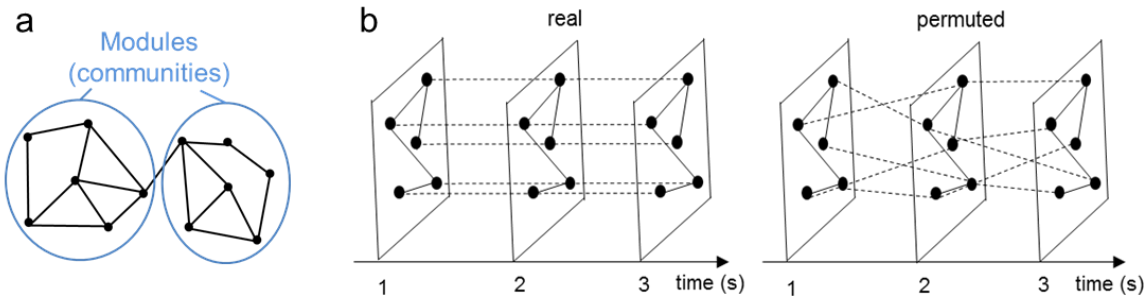


**Figure 5.2.** Schematic of network modules and multilayer networks. **(a)** Modules or communities refer to sets of nodes that are more highly interconnected than expected in an appropriate statistical null model. **(b)** In multilayer networks, consecutive time windows were connected by linking each node to itself for real networks or linking nodes randomly to create permuted networks as nodal null models.

Because of the near degeneracy of the modularity landscape (Good et al. 2010), the modularity quality function was optimized 100 times and a consensus partition was constructed for each network at the resting state and for each network at the onset of anomalous realignment, separately for both region types (AR, NR) in each specimen. To quantify how well the network was segregated into modules, the modularity was calculated using the consensus partition for each state (resting, onset of anomalous realignment) and region (AR, NR). To determine the statistical significance of these modularity values, commonly used comparative benchmark networks were constructed

by rewiring each collagen network 20 times while preserving the number of nodes, the number of edges, and the degree distribution. The *degree* of a node is defined by the number of connections emanating from that node. In this way, 100 benchmark null models were created and an optimized modularity value was acquired from each null model. The mean modularity was computed over those 100 benchmark networks and compared to that observed in the real network.

Since network size and connectivity density may influence graph properties (van Wijk et al. 2010), the relationships between modularity and each of the mean node degree and connection strength were evaluated. Average node degree was defined as the total number of edges divided by the number of nodes. Average *weighted* node degree was defined as the sum of edge weights in the network divided by the number of nodes. Correlations between modularity and weighted and unweighted node degrees were evaluated using linear regression models. To further assess the dependency of modularity on node degree, the number of edges after stretch was fixed to be the same as that observed at the resting state by preserving the strongest connections. The modularity of the collagen networks before and after stretch, in regions with and without anomalous fiber realignment, was computed and compared across states.

To visualize community structure, the Fruchtermann-Reingold algorithm (Fruchterman and Reingold 1991) was used to determine the placement of communities for each network, and the Kamada-Kawai algorithm (Kamada and Kawai 1989) was employed to position nodes within a community (Traud et al. 2009).

### 5.3.4. Dynamic Community Detection & Tissue Mechanics

The evolvability of the collagen network was investigated; its relationship to changes in the mechanical responses of the facet capsular ligament during loading was also evaluated using dynamic community detection. Dynamic modular structure was evaluated using a multilayer network framework created by linking nodes between consecutive time steps (Mucha et al. 2010) (Figure 5.2b). Layers in the multilayer network represent time windows that were 1s apart, starting from the baseline resting state and continuing through to the first detection of anomalous fiber realignment. In the multilayer network, identity links connected nodes in a given time window to themselves in the previous and subsequent time windows (Figure 5.2b). The multilayer modularity index were optimized over partitions of nodes into communities over time (Mucha et al. 2010). After 100 times of optimization, a consensus partition was determined using the method outlined by Bassett et al. (2013a).

To quantify statistical significance, 100 nodal null model networks were constructed for each real network by permuting the inter-layer connections uniformly at random (Bassett et al. 2011) (Figure 5.2b). To describe the evolution of communities in collagen networks during loading, four diagnostics were calculated (Bassett et al. 2011): the multilayer modularity index, the number of modules, stationarity, and flexibility. The mathematical definitions for these dynamic network diagnostics are detailed in Appendix H. Values of these diagnostics estimated in the real networks were compared to the mean values of the same diagnostics averaged over the set of 100 nodal null model networks constructed for each real network. Differences in network diagnostics between the AR

and NR regions were assessed to investigate the relationships between anomalous fiber realignment and dynamic properties of the community structure of the tissue.

To study the associations between dynamic features of the local collagen network and tissue mechanics, linear regressions were used to measure the correlations between the network flexibility and the forces and stresses generated in the tissue at the onset of anomalous realignment.

### 5.3.5. Statistics

All computations and statistical tests were performed using MATLAB and JMP (version 11; SAS Institute; Cary, NC). The Brain Connectivity Toolbox (Rubinov and Sporns 2010), community detection code (Jutla et al. 2011) and nodal null models (Mucha et al. 2010; Bassett et al. 2011) were used to implement the network computations.

Paired t-tests were used to test differences in modularity and the number of modules before and after stretch in AR and NR regions, and between real and randomized networks, both of which were further verified using nonparametric permutation tests. For the case of dynamic community detection on multilayer networks, the differences in the four network diagnostics (modularity, number of modules, stationarity, flexibility) were computed between real networks and nodal null models. Whether these differences were significantly different from zero was tested using one-sample t-tests. Paired t-tests evaluated the differences in network diagnostics between the

two regions (AR and NR) of the facet capsular ligament. Significance of all linear regressions were tested using separate f-tests, with significance at 0.05.

## 5.4. Results

Networks of AR and NR regions had similar sizes: 39.4±7.4 nodes and 39.7±4.5 nodes, respectively. The two network sizes were not statistically different from one another ($p=0.924$). Individual diagnostics values for the AR and NR networks of each sample are summarized in Appendix H.

### 5.4.1. Static Modular Structure

Regions with anomalous fiber realignment exhibit heightened modular structure in the resting state compared to the state in which the ligament was stretched. Specifically, AR regions display decreases in both the modularity ($p=0.030$) and the number of modules ($p=0.015$) after loading compared to rest (Figure 5.3). No difference is observed in NR regions after loading compared to rest (Figure 5.3b). These results suggest that more robust collagen fiber reorientation altering the network architecture occurs during loading in regions sustaining local fiber damage.

In the AR regions, significant increases are found in the unweighted ($p=0.017$) and weighted ($p=0.007$) node degrees at the onset of anomalous realignment with respect to rest. Both the unweighted ($R=-0.471$; $p=0.011$) and the weighted ($R=-0.642$; $p<0.001$) node degrees display significant negative correlations with modularity (Figure 5.4). After fixing the unweighted node degree of the stretched networks to be the same as that of the

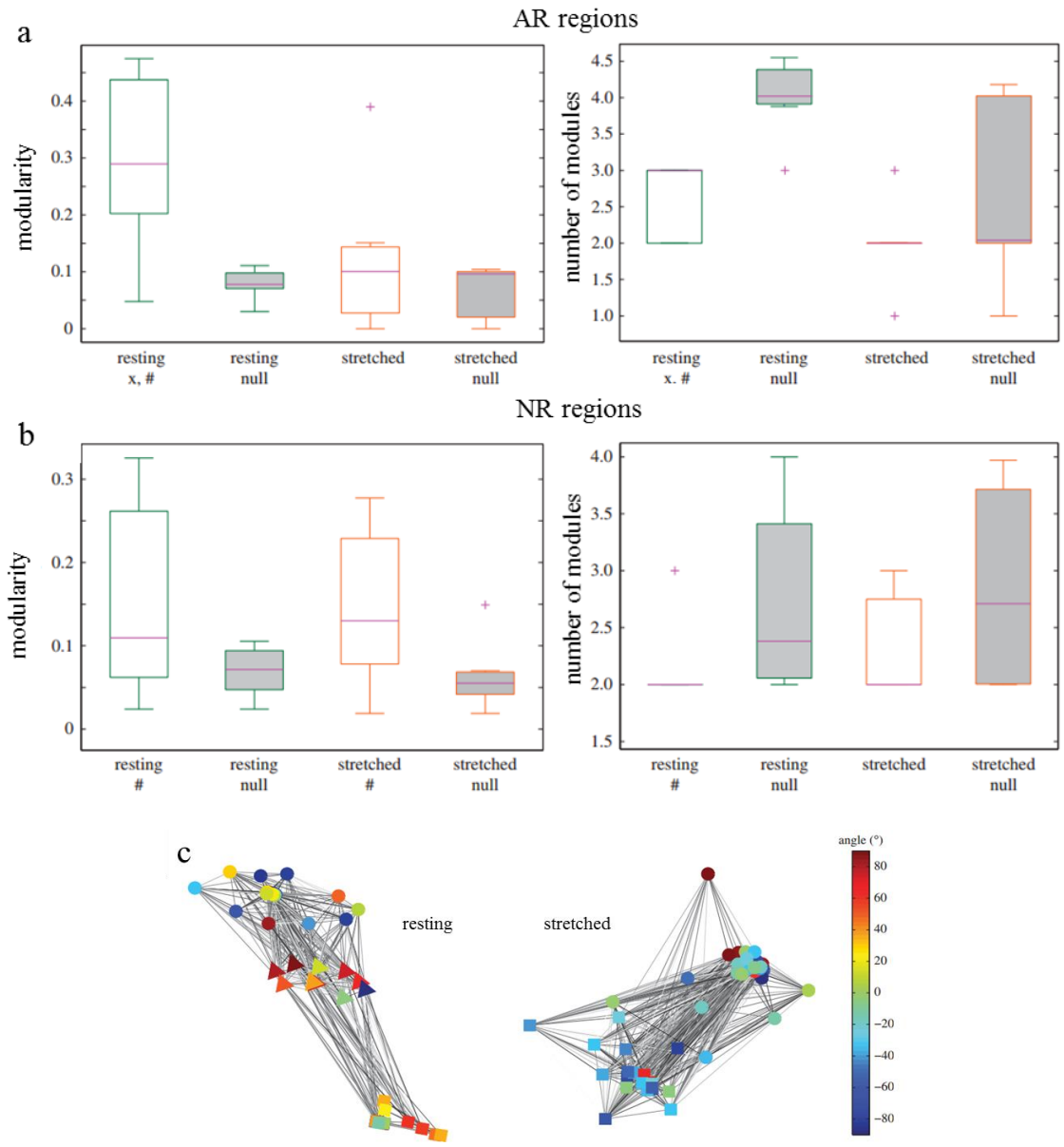


**Figure 5.3.** Static modular structures. **(a)** Modularity and the number of modules of collagen networks in regions with anomalous realignment show significant changes from the non-random resting state (green boxes) to the random state at the onset of anomalous realignment (orange boxes). **(b)** In contrast, regions with normal realignment display no difference before (green boxes) and after (orange boxes) stretch. Below each boxplot, a single cross (×) represents differences between rest and the onset of atypical realignment ($p<0.031$); the pound sign (#) represents differences between real and randomized networks ($p<0.035$). **(c)** Visualization of community structures of a representative AR region. Force-directed placement of modules and nodes was used. Module assignment is indicated by node shape. Node color shows the mean fiber angle at a given node. Edge strength is displayed in grayscale with black representing the maximum weight.

resting-state networks by preserving the strongest connections, statistical differences are no longer detectable for modularity or weighted node degree between the resting and the stretched networks for either the AR or NR regions. These findings indicate that nodal-level changes play an important role in shaping the modular structure of the collagen network during facet capsular ligament loading.

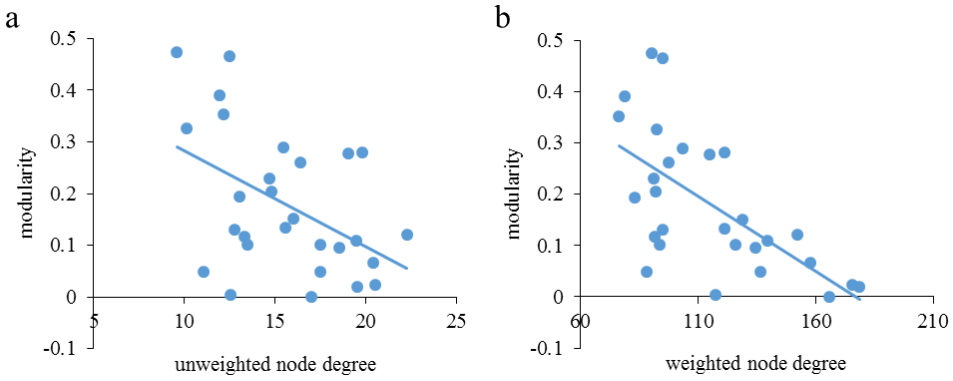


**Figure 5.4.** Correlations between modularity and both unweighted and weighted node degrees. **(a)** Modularity is significantly correlated with the unweighted node degree ($R=-0.437$; $p=0.0114$). **(b)** A stronger negative correlation is found between modularity and the weighted node degree ($R=-0.642$; $p=0.0002$).

Collagen networks in the AR regions display topological alterations from rest to the onset of anomalous realignment. Only anomalously realigned regions under stretch show similar modularity and number of modules as null model networks, while the other three networks (AR region at rest, NR region at rest, NR region at the onset of anomalous realignment) exhibit significantly heightened ($p<0.035$) modular structure in comparison to the null model networks (Figure 5.3). The decreased modularity and the number of modules that are comparable to random levels in the anomalously realigned region after stretch is likely driven by an increase in the number of inter-modular connections as the alignment directions become more similar between modules after loading (Figure 5.3c).

### 5.4.2. Dynamic Modular Structure

Dynamic community detection on multilayer networks reveals that the collagen network reorganizes smoothly and adaptively over time. For both of the AR and NR regions, collagen fiber networks exhibit significantly higher modularity ($p<0.013$) than the null model (Figure 5.5), indicating the presence of long-lasting modules that reflect coordinated fiber movements. In comparison to dynamic null model networks in both the AR and NR regions, a significant increase is found in stationarity, which measures the maintenance of nodal composition of modules over time ($p<0.004$). A significant decrease is observed in flexibility, which characterizes the altered nodal allegiance to modules, ($p<0.004$), indicating a smooth temporal transition between the resting and the stretched states (Figure 5.5). There is no difference in the number of modules between the real and null model networks (Figure 5.5). Together, these findings suggest coordinated realignment of fibers to smoothly adapt to macroscopic ligament loading.

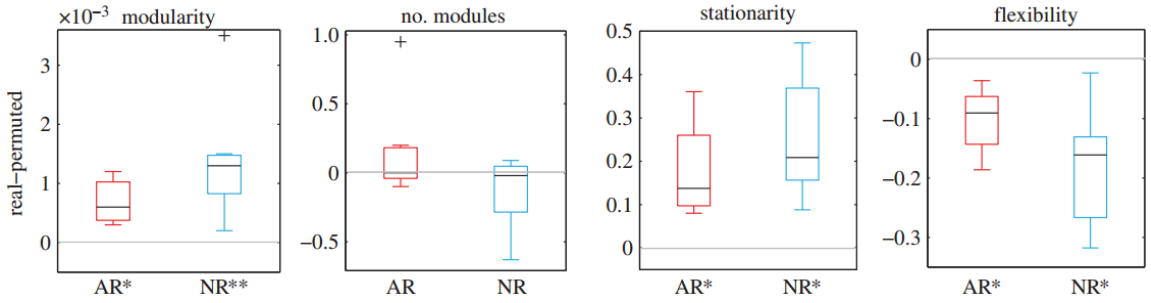


**Figure 5.5.** Network diagnostics of multilayer networks. Significant differences in modularity, stationarity, and flexibility are found between real and permuted networks for both regions with and without AR. No difference in the number of modules is detected. Asterisks are used below each plot to indicate significant differences from zero (grey line). A single asterisk (*) indicates $p<0.004$; double asterisks (**) indicate $p=0.013$.

### 5.4.3. Regional Differences in Flexibility

Differences in flexibility and its relationships to facet capsular ligament mechanics are found in regions with and without anomalous realignment. Flexibility is significantly increased (p=0.029) in the AR regions compared to the NR regions in the same sample as tested by a paired one-tailed t-test (Figure 5.6a). Significant correlations between the flexibility of the NR regions and each of the stress (R=0.890; p=0.007) and force (R=0.877; p=0.010) developed in the facet capsular ligament are observed (Figures 5.6b & 5.6c). Whereas, although trending the same as the NR regions, AR regions show no association between flexibility and either the facet capsular ligament force or stress (Figures 5.6b & 5.6c). Larger differences in flexibility between the AR and NR regions occur in samples that produce lower forces and stresses at the onset of anomalous fiber realignment (Figures 5.6b & 5.6c). These flexibility-related regional differences suggest

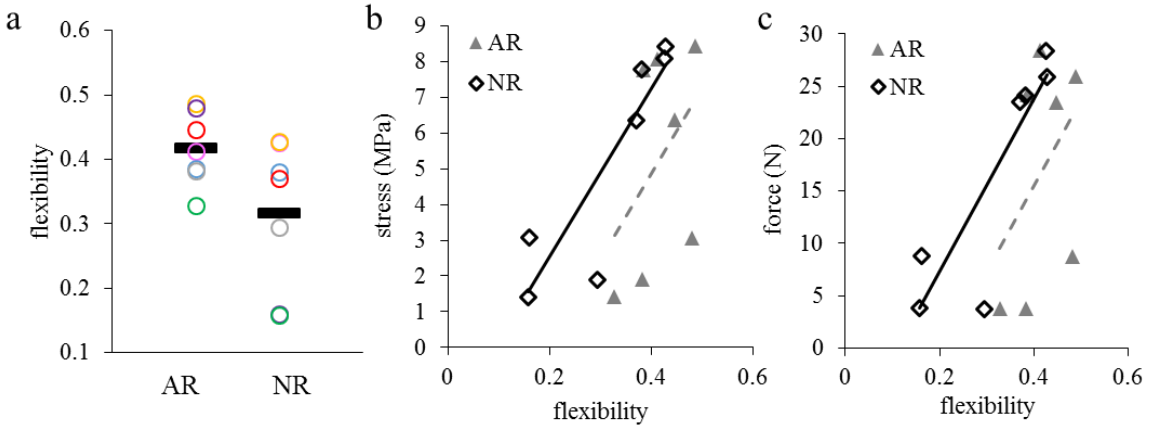


**Figure 5.6.** Regional differences in flexibility. **(a)** Regions with anomalous realignment (AR) exhibit significantly higher flexibility than normally realigned (NR) regions. Open circles (○) in the same color represent flexibility from the same facet capsular ligament sample; black bars (▬) indicate the mean flexibility in each region. Correlations between flexibility and **(b)** stress and **(c)** force in the facet capsular ligament at the onset of anomalous realignment are only significant in regions with NR (R=0.890, p=0.007 for stress; R=0.877, p=0.010 for force), but not in regions sustaining NR.

that abnormal reorganization of collagen networks over time may contribute to the mechanical events that occur at the first detection of anomalous realignment, which associates with the impaired mechanical integrity of the facet capsular ligament.

## 5.5. Discussion

Collagen fiber realignment is a possible mechanism by which force from macroscopic facet capsular ligament stretch deforms and activates pain fibers embedded in the collagen matrix. This work used analytic tools from the field of complex systems to investigate the stretch-induced collagen reorganization in the human facet capsular ligament, whose loss of structural integrity may lead to changes in tissue mechanics and cellular responses (Kallakuri et al. 2008; Bogduk 2011; Winkelstein 2011; Dong et al. 2012). Fiber alignment maps generated using QPLI were converted into weighted collagen alignment networks based on similarity in fiber alignment directions. Community detection methods reveal differences in the modular structure of the constructed collagen networks before and after tensile loading in regions with previously identified anomalous fiber realignment leading to tissue failure (Figure 5.3). Specifically, regions with anomalous fiber realignment, but not those with normal realignment, exhibit significantly decreased modularity at the onset of atypical fiber realignment compared to the resting state (Figure 5.3). This decrease in AR regions leads to modularity that is no longer different from that of the null model network (Figure 5.3). Dynamic community detection on multilayer temporal networks from rest to the onset of anomalous realignment uncovers significantly heightened modular structure as well as higher

stationarity and lower flexibility in the real collagen networks with respect to dynamic null model networks in both AR and NR regions (Figure 5.5). These dynamic features in the real networks suggest a smooth and adaptive process of network reorganization during loading. Significant increases in flexibility and loss of correlation between flexibility and facet capsular ligament mechanics are found in the AR regions compared to NR regions (Figure 5.6), providing evidence of the contribution of local collagen network reorganization to impaired mechanical integrity of the ligament observed at the onset of anomalous fiber realignment.

### 5.5.1. A Stretch-Induced Decrease in Modularity

The finding that local collagen networks of the facet capsular ligament are modular at rest (Figure 5.3) is consistent with the facet capsular ligament morphology. Macroscopic and microscopic investigations have revealed that the human facet capsular ligament is composed of irregular connective tissues and parallel bundles of collagenous fibers that run in different directions (Yamashita et al. 1996; Kallakuri et al. 2012). In the inferior region of the joint, the fibers run in a superior-medial to inferior-lateral direction, whereas in the superior and middle part of the joint, the fibers cross the joint space in the medial-to-lateral direction (Yamashita et al. 1996). This well-organized fiber orientation composed of more than one preferred alignment direction in the facet capsular ligament is expected to provide heightened modular structures in the collagen networks than random networks as shown using static community detection (Figure 5.3).

Modularity decreases from rest to the onset of anomalous fiber realignment only in regions that developed atypical fiber reorganization (Figure 5.3). Increases in the mean node degree and average connection strength are potential drivers of the decrease in modularity, as quantitatively confirmed by the significant negative correlations between modularity and both weighted and unweighted average node degrees (Figure 5.4). Thresholding the stretched collagen networks to decrease the number of connections to the resting level while preserving the strongest connections eliminates the difference in modularity between the resting and the stretched states (Figure 5.4). This finding suggests that loading-induced generation of substantially more weak connections in regions sustaining anomalous fiber realignment plays an important role in collagen network reorganization towards the impaired state.

The modular structure of the collagen network at rest is disrupted during stretch of the facet capsular ligament and undergoes a transition to random topology in the regions with anomalous fiber realignment (Figure 5.3). Tensile stretch is known to realign collagen fibers towards the direction of loading (Vader et al. 2009; Lake and Barocas 2011), which is expected to decrease the angle differences between collagen bundles aligned in different directions. Substantial fiber realignment with decreasing angle differences during tensile loading can lead to an increase in inter-modular connections at the network scale and can result in altered topology; this notion was qualitatively supported by visualization of the network (Figure 5.3). The structural shift from the modular architecture to a random architecture is likely driven by complex topological changes rather than simply an increase in the node degree. Collagen networks

before and after stretch were both compared quantitatively to their respective null model networks with the same node degree, but exhibit different structural features. It is important to understand the topological contributions to the altered network architecture, since network-level abnormality may be more detectable and more related to mechanical changes in the macro-scale than nodal-level changes.

### 5.5.2. Dynamic Fiber Reorganization During Loading

Resolving how external loading regulates cellular behaviors is often confounded by dynamic collagen fiber reorganization in the extracellular matrix. Defining the time-dependent fiber kinematics continues to become more feasible due to advancing imaging techniques and computational models (Tower et al. 2002; Quinn and Winkelstein 2009; Sander et al. 2009a; Wang et al. 2014). Yet, quantification of coordinated reorganization across spatially distributed fibers over time in real human tissue remains a challenge due to a lack of analytic tools. This challenge was addressed in this work using graph theoretical tools – particularly dynamic community detection of collagen networks – to explore the temporally-evolving network architecture of this biological material. Higher stationarity, lower flexibility, and heightened modular structure of dynamic collagen networks compared to dynamic network null models indicate the existence of enduring modules, which implies that collagen fibers collectively and smoothly adapt to facet capsular ligament loading in a coordinated manner. This stretch-induced adaptive realignment of collagen fibers may modulate mechanical behaviors of the facet capsular ligament as well as other tissues with complex geometry and anatomy, since collagen

fiber realignment contributes to the inhomogeneity and nonlinear stress-strain relationships of the material (Lake et al. 2009).

Mechanical events, including material yield or partial failure indicated by a sudden decrease in force with increasing displacement, occurred at the first detection of anomalous realignment for every specimen included in this study (Quinn and Winkelstein 2008; Quinn and Winkelstein 2009). In addition to those observations at the onset of anomalous realignment, there is a correlation between tissue forces and flexibility *only* in the NR regions, but not in the AR regions, at the first occurrence of tissue yield and visible rupture that occurred before and after the first detection of atypical reorganization (Figure 5.7). At the eventual gross failure, no correlation was detected between tissue forces and the flexibility measured in either the NR or AR regions (Figure 5.7). The loss of association between facet capsular ligament mechanical properties and flexibility that occurs before failure in anomalously realigned regions (Figure 5.6) suggests that dynamic changes of mescoscopic collagen networks may contribute to the subfailure impairment of mechanical integrity at the tissue level. The relationships found between collagen fiber realignment and the mechanical parameters of the ligament imply a structure-function correlation in the facet capsular ligament. Anomalous fiber realignment develops at strains significantly lower than those at rupture and predicts the region of visible failure (Quinn and Winkelstein 2009). Since significant differences in flexibility are observed between AR and NR regions from rest to the onset of anomalous realignment (Figure 5.6), flexibility may be used as a predictor of microstructural abnormality that may lead to eventual ligament failure.

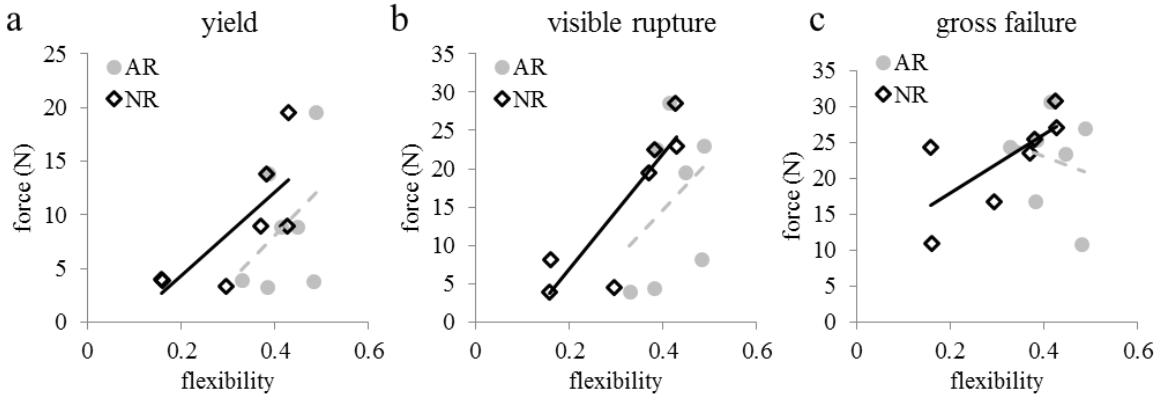


**Figure 5.7.** Relationships between tissue force and nodal flexibility at yield and failure. Significant correlations between flexibility and force at the **(a)** first occurrence of yield (R=0.759; p=0.0476) and **(b)** visible rupture (R=0.879; p=0.0092) are found only in the NR regions, but not in regions sustaining AR. **(c)** Force and flexibility are not significantly associated in either the NR or AR region at gross failure.

Fiber alignment-based measurements to detect sub-failure tissue damage likely have higher sensitivity than the bulk strain measurements. Fiber strains in computationally modeled fibrous networks during uniaxial tensile loading can vary spatially and exceed the applied bulk strain depending on the fiber orientation (Zhang et al. 2016b). The cascade of fiber failure, load redistribution and reorientation of intact fibers that leads to anomalous realignment at the micro-scale can be complex and non-uniform, particularly considering the structural heterogeneity of the facet capsular ligament. Therefore, those microscopic changes may not directly align with macroscopic strain measurements. However, the more precise measurements of altered tissue structure instead provide higher resolution to probe tissue impairment in the subfailure regime. In addition, macroscopic tissue strains were typically measured in two dimensions with surface markers, while the QPLI technique captures the average fiber alignment response

along the third dimension of the tissue's thickness. Since the facet capsular ligament is non-uniform through its thickness, alignment-based measurements, such as flexibility, may be more predictive of tissue damage and failure than two-dimensional strains.

### 5.5.3. Methodological Considerations

There are several methodological considerations relevant to this work. First, it remains an open question how to determine certain input parameters used in this technique, including the pixel window size used to define nodes and the cut-off threshold used to establish connections between nodes. Changes in the input parameters can alter the network size and connection density, which may affect network properties (van Wijk et al. 2010). The parameters used to construct the networks in the current study were chosen based on previously assessed accuracy of the QPLI techniques. Small perturbations of the pixel window size and the cut-off angle threshold vary the network size and density. However, those changes are not sufficient to alter the finding that the loading-induced changes in modularity only occurred in the AR regions, but not in the NR regions (Figure 5.8), suggesting that this technique is robust to small variations in input parameters. Nevertheless, systematic testing of different thresholds and other relevant input parameters would determine the effects that diverse thresholding methods (Rubinov and Sporns 2010; Lohse et al. 2014) and parameter choices might have on detecting changes in collagen network structure. Second, there may be additional means for converting the angle differences into edge weights for collagen network construction. In this study, the angle difference was evenly scored from 1 to 10 to generate the

connection weights. An alternative is to assign weights based on the probability distribution of the alignment angle difference. Another possible approach is to study the fully weighted network. However, the angle difference still needs to be converted to connection strength since those two quantities are inversely related. More evaluation is needed to determine the optimal method for weight assignment.

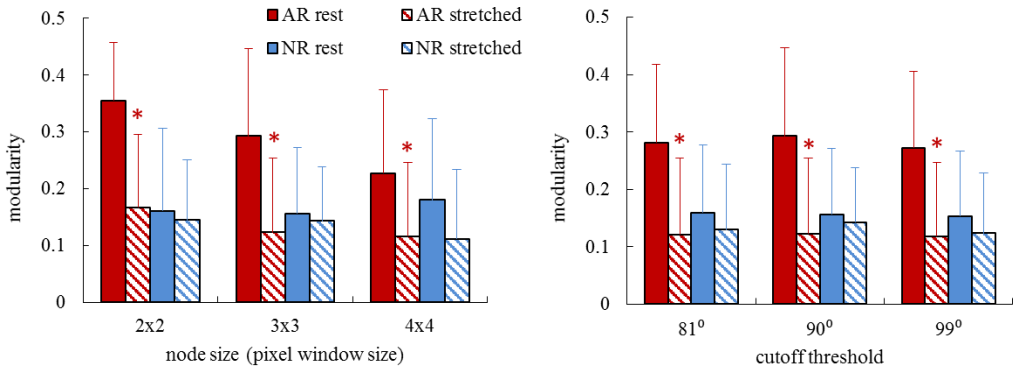


**Figure 5.8.** Modularity of networks in different regions at different states, with changes in the node size and the cutoff threshold. Significant decreases (*p<0.035) in modularity after loading as compared to the resting state only occur in the AR region, but not in the NR region, despite altered network parameters.

An alternative approach to quantifying the microstructure of collagen matrix is to use two-point or higher order correlation functions. The two-point correlation function is a widely used statistic that describes the spatial heterogeneity of the material morphology (Jiao et al. 2007; Jones et al. 2014). It defines the distribution of a set of point processes by comparing each point with every other point in the measured space (Jiao et al. 2007; Baniassadi et al. 2012). Statistical pair correlation functions are typically computed via analysis of images obtained using confocal, scanning electron microscopy, or small x-ray scattering techniques (Baniassadi et al. 2012; Jones et al. 2014). For example, two-point correlation has been used to measure the spatial fluctuations of collagen density and

orientation imaged by confocal microscopy during assembly of Type I collagen gels (Jones et al. 2014). However, the correlation functions capture the probability distribution and cannot uniquely determine the organization of collagen fiber networks. Moreover, many different network topologies can be constructed from the same probability distribution. The two-point correlation method has been recently used to identify sub-regions in ligaments where collagen fibers exhibit similar orientations and to compare the size of those sub-regions between cervical and lumbar facet capules (Ban et al. 2017). However, the application of N-point correlation functions to QPLI data for larger-scale collagen configurations requires further investigation, in order to optimize the analytic approaches for quantifying multi-scale collagen reorganization.

Although network construction techniques should be further tested and improved in future studies, as well as be adjusted for applications on different tissue types, this study demonstrates the relevance and significance of using community detection to define and understand loading-induced collagen reorganization. The successful implementation of these graph theoretic techniques on collagen networks can have broader impact in quantifying the organization and defining the structure-function relationships of other fibrous connective tissues and heterogeneous materials.

## 5.6. Conclusions & Integration

Local collagen disorganization is an important indicator for the loss of tissue homeostasis and eventual structural failure (Quinn and Winkelstein 2008; Quinn and Winkelstein 2009; Voycheck et al. 2014). In the context of pain from facet joint capsule

stretch, collagen organization and fiber realignment have been demonstrated to affect afferent activation and macroscopic forces using three-dimensional in vitro models (Zhang et al. 2016b; Zhang et al. 2017b). However, unlike simplified collagen gel constructs, human cervical facet capsular ligaments display complex structural patterns that vary from sub-region to sub-region and from sample to sample (Quinn and Winkelstein 2008; Ban et al. 2017). In order to relate the stretch-induced structural changes to the altered tissue mechanics and even to cellular behaviors in the facet capsular ligament, it is important to fully define the collagen reorganization patterns in different sub-regions of this ligament and their contributions to tissue-level stresses and strains during ligament loading. Using tools from the field of complex systems, the studies in this chapter identify coordinated collagen fiber movement in the human cervical facet capsular ligament based on polarized light images (Figures 5.1 & 5.5). A steady and adaptive transition of the collagen network organization is observed in the AR regions from the resting state with heightened modular architecture to the onset of anomalous realignment with random structure (Figures 5.3 & 5.5). Differences in stretch-induced changes in modularity and flexibility between anomalously and normally realigned regions and the loss of association between flexibility and ligament mechanics in regions sustaining anomalous realignment could reveal region-specific dynamic structural changes and would be promising in detecting and predicting microscopic and macroscopic tissue failures.

The network analyses described in this chapter provide a method to analyze and integrate the micro-scale and macro-scale tissue mechanics and how they evolve across

time and length scales. The findings that ligament regions with anomalous fiber realignment correspond to more evident stretch-induced changes than regions with normal reorganization (Figures 5.3 & 5.6) is consistent with findings based on vector correlation (Quinn and Winkelstein 2009; Quinn et al. 2010a). Unlike prior studies of collagen fiber realignment that largely identified fiber or pixel-level changes (Quinn and Winkelstein 2009; Sander et al. 2009a; Quinn et al. 2010a; Hadi et al. 2012a), network-based methods provide novel access to *regional* differences in collagen network responses to ligament loading. Moreover, this approach provides new diagnostic variables to quantify the coordinated movement of fibers over time during the evolution of meso-scale collagen networks (Figures 5.5 & 5.6).

Although these image-based network analysis tools are capable of connecting the local collagen disorganization to larger-scale impairments of macroscopic mechanical integrity, they only focus on structural changes and do not predict local the stresses and strains that are difficult to measure experimentally. Complementing the studies in this chapter, work described in Chapter 6 assesses the multi-scale responses of the cervical facet capsule during stretch by constructing image-based, finite-element mechanical models using the same set of polarized light images as detailed in this chapter. The studies in Chapter 6 provide a possible mechanical basis of anomalous fiber realignment and further define changes in the ECM microenvironment during stretch of the human cervical facet capsular ligaments. Further, to understand how ligament mechanics may modulate neuronal nociception, the role of integrin-mediated mechnotransduction in facet joint pain from capsule distraction is investigated in Chapter 7.

# Chapter 6

# Multi-Scale Mechanics of the Cervical Facet Capsular Ligament & Effects on Local Collagen Disorganization

*This chapter has been adapted from:*

Zhang S, Zarei V, Winkelstein BA, Barocas VH. Multi-scale mechanics of the cervical facet capsular ligament, with particular emphasis on anomalous fiber realignment prior to tissue failure. *Biomechanics and Modeling in Mechanobiology*, in press, doi: 10.1007/s10237-017-0949-8.

## 6.1. Overview

The facet capsular ligaments, as a common source of pain from neck trauma, exhibit complex structure-function relationships during their supraphysiologic stretch (Lee et al. 2004a; Lee et al. 2006; Quinn et al. 2007; Quinn and Winkelstein 2008; Zhang et al. 2016a). Traditional mechanical metrics, like macroscopic strains, that predict the tissue's susceptibility to damage lack the resolution to localize the microstructural abnormalities that accompany decreases in the tissue mechanical strength during subfailure loading of this ligament (Quinn and Winkelstein 2009). The cervical facet capsules exhibit both structural and mechanical heterogeneity across different length scales (multi-scale) from fibers to tissue, as described in Section 1.1. That architectural complexity is suspected to contribute to the experimentally observed lack of co-localization between macroscopic strain and local collagen disorganization (Quinn and

Winkelstein 2008; Quinn and Winkelstein 2009; Kallakuri et al. 2012; Ban et al. 2017). Based on structural data of the human cervical facet capsular ligament obtained by QPLI (Quinn and Winkelstein 2009), computational work has characterized the spatial variation in that tissue's fibrous architecture (Ban et al. 2017). Further studies in Chapter 5 revealed regional differences in collagen reorganization at the onset of anomalous fiber realignment (Zhang et al. 2016a). However, those prior studies examined only the collagen architecture, but not the spatial variations in stresses or strains or possible associations between those structural and mechanical changes during ligament stretch. Challenges in experimentally measuring the stresses and strains of single fibers or local networks, together with the structural heterogeneity of this ligament, hinder the full definition of its mechanical environment and understanding the effects of altered tissue mechanics on sensory function during supraphysiologic facet capsule stretch.

Finite element-based multi-scale mechanical models, which link the local fibrous networks to the tissue continuum, enable both prediction of strains and stresses of local collagen fibers and networks that otherwise are challenging to measure experimentally and evaluation of the relationships between micro-, meso- and macro-scale mechanics in heterogeneous tissues (Hadi et al. 2012a; Aghvami et al. 2013; Lai et al. 2013). Multi-scale models successfully describe the non-uniform fiber forces and orientation (Sander et al. 2009a; Hadi and Barocas 2013; Lai et al. 2013) that can affect cellular mechanotransduction and bridge the microscopic and macroscopic tissue failure responses in vitro in collagen constructs. The mechanical behaviors of the human *lumbar* facet capsular ligament can be captured by image-based multi-scale models that account

for the ligament's structural heterogeneity across different scales (Zarei et al. 2017). Multi-scale models are hypothesized to better represent the mechanical and structural complexities of the cervical facet capsular ligament in comparison to finite element models of only the tissue continuum or discrete fibers (Zhang et al. 2016b).

This chapter summarizes a subset of studies under Aim 1b, which define the multi-scale mechanics of the human cervical facet capsular ligament with particular emphasis on anomalous fiber realignment using finite element-based models. Based on the same set of QPLI data (Quinn and Winkelstein 2009) used in the studies in Chapter 5 (Zhang et al. 2016a), subject-specific models were constructed to predict the mechanical responses of the ligament under stretch in the context of damage detection in the collagenous network. The model performance was evaluated by comparing the predicted tissue force, macroscopic strains and fiber alignment to those corresponding outcomes measured experimentally. To investigate whether stresses and deformations at the network and fiber scales relate to microstructural tissue damage, macro-scale stresses and strains and fiber-level stretch were generated by the simulations, and their spatial location was compared to that of the experimentally detected anomalous fiber alignment. The work in this chapter elucidates a potential mechanical basis for predicting microscopic tissue damage and for defining the relationships between macroscopic ligament deformations and micro-scale matrix damage in the subfailure loading regime.

## 6.2. Relevant Background

Supraphysiologic tissue loading can alter the mechanical and sensory functions of

the cervical facet capsular ligament even in the absence of its overt, macrostructural failure (Lu et al. 2005a; Lee et al. 2008; Quinn and Winkelstein 2008; Quinn and Winkelstein 2009; Quinn et al. 2010b; Crosby et al. 2014). Subfailure biomechanical signals generated in the facet capsule underlie its pathophysiologic changes, leading to pain (Lord et al. 1996; Lee et al. 2004a; Cavanaugh et al. 2006; Dong et al. 2012; Crosby et al. 2014). Tensile strains that exceed the physiologic range, but are still below the failure threshold for the facet capsular ligament, induce persistent pain in vivo (Lee et al. 2008; Dong et al. 2012; Ita et al. 2017). However, how the microstructural mechanics are altered during ligament loading are still not well-understood, nor is how the tissue-level deformations relate to local loading that may influence the nerve afferents embedded in the ligament.

The fibrous structure of the cervical facet capsular ligament is anisotropic, with the collagen fibers being strongly aligned in some sub-regions and unaligned in others (Kallakuri et al. 2012; Ban et al. 2017). Varied matrix organization can lead not only to heterogeneous stresses and strains in the ligament (Quinn and Winkelstein 2008; Quinn and Winkelstein 2009; Quinn and Winkelstein 2010), but also to the non-uniform distribution of loads and local matrix deformation. During traumatic tissue loading, that heterogeneity can lead to activation and/or injury of some afferents but not the others in the ligament depending on their relative spatial location. The complex tissue structure and the lack of visible tissue rupture during painful facet capsule stretch (Lee et al. 2006; Quinn and Winkelstein 2008; Quinn and Winkelstein 2009) complicate the identification

of regions in the cervical facet capsular ligament that may be prone to neuronal activation and/or tissue failure.

Macroscopic strain is commonly used as a metric to characterize the mechanical tolerance of soft tissues (Siegmund et al. 2001; Robinson and Tranquillo 2009; Voycheck et al. 2014); but, it lacks the resolution to localize microscopic alterations in the subfailure loading regime (Quinn and Winkelstein 2008; Quinn and Winkelstein 2009). As such, more sensitive, image-based techniques that detect microstructural changes have been developed and utilized (Tower et al. 2002; Park and de Boer 2008; Quinn and Winkelstein 2009; Voycheck et al. 2014). For example, QPLI has been used to assess collagen kinematics in real-time during loading of the isolated cervical facet capsular ligament (Quinn and Winkelstein 2008; Quinn et al. 2010a) and reveals that anomalous fiber realignment occurs prior to visible rupture and in areas of eventual tissue rupture (Quinn and Winkelstein 2009). The onset of anomalous fiber realignment typically accompanies signs of compromised tissue integrity, like decreased tissue stiffness, and occurs at strains that induce pain in vivo (Quinn and Winkelstein 2008; Quinn and Winkelstein 2009; Dong and Winkelstein 2010). Although excess fiber rotation indicates microscopic tissue damage and relates to changes in the tissue's macromechanics (Quinn and Winkelstein 2008; Quinn and Winkelstein 2009; Voycheck et al. 2014), the cause of anomalous fiber realignment and its effects on local mechanics are less well-known, in part due to the difficultly in experimentally measuring tissue micromechanics. Further, predicting when and where microstructural abnormalities may develop in the cervical

facet capsular ligament during its loading is confounded by the high inter-subject variability in the fibrous tissue structure (Ban et al. 2017).

Multi-scale computational models are useful tools to probe the structure-function relationships in heterogeneous tissues (Breuls et al. 2002; Weinberg et al. 2010; Erdemir et al. 2015; Thunes et al. 2016). Although fully macro-scale modeling approaches are able to simulate the macroscopic tissue behaviors and average fiber rotations, those models cannot accurately predict rotations of individual fibers and over-estimate the fiber stretch (Chandran and Barocas 2006). To capture the fine details of the complex fibrous architecture of soft tissues and collagen-based tissue analogs and to predict microstructural mechanics, a finite element-based multi-scale model has been developed that incorporates microstructural details that can be obtained using imaging techniques into the macroscopic tissue framework (Chandran and Barocas 2007; Sander et al. 2009b; Zarei et al. 2017). That multi-scale model has been employed to describe the heterogeneity of fiber forces and orientations in the collagen matrix during stretch (Sander et al. 2009a), to assess the effects of fiber alignment on macro-scale mechanics of collagen tissue analogs (Hadi and Barocas 2013), and to predict tissue-level failure based on fiber damage (Hadi et al. 2012a; Vanderheiden et al. 2015). Furthermore, sample-specific multi-scale models constructed using collagen organization data from optical coherence tomography show promise in capturing the structural and mechanical complexities of the lumbar facet capsular ligaments (Zarei et al. 2017). Therefore, image-based multi-scale modeling is hypothesized as a feasible approach to predict the macro-

and micro-scale tissue behaviors relevant to damage detection in the cervical facet capsular ligament.

The goals of the work presented in this chapter were to develop subject-specific multi-scale models of the cervical facet capsular ligament based on QPLI data and to use those models to evaluate different micro- and macro-scale mechanical parameters as predictors for microscopic tissue damage. Separate models were constructed for different human facet capsule specimens based on their geometries, fibrous structures, and force-displacement responses. To test the model performance, the predicted tissue strains and fiber orientation were compared to those measured experimentally. Several mechanical metrics, including high-resolution macro-scale stresses and strains and fiber-level stretch, were assessed in simulations, and their co-localization with the experimentally detected anomalous fiber alignment was evaluated.

## 6.3. Methods

### 6.3.1. Image-Based Multi-Scale Model

As reported in Chapter 5, tissue-level mechanics and collagen fiber orientation data were derived previously from experiment using an integrated mechanical testing and polarized light imaging system (Quinn and Winkelstein 2009); the experimental setup and data acquisition were briefly described in Section 5.3 of Chapter 5. The human cervical facet capsular ligament samples used in this chapter are the same as those reported in Chapter 5 and Appendix G. The seven specimens included in these studies are considered representative of the typical facet capsular ligament since they have varied

force-displacement relationships, distinct fibrous structures and anomalous fiber realignment (AR) that develops at different sub-regions and displacements (Quinn and Winkelstein 2009; Ban et al. 2017). Previous work applying vector correlation on consecutive QPLI images detected the onset of AR in the cervical facet capsular ligament prior to its rupture (Quinn and Winkelstein 2009). As described in Chapter 5, AR occurs when local fiber directions change significantly more than expected in the majority of the tissue and serves as an important predictor of eventual tissue failure (Quinn and Winkelstein 2008; Quinn and Winkelstein 2009; Quinn et al. 2010a).

An image-based multi-scale finite element method, as described in previous studies (Sander et al. 2009a; Zarei et al. 2017), was used to construct separate computational models for each cervical facet capsular ligament based on the inferred tissue structure from QPLI. Briefly, in this method, each finite element contains eight representative volume elements (RVEs) located at each of the eight Gauss integration points (Figure 6.1). These RVEs are composed of a network of fibers embedded in a Neo-Hookean matrix (Figure 6.1). The fiber network is constructed using the derived local collagen fiber orientations. The fiber network and the Neo-Hookean matrix are not coupled, allowing the network to deform non-affinely, but they are constrained to have the same macroscopic-scale deformation (Alford and Taber 2008; Ateshian et al. 2013). Upon deformation of each element, the underlying RVEs deform and generate stress, which is averaged and passed up to the macro-scale. This process iterates until the equilibrium is achieved.

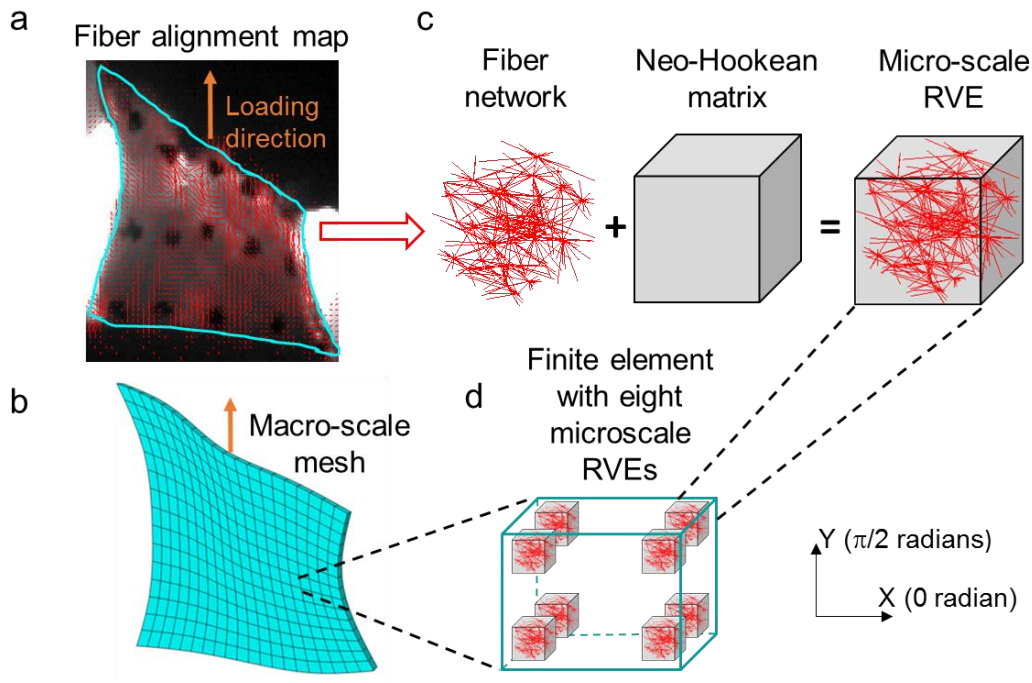


**Figure 6.1.** Schematic showing multi-scale model construction. **(a)** Polarized light images of the cervical facet capsular ligament were used to create **(b)** the macro-scale tissue mesh and to derive **(c)** the local fiber orientation for the representative volume elements (RVEs). Micro-scale RVEs are **(d)** located at the eight Gauss integration points in each finite element and comprised of a fiber network in a neo-Hookean matrix. The network and matrix deform independently during uniaxial tension simulating the experiment.

Individual fibers in the fiber networks of the RVEs are governed by the following phenomenological constitutive equation (Billiar and Sacks 2000):

$$F = A[exp(BE) - 1],$$

where $F$ and $E$ are force and Green strain for each fiber, and $A$ and $B$ are two constitutive constants. Based on previous models of the lumbar facet capsule (Zarei et al. 2017), the Neo-Hookean matrix inside the RVEs was assumed to have low compressibility (Poisson's ratio $\nu$=0.48) with minimal change in ligament volume. Therefore, there were

three fitting parameters, namely the two constitutive constants *A* and *B* for fibers, and the shear modulus of the Neo-Hookean matrix $G_{mat}$.

QPLI data and sample geometry in the undeformed state were used to construct separate models for each individual cervical facet capsular ligament. First, based on the polarized light images taken in the pre-stressed reference position, a geometry representing the shape of the tissue was created and meshed with eight node linear hexahedral elements in Abaqus CAE (version 6.11-1; Dassault Systems Americas Corp.; Waltham, MA) (Figure 6.1). Each tissue continuum was meshed into approximately 300 finite elements based on convergence studies performed using 280-760 elements. Next, fiber alignment maps derived from the QPLI data were registered to the created tissue geometries. A previously developed tensor-based averaging method (Zarei et al. 2017) was then used to coarsen the high-resolution QPLI orientation map and to acquire the mean fiber orientation and alignment strength for each finite element.

To generate fiber networks in each RVE based on the elemental fiber orientation and alignment strength, isotropic Delaunay networks composed of interconnected fibers were first created using random seed points in the 3D space. The fibers were linked to each other at their contact points by rigid, freely rotating crosslinks. Each network was stretched geometrically according to the local alignment strength and rotated such that the primary network orientation was aligned with the element's calculated fiber orientation. The transformed network was then cropped to a cubic unit subsection to be used in the RVEs. The number of fibers in the final cubic network was controlled to be in the range from 350 to 450 fibers, and the eight RVEs in the same finite element all contained the

same initial fiber network. Those fiber networks were constructed in MATLAB (R2014a). The dimension of a single RVE is on the order of 10-30μm, which is much smaller than the length scale for structural variation (300-400μm) observed in the same set of human cervical facet capsular ligaments (Ban et al. 2017). Therefore, the structural variation in actual ligaments is sufficiently small so that a smooth interpolation between RVEs is acceptable.

The geometric data obtained from Abaqus CAE and MATLAB were input into an in-house C-based multi-scale computational framework (Chandran and Barocas 2007; Lai et al. 2013; Zarei et al. 2017). The multi-scale code was executed on an IBM BladeCenter Linux Cluster at the Minnesota Supercomputing Institute. To simulate the experimental loading of the isolated facet capsule from its tensile loading during neck trauma, the upper boundary in the constructed model was pulled uniaxially along the vertical direction (Figure 6.1); the bottom boundary was fixed, and the lateral boundaries were unconstrained. No lateral contraction was allowed along the upper and bottom boundaries in order to mimic the constrained ligament-bone attachment. Boundary forces were computed as a function of the applied displacement during each simulation. The force-displacement results from the model were matched to those from the experiments by tuning the three fitting parameters, $A$, $B$, and $G_{mat}$ using trial and error. Specifically, one parameter at a time was adjusted and the match between the resulting force-displacement responses from the model and the experiment were visually assessed. When a good match was observed, the coefficient of determination ($R^2$) was calculated to ensure high agreement between model and experiment. Although the trial-and-error

method cannot guarantee the uniqueness of the fit, high accuracy of the estimated parameters was ensured by calculating the ellipsoidal confidence region around the center of these final choices (Draper and Smith 2014). The width of the 95% confidence interval of the sample with the lowest $R^2$ is as low as about 1% of the estimated values for all three fitting parameters. The average RVE Cauchy stress (sum of the fiber network and the Neo-Hookean matrix contributions) and the resultant Green strain were also calculated at different displacements, based on which the maximum principal stress and strain fields were generated for each sample simulation. Nodal displacements of the FE mesh and fiber networks were recorded during simulations to track the macro-scale model deformation and the micro-scale fiber stretch and orientation.

### 6.3.2. Comparison Between Experiments & Subject-Specific Models

The force-displacement responses from the experiment and the model were compared by measuring the coefficient of determination and the root mean squared error (RMSE). Model nodes that were closest to the locations of the experimental fiducial markers were tracked during the simulation to compute the regional strain at 50% displacement towards the onset of AR and *at* the onset of AR that indicates excessive local collagen reorganization and possible fiber failure. For example, if AR initially occurred at 3mm of displacement, points were analyzed at 1.5mm displacement and at 3mm displacement. Maximum principal strains in each of the four-node sub-regions were calculated using LS-DYNA (Livermore Software Technology Corp.; Livermore, CA) (Quinn et al. 2007). The spatial distribution of the maximum principal strains was

visualized and the locations of the measured and predicted peak strains were compared. To test whether the model generated strain magnitudes that were within a similar range as those from the experiment, paired t-tests compared the experimental and predicted peak maximum principal strain in each sample. Strain direction was measured as the angle from the horizontal direction. Circular variance, which captures the variation in a set of dihedral angles, was calculated as a measure of the heterogeneity in strain directions acquired from different sub-regions within the same sample. A lower circular variance indicates higher similarity in regional strain directions within the given sample. Circular variances were computed for each specimen and its corresponding model and were compared between the experiment and model using paired t-tests. Since a total of four strain-related comparisons were compared between the model and experiment, Bonferroni correction was performed to counteract the errors that may arise from multiple comparisons by adjusting the significance level from 0.05 to 0.05/4=0.0125.

Pixel-wise and elemental-wise color maps showing the local fiber orientations were generated for the experiment and the model, respectively. The fiber orientation maps measured from the experiment and those predicted by the model were visually compared to examine whether the experimental fiber organization displays a different spatial profile from the model prediction. The angle distribution functions normalized by total counts of fiber angles were generated at displacements equal to 20%, 50%, and 100% of the displacement at the onset of anomalous fiber reorganization for both of the experiment and the model.

Several additional metrics characterizing tissue mechanics from the model were compared with the development of anomalous fiber realignment measured experimentally. To do this, the macroscopic maximum principal stress, macroscopic strain, and micro-scale fiber stretch were derived, normalized and correlated to the initiation of anomalous fiber realignment, using the same approach for each comparison. First, the AR locations identified in the experiment were spatially mapped to the model by overlying the model mesh on the polarized light images at the onset of AR. Finite elements that co-localized with tissue domains sustaining anomalous fiber realignment were assigned an AR score of 1 (AR elements) and 0 otherwise (normal realignment; NR elements). The metric of interest was calculated across the eight RVEs for each finite element. Using these measurements, a score was computed for each finite element to indicate the degree of change in mechanics and chance of tissue damage at different spatial locations across the entire tissue domain. Each metric was mapped to the range from 0 to 1 using min-max scaling $x_{normalized} = \frac{x - min(x)}{max(x) - min(x)}$, and the data were smoothed by a $3 \times 3$ average filter; a score closer to 1 indicates the condition more prone to tissue impairment (e.g., higher maximum principal strain). Paired t-tests compared the average scores of AR elements and NR elements from all samples. Logistic regression of the AR score against each of the mean stress, strain and fiber stretch ratio scores determined the relationships between different mechanical metrics and the development of anomalous collagen realignment. Bonferroni correction was performed to adjust the significance level from 0.05 to 0.0167 for the three paired t-tests.

## 6.4. Results

### 6.4.1. Model Capability to Predict Tissue Force, Regional Strain & Fiber Alignment

The force-displacement responses of the ligament in the subfailure loading regime are well predicted by the model for all specimens (Figure 6.2). The experimentally acquired and computationally predicted force-displacement curves demonstrate high similarity, even for the sample with the lowest coefficient of determination (Figure 6.2a). The experimental and predicted force-displacement responses for each sample are detailed in Appendix I. The agreement in forces between the experiment and model is further confirmed quantitatively by high $R^2$ values and low RMSEs. The average $R^2$ value is 0.99±0.01, indicating nearly perfect goodness-of-fit; the RMSE is 0.37±0.42N, which is less than 3% of the mean maximum force from the seven samples (Figure 6.2b).

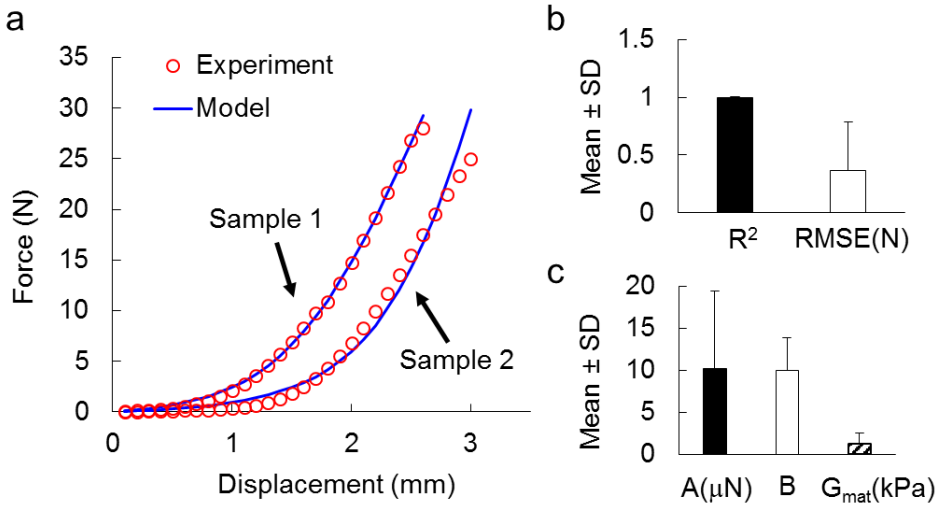


**Figure 6.2.** Force-displacement responses and model fitting parameters. **(a)** Two representative samples demonstrate the agreement in force-displacement responses between the experiment and model. Samples 1 and 2 have the highest and lowest coefficient of determination ($R^2$) among the seven samples, respectively. **(b)** High $R^2$ (close to 1) and low root mean squared error (RMSE) values verify the accuracy in force prediction. **(c)** The best-fit parameters for the multi-scale model show large variations across the different samples. Error bars represent the standard deviation (SD).

The fitting parameters used to tune the forces vary from sample to sample. The average best-fit values for parameters *A*, *B*, and $G_{mat}$ across all samples are 10.2±9.2μN, 10.0±3.9 and 1.2±1.3kPa, respectively (Figure 6.2c). The large variation observed in the fiber stiffness (*A*) and matrix shear modulus ($G_{mat}$) (Figure 6.2c) demonstrate the inter-subject variability in mechanical properties of the cervical facet capsular ligaments.

The accuracy of the multi-scale model in predicting regional strains also differs across the samples. The locations of the peak maximum principal strain are correctly predicted in two samples; another three samples have experimental peak strains located in regions that corresponded to areas of high, but not peak maximum principal strain in the model. The predicted and experimentally measured strain fields in the other two samples are dissimilar. The maximum principal strains from the experiment and the model for all samples are provided in Appendix I. Although Sample 1 (Specimen #4 in Appendix F) exhibits high agreement in the force-displacement responses (Figure 6.2a), the predicted maximum principal strain is substantially different from the measured strain with regards to the location, magnitude and direction of the peak maximum principal strain (Figure 6.3). In contrast, the model for Sample 2 (Specimen #2 in Appendix F) accurately predicts the location of the peak strain, and the simulated peak maximum principal strain exhibits both similar magnitude and direction to that observed experimentally (Figure 6.3). Comparing the experimental and simulation results of all seven samples, no significant difference ($p>0.37$) is detected in the magnitude of the peak maximum principal strain at either 50% AR displacement or the onset of AR (Figure 6.4a). Overall, the predicted maximum principal strain (0.46±0.16 at 50% AR displacement; 1.12±0.46

at onset of AR) is slightly larger than the experimentally measured strains (0.39±0.33 at 50% AR displacement; 0.86±0.54 at onset of AR). Differences in strain direction also exist. The directions of the maximum principal strain in the model are mostly aligned along the loading direction, while the strain directions in the experiment are highly non-uniform (Figure 6.3). The circular variance of strain directions is significantly higher in the experiment than in the model at 50% AR displacement (p=0.001); although no significant difference is detected at the onset of AR (p=0.028; greater than the Bonferroni corrected p-value of 0.0125), the circular variance of strain directions predicted by the model is consistently lower than that measured for each of the corresponding experimental samples (Figure 6.4b).

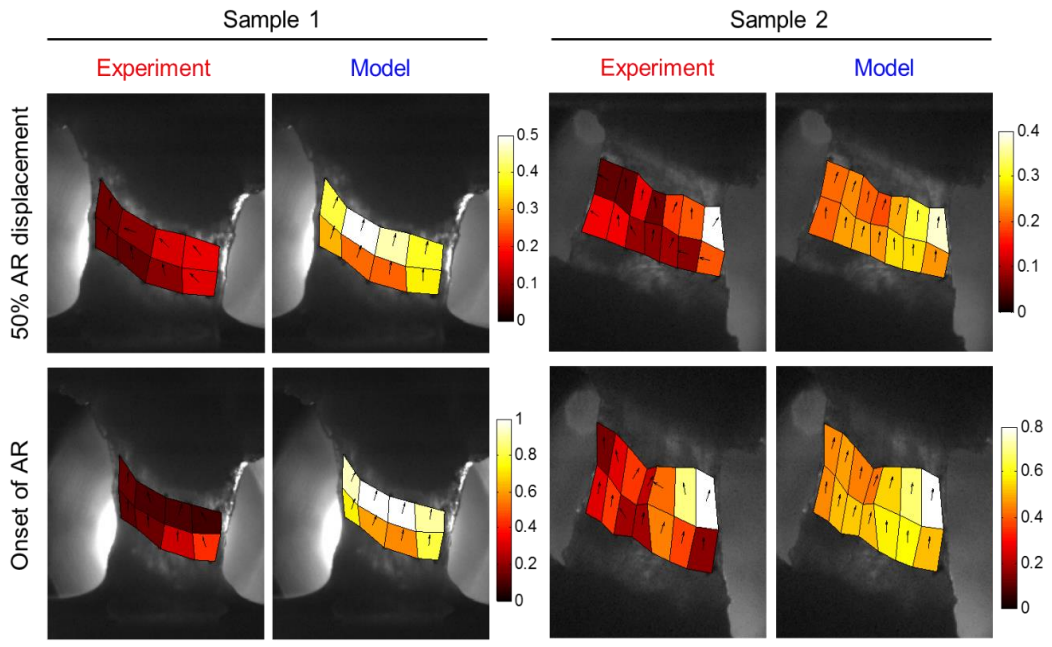


**Figure 6.3.** Comparison of regional maximum principal strain profiles between the experiment and model for the samples shown in Figure 6.2. The arrows indicate the direction of maximum principal strains. Strain maps of these two representative samples show heterogeneous strain directions in the experiment and uniform strain directions in the model. The location and magnitude of the peak strain are well predicted in Sample 2, but not Sample 1, at both 50% AR displacement and the onset of AR.

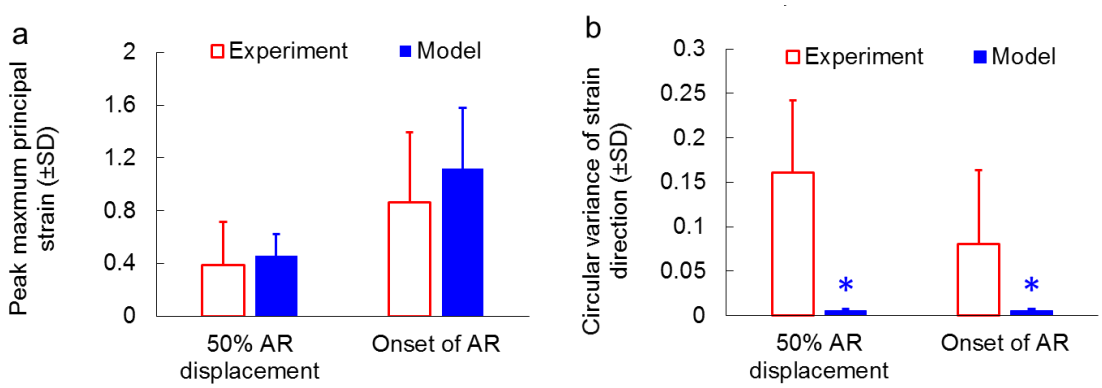


**Figure 6.4.** Quantification of mean regional maximum principal strain profiles for all samples. **(a)** The peak maximum principal strains from the experiment and model for all seven samples are not different at either 50% AR displacement ($p=0.629$) or the onset of AR ($p=0.380$). **(b)** The circular variances of strain directions between the experiment and model at both 50% AR displacement and the onset of AR are significantly lower in the model ($*p<0.028$), indicating more consistent regional strain directions in the model than in the experiment. Error bars indicate the standard deviations.

In addition to discrepancies observed in the macro-scale strain directions, the experiment and model also show differences in the orientation of the microscopic networks during loading. The alignment maps derived from QPLI and the simulated fiber orientation maps have similar distributions at the pre-stressed reference position for all seven samples, verifying the accuracy of the tensor averaging method (Figure 6.5). The predicted fiber alignment maps remain similar to those of the experimental measurements at small displacements, but the differences become more evident with increasing applied deformation (Figure 6.5). In the simulations, the fibers reorient towards the vertical loading direction; the inferred reorganization of the collagenous structure from QPLI is non-uniform within each sample and between different specimens (Figure 6.5).

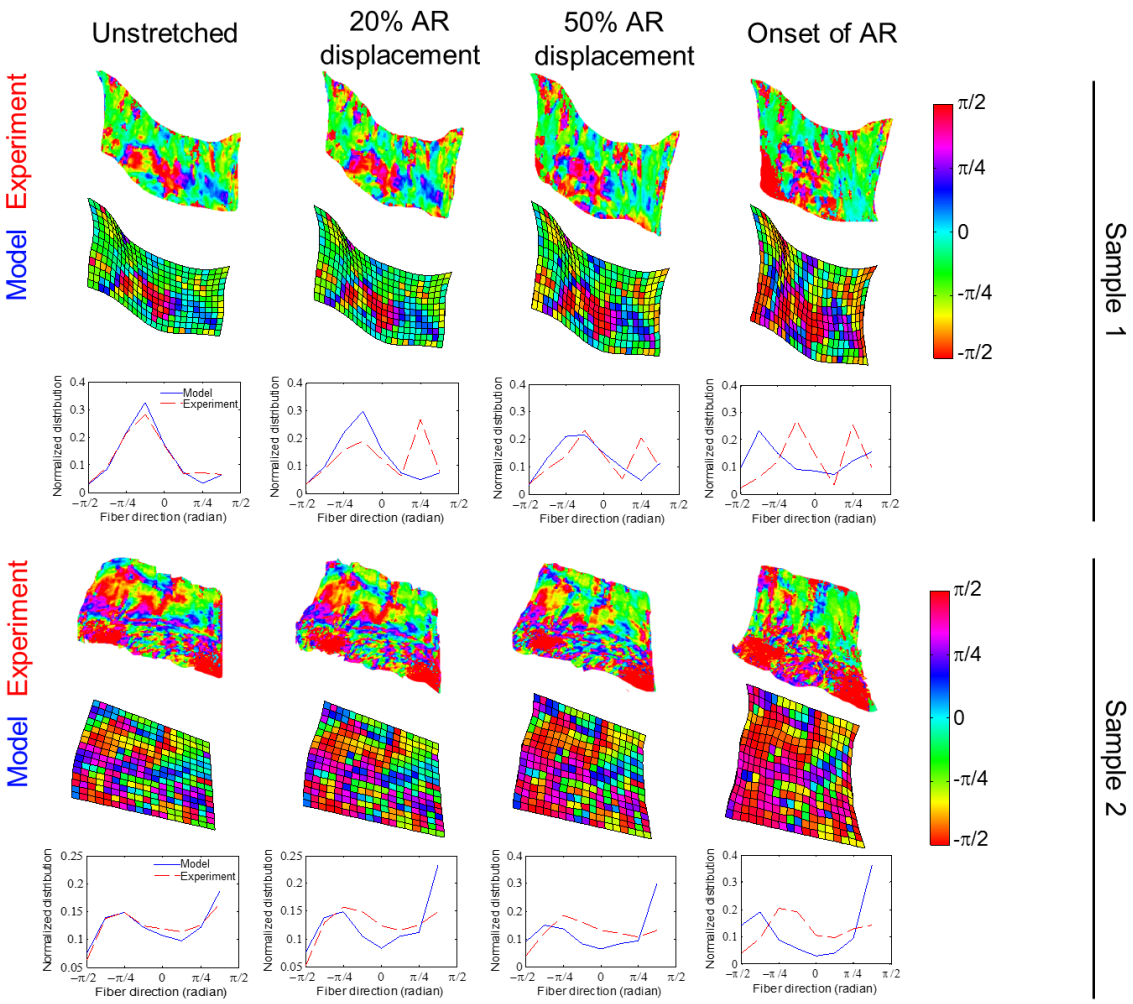


**Figure 6.5.** Comparison of fiber orientations between the experiment and model. Alignment maps and angle distributions are shown for the samples shown in Figure 6.2 at several displacements up to the onset of anomalous fiber realignment (AR). Differences in the simulated and experimentally measured fiber orientations are minimal initially in the pre-stressed resting configuration. The discrepancy between the two is amplified with increased tissue deformation.

### 6.4.2. Associations Between Anomalous Fiber Realginment Onset & Multi-Scale Mechanics

The development of anomalous fiber realignment in the facet capsular ligament associates with the microscopic fiber stretch, but not with the macro-scale maximum

principal stress or maximum principal strain calculated by the multi-scale model (Figures 6.6 & 6.7). The fiber stretch ratio map, maximum principal stress field, and maximum principal strain field obtained from the same sample model exhibit different patterns (Figure 6.6). The predicted fiber stretch and tissue stresses and strains are highly heterogeneous within each sample and between different samples (Figure 6.6). Most of the finite elements whose regions sustained AR in the experiment co-localize with regions of high fiber stretch ratio in the model (Figure 6.6). The spatial distribution of anomalous fiber realignment and predicted fiber stretch ratio, maximum principal stress and maximum principal strain for each of the seven samples are provided in Appendix I.

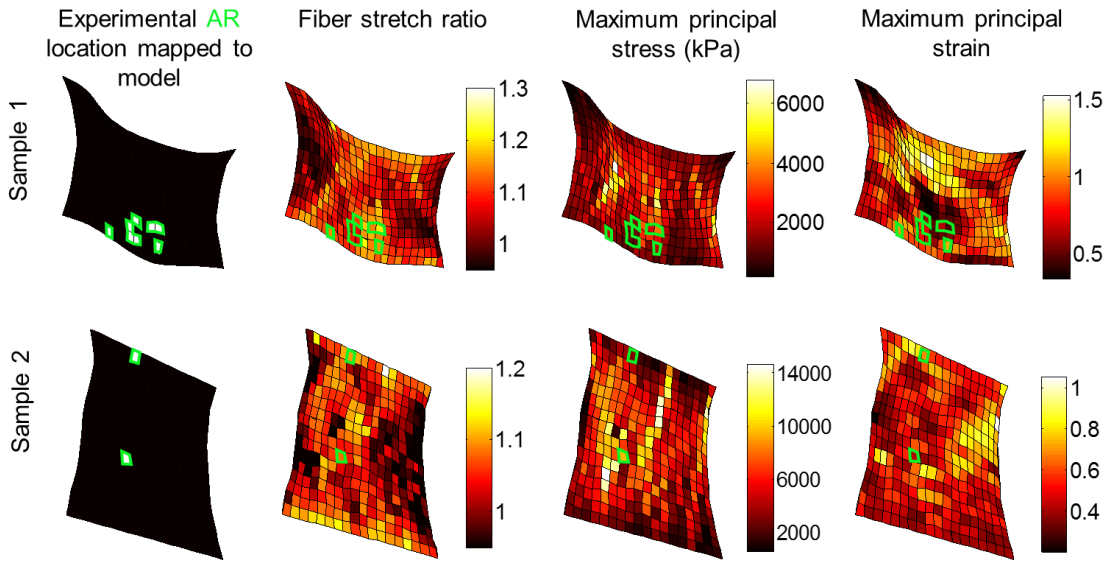


**Figure 6.6.** The spatial distribution of anomalous fiber realignment (AR) and predicted fiber stretch ratio, maximum principal stress and maximum principal strain for two representative samples. The simulated mechanical outcomes display heterogeneous spatial patterns. Anomalous fiber realignment mapped to the model (shown by the white elements in plots in 1$^{st}$ column) tends to locate in regions with high fiber stretch ratio (shown in maps in 2$^{nd}$ column). Green boxes outline locations of the experimental AR mapped to the model in all maps.

Significant association between AR occurrence and fiber stretch is detected by logistic regression ($p<0.009$) (Figure 6.7a). For all seven samples, the average fiber stretch score is higher in the elements that sustain AR than in those that do not (Figure 6.7a), leading to a significant difference in fiber stretch scores between AR (anomalously realigned) and NR (normally realigned) elements ($p<0.002$) (Figure 6.7b). Some, but not all, AR elements have high stresses; the logistic regression shows no significant correlation between the development of AR and the stress magnitude ($p=0.171$) (Figures 6.6 & 6.7c). Although the mean stress score is higher in AR elements than in the NR

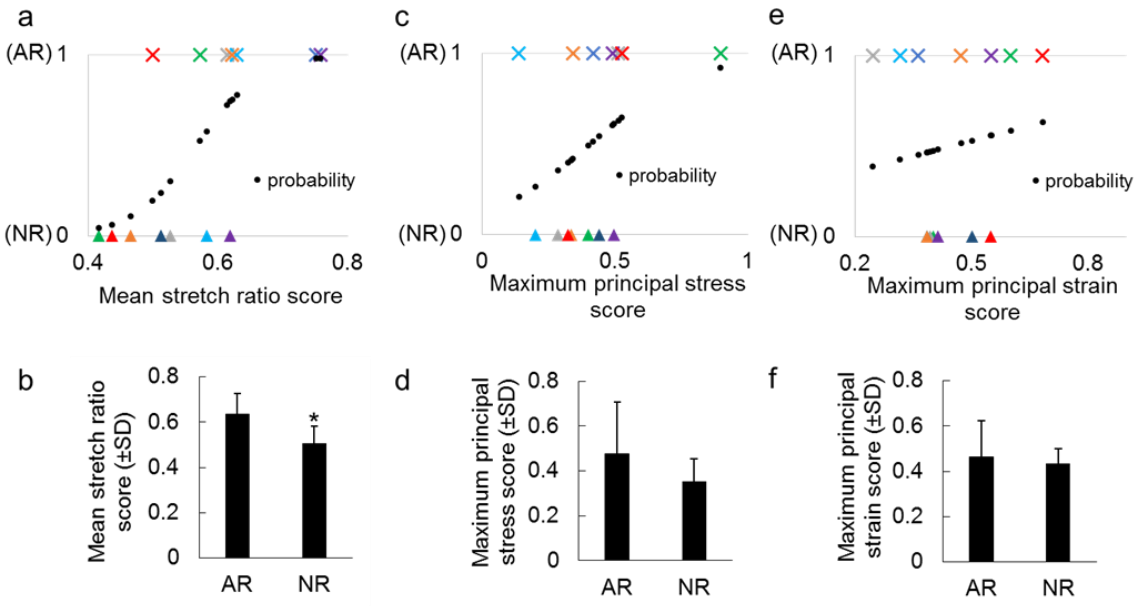


**Figure 6.7.** Comparison of damage scores in regions with and without anomalous fiber realignment. The stretch ratio score **(a)** is significantly correlated with the occurrence of AR by logistic regression ($p<0.009$) and **(b)** significantly higher values in anomalous realignment (AR) than in normal realignment (NR) elements (*$p<0.002$). No significant association is detected between the development of AR and the **(c)** maximum principal stress score or **(e)** maximum principal strain score. Neither **(d)** the maximum principal stress score nor **(f)** the maximum principal strain score differs between AR and NR regions. Symbols with the same color in **(a), (c)** and **(e)** represent the AR (×) and NR (▲) elements from the same specimen. Predicted probability (•) from logistic regression models is also shown in **(a), (c)** and **(e)**. Error bars are standard deviations.

elements, the difference is not significant ($p=0.081$) (Figure 6.7d). Similar to stress, the predicted maximum principal strain does not associate with the emergence of AR and neither does the mean strain magnitude differ between the AR and NR elements ($p>0.3$) (Figures 6.6 & 6.7). The damage scores of elemental stresses, elemental strains and fiber stretch for each sample are detailed in Appendix I.

## 6.5. Discussion

These studies used image-based sample-specific multi-scale models to simulate the mechanical behavior of the isolated cervical facet capsular ligament during uniaxial tension, a common injury modality for this ligament in vivo (Panjabi et al. 1998a; Winkelstein et al. 2000; Siegmund et al. 2001). The models exhibit varied capabilities in predicting different kinematic and kinetic outcomes across the multiple length scales of the tissue as a whole, the ligament sub-regions and the local networks and fibers (Figures 6.2-6.5). There was a mismatch between the model and experimental findings in terms of fiber organization at large tissue stretch (Figure 6.5), possibly due to limitations in the model and/or the imaging methods. Nonetheless, the models precisely simulated the force-displacement responses for all samples and showed promise in predicting the magnitude and location of peak regional strains at two different displacements (Figures 6.2-6.4). To investigate possible causes for abnormal collagen organization in the facet capsular ligament, those multi-scale models were employed to evaluate the relationships between the development of abnormal fiber realignment and each of the fiber-level stretch and network-level stresses and strains. Since fiber stretch has the highest

correlation with the occurrence of AR (Figures 6.6 & 6.7), excess fiber strains may contribute to local collagen disorganization and eventual tissue failure. Previous experimental studies of soft tissues have revealed complex relationships between collagen fiber alignment and macroscopic deformation in the context of tissue failure prediction (Quinn and Winkelstein 2009; Alavi et al. 2013; Voycheck et al. 2014). For example, the maximum principal strain and collagen fiber alignment measured in the glenohumeral joint capsule prior to failure are significantly correlated in the region of tissue failure (Voycheck et al. 2014), despite that the lack of co-localization between the peak regional strains and the failure-predicting anomalous fiber realignment has been found in the cervical facet capsular ligament (Quinn and Winkelstein 2009). Complementing those prior experiments, the studies in this chapter provide a multi-scale computational approach to further quantify the complicated relationships between the various micro-, meso- and macro-scale mechanical responses in heterogeneous tissues. This method complements and expands the understanding of potential mechanical causes for microstructural ligament damage that may lead to eventual failure of the cervical facet capsule.

By incorporating sample-specific fiber architecture to account for the large structural variation in the cervical facet capsules (Quinn and Winkelstein 2008; Kallakuri et al. 2012; Ban et al. 2017), these sample-specific models capture the non-uniform multi-scale mechanics of this ligament. Macroscopically, the subfailure force-displacement responses during stretch of isolated ligaments are predicted with high accuracy in the simulations (Figure 6.2). By estimating the magnitude of peak strains and identifying

regions that may undergo large strains during loading (Figures 6.3 & 6.4), this approach also shows promise in capturing the heterogeneity in the local strain distribution within and across samples. However, not all experimental tissue-level strain fields are predicted accurately, as observed with strain maps for some samples (Figure 6.3). The inaccurate strain estimation may have arisen from simplifications due to insufficient experimental characterization of the structural variation or fiber density in the cervical facet capsular ligament. By assuming that any structural variability through the ligament thickness can be ignored, or homogenization of collagen fiber density across the finite element mesh, the model likely does not simulate fully the exact fibrous architecture of the facet capsule and cannot accurately capture the structure-dependent mechanical responses (Jaumard et al. 2011; Iorio et al. 2016). The prediction accuracy of regional strains could be enhanced by performing a localized fit of the model parameters, $A$, $B$, and $G_{mat}$, using the macroscopic displacement data, which could lead to the overall improvement of the model performance. At the fiber scale, the tensor averaging method enables consistency between the initial fiber orientations in the model and those acquired experimentally at the pre-stressed resting configuration (Figure 6.5). Yet, this type of model does not accurately simulate the network reorganization that is observed experimentally during ligament loading, especially at larger strains (Figure 6.5). These discrepancies between the model and the experiment raise additional questions regarding the model and the imaging techniques. First, it is unclear whether certain material behaviors (i.e. viscoelasticity and microstructural failure) that are missing in the computational model play important roles in modulating tissue-level strains and network reorganization during

loading of the cervical facet capsular ligaments. Second, whether polarized-light imaging provides sufficient structural detail to construct a comprehensive multi-scale model is still unclear. Incorporating time-dependent tissue behaviors, fiber failure and depth-specific fiber organization from other imaging modalities may enhance the performance of the current multi-scale model. Limitations and possible improvements related to the above two issues are further discussed in the next section.

### 6.5.1. Methodological Considerations

Theoretically and experimentally, collagen fibers in many soft tissues and engineered tissue analogs have been observed to realign towards the loading direction during uniaxial tension (Tower et al. 2002; Vader et al. 2009; Voycheck et al. 2014; Zhang et al. 2016b). However, the alignment maps derived from QPLI suggest that collagen fibers in the cervical facet capsular ligament rotate in different directions during stretch, with some fibers even reorienting away from the primary loading axis (Figure 6.5) (Quinn and Winkelstein 2008; Ban et al. 2017). The differences in fiber orientation distribution observed in both the simulations and experiments become more apparent as the applied tissue deformation increases (Figure 6.5). One possible reason for this discrepancy is the emergence of microstructural failure prior to visible rupture of the actual tissue (Quinn and Winkelstein 2008; Quinn and Winkelstein 2009) that was not simulated in the model. The source of microstructural damage may be failure of individual fibers or fiber bundles, and/or breakdown of non-fibrillar matrix. Since the collagen fibers closely interact with other fibers in the local network and the surrounding

non-fibrillar matrix, failure of any of these components could impact the motion of fibers as they realign and elongate to accommodate tissue deformation.

Measuring fiber and/or matrix failure in real-time during tissue loading is challenging, but the occurrence of either or both may be reflected in the altered collagen kinematics (e.g. anomalous collagen realignment). Anomalous collagen realignment could result from stress redistribution among the remaining undamaged fibers upon failure of the load-bearing fibers, and/or from fiber rotation away from the non-fibrillar matrix when the interactions between the two are compromised. In the current study, neither fiber failure nor matrix failure was incorporated. Nonetheless, the predicted maximum fiber stretch at the onset of anomalous fiber realignment (1.23-1.66) in all samples (Figure 6.6) exceeds the breaking threshold (6-22%) of collagen fibers estimated from other ligament and tendons (Morgan and Mitton 1960; Liao and Belkoff 1999b; Yamamoto et al. 1999; Svensson et al. 2013). This difference suggests that microscopic collagen failure likely occurs prior to the detection of abnormal fiber reorientation. It could also indicate that fibers in the facet capsule are substantially crimped in the initial unloaded resting configuration, which would be reflected as greater apparent fiber stretch in the model than actually occurs in the tissue. Although the fibers are modeled as straight lines, the early compliant tissue responses due to crimping is simulated by fiber realignment in the current model (Figure 6.5).

The ability of the current model to accurately predict fiber strain and failure is further limited by simplified fiber-fiber interactions. The crosslinks were constructed with arbitrary density and distribution at the points of contact between fibers that were

positioned according to the imaging data. Those crosslinks enabled only fiber rotation but not fiber bending or sliding, which is an approximation based on previous experimental observations in collagen-based tissue analogs (Chandran and Barocas 2004). Although the predicted macroscopic force-displacement responses match those observed in experiments (Figure 6.2), more work is needed to elucidate the details of the fiber-fiber interactions. Nevertheless, the occurrence of anomalous fiber realignment in regions of high fiber stretch ratio (Figure 6.6) implies that fiber-level impairment is involved in the development of local collagen disorganization leading to eventual gross failure. In addition to microstructural damage, the varying quantities of elastic fibers and ground substances in the facet capsule (Yahia and Garzon 1993; Yamashita et al. 1996) may also affect the motion and deformation of the local fibrous networks. The interspersed elastin fibers in close association with the collagenous structure accommodate macroscopic deformations by allowing the tissue to stretch and recoil, and the proteoglycans could affect the collagen networks by connecting fibers into dense bundles (Jaumard et al. 2011; Green et al. 2014). Although other fibrillary components could be introduced to individual RVEs by modulating the assigned fiber properties (Witzenburg et al. 2017), their distribution and orientation cannot be directly acquired experimentally using QPLI due to the lack of birefringence. Additional studies using immunohistochemistry and/or confocal microscopy would provide more detailed structural information about the different fibrillar and non-fibrillar components in the facet capsular ligament and would improve the current model.

Polarized light imaging has been widely used to evaluate matrix reorganization and its relationships to macro-scale mechanical responses in simple collagen-based tissue analogs (Sander et al. 2009a; Raghupathy et al. 2011; Zhang et al. 2016b). Although this imaging tool has also been employed to study the structure-function relationships in tissues (Tower et al. 2002; Quinn and Winkelstein 2008; Quinn et al. 2010a), limitations of QPLI become obvious and confound the structural findings when applied to complex tissue systems. One pitfall of this technique that affects the construction of multi-scale models is its limited resolution. Despite having an adjustable resolution, QPLI produces pixel-wise alignment measurements, which correspond to the average angle from a fiber group containing an unknown number of fibers that may only be partially captured within a given pixel. Such measurements do not provide sufficient information about fiber density or fiber length to be translated directly into detailed RVE networks on the scale of 10-20μm (Hadi et al. 2012a). Therefore, other imaging methods, such as second harmonic generation microscopy (Chen et al. 2012) and scanning electron microscopy (Provenzano and Vanderby 2006; Zarei et al. 2017), may prove necessary to assess the collagen fibrillary structure in normal unloaded ligament tissues in order to construct more precise and detailed models. In this study, fiber networks were assumed to be identical through the sample thickness, because the orientation derived from QPLI is the thickness-averaged alignment (Tower et al. 2002; Quinn and Winkelstein 2008). Although the model thickness for each simulation was determined based on the average thickness of individual specimens measured experimentally and so *actually* varies from sample to sample, a uniform sample-specific thickness was assumed for each model.

Varied tissue thickness, as well as non-uniform fiber density in the actual ligament specimens, can affect both the degree of light transmission and depolarization, leading to inconsistent estimation of fiber alignment. Depth-dependent collagenous structure may be better captured by other imaging modalities, such as polarization-sensitive optical coherence tomography (Park and de Boer 2008; Claeson et al. 2015, Zarei et al. 2017). Incorporating depth-dependent structural variation can provide additional structural information to construct a more detailed model that better recapitulates the non-uniform fiber motions in the 3D space. Enhanced imaging resolution to describe the alignment of single fibers would likely improve the model's prediction of fiber reorganization and would enable finer strain measurement by tracking fiber alignment in the heterogeneous facet capsular ligament.

### 6.5.2. Relationships Between Multi-Scale Mechanics & Implications for Pain

Despite the enumerated methodological issues and caveats above, the current modeling approach complements the experimental assessment of the cervical facet capsular ligament and further elucidates the multi-scale nature of the ligament's response to tensile loading. The consistent force-displacement curves (Figure 6.2) and discrepancies in regional strains and fiber reorganization (Figures 6.3 & 6.5) observed in the experiment and model suggest that the underlying microscopic collagen structure may impact the regional strains more than tissue-level forces. The differences in fiber realignment between the model and experiment do not affect the model's ability to predict the force-displacement responses (Figure 6.2), likely because the effects of the

microstructure on the bulk force are subtle and can only be captured at large strains. In contrast, different fiber realignment patterns during loading – non-uniform in the experiment and uniformly towards the loading direction in the model – seem to affect the primary direction of regional strains, leading to maximum principal strains that are non-uniformly oriented in the experiment and vertically aligned with loading direction in the model (Figures 6.3 & 6.5). The association between collagen fiber alignment and tissue strains has also been implicated previously in a study using fiber orientation to establish full field strains in the cervical facet capsule (Quinn and Winkelstein 2010). Tissue strain and fiber alignment were found to be correlated in the glenohumeral capsule in tensile loading experiments and suggested as predictors for tissue failure (Voycheck et al. 2014).

Macroscopic strain measurements are common mechanical metrics that define the injury thresholds of soft tissues (Siegmund et al. 2001; Robinson and Tranquillo 2009; Voycheck et al. 2014). Despite possible associations between collagen fiber alignment and macro-scale strains, the disconnect between the location of microstructural tissue damage indicated by anomalous fiber realignment and the region of maximum principal strain in the cervical facet capsular ligament has been observed previously (Quinn and Winkelstein 2009). The lack of correlation between macroscopic strains and/or stresses and microstructural abnormalities may occur in anisotropic tissues because large tissue deformations and stresses in the fiber alignment direction can be borne by the elongation and strength of the fiber bundles; whereas, strains perpendicular to the aligned fibers have less impact on the microstructure during loading (Korenczuk et al. 2017). This disconnect between mechanical metrics of local collagen disorganization and tissue-level damage

points to the importance of investigating both macro- and micro-scale mechanics in defining and predicting damage in the cervical facet capsule and other heterogeneous soft tissues.

By meshing the tissue continuum into finite elements and incorporating micro-scale RVEs in each element, the multi-scale model increases the resolution of strain measurements from *regional* strains to strains of the *local networks and fibers* (Figures 6.3 & 6.6) that are challenging to assess experimentally. Similar to regional strains computed by tracking fiducial markers experimentally, the predicted elemental strains do not effectively indicate where microstructural tissue damage is initiated (Figures 6.6 & 6.7). Elemental maximum principal stresses, on the other hand, exhibit different spatial distributions from the element strains and are high in regions of anomalous realignment in some cases (Figure 6.6). But, the elemental stresses still lack sensitivity in accurately predicting the location of collagen disorganization (Figures 6.6 & 6.7). The same correlation analysis between AR development and different damage scores was repeated using elemental von Mises stresses and strains; a similar lack of correlation was found as when maximum principal stresses and strains were used (Figure 6.8). There is no significant correlation between the development of AR and the von Mises stress ($p=0.181$) (Figure 6.8a). The mean von Mises stress score is higher in AR elements than in NR elements, but the difference is not significant ($p=0.086$) (Figure 6.8b). Similarly, the predicted von Mises strain does not correlate with AR onset and neither does the von Mises strain score differ between the AR and NR elements ($p>0.3$) (Figures 6.8c & 6.8d). The von Mises stress and strain scores for each sample were summarized in Appendix I.

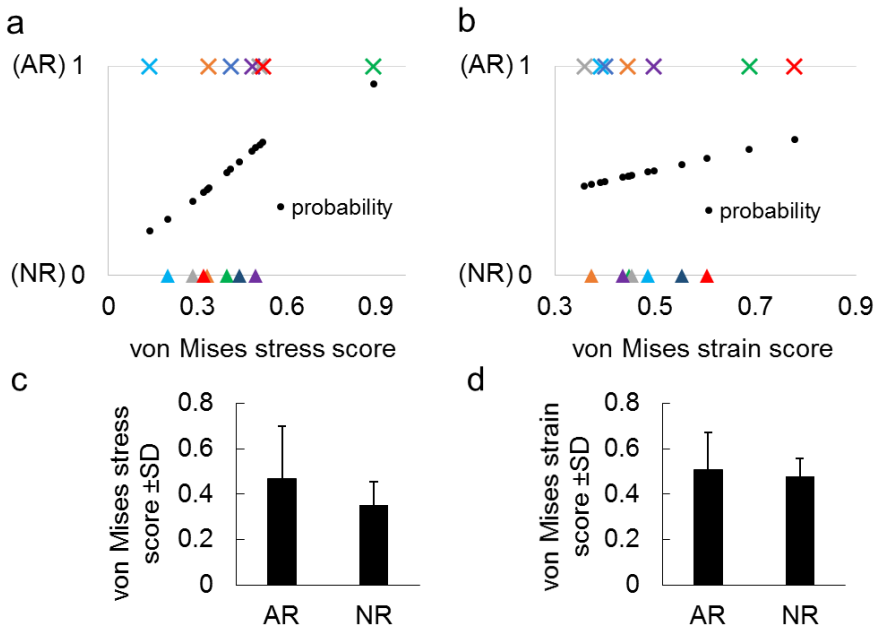


**Figure 6.8.** Relationships between AR onset and each of von Mises stress and von Mises strain. No significant association is detected between the development of AR and **(a)** the von Mises stress score or **(b)** the von Mises strain score. Neither **(c)** the von Mises stress score nor **(d)** the von Mises strain score differs between AR and NR regions. Symbols with the same color in **(a)** and **(b)** represent the AR (×) and NR(▲) elements from the same specimen. Predicted probability from logistic regression models are shown in **(a)** and **(b)**. Error bars show the standard deviations.

Among all of the mechanical variables examined, fiber stretch ratio appears to be the best metric in terms of detecting tissue domains prone to structural abnormality indicated by collagen disorganization, because regions sustaining anomalous fiber realignment show higher fiber-level stretch in *all* of the samples evaluated (Figures 6.6 & 6.7). The studies summarized in Chapter 4 utilized a finite element-based discrete fiber network model to simulate collagen tissue analogs (Zhang et al. 2016b). Simulation results from the discrete fiber model demonstrate that at a maximum fiber strain of ~15% (strain >4% in most fibers along the loading direction), neurons in the collagen matrix

increase their expression of pERK, a marker for pain-related neuronal activation (Ji et al. 1999; Dina et al. 2005; Gao and Ji 2009; Kras et al. 2013c; Crosby et al. 2014). In all seven samples, the high fiber stretch ratios (1.23-1.66) in this multi-scale model exceed the previously defined threshold (~1.1) for neuronal activation (Zhang et al. 2016b). Large deformation of fibers could be transferred to neuronal deformations via cell-collagen adhesions (Tomaselli et al. 1993; Khalsa et al. 2000), presenting a possible mechanism by which excessive ligament stretch induces nociception.

Failure of load-bearing fibers in the facet capsular ligament likely occurs under excessive stretch, and leads to stress redistribution among intact fibers and subsequent fiber reorientation to accommodate the macroscopic deformation. Fiber reorganization can exert local forces on the cells embedded in the fibrous networks and can form stress concentrations at cell-collagen adhesions (Cullen et al. 2007a; Sander et al. 2009a; Cao et al. 2015). Neuronal loading as a result of noxious mechanical stimuli is a potential mechanism to initiate neuronal signaling cascades that elicit pain. An association between fiber-level changes of collagen and neuronal responses is supported by the observation that abnormal fiber realignment occurs at capsule strains that induces facet pain in vivo (Quinn and Winkelstein 2009; Dong et al. 2012). Collectively, these findings suggest that correlated fiber-level responses, such as anomalous realignment and excessive stretch or failure in the subfailure tissue loading regime, likely underlie the pathophysiologic responses of the cervical facet capsular ligament and its role in facet joint pain.

## 6.6. Conclusions & Integration

The studies in this chapter utilized imaging-based finite-element models to predict the heterogeneous, multi-scale mechanical responses of the cervical facet capsular ligament under tensile loading. This modeling approach precisely simulates the force-displacement responses for all samples and shows promise in predicting the magnitude and location of peak regional strains at two different displacements that are relevant to the development of AR (Figures 6.2-6.4). Yet, there is an evident loss of agreement for fiber organization at large tissue stretches (>20% AR displacement) (Figure 6.5). The variability in model performance when predicting tissue-level force responses, regional surface strains and fiber realignment is likely associated with limitations related to the imaging technique and the model itself. The highly heterogeneous fibrous architecture and the structural and mechanical contributions of non-fibrillar components in the facet capsular ligament (Yamashita et al. 1996; Quinn and Winkelstein 2008; Jaumard et al. 2011; Kallakuri et al. 2012; Ban et al. 2017) cannot be fully captured by QPLI. In addition, this imaging-based model does not simulate the fiber failure responses of the ligament, which tends to occur at high capsule strains and prevents the normal realignment of fiber towards the loading direction (Quinn and Winkelstein 2008; Quinn and Winkelstein 2009). Combining QPLI with other imaging modalities that capture the depth-dependent structural variation, the crosslink density and fiber failure could provide more structural information to improve the current model. Nevertheless, by incorporating sample-specific fibrous structures, the model shows promise in identifying tissue domains that may be prone to microstructural damage during loading prior to visual

rupture (Figures 6.6 & 6.7). Fiber-level measurements are implicated as more sensitive than macroscopic stresses or strains in detecting microstructural tissue damage and may have direct impact on the sensory afferents that innervate the facet capsule.

Identifying sub-regions of the facet capsular ligament where collagen disorganization and nociceptor activation may occur is confounded by its non-uniform fibrous structure and suffers from a current lack of experimental techniques. The studies in this chapter and Chapter 5 were performed in order to characterize the local mechanical environment in the facet capsule that may affect the nerve fibers which innervate that ligament, as proposed in Aim 1. The work in both chapters begins to define the multi-scale mechanics of the human cervical facet capsular ligament using computational frameworks that incorporate the tissue's structural heterogeneity. Both approaches emphasize the onset of microstructural abnormalities as evidenced by local collagen disorganization. Collectively, these computational findings suggest that the development of anomalous fiber realignment is related to fiber-level stretch, fiber failure and reorganization of the local fibrous networks.

Despite evidence suggesting complex alterations in the local ECM environment during ligament stretch as presented in Chapters 4 through 6, the molecular mechanisms by which external mechanical stimuli are translated into pain signals following facet joint trauma remain unknown. The models do not include any cellular component, but the predicted fiber-level perturbations likely play a role in modulating the physical properties of the integrin-mediated cell-ECM adhesion complex (Kong et al. 2010; Cao et al. 2015). Given the previously established contributions of integrins in mechanotransduction and

chemically-induced pain (Dina et al. 2004; Khalsa et al. 2004; Schwartz 2010), the studies in Chapter 7 begin to evaluate the involvement of integrin signaling in facet capsular ligament pain using integrated in vivo and in vitro approaches. Further, work presented in Chapter 8 tests the role of intracellular RhoA/ROCK pathway, which is involved in integrin-mediated mechanotransduction (Marjoram et al. 2014; Freedman et al. 2015), in facet joint pain from capsule distraction.

# Chapter 7

# Integrin Signaling in Mechanically-Induced Facet Joint Pain

*Parts of this chapter have been adapted from:*

Zhang S, Zhao E, Winkelstein BA. A nociceptive role for integrin signaling in pain after mechanical injury to the spinal facet capsular ligament. *Annals of Biomedical Engineering*, in press.

Zhang S, Kartha S, Winkelstein BA. Techniques for multiscale neuronal regulation via therapeutic materials and drug design. *ACS Biomaterials Science & Engineering*, in press, doi: 10.1021/acsbiomaterials.7b00012.

## 7.1. Overview

Excessive stretch of the facet capsular ligament is a common injury that induces morphological and functional changes in the afferent neurons of that ligament and can lead to pain (Cavanaugh et al. 2006; Kallakuri et al. 2008; Bogduk 2011; Dong et al. 2012; Crosby et al. 2014). Current treatments for facet joint pain have major drawbacks, like limited specificity and effectiveness, partially due to a lack of understanding of the local mechanisms by which excess capsule distraction activates joint afferents. Work in earlier chapters in this thesis has begun to identify changes in the micromechanical environment of the facet capsular ligament during its loading, and to define the relationships between ECM mechanics and neuronal activation and nociception. As shown in the studies presented in Chapters 3 through 6, macroscopic strains that are painful in innervated tissues, which can produce substantial collagen fiber reorganization

and extension, regulate afferent expression of pERK and SP (Zhang et al. 2016a; Zhang et al. 2016b; Zhang et al. 2017b; Zhang et al. 2017c). Yet, further investigation into the molecular pathways that translate macroscopic tissue deformations and the associated micromechanical changes in to intracellular pain signals is needed to fully define the local neuronal mechanosensing processes involved in ligament trauma. Blocking the cell signaling cascades that mediate mechanotransduction of pain may prevent or attenuate nociceptive responses that are elicited by excess facet capsule stretch. Disrupting the neuronal sensing of painful mechanical stimuli may provide a potential therapeutic strategy for pain relief.

Integrins are important cell surface receptors that modulate cell adhesion and regulate mechanotransduction via iteractions with the ECM and the actin cytoskeleton (Schwartz 2010; Ross et al. 2013). Integrin-dependent pathways can mediate neuronal morphology following axonal injury and are activated in cutaneous mechanoreceptors in response to skin stretch (Khalsa et al. 2004; Hemphill et al. 2011). Because excessive stretch of the facet capsular ligament induces morphological changes and activation of the embedded afferents (Lu et al. 2005a; Kallakuri et al. 2008; Crosby et al. 2014), integrins may mediate signal transduction from external tissue deformations into neuronal nociception via focal adhesions. Furthermore, integrins, such as the β1 integrins which are expressed by sensory neurons, have been implicated in chronic pain from inflammation and neuropathy (Khalsa et al. 2000; Dina et al. 2004; Malik-Hall et al. 2005). Based on those prior findings, neuronal integrin signaling is hypothesized to contribute to nociceptive signaling from mechanical loading to an innervated ligament.

The studies in this chapter, which correspond to work under Aim 3a, investigated the role of the integrin subunit β1 in mechanically-induced pain signaling using complementary in vivo and in vitro studies. The first set of in vivo experiments (presented in Section 7.3) includes two sub-studies performed in the rat. An anatomical study was performed to characterize the constitutive expression of the integrin subunit β1 in various sub-populations of DRG neurons, including those that innervate the facet joint as identified by retrograde neuronal tracing (Kras et al. 2013b). The second in vivo experiment measured changes in the integrin subunit β1 expression in the DRG at seven days after a painful facet joint distraction using a previously developed rat model (Dong et al. 2012; Kras et al. 2013b; Crosby et al. 2013; Crosby et al. 2014; Kras et al. 2015b). To test for possible nociceptive effects of β1 integrin inhibition, two in vitro studies (presented in Section 7.4) were conducted using the NCC system for biaxial stretch that was introduced in (Chapter 3; Zhang et al. 2017a). Those in vitro studies utilized two different types of integrin inhibitors to evaluate the effects of blocking β1 integrins on stretch-induced SP expression in NCCs. In the first in vitro experiment, the β1 integrin was blocked by the arginylglycylaspartic acid (RGD) peptide; the second NCC study used a small-molecule inhibitor to specifically inhibit the α2β1 integrin, which is the primary receptor for Type I collagen. In both in vitro studies, integrin inhibition was performed before biaxial NCC stretch was applied to generate strains that increase SP expression in the DRG (Zhang et al. 2017b). One day after gel loading, axonal SP expression was measured as a marker for nociception (Lee and Winkelstein 2009; Basbaum et al. 2009; Zhang et al. 2017b). Results from those in vitro studies are

integrated and discussed together in Section 7.5. The findings summarized in this chapter reveal a role of the integrin subunit β1 in mediating SP expression and its potential involvement in facet joint pain from mechanical injury.

## 7.2. Relevant Background

Biomechanical, animal and clinical studies have identified the cervical facet capsular ligament as a source of pain from neck trauma (Panjabi et al. 1998a; Lee et al. 2004a; Bogduk 2011; Winkelstein 2011), owing to its mechanical vulnerability (Panjabi et al. 1998a; Jaumard et al. 2011) and its innervation by pain-detecting nociceptors (McLain and Pickar 1998; Kallakuri et al. 2012; Kras et al. 2013b). Although supraphysiologic deformation of the facet capsule induces pain (Bogduk and Yoganandan 2001; Lee et al. 2008; Dong et al. 2012; Kras et al. 2013b; Crosby et al. 2013), the local cellular and molecular mechanisms that translate the macroscopic tissue strains into nociceptive signals in afferents are still unknown, hampering the development of effective treatments for facet joint-mediated pain.

Integrins are transmembrane receptors that mediate cell adhesion to the ECM and regulate bidirectional signaling and force balance between a cell and the surrounding ECM (Chicurel et al. 1998; Hynes 2002). Various α and β subunits comprising integrins are expressed in a wide range of cells, including primary sensory neurons (Tomaselli et al. 1993; Hynes 2002). Integrins, particularly those that contain the subunit β1, have been shown to play a role in modulating the electrophysiological and morphological properties of neurons after mechanical insults in their surrounding ECM (Khalsa et al. 2004;

Hemphill et al. 2011). For instance, blocking the α2β1 integrin expressed on peripheral nerve endings has been shown to reduce the reactivity of cutaneous mechanoreceptors to skin stretch (Khalsa et al. 2000; Khalsa et al. 2004).

Painful stretch of the cervical facet capsular ligament is a complex injury involving not only direct mechanical insults, but also secondary inflammatory cascades. Increased nerve growth factor (NGF) in the facet joint and upregulation of the prostaglandin $E_2$ ($PGE_2$) receptor in DRG neurons accompany behavioral hypersensitivity induced by painful cervical facet trauma in the rat (Kras et al. 2013a; Kras et al. 2015a). Both NGF and $PGE_2$ are known to mediate inflammatory pain and can induce behavioral sensitivity when injected intradermally (Dina et al. 2004; Malik-Hall et al. 2005). Further, functionally blocking or knocking down certain integrin subunits, such as the integrin subunit β1, has been shown to prevent the pain induced by NGF or $PGE_2$ (Dina et al. 2004; Malik-Hall et al. 2005). Since integrins can be mechanically and chemically coupled to both the ECM and the cell cytoskeleton (Chicurel et al. 1998; Hynes 2002), they may be important for translating the external stimuli to neuronal loading and pain signals in the facet capsular ligament.

The studies in this chapter tested the hypothesis that integrin-dependent pathways, especially those involving the subunit β1, contribute to nociception from facet capsule injury using complementary in vivo and in vitro studies. First, constitutive expression of the integrin subunit β1 in naïve normal rats was confirmed and assessed in the different sub-populations of DRG neurons, including the peptidergic and non-peptidergic neurons. Both of those sub-types of DRG neurons have been shown to be involved in the

transmission of pain signals but via different mechanisms (Braz et al. 2005; Basbaum et al. 2009; Kras et al. 2015b). The integrin subunit β1 and the afferents that innervate the facet joint were co-labeled in the DRG to test for β1 integrin expression by afferents from the involved joint. Expression of the integrin subunit β1 was also assessed in the DRG seven days after facet capsule stretch when pain is still present, in order to evaluate the association between regulation of integrins and mechanically-induced pain in vivo.

In the parallel in vitro studies, the DRG-collagen NCC model described in (Chapter 3; Zhang et al. 2017a), which simulates the innervated facet capsular ligament, was used to investigate if, and how, tissue matrix deformation modulates local axonal responses via integrin-dependent pathways in the context of pain. Separate studies tested if β1 integrins facilitate the translation of NCC stretch into neuronal signaling by blocking integrins with either a subunit β1-specific inhibitor or an α2β1 integrin inhibitor. The integrin subunit β1 can form heterodimers with several different α subunits, leading to varied responses to mechanical and chemical cues (Hynes 2002). The α2β1 integrin is the primary receptor for Type I collagen, which is a major component of the facet capsular ligament (Jenkins et al. 1999; Jokinen et al. 2004; Jaumard et al. 2011). Phosphorylation of focal adhesion kinase (FAK) was measured as a read-out of activated integrin signaling (Ribeiro et al. 2013). To investigate whether integrin inhibition affects neuronal processing of noxious mechanical stimuli, expression of the pain neurotransmitter substance P was measured after NCC stretch as a nociceptive signal and pain predictor.

## 7.3. Integrin Subunit β1 Expression in the DRG

### 7.3.1. Methods

#### 7.3.1.1. Characterization of the Integrin Subunit β1 in the DRG

All experimental procedures involving rats were approved by the University of Pennsylvania Institutional Animal Care and Use Committee and carried out under the guidelines of the Committee for Research and Ethical Issues of the International Association for the Study of Pain (Zimmermann 1983). The in vivo experiments were performed using adult male Holtzman rats (300-450g; Envigo; Indianapolis, IN). Rats were housed with 12-12 hour light–dark cycle, provided environmental enrichment, and given free access to food and water. All surgical procedures were performed under inhalation isoflurane anesthesia (4% induction, 2.5% maintenance). Two groups of naïve rats were used to characterize the integrin subunit β1 expression in different types of DRG neurons. In the first group (n=4) of rats, the expression of the integrin subunit β1 was measured in peptidergic and non-peptidergic neurons, both of which have been shown to innervate the facet joint and to mediate pain after its injury (Kras et al. 2013b; Kras et al. 2015b; Weisshaar et al. 2017). To specifically evaluate if the DRG neurons that specifically innervate the facet joint express the integrin subunit β1, a separate group of rats (n=4) was injected with a retrograde neuronal tracer into the facet joint.

##### 7.3.1.1.1. Intra-Articular Injection of Neuronal Tracer & DRG Harvest

In the retrograde tracing study, rats received intra-articular injections in the bilateral C6/C7 facet of the retrograde neuronal tracing molecule, cholera toxin subunit B

(CTb) conjugated to the fluorescent dye Alexa Fluor 488 (20μg in 5μL of PBS; Life Technologies; Carlsbad, CA) as previously reported (Kras et al. 2013b). The bilateral C6/C7 facet joints were exposed by making a midline incision over the back of the neck. The CTb solution was injected into the bilateral facet joints using a 10μL syringe with a 33-gauge beveled needle (Figure 7.1). After injection, wounds were closed using 3-0 polyester sutures and surgical staples. The neuronal tracer was allowed sufficient time to be retrogradely transported from the peripheral terminal in the facet joint to the DRG before the DRG was harvested for immunohistochemistry and confocal microscopy (Figure 7.1). On day 10 after CTb injection, rats were anesthetized with sodium pentobarbital (65 mg/kg) and perfused transcardially with chilled PBS and 4% PFA in PBS (pH7.4). The C7 DRGs were dissected and post-fixed in 4% PFA in PBS at 4°C for one day. DRGs were then incubated in 30% sucrose at 4°C for one week and freeze-mounted in Tissue-Tek OCT Compound (Sakura Finetek; Torrance, CA).

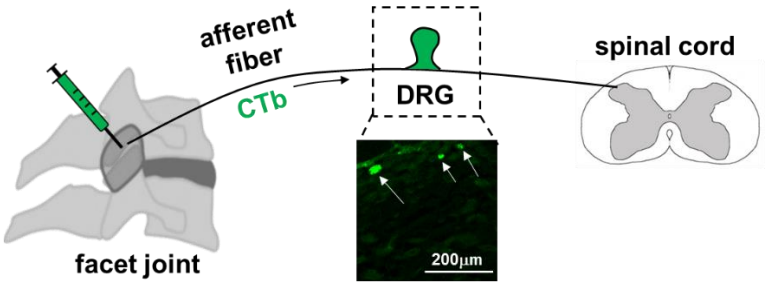


**Figure 7.1.** Overview of intra-articular CTb injection and DRG assessment. The fluorescent CTb injected into the bilateral facets is transported from the C6/C7 joint terminal to the DRG along the afferents that innervate the facet. The C7 DRG was harvested ten days after CTb injection and imaged by confocal microscopy to visualize CTb-positive joint afferents (white arrows).

#### 7.3.1.1.2. Immunohistochemistry by Neuron Type

To analyze neuronal expression of the integrin subunit β1 in peptidergic and non-peptidergic neurons, DRG tissue was harvested from un-operated naïve rats via transcardial perfusion and fixed with 4% PFA as described in Section 7.3.1.1. Each DRG was sectioned into 14μm-thick slices longitudinally and mounted on Superfrost Plus slides (Thermal Fisher Scientific; Waltham, MA) for immunohistochemistry. Isolectin B4 (IB4) and SP were labeled as markers for non-peptidergic and peptidergic neurons, respectively (Basbaum et al. 2009).

DRG sections were blocked in 10% normal goat serum with 0.3% Triton-X PBS for 2 hours at room temperature. Sections were then incubated overnight at 4°C with primary antibodies, including guinea pig anti-substance P (1:500; Neuromics; Bloomington, MN), biotinylated IB4 (5μg/ml; Sigma-Aldrich Corp.; St. Louis, MO) and rabbit anti-integrin subunit β1 (1:100; Santa Cruz Biotechnology; Santa Cruz, CA). The next day, sections were fluorescently labeled with secondary antibodies for goat anti–guinea pig 633 (1:1000, Invitrogen; Carlsbad, CA), fluorescein (DTAF)–conjugated streptavidin (1:500, Jackson ImmunoResearch; West Grove, PA) and goat anti–rabbit Alexa Fluor 546 (1:1000, Invitrogen; Carlsbad, CA). Images from 5-6 tissue sections for each rat were taken using the 20X objective of a Zeiss 710 confocal microscope (Carl Zeiss Microscopy, LLC; Thornwood, NY). In the naïve DRGs, the percentage of SP-positive neurons and the percentage of IB4-positive neurons that express the integrin subunit β1 was separately measured by visually comparing the amount of positive labeling to the levels of background fluorescence in each image (Dong et al. 2012). The

paired percentages of integrin subunit β1-expressing neurons in peptidergic and non-peptidergic populations was compared using a non-parametric Wilcoxon singed-rank test.

DRGs harvested from the rats receiving CTb injection were also sectioned, fluorescently labeled and imaged for integrin subunit β1 using the same methods detailed above. The existence of neurons displaying both CTb uptake and positive integrin subunit β1 expression was verified by visual inspection only.

#### 7.3.1.2. Integrin Subunit β1 Expression in the DRG after Painful Facet Joint Distraction

##### 7.3.1.2.1. Surgical Procedures for Facet Joint Distraction

To assess any pain- or injury-related changes in the expression of the integrin subunit β1 in DRG neurons, separate groups of rats received either a facet joint distraction applied to the C6/C7 facet joints (n=4) or a sham control surgery with no stretch (n=5), as described previously (Kras et al. 2013b). Rats were anesthetized with isoflurane (4% for induction; 2-3% for maintenance) and placed in a prone position on the surgical platform. After exposing the bilateral C6/C7 facet joints, the interspinous ligaments and ligamentum flavum from the C5 to T1 levels were transected so the C6 and C7 laminae could be rigidly attached to microforceps and distracted on a customized loading device (Dong et al. 2012; Kras et al. 2013b; Crosby et al. 2014) (Figure 7.2). Painful tensile facet capsule stretch injury was imposed by translating the C6 microforceps rostrally by 2.5mm as recorded by a linear variable differential transducer (LVDT) (to impose ~13% capsule strain) at 15mm/s (~500%/s) while holding the C7

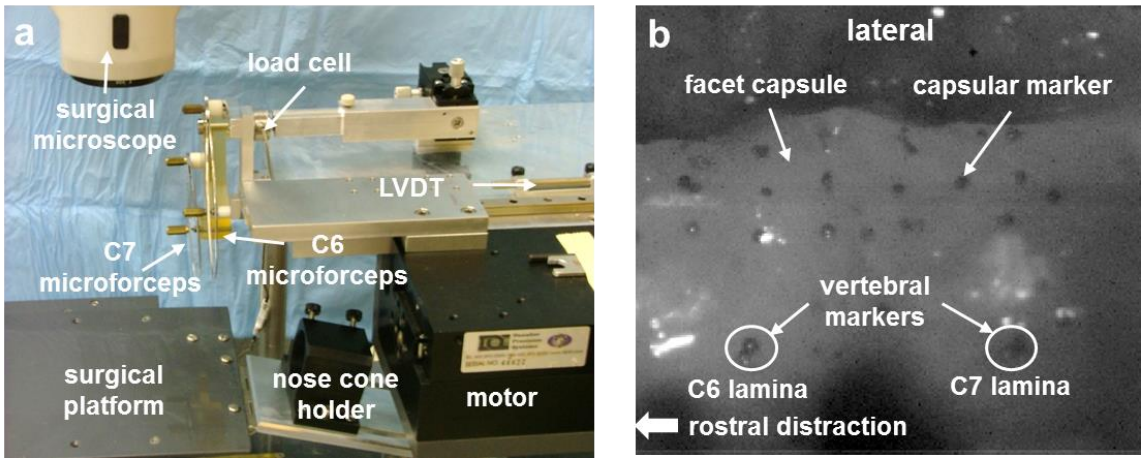


**Figure 7.2.** Experimental setup for facet joint distraction in the rat. **(a)** Customized facet loading device equipped with a surgical microscope connected to a high speed camera for marker tracking, microforceps to fix the C7 vertebra and translate the C6 vertebra via a stepper motor, a nose cone holder for anesthesia delivery to rats positioned on the surgical platform, and a load cell and a LVDT to record the imposed force and C6 microforceps displacement, respectively. **(b)** Image of the facet joint with two vertebral markers placed on the laminae of the C6 and C7 vertebrae and a grid of capsular markers placed on the C6/C7 capsule. The markers are used to quantify the magnitude of the applied distraction.

vertebra fixed (Dong et al. 2012; Kras et al. 2013b) (Figure 7.2). Strains of the C6/C7 facet capsular ligament were targeted to exceed its maximum non-painful physiologic strain (~6%) (Panjabi et al. 1998a; Dong et al. 2012) and to be below the peak ligament strain (~35%) experienced during painful traumatic loading (Ita et al. 2017a; Ita et al. 2017b). Target strains are comparable to those which activate afferents in the facet capsule (Lu et al. 2005a; Lu et al. 2005b), and the applied strain rate simulates the capsule stretch rate in whiplash injury (Panjabi et al. 1998a; Panjabi et al. 1998b; Stemper et al. 2005; Dong et al. 2012). A grid of polystyrene beads was placed on the right C6/C7 facet laminae and the joint capsule prior to distraction and was tracked by a Phantom v4.3 CCD camera (Vision Research; Wayne, IN) during joint distraction to measure the

imposed capsule stretch (Figure 7.2). The positions of the vertebral and capsular markers before joint distraction and at the maximum capsule stretch were used to calculate the applied vertebral and capsular displacements and the maximum principal strains across the facet capsule using LS-DYNA software (Livermore Software Technology Corp.; Livermore, CA) (Lee et al. 2004a; Dong et al. 2012). A separate group of rats received a sham surgery with attachment to the loading device but no joint distraction.

#### 7.3.1.2.2. Behavioral Assessment of Mechanical Hyperalgesia

Pain was assessed before (day 0) and on days 1 and 7 after the injury or sham surgeries by measuring the withdrawal threshold of the forepaws to stimulation by von Frey filaments of increasing strengths from 0.6-26g (0.6, 1.4, 2, 4, 6, 8, 10, 15 and 26g; Stoelting Co., Wood Dale, IL) (Chaplan et al. 1994; Kras et al. 2013b). Beginning with the 0.6g filament, each filament was applied five times to the plantar surface of the forepaw. If two consecutive filament strengths evoked a withdrawal, licking, or shaking of the forepaw, the lower of those filament strengths was taken as the withdrawal threshold. Three rounds of testing were performed on the left and right forepaws separately on each testing day; the average of the left and right forepaw response thresholds from all rounds in a session was taken as the forepaw withdrawal threshold for each rat. A two-way repeated-measures ANOVA with Tukey HSD test (JMP11 software) identified significant differences in withdrawal thresholds between groups over time.

#### 7.3.1.2.3. Immunohistochemistry & Quantification of the Integrin Subunit β1

On day 7 after behavioral testing, rats were anesthetized with sodium pentobarbital (65mg/kg) and perfused transcardially with PBS and 4% PFA as described in Section 7.3.1.1.1. DRGs at C7 were harvested from rats undergoing surgery, as well as from the naïve un-operated rats (n=3) to serve as negative controls for immunohistochemistry and analyses. DRGs were sectioned and mounted on slides, as described in Section 7.3.1.1.2. Tissue sections were blocked in 1% normal donkey serum with 0.3% Triton-X PBS, immunolabeled for the integrin subunit β1 (1:100; Santa Cruz Biotechnology; Santa Cruz, CA) and the neuronal marker microtubule-associated protein 2 (MAP2; 1:500; Aves Labs; Tigard, OR), and imaged using a Zeiss 710 confocal microscope. The small-diameter (4-21μm) and medium-diameter (21-40μm) sized DRG neurons are primarily nociceptors (Julius and Basbaum 2001; Dubin and Patapoutian 2010) and exhibit different expression profiles after painful facet joint distraction (Weisshaar et al. 2010; Dong et al. 2012). Accordingly, the average intensity of the integrin subunit β1 labeling was quantified in each of those populations of neurons separately using ImageJ software and normalized to the expression in size-matched neurons from naïve rats. Differences in β1 integrin expression between the injury and sham groups were compared separately in small- and medium-diameter DRG neurons using t-tests.

### 7.3.2. Results

#### 7.3.2.1. Constitutive Expression of the Integrin Subunit β1 in DRG Neurons

The integrin subunit β1 is highly expressed in SP-positive peptidergic neurons of the uninjured DRG (Figure 7.3). From the four un-operated naïve rats, 490 SP-positive (peptidergic) neurons and 636 IB4-positive (non-peptidergic) neurons were evaluated. Among the SP-positive neurons, 81±15% exhibit expression of integrin subunit β1 (Figure 7.3b). In contrast, only 50±6% of the neurons that express IB4 are positive for the integrin β1 subunit, which is significantly lower ($p<0.001$) than the percentage in neurons expressing SP (Figure 7.3b). The percent positive neuron data for individual rats is listed in Appendix J, which details the quantification of immunolabeling. Although not all CTb-positive neurons show a detectable level of the integrin subunit β1, co-localization of the β1 subunit with CTb-positive neurons in the C7 DRG was found by visual inspection (Figure 7.3c), suggesting that some of the afferents that innervate the C6/C7 facet capsule express the integrin subunit β1.

#### 7.3.2.2. Integrin Subunit β1 Up-Regulation in Afferents after Painful Facet Distraction

A painful facet joint injury appears to increase the expression of the integrin subunit β1 in the DRG neurons that have small- or medium-diameter as compared to expression in size-matched neurons in sham-operated rats (Figure 7.4). Indeed, facet joint distraction imposing a capsular MPS of 13.3±3.8% induces behavioral hypersensitivity that develops as early as one day and lasts for at least seven days, as evidenced by a

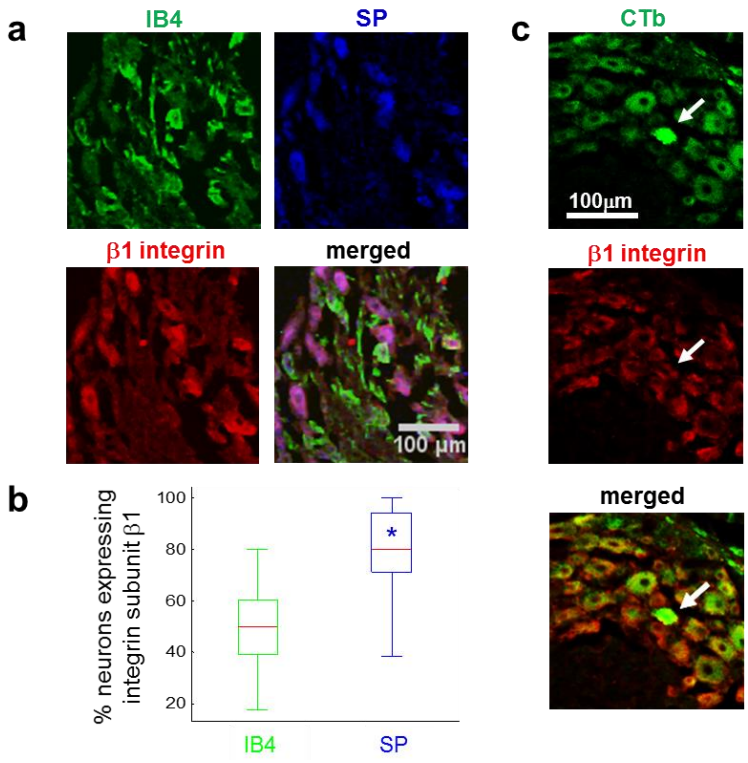


**Figure 7.3.** Expression of the integrin subunit β1 in neurons in the rat C7 DRG. **(a)** Representative images and **(b)** quantification show localization of the integrin subunit β1 in both IB4-positive neurons (co-localization shown in yellow) and SP-positive neurons (co-localization shown in pink), and that expression is significantly higher (*p<0.001) in SP-positive neurons. The box plot shows the interquartile range (box height), sample median (red line), and maximum and minimum values (whiskers). **(c)** Some CTb-positive neurons that innervate the facet joint also express the integrin subunit β1. Arrows point to an afferent neuron with co-localized CTb tracer and the integrin subunit β1. The scale bar in **(a)** and **(c)** is 100µm and applies to all images in the same panel.

significantly decreased forepaw withdrawal threshold from baseline (day 0) at day one (p=0.014) and day seven (p=0.020) (Figure 7.4a). Forepaw withdrawal thresholds and the imposed joint distraction and capsular strains for each rat in this study are summarized in Appendix K. At day seven, DRG expression of the integrin subunit β1 is significantly greater in the injury group than in shams for both small-diameter (p<0.001; 129 neurons for injury; 204 neurons for sham) and medium-diameter (p=0.005; 247 for injury; 311

neurons for sham) neurons (Figure 7.4). Quantification of the integrin subunit β1 expression for individual rats can be found in Appendix J.

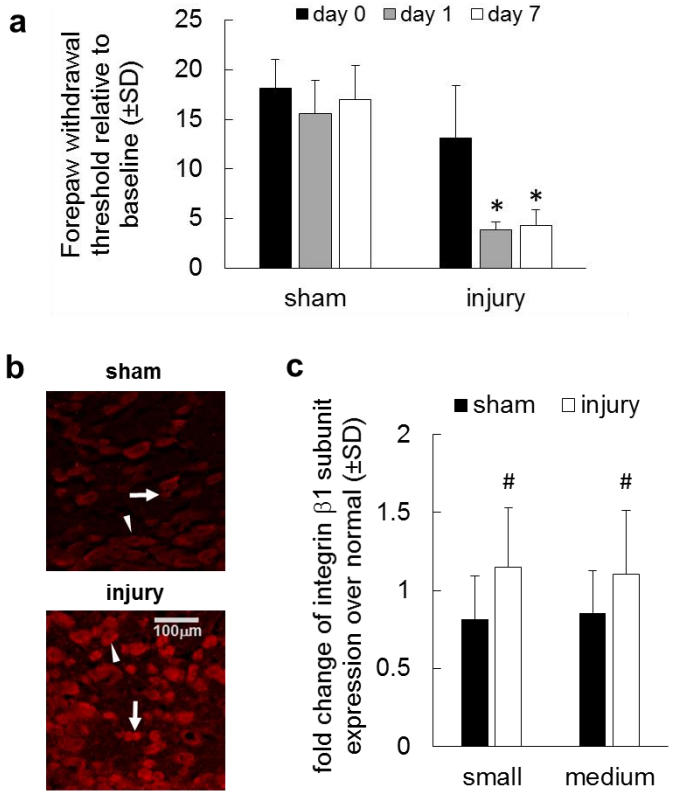


**Figure 7.4.** Expression of the integrin subunit β1 after painful facet capsule injury. **(a)** The forepaw withdrawal threshold significantly decreases (*p≤0.020) at days 1 and 7 from baseline pre-injury levels (day 0) only in rats receiving facet injury. **(b)** Representative images and **(c)** intensity quantification reveal significantly more (#p≤0.005) expression of the integrin subunit β1 in small-diameter (arrows) and medium-diameter (arrow heads) DRG neurons after a painful facet injury.

## 7.4. Effects of β1 Integrin Inhibition on Stretch-Induced substance P Expression

Given the evidence of integrin subunit β1 expression in neurons that innervate the facet capsular ligament (Figure 7.3) and its up-regulation in the DRG following painful

facet joint distraction (Figure 7.4), β1 integrin modulation of the transduction of stretch into nociceptive signals was assessed using the NCC system, with and without blocking integrins. To probe the roles of the integrin subunit β1 and the specific β1 integrins that mediate cell adhesion to Type I collagen, a subunit β1-specific inhibitor or an inhibitor for the collagen-binding α2β1 integrin was used in separate studies. The study using an RGD peptide to block the integrin subunit β1 is summarized in Section 7.4.1 and the study using TC-I15 to inhibit the α2β1 integrin is summarized in Section 7.4.2. In both studies, the expression of SP was measured as a marker of nociceptive signaling. The relationship between local SP expression levels and macroscopic strain of the surrounding ECM, with and without integrin inhibition, was also evaluated in the TC-I15 treatment study.

### 7.4.1. Inhibition of Integrin Subunit β1 by RGD Peptide

#### 7.4.1.1. Methods

As described in Sections 3.3 and 3.4 (Zhang et al. 2017b), cruciform NCCs with random fiber organization were made using rat tail collagen I (2mg/ml; Corning; Corning, NY) to encapsulate DRG explants harvested from embryonic day 18 Sprague-Dawley rats and cultured for six days. Integrins were blocked using an RGD peptide (Sigma-Aldrich Corp.; St. Louis, MO) that binds to the β1 subunit (Bonfoco et al. 2000).

A pilot study was first performed using different peptide concentrations and incubation times to ensure effective inhibition of β1 integrin activation while minimizing other effects to neurons, such as altered morphology. After DRG plating, either 0.5mM

(n=2/time point) or 1mM RGD (n=3/time point) was applied for each of one or six days. All NCCs were cultured for six days and were fixed with 4% PFA at day 6. Morphological changes and integrin signaling, as indicated by phosphorylation of the focal adhesion kinase (FAK; FAKpY397), were measured by fluorescent labeling for βIII-tubulin (1:200; Abcam; Cambridge, MA) and phosphorylated FAK (pFAK; 1:200; Santa Cruz Biotechnology; Santa Cruz, CA), respectively, using methods described in Section 3.3. Axonal outgrowth and pFAK expression in treated NCCs were compared to baseline levels in untreated controls (n=2). Differences in axon morphology and density were assessed by visual inspection. For each RGD concentration, a separate one-way ANOVA tested the difference between pFAK expression after one day of incubation, six days of incubation, and in untreated controls.

Based on that work, NCCs were incubated in subsequent studies with 1mM RGD for one day before stretch to evaluate the effect of loading on SP expression with and without β1 integrin inhibition. To evaluate the extent of morphological changes and integrin (in)activation, axonal morphology and the ratio of pFAK to total FAK were assessed by immunolabeling in unloaded NCCs, with and without RGD treatment (n=3/group). Treated and untreated cruciform-shaped NCCs (n=3/group) underwent equibiaxial stretch as described in Section 3.4. Briefly, cruciform NCCs were loaded onto a planar biaxial testing machine equipped with a bio-bath filled with PBS maintained at 37°C. NCCs were stretched equibiaxially to 1.5mm (to apply ~20% strain) at 0.3mm/s (~4%/s) in order to simulate sub-failure strains that induce pain in vivo (Dong et al. 2012; Kras et al. 2013b; Crosby et al. 2014) (see also Chapter 3). The applied strain was

measured by tracking both the fiducial markers drawn on the NCC surface and the embedded visible DRGs using a high-speed camera. Based on the marker and DRG positions before and after stretch, the regional MPS in all non-overlapping four-node sub-regions across the surface of the NCC was computed in LS-DYNA (Zhang et al. 2016b; Zhang et al. 2017b). In particular, the mean MPS of each NCC was compared between RGD-treated and untreated groups using a t-test. Unloaded NCCs (n=2/group), with and without RGD treatment, were included to provide the baseline neuronal responses without stretch and to control for differences between experimental runs. Immediately after mechanical loading, NCCs were released from the grips of the testing machine, washed with fresh PBS with 1% Pen-Strep (Thermo Fisher Scientific; Waltham, MA) and transferred to pre-warmed culture media supplemented with 1% Pen-Strep for one day. After that time, the NCCs were fixed with 4% PFA. Axonal SP expression was measured by florescent labeling (1:500; Neuromics; Bloomington, MN) and normalized to the respective unloaded untreated controls from the corresponding experimental run. FAK phosphorylation and SP expression were compared with separate t-tests between treated and untreated groups.

#### 7.4.1.2. Results

In the pilot study determining the incubation time and concentration, RGD incubation for six days at either concentration (0.5mM or 1mM) leads to growth of more but thinner axons than in controls (Figure 7.5). After one day of incubation, no evident morphological changes are observed in neurons for either concentration at six days in

culture (Figure 7.5). Integrin inhibition with 1mM, but not 0.5mM, of RGD significantly decreases (p=0.01) pFAK as compared to untreated controls (Figure 7.5). Therefore, one day incubation with 1mM RGD peptide was chosen for subsequent studies.

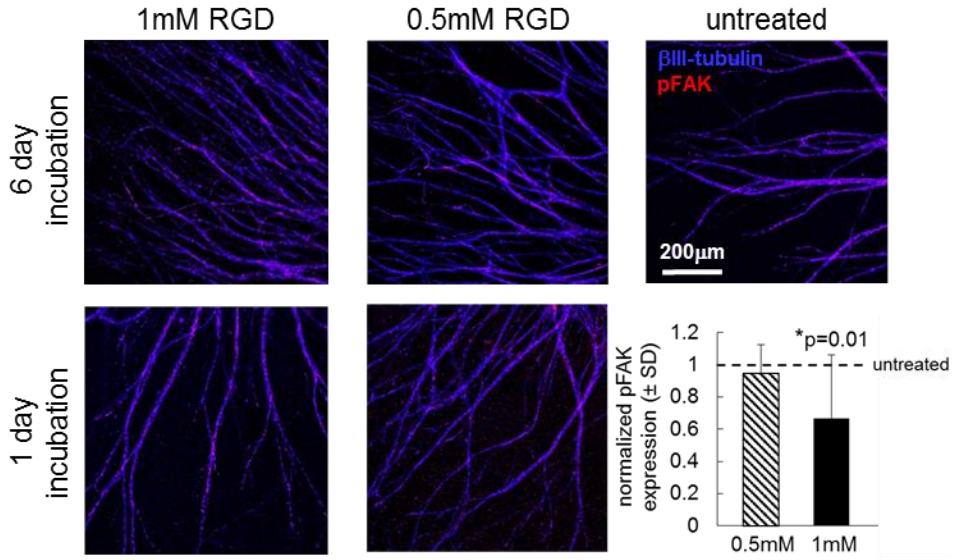


**Figure 7.5**. Axonal outgrowth and pFAK expression after RGD treatment for different concentrations and incubation times. Representative images show higher axon density after six days of incubation, but not one day of incubation, with both 0.5mM and 1mM RGD, as compared to the untreated control. After one day of incubation, the pFAK expression is only significantly decreased for the 1mM RGD inhibition (*p=0.01) relative to untreated control levels (dotted line). The scale bar is 200μm and applies to all images**.**

Inhibition of β1 integrins by the RGD peptide decreases the baseline level of FAK phosphorylation and reduces SP expression after NCC loading. Consistent with pilot results (Figure 7.5), integrin inhibition with 1mM RGD one day before loading does not induce morphological changes but significantly lowers (p=0.03) FAK phosphorylation (Figure 7.6a), indicating altered integrin signaling. Although the strains in treated (21.8±8.5%) and untreated (20.6±4.8%) NCCs are not different (p=0.8), integrin inhibition significantly decreases (p=0.04) the SP expression after loading (Figure 7.6b).

The quantified protein expression and imposed MPS for individual NCCs are summarized in Appendix C and Appendix F, respectively.

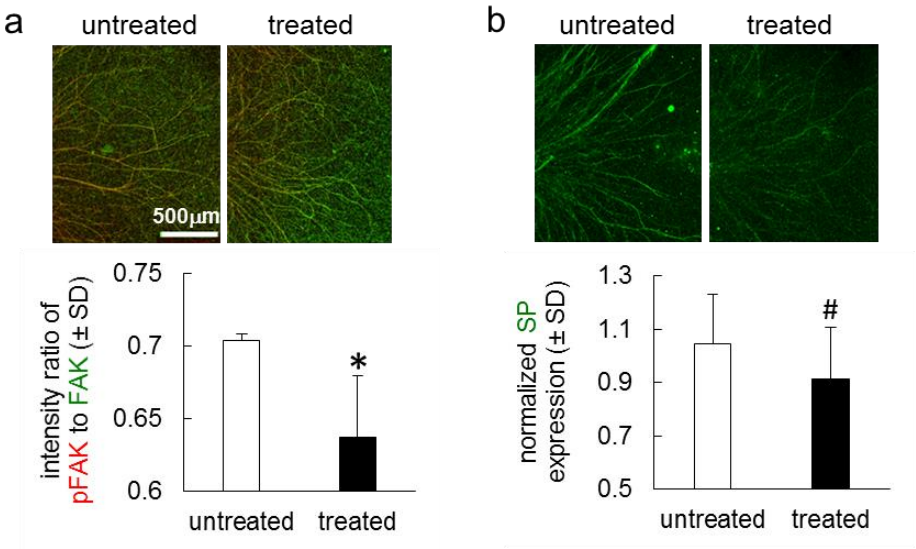


**Figure 7.6.** Effects of β1 integrin inhibition by RGD on FAK phosphorylation and SP expression in NCCs. **(a)** Representative images and quantification of the ratio of pFAK (red) to total FAK (green) after stretch simulating painful strains show FAK phosphorylation decreases (*p=0.03) with integrin inhibition. **(b)** Expression of the nociceptive neuropeptide SP shows a similar decreased expression in axons after stretch (#p=0.04) with integrin inhibition. The scale bar in **(a)** is 500μm and applies to all images in panels **(a)** and **(b).**

### 7.4.2. Small-Molecule Inhibition of Collagen-Binding α2β1 Integrins

#### 7.4.2.1. Methods

The α2β1 integrin is the primary functional receptor that mediates cell adhesion to Type I collagen (Jokinen et al. 2004), a major component of the facet capsular ligament (Jaumard et al. 2011) and the NCC gels used throughout this thesis (Zhang et al. 2016b; Zhang et al. 2017b). The presence of the α2β1 integrin in the DRG explant culture was confirmed by immunolabeling against the integrin subunits α2 and β1 (both at 1:100; Santa Cruz Biotechnology) and visualizing the co-localization of the two

subunits. All fluorescent labeling for NCCs was performed by blocking the gels with 1% donkey serum in 0.3% Triton-X PBS for 2 hours at room temperature, incubating them with primary antibodies overnight at 4°C and fluorescent labeling with corresponding secondary antibodies for 2 hours at room temperature.

After confirming the expression of the subunits of the α2β1 integrin in the NCCs, activation of the α2β1 integrin was inhibited to evaluate whether neurotransmitter expression that is induced by loading (Zhang et al. 2017b) depends on the integrin subunit β1. The allosteric inhibitor TC-I15 (Tocris Bioscience; Minneapolis, MN) that blocks interactions between the integrin subunits α2 and β1 was used to prevent the activation of the α2β1 integrin (Miller et al. 2009; Borza et al. 2012). Separate groups of NCCs were treated with 10μM (n=4), 100μM (n=5), and 1000μM (n=5) TC-I15 at 36 hours before undergoing mechanical loading. Additional NCCs underwent treatment with TC-I15 but no mechanical loading (n=3/concentration); untreated NCCs (n=5 loaded; n=6 unloaded) also were included as controls. All sets of controls were evaluated for neuronal neurite density and neuropeptide expression.

At day seven in vitro, the DRG cultures underwent mechanical loading. The imposed strains (~20%) have been shown to increase the expression of SP and pERK in NCCs (Zhang et al. 2017b) and to activate nociceptors and lead to pain in vivo (Lu et al. 2005a; Dong et al. 2012). NCCs were cultured for one day after stretch as described in Section 3.3 and Section 7.4.1 above. To evaluate the effects of integrin inhibition before mechanical testing on neurite density, axonal expression of βIII-tubulin was visualized using immunolabeling and confocal microscopy. Three randomly selected regions of

interest were evaluated from each unloaded control NCCs (n=3 NCCs/group). Two blinded assessors scored the images using a three-point scale based on neurite density: a score of 0 indicates mild axon outgrowth and branching, a score of 1 represents moderate axon outgrowth and branching, and a score of 2 is assigned to robust axon outgrowth and branching (Hubbard et al. 2008; Nicholson et al. 2014). The average score for each group was compared using a non-parametric Kruskal-Wallis rank-sum test in JMP11.

The axonal expression of SP was measured in DRGs at one day after NCC stretch using a guinea pig SP antibody (1:500; Neuromics; Bloomington, MN) and confocal microscopy for NCCs with and without integrin inhibition. The methods of fluorescent labeling and imaging were detailed in Section 3.4. The average intensity of SP labeling in axons was quantified using the ImageJ software and normalized to levels in untreated unloaded control gels to ensure appropriate comparison between different experimental runs. The normalized SP expression was compared across different groups using a two-way ANOVA, with the loading group and treatment condition as the two factors. To evaluate the relationship between SP expression and the applied NCC strain in untreated NCCs and those pre-incubated with various concentrations of the $\alpha 2\beta 1$ inhibitor, local SP expression was mapped to the regional strain measured in the same sub-region of the gel (Zhang et al. 2016b). The MPS for unloaded control gels was taken as 0. The associations between SP expression and MPS were evaluated using linear regression models (Zhang et al. 2016b), with F-tests assessing the significance of each of the regressions in JMP11.

### 7.4.2.2. Results

Co-localization of the integrin subunits α2 and β1 in axons is observed in the neuronal NCC cultures, confirming the existence of α2β1 integrins (Figure 7.7a). The neurite density score describing neurite density on the day of mechanical loading is not different between NCCs regardless of whether they received inhibition treatment or not; in addition, the inhibitor concentration does not affect the density score (Figure 7.7). the gel surface is not different between any loaded group (MPS=20.5±3.5%), indicating

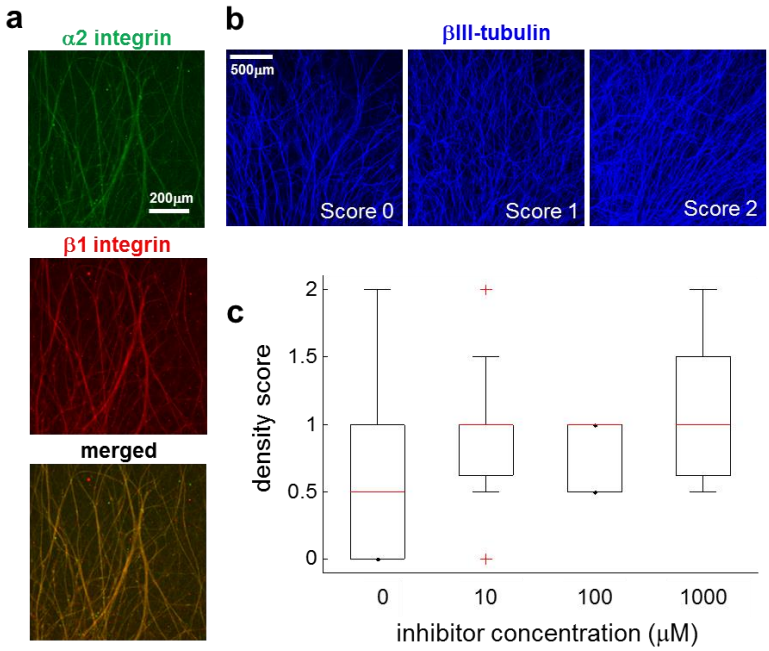


**Figure 7.7.** Characterization of integrin subunit expression and neurite density in the DRG-collagen NCCs. **(a)** Abundant expression of the α2 (green) and β1 (red) integrin subunits and their co-localization (yellow) are evident in axons in the NCC. The scale bar is 200μm and applies to all images. **(b)** Representative images showing the scoring scheme used to evaluate neurite density as visualized by immunolabeling of βIII-tubulin: a score of 0 is low density, and a score of 2 is robust axon outgrowth and branching. The scale bar represents 500μm and applies to all images. **(c)** The density scores are not different between NCCs with or without the α2β1 integrin inhibitor, regardless of inhibition concentration. The box plot shows the interquartile range (IQR; box height), sample median (red line), maximum and minimum values within 1.5 IQR away from the box (whiskers) and outliers (+).

that all loaded groups underwent the same degree of macroscopic deformation. The MPS values for individual NCCs are detailed in Appendix F. There is no difference in the levels of SP expression in unloaded control NCCs, with and without TC-I15 treatment (Figure 7.8). In untreated NCCs, substance P is significantly upregulated after stretch as

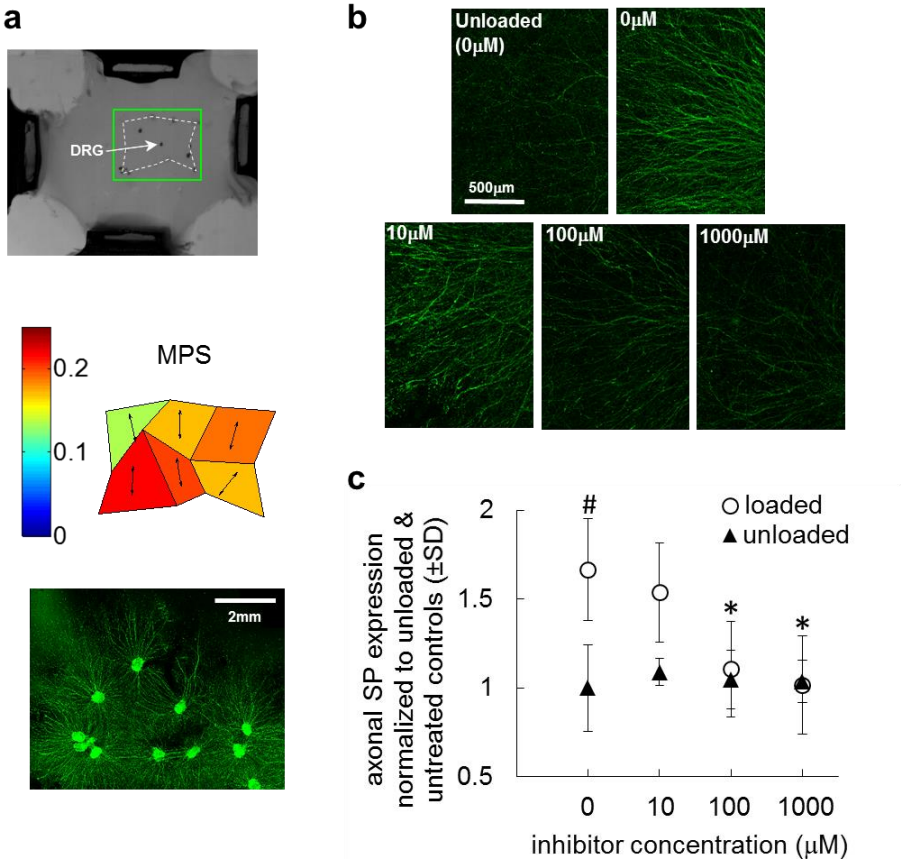


**Figure 7.8.** Stretch-induced SP expression decreases after integrin inhibition in NCCs. **(a)** Sample images show an NCC in a stretched configuration, with the region used for strain calculation (white dashed-line box) and for SP assessment (green solid-line box). The corresponding strain map and SP expression for that NCC are also shown, within the same region of interest. **(b)** Representative images showing variable axonal SP expression in an unloaded untreated control and in loaded NCCs that received TC-I15 treatment (0, 10, 100, 1000μM). **(c)** Quantification of normalized axonal SP showing significantly greater expression in loaded untreated NCCs as compared to unloaded untreated controls ($^{\#}p=0.003$) and loaded NCCs treated with 100 or 1000μM of TC-I15 ($^{*}p<0.03$).

compared to levels of SP in unloaded controls (p=0.003) (Figure 7.8). Although treated and untreated NCCs exhibit similar neurite density and undergo comparable strain severity, inhibiting α2β1 integrins with 100μM or 1000μM TC-I15 significantly lowers the SP expression after loading (p<0.03) (Figure 7.8). The expression of substance P in TC-I15-treated NCCs is not different from the corresponding untreated controls, regardless of the inhibitor concentration (Figure 7.8). Detailed SP expression data for each NCC is summarized in Appendix C.

Integrin inhibition does alter the relationship between SP expression and regional strains in the NCC (Figure 7.9). Mapping the local SP expression to the regional MPS in the same sub-region of the NCC (Figure 7.8a) the axonal SP expression is significantly

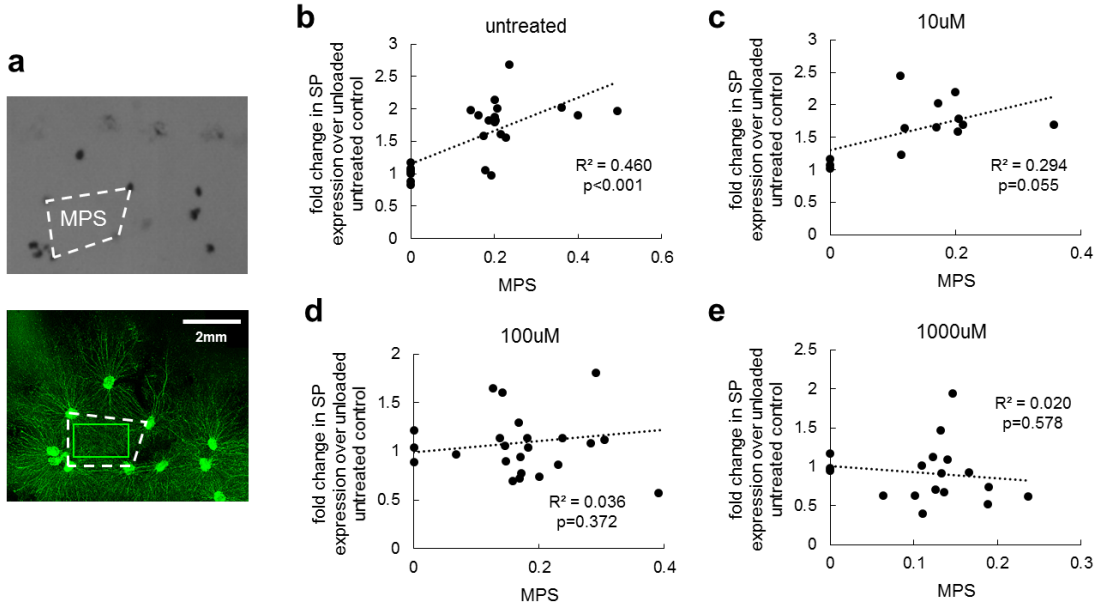


**Figure 7.9.** Linear correlations between strain and SP with and without integrin inhibition. **(a)** Representative images show the mapping between regional strain (dashed line box) and the local SP assessment (solid line box) from the same sub-region of an NCC. Linear regressions of normalized SP expression against regional strain reveal only a **(b)** significant correlation in the case without inhibition of the α2β1 integrin; **(c)-(e)** there is no significant association after treatment with 10, 100 or 1000μM of the TC-I15 inhibitor.

correlated ($R^2$=0.460; p<0.001) with regional MPS in untreated NCCs (Figure 7.9b). However, there is no significant linear correlation detected between SP expression and regional MPS with the presence of 10μM ($R^2$=0.294; p=0.055), 100μM ($R^2$=0.036; p=0.372) or 1000μM ($R^2$=0.020; p=578) of the α2β1 integrin blocker (Figure 7.9).

## 7.5. Discussion

Consistent with previous work (Wallquist et al. 2004), the integrin subunit β1 is highly expressed in DRG neurons (Figure 7.3). Integrin subunit β1 expression is evident in nearly all (81±15%) of the peptidergic afferents in the DRG (Figure 7.3), which themselves account for over one-half of the afferents innervating the facet joint in rats and have been shown to be critical in initiating facet joint pain (Kras et al. 2013b; Kras et al. 2015b). The integrin subunit β1 is expressed on DRG neurons whose peripheral terminals reside in the C6/C7 facet joint (Figure 7.3) and is upregulated in both small- and medium-diameter DRG neurons at seven days after painful facet capsule stretch (Figure 7.4). The imposed capsular ligament strains (13.3±3.8%) are comparable to strains (5-15%) that activate group III and group IV nociceptors in the cervical facet capsule (Lu et al. 2005a; Lu et al. 2005b) and strains (8-12%) that induce pain (Dong et al. 2012). Of note, the facet capsule injury used in Section 7.3 produces forepaw withdrawal thresholds that are lower than those in uninjured sham rats (Figure 7.4) and are similar to prior reports (Dong et al. 2012; Kras et al. 2015a). The presence of the β1 subunit in DRG neurons that innervate the facet joint suggests their ability to sense facet joint loading via integrin-mediated mechanotransduction; up-regulation of the β1

integrins a week after painful facet capsule stretch (Figure 7.4) may be a response to nerve injury and/or joint inflammation from facet injury (Dina et al. 2004; Wallquist et al. 2004).

Pre-incubation of the NCCs with RGD peptides, which are known to inhibit β1 integrin-dependent hyperalgesia (Dina et al. 2005; Malik-Hall et al. 2005), significantly reduces pFAK (Figure 7.6), a marker for altered integrin signaling (Guan 1997). Further, for NCCs undergoing tensile loading to strains that are sufficient for afferent activation (Lu et al. 2005a; Zhang et al. 2017b), axonal expression of SP is significantly lower after RGD treatment than expression in untreated NCCs (Figure 7.6), suggesting the involvement of integrin-dependent neuron-collagen adhesion in modulating mechanically-induced nociception. In addition, inhibiting the primary Type I collagen receptor, the α2β1 integrin, before NCC stretch prevents the upregulation of axonal SP that results from loading and weakens the positive correlation between local SP expression and strain in a dose-dependent manner (Figures 7.8 & 7.9). Since the treated and untreated NCCs exhibit similar neurite density and underwent the same degree of stretch, any difference in protein expression between the loaded untreated group and the loaded treated group can be attributed to the inhibition of the α2β1 integrin. Collectively, findings in these studies point to a potential role of integrins, especially those that contain the β1 subunit, in the sensitization of nociceptors from supraphysiologic ligament stretch at the cell-matrix interface. Since input from peptidergic facet joint afferents is required for pain from capsule stretch injury (Kras et al. 2013b; Kras et al. 2015b) and the majority of the SP-positive peptidergic neurons express β1 integrins (Figure 7.3), the in

vitro finding that DRG SP expression is affected by β1 integrin inhibition (Figures 7.6, 7.8 & 7.9) suggests that β1 integrins may contribute to the development of facet pain from capsule stretch via SP-dependent mechanisms.

Substance P has both pro-inflammatory and neurotransmitter effects in modulating pain. It has been shown to be elevated in the innervated tissue and/or DRG in models of knee and facet joint pain (Lee and Winkelstein 2009; He et al. 2016; Koeck et al. 2016). Additionally, since ablating peptidergic joint afferents using a targeted SP conjugated neurotoxin prevents pain after facet joint injury that causes pain (Kras et al. 2015b), SP-positive peptidergic afferents are hypothesized to respond directly to deformations in the tissue they innervate and to, at least in part, initiate mechanically-induced facet joint pain. Since the β1 integrin has a role in mediating cell-ECM interactions (Khalsa et al. 2004; Schwartz 2010) and neuronal mechanosensing, and it is preferentially expressed in SP-positive peptidergic afferents (Figure 7.3), the hypotheses that β1 integrin activation occurs in response to an altered microenvironment in joint trauma and mediates SP in neurons are supported. The in vitro findings that blocking β1 integrins and inhibiting specific collagen-binding α2β1 integrins prevent the axonal SP expression after tensile loading (Figures 7.6, 7.8 & 7.9) suggest that SP may be directly modulated by mechanically-induced integrin activation.

However, the specific signaling cascades involved in integrin-dependent SP production and release are unknown and requires further investigation. It is possible that integrin activation triggers increases in substance P via cytoskeletal regulation, because the cytoskeleton interacts with integrins (Hynes 2002; Ross et al. 2013), can contribute to

second messenger signaling for inflammatory pain (Bhave and Gereau 2003; Dina et al. 2003), and modulates N-methyl-D-aspartate receptor activity that alters SP release from the primary afferents (Liu et al. 1997; Lei et al. 2001). In addition, ERK signaling, which can mediate inflammatory pain via the integrin subunit β1 (Dina et al. 2005), and SP are both elevated in response to neuronal injury in a strain-dependent manner (Zhang et al. 2016b) (Figure 7.9) and have direct effects on each other in primary sensory afferents (Ma et al. 2001; Tang et al. 2007). As such, specific second messenger cascades that interact with the integrin subunit β1, including the ERK pathway, may play critical roles in altering SP expression via integrin activation. To define the mechanisms by which β1 integrins regulate substance P expression in primary afferents, investigating how downstream effectors of activated integrins, such as different cytoskeletal components and second messenger molecules, induce production of substance P is needed. Identifying β1 integrin-dependent intracellular events not only would provide an array of molecules that could be pharmacologically targeted to attenuate β1 integrin-mediated nociceptive signaling, but also would help determine whether the β1 integrin mediates facet pain via mechanotransductive and/or inflammatory signaling cascades.

The role of β1 integrins and FAK in mediating tissue inflammation and the development of inflammatory pain has been characterized previously (Dina et al. 2003; Dina et al. 2004; Dina et al. 2005; Lian et al. 2015). Yet, understanding if, and how, integrins contribute to nociceptors' responses to the mechanical changes of their surrounding tissue during loading is complex. Defining how the integrin subunits regulate mechanotransduction cascades of afferents to ligament injury is challenging partly due to

the difficulty in decoupling the mechanical stimuli from the rapidly developing local inflammatory responses after joint trauma (Dong et al. 2013b; Kras et al. 2015a). Even in the three-dimensional DRG explant culture model used here, neurons themselves produce inflammatory mediators (Basbaum et al. 2009; Kras et al. 2013c; Dubový et al. 2013; Kras et al. 2015b); but, the number of glial and immune cells is largely reduced, eliminating a host of inflammatory factors that sensitize neurons (Basbaum et al. 2009; Chang and Winkelstein 2011; Mietto et al. 2015a). The NCC model *does* enable mapping local physiological responses (like substance P) to the applied macroscopic strain and local regional mechanics (Figures 7.8 & 7.9). As such, it provides a simplified microenvironment suitable to investigate the role of integrins and other mediators of cell-ECM interactions in neuronal mechanosensing of its surrounding microenvironment.

Although SP is a well-known nociceptive mediator, its expression in sensory neurons is only a proxy for pain and no in vitro system can link integrin activation to the integrated responses, like pain, that are afforded by in vivo systems. The effects of integrin inhibition on the development of pain from ligament trauma was not investigated in vivo; but, altered integrin subunit β1 expression was evaluated in nociceptors in parallel with pain (Figure 7.4). At that same time after painful facet joint injury when concurrent increases in the integrin subunit β1 expression and pain are detected (Figure 7.4), upregulation of both SP and protein kinase C-ε (PKCε) is evident in the DRG (Lee and Winkelstein 2009; Weisshaar et al. 2010; Dong et al. 2012). Although pain-inducing PKCε signaling in primary afferent nociceptors has been shown to depend on the integrin β1 (Dina et al. 2005), no causal relationships have been defined between its increase and

increased expression of SP and/or PKCε in the DRG after painful facet injury. Nonetheless, these findings support the notion that the integrin subunit β1 may be needed in order to maintain facet pain via well-defined nociceptive signaling cascades involving the SP and PKCε pathways. Despite the fact that this study provides the first evidence for the integrin subunit β1 as a potential mediator of ligament pain from mechanical trauma, it remains unclear whether the β1 integrins broadly control nociception from mechanotransduction or selectively interact with particular second messenger cascades that are essential for pain development or maintenance. Further, it also remains unknown if β1 integrins play similar roles in mechanically- and/or chemically-induced pain.

## 7.6. Conclusions & Integration

The current results, together with prior reports, begin to elucidate possible mechanisms by which integrins, the subunit β1 in particular, mediate nociceptor responses to their altered mechanical and/or chemical environment that arises during and after painful facet injury. The facet capsular ligament is primarily composed of heterogeneously organized dense collagen fibers (Quinn and Winkelstein 2008; Ban et al. 2017), which can be reorganized and stretched and can activate neurons embedded in them during supraphysiologic ligament loading, as suggested by findings in Chapters 3 through 6 and other studies (Quinn and Winkelstein 2008; Quinn and Winkelstein 2009; Quinn et al. 2010a; Zhang et al. 2016a; Zhang et al. 2016b; Zhang et al. 2017b; Zhang et al. 2017c). Integrins and focal adhesions at the interface between afferents and their surrounding collagen may be activated by ligament loading, generate stress

concentrations and/or induce changes in electrophysiological signaling, morphological impairment and neurotransmitter regulation (Hynes 2002; Khalsa et al. 2004; Hemphill et al. 2011). Tissue inflammation involving NGF and $PGE_2$ after facet injury may also activate integrins (Dina et al. 2005; Malik-Hall et al. 2005; Kras et al. 2013a; Kras et al. 2015a). Inflammatory mediators binding to their cell membrane receptors can trigger intracellular mechanisms that impact integrins from inside the axons (Hynes 2002; Malik-Hall et al. 2005; Kras et al. 2013a; Kras et al. 2015b; Ferrari and Levine 2015). Activated integrins can regulate both focal adhesions and the cytoskeleton, initiating second messenger cascades, such as the ERK and the PKC pathways, that lead to pain (Hynes 2002; Bershadsky et al. 2003; Dina et al. 2005; Malik-Hall et al. 2005; Ferrari and Levine 2015).

The increased expression of integrin subunit β1 a few days after a painful facet capsule injury (Figure 7.4) points to possible interactions between sustained pain signaling in nociceptors and regulation of integrins in those neurons. Further, blocking β1 integrins with two types of inhibitors decreases axonal SP in DRG neurons in NCCs undergoing tensile strains sufficient to activate afferents and to induce pain in vivo (Lu et al. 2005a; Cavanaugh et al. 2006; Dong et al. 2012; Kras et al. 2013b; Crosby et al. 2014) (Figures 7.6 & 7.8). Since neuronal SP expression has been shown to increase after stretch of NCCs with varied collagen organization (Zhang et al. 2017b) and after painful facet joint distraction (Lee and Winkelstein 2009), the reduced SP in neurons after integrin inhibition suggests the β1 integrin, in particular the α2β1 integrin, to be a potential mediator of nociceptor sensitization from supraphysiologic tissue deformation.

Given that stretch-induced up-regulation of the integrin subunit β1 accompanies facet pain in vivo (Figure 7.4) and the β1 integrin-dependent regulation of substance P in NCCs (Figures 7.6, 7.8 & 7.9), inhibiting β1 integrin signaling may be a potential therapeutic strategy for treating facet capsular ligament pain.

These studies support an emerging schema for integrin-dependent mechanically-induced facet joint pain. However, to fully define the role of integrins in the initiation and maintenance of traumatic facet joint pain, the temporal expression of different integrin subunits in primary afferents, which mediate neuronal activation and inflammatory and neuropathic pain (Khalsa et al. 2004; Dina et al. 2004), after painful capsule stretch is needed. Probing the intracellular pathways that are downstream of integrin activation, like FAK, Src and actin (Guilluy et al. 2011; Ross et al. 2013; Lian et al. 2015), is also needed, in order to fully understand the integrin signaling cascades and to reveal other possible drug targets. The cell adhesion complex interacts with the cytoskeleton (Renaudin et al. 1999; Negreiros et al. 2003; Spanjaard and de Rooij 2013), which is regulated by the RhoA/ROCK pathway (Marjoram et al. 2014; Freedman et al. 2015), and has been shown to mediate inflammatory pain (Bhave and Gereau 2003; Dina et al. 2003). Stresses transmitted through adhesion receptors can trigger the activation of RhoA (Marjoram et al. 2014). Activated RhoA/ROCK can not only facilitate cellular force balance via regulation of the cytoskeleton, but can also underlie the pathogenesis of neuropathy (Ohsawa and Kamei 2010). Based on previous evidence supporting a role of the RhoA/ROCK signaling in neuropathic and inflammatory pain (Tatsumi et al. 2005; Mueller et al. 2005; Paiva-Lima et al. 2014), studies presented in Chapter 8 begin to

investigate the contributions of RhoA and its associated protein kinase in the development of facet joint pain from its mechanical loading.

# Chapter 8

# Contributions of the RhoA/ROCK Pathway in Mechanically-Induced Facet Joint Pain

*This chapter has been adapted from:*

Zhang S, Weisshaar CL, Zeeman ME, Winkelstein BA. The RhoA/ROCK pathway mediates pain and central sensitization after mechanical injury to the spinal facet joint. *Journal of Neuroscience*, submitted.

## 8.1. Overview

Mechanical trauma to innervated joint tissues, like the capsular ligament enclosing the spinal facet joint, can induce pain. Excessive stretch of the cervical facet capsular ligament activates its afferents, alters neurotransmitter expression in the DRG, and induces neuronal hyperexcitability and inflammatory responses in the spinal cord, all of which are also associated with pain (Lu et al. 2005b; Cavanaugh et al. 2006; Lee and Winkelstein 2009; Quinn et al. 2010b; Kras et al. 2013b; Crosby et al. 2014). Despite mechanical loading of the facet capsule leading to pain, the local neuronal mechanisms by which noxious mechanical stimuli are translated into pain signals are still not well-defined. Therefore, current facet pain therapies do not target any specific intracellular mechanotransduction pathways, but rather block afferent signaling by neuronal ablation or using anesthetics that often lead to varied and ineffective clinical outcomes (Kwan and Fiel 2002; Bogduk 2011; MacVicar et al. 2012).

The findings in Chapter 7 suggest that integrin-dependent neuron-ECM adhesion in collagenous tissue plays a role in mediating nociceptive responses to tissue stretch (Zhang et al. 2017d). Further, fiber realignment and deformation in the human cervical facet capsular ligament, as shown in the studies reported in Chapters 5 and 6 (Zhang et al. 2016a; Zhang et al. 2017c), can generate local forces (Sander et al. 2009a). Those local forces can be transmitted by neuronal adhesion molecules to activate intracellular signaling cascades (Hemphill et al. 2011; Delmas et al. 2011; Ross et al. 2013). One downstream effector of cell adhesion-mediated mechanotransduction is the RhoA/ROCK pathway (Lessey et al. 2012; Marjoram et al. 2014). Mechanical stress on and to cells can upregulate RhoA activity; active RhoA binds and activates the Rho kinase ROCK, triggering a host of cell signaling cascades, including those involved in stretch-induced neural injury and pain from inflammation and neuropathy (Mueller et al. 2005; Tatsumi et al. 2005; Ohsawa and Kamei 2010; Hemphill et al. 2011; Paiva-Lima et al. 2014).

Since RhoA and ROCK are both cellular mechanotransducers (Marjoram et al. 2014) and are modulated in neuropathic and inflammatory pain (Tatsumi et al. 2005; Hang et al. 2013), the studies in this chapter, which are under Aim 3, evaluated the involvement of the RhoA/ROCK pathway in ligament pain from mechanical injury, using integrated in vivo and in vitro approaches. RhoA activity was first measured in the DRGs from either rats that underwent a painful facet joint distraction and or stretched NCCs. Based on findings of increased RhoA activity shortly after stretch in both systems, ROCK inhibition was performed in parallel studies both in vitro and in vivo to further probe the role of the RhoA/ROCK pathway in stretch-induced nociception. Expression of the

neuropeptide substance P was measured as a marker of nociception after NCC stretch, in the presence or absence of the ROCK inhibitor Y27632. Given decreases in substance P expression in stretched NCCs with Y27632 treatment, intra-articular ROCK inhibition at the time of facet capsule stretch was performed to test if the RhoA/ROCK pathway contributes to the behavioral hypersensitivity that is elicited by mechanical injury in the rat. To probe potential mechanisms by which ROCK may alter nociception, spinal glial and neuronal responses were evaluated early after capsule stretch by measuring microglial activation, substance P expression and neuronal excitability. Findings presented in this chapter suggest that the RhoA/ROCK pathway contributes to the onset of facet joint pain from its mechanical injury, likely via modulating substance P-mediated nociceptive transmission and microglia-dependent mechanisms that initiate central sensitization.

## 8.2. Relevant Background

In addition to stabilizing joints and transmitting loads, ligaments have important sensory functions via proprioception and nociception from afferent innervation (Schultz et al. 1984; Petrie et al. 1998; Chen et al. 2006; Kallakuri et al. 2012). The capsular ligaments enclosing the bilateral facet joints between spinal vertebrae are innervated by mechanoreceptors and nociceptors (McLain 1994; Chen et al. 2006). Facet joints are a common source of neck and low back pain, and are implicated in over 50% of neck pain patients (Côté et al. 2004; Strine and Hootman 2007; van Eerd et al. 2010). Cervical facet capsule stretch exceeding its physiologic range is a common painful injury from

traumatic spinal loading (Panjabi et al. 1998a; Bogduk 2011; Winkelstein 2011). Supraphysiologic stretch of the cervical facet capsular ligament can activate its afferents (Lu et al. 2005b; Lu et al. 2005a); early afferent activity is requisite for pain development (Crosby et al. 2014). Excessive facet capsule stretch also regulates neuropeptide expression in the DRG, activates spinal glia, and potentiates spinal neuronal excitability, all of which are associated with persistent pain (Cavanaugh et al. 2006; Lee and Winkelstein 2009; Quinn et al. 2010b; Weisshaar et al. 2010). Despite mounting evidence of facet capsule injury leading to central sensitization and pain (Quinn et al. 2010b; Bogduk 2011; Dong et al. 2012; Smith et al. 2014), the molecular pathways translating mechanical stimuli into nociceptive signals in afferents are not well understood, hampering effective therapies for facet pain.

Mechanical stimuli can trigger a host of intracellular signing cascades, several of which convert the Rho family GTPase RhoA from the inactive GDP-bound form to the active GTP-bound state (Lessey et al. 2012). Mechanical loading to the ECM can increase RhoA activity via the adhesion complexes mediating cell-matrix interactions (Marjoram et al. 2014). Active RhoA activates Rho associated protein kinase (ROCK), triggering cytoskeletal regulation, protein synthesis and synaptic signaling among other downstream responses (Luo 2000; Mueller et al. 2005; McMullan et al. 2006; González-Forero et al. 2012). In addition to its role in mechanotransduction, the RhoA/ROCK pathway is also involved in the pathogenesis of pain via inflammatory signaling and/or regulating actin dynamics (Nörenberg et al. 1999; Inoue et al. 2004; Tatsumi et al. 2005; Paiva-Lima et al. 2014). Preemptively inhibiting ROCK either intrathecally or

systemically in mice prevents the typical development of pain after nerve injury (Inoue et al. 2004). Carrageenan-induced hyperalgesia is attenuated by local treatment with the ROCK inhibitor Y27632 (Paiva-Lima et al. 2014). Although ROCK inhibitors are analgesic in neuropathic and inflammatory pain, it is unknown if, and how, the RhoA/ROCK pathway mediates nociception from mechanical injury of innervated ligaments like the facet capsule.

Because facet pain from capsular ligament stretch involves both primary mechanical afferent insults and secondary tissue inflammation (Lu et al. 2005b; Kallakuri et al. 2008; Crosby et al. 2014; Kras et al. 2015a; Kras et al. 2015b), the RhoA/ROCK pathway was hypothesized to contribute to traumatic facet pain onset. Complementary in vivo and in vitro experiments tested this hypothesis. First, RhoA activity was assessed in DRGs using both capsule stretch in vivo (Crosby et al. 2013) and an in vitro neuron-collagen construct system enabling well-controlled stretch and measurement of local mechanical and neuronal responses (Zhang et al. 2017b). To probe the role of the RhoA/ROCK pathway in nociception from mechanical loading, ROCK inhibition was also utilized with NCCs. Because substance P is produced by facet afferents and transmits nociceptive signals (Lee and Winkelstein 2009; Kras et al. 2015b), it was measured in the NCCs after loading, with and without the ROCK inhibitor Y27632. Based on reduced substance P after stretch with Y27632 in vitro, the effects of intra-articular ROCK inhibition on behavioral sensitivity and DRG substance P expression was further tested in the rat. Since substance P release in the spinal cord contributes to central

sensitization (Basbaum et al. 2009), spinal substance P, glial activation and neuronal excitability were also assessed.

## 8.3. Methods

Complementary in vivo and in vitro studies were performed to investigate whether mechanical trauma to the innervated facet capsule regulates RhoA activity in the DRG and if, and how, trauma-induced facet joint pain is mediated by local inhibition of the RhoA/ROCK pathway. The in vivo rat model of painful facet joint injury simulates whiplash-like facet capsule stretch and induces spinal neuronal plasticity and pain within one day (Panjabi et al. 1998a; Dong et al. 2012; Crosby et al. 2013). The in vitro NCC system integrates DRGs in collagen to simulate innervated ligament tissue (Zhang et al. 2017b); the three-dimensional DRG-collagen culture was used to isolate the effects of mechanical loading that is difficult to decouple from the system responses that occur in vivo, to assess early changes in RhoA activity that cannot be measured in vivo due to the confounding effects of anesthesia, and to correlate ECM strains with local expression of substance P.

All experimental procedures were approved by the University of Pennsylvania Institutional Animal Care and Use Committee and carried out under the guidelines of the Committee for Research and Ethical Issues of the International Association for the Study of Pain (Zimmermann 1983). In vivo experiments were performed using adult male Holtzman rats (370-470g; Envigo; Indianapolis, IN). Rats were housed with 12-12 hour light–dark cycle and given environmental enrichment and free access to food and water.

All surgical procedures were performed under inhalation isoflurane anesthesia (4% induction, 2.5% maintenance). All in vitro experiments were performed using DRGs harvested from embryonic day 18 Sprague-Dawley rats (kind gift from the CNS Cell Culture Service Center of the Mahoney Institute of Neuroscience at the University of Pennsylvania) from all spinal levels and sterilely isolated in Hank's Balanced Salt Solution (HBSS; Thermo Fisher Scientific; Waltham, MA).

### 8.3.1. RhoA Activity after Stretch Injury

#### 8.3.1.1. Facet Joint Injury

The effects of facet joint injury and capsule stretch on RhoA activity were evaluated in the DRG. Separate groups of rats underwent either a dynamic joint injury imposed across the bilateral C6/C7 facet joints (*injury*; n=4) or a sham control surgery with no injury (*sham*; n=2), as described previously (Crosby et al. 2013). Briefly, the bilateral C6/C7 facet joints were exposed and the C6 and C7 laminae were rigidly attached to microforceps mounted on a customized loading device (Dong et al. 2012; Crosby et al. 2013; Weisshaar and Winkelstein 2014; Kras et al. 2015a). To impose capsule stretch, C6 was translated rostrally by 2.5mm while the C7 vertebra was held fixed (Dong et al. 2012; Crosby et al. 2013; Weisshaar and Winkelstein 2014; Kras et al. 2015a). A separate group received a sham surgery with attachment to the loading device but no joint injury. At one day after the surgical procedures, rats were transcardially perfused with 300mL of chilled phosphate-buffered saline solution (PBS). DRG tissue at the C6 level was freshly harvested and stored at -80°C before assessing RhoA activity.

#### 8.3.1.2. Neuron-Collagen Construct Culture & Stretch

Collagen gels were made using rat tail Type I collagen (2mg/ml; Corning Inc., Corning, NY) cast overnight in 12-well tissue culture plates at 37°C. To dissect DRGs from embryonic day 18 Sprague-Dawley rats, the spine was exposed and the spinal cord was removed. DRGs were isolated using fine forceps and approximately 5-10 DRGs were plated on each collagen gel. Neurons were allowed to attach and grow axons for three days before the supplemental collagen solution was added to encapsulate them in the NCC construct. NCCs were cultured in neurobasal medium supplemented by 1% GlutaMAX, 2% B-27, and 1% Fetal Bovine Serum (FBS) (all from Thermo Fisher Scientific; Waltham, MA). In addition, 10ng/mL 2.5S nerve growth factor (Thermo Fisher Scientific; Waltham, MA), 2mg/mL glucose (Sigma-Aldrich Corp.; St. Louis, MO), 10mM FdU (Sigma-Aldrich Corp.; St. Louis, MO) and 10mM uridine (Sigma-Aldrich Corp.; St. Louis, MO) were supplemented to favor proliferation of neurons over non-neuronal cells (Cullen et al. 2012; Zhang et al. 2017b).

At day seven in vitro, NCCs were cut into a cruciform shape to undergo biaxial stretch as described previously (Zhang et al. 2017d). A planar testing machine (574LE2; TestResources; Shakopee, MN) equipped with a bio-bath filled with PBS maintained at 37°C was used to stretch the NCCs along each arm of the cruciform to 1.5mm at 0.3mm/s. This amount of stretch has been shown to impose strains (~20%) simulating those that induce pain in vivo (Lee et al. 2004b; Lee et al. 2006; Dong et al. 2012). Immediately after stretch, NCCs were released from the testing machine, washed with fresh PBS with 1% Pen-Strep (Thermo Fisher Scientific; Waltham, MA) and transferred

to pre-warmed culture media supplemented by 1% Pen-Strep. Either 30 minutes (n=3) or 6 hours (n=5), the NCCs were rinsed with cold PBS and any residual PBS and culture medium was removed by blotting the edge of the gel (Keely et al. 2007). Each NCC was then snap frozen using liquid nitrogen and stored at -80°C before RhoA activity was measured. Unstretched NCCs also were included as controls for the evaluation of RhoA activity at each time point (n=3 at 30 minutes; n=5 at 6 hours).

#### 8.3.1.3. RhoA Activity Assay

RhoA activity was measured using a RhoA G-LISA Kit (BK124; Cytoskeleton; Denver, CO) and normalized to the total RhoA measured by a RhoA ELISA Kit (BK150; Cytoskeleton; Denver, CO), according to manufacturer methods. Each DRG was homogenized in 75mL of the lysis buffer provided in the G-LISA Kit; the tissue was grinded on ice with a pellet pestle motor until no visible pieces were left. To collect cell lysate from the NCCs, each NCC was grinded on ice in 50mL of G-LISA lysis buffer and quickly sheared through an 18-gauge needle (Keely et al. 2007). All of the homogenized samples were centrifuged at 14,000rpm at 4°C for 2 minutes and the supernatant was collected. The total concentration of protein in the supernatant was measured using a Pierce BCA Protein Assay Kit (Thermo Fisher Scientific; Waltham, MA). Supplemental lysis buffer was added to equalize the protein concentration in all samples so that 0.7mg/mL of lysate was used for the G-LISA and 1mg/mL of lysate was used for the ELISA.

The G-LISA RhoA assay used a 96-well plate that was coated with a Rho-GTP-binding protein. Only the active GTP-bound Rho in lysates were bound to the well plate, while other proteins including the inactive GDP-bound Rho were removed during multiple washing steps. The bound active RhoA was detected with a RhoA specific antibody followed by incubation with a secondary antibody conjugated to horseradish peroxidase (HRP) and an HRP detection reagent. In order to compare RhoA activity between samples, active RhoA was normalized to the total RhoA in the lysate from the same sample. The total RhoA ELISA assay was performed using a 96-well plate that was pre-coated with anti-Rho IgY antibody for high-affinity binding of all Rho isotypes. The bound RhoA is recognized by incubation with a selective RhoA antibody followed by subsequent signal detection with a secondary antibody HRP conjugate. Each of the active RhoA and total RhoA signals was read by measuring absorbance at 490nm using a microplate reader (Infinite M200; Tecan Life Sciences; San Jose, CA). RhoA activity was calculated as the active RhoA absorbance divided by the total RhoA absorbance. The results are expressed as RhoA activity relative to the corresponding unstretched control DRGs or NCCs.

### 8.3.2. ROCK Inhibition & substance P Expression after NCC Stretch

#### 8.3.2.1. ROCK Inhibition in Vitro

ROCK inhibition was performed on a separate set of NCCs immediately after undergoing stretch along each arm of the cruciform to 1.5mm at 0.3mm/s. After stretch NCCs were removed from the testing machine and incubated for one day in 1mL of 1%

Pen-Strep supplemented culture medium either with (n=6) or without (n=8) of 10μM of the ROCK inhibitor Y27632 (Selleckchem; Houston, TX) (Fournier et al. 2003; Joshi et al. 2015). This inhibitor concentration and incubation time were selected because they were found in previous in vitro studies to promote neurite outgrowth (Fournier et al. 2003; Joshi et al. 2015). In addition, substance P increases at this time point after stretch in this same system (Zhang et al. 2017b). Unstretched untreated NCCs (n=7) and unstretched Y27632-treated NCCs (n=6) were included as negative controls for the assessment of substance P expression. At one day after stretch, NCCs were fixed with 4% paraformaldehyde (PFA) in PBS (pH7.4) for immunolabeling of substance P.

#### 8.3.2.2. Measurement of NCC Strain

Strains across the NCC surface were calculated in order to measure the extent of mechanical injury imposed on NCCs that received ROCK inhibition and those that did not and to enable correlations between strains and local substance P expression in different sub-regions of the NCC. A grid of markers was drawn on each NCC surface before stretch and it was tracked during stretch by a high speed camera (Phantom-v9.1; Vision Research Inc.; Wayne, NJ). Together with visible DRGs, the markers were used to designate four-node sub-regions covering the area of the NCC containing the DRGs. Maximum principal strain (MPS) quantifies the greatest change in length along any direction in each sub-region of the NCC and captures the most injurious strain; it was computed in each NCC region using LS-DYNA (Livermore Software Technology Corp.;

Livermore, CA) (Zhang et al. 2017b). MPS was taken as zero for unstretched control NCCs.

#### 8.3.2.3. Immunolabeling & Analysis of Axonal substance P Expression

Axonal expression of substance P was measured in fixed NCCs using immunofluorescent labeling. First, NCCs were blocked in 1% normal donkey serum with 0.3% Triton-X PBS for two hours at room temperature, followed by overnight incubation at 4°C with chicken anti-βIII tubulin (1:200; Abcam; Cambridge, MA) and guinea pig anti-substance P (1:500; Neuromics; Bloomington, MN) primary antibodies. The next day, NCCs were incubated with donkey anti-chicken Alexa Fluor 647 (1:1000; Invitrogen; Carlsbad, CA) and donkey anti-guinea pig Alexa Fluor 488 (1:1000; Jackson ImunoResearch Labs; West Grove, PA) secondary antibodies. DRGs in each NCC were imaged to capture βIII tubulin and substance P labeling using a Zeiss 710 confocal microscope (Carl Zeiss Microscopy; Thornwood, NY) and processed in ImageJ (National Institutes of Health; Bethesda, MD) for background subtraction and intensity measurement. To quantify the expression of substance P, four to eight axons were randomly selected from each DRG and outlined based on the βIII tubulin labeling. The average intensity of substance P labeling per unit area in those outlined axons was measured and normalized to the level in comparable unstretched, untreated control NCCs to ensure appropriate comparison. The number of axons analyzed was 182 for the *stretched, untreated* group, 117 for the *stretched, treated* group, 90 for the *unstretched, untreated* group, and 81 for the *unstretched, treated* group. To evaluate the relationship

between substance P expression and the applied NCC strain in untreated NCCs and those treated with Y27632, local substance P expression was mapped to the regional strain measured in the same sub-region of the gel (Zhang et al. 2016b; Zhang et al. 2017d).

### 8.3.3. ROCK Inhibition in Vivo

#### 8.3.3.1. Intra-Articular ROCK Inhibition

Immediately after facet joint injury, rats were randomly selected to receive a bilateral C6/C7 intra-articular injection of either the ROCK inhibitor Y27632 at a dose of 500μg (Paiva-Lima et al. 2014) in 10μL of saline (*injury+Y27632*; n=12) or the same volume of only the vehicle saline (*injury+veh*; n=11). The severity of the applied stretch injury was quantified by tracking markers on the laminar bones of the vertebrae and the facet capsule during its stretch (Lee et al. 2006; Quinn et al. 2010b; Dong et al. 2012). Vertebral and capsular displacement and the MPS across the capsule were measured and compared between groups to ensure that the imposed stretch was not different between the inhibitor and vehicle treatment groups. A separate group of rats (*sham+veh*; n=12) received sham surgery and saline vehicle injection but no joint injury to serve as surgical controls.

#### 8.3.3.2. Assessment of Mechanical Hyperalgesia

Behavioral sensitivity was assessed in the forepaw before (day 0), eight hours and one day after surgical procedures. Mechanical hyperalgesia was quantified as the withdrawal threshold of the bilateral forepaws to mechanical stimulation applied by von

Frey filaments of increasing strengths from 0.6-26g (Stoelting Co., Wood Dale, IL) (Chaplan et al. 1994; Dong et al. 2012; Crosby et al. 2013; Kras et al. 2013a; Corder et al. 2017). Briefly, each filament was applied five times to the plantar surface of the left and right forepaws separately. If two consecutive filament strengths evoked withdrawal, shaking or licking of the forepaw, the lower filament strength was recorded as the paw withdrawal threshold. During each testing session, three rounds of stimulation were performed with ten minutes of rest between each round. The average of the left and right forepaw response thresholds from all rounds at each time point was taken as the forepaw withdrawal threshold for each rat.

#### 8.3.3.3. Fluorescent Immunohistochemistry of DRG & Spinal Cord Tissue

After behavioral testing on day one, a subset of rats (*injury+veh* n=6; *injury+Y27632* n=6; *sham+veh* n=5) was anesthetized with sodium pentobarbital (65 mg/kg) and perfused transcardially with PBS and 4% PFA in PBS. The C7 DRG and spinal cord tissues were harvested, post-fixed in 4% PFA in PBS at 4°C for one day, incubated in 30% sucrose at 4°C for one week and freeze-mounted in Tissue-Tek OCT Compound (Sakura Finetek; Torrance, CA). DRG and spinal cord from un-operated naïve rats (n=2) were also included as normal controls for all tissue assays. The spinal cord with DRGs attached was sectioned axially into 14μm-thick slices and mounted on Superfrost Plus slides (Thermal Fisher Scientific; Waltham, MA) for immunohistochemistry (IHC). Tissue sections were blocked in 1% normal donkey serum with 0.3% Triton-X PBS and fluorescently labeled for substance P and the microglial

marker ionized calcium binding adaptor molecule 1 (Iba1). Tissue slices were incubated with guinea pig anti-substance P (1:500; Neuromics; Bloomington, MN) and rabbit anti-Iba1 (1:1000; Wako; Richmond, VA) antibodies overnight at 4°C. The next day, sections were incubated with the secondary antibodies donkey anti-rabbit 555 (1:1000; Invitrogen; Carlsbad, CA) and donkey anti-guinea pig 488 (1:1000; Jackson ImunoResearch Labs; West Grove, PA). Slides were imaged using an Olympus BX51 microscope (Olympus, Tokyo, Japan) with the 20X objective (1360x1024 pixels).

Uniform-sized regions of interested (ROI) in the DRG (472×472 pixels) and in the superficial (laminae I-II; 750×150 pixels) and deep (laminae III-V; 600×380 pixels) dorsal horn were cropped from each image for standard analysis of the amount of positively labeled pixels (Zhang et al. 2013; Nicholson et al. 2014). The percentage of substance P-positive neurons was counted in the small-diameter (4-21μm) and medium-diameter (21-40μm) sized DRG neurons, because those populations of neurons are primarily nociceptors and exhibit different protein expression profiles after painful facet joint injury (Julius and Basbaum 2001; Weisshaar et al. 2010; Dong et al. 2012). Expression of substance P was measured in three slices for each rat, leading to a total count of analysis on 482 DRG neurons for the *injury+veh* group, 460 neurons for the *injury+Y27632* group, and 355 DRG neurons for the *sham+veh* group. Automated densitometry measured the percentage of positively-labeled pixels for substance P and Iba1 separately in the superficial dorsal horn using a customized script in MATLAB (R2014a; MathWorks, Inc; Natick, MA) (Zhang et al. 2013; Nicholson et al. 2014). Since most peptidergic nociceptors synapse with spinal neurons in the superficial dorsal horn

(Basbaum et al. 2009), substance P expression was only quantified in laminae I-II. However, since glial activation has been shown to occur throughout the dorsal horn in rodent models of joint and neuropathic pain (Rothman et al. 2009; Weisshaar and Winkelstein 2014; Guan et al. 2015), Iba1 expression was assessed in both laminae I-II in the superficial dorsal horn and III-V in the deep dorsal horn using automated densitometry. For each rat, six to nine spinal cord sections were analyzed. Quantified substance P and Iba1 labeling in the spinal cord was expressed as fold-change over normal levels in the un-operated naïve rats.

#### 8.3.3.4. Electrophysiological Recordings from the Spinal Dorsal Horn

Following behavioral testing on day one, electrophysiological recordings of spinal neurons were performed on a subset of rats (*injury+veh* n=5; *injury+Y27632* n=6; *sham+veh* n=6) as described previously (Crosby et al. 2014; Nicholson et al. 2014; Weisshaar and Winkelstein 2014). Rats were anesthetized with an intraperitoneal injection of 45mg/kg sodium pentobarbital and the cervical (C6-C8) dorsal horns were exposed by laminectomy. Temperature was maintained at 34-36°C by placing the rat on a heating pad with feedback from a rectal probe (Physitemp; Clifton, NJ), and a tracheotomy was performed to allow for mechanical ventilation (40-50 cycles/min) and monitoring of $CO_2$ levels (Harvard Small Animal Ventilator Model 683; Harvard Apparatus; Holliston, MA). A stereotactic frame anchored the head and T2 spinal process while a micropositioner was used to insert a carbon fiber electrode (#E1011; Kation Scientific; Minneapolis, MN) into the dorsal horn (100-970μm depth) at the C6-C8 spinal

cord to allow for extracellular recordings of neurons (*injury+veh* n=49 neurons; *injury+Y27632* n=52 neurons; *sham+veh* n=52 neurons).

Neuronal firing was evoked using either non-painful (brush, 1.4g and 4g von Frey filaments) or painful (10g and 26g von Frey filaments, pinch) stimuli applied to the receptive field on the forepaw. The stimulation was applied in the following order: ten light brushes over ten seconds, five consecutive one-second stimulations separated by one-second of rest with 1.4g, 4g, 10g then 26g von Frey filaments, and finally a ten-second pinch; between application of each different stimulus, a one-minute rest period was maintained. Signals were amplified with a gain of $10^3$ and conditioned using a 0.3-3kHz bandpass filter (World Precision Instruments; Sarasota, FL) and a 60Hz HumBug adaptive filter (Quest Scientific; North Vancouver, BC). The recorded potentials were sampled at a rate of 25kHz and monitored with a speaker (A-M Systems; Carlsborg, WA) for audio feedback. Spike2 software (CED; Cambridge, UK) was used to sort individual potentials, ensuring that only a single neuron was counted at each site of recording. The resultant spikes were log-transformed to reduce any skewness in the spike distribution.

Based on the firing patterns in response to different stimulations, neurons were classified as low-threshold mechanoreceptive (LTM), nociceptive specific (NS), or wide dynamic range (WDR) (Saito et al. 2008; Quinn et al. 2010b; Zhang et al. 2013). LTM neurons were taken as those that respond maximally to the light brushing, while NS neurons responded only to noxious pinch; neurons that showed a graded response to increasing filament strength were classified as WDR neurons (Woolf and Fitzgerald 1983; Saito et al. 2008). The relative percentage of neurons in each phenotypic

classification was measured to assess if there is any shift in relative phenotypic responses induced by painful facet joint injury and/or ROCK inhibition.

### 8.3.4. Experimental Design & Statistical Analysis

The first study evaluated whether mechanical loading of the innervated facet capsule induces RhoA activation in the DRG at early times after joint injury. RhoA activity in the DRG at one day was compared between groups undergoing stretch (*injury* n=4) and not (*sham* n=2) in the rat. In addition, in parallel, RhoA activity was compared between NCCs undergoing stretch and not at 30 minutes (n=3/group) and six hours (n=5/group). For the in vivo and in vitro experiments, differences in RhoA activity between the stretched and unstretched groups were tested using separate t-tests.

Based on findings that stretch up-regulates RhoA activity in DRG neurons, the role of ROCK in mediating stretch-induced substance P expression was evaluated via its inhibition in DRG-collagen constructs. The effects of ROCK inhibition on the axonal substance P expression were tested using four different NCC groups (*stretched, untreated* n=8 NCCs; *stretched, treated* n=6 NCCs; *unstretched, untreated* n=7 NCCs; *unstretched, treated* n=6 NCCs). A two-way analysis of variance (ANOVA) with post-hoc Tukey's HSD test compared substance P expression in stretched NCCs with and without ROCK inhibition and that between stretched NCCs and their respective unstretched controls. Linear regression analysis was implemented to define the relationship between the average local substance P expression and the regional MPS in vitro with and without

ROCK inhibition (*untreated* n=198 axons from 35 regions; *treated* n=198 axons from 41 regions); an f test was performed to assess the significance of the regression.

A final set of experiments tested whether intra-articular ROCK inhibition attenuates facet pain from its mechanical stretch injury and modulates DRG substance P expression in the DRG and/or aspects of the spinal central sensitization response in vivo. To assess pain responses, a repeated-measures ANOVA with post-hoc Tukey's HSD test compared the forepaw withdrawal thresholds between groups (*injury+veh* n=11; *injury+Y27632* n=12; *sham+veh* n=12) at each time point (day 0, 8 hours, day 1). The expression of substance P in the DRG and Iba1 in the spinal cord from the in vivo experiments was statistically compared between groups (*injury+veh* n=6; *injury+Y27632* n=6; *sham+veh* n=5) using separate one-way ANOVAs with post-hoc Tukey's HSD tests. To evaluate changes in the spinal neuronal excitability after facet injury with ROCK inhibition, the number of evoked spikes was compared between the *injury+veh* (n=49 neurons from six rats), *injury+Y27632* (n=52 neurons from six rats), and *sham+veh* (n=52 neurons from six rats) groups using a two-way ANOVA for overall significance and separate one-way ANOVAs at each filament strength, all with post-hoc Tukey's HSD tests. A Pearson's Chi-Squared test compared the number of the different types of neurons (LTM, NS, WDR) identified in the spinal cord between the three groups.

Separate t-tests compared the applied strains and/or displacements between groups that received ROCK inhibition and those that did not in each of the in vitro and in vivo studies to ensure consistent loading between groups. All t-tests were conducted in

MATLAB and the other statistical tests were performed using JMP11 software (SAS Institute; Cary, NC). The significance level was set to 0.05.

## 8.4. Results

### 8.4.1. Stretch-Induced RhoA Activation in the DRG

Both an injurious facet joint stretch in vivo and NCC stretch to comparable degrees in vitro induce RhoA activation in DRG neurons early after stretch (Figure 8.1); strain of 16.0±3.9% was induced in the NCCs in which RhoA activity was measured. Strains imposed on the NCCs and the facet capsular ligaments are summarized in Appendix F and Appendix K, respectively. Rats receiving facet joint injury exhibit significantly higher RhoA activity in the DRG as compared to unstretched sham rats at day one ($t(4)=2.21$, $p=0.046$, one-tailed t-test). RhoA activity in the *injury* group is 1.63±0.38 times the level in the corresponding *sham* group (Figure 8.1a). Similar to in vivo results, mechanical loading of the NCCs in vitro also significantly increases RhoA

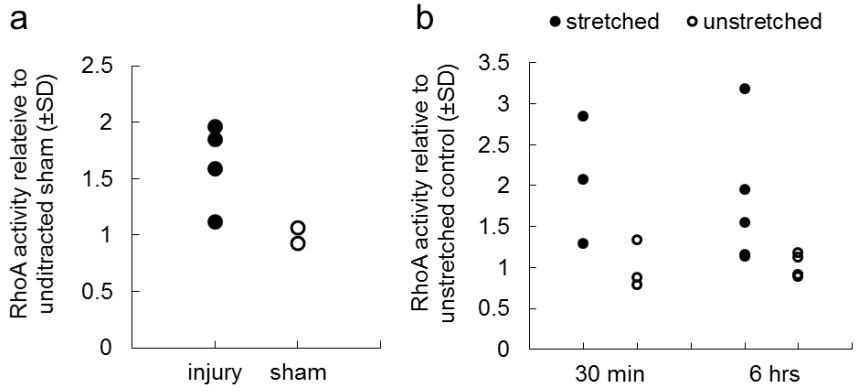


**Figure 8.1.** Stretch-induced RhoA activation in the DRG. RhoA activity quantified as the ratio of active-to-total RhoA is up-regulated by **(a)** a cervical facet joint stretch injury as compared to sham procedures in the rat ($p=0.046$) and **(b)** NCC stretch relative to levels in unstretched control gels at 30 minutes ($p=0.045$) and 6 hours ($p=0.037$).

activity in the associated DRGs. RhoA activity after NCC stretch increases by 2.1±0.78 times at 30 minutes ($t(4)=2.22$, $p=0.045$, one-tailed t-test) and 1.8±0.84 times at six hours ($t(8)=2.06$, $p=0.037$, one-tailed t-test) over levels in unstretched controls (Figure 8.1b). RhoA activity after facet capsule stretch and NCC stretch is detailed in Appendix L.

### 8.4.2. Prevention of Stretch-Induced substance P by ROCK Inhibition in Vitro

The untreated and treated NCCs underwent comparable strains ($t(12)=0.042$, $p=0.967$, two-tailed t-test); the average MPS was 18.7±2.8% for the treated NCCs and 18.8±3.4% for the untreated NCCs, respectively. The increase in substance P expression in the DRG that is induced one day after NCC stretch is prevented with ROCK inhibition ($F(3, 23)=5.21$, $p=0.007$, ANOVA) (Figure 8.2). In the absence of the inhibitor Y27632, substance P expression increases by 1.3±0.1-fold after NCC stretch as compared to unstretched controls ($p=0.047$, post-hoc Tukey HSD) (Figures 8.2a & 8.2b). In contrast, Y27632 treatment of stretched NCCs significantly decreases substance P expression ($p=0.006$, post-hoc Tukey HSD) to levels that are not different from expression in unloaded control NCCs ($p>0.463$, post-hoc Tukey HSD) (Figures 8.2a & 8.2b). The substance P expression and MPS for individual NCCs are provided in Appendix C and Appendix F, respectively.

Axonal substance P expression is positively correlated with the injury severity as measured by MPS in NCCs undergoing stretch without ROCK inhibition ($R^2=0.268$, $F(1, 33)=12.1$, $p=0.002$, linear regression) (Figure 8.2c). However, ROCK inhibition abolishes that strain-dependent up-regulation in substance P (Figure 8.2c); for Y27632-treated

NCCs, the positive correlation between the expression of substance P and MPS is no longer evident ($R^2$=0.040, F(1, 39)=1.61, p=0.211, linear regression) (Figure 8.2c).

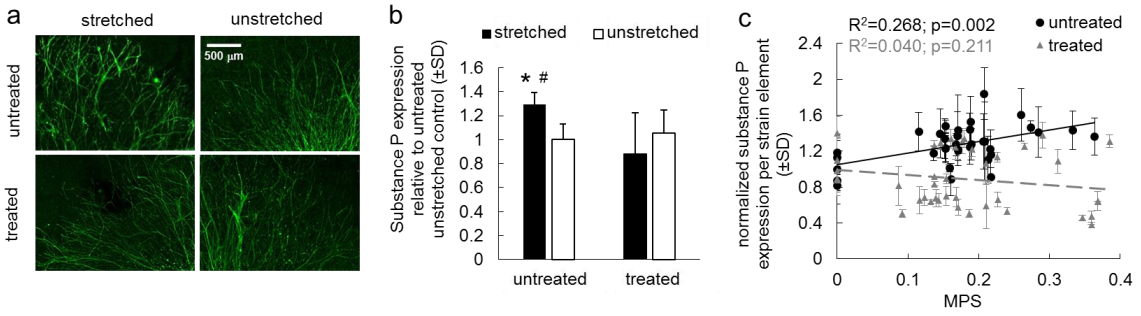


**Figure 8.2.** ROCK inhibition prevents the strain-dependent elevation of substance P in NCCs at day one. **(a)** Representative images and **(b)** quantification of axonal substance P expression show that expression in stretched NCCs receiving no Y27632 treatment (untreated) exceeds that in untreated unstretched controls (*p=0.047) and in Y27632 treated stretched NCCs ($^{\#}$p=0.006). **(c)** The positive correlation ($R^2$=0.268, p=0.002) between substance P expression and local strain (MPS) is abolished by ROCK inhibition ($R^2$=0.040, p=0.211). The scale bar is 500μm and applies to all images in **(a)**. Error bars indicate the standard deviation (SD).

### 8.4.3. ROCK Inhibition is Anti-Nociceptive in Vivo

The severity of the imposed mechanical stretch injury was not different between the two groups receiving injury (*injury+veh*, *injury+Y27632*) regardless of receiving treatment. The mean vertebral displacement was 0.52±0.21mm for the *injury+veh* group and was 0.51±0.13mm for the *injury+Y27632* group (t(21)=0.139, p=0.891, two-tailed t-test); the mean capsule displacement was 0.27±0.11mm for the *injury+veh* group and 0.30±0.09mm for the *injury+Y27632* group (t(21)=0.646, p=0.525, two-tailed t-test). Rats receiving vehicle treatment sustained a capsular MPS of 10±4% and peak MPS of 22±12%; the capsule strains were similar in the rats that received ROCK inhibition

(average: t(21)=0.529, p=0.603, two-tailed t-test; peak: t(21)=0.383, p=0.706, two-tailed t-test), with a mean MPS of 11±4% and a peak MPS of 23±10%.

Despite undergoing comparable facet joint stretch injuries, only the rats receiving a saline vehicle injection intra-articularly (*injury+veh*) developed behavioral sensitivity (Figure 8.3). Differences in mechanical hyperalgesia were observed over time in the *injury+veh* group and between groups ($F(4, 64)=16.9$, $p<0.0001$, repeated measures ANOVA); the forepaw withdrawal threshold is significantly lowered from baseline (day 0) at both eight hours and one day ($p<0.0001$ for both time points, post-hoc Tukey HSD) after facet joint stretch (Figure 8.3). In contrast, the withdrawal thresholds of the group

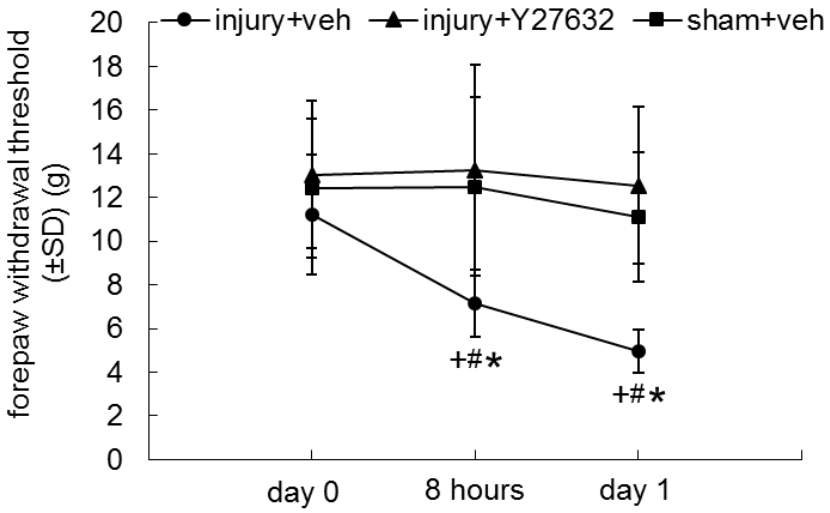


**Figure 8.3.** Intra-articular ROCK inhibition prevents mechanical hyperalgesia within one day after painful facet joint stretch injury. Facet joint stretch decreases the forepaw withdrawal threshold at eight hours and one day in the *injury+veh* group as compared to that before injury (day 0) ($^{+}p<0.0001$) and corresponding levels in the *injury+Y27632* group ($^{\#}p\leq0.002$) and in the *sham+veh* group ($^{*}p\leq0.009$). Neither the *injury+Y27632* nor *sham+veh* group exhibit altered thresholds from pre-injury baseline (day 0) levels ($p\geq0.311$). Error bars indicate the standard deviation (SD).

undergoing stretch injury with ROCK inhibition (eight hours p=1, one day p=0.993, post-hoc Tukey HSD) and the group undergoing sham surgery (eight hours p=1, one day p=0.311, post-hoc Tukey HSD) are not altered from their corresponding baseline (day 0) uninjured values (Figure 3). At both eight hours and one day, the forepaw withdrawal threshold in the *injury+veh* group is significantly lower than for the *injury+Y27632* group (eight hours p=0.002, one day p<0.0001, post-hoc Tukey HSD) and the *sham+veh* group (eigth hours p=0.009, one day p=0.002, post-hoc Tukey HSD) (Figure 8.3). The forepaw withdrawal thresholds of each rat as well as their facet joint distraction mechanics are summarized in Appendix K.

The differences in substance P expression in the DRG at day one parallel the behavioral responses, with differences between groups ($F(2,14)=4.13$, $p=0.039$, ANOVA). The *injury+veh* group exhibits a significantly higher percentage of substance P-positive small- and medium-diameter neurons than in the *injury+Y27632* group (p=0.048, post-hoc Tukey HSD) (Figure 8.4). The percent of substance P-positive afferents in DRGs of rats receiving ROCK inhibition is similar to that in un-operated naïve rats and is not different from that in sham-operated rats (p=0.963, post-hoc Tukey HSD) (Figure 8.4). No difference is detected in the percent of substance P-positive DRG neurons between the *sham+veh* and *injury+veh* groups (p=0.096, post-hoc Tukey HSD).

Intra-articular ROCK inhibition not only reduces substance P expression in the DRG, but also exhibits differences in spinal substance P between treated and untreated groups one day after facet joint injury ($F(2, 14)=4.67$, $p=0.028$, ANOVA) (Figure 8.5). The amount of substance P in the superficial dorsal horn in the *injury+Y27632* group is

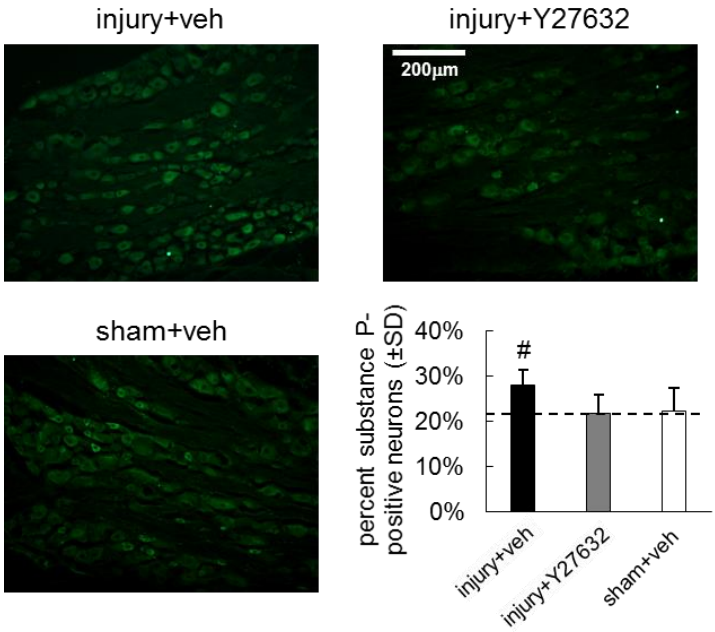


**Figure 8.4.** Intra-articular ROCK inhibition reduces the percent substance P-positive DRG neurons at one day after painful facet joint stretch injury. Representative images and quantification demonstrate that the percentage of DRG neurons that display positive substance P labeling in the *injury+Y27632* group is significantly lower than that in the *injury+veh* group ($^{\#}$p=0.048) and not different from the level in the *sham+veh* group (p=0.963). The dotted line indicates the percent substance P-positive neurons in the un-operated naïve rats. The scale bar is 200μm and applies to all images. Error bars indicate the standard deviation (SD).

significantly lower than that in the *injury+veh* group (p=0.046, post-hoc Tukey HSD) and comparable to the level in normal un-operated rats (fold changes close to one) (Figure 8.5). As with the percent of substance P-positive neurons in the DRG, no difference in spinal substance P expression is found between the *sham+veh* group and either the *injury+Y27632* group (p=0.053, post-hoc Tukey HSD) or the *injury+veh* group (p=0.999, post-hoc Tukey HSD) (Figure 8.5).

In addition to spinal substance P expression, spinal microglial activation is found to be different across groups in the superficial dorsal horn ($F(2, 14)=28.6$, $p<0.0001$, ANOVA) and in the deep dorsal horn ($F(2, 14)=4.30$, $p=0.035$, ANOVA) at day one

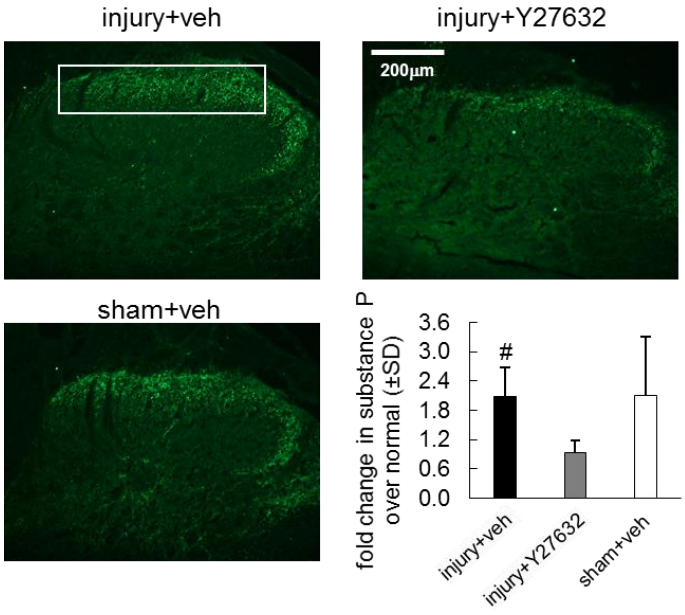


**Figure 8.5.** Intra-articular ROCK inhibition reduces substance P expression in the superficial dorsal horn at one day after painful facet joint stretch injury. Representative images and quantification demonstrate that the percent pixels labeled positively for substance P (normalized over the level in un-operated naïve rats) in the *injury+Y27632* group is significantly lower than that in the *injury+veh* group ($^{\#}p=0.046$). The normalized spinal substance P expression in the *sham+veh* group is not different from either of the injury groups, regardless of treatment ($p \geq 0.053$). The rectangular box indicates the region of interest in the superficial dorsal horn. The scale bar is 200µm and applies to all images. Error bars indicate the standard deviation (SD).

(Figure 8.6). There is significantly more Iba1 expression in the superficial dorsal horn in the *injury+veh* group as compared to the *sham+veh* group (p=0.0008, post-hoc Tukey HSD) (Figure 8.6). Intra-articular ROCK inhibition after facet injury significantly lowers that Iba1 expression in both the superficial ($p<0.0001$, post-hoc Tukey HSD) and deep (p=0.028, post-hoc Tukey HSD) dorsal horns relative to corresponding levels in the injured, vehicle-treated rats (Figure 8.6). The Iba1 expression in the *injury+Y27632* group is similar to levels in normal un-operated rats (fold changes close to one) and not different from that in the *sham+veh* group (p=0.099, post-hoc Tukey HSD) in both

regions of the dorsal horn (Figure 8.6). Measurements of protein expression, including substance P in the DRG and spinal cord and spinal Iba1, are detailed in Appendix J.

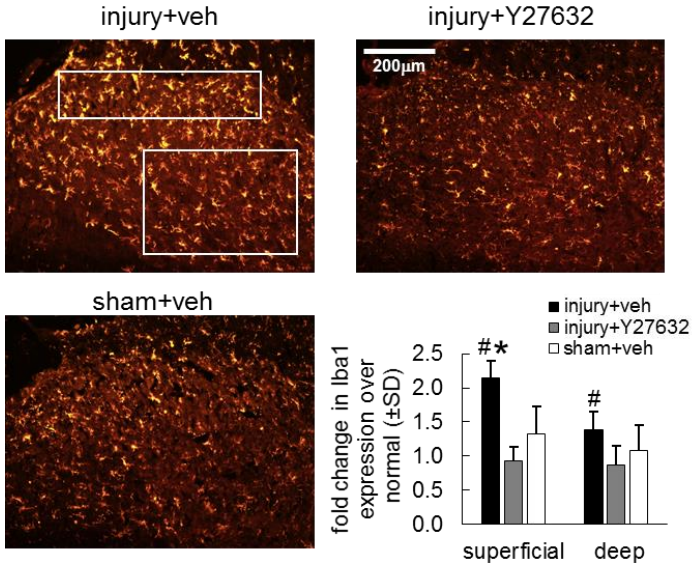


**Figure 8.6.** Intra-articular ROCK inhibition reduces Iba1 labeling in the spinal dorsal horn at one day after painful facet joint stretch injury. Representative images and quantification show that the percent pixels labeled positively for Iba1 (normalized over the level in un-operated naïve rats) in the *injury+veh* group is significantly higher than that in the *injury+Y27632* group in both the superficial ($^{\#}p<0.0001$) and deep ($^{\#}p=0.028$) dorsal horns. The normalized Iba1 expression in the *injury+veh* group is also significantly higher than the level in the *sham+veh* group but only in the superficial dorsal horn (*p=0.0008). The rectangular boxes indicate the regions of interest in the superficial and deep dorsal horns. The scale bar is 200μm and applies to all images. Error bars indicate the standard deviation (SD).

Intra-articular ROCK inhibition immediately after facet capsule stretch also attenuates the spinal neuronal hyperexcitability that is typically induced by that painful joint injury. Overall, the evoked firing in the spinal dorsal horn is different between the three groups across the non-noxious and noxious stimuli at day one ($F(17, 900)=17.4$, $p<0.0001$, ANOVA). Regardless of the applied stimulus strength, the number of evoked spikes is significantly higher in the *injury+veh* group than in the *sham+veh* group

(p<0.026, post-hoc Tukey HSD) (Figure 8.7). The increases in neuronal firing that are evident in response to painful filament stimulations (10g and 26g) after a facet joint stretch injury are abolished by ROCK inhibition; 10g and 26g stimulations induce fewer

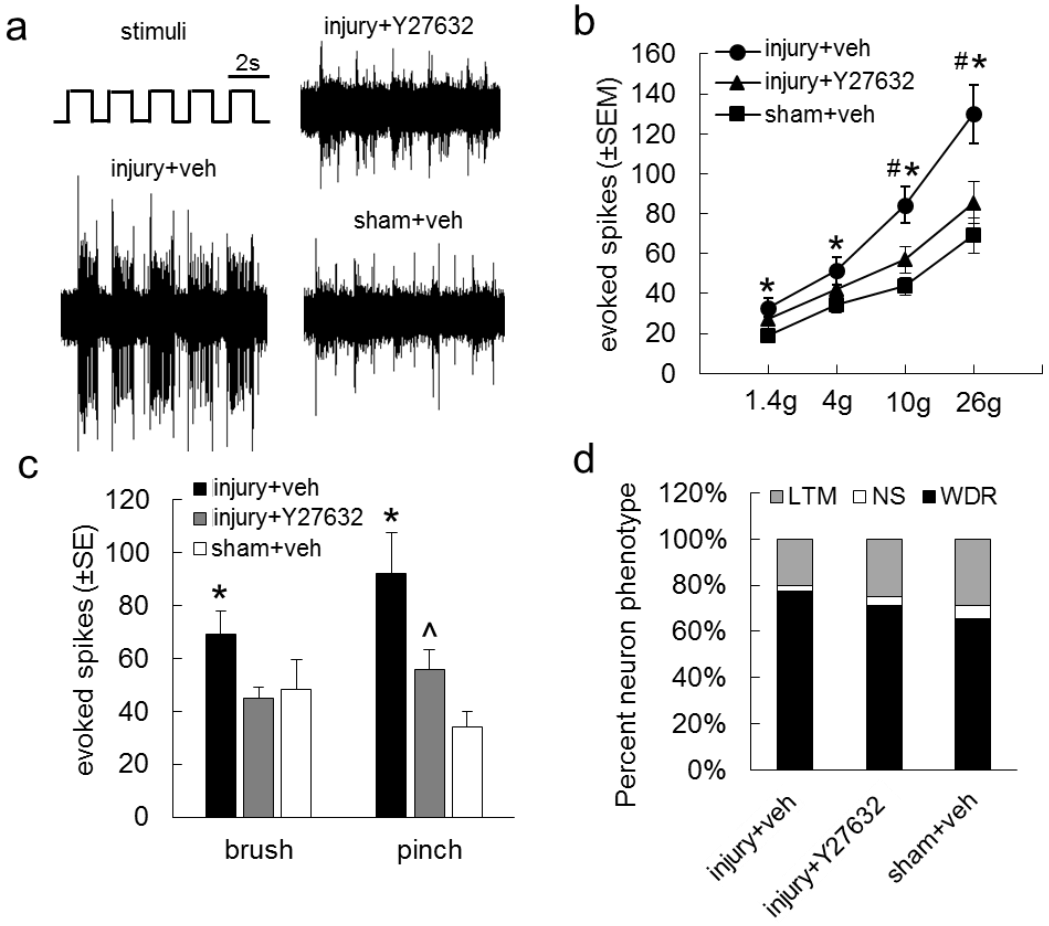


**Figure 8.7.** Intra-articular ROCK inhibition attenuates the neuronal hyperexcitability in the spinal dorsal horn at one day after painful facet joint stretch injury. **(a)** Representative neuronal traces evoked by stimulation with a 26g von Frey filament and spike counts evoked by **(b)** von Frey filaments and **(c)** light brushing or noxious pinch exhibit fewer spikes evoked by the 10g and 26g stimulations in the *injury+Y27632* group than in the *injury+veh* group ($^{\#}p \leq 0.019$). Regardless of the applied stimulus strength, the evoked neuronal firing in the *sham+veh* group is significantly lower than that in the *injury+veh* group (*p<0.026), but not different from the number of spikes in the *injury+Y27632* group (p>0.251) except for noxious pinch ($^{\wedge}p=0.024$). Error bars indicate the standard error of mean (SEM). **(d)** There is no difference in the numbers of neurons classified as LTM, NS, and WDR between any group (p=0.361).

spikes with the Y27632 treatment than for the saline vehicle treatment (10g p=0.011, 26g p=0.019, post-hoc Tukey HSD) (Figures 8.7a & 8.7b). In fact, the *injury+Y27632* group and the *sham+veh* group display similar numbers of evoked spikes for all stimulation strengths (p>0.251, post-hoc Tukey HSD) except for a noxious pinch (Figure 8.7). A pinch evokes significantly fewer neuronal spikes in the sham-operated rats compared to that in the *injury+Y27632* group (p=0.024, post-hoc Tukey HSD), which is lower than, but not significantly different from, the number of pinch-evoked spikes in the *injury+veh* group (p=0.068, post-hoc Tukey HSD) (Figure 8.7c). Although each of these groups exhibit different firing response patterns to increasing stimulus strength (Figures 8.7b & 8.7c), the numbers of neurons classified as LTM, NS and WDR neurons at day one are not different ($\chi^2(4, N = 110)=4.346$, p=0.361) (Figure 8.7d). The quantification of spike counts of individual dorsal horn neurons is summarized in Appendix M.

## 8.5. Discussion

The Rho/ROCK pathway may be activated by stretch of the fibrous facet capsule via neuronal mechanotransduction. The activity of RhoA in neurons is known to be regulated by mechanical inputs. For example, direct mechanical trauma to neural tissue, like the spinal cord and peripheral nerves, activates RhoA in neurons within 30 minutes and it lasts for up to seven days (Dubreuil et al. 2003; Yamagishi et al. 2005; Cheng et al. 2008). Similarly, facet capsule injury and NCC stretch both increase RhoA activity in DRG neurons within one day (Figure 8.1). The loading severities (i.e strains) used in vivo with facet capsule stretch and in vitro for NCC loading also induce pain and lead to

restructuring of the ECM (Quinn et al. 2007; Zhang et al. 2016b), which can produce local forces in fibers that are sensed by the cells that adhere to the ECM (Sander et al. 2009a). Forces in the ECM can be transmitted to cells through cell adhesion receptors, like integrins, and regulate the intracellular guanine nucleotide exchange factors that activate RhoA (Guilluy et al. 2011; Lessey et al. 2012; Marjoram et al. 2014). Therefore, increased RhoA activity in afferents after facet joint injury (Figure 8.1) may be triggered by the mechanical coupling of neurons and the restructuring ECM during ligament stretch. Although mechanotransduction processes in neurons were not assessed in this study, integrin-dependent mecahnotransduction, RhoA/ROCK activation and neuronal dysfunction have been previously related to each other since ROCK inhibition can attenuate integrin-mediated mechanical injury in axons (Hemphill et al. 2011).

Since this NCC system utilizes isolated DRG explants, it minimizes the confounding effects of any inflammatory response (Zhang et al. 2017d), providing a simplified microenvironment suitable to investigate mechanically-induced nociception. In addition to isolating the mechanical effects, the NCC system also enables direct mapping of the neuronal responses to the local strains imposed on their surrounding ECM (Figure 8.2). As such, it can be used to define the role of RhoA/ROCK in neuronal mechanosensing of the surrounding ECM. In fact, by measuring strain-dependent substance P expression, this and previous NCC experiments reveal a possible connection between integrin and ROCK in mediating neuronal nociception following mechanical stimuli (Zhang et al. 2017d). The positive correlation found in the DRG-collagen in vitro tests between axonal substance P and regional MPS is similarly abolished by Y27632

treatment (Figure 8.2) as by the allosteric inhibition of the α2β1 integrin (Zhang et al. 2017d), suggesting that external forces transmitted through collagen-binding integrins may regulate substance P expression via the intracellular RhoA/ROCK pathway. Furthermore, although RhoA activity can also be increased via inflammatory pathways and ROCK inhibition attenuates pain from inflammation (Inoue et al. 2004; Tatsumi et al. 2005; Paiva-Lima et al. 2014; Wu and Xu 2016), early RhoA activation after facet joint distraction (Figure 8.1) is unlikely triggered by inflammatory contributions in the tissue or joint. Although this study found that intra-articular injection of the ROCK inhibitor Y27632 at injury prevents pain onset (Figure 8.3), similar injection of the non-steroidal anti-inflammatory drug ketorolac immediately after injury did *not* prevent or attenuate pain (Dong et al. 2011; Dong et al. 2013b). Together, these findings support the hypothesis that the activity of RhoA/ROCK is increased by mechanical signals present in the ECM *during* facet capsule stretch via cell adhesion-mediated mechanotransduction.

Blocking the Rho kinase ROCK in the facet joint at the time of mechanical injury not only prevents the development of mechanical hyperalgesia (Figure 8.3) but also prevents the elevated spinal neuronal responses to noxious stimuli (Figure 8.7), both of which are typical early (one day) after a painful facet capsule stretch (Dong et al. 2012; Crosby et al. 2013; Crosby et al. 2014; Kras et al. 2015a). Paralleling the reduced behavioral sensitivity and neuronal excitability at that time point, intra-articular ROCK inhibition also decreases substance P and Iba1 immunoreactivity in the spinal cord (Figures 8.5 & 8.6). Although ROCK inhibition does attenuate neuropathic and inflammatory pain (Inoue et al. 2004; Tatsumi et al. 2005; Yoshimi et al. 2010b; Ohsawa

and Kamei 2010; Paiva-Lima et al. 2014), the current findings suggest, for the first time, that peripheral intra-articular ROCK inhibition prevents pain after joint injury possibly via down-regulation of injury-associated neurotransmitter expression in, and release from, afferents that themselves contribute to establishing the spinal responses that are typically involved in centrally-mediated pain (Figures 8.3 & 8.5-8.7) (Afrah et al. 2002; Basbaum et al. 2009; Kras et al. 2013b; He et al. 2016).

Since intra-articular ROCK inhibition immediately after a painful facet capsule stretch prevents behavioral hypersensitivity within one day (Figures 8.3 & 8.7), *early* activation of the RhoA/ROCK pathway in joint afferents may be important for pain development from joint injury. Although this ROCK inhibitor does not *specifically* target only afferent neurons, increased RhoA activity in the DRG at both 30 minutes and six hours after NCC stretch and at one day after facet capsule stretch (Figure 8.1) demonstrate the RhoA/ROCK pathway being rapidly activated in DRG neurons by excessive stretch of their axons. In fact, facet capsular ligament loading to the extent that generates strains comparable to those in the current study also activates the afferents that innervate the joint capsule (Lu et al. 2005b; Lu et al. 2005a). Further, early afferent activity has been shown to be *required* for pain to develop after facet joint stretch (Crosby et al. 2014); blocking afferent activity in the facet with the anesthetic bupivacaine during the same mechanical injury abolishes behavioral hypersensitivity, but is ineffective if given at eight hours after injury when pain has already developed (Figure 8.3) (Crosby et al. 2014). Since the Y27632 treatment given at injury is anti-nociceptive

(Figure 8.3), activation of the RhoA/ROCK pathway is likely an early response in afferents in response to stretch and is possibly critical for pain initiation.

Decreases in the spinal neuronal excitability evoked by noxious stimuli after ROCK inhibition (Figure 8.7) suggest reduced synaptic transmission between the primary afferents and the dorsal horn neurons. Activation of intra-articular ROCK by injury may facilitate synaptic signaling by increasing substance P release from the afferent to the spinal cord, because ROCK inhibition after stretch reduces substance P both in DRG neurons and in the superficial spinal dorsal horn (Figures 8.2, 8.4 & 8.5) where the peptidergic afferents synapse with spinal neurons (Basbaum et al. 2009). Both inhibiting ROCK in the facet joint (Figure 8.3) and ablating substance P-expression peptidergic joint afferents similarly prevent pain onset from mechanical injury (Kras et al. 2015b). Yet, the mechanisms by which the RhoA/ROCK pathway mediates substance P up-regulation and release is not well understood. ROCK signaling is hypothesized to be involved in neurotransmission by regulating the afferent cytoskeleton, which is critical in the development of inflammatory pain (Dina et al. 2003). Substance P release from primary afferents in the spinal cord is modulated by the activity of pre-synaptic N-methyl-D-aspartate (NMDA) receptors (Liu et al. 1997). Further, activity of the NMDA receptors on neurons can be modulated by the RhoA/ROCK pathway via its regulation of F-actin (Nörenberg et al. 1999; Lei et al. 2001). In that case, RhoA/ROCK, acting via cytoskeletal components, may activate NMDA receptors on the central terminals of afferents that facilitate the release of neurotransmitter, like substance P, for nociceptive transmission. In fact, ROCK signaling has been shown to maintain afferent synaptic

strength by myosin light chain phosphorylation that stabilizes the size of the readily releasable pool of synaptic vesicles (González-Forero et al. 2012), which may be another cytoskeleton-dependent mechanism mediating substance P release. Substance P can bind to neurokinin receptors on spinal neurons, which are required for facet joint pain initiation (Weisshaar and Winkelstein 2014). However, substance P receptors are not well-predicted by the amount of substance P in the spinal cord (Abbadie et al. 1996), which may explain why the *sham+veh* group and the *injury+veh* group exhibit similar levels of substance P, but different pain responses (Figures 8.3 & 8.5). Accordingly, additional work assessing the activation of the neurokinin receptor after facet capsule stretch with and without ROCK inhibition, would better define the substance P-dependent mechanisms by which afferent RhoA/ROCK signaling increases spinal neuronal excitability.

The RhoA/ROCK pathway may also indirectly mediate the activity of dorsal horn neurons via microglial activation (Figure 8.6). Activated microglia release a range of inflammatory mediators, such as the brain-derived neurotrophic factor (BDNF) (Ulmann et al. 2008; Basbaum et al. 2009), which promotes neuronal hyperexcitability in the spinal dorsal horn (Coull et al. 2005; Basbaum et al. 2009) and mediates pain after facet capsule stretch (Kras et al. 2013c). The signaling cascades that link RhoA/ROCK activation in afferents to microglial activation in the spinal cord are still not defined; the excitatory neurotransmitter glutamate which is critical for central sensitization (Latremoliere and Woolf 2009; Basbaum et al. 2009) may be involved. ROCK signaling in neurons can strengthen the glutamatergic synaptic inputs via cytoskeletal regulation

(González-Forero et al. 2012) and glutamate can induce functional changes in microglia by acting on their glutamate receptors (Domercq et al. 2013). Although this study found that intra-articular ROCK inhibition can prevent facet pain similar to blocking joint activity which induces spinal sensitization via glutamatergic signaling (Crosby et al. 2014), it does not directly assess if, and how, afferent RhoA/ROCK contributes to central sensitization and/or facet pain, nor does it evaluate how spinal glia are activated/inactivated and/or measure any associated glutamatergic signaling.

In addition to enhancing a mechanistic understanding of joint pain from ligament injury, this study provides novel evidence supporting peripheral ROCK as a promising drug target for mechanically-induced facet pain. Although ROCK inhibition has been shown in pre-clinical studies to prevent or attenuate inflammatory pain from biochemical mediators and neuropathic pain from peripheral nerve or spinal cord injury (Inoue et al. 2004; Tatsumi et al. 2005; Ohsawa and Kamei 2010; Hang et al. 2013; Paiva-Lima et al. 2014), this is the first study demonstrating the possible utility of ROCK inhibitors in treating joint pain from mechanical injury. Compared to existing facet pain therapies that target joint afferents by anesthetic joint injections or radiofrequency neurotamy (Barnsley et al. 1994; Kwan and Fiel 2002; Bogduk 2011; Smith et al. 2014), intra-articular ROCK inhibition may be more selective and more effective since it intervenes in a *specific* cell-signaling cascade. The effects of intra-articular ROCK inhibition on pain beyond one day, which typically last for three to four weeks after joint injury (Ita et al. 2017b), remain untested. However, prior work showing that blocking joint afferent activity at facet injury prevents pain for at least seven days (Crosby et al. 2014) suggests possible

longer-term analgesic effects of locally attenuating afferent ROCK signaling. Furthermore, because afferent neuronal RhoA/ROCK can be activated by both mechanotransduction and chemical stimuli (Inoue et al. 2004; Tatsumi et al. 2005; Lessey et al. 2012; Paiva-Lima et al. 2014; Wu and Xu 2016), pain from primary mechanical facet trauma that itself induces secondary inflammatory responses (Dong et al. 2013b; Crosby et al. 2014; Kras et al. 2015a) may be prevented or attenuated by inhibiting ROCK at the injury source. However, since ROCK inhibitors have a short half-life (no more than a few hours) in the human (Liao et al. 2007; Feng et al. 2016), effective maintenance of pain relief may require repeated dosing. The current study, while cast in the context of the spinal facet joint and its capsule, also provides insight to more broadly understand the nociceptive effects of ROCK and the mechanisms of pain from mechanical injury of other innervated joint ligaments, such as the knee and shoulder joint capsules.

## 8.6. Conclusions & Integration

Collectively, findings in this and previous studies begin to suggest possible mechanisms by which RhoA/ROCK in afferents may contribute to pain from facet joint trauma. Stretch of the innervated facet capsular ligament can activate RhoA/ROCK signaling in DRG neurons (Figure 8.1), potentially via cell-ECM mediated mechanotransduction (Lessey et al. 2012; Marjoram et al. 2014; Zhang et al. 2017d) (Figure 8.2). Restructuring of the ECM is evident in both the human and rat facet capsular ligaments and the NCC system at painful strains (Quinn et al. 2007; Quinn and

Winkelstein 2009; Zhang et al. 2016a; Zhang et al. 2016b). Local forces produced by fiber reorganization (Sander et al. 2009a) can be transmitted through cell adhesion receptors, such as integrins, and regulate the guanine nucleotide exchange factors that are required for activating RhoA (Guilluy et al. 2011; Marjoram et al. 2014). Mechanically activated β1 integrins and RhoA/ROCK may mediate substance P up-regulation in the nociceptors that innervate the facet capsule (Zhang et al. 2017a; Zhang et al. 2017c) (Figures 8.2 & 8.4), as well as substance P release into the spinal cord (Liu et al., 1997; Nörenberg et al., 1999) (Figure 8.5). Since substance P and/or other neurotransmitters from the primary afferents can activate microglia in the spinal cord (Basbaum et al., 2009; Zhu et al., 2014) (Figure 8.6) and both neurotransmitters and mediators released by microglia contribute to hyperexcitability of dorsal horn neurons (Tsuda et al. 2003; Coull et al. 2005; Ulmann et al. 2008; Basbaum et al. 2009), afferent RhoA/ROCK likely mediates central sensitization and pain via increased synaptic transmission and glial activation (Figures 8.3 & 8.7).

The nociceptive role of the RhoA/ROCK pathway has been focused on mostly in neuropathy and inflammation (Inoue et al. 2004; Tatsumi et al. 2005; Mueller et al. 2005; Hang et al. 2013; Paiva-Lima et al. 2014). The work presented in this chapter is the first to identify ROCK as a potent mediator of painful mechanical trauma to an innervated ligament and a potential therapeutic target for joint pain. Although the long-term effects of intra-articular ROCK inhibition on pain relief remain untested, the analgesic effects of inhibiting afferent ROCK in the facet joint might persist since a prior study with this rat model prevented pain for at least seven days by blocking afferent signaling at the time of

facet injury (Crosby et al. 2014). Early Y27632 treatment likely *only* targets RhoA/ROCK activation by mechanotransduction, but intra-articular ROCK inhibition at later times may attenuate pain via mediating the secondary inflammation that occurs and induces nociception following facet joint trauma (Dong et al. 2013b; Kras et al. 2015a). This is particularly encouraging given the effectiveness of ROCK inhibition in mitigating inflammatory pain that has been previously reported (Tatsumi et al. 2005; Paiva-Lima et al. 2014). Although the studies in this and previous chapters are cast in the light of cervical facet capsular ligaments, they may also have implications for more broadly understanding the mechanotransduction processes and for developing therapeutic strategies for pain from mechanical injury of other innervated joint ligaments.

# Chapter 9

# Synthesis & Future Work

## 9.1. Introduction

Ligaments have been traditionally viewed as joint stabilizers with important structural and functional roles. However, they have been increasingly recognized as sensory organs for proprioception and nociception due to their afferent innervation (Schultz et al. 1984; Halata et al. 1985; McLain 1994; Petrie et al. 1997; Petrie et al. 1998; Guanche et al. 1999). Because of their mechanical and neurophysiological properties, ligaments that undergo abnormal loading are also the source of several musculoskeletal disorders, such as chronic pain (Solomonow 2004; Cavanaugh et al. 2006; Winkelstein 2011). The generation of acute pain is normally a protective mechanism that signals the central nervous system of potential or received tissue damage (Woolf and Salter 2000b; Steeds 2009). However, aberrant and/or prolonged nociceptive processing can develop into a chronic neurological disorder (Dubner and Ruda 1992; Markenson 1996; Ita et al. 2017b). As a major clinical, social and economic problem, chronic pain affects over 100 million adults in the United States, with an annual cost exceeding $500 billion (Institute of Medicine 2011). A substantial portion of the general population is affected by chronic neck pain and approximately 50% of the chronic neck pain cases result from trauma (Côté et al. 1998; Côté et al. 2000; Côté et al. 2004; Strine

and Hootman 2007; Hogg-Johnson et al. 2008). The spinal facet joint is a common source of chronic neck pain from abnormal spinal motions, which can injure the innervated capsular ligament that encloses the facet (Siegmund et al. 2001; Cavanaugh et al. 2006; van Eerd et al. 2010; Bogduk 2011; Jaumard et al. 2011). The cervical facet capsule is a prototypical ligament that has important sensory functions and has been demonstrated to be innervated by mechanoreceptors and nociceptors (McLain 1994; Kallakuri et al. 2012).

The involvement of the facet capsular ligament in joint-related neck pain has been extensively implicated by previous biomechanical studies in cadavers and in vivo models (Panjabi et al. 1998a; Pearson et al. 2004; Cavanaugh et al. 2006; Lee et al. 2008; Dong et al. 2012). This ligament can stretch beyond its physiologic range during neck trauma (Panjabi et al. 1998a; Pearson et al. 2004), and the magnitude of its stretch has been shown to modulate neuronal activation patterns and behavioral outcomes (Lu et al. 2005a; Lee and Winkelstein 2009; Dong et al. 2012). Although supraphysiologic stretch of the cervical facet capsule can lead to pain (Lord et al. 1996; Ita et al. 2017b), many patients with facet pain do not have any visible lesions in their capsular ligament (Pettersson et al. 1997; Voyvodic et al. 1997). The lack of visible tissue damage that is observed clinically is consistent with animal studies finding that subfailure capsule stretch, without gross tissue rupture, is sufficient to activate nociceptors and to induce pain (Lu et al. 2005b; Lee and Winkelstein 2009; Quinn et al. 2010b). In addition to the absence of overt, macroscopic facet capsular ligament failure at both non-painful and painful ligament strains, the fact that gross facet capsule failure induces pain that is only

*transient* (Lee et al. 2008) suggests that traditional macro-scale metrics that are often used to describe tissue injury are not useful for specifically predicting the effects of ligament loading on neuronal nociception and/or dysfunction. Despite continued efforts to measure the microstructural mechanics of the facet capsular ligament during stretch (Quinn et al. 2007; Quinn and Winkelstein 2008; Lee and Winkelstein 2012; Ban et al. 2017; Zarei et al. 2017), the complex relationships between the mechanical and nociceptive functions of the facet capsule were not well understood before the work in this thesis, largely due to the lack of cellular assessment in those prior biomechanical studies.

Work reported in this thesis begins to uncover the mechanotransduction processes that can occur in innervated tissue and that lead to neuronal activation and nociception after trauma to the facet. The overall goal of this thesis was to answer two major questions that are important for understanding how tissue deformation relates to pain onset from the facet capsular ligament, and likely other innervated connective tissues as well. The first question involved determining how the mechanical environment of neurons is affected by the interplay between tissue-level mechanics and the organization of the fiber networks. Secondly, work sought to define if, and how, local fiber kinematics affect neuronal activation and nociception. Integrated findings here support the **hypothesis** that subfailure stretch of the cervical facet capsular ligament exceeding its physiologic range alters the local biomechanics of the collagen networks and fibers in that ligament, which directly mediates the responses of the embedded neurons and activates neuronal intracellular pathways via cell-ECM adhesions, leading to pain.

By assessing the local biomechanical changes that accommodate macroscopic tissue loading and modulate neuronal signaling, results in Chapter 3 through Chapter 6 suggest that the spatially heterogeneous fiber organization and deformations that occur during ligament loading likely have micro-scale contributions to neuronal activation in the facet capsule. Furthermore, studies in Chapter 7 and Chapter 8 identify specific signaling molecules that are involved in mechanotransduction, including the adhesion molecule integrin subunit β1 and the intracellular Rho kinase ROCK, that mediate mechanically-induced nociception from the facet joint. In addition to enhancing the mechanistic understanding of mechanotransduction processes in neurons within fibrous connective tissues, this work presents a multi-faceted approach that integrates computational modeling, a cell culture model and whole animal experiments to study the multi-scale interactions between soft tissue mechanics, nociceptive signaling and pain. Although these in silico, in vitro and in vivo models have limitations, the studies in this thesis define the contribution of collagen organization-mediated mechanotransduction to neuronal nociception and dysfunction at painful ligament strains. Of note, other factors, such as the biochemical environment and prior sensitization of neurons and activation of non-neuronal cell populations, can also modulate the heterogeneous responses of neurons to mechanical stimuli, but they were not examined under this thesis.

This chapter summarizes and synthesizes the key findings of this thesis as a whole (Section 9.2) and identifies and discusses areas for future studies based on that work (Section 9.3). The main results of this thesis are discussed in the context of the broader literature related to facet capsular ligament mechanics, neuronal mechanisms of pain and

cellular signaling cascades in mechanotransduction. Possible future directions are suggested along with a discussion of the limitations of the current work, which may inspire new clinically-relevant, basic science hypotheses and/or improvements in the research models used here. Although the mechanotransduction processes investigated in this thesis are cast in the light of cervical facet pain, the findings could be extended to have broader influence on understanding pain from other joint capsules. Further, the image-based computational models and the neuron-collagen construct (NCC) system developed in this thesis have the potential to be extended and applied to other innervated ligaments or fibrous connective tissues from which pain originates.

## 9.2. Summary & Synthesis of Major Findings

The mechanical state of the facet joint is encoded by mechanoreceptors and nociceptors that innervate the facet capsular ligament (McLain 1994; Chen et al. 2006; Kallakuri et al. 2012). Physiologic facet capsule strains (<6%) during normal spinal motions activate only low-threshold mechanoreceptors for proprioception, but not nociceptors for pain sensation (Panjabi et al. 1998; Lu et al. 2005a; Lu et al. 2005b). In contrast, traumatic loading of the cervical spine producing facet capsular strains of approximately 35% can activate high-threshold mechanosenstive nociceptors and induce prolonged afterdischarges in low-threshold receptors, and have been shown to lead to subsequent neuronal dysfunction and pain (Panjabi et al. 1998a; Lu et al. 2005a; Cavanaugh et al. 2006; Dong et al. 2012; Crosby and Winkelstein 2016). Integrated biomechanical and computational studies have shown that the collagenous ECM in the

facet capsular ligament restructures differently at physiologic and supraphysiologic strains (Quinn and Winkelstein 2009; Quinn et al. 2010a; Ban et al. 2017; Zhang et al. 2017c) (Figure 9.1). Image-based assessments of the ECM structure and neuronal protein

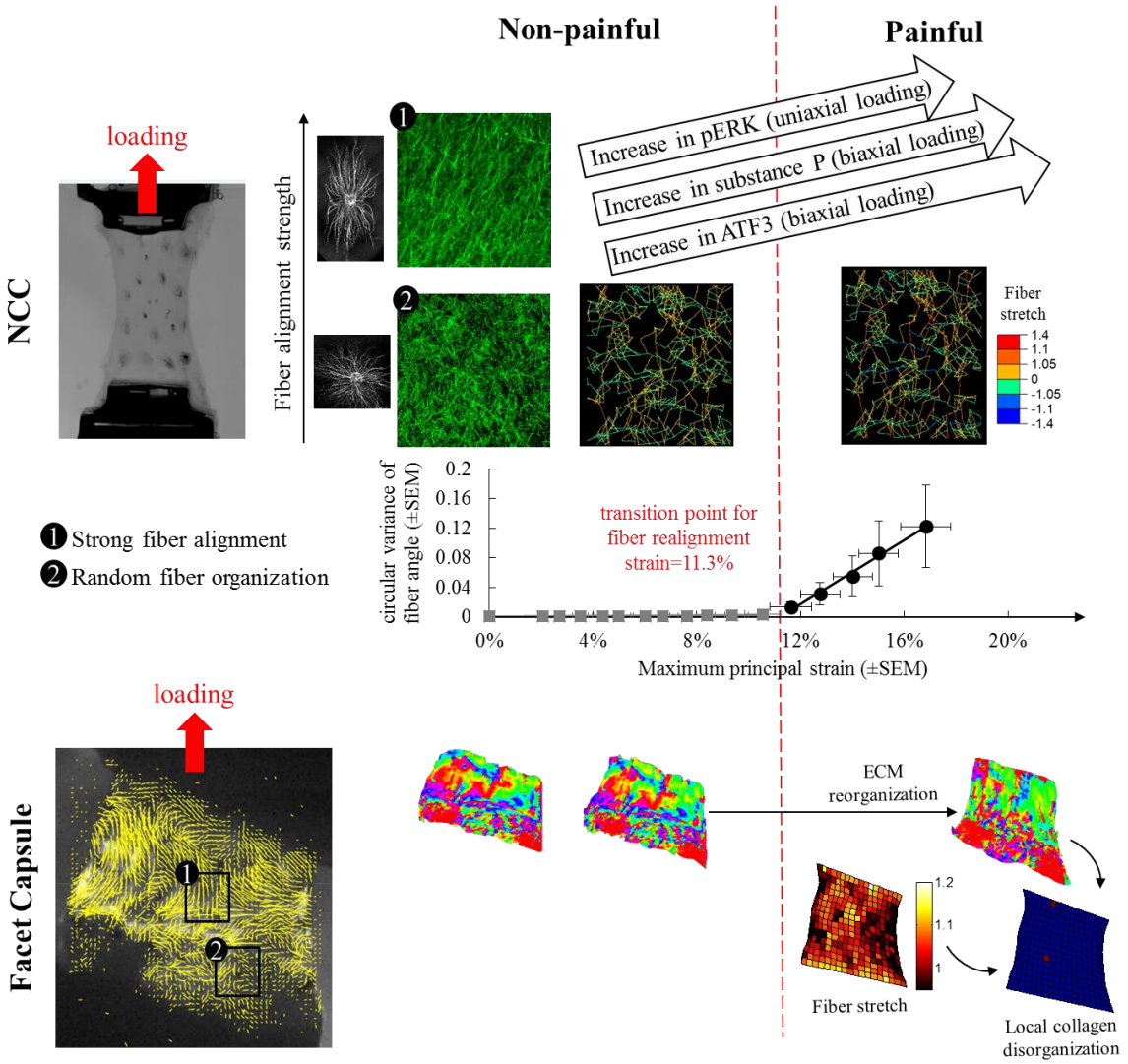


**Figure 9.1.** Different microstructural mechanics during non-painful and painful facet loading are associated with varied neuronal responses to uniaxial stretch. In both the NCC model and isolated human cervical facet capsule, network reorganization, fiber realignment and fiber stretch are observed at painful strains (>11%). At similar macroscopic strains, up-regulation of pERK, ATF3 and substance P are evident in the NCC system, and they increase with greater initial fiber alignment (anisotropy) in the NCCs during uniaxial or biaxial loading.

expression at different macroscopic strains suggest that distinct collagen organization and fiber kinematics are associated with differential afferent responses to stretch (Quinn et al. 2007; Lee and Winkelstein 2009; Sander et al. 2009a; Dong et al. 2012; Zhang et al. 2016b; Zhang et al. 2017b) (Figure 9.1). Afferent activation, nociceptive signaling and injury responses are critical in mediating central sensitization and pain (Lee et al. 2008; Steeds 2009; Basbaum et al. 2009; Crosby et al. 2014) (Figures 8.3 & 8.7).

During non-painful physiologic capsule stretch, the reorganization of collagen networks in the cervical facet capsular ligament is not evident (Quinn et al. 2007; Zhang et al. 2017c) (Figure 9.1). The applied macroscopic deformation in those cases may be accommodated by collagen fiber bending or uncramping more than fiber realigning or stretching along the loading direction (Liao and Belkoff 1999; Sacks 2003; Franchi et al. 2010; Miller et al. 2012a). Minimal changes in the collagen architecture at small ligament strains correspond to the initial compliant mechanical responses reported for the facet capsule during uniaxial tensile testing (Quinn and Winkelstein 2008; Quinn et al. 2010a). The low macroscopic tissue forces may be due to small fiber elongation and low local stresses in a large number of fibers that have not been reoriented to be along the direction of loading (Nair et al. 2014; Zhang et al. 2016b). However, afferents innervating the facet capsule can still be loaded by non-painful strains due to the collagen fiber motions and deformation of the surrounding ECM, but at levels below the threshold for activating the mechanosensing molecules on nociceptors, like integrins and/or ion channels (Dina et al. 2005; Raoux et al. 2007; Delmas et al. 2011). Accordingly, nociceptors are not responsive to small facet capsule strains and exhibit similar neuropeptide expression as

compared to unloaded neurons and no glutamatergic changes (Lu et al. 2005b; Dong et al. 2012; Zhang et al. 2017d) (Figures 4.11 & 8.2). The absence of nociceptive responses in afferents leads to the absence of spinal neuronal plasticity or pain (Lee and Winkelstein 2009; Quinn et al. 2010b; Dong et al. 2012).

More robust structural remodeling of the ECM is produced in the cervical facet capsular ligament by strains that induce pain than by those that do not (Lu et al. 2005a; Quinn et al. 2007; Quinn and Winkelstein 2009; Dong et al. 2012; Ban et al. 2017; Zhang et al. 2017c) (Figure 9.1). The "transition strain" in collagen networks from minimal to evident fiber realignment towards the uniaxial stretch direction is comparable to those thresholds for strain hardening (a rapid increase in force with small deformation) and rapid neuronal ERK phosphorylation in similar collagen matrices (Roeder et al. 2002; Zhang et al. 2016b). Similar biphasic responses of the ECM mechanics and neuronal ERK phosphorylation suggest possible associations between fiber orientation, tissue stress and neuronal activation (Figure 9.1). As collagen fibers become aligned towards the loading direction at large macroscopic strains, greater fiber-level stretches are produced (Zhang et al. 2016b) (Figure 9.1). Larger fiber strains can lead to higher fiber forces and contribute to the overall increases in stress in the ECM at painful strains (Quinn and Winkelstein 2008; Sander et al. 2009a; Nair et al. 2014; Zhang et al. 2016b; Zhang et al. 2017b). Parallel collagen fiber alignment in the loading direction and the associated high force in the ECM increase the extent of neuronal ERK activation after supraphysiologic stretch as compared to that in networks with random collagen organization (Zhang et al. 2017b) (Figure 9.1). In addition to ERK-mediated neuronal

plasticity (Ji et al. 1999; Dina et al. 2005; Gao and Ji 2009), nociceptive neurotransmitter expression and the degree of axonal injury can also be regulated by collagen organization in response to tissue stretch (Figures 3.7 & 3.8), further supporting the association between fiber alignment and neuronal nociception and dysfunction.

Even for relatively simple uniaxial stretch of isotropic networks, ECM restructuring and deformation is heterogeneous at the fiber level, presenting a range of tensile and compressive fiber forces that may present differential mechanical inputs to the neurons that adhere to the collagen fibers (Sander et al. 2009a; Zhang et al. 2016b) (Figure 9.1). The collagen structure in the human cervical facet capsule is highly non-uniform; it contains sub-regions with parallel collagen bundles and those with irregularly organized fibers, which collectively form wavy patterns that accommodate capsular deformations under complex spinal motions (Siegmund et al. 2000; Quinn and Winkelstein 2008; Kallakuri et al. 2012; Ban et al. 2017; Zhang et al. 2017c) (Figure 9.1). That non-homogeneous collagen architecture likely presents a complex array of orientation-dependent mechanical stimuli to the embedded neurons during supraphysiologic stretch. In fact, at high capsule strains, the human facet capsular ligament exhibits spatially heterogeneous reorganization; one or a few sub-regions show substantial network-level restructuring and develop localized collagen disorganization that are absent in the majority of the tissue (Quinn and Winkelstein 2009; Zhang et al. 2016a; Zhang et al. 2017c) (Figure 9.1). Excessive fiber realignment that occurs at painful strains may involve a host of local mechanical changes, including high stretch of fibers close to, or beyond, their failure threshold and stress redistribution in collagen

networks due to failure of load-bearing fibers (Liao and Belkoff 1999; Quinn and Winkelstein 2009; Zhang et al. 2017c). That microstructural ECM damage at supraphysiologic strains may suddenly alter the fiber force that is exerted on neurons via collagen-binding receptors and lead to pain-related neuronal signaling even without overt macroscopic failure in the facet capsule (Zhang et al. 2016b; Zhang et al. 2017d). Therefore, the variation and/or transition between local collagen organization is a possible mechanism by which pain may develop from facet joints in whiplash patients, even in those with no apparent lesion to the capsule (Pettersson et al. 1997; Voyvodic et al. 1997; Kwan and Fiel 2002).

Local forces produced by fiber reorganization (Sander et al. 2009a; Zhang et al. 2016b) in the painful loading regime could form stress concentrations at the site of neuron-ECM adhesions and be translated in to intracellular nociceptive signals via cellular mechanotransduction (Cullen et al. 2007a; Guilluy et al. 2011; Hemphill et al. 2011; Ross et al. 2013). The integrins are important adhesion molecules, some of which have dual roles in force transmission and nociception (Dina et al. 2004; Ross et al. 2013; Ferrari and Levine 2015; Zhang et al. 2017a; Zhang et al. 2017d). The primary collagen-binding integrin, the α2β1 integrin (Jokinen et al. 2004), is found at the peripheral terminal of afferents (Khalsa et al. 2000) and DRG neurons that innervate the facet joint (Zhang et al. 2017d), and is implicated in modulating the mechanosensitivity and nociceptive responses of afferents to tissue stretch (Khalsa et al. 2004; Zhang et al. 2017d). Integrins may mediate mechanically-induced neuronal dysfunction and pain via the downstream RhoA/ROCK pathway (Guilluy et al. 2011; Hemphill et al. 2011; Lessey

et al. 2012; Zhang et al. 2017d) (Figures 8.2 & 9.2). Forces transmitted through integrins can regulate the guanine nucleotide exchange factors that are required for activating RhoA (Guilluy et al. 2011; Marjoram et al. 2014). Activated RhoA/ROCK, via cytoskeletal regulation, can activate intracellular ERK signaling and facilitate synaptic transmission (Liu et al. 1997; Nörenberg et al. 1999; González-Forero et al. 2012; Hirata et al. 2017) (Figures 8.2, 8.4, 8.5 & 9.2). Both the activation of the ERK pathway and regulation of neurotransmitters are important processes involved in integrin-mediated nociception (Dina et al. 2005; Zhang et al. 2017d).

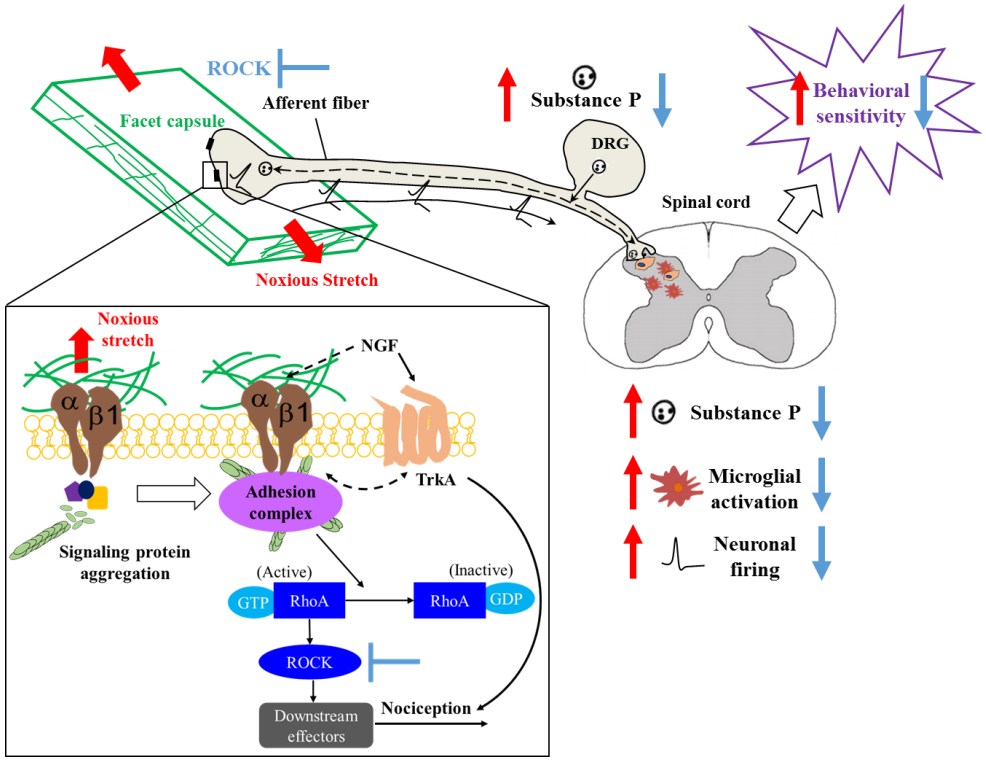


**Figure 9.2.** Schematic showing possible partial mechanisms involving the RhoA/ROCK pathway that mediate pain from facet capsule stretch. Facet joint distraction (red arrows) activates the β1 integrin-mediated RhoA/ROCK pathway via mechanotransduction and NGF-mediated tissue inflammation, leading to behavioral hypersensitivity. Intra-articular ROCK inhibition (blue arrows) immediately after painful facet capsule stretch prevents pain, reduces substance P in the DRG, and attenuates microglial activation and neuronal hyperexcitability in the spinal cord.

At extreme facet capsule strains, gross ligament failure can occur in sub-regions of the facet capsule that sustain excessive collagen realignment and fiber-level damages due to large fiber stretch (Quinn and Winkelstein 2009; Quinn and Winkelstein 2011; Hadi et al. 2012a; Hadi and Barocas 2013; Zhang et al. 2016a; Zhang et al. 2017c). Tearing of the cervical facet capsule can lead to morphological changes, such as focal swelling, in afferents (Kallakuri et al. 2008) that may be due to axotomy and are similar to those seen in direct injury to the CNS (Maxwell and Graham 1997; Bain et al. 2001; Tang-Schomer et al. 2010). Neuronal dysfunction from traumatic loading of the ECM is likely modulated by mechnotransduction mechanisms, including the integrin-mediated RhoA/ROCK signaling, because the severity of neuronal injury depends on the collagen fiber organization, density of cell-ECM adhesion and the activity of ROCK (Cullen et al. 2007a; Hemphill et al. 2011) (Figure 3.8). However, cervical facet capsule loading to failure that could damage afferents and disrupt axonal transport (Kallakuri et al. 2008; Tang-Schomer et al. 2010) induces only transient pain (Lee et al. 2008), likely owing to interrupted afferent signaling. These findings together suggest the magnitude of capsule strain regulates the afferent dysfunction, which plays a critical role in pain initiation from injured joints.

Persistent spinal modifications and behavioral hypersensitivity in response to painful stretch of the facet capsular ligament require afferent activity and neurotransmitter-mediated synaptic transmission between the peripheral afferents and the dorsal horn neurons (Crosby et al. 2013; Kras et al. 2015b; Weisshaar et al. 2017). Activation of nociceptors at the peripheral terminal triggers a complex cascade of

electrophysiological and biochemical events that convey the nociceptive messages from the periphery to the higher order pathways in the spinal cord and the brain (Steeds 2009; Basbaum et al. 2009; Woolf 2011) (Figure 9.2). The rapid activation of the RhoA/ROCK pathway in afferents that occurs after supraphysiologic facet capsule stretch has been shown here to contribute to central sensitization and pain onset (Figures 8.3 & 8.7), likely through increased nociceptive signaling in afferents and also spinal microglial activation (Figures 8.4-8.6 & 9.2). Both afferent neurons and spinal glia can release neurotransmitters and/or inflammatory mediators that sensitize dorsal horn neurons, leading to heightened spinal neuronal excitability and nociceptive transmission to the brain (Henry 1993; Khasabov et al. 2002; Ulmann et al. 2008; Basbaum et al. 2009; Domercq et al. 2013; Dong et al. 2013a).

Painful facet capsule stretch induces not only primary mechanical insults but also secondary inflammation in the affected peripheral tissues, such as NGF- and $PGE_2$-mediated cascades (Kras et al. 2013a; Kras et al. 2015a). Both mechanical and chemical stimuli can activate both integrin and RhoA/ROCK signaling in afferents (Dina et al. 2004; Malik-Hall et al. 2005; Tatsumi et al. 2005; Paiva-Lima et al. 2014; Zhang et al. 2017d) (Figures 8.2 & 9.2). Integrating evidence from this thesis and prior work suggests that the rapid RhoA/ROCK activation that occurs within 30 minutes after painful stretch likely results from the mechanical insult in the facet capsular ligament. Unlike ROCK inhibition in the facet joint preventing pain onset (Figure 8.3), intra-articular administration of the non-steroidal anti-inflammatory drug ketorolac, which targets the $PGE_2$-dependent pathways, immediately after capsule stretch does *not* prevent or

attenuate pain (Dong et al. 2011; Dong et al. 2013b). In addition, a recent pilot study investigated whether NGF-mediated painful joint inflammation activates afferent RhoA in the rat. Behavioral sensitivity and RhoA activity in the DRG were both measured at one day after intra-articular NGF injection (3μg; Kras et al. 2015b). Increased behavioral sensitivity was found despite RhoA activity being unchanged (Figure 9.3); those findings suggest that intra-articular NGF induces pain via mechanisms that do not involve RhoA/ROCK activation in DRG neurons (Figure 9.2). These pilot findings further support the notion that RhoA/ROCK-mediated nociception shortly after facet capsule stretch (Figures 8.1-8.7, 9.2) may be triggered by mechanical stimuli rather than by early tissue inflammatory cascades.

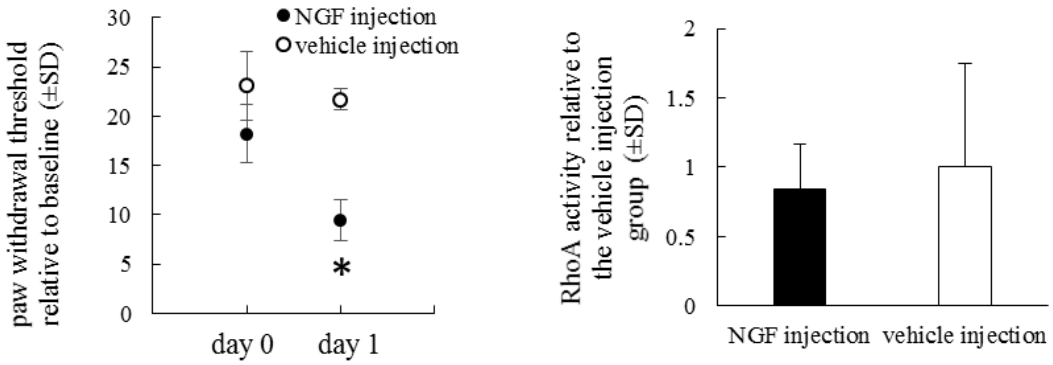


**Figure 9.3.** Intra-articular NGF injection induces behavioral hypersensitivity without altering RhoA activity in the DRG at day one. Although injection of 3μg of rat NGF (n=6 rats) but not PBS vehicle (n=3 rats) into the facet joint, significantly decreases the paw withdrawal threshold at day one (*p=0.002) relative to the baseline level (day 0), no difference in the RhoA activity is found in the DRG at day one.

In contrast, the *maintenance* of facet joint pain may be due to inflammation-mediated changes in the peripheral afferents. At seven days after facet capsule stretch, when pain is still present, the expression of the integrin subunit β1, but not the integrin

subunit α2, is increased in DRG neurons (Zhang et al. 2017d) (Figure 9.4). This finding suggests that β1 integrins other than the specific collagen I-binding α2β1 integrin may have a role in maintaining facet pain. In fact, the integrin subunit β1 in afferents has been shown to mediate inflammatory pain induced by $PGE_2$ and NGF (Dina et al. 2004; Malik-Hall et al. 2005); those inflammatory mediators, in particular, can act on β1 integrins directly (Staniszewska et al. 2008) and/or through intracellular signaling that is triggered by their binding to other cell membrane receptors, like the prostaglandin E2 receptor and Tropomyosin receptor kinase A (TrkA) (Dina et al. 2004; Malik-Hall et al. 2005; Ferrari and Levine 2015). Although targeting the integrin-mediated RhoA/ROCK pathway in afferents is implicated by the work in this thesis and previous studies to attenuate nociception from both mechanical and biochemical stimulation (Dina et al. 2004; Malik-Hall et al. 2005; Tatsumi et al. 2005; Paiva-Lima et al. 2014; Zhang et al. 2017d) (Figures 8.3 & 9.2), different therapeutic strategies are likely needed to prevent

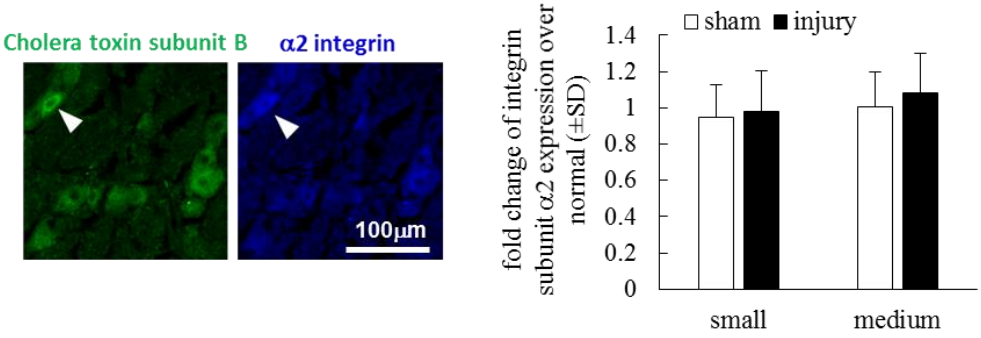


**Figure 9.4.** Expression of the integrin subunit α2 in the rat DRG. Representative images show that some CTb-positive neurons that innervate the facet joint express the integrin subunit α2. Arrow heads point to an afferent neuron with co-localized CTb tracer and the integrin subunit α2. Intensity quantification shows no change in the expression of the integrin subunit α2 in small-diameter or medium-diameter DRG neurons on day seven after a painful facet injury (n=4 rats) as compared to after a sham sugergy (n=5 rats).

and alleviate traumatic facet join pain depending on the type of noxious stimuli that are present temporally.

Findings in this thesis and those from previous studies begin to suggest possible mechanical and signaling events that contribute to mechanically-induced pain from innervated peripheral tissue, like the facet capsular ligament (Figure 9.5). In healthy uninjured ligaments, collagen fibers are relaxed and nociceptors are silent with only brief firing; dorsal horn neurons are not sensitized due to the absence of nociceptive inputs from the primary afferents (Petrenko et al. 2003; Franchi et al. 2010; Jaumard et al. 2011) (Figure 9.5a). During stretch injury that produces painful strains (Figure 9.5b), the ECM in the ligament can undergo substantial network reorganization and excessive fiber stretch (Quinn et al. 2007; Quinn and Winkelstein 2009; Zhang et al. 2016a; Zhang et al. 2017c) (Figure 9.5b). Fiber forces detected by integrins may lead to the assembly of the adhesion machinery, activating the RhoA/ROCK pathway that can modulate synaptic strength via its action on actin filaments (Liu et al. 1997; Nörenberg et al. 1999; González-Forero et al. 2012; Lessey et al. 2012; Marjoram et al. 2014; Humphrey et al. 2014; Zhang et al. 2017a; Zhang et al. 2017d) (Chapter 8). Activated integrins can also interact with the second messenger cascades, like the ERK pathway, which regulate neuronal excitability by modulating the gating properties of ion channels (Bhave and Gereau 2003; Dina et al. 2005; Stamboulian et al. 2010). In addition, ECM deformation can directly activate stretch-activated ion channels and thus increase afferent activity (Lu et al. 2005b; Raoux et al. 2007).

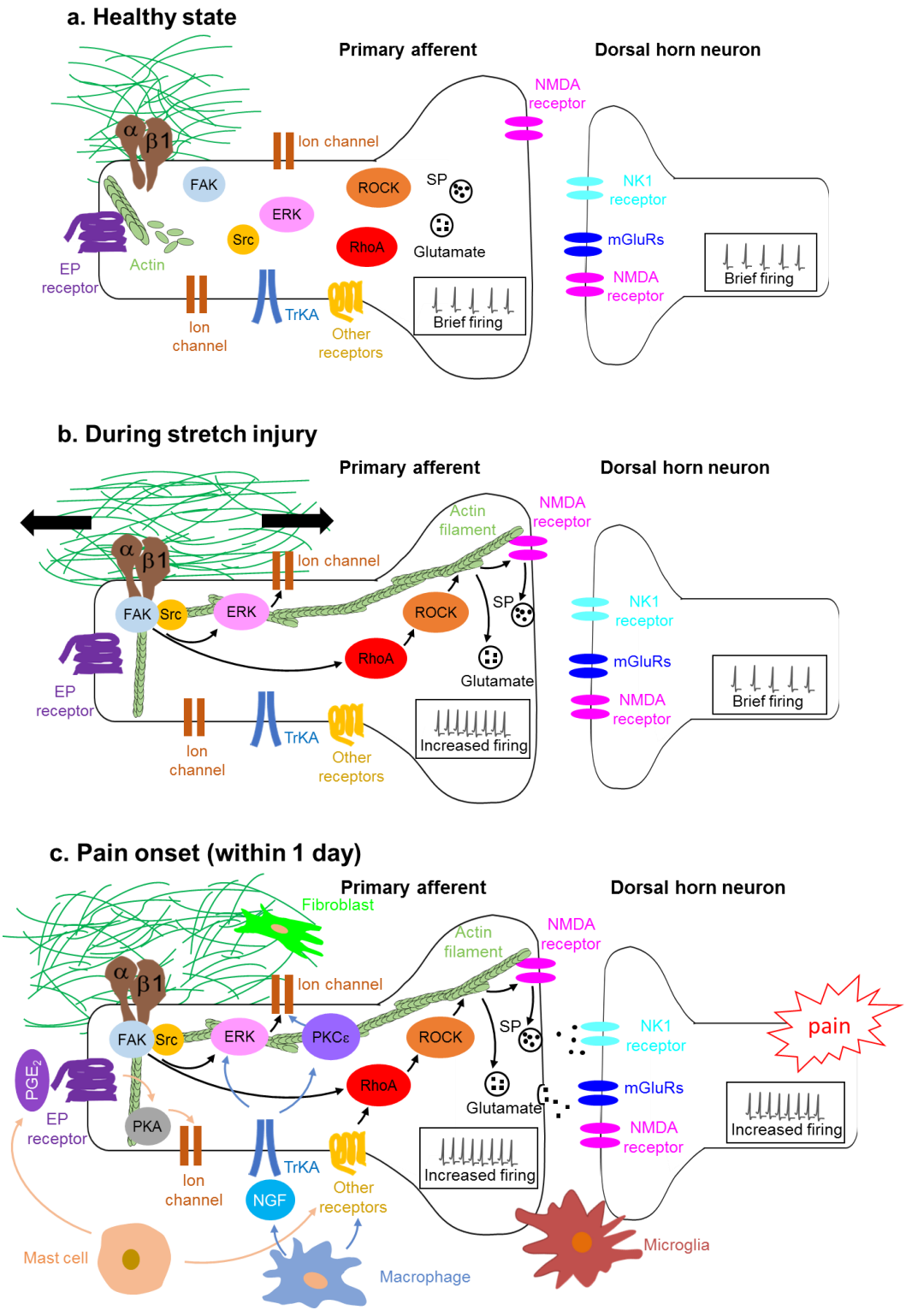


Note: figure continued on next page.

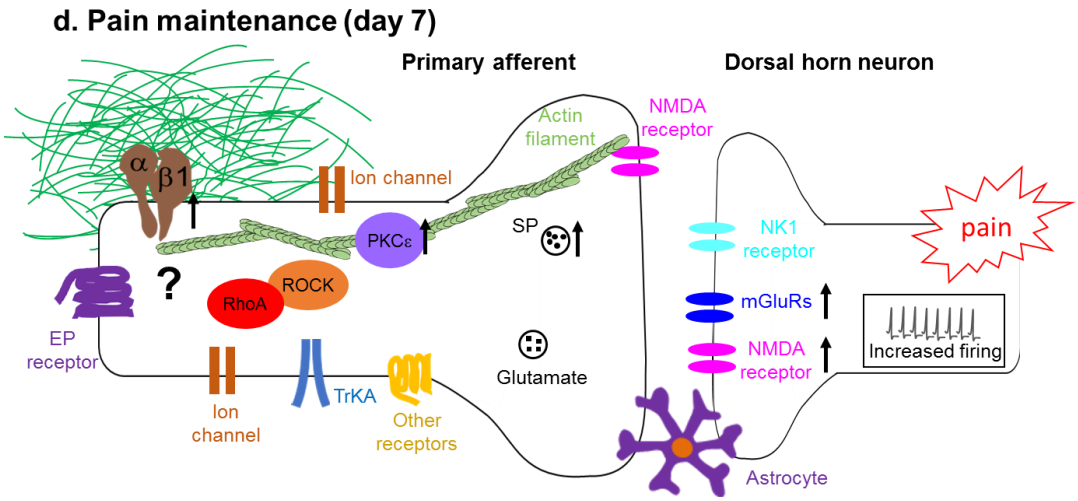


**Figure 9.5.** Schematic showing possible partial mechanisms mediating pain from facet capsule stretch. **(a)** In the healthy uninjured state, fibers in the ECM are relaxed and the neurons exhibit only brief activity. **(b)** During stretch injury, **(c)** at pain onset and **(d)** as pain persists at later times, the ECM can be restructured, damaged and remodeled; an altered mechanical and cellular environment in the ECM may activate afferents by triggering cell receptor-mediated intracellular signaling cascades. Activated afferents can release neurotransmitters to sensitize dorsal horn neurons and activate spinal glia, leading to sustained pain.

Shortly after painful stretch (Figure 9.5c), fibroblasts may remodel the damaged ECM and they can influence neuronal responses via collagen deposition and/or release of matrix metalloproteases (Jaumard et al. 2011; Fujioka et al. 2012a; Lindner et al. 2012; Freedman et al. 2015). Tissue injury may lead to activation and infiltration of macrophages and mast cells; those cells can release inflammatory mediators, like NGF and PGE2, that modulate ion channel activities through protein kinase A (PKA), protein kinase C (PKC) and/or ERK-mediated pathways (Bhave and Gereau 2003; Malik-Hall et al. 2005; Basbaum et al. 2009; Kras et al. 2013a; Ferrari and Levine 2015; Kras et al. 2015b). Immune responses may also lead to the production of biochemical factors that further activate the RhoA/ROCK, contributing to the release of neurotransmitter into the

spinal dorsal horn (Mueller et al. 2005; Paiva-Lima et al. 2014) (Chapter 8). Neurotransmitters, like glutamate and substance P, can act on their post-synaptic receptors and increase the excitability of dorsal horn neurons (Petrenko et al. 2003; Basbaum et al. 2009; Weisshaar and Winkelstein 2014; Crosby et al. 2014). Furthermore, glutamate can activate microglia, which modulates synaptic transmission and neuronal firing (Coull et al. 2005; Ulmann et al. 2008; Domercq et al. 2013) (Chapter 8).

Central sensitization and pain can last for at least seven days after facet joint injury in the rat (Quinn et al. 2010b; Crosby et al. 2014; Ita et al. 2017b). After a painful facet injury (Figure 9.5d), increases in glutamate receptors and astrocyte activation are evident in the spinal dorsal horn (Dong et al. 2012; Crosby et al. 2014; Crosby and Winkelstein 2016). Accompanying spinal cord modifications and pain, the expression of substance P, PKCε and the integrin subunit β1 is increased in DRG neurons (Lee and Winkelstein 2009; Weisshaar et al. 2010; Dong et al. 2012; Zhang et al. 2017d). A collagenous scar can also form after facet capsule injury (Jaumard et al. 2011). Yet, it remains unclear if changes in the ECM environment days after an initial mechanical insult could affect integrin, RhoA/ROCK and/or actin-mediated neuronal responses. Changes in afferent signaling at later times and their contributions to the maintenance of pain require further investigation.

## 9.3. Limitations & Future Work

Findings in this thesis constitute a substantial step towards understanding the multi-scale relationship(s) between the biomechanical and nociceptive responses of the

facet capsular ligaments and their resident afferents. However, there are always several caveats related to experimental and computational models, and those used in this thesis are not without limitations. As such, there are also unanswered questions that must be considered when integrating findings from the work in this thesis. This section highlights several important limitations and discusses areas that require continued efforts to better interpret the findings presented in this thesis.

Although intra-articular ROCK inhibition prevents the onset of pain, the effects of ROCK inhibition at later time points were not evaluated nor was a dose response study performed. RhoA/ROCK in afferents is activated by mechanical stimuli within one day after painful facet capsule injury (Chapter 8); but, it is not known how long that RhoA/ROCK activity remains increased and/or whether that pathway can be re-activated at a later time or to a greater extent by secondary cascades like joint inflammation. Nevertheless, since inhibition of the RhoA/ROCK pathway days after painful neuropathy or inflammatory arthritis has been reported to transiently alleviate pain (Tatsumi et al. 2005; Yoshimi et al. 2010a), it is possible that RhoA/ROCK may have long-term involvement in pain from joint trauma. Additional inhibition studies are needed to study both the time course of RhoA/ROCK activation in this model and to define the temporal effects of a single dose on preventing pain. Of note, the role of ROCK in nociception is still controversial; a lower dose (25μg) of Y27632, the same ROCK inhibitor used in the studies in Chapter 8, was pro-nociceptive (i.e. painful), while a higher dose (500μg) was found to be anti-nociceptive when given to rats with an inflamed paw (Paiva-Lima et al. 2014). Since ROCK inhibition was performed using only the high dose (500μg) in the

studies in this thesis, other doses should be evaluated to determine if RhoA/ROCK has similar dual effects in facet joint pain and to determine if a lower dose is equally effective.

The involvement of integrin in facet pain from capsule stretch is supported by the increased expression of the integrin subunit β1 and reduced substance P expression by its inhibition after stretch (Zhang et al. 2017d). However, the role of integrin subunits other than α2 and β1, including α1, α3 and α5 that are expressed in afferents and mediate inflammatory hyperalgesia (Dina et al. 2004; Dina et al. 2005), is undefined for pain from mechanical facet trauma. Prior work has shown that several α subunits, but *not* the β1 subunit, selectively interact with second messengers in afferents to signal inflammatory pain (Dina et al. 2005). As such, integrin subunits that were not examined in this thesis also may mediate facet joint pain via afferent signaling cascades that are different from those triggered by β1 integrin activation. Investigating the downstream effects of blocking other integrin subunits is needed. Further characterizing integrin expression on the afferent terminals in the facet capsule is needed as well, since the location of integrins on the plasma membrane may be critical for their interaction with the ECM and/or their coupling with membrane receptors for inflammatory mediators (Dina et al. 2005; Ferrari and Levine 2015). Such studies would more fully define the contributions of different integrins in mediating nociception after mechanical facet trauma and potentially uncover new molecular targets for treating facet pain.

Since the integrin subunit β1 is expressed in the majority of substance P-positive afferents (Zhang et al. 2017d) and substance P-producing peptidergic C fibers have been

shown to be important in a variety of painful conditions, including joint pain (Henry 1993; Lee and Winkelstein 2009; Kras et al. 2015b; He et al. 2016), substance P was used as a mediator and marker for pain or nociception in most of the in vivo and in vitro studies in this thesis. However, other types of nociceptors, including Aδ and non-peptidergic C fibers, are also found in the facet capsule and believed to contribute to pain onset from facet trauma (Chen et al. 2006; Weisshaar et al. 2017). Different types of nociceptors not only produce different neurotransmitters, but also synapse with, and sensitize, distinct groups of neurons in the spinal dorsal horn (Braz et al. 2005; Basbaum et al. 2009; Todd 2010). Despite previous evidence for different nociceptor classes engaging in different pain circuits in the CNS (Braz et al. 2005; Todd 2010), it is unknown whether their peripheral terminals respond to micro- and/or macro-scale mechanical stimuli in the facet capsular ligament to the same degree and through similar mechanisms. The expression of the integrin subunit β1 in IB4-positive neurons (Zhang et al. 2017d), which is also required for the development of pain from facet capsular ligament injury (Weisshaar et al. 2017), suggests possible utilization of integrins for nociception in non-peptidergic neurons via substance P-independent mechanisms. As such, additional work is needed to examine if and how different ligament loading affects pain pathways that arise from the Aδ nociceptors and different sub-types of C fibers. That work would more fully define the selectivity of nociceptors in signaling facet pain from its capsule injury and identify more definitively if it is strain magnitude dependent.

Besides only measuring substance P expression as a marker for nociception, the in vitro studies with the NCC system have other limitations, including not measuring the

responses of cells during loading. The simultaneous assessment of the ECM restructuring and neuronal mechanics and activation in real-time is extremely challenging, Yet, knowing how the local network strains and fiber motions deform axons and alter their activity during tissue loading is important to fully define the local mechanisms responsible for mechanosensing of primary afferents in ligaments. Since calcium signaling controls key functions in neurons including synaptic transmission in pain (Petrenko et al. 2003; Grienberger and Konnerth 2012), measuring real-time calcium signals in nociceptor as a marker for their activation would enable the detection of aberrant and/or prolonged nociceptive signaling during ECM reorganization. Measuring neuronal deformation, integrin activation, and calcium signaling together would help to define the mechanical and/or physiological tolerance of neurons at the micro-scale. Additional work developing an experimental system that integrates mechanical loading and measurement with real-time imaging of collagen and neurons during stretch would provide evidence to directly evaluate the relationships between collagen fiber kinematics and neuronal (dys)function.

The loading rate used for studies with the NCCs does not simulate the high-speed loading that is often experienced during facet joint trauma. The strain rates used in the studies reported in Chapter 4 are 1%/s and 7%/s (Zhang et al. 2016b), which are similar to the quasi-static rates that are often used for tensile testing of isolated ligaments (Crisco et al. 2002; Bonner et al. 2015). Although neuronal dysfunction in response to loading has been shown to depend on the strain rate (Singh et al. 2006; Cullen et al. 2007b), no difference in pERK production was found between NCCs tested at these two rates (1% &

7%) (Zhang et al. 2016b). However, the lack of difference may be due to the fact that there is only a seven-fold difference between the two distraction rates tested. Those rates were limited by technical constraints of the mechanical testing device and its inability to reliably impose the relatively small displacement (4mm) at higher rates, as well as challenges of imaging NCCs with much larger dimensions. Although facet capsule strains from comparable quasi-static loading do activate the embedded afferents and induce pain in vivo (Lee et al. 2004a; Lu et al. 2005b; Quinn et al. 2010b), the more severe neuronal injury that occurs more often at high rate loading, like electrophysiological abnormality, morphological impairment and even cell death (Geddes et al. 2003; Hemphill et al. 2011; Cullen et al. 2011), may not be captured at the lower rate of loading. Using the planar biaxial testing device to investigate the stretch-induced nociceptive responses in random and aligned NCCs in the studies presented in Chapter 3 did enable the strain rate to be increased from 7%/s to 23%/s (Zhang et al. 2017b). Nevertheless, even that rate (23%) is much lower than that reported during traumatic joint loading (500%/s) (Panjabi et al. 1998a; Panjabi et al. 1998b; Stemper et al. 2005; Dong et al. 2012; Kras et al. 2013b; Crosby et al. 2013). As such, the neuronal dysfunction that was observed in the NCC system here are expected to be less severe than that which occurs during high-rate facet trauma. More robust neuronal activation, prolonged nociceptive responses and even cell death may be induced by traumatic ligament loading and responsible for persistent facet pain. However, that remains to be tested and is speculative based on the strain rate-dependent neuronal injury responses reported in previous studies (Singh et al. 2006; Cullen et al. 2007a; Cullen et al. 2007b).

Although the NCC system does enable measuring and mapping between neuronal responses and the fiber kinematics and macroscopic strain of their surrounding ECM, the NCC models *are* different from innervated ligaments with regards to neuroanatomy, ECM composition and fiber density of the ECM. The facet capsule is innervated by nerve endings (McLain 1994; Kallakuri et al. 2012), but the NCC system encloses whole DRG neurons including both their somas and axons. As such, it cannot be ruled out that *both* the cell bodies and axons undergo injury during NCC stretch. Loading the entire neuron may increase the injury severity it experiences as compared to stretching *only* the axonal ending. Although the neuronal soma is believed to have a significantly higher threshold for adhesion-mediated mechanical failure than neurites (Hemphill et al. 2011), the in vitro studies with the NCCs system in this thesis may still be overestimating the degree of afferent dysfunction for the given loading condition because the cell bodies are also loaded and exhibit increased pERK expression (Chapter 4). Yet, the inability of the current system to leave the neuronal soma intact during NCC stretch could be overcome by developing new bioreactor systems or ligament-on-a-chip systems, which may have separate compartments and/or unevenly distributed load for neuronal soma and axons (Pfister et al. 2006; Siddique et al. 2014) to better mimic the anatomy of the facet capsular ligament.

The NCCs also use *only* collagen, the major ECM component in ligaments, and ignore the contributions of the other fibrillar and non-fibrillar components that are present in the facet capsule (Yamashita et al. 1996; Jaumard et al. 2011). Since the coupled collagen and elastin responses and non-fibrillar materials have also been shown to affect

tissue mechanics (Jaumard et al. 2011; Lake et al. 2011; Lake et al. 2012; Witzenburg et al. 2017) and RGD-binding integrin activation (Hynes 2002; Midwood and Schwarzbauer 2002), different ECM components likely differentially mediate neuronal responses to loading. Accordingly, studies using neuronal cultures with varied ECM compositions could define the role of different ECM components in mediating mechanically-induced neuronal nociceptive signals and test whether collagen, the major structural component of joint capsules, also dominates the nociceptive function(s) of innervated ligament tissue.

Besides ECM composition, the contribution of fiber density to nociceptor activation remains unknown. The concentration of collagen (2mg/mL) that was used in studies with the NCC system (Zhang et al. 2016b) has been used in previous studies of three-dimensional collagen substrates (Roeder et al. 2002; Chieh et al. 2010) and is suitably strong to undergo mechanical testing. However, that collagen density is *substantially* lower than that of the native ligament (30-40mg/mL) (Miller and Rhodes 1982) and does not currently capture the possible spatial variation that exists in the heterogeneous facet capsule (Yamashita et al. 1996; Kallakuri et al. 2012). Neuronal viability after mechanical loading has been shown to decrease with increasing collagen concentration in the surrounding matrix (Cullen et al. 2007a), likely due to an increased complex modulus of the matrix material and increased load transmission from ECM neurons via adhesion-mediated mechanotransduction. As such, the higher collagen fiber density that is evident in the native ligament may lead to higher neuronal stresses and more robust neuronal activation, nociception or even injury and degeneration that cannot be captured by the NCC model. It is challenging to replicate that high fiber density of

native ligaments in vitro, but computational models do enable investigation of how, and to what extent, different fiber volume fractions alter the local mechanics of individual axons.

Although the finite element-based multi-scale model used in the studies in Chapter 6 was constructed using the geometry and fibrous structure of human cervical facet capsule specimens (Zhang et al. 2017c), that computational model also lacks the accurate incorporation of different fibrillar and non-fibrillar components, primarily due to the limitations with using the QPLI technique (Tower et al. 2002; Quinn 2010; Zhang et al. 2017c). QPLI *only* assesses the orientation of birefringent collagen and provides an *average* measurement *through* the sample thickness (Tower et al. 2002; Quinn 2010). The accuracy of such an image-based computational model may be improved by defining the distribution and density of different fibrillar and non-fibrillar components in the facet capsular ligament using immunohistochemistry, confocal microscopy and other imaging modalities that measure depth-dependent collagenous architecture, like polarization-sensitive optical coherence tomography (Park and de Boer 2008; Claeson et al. 2015, Zarei et al. 2017). The depth-dependent fibrous structure can be simulated using the multi-scale model by meshing the tissue continuum into different layers and incorporating different micro-scale networks in each finite element. By so doing, the multi-scale computational model would more accurately predict the network and fiber stresses and strains at the micro-scale that have been found to affect the mechanotransduction processes of resident neurons (Zhang et al. 2016b; Zhang et al. 2017b).

In addition to the caveats associated with the structure of the fiber networks in the multi-scale model, the absence of certain material behaviors, like fiber failure and tissue viscoelasticity, may also lead to the inaccurate model prediction of regional strains and fiber realignment (Zhang et al. 2017c). For example, the predicted maximum fiber stretch at the onset of anomalous fiber realignment (1.23-1.66) in all samples (Zhang et al. 2017c) exceeds the breaking threshold (6-22%) of collagen fibers that was estimated from other ligaments and tendons (Morgan and Mitton 1960; Liao and Belkoff 1999; Yamamoto et al. 1999). The high fiber strain predicted in the multi-scale model indicates possible fiber failure prior to the development of anomalous collagen realignment. Damage of discrete fibers associated with collagen disorganization could strongly shape the macroscopic failure responses of the tissue (Quinn and Winkelstein 2009; Hadi et al. 2012a), which could lead to a sudden change in force on not only the neurons adhered to the failed fibers but also the other cells remote from the lesion site. Computational models and/or other approaches that incorporate fiber failure responses would enable more accurate prediction of local reorganization and stress redistribution among intact fibers in different sub-regions of a heterogeneous tissue. Better descriptions of the complex mechanical signals that may sensitize neurons during facet capsule stretch would enable more precise evaluation of the possible micro-scale contributions of collagen networks and fibers to transferring forces from and deformations of the ECM to neurons.

Viscoelasticity was also omitted in the computational models used in this thesis and should be considered in any ligament model, because it determines the time-history

dependence of the mechanical properties of soft tissues. High-rate loading, which is relevant in the context of facet capsule injury from neck trauma (Panjabi et al. 1998b; Pearson et al. 2004; Dong et al. 2012), limits the time for a viscoelastic ligament and its nerves to adapt to, and relax in response to, macroscopic tissue deformation (Crisco et al. 2002; Topp and Boyd 2006; De Vita and Slaughter 2006; Laplaca and Prado 2010). Fiber-level relaxation could modulate both the macroscopic viscoelastic behavior (Xu et al. 2013) and rate-dependent changes in the neurons that are adhered to those relaxed fibers. As such, modeling the viscoelastic properties of the collagen-based ECM across length scales is needed to more fully capture the time-dependent mechanical and nociception responses of the facet capsular ligament during its dynamic and other loading scenarios.

Finally, a major limitation of both the multi-scale model and the discrete fiber network model is their lack of neural components. As such, those models are incapable of predicting the effects of tissue-level deformation and micro-scale network reorganization on *neuronal* stresses and strains. The computational models used in this thesis collectively provide a more detailed description of the microscopic mechanics of the facet capsular ligament that are difficult to measure experimentally (Zhang et al. 2017c). However, since they do not measure neuronal strains, they are not able to define the microscopic biomechanical thresholds for neuronal activation and nociception. Incorporating methods to include neurons and to assess their mechanical responses would go a long way in integrating mechanical and cellular information at different length scales from biomechanical, cell culture and animal studies. Such models, if accurate and

properly validated, could be used to predict not only the mechanical abnormalities in ligaments, but also the thresholds for neuronal dysfunction that causes pain.

Although this thesis focuses on understanding the relationships between tissue biomechanics and nociception in ligament pain (Figure 9.5), there are many factors other than the magnitude of tissue strain and the extent of fiber alignment that can contribute to the heterogeneous neuronal responses to ligament stretch. For example, prior exposure of neurons to biochemical sensitizers can alter their nociceptive properties. Such predisposing implications include lowering their response threshold to mechanical stimuli and/or more readily enabling the transition from acute to chronic states. Neither facet capsule stretch at physiologic strains nor a low dose (1μg) of intra-articular NGF induce facet pain (Dong et al. 2012; Sperry et al. 2017). However, exposing joint afferents to that low dose of NGF (less than that used in Figure 9.3) prior to a non-painful facet capsule distraction *does* induce pain that persists for at least seven days (Sperry et al. 2017). That finding suggests that even slightly elevated levels of NGF, for example, that accompany facet joint inflammation may sensitize nociceptors, making them more susceptible to dysfunction upon undergoing subsequent mechanical loading. In addition, a prior history of nociception can convert short-lasting behavioral hypersensitivity induced by the inflammatory mediator $PGE_2$ in to long-term pain (Ferrari and Levine 2015). The short-lasting hyperalgesia induced by $PGE_2$ alone depends on protein kinase A signaling, while $PGE_2$ exposure subsequent to a resolved pain bout can activate an additional protein kinase C-mediated singling cascade in the primed nociceptors that is responsible for their latent hyper-responsiveness (Ferrari and Levine 2015). Given that

finding, supraphysiologic ligament stretch subsequent to a prior painful joint loading or exposure to inflammation are more likely to induce sustained nociceptive signaling and lead to prolonged pain, as compared to the single stretch that was studied in this thesis.

Besides the neuron-ECM interactions that were investigated in this thesis, direct or indirect communication between the activated nociceptors and other neurons and/or non-neuronal cells may also modulate nociceptor responses to mechanical stimuli and contribute to pain (Devor and Wall 1990; Basbaum et al. 2009; Mietto et al. 2015b). Cross-excitation can occur between clustered afferent neurons in the DRG after nerve injury (Devor and Wall 1990), forming a functionally and structurally connected neuronal network. Activity of neurons in such networks are modulated by intrinsic factors, like force and synaptic transmission between affected joint afferents and intact neurons, and by extrinsic factors, such as the biochemical mediators released by non-neuronal cells (Devor and Wall 1990; Julius and Basbaum 2001; Patel et al. 2015). In response to tissue injury, macrophages and glia release a range of inflammatory factors, including cytokines and neurotrophins, that sensitize neurons (Basbaum et al. 2009; Mietto et al. 2015a). Moreover, capsular strains that damage the ECM microstructure can also activate fibroblasts for ECM remodeling and repair (Jaumard et al. 2011; Freedman et al. 2015), which may contribute to neuronal plasticity by ECM deposition and/or secretion of matrix metalloproteinases (Lindner et al. 2012; Fujioka et al. 2012b). Cell-cell interactions in the facet capsular ligament-DRG peripheral system may activate intact afferents and/or hyperexcite the already affected nociceptors (Devor and Wall 1990; Basbaum et al. 2009), increasing the sensory inputs to the spinal cord and contributing to

the development of central sensitization. The responses and involvement of such neuronal networks in facet pain from mechanical injury could be explored by expanding studies using the network analysis tools that were introduced in Chapter 5. Additional efforts examining the non-mechanical signals that are present in the facet joint and its capsular ligament prior to, and after, its mechanical stretch could reveal the further heterogeneity of this complex tissue system and the pathogenesis of other painful conditions.

Overall, the work reported in this thesis did not assess the *integrated* mechanotransduction processes in the facet capsular ligament as a *system* across length and time scales. However, the studies presented here *did* investigate *separately* the relationships between macroscopic strain and each of network-level and fiber-level mechanics (Aim 1), the effects of tissue strain and collagen organization on neuronal activation and dysfunction (Aim 2), and the contributions of molecular mechanotransducers to facet pain (Aim 3). Several mechanical and cellular responses that integrate the tissue, neuron and molecular pathways to form a complete system for mechanosensing and pain were not explicitly measured. For instance, how the restructuring and stressing of local collagen networks, which accommodate tissue-level deformations, distort the neuronal cell membrane and alter the force between collagen fibers and integrin receptors was not measured. Further, it is unknown how neuronal deformation and/or integrin-dependent force transmission trigger downstream intracellular events, including RhoA/ROCK activation, second messenger signaling cascades and subsequent nociceptor firing and synaptic transmission. In addition, the majority of the studies presented in this thesis only assessed the nociceptive changes at

early times (within one day) after the mechanical insult. Although it has been shown that afferent activity within eight hours is critical for the initiation of facet pain (Crosby et al. 2013; Crosby et al. 2014), that pain can persists for at least 21 days after a single capsule stretch (Ita et al. 2017b). As such, understanding how transient mechanotransduction in joint afferents can lead to central sensitization and pain that lasts for weeks is critically important, especially for clinical relevance. The simultaneous assessment of the different ECM, cellular and molecular components in the ligament system over long time scales would provide a more comprehensive biomechanical injury mechanism that lead to chronic joint pain.

## 9.4. Summary

Collectively, the studies presented in this thesis begin to provide a biomechanical and cellular schema for mechanically-induced pain in the innervated, heterogeneous and multi-scale facet capsular ligament (Figure 9.5). The magnitude of macroscopic strains, convolved with the organization and mechanical responses of the fibrous ECM, induces a complex array of mechanical stimuli that differentially modulate the neuronal responses to ligament loading at different locations in the facet capsule. Unlike physiologic strains that do not induce structural changes in the facet capsular ligament, larger pain-producing strains can also induce substantial network reorganization and high fiber deformation in the ligament. Changes in the local mechanical environment of neurons may be transferred to concentrated neuronal loading at cell-ECM adhesion sites and activate intracellular signaling cascades, like the RhoA/ROCK pathway, via integrin-mediated

mechanotransduction. Activated RhoA/ROCK in afferents facilitates the translation of facet capsule strains to nociceptive signals. Blocking that signaling cascade in the mechanically-injured facet joint attenuates spinal inflammation and neuronal hyperexcitability remote from the injury site and prevents pain (Chapter 8). Using integrated experimental and computational approaches, the work in this thesis enhances the basic understanding of the relationship(s) between mechanical and nociceptive functions of the cervical facet capsular ligament. Biomechanical and neuronal mechanisms defined in the studies here have potential clinical impact because they suggest micromechanical metrics that may better predict neuronal dysfunction in the facet capsule than macroscopic joint kinematics and provide novel molecular therapeutic targets for facet pain. Further, since much of the mechanotransductive and nociceptive processes defined in this thesis have direct translation to other innervated joints, these findings could be informative in understanding and treating pain in a host of other joints and associated pathologies that result from mechanical injury.

# APPENDIX A

# MATLAB Code to Generate Collagen Alignment Maps from QPLI Data

This appendix contains three customized MATLAB functions used in the studies throughout this thesis to create fiber alignment maps from polarized light images. The general MATLAB code below was adapted from prior work performed in the lab (Quinn and Winkelstein 2008; Quinn 2010).

Three functions (*initializeQPLI.m, prepsample3.m, analyzesampleIM3.m*) were created as separate MATLAB files to calculate and plot fiber orientations based on polarized light images. The main file that needs to be run by the user contains the function *initializeQPLI.m*, which calls *prepsample3.m*. The function *prepsample3.m* displays a multi-page TIFF file created by the camera that monitors the polarizer rotation. The user must identify the first image in which the line mark on the rotating polarizer is approximately positioned horizontally. In addition, the user needs to digitize the exact polarizer orientation within the frame identified as the first image. Based on the user input, *initializeQPLI.m* then calculates a polarizer orientation for every image. The multi-page TIFF file containing the light intensity information is also loaded into MATLAB via *initializeQPLI.m* and analyzed by calling *analyzesampleIM3.m*. The function *analyzesampleIM3.m* computes the fiber direction and retardation for each pixel

using the harmonic analysis as described previously (Quinn and Winkelstein 2008; Quinn and Winkelstein 2009). Based on the extracted fiber direction and retardation, *initializeQPLI.m* generates a fiber alignment map similar to those maps shown in Chapter 4.

## initializeQPLI.m

```
%% This script was written to generate fiber alignment maps
%% Written by Kyle Quinn
%% Modified by Sijia Zhang in 2013
clear all

% user must modify these values prior to running the program
specID='05mm_s-8mm-6-static'; % text string that is used to identify the proper folder and files
zer=0; % force balance in Newtons corresponding to the true zero Newtons
ypix=800; % y-coordinate in pixels where polarizer in Rotation camera images is at 0 deg

% defines start
imgstart=1;
imginf=imfinfo([specID,'_img.tif']);
clear I
imgend=round(length(imginf)/20)-1;

% define polarizer position during acquisition and ROI at initial positions
disp('please digitize QPLI polarizer position and ROIs...');
[beg angCOR intpROI dc]=prepsample3([specID,'_img.tif'],[specID,'_rot.tif'],ypix,imgstart,imgend)
save PREPDONE

% define ROI for QPLI analysis
intpROI=[min(intpROI(:,1)) min(intpROI(:,2)) max(intpROI(:,3)) max(intpROI(:,4))]


%%
% PLOT FIBER ALIGNMENT MAPS

% sets baseline (DC) intensity of pixels by finding median value in the ROI
clear all
load PREPDONE
h=figure;

ii=1;
intpROI=[min(intpROI(:,1)) min(intpROI(:,2)) max(intpROI(:,3)) max(intpROI(:,4))]
dcim1=imread('dc.tif');
dcim=uint8(dcim1);
dc_crop=dcim(intpROI(2):intpROI(4),intpROI(1):intpROI(3));
dc=double(median(reshape(dc_crop,1,[])));

clear I

SNRs=ones(size(dc_crop,1),size(dc_crop,2),round(1*round(imgend)-1)-1);
inten=zeros(size(dc_crop,1),size(dc_crop,2),round(1*round(imgend)-1)-1);
Rv=ones(size(dc_crop,1),size(dc_crop,2),round(1*round(imgend)-1)-1);
tic
for j=2:round(imgend)-round(imgstart)
    ad=20*j-20;
    clear I
    for i=beg+ad:beg+ad+19
        img=imread([specID,'_img.tif'],i);
```

```
        Io(:,:,i-beg-ad+1)=img(intpROI(2):intpROI(4),intpROI(1):intpROI(3));
        imga=imread([specID,'_img.tif'],i+20);
        Ia(:,:,i-beg-ad+1)=imga(intpROI(2):intpROI(4),intpROI(1):intpROI(3));
        imgb=imread([specID,'_img.tif'],i-20);
        Ib(:,:,i-beg-ad+1)=imgb(intpROI(2):intpROI(4),intpROI(1):intpROI(3));
    end

    I=.25*Ib+.5*Io+.25*Ia;
    %Finds pixel intensities over the course of the polarizer rotation

    jj=j-round(imgstart)+1;
    disp((jj-1)/(round(imgend-imgstart))*100);


    [alphaS deltaS ptp err snr]=analyzesampleIM3(I,0,1,dc,angCOR);

    image(uint8(round(mean(I,3))),'CDataMapping','scaled')
    colormap(gray);

    hold on;
    snrx=snr.^(1-isinf(snr));

    [X,Y] = meshgrid(2:5:size(alphaS,2)-1,2:4:size(alphaS,1)-1);
    clear u v
    for i=1:size(X,1)
        for j=1:size(Y,2)
            alp(i,j)=alphaS(Y(i,j),X(i,j));
            del(i,j)=sin(deltaS(Y(i,j),X(i,j)));
            if snrx(Y(i,j),X(i,j))>2
                u(i,j)=cos(alp(i,j))*del(i,j)*10;
                v(i,j)=sin(alp(i,j))*del(i,j)*10;
            else
                u(i,j)=0;
                v(i,j)=0;
            end
        end
    end

    u=reshape(u,1,[]);
    v=reshape(v,1,[]);
    ind=find((u.^2+v.^2)>.00002);
    X=reshape(X,1,[]);
    Y=reshape(Y,1,[]);

    quiver([X(ind) X(ind) 1],[Y(ind) Y(ind) 1],[u(ind) -u(ind) 1],[-v(ind) v(ind) 1],.5,'r-
','ShowArrowHead','off','LineWidth',.5)
    title((jj-1)/5)
    axis image

   drawnow;
    hold off

end
```

## prepsample3.m

```
function [beg angCOR intpROI dc]=prepsample2(imgfile,rotfile,zpix,imgstart,imgend)

figure;
disp('getinfo')
A=imfinfo(rotfile);
disp('gotinfo')
for i=1:length(A)
rotat=imread(rotfile,i);
image(rotat,'CDataMapping','scaled');
colormap('gray');
title(num2str(i));
axis image;
hold on;
plot([0 size(rotat,2)],[zpix zpix]);
% set(gcf)
k=waitforbuttonpress;
if k==0
   beg=i
   break
end
drawnow;
end

%%

% determine the offset the beg frame has from true zero deg
rotat=imread(rotfile,beg);
rotat2=imread(rotfile,1);
subplot(1,2,1);
image(rotat,'CDataMapping','scaled');
colormap('gray');
hold on;
plot([0 size(rotat2,2)],[zpix zpix]);
title('first click on 0 deg mark, then next tick closest to shaft');
axis image;
subplot(1,2,2);
image(rotat2,'CDataMapping','scaled');
colormap('gray');
axis image;
[x,y] = ginput(2);
ninedegdist=abs(y(1)-y(2));
angCOR=(y(1)-zpix)/ninedegdist*pi/20-.08482;% -((rottrig-imgtrig)/1000*4500+4.0275)/180*pi;

%%
% find the appropriate area of interest
iww=1;
clear rotat rotat2
for iw=round(20*imgstart):200:round(20*imgend);
   rotat(:,:,iww)=imread(imgfile,iw);
   iww=iww+1;
end
```

```
rotat2=mean(rotat,3);

% rotat=imread(imgfile,round(20*imgstart));
image(rotat2,'CDataMapping','scaled');
colormap('gray');
axis image;


k = waitforbuttonpress;
point1 = get(gca,'CurrentPoint');    % button down detected
finalRect = rbbox;                   % return figure units
point2 = get(gca,'CurrentPoint');    % button up detected
point1 = point1(1,1:2);              % extract x and y
point2 = point2(1,1:2);
point1=round(point1);
point2=round(point2);
p1 = min(point1,point2);             % calculate locations
offset = abs(point1-point2);         % and dimensions
x = [p1(1) p1(1)+offset(1) p1(1)+offset(1) p1(1) p1(1)];
y = [p1(2) p1(2) p1(2)+offset(2) p1(2)+offset(2) p1(2)];
hold on
axis manual
plot(x,y)
% find the appropriate area of interest
intpROI(1,:)=[point1 point2];

% rotat=imread(imgfile,round(20*imgend));
image(rotat2,'CDataMapping','scaled');
colormap('gray');
axis image;
k = waitforbuttonpress;
point1 = get(gca,'CurrentPoint');    % button down detected
finalRect = rbbox;                   % return figure units
point2 = get(gca,'CurrentPoint');    % button up detected
point1 = point1(1,1:2);              % extract x and y
point2 = point2(1,1:2);
point1=round(point1);
point2=round(point2);
p1 = min(point1,point2);             % calculate locations
offset = abs(point1-point2);         % and dimensions
x = [p1(1) p1(1)+offset(1) p1(1)+offset(1) p1(1) p1(1)];
y = [p1(2) p1(2) p1(2)+offset(2) p1(2)+offset(2) p1(2)];
hold on
axis manual
plot(x,y)
intpROI(2,:)=[point1 point2];

%%
% find dc shift

dc=0;
```

## analyzesampleIM3.m

```
function [alphaS deltaS ptp err snr]=analyzesampleIM3(I2,angP,scale,dc,angCOR)

ang=0:.05*pi:.95*pi;
ang=ang+angCOR;
sumA=0;
sumB=0;
sumC=0;
N=20;
I2=double(I2);
for i=1:N
   sumA=sumA+I2(:,:,i);
   sumB=sumB+I2(:,:,i)*cos(2*(ang(i)+angP));
   sumC=sumC+I2(:,:,i)*sin(2*(ang(i)+angP));
end
A=sumA/N;
B=sumB*2/N;
C=sumC*2/N;

for i=1:N
calcSig(:,:,i)=A+B*cos(2*ang(i))+C*sin(2*ang(i));
end
err=I2-calcSig;

dc=double(dc);
scale=double(scale);
scale=scale*(A-dc-.000001);


ptp=sqrt(B.^2+C.^2);
snr=10*(ptp.^2)./sum(err.^2,3);

B=B./scale;
C=C./scale;
alphaS=.5*atan2(-B,C);
deltaS=acos(sqrt(1-B.^2-C.^2));
```

# APPENDIX B

# Quantification of Alignment of Collagen Fibers & Axons

This appendix summarizes the quantitative measurements of collagen fiber alignment and axon alignment in the random and aligned NCCs, which were used in the studies presented in Chapter 3. Collagen organization data were acquired by QPLI and the circular variance of the extracted fiber angles was calculated. A higher circular variance indicates a lower degree of alignment. Axonal outgrowth was visualized using fluorescent labeling and confocal microscopy; the anisotropy in axon alignment was quantified as the ratio of the minor axis of alignment to the major axis of alignment by performing image analysis using a Fourier transform method (Sander and Barocas 2009; Susilo et al. 2015). A lower minor-to-major-axis ratio indicates a higher degree of axon alignment. Table B.1 details the circular variance that characterizes the variation in collagen fiber orientation angles collected from the entire area of each unloaded control NCC. Table B.2 details the minor-to-major-axis ratio of axon alignment in one confocal tile scan from each unloaded control NCC.

**Table B.1. Circular variance of collagen fiber alignment angles in NCC samples.**

| Sample | Group | Circular variance |
|---|---|---|
| 1 | random NCC | 0.0060 |
| 2 | random NCC | 0.0027 |
| 3 | random NCC | 0.0035 |
| 4 | random NCC | 0.0051 |
| 5 | random NCC | 0.0039 |
| 6 | random NCC | 0.0017 |
| 7 | random NCC | 0.0039 |
| 8 | random NCC | 0.0075 |
| 9 | aligned NCC | 0.0022 |
| 10 | aligned NCC | 0.0008 |
| 11 | aligned NCC | 0.0008 |
| 12 | aligned NCC | 0.0035 |
| 13 | aligned NCC | 0.0025 |
| 14 | aligned NCC | 0.0012 |
| 15 | aligned NCC | 0.0018 |
| 16 | aligned NCC | 0.0037 |
| 17 | aligned NCC | 0.0034 |

**Table B.2. Minor-to-major-axis ratio of axon alignment in NCC samples.**

| Sample | Group | Minor-to-major-axis ratio |
|---|---|---|
| 1 | random NCC | 0.820 |
| 2 | random NCC | 0.820 |
| 3 | random NCC | 0.614 |
| 4 | random NCC | 0.857 |
| 5 | random NCC | 0.886 |
| 6 | random NCC | 0.763 |
| 7 | random NCC | 0.535 |
| 8 | random NCC | 0.713 |
| 9 | aligned NCC | 0.250 |
| 10 | aligned NCC | 0.214 |
| 11 | aligned NCC | 0.261 |
| 12 | aligned NCC | 0.695 |
| 13 | aligned NCC | 0.224 |
| 14 | aligned NCC | 0.555 |
| 15 | aligned NCC | 0.642 |
| 16 | aligned NCC | 0.293 |
| 17 | aligned NCC | 0.370 |

# APPENDIX C

# Stretch-Induced Protein Expression in Neuron-Collagen Constructs

This appendix summarizes the quantification of immunolabeled proteins in the NCCs used in the studies throughout this thesis. The corresponding maximum principal strain (MPS) for each NCC listed in this appendix is provided in either the chapter containing the work or in the following Appendix F. In each table and figure, the quantified protein expression and raw images are identified by the study group, gel number and corresponding region of interest (ROI) number or DRG number.

Table C.1 details the quantification of axonal substance P (SP) and phosphorylated ERK (pERK) expression at day 1 after uniaxial stretch of random and aligned NCCs in the studies presented in Chapter 3. The expression of SP and pERK is normalized to the mean level in their respective unloaded controls, whose protein expression is also included in Table C.1. The corresponding images, with SP, pERK and βIII-tubulin (for neuronal structure) co-labeled, are included in Figure C.1. Similarly, Table C.2 summarizes the quantification of normalized SP and pERK expression at day 1 in unstretched and biaxially stretched NCCs having either random or aligned collagen organization, which were also used in the studies included in Chapter 3. The corresponding images are shown in Figure C.2. In the studies presented in Chapter 3,

immunolabeling of activating transcription factor 3 (ATF3) was also quantified in ROIs taken from each strain element. Figure C.3 summarizes the strain maps of each biaxially stretched NCC with quantification of its ATF3 expression overlaid on each corresponding strain element. Since unloaded control NCCs do not have associated strain maps, their ATF3 expression is listed in Table C.3. Immunofluorescence images showing ATF3 expression in loaded and unloaded NCCs with varied fiber alignment are itemized in Figure C.4.

The quantification of the pERK expression from the studies presented in Chapter 4 is summarized in Table C.4 and Table C.5, with corresponding images shown in Figures C.5 and C.6. Two types of NCCs were used: cortical-collagen constructs and DRG-collagen constructs. The cortical-collagen constructs underwent uniaxial stretch in one of the following loading conditions: 0.5mm/s to 4mm (n=8), 3.5mm/s to 8mm (n=7), 0.5mm/s to 8mm (n=9) and 3.5mm/s to 8mm (n=9). Immunolabeling of pERK in each cortical-collagen gel was quantified by densitometry using a custom MATLAB code that is provided in Appendix D; protein expression was quantified as the fraction of positively-labeled pixels in each image (30 images/NCC) and normalized to the unloaded control level. Normalized pERK in cortical-collagen gels is summarized in Table C.4 and the corresponding images are shown in Figure C.5. Due to an unequal number of samples in each loading group, some sections of Table C.4 do not have data and are indicated by a dash (–). Table C.5 details the normalized pERK expression measured in the DRG-collagen gels that underwent stretch to 4mm or 8mm at 0.5mm/s. Immunolabeling of

pERK was quantified by measuring the intensity/unit area in the cell bodies and axons of each DRG. Corresponding images are summarized in Figure C.6.

Table C.6 details the ratio of phosphorylated focal adhesion kinase (pFAK) to the total amount of FAK in the axons of each unloaded NCC with and without the β1 inhibitor RGD peptide, as described in Chapter 7. Figure C.7 compiles the corresponding images that show the co-labeled pFAK and FAK. Table C.7 details the quantification of axonal SP expression at day 1 in the associated DRGs of unstretched and stretched NCCs, with and without RGD treatment. The expression of SP is normalized to the average level in unloaded untreated controls. The corresponding images are summarized in Figure C.8. In addition, in the studies presented in Chapter 7, the α2β1 integrins that bind to Collagen I were specifically blocked using a small molecule inhibitor TC-I15. Table C.8 summarizes the quantification of axonal SP expression, which was normalized to the unloaded untreated control level, at day 1 in unstretched and stretched NCCs, with and without TC-I15 treatment. Figure C.9 shows the corresponding immunofluorescence images of SP.

Lastly, SP expression in NCCs in the ROCK inhibition (inhibitor Y27632) studies presented in Chapter 8 is summarized in Table C.9 and Figure C.10. Table C.9 details the quantification of axonal SP expression, normalized to the unloaded untreated control level, at day 1 in unstretched and stretched NCCs, with and without Y27632 treatment. Figure C.10 shows the corresponding images.

**Table C.1. Quantification of SP & pERK expression normalized to respective unloaded controls at day 1 in unstretched & uniaxially stretched NCCs with random or aligned collagen organization (Chapter 3).**

| Random NCCs | | | | | | | |
|---|---|---|---|---|---|---|---|
| | | ROI 1 | | ROI 2 | | ROI 3 | |
| Group | Gel | SP | pERK | SP | pERK | SP | pERK |
| Unstretched | UC-R1 | 1.34 | 0.95 | 1.20 | 1.13 | 1.15 | 1.09 |
| | UC-R2 | 0.82 | 1.01 | 1.07 | 0.84 | 0.84 | 0.98 |
| | UC-R3 | 0.81 | 0.94 | 0.93 | 1.14 | 0.84 | 0.92 |
| | UC-R4 | 1.85 | 0.71 | 0.36 | 0.74 | 2.90 | 0.31 |
| | UC-R5 | 0.25 | 1.38 | 0.47 | 0.73 | 0.18 | 2.13 |
| | UC-R6 | 1.55 | 0.63 | 1.16 | 0.75 | 1.19 | 1.42 |
| | UC-R7 | 0.80 | 0.68 | 0.57 | 0.93 | 0.73 | 1.58 |
| Stretched | U-R1 | 1.53 | 1.90 | 1.45 | 4.31 | 0.67 | 3.05 |
| | U-R2 | 4.47 | 3.57 | 1.26 | 4.02 | 4.73 | 1.36 |
| | U-R3 | 1.81 | 3.59 | 5.96 | 2.50 | 1.60 | 3.07 |
| | U-R4 | 1.05 | 1.24 | 0.89 | 0.96 | 1.09 | 1.15 |
| | U-R5 | 1.30 | 0.97 | 1.22 | 1.03 | 1.03 | 0.85 |
| | U-R6 | 1.29 | 1.30 | 1.04 | 0.80 | 1.33 | 0.90 |
| | U-R7 | 1.78 | 1.05 | 1.81 | 1.23 | 1.40 | 1.79 |
| | U-R8 | 1.81 | 0.60 | 2.27 | 1.19 | 1.79 | 1.79 |
| **Aligned NCCs** | | | | | | | |
| | | ROI 1 | | ROI 2 | | ROI 3 | |
| Group | Gel | SP | pERK | SP | pERK | SP | pERK |
| Unstretched | UC-A1 | 1.19 | 0.95 | 0.84 | 0.78 | 0.83 | 1.00 |
| | UC-A2 | 1.09 | 1.08 | 1.01 | 1.04 | 1.04 | 1.14 |
| | UC-A3 | 0.90 | 1.51 | 0.81 | 1.88 | 0.49 | 0.90 |
| | UC-A4 | 0.86 | 0.23 | 1.65 | 0.28 | 0.62 | 0.93 |
| | UC-A5 | 1.05 | 0.13 | 1.57 | 1.59 | 1.06 | 1.55 |
| | UC-A6 | 1.55 | 1.48 | 1.25 | 0.42 | 0.49 | 1.90 |
| | UC-A7 | 0.72 | 0.79 | 1.15 | 1.18 | 0.84 | 0.23 |
| Stretched | U-A1 | 2.81 | 0.66 | 1.07 | 4.47 | 0.88 | 2.65 |
| | U-A2 | 2.02 | 2.34 | 3.04 | 2.30 | 3.72 | 5.00 |
| | U-A3 | 1.70 | 1.50 | 1.49 | 5.00 | 1.53 | 4.17 |
| | U-A4 | 0.84 | 4.71 | 2.77 | 1.85 | 2.47 | 0.74 |
| | U-A5 | 2.15 | 2.06 | 2.32 | 2.23 | 2.76 | 1.51 |
| | U-A6 | 2.40 | 1.77 | 2.58 | 1.82 | 2.63 | 1.99 |
| | U-A7 | 2.34 | 2.93 | 2.83 | 1.41 | 1.99 | 2.66 |
| | U-A8 | 1.68 | 3.32 | 1.71 | 1.74 | 1.84 | 2.16 |

**Figure C.1. Immunofluoresence images showing the expression of SP (green), pERK (red) & βIII-tubulin (blue) at day 1 in unstretched & uniaxially stretched NCCs with random or aligned collagen organization.**

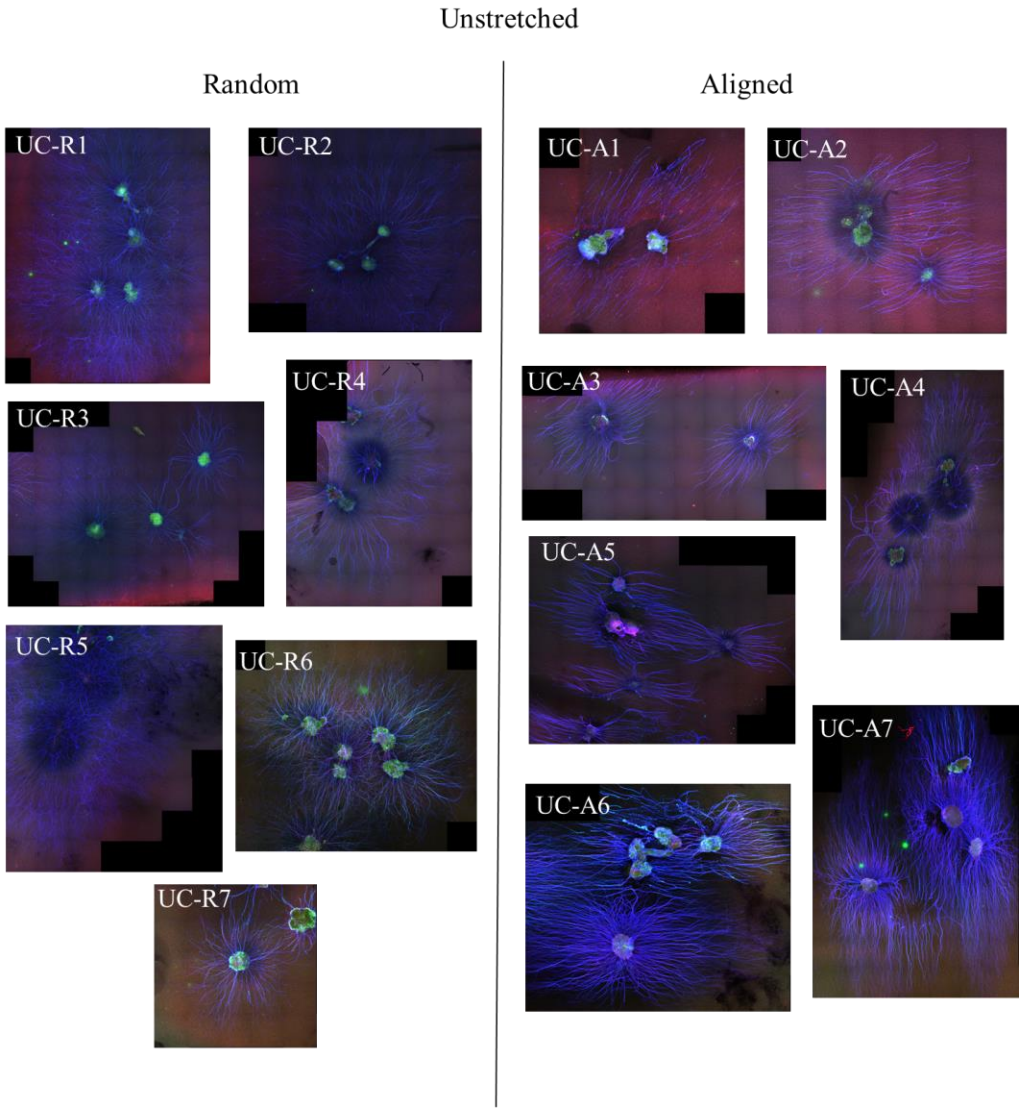


**Note:** Figure is continued on the next page.

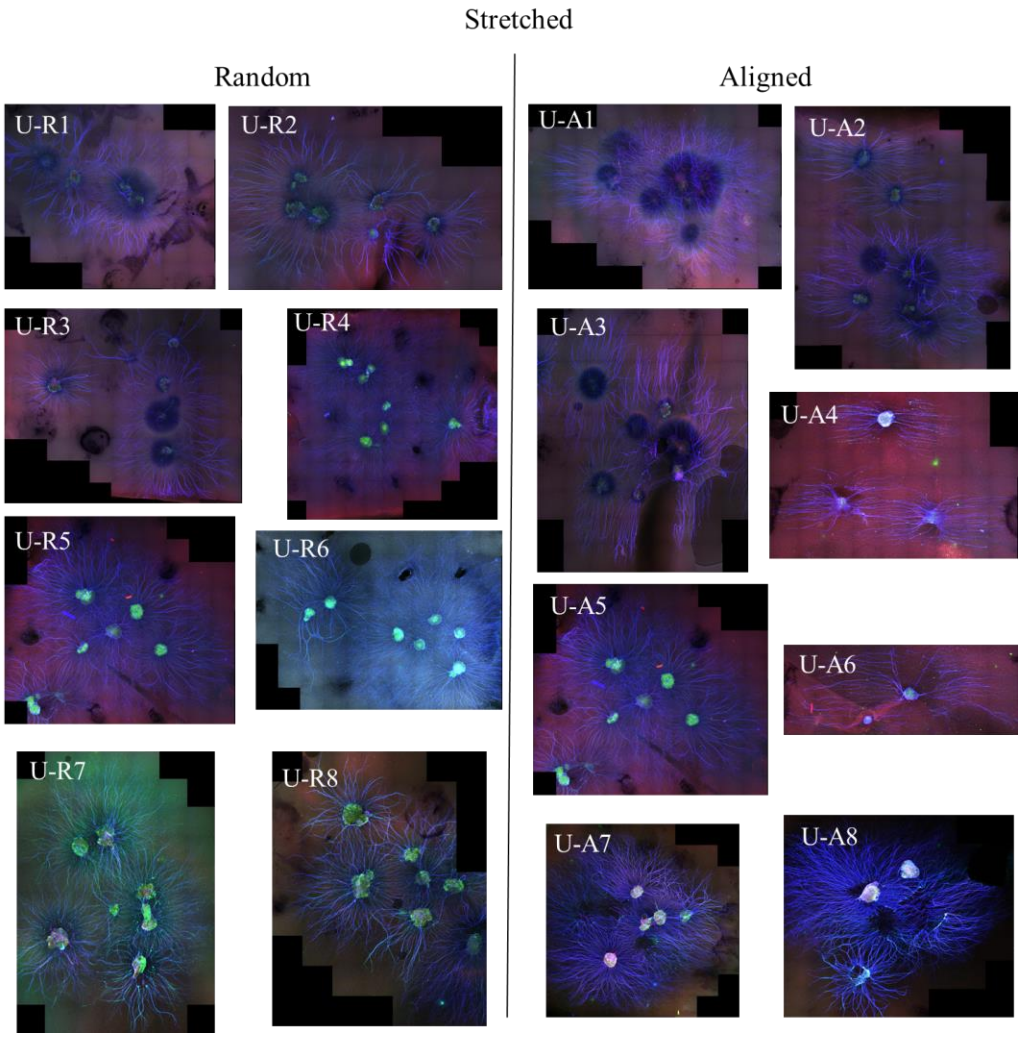
Stretched
Random
Aligned
U-R1
U-R2
U-R3
U-R4
U-R5
U-R6
U-R7
U-R8
U-A1
U-A2
U-A3
U-A4
U-A5
U-A6
U-A7
U-A8

**Table C.2. Quantification of SP & pERK expression normalized to respective unloaded controls at day 1 in unstretched & biaxially stretched NCCs with random or aligned collagen organization (Chapter 3).**

| Random NCCs | | | | | | | |
|---|---|---|---|---|---|---|---|
| | | ROI 1 | | ROI 2 | | ROI 3 | |
| Group | Gel | SP | pERK | SP | pERK | SP | pERK |
| Unstretched | BC-R1 | 1.55 | 0.63 | 1.16 | 0.75 | 1.19 | 1.42 |
| | BC-R2 | 0.80 | 0.68 | 0.57 | 0.93 | 0.73 | 1.58 |
| | BC-R3 | 1.01 | 1.27 | 2.04 | 0.82 | 0.55 | 0.97 |
| | BC-R4 | 0.92 | 1.18 | 1.07 | 0.47 | 0.41 | 1.29 |
| | BC-R5 | 0.69 | 0.51 | 1.72 | 2.19 | 0.59 | 0.30 |
| Stretched | B-R1 | 2.17 | 2.64 | 3.31 | 1.72 | 1.09 | 2.15 |
| | B-R2 | 1.51 | 1.14 | 1.13 | 0.81 | 1.02 | 1.54 |
| | B-R3 | 0.71 | 0.79 | 1.92 | 1.27 | 0.88 | 1.06 |
| | B-R4 | 1.33 | 0.28 | 2.12 | 0.67 | 1.48 | 4.99 |
| | B-R5 | 0.84 | 2.64 | 0.44 | 2.71 | 0.79 | 2.24 |
| | B-R6 | 1.53 | 2.40 | 1.90 | 3.29 | 2.38 | 1.56 |
| | B-R7 | 1.38 | 2.30 | 1.76 | 3.08 | 2.34 | 1.60 |
| | B-R8 | 1.51 | 2.49 | 1.98 | 3.12 | 2.18 | 1.63 |
| **Aligned NCCs** | | | | | | | |
| | | ROI 1 | | ROI 2 | | ROI 3 | |
| Group | Gel | SP | pERK | SP | pERK | SP | pERK |
| Unstretched | BC-A1 | 1.55 | 1.48 | 1.25 | 0.42 | 0.49 | 1.90 |
| | BC-A2 | 0.72 | 0.79 | 1.15 | 1.18 | 0.84 | 0.23 |
| | BC-A3 | 1.08 | 1.09 | 1.49 | 0.95 | 0.80 | 1.08 |
| | BC-A4 | 0.90 | 0.84 | 0.96 | 1.17 | 0.76 | 0.87 |
| | BC-A5 | 0.83 | 0.33 | 0.84 | 1.11 | 1.33 | 1.56 |
| Stretched | B-A1 | 1.55 | 4.15 | 1.42 | 3.51 | 1.18 | 1.89 |
| | B-A2 | 3.39 | 2.39 | 1.98 | 3.05 | 2.93 | 0.77 |
| | B-A3 | 3.29 | 4.14 | 2.91 | 3.62 | 3.28 | 4.87 |
| | B-A4 | 1.82 | 4.55 | 2.77 | 4.90 | 2.56 | 4.15 |
| | B-A5 | 2.81 | 3.33 | 3.69 | 3.23 | 2.19 | 3.23 |
| | B-A6 | 1.19 | 2.05 | 1.60 | 0.61 | 1.82 | 1.22 |
| | B-A7 | 0.70 | 1.80 | 1.72 | 1.46 | 1.46 | 2.92 |
| | B-A8 | 0.97 | 0.99 | 1.18 | 0.46 | 1.40 | 1.66 |

**Figure C.2. Immunofluoresence images showing the expression of SP (green), pERK (red) & βIII-tubulin (blue) at day 1 in unstretched & biaxially stretched NCCs with random or aligned collagen organization.**

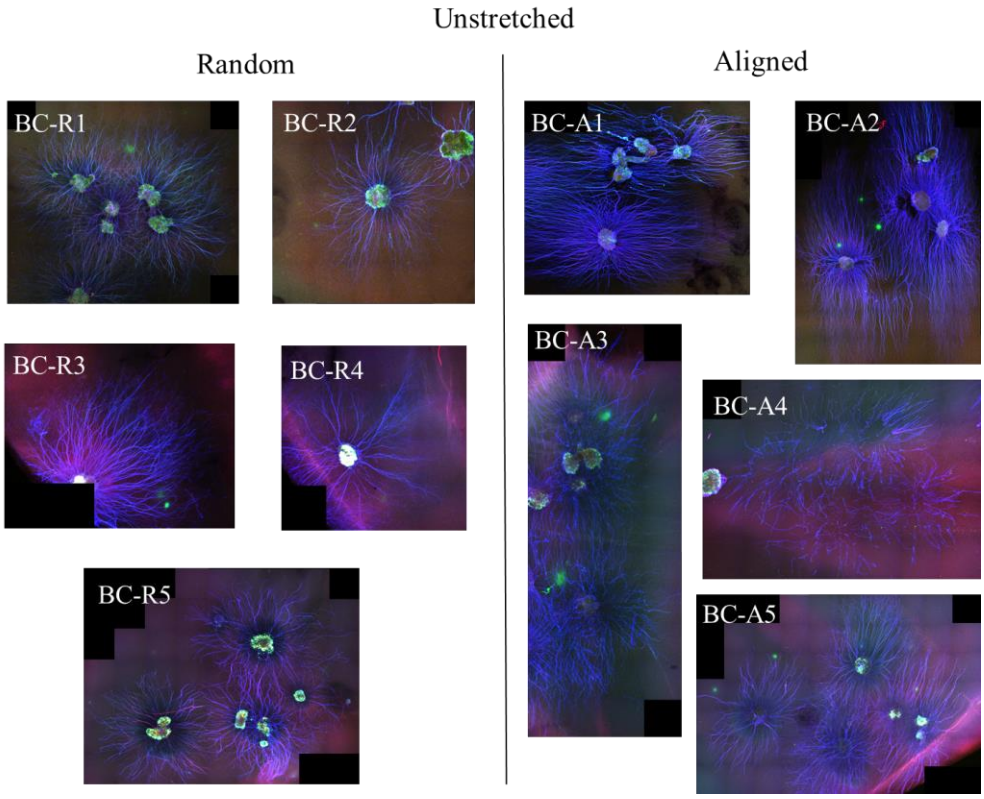


**Note:** Figure is continued on the next page.

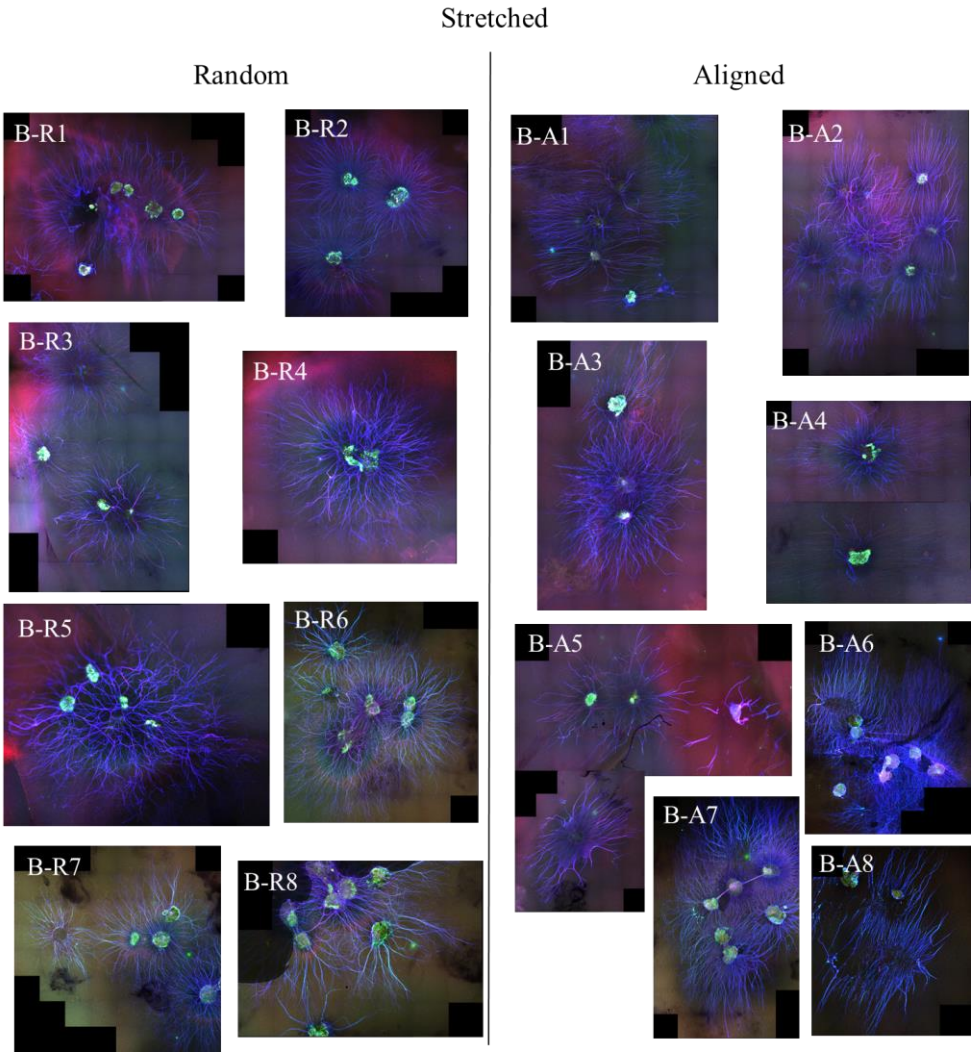
Stretched
Random
Aligned
B-R1
B-R2
B-R3
B-R4
B-R5
B-R6
B-R7
B-R8
B-A1
B-A2
B-A3
B-A4
B-A5
B-A6
B-A7
B-A8

**Figure C.3. Quantification of normalized ATF3 expression over unloaded controls in each strain element at day 1 after NCC stretch, overlaid on the corresponding strain maps (Chapter 3).**

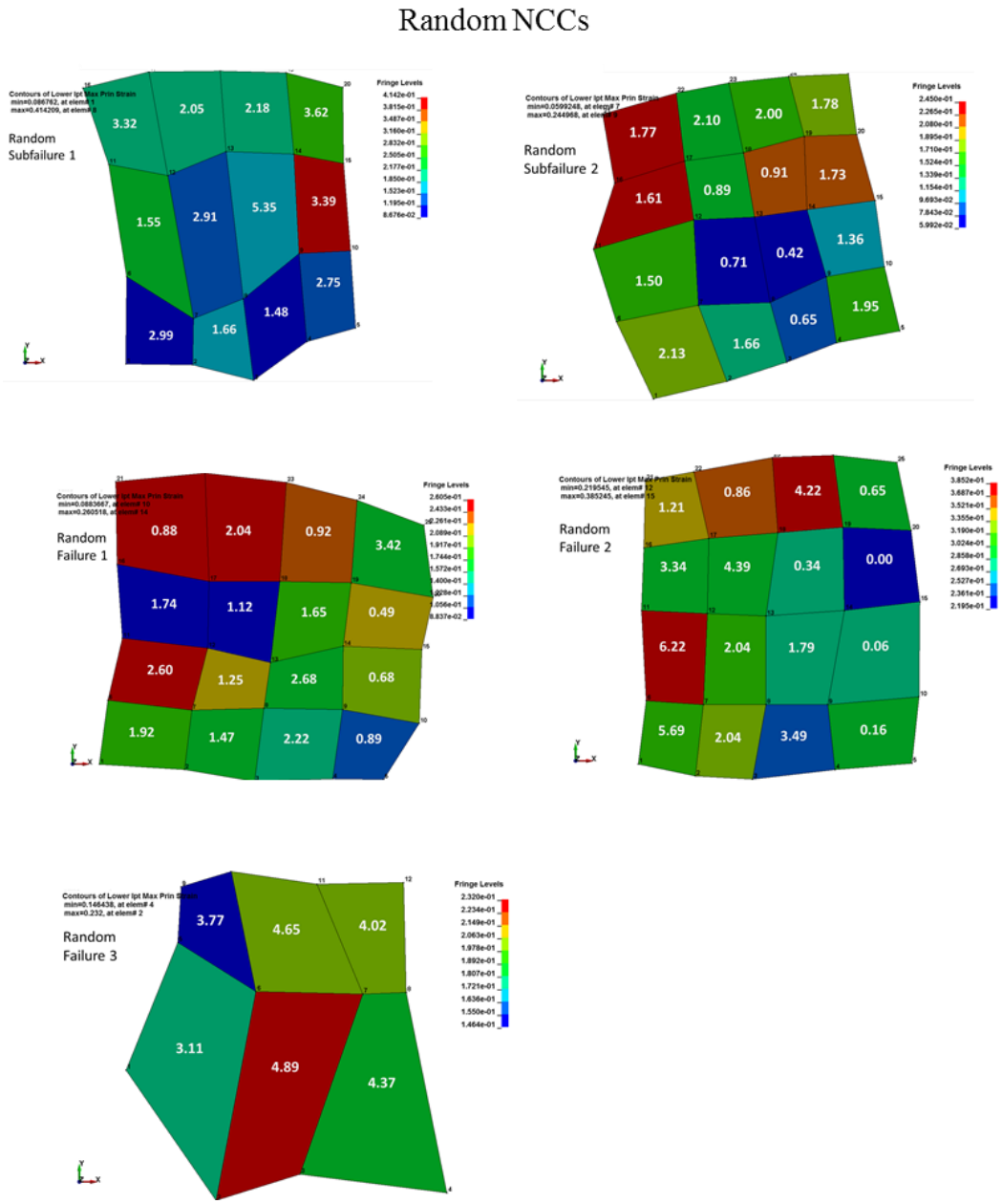


**Note:** Numbers on elements are normalized ATF3 for that element. Figure is continued on the next page.

# Aligned NCCs

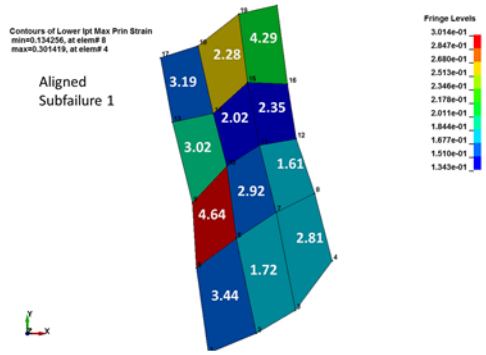


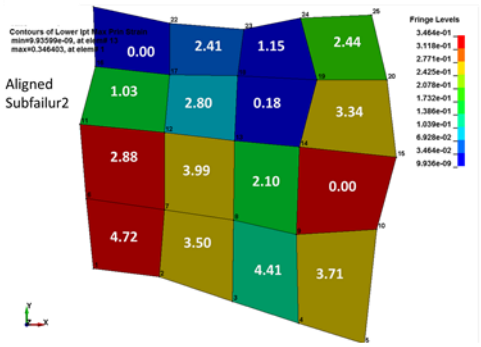


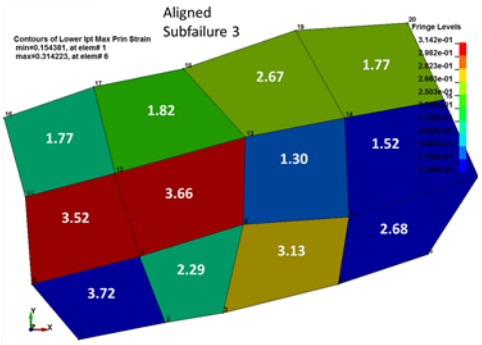


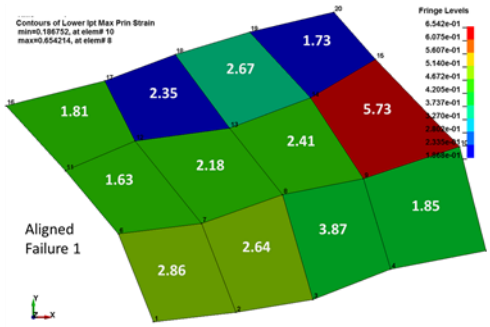


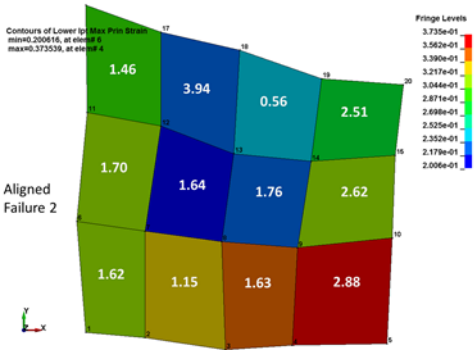


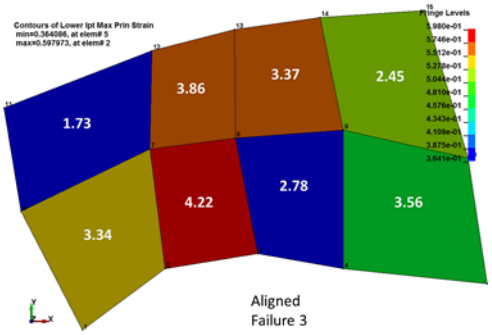

**Table C.3. Quantification of normalized ATF3 expression in unloaded control NCCs with random or aligned collagen organization (Chapter 3).**

| Random | | Aligned | |
|---|---|---|---|
| **Gel #** | **Normalized ATF3** | **Gel #** | **Normalized ATF3** |
| 1 | 1.24 | 1 | 0.89 |
| | 1.47 | | 0.80 |
| | 0.77 | | 1.34 |
| | 0.81 | | 0.58 |
| | 1.06 | | 0.49 |
| | 0.95 | | 0.34 |
| | 1.60 | | 1.22 |
| | 0.70 | | 1.21 |
| | 0.61 | | 0.78 |
| | 0.42 | | 1.19 |
| | 1.49 | | 0.86 |
| | 1.48 | | 1.07 |
| | 0.95 | | 1.37 |
| | 1.21 | | 1.60 |
| 2 | 1.13 | 2 | 0.94 |
| | 1.02 | | 0.88 |
| | 1.23 | | 1.38 |
| | 1.07 | | 0.65 |
| | 1.13 | | 0.51 |
| | 1.07 | | 0.35 |
| | 0.87 | | 1.17 |
| | 0.78 | | 1.35 |
| | 0.81 | | 0.77 |
| | 0.86 | | 1.28 |
| | 0.85 | | 0.87 |
| | 0.96 | | 1.10 |
| | 0.73 | | 1.54 |
| | 0.70 | | 1.55 |
| | – | | 1.64 |

**Figure C.4. Immunofluorescence images showing the ATF3 (red) & βIII-tubulin (blue) in unstretched & stretched NCCs with random or aligned collagen organization.**

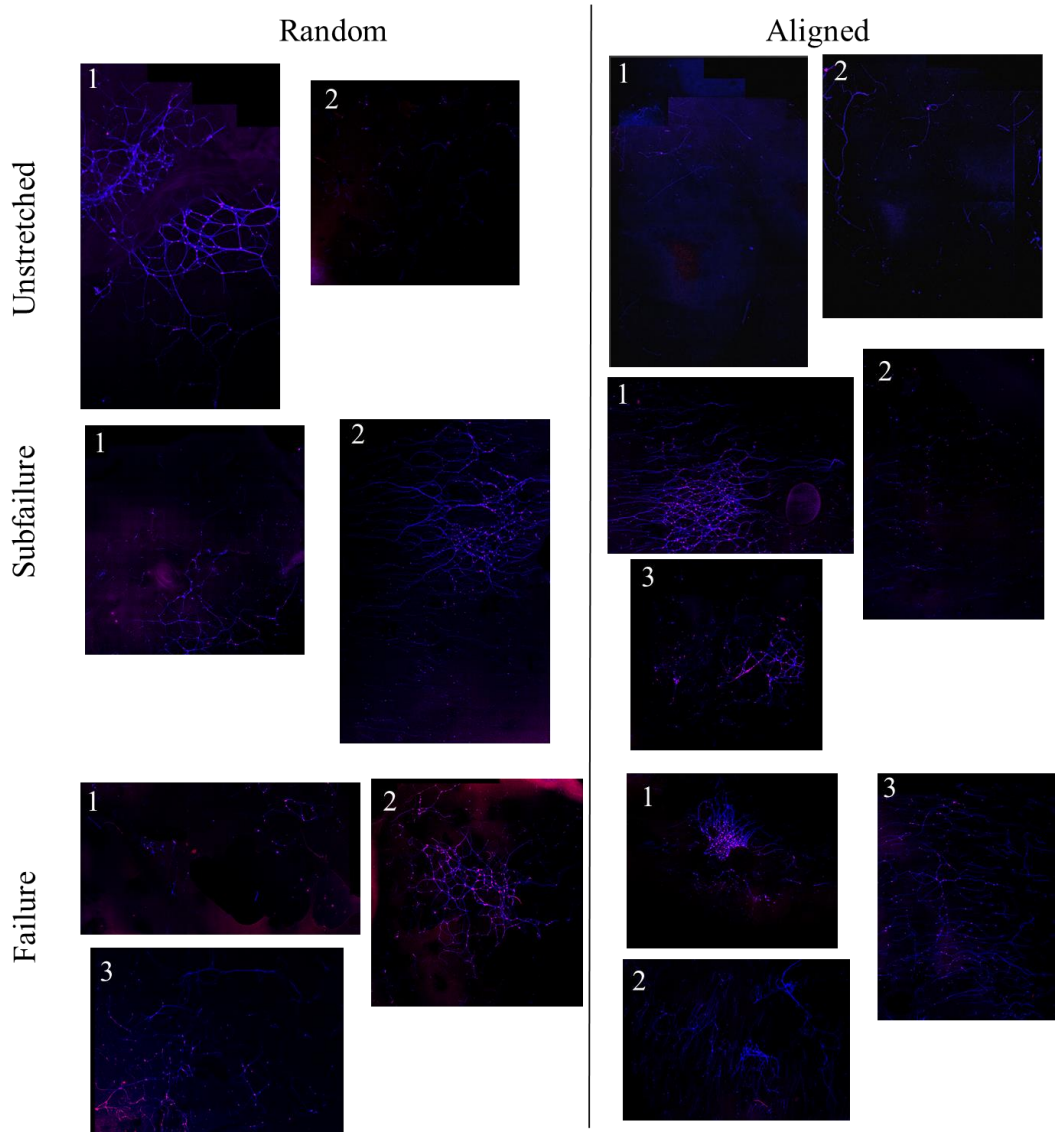

**Table C.4. Densitometric quantification of pERK in cortical-collagen constructs immediately after stretch to 4mm or 8mm at 0.5mm/s or 3.5mm/s (Chapter 4).**

| 4mm, 0.5mm/s | | | | | | | | | | | |
|---|---|---|---|---|---|---|---|---|---|---|---|
| **Gel** | **Image** | **pERK** | **Gel** | **Image** | **pERK** | **Gel** | **Image** | **pERK** | **Gel** | **Image** | **pERK** |
| 1 | 1 | 1.38 | 2 | 1 | 0.50 | 3 | 1 | 1.51 | 4 | 1 | 0.20 |
| | 2 | 1.09 | | 2 | 0.36 | | 2 | 1.79 | | 2 | 0.41 |
| | 3 | 1.16 | | 3 | 0.31 | | 3 | 1.75 | | 3 | 0.38 |
| | 4 | 1.00 | | 4 | 0.92 | | 4 | 1.26 | | 4 | 1.12 |
| | 5 | 0.99 | | 5 | 0.71 | | 5 | 0.91 | | 5 | 0.58 |
| | 6 | 0.89 | | 6 | 0.73 | | 6 | 1.63 | | 6 | 0.73 |
| | 7 | 1.38 | | 7 | 0.79 | | 7 | 1.04 | | 7 | 0.12 |
| | 8 | 1.75 | | 8 | 0.80 | | 8 | 1.16 | | 8 | 0.26 |
| | 9 | 0.83 | | 9 | 0.77 | | 9 | 1.10 | | 9 | 0.73 |
| | 10 | 1.10 | | 10 | 0.47 | | 10 | 0.89 | | 10 | 0.53 |
| | 11 | 0.62 | | 11 | 0.43 | | 11 | 0.98 | | 11 | 0.17 |
| | 12 | 1.01 | | 12 | 0.42 | | 12 | 1.19 | | 12 | 0.27 |
| | 13 | 0.50 | | 13 | 0.55 | | 13 | 0.94 | | 13 | 0.50 |
| | 14 | 1.07 | | 14 | 0.57 | | 14 | 0.81 | | 14 | 1.07 |
| | 15 | 1.35 | | 15 | 0.64 | | 15 | 0.92 | | 15 | 0.76 |
| | 16 | 0.71 | | 16 | 0.45 | | 16 | 1.18 | | 16 | 0.27 |
| | 17 | 0.72 | | 17 | 0.47 | | 17 | 0.92 | | 17 | 0.24 |
| | 18 | 1.02 | | 18 | 0.40 | | 18 | 1.04 | | 18 | 0.27 |
| | 19 | 0.31 | | 19 | 0.56 | | 19 | 0.79 | | 19 | 0.19 |
| | 20 | 0.47 | | 20 | 0.47 | | 20 | 0.95 | | 20 | 0.31 |
| | 21 | 0.14 | | 21 | 0.58 | | 21 | 0.99 | | 21 | 0.33 |
| | 22 | 1.06 | | 22 | 0.51 | | 22 | 1.41 | | 22 | 0.76 |
| | 23 | 0.94 | | 23 | 0.57 | | 23 | 1.29 | | 23 | 1.07 |
| | 24 | 0.88 | | 24 | 0.86 | | 24 | 1.09 | | 24 | 0.93 |
| | 25 | 0.25 | | 25 | 1.13 | | 25 | 0.40 | | 25 | 1.75 |
| | 26 | 0.24 | | 26 | 1.41 | | 26 | 0.51 | | 26 | 1.20 |
| | 27 | 0.25 | | 27 | 0.83 | | 27 | 0.36 | | 27 | 0.67 |
| | 28 | 0.91 | | 28 | 1.13 | | 28 | 1.34 | | 28 | 1.15 |
| | 29 | 1.03 | | 29 | 1.26 | | 29 | 1.01 | | 29 | 1.13 |
| | 30 | 0.98 | | 30 | 1.00 | | 30 | 0.91 | | 30 | 1.03 |
| 5 | 1 | 0.94 | 6 | 1 | 0.75 | 7 | 1 | 0.48 | 8 | 1 | 0.88 |
| | 2 | 0.36 | | 2 | 0.85 | | 2 | 0.68 | | 2 | 1.03 |
| | 3 | 0.53 | | 3 | 0.86 | | 3 | 0.96 | | 3 | 0.79 |
| | 4 | 1.30 | | 4 | 1.04 | | 4 | 0.09 | | 4 | 0.96 |
| | 5 | 1.47 | | 5 | 0.94 | | 5 | 0.09 | | 5 | 0.86 |
| | 6 | 1.45 | | 6 | 0.60 | | 6 | 0.09 | | 6 | 1.07 |
| | 7 | 1.42 | | 7 | 1.30 | | 7 | 0.87 | | 7 | 0.89 |
| | 8 | 0.55 | | 8 | 1.48 | | 8 | 1.01 | | 8 | 0.70 |
| | 9 | 0.84 | | 9 | 1.08 | | 9 | 0.69 | | 9 | 0.75 |
| | 10 | 0.81 | | 10 | 1.11 | | 10 | 1.00 | | 10 | 1.14 |
| | 11 | 0.52 | | 11 | 0.96 | | 11 | 1.00 | | 11 | 0.97 |
| | 12 | 0.60 | | 12 | 0.89 | | 12 | 1.15 | | 12 | 0.97 |
| | 13 | 0.34 | | 13 | 0.69 | | 13 | 1.03 | | 13 | 1.20 |
| | 14 | 0.52 | | 14 | 0.73 | | 14 | 1.19 | | 14 | 0.98 |
| | 15 | 0.54 | | 15 | 0.33 | | 15 | 1.25 | | 15 | 1.10 |

**Note:** Table is continued on the next page.

| 4mm, 0.5mm/s | | | | | | | | | | |
|---|---|---|---|---|---|---|---|---|---|---|
| **Gel** | **Image** | **pERK** | **Gel** | **Image** | **pERK** | **Gel** | **Image** | **pERK** | **Gel** | **Image** | **pERK** |
| | 16 | 0.64 | | 16 | 0.19 | | 16 | 1.12 | | 16 | 0.98 |
| | 17 | 1.30 | | 17 | 0.47 | | 17 | 0.47 | | 17 | 1.51 |
| | 18 | 1.14 | | 18 | 0.78 | | 18 | 0.90 | | 18 | 0.82 |
| | 19 | 0.92 | | 19 | 0.73 | | 19 | 0.87 | | 19 | 0.90 |
| | 20 | 0.87 | | 20 | 0.85 | | 20 | 1.40 | | 20 | 0.83 |
| | 21 | 0.97 | | 21 | 0.41 | | 21 | 1.61 | | 21 | 0.77 |
| | 22 | 1.78 | | 22 | 0.85 | | 22 | 1.07 | | 22 | 0.79 |
| 5 | 23 | 1.04 | 6 | 23 | 0.75 | 7 | 23 | 2.00 | 8 | 23 | 0.66 |
| | 24 | 0.49 | | 24 | 0.25 | | 24 | 1.41 | | 24 | 0.86 |
| | 25 | 1.51 | | 25 | 0.19 | | 25 | 0.91 | | 25 | 0.76 |
| | 26 | 1.50 | | 26 | 0.06 | | 26 | 1.31 | | 26 | 0.80 |
| | 27 | 1.02 | | 27 | 0.52 | | 27 | 1.22 | | 27 | 0.82 |
| | 28 | 1.63 | | 28 | 0.70 | | 28 | 0.62 | | 28 | 0.87 |
| | 29 | 2.05 | | 29 | 0.22 | | 29 | 0.36 | | 29 | 0.85 |
| | 30 | 1.91 | | 30 | 0.46 | | 30 | 0.21 | | 30 | 0.83 |
| **4mm, 3.5mm/s** | | | | | | | | | | |
| **Gel** | **Image** | **pERK** | **Gel** | **Image** | **pERK** | **Gel** | **Image** | **pERK** | **Gel** | **Image** | **pERK** |
| | 1 | 1.29 | | 1 | 1.60 | | 1 | 1.40 | | 1 | 0.35 |
| | 2 | 1.55 | | 2 | 1.60 | | 2 | 0.70 | | 2 | 0.45 |
| | 3 | 1.89 | | 3 | 1.36 | | 3 | 0.75 | | 3 | 0.36 |
| | 4 | 1.77 | | 4 | 2.00 | | 4 | 0.83 | | 4 | 1.71 |
| | 5 | 1.96 | | 5 | 1.90 | | 5 | 1.12 | | 5 | 0.40 |
| | 6 | 0.78 | | 6 | 1.15 | | 6 | 1.57 | | 6 | 0.39 |
| | 7 | 1.95 | | 7 | 1.93 | | 7 | 1.18 | | 7 | 0.59 |
| | 8 | 1.08 | | 8 | 1.74 | | 8 | 1.30 | | 8 | 0.49 |
| | 9 | 1.57 | | 9 | 1.53 | | 9 | 1.19 | | 9 | 0.45 |
| | 10 | 1.67 | | 10 | 1.01 | | 10 | 0.43 | | 10 | 0.47 |
| | 11 | 1.93 | | 11 | 1.17 | | 11 | 0.66 | | 11 | 0.64 |
| | 12 | 0.68 | | 12 | 1.42 | | 12 | 0.62 | | 12 | 0.57 |
| | 13 | 0.35 | | 13 | 1.40 | | 13 | 1.55 | | 13 | 0.95 |
| | 14 | 0.59 | | 14 | 1.45 | | 14 | 1.22 | | 14 | 1.04 |
| | 15 | 0.92 | | 15 | 1.21 | | 15 | 1.30 | | 15 | 1.02 |
| 1 | 16 | 0.62 | 2 | 16 | 1.35 | 3 | 16 | 0.81 | 4 | 16 | 0.60 |
| | 17 | 0.91 | | 17 | 1.01 | | 17 | 0.82 | | 17 | 0.63 |
| | 18 | 0.94 | | 18 | 1.42 | | 18 | 0.31 | | 18 | 0.71 |
| | 19 | 0.98 | | 19 | 1.39 | | 19 | 1.44 | | 19 | 1.32 |
| | 20 | 0.92 | | 20 | 1.40 | | 20 | 1.38 | | 20 | 1.30 |
| | 21 | 0.91 | | 21 | 1.42 | | 21 | 1.19 | | 21 | 1.09 |
| | 22 | 0.74 | | 22 | 1.30 | | 22 | 0.24 | | 22 | 2.02 |
| | 23 | 0.43 | | 23 | 1.11 | | 23 | 0.17 | | 23 | 1.84 |
| | 24 | 0.50 | | 24 | 1.47 | | 24 | 0.94 | | 24 | 1.85 |
| | 25 | 0.73 | | 25 | 1.49 | | 25 | 1.44 | | 25 | 1.32 |
| | 26 | 0.41 | | 26 | 1.46 | | 26 | 1.30 | | 26 | 1.40 |
| | 27 | 0.58 | | 27 | 1.39 | | 27 | 1.10 | | 27 | 1.62 |
| | 28 | 0.87 | | 28 | 1.55 | | 28 | 0.91 | | 28 | 0.78 |
| | 29 | 1.02 | | 29 | 1.92 | | 29 | 0.99 | | 29 | 0.84 |
| | 30 | 0.66 | | 30 | 0.98 | | 30 | 1.11 | | 30 | 0.74 |
| | 1 | 0.62 | | 1 | 1.09 | | 1 | 0.42 | | | |
| | 2 | 0.73 | | 2 | 1.20 | | 2 | 0.68 | | | |
| 5 | 3 | 0.64 | 6 | 3 | 1.44 | 7 | 3 | 1.71 | – | – | |
| | 4 | 1.83 | | 4 | 1.28 | | 4 | 1.07 | | | |
| | 5 | 1.67 | | 5 | 1.17 | | 5 | 1.22 | | | |

**Note:** Table is continued on the next page.

| 4mm, 3.5mm/s | | | | | | | | | | |
|---|---|---|---|---|---|---|---|---|---|---|
| **Gel** | **Image** | **pERK** | **Gel** | **Image** | **pERK** | **Gel** | **Image** | **pERK** | **Gel** | **Image** | **pERK** |
| | 6 | 1.68 | | 6 | 1.28 | | 6 | 1.58 | | | |
| | 7 | 0.61 | | 7 | 1.03 | | 7 | 1.15 | | | |
| | 8 | 0.64 | | 8 | 0.94 | | 8 | 1.43 | | | |
| | 9 | 0.69 | | 9 | 0.91 | | 9 | 1.53 | | | |
| | 10 | 2.20 | | 10 | 0.39 | | 10 | 0.65 | | | |
| | 11 | 1.77 | | 11 | 0.42 | | 11 | 0.99 | | | |
| | 12 | 1.97 | | 12 | 0.60 | | 12 | 0.82 | | | |
| | 13 | 1.48 | | 13 | 0.75 | | 13 | 0.69 | | | |
| | 14 | 1.31 | | 14 | 0.92 | | 14 | 0.60 | | | |
| | 15 | 0.91 | | 15 | 0.64 | | 15 | 0.90 | | | |
| | 16 | 0.62 | | 16 | 0.64 | | 16 | 1.07 | | | |
| | 17 | 0.59 | | 17 | 0.67 | | 17 | 0.99 | | | |
| 5 | 18 | 0.89 | 6 | 18 | 0.57 | 7 | 18 | 0.88 | – | – | |
| | 19 | 0.96 | | 19 | 0.78 | | 19 | 0.41 | | | |
| | 20 | 1.08 | | 20 | 0.61 | | 20 | 0.45 | | | |
| | 21 | 0.87 | | 21 | 0.84 | | 21 | 0.55 | | | |
| | 22 | 1.02 | | 22 | 1.65 | | 22 | 0.60 | | | |
| | 23 | 0.94 | | 23 | 1.22 | | 23 | 0.74 | | | |
| | 24 | 0.79 | | 24 | 1.15 | | 24 | 0.66 | | | |
| | 25 | 0.87 | | 25 | 0.46 | | 25 | 0.68 | | | |
| | 26 | 0.86 | | 26 | 0.71 | | 26 | 0.77 | | | |
| | 27 | 0.85 | | 27 | 0.55 | | 27 | 0.78 | | | |
| | 28 | 1.44 | | 28 | 1.40 | | 28 | 0.45 | | | |
| | 29 | 1.37 | | 29 | 1.41 | | 29 | 0.48 | | | |
| | 30 | 1.42 | | 30 | 1.39 | | 30 | 0.38 | | | |

| 8mm, 0.5mm/s | | | | | | | | | | |
|---|---|---|---|---|---|---|---|---|---|---|
| **Gel** | **Image** | **pERK** | **Gel** | **Image** | **pERK** | **Gel** | **Image** | **pERK** | **Gel** | **Image** | **pERK** |
| | 1 | 1.18 | | 1 | 1.47 | | 1 | 1.21 | | 1 | 2.08 |
| | 2 | 1.18 | | 2 | 1.21 | | 2 | 0.87 | | 2 | 2.10 |
| | 3 | 1.01 | | 3 | 1.56 | | 3 | 0.99 | | 3 | 1.84 |
| | 4 | 1.38 | | 4 | 1.57 | | 4 | 2.36 | | 4 | 1.85 |
| | 5 | 0.94 | | 5 | 1.84 | | 5 | 2.05 | | 5 | 2.16 |
| | 6 | 0.78 | | 6 | 1.52 | | 6 | 1.71 | | 6 | 2.24 |
| | 7 | 0.70 | | 7 | 1.63 | | 7 | 1.50 | | 7 | 1.43 |
| | 8 | 0.24 | | 8 | 1.42 | | 8 | 1.71 | | 8 | 1.26 |
| | 9 | 0.65 | | 9 | 1.30 | | 9 | 1.30 | | 9 | 0.98 |
| | 10 | 1.20 | | 10 | 1.36 | | 10 | 0.74 | | 10 | 1.67 |
| | 11 | 0.57 | | 11 | 1.19 | | 11 | 0.71 | | 11 | 1.67 |
| | 12 | 0.59 | | 12 | 1.72 | | 12 | 0.61 | | 12 | 1.43 |
| 1 | 13 | 0.49 | 2 | 13 | 0.98 | 3 | 13 | 0.70 | 4 | 13 | 1.57 |
| | 14 | 0.34 | | 14 | 0.46 | | 14 | 0.46 | | 14 | 1.65 |
| | 15 | 0.35 | | 15 | 1.00 | | 15 | 0.67 | | 15 | 1.55 |
| | 16 | 0.64 | | 16 | 2.21 | | 16 | 0.82 | | 16 | 0.57 |
| | 17 | 0.97 | | 17 | 2.04 | | 17 | 0.53 | | 17 | 1.30 |
| | 18 | 0.46 | | 18 | 0.73 | | 18 | 0.88 | | 18 | 1.47 |
| | 19 | 0.35 | | 19 | 1.63 | | 19 | 0.78 | | 19 | 0.98 |
| | 20 | 0.46 | | 20 | 1.36 | | 20 | 0.86 | | 20 | 0.94 |
| | 21 | 0.52 | | 21 | 1.57 | | 21 | 1.12 | | 21 | 1.00 |
| | 22 | 0.47 | | 22 | 1.05 | | 22 | 0.94 | | 22 | 1.71 |
| | 23 | 0.43 | | 23 | 0.77 | | 23 | 1.57 | | 23 | 1.62 |
| | 24 | 0.70 | | 24 | 2.08 | | 24 | 1.59 | | 24 | 2.11 |
| | 25 | 0.29 | | 25 | 1.32 | | 25 | 1.25 | | 25 | 1.16 |

**Note:** Table is continued on the next page.

| 8mm, 0.5mm/s | | | | | | | | | | | |
|---|---|---|---|---|---|---|---|---|---|---|---|
| **Gel** | **Image** | **pERK** | **Gel** | **Image** | **pERK** | **Gel** | **Image** | **pERK** | **Gel** | **Image** | **pERK** |
| 1 | 26 | 0.50 | 2 | 26 | 0.76 | 3 | 26 | 1.56 | 4 | 26 | 1.16 |
| | 27 | 0.27 | | 27 | 0.84 | | 27 | 1.89 | | 27 | 1.41 |
| | 28 | 1.25 | | 28 | 1.51 | | 28 | 2.18 | | 28 | 2.10 |
| | 29 | 0.86 | | 29 | 1.55 | | 29 | 2.29 | | 29 | 2.02 |
| | 30 | 1.09 | | 30 | 0.86 | | 30 | 2.12 | | 30 | 1.87 |
| 5 | 1 | 2.81 | 6 | 1 | 1.45 | 7 | 1 | 0.53 | 8 | 1 | 1.30 |
| | 2 | 2.80 | | 2 | 0.84 | | 2 | 0.09 | | 2 | 1.22 |
| | 3 | 2.89 | | 3 | 1.34 | | 3 | 0.74 | | 3 | 1.43 |
| | 4 | 3.74 | | 4 | 1.39 | | 4 | 0.67 | | 4 | 1.34 |
| | 5 | 2.74 | | 5 | 1.93 | | 5 | 0.91 | | 5 | 1.55 |
| | 6 | 3.17 | | 6 | 1.05 | | 6 | 1.20 | | 6 | 1.22 |
| | 7 | 2.56 | | 7 | 0.87 | | 7 | 0.84 | | 7 | 1.20 |
| | 8 | 2.93 | | 8 | 0.82 | | 8 | 0.99 | | 8 | 1.19 |
| | 9 | 2.84 | | 9 | 1.05 | | 9 | 0.38 | | 9 | 0.99 |
| | 10 | 2.36 | | 10 | 1.44 | | 10 | 0.74 | | 10 | 1.36 |
| | 11 | 2.19 | | 11 | 1.02 | | 11 | 0.81 | | 11 | 1.48 |
| | 12 | 2.15 | | 12 | 2.02 | | 12 | 0.05 | | 12 | 1.47 |
| | 13 | 1.26 | | 13 | 0.45 | | 13 | 1.19 | | 13 | 1.45 |
| | 14 | 1.34 | | 14 | 0.72 | | 14 | 1.14 | | 14 | 1.21 |
| | 15 | 1.40 | | 15 | 1.51 | | 15 | 1.05 | | 15 | 1.67 |
| | 16 | 2.07 | | 16 | 0.84 | | 16 | 1.15 | | 16 | 2.82 |
| | 17 | 2.20 | | 17 | 1.22 | | 17 | 1.07 | | 17 | 2.34 |
| | 18 | 1.98 | | 18 | 1.35 | | 18 | 1.08 | | 18 | 2.68 |
| | 19 | 1.83 | | 19 | 1.00 | | 19 | 1.28 | | 19 | 1.31 |
| | 20 | 1.62 | | 20 | 1.20 | | 20 | 1.68 | | 20 | 1.36 |
| | 21 | 1.51 | | 21 | 0.82 | | 21 | 1.74 | | 21 | 1.59 |
| | 22 | 2.48 | | 22 | 1.69 | | 22 | 1.16 | | 22 | 0.98 |
| | 23 | 2.07 | | 23 | 0.84 | | 23 | 1.12 | | 23 | 0.88 |
| | 24 | 2.37 | | 24 | 2.00 | | 24 | 1.07 | | 24 | 1.29 |
| | 25 | 1.94 | | 25 | 0.42 | | 25 | 1.30 | | 25 | 1.33 |
| | 26 | 1.84 | | 26 | 0.70 | | 26 | 1.10 | | 26 | 1.39 |
| | 27 | 2.13 | | 27 | 1.42 | | 27 | 1.24 | | 27 | 1.49 |
| | 28 | 2.79 | | 28 | 1.47 | | 28 | 0.80 | | 28 | 1.59 |
| | 29 | 2.26 | | 29 | 0.74 | | 29 | 0.88 | | 29 | 1.67 |
| | 30 | 2.48 | | 30 | 1.57 | | 30 | 0.95 | | 30 | 1.63 |
| 9 | 1 | 1.16 | – | – | | – | – | | – | – | |
| | 2 | 1.38 | | | | | | | | | |
| | 3 | 1.40 | | | | | | | | | |
| | 4 | 1.18 | | | | | | | | | |
| | 5 | 1.25 | | | | | | | | | |
| | 6 | 1.15 | | | | | | | | | |
| | 7 | 1.48 | | | | | | | | | |
| | 8 | 1.72 | | | | | | | | | |
| | 9 | 1.42 | | | | | | | | | |
| | 10 | 1.16 | | | | | | | | | |
| | 11 | 1.19 | | | | | | | | | |
| | 12 | 1.21 | | | | | | | | | |
| | 13 | 1.64 | | | | | | | | | |
| | 14 | 1.59 | | | | | | | | | |
| | 15 | 1.64 | | | | | | | | | |
| | 16 | 1.70 | | | | | | | | | |
| | 17 | 1.52 | | | | | | | | | |

**Note:** Table is continued on the next page.

| 8mm, 0.5mm/s | | | | | | | | | | |
|---|---|---|---|---|---|---|---|---|---|---|
| **Gel** | **Image** | **pERK** | **Gel** | **Image** | **pERK** | **Gel** | **Image** | **pERK** | **Gel** | **Image** | **pERK** |
| 9 | 18 | 1.11 | – | – | | – | – | | – | – | |
| | 19 | 1.72 | | | | | | | | | |
| | 20 | 1.69 | | | | | | | | | |
| | 21 | 1.62 | | | | | | | | | |
| | 22 | 1.61 | | | | | | | | | |
| | 23 | 1.46 | | | | | | | | | |
| | 24 | 1.49 | | | | | | | | | |
| | 25 | 1.77 | | | | | | | | | |
| | 26 | 1.62 | | | | | | | | | |
| | 27 | 1.73 | | | | | | | | | |
| | 28 | 1.50 | | | | | | | | | |
| | 29 | 0.76 | | | | | | | | | |
| | 30 | 0.61 | | | | | | | | | |

| 8mm, 3.5mm/s | | | | | | | | | | |
|---|---|---|---|---|---|---|---|---|---|---|
| **Gel** | **Image** | **pERK** | **Gel** | **Image** | **pERK** | **Gel** | **Image** | **pERK** | **Gel** | **Image** | **pERK** |
| 1 | 1 | 1.17 | 2 | 1 | 1.69 | 3 | 1 | 1.17 | 4 | 1 | 0.72 |
| | 2 | 1.10 | | 2 | 0.25 | | 2 | 0.93 | | 2 | 1.73 |
| | 3 | 1.44 | | 3 | 0.30 | | 3 | 1.55 | | 3 | 0.87 |
| | 4 | 1.35 | | 4 | 0.28 | | 4 | 1.82 | | 4 | 1.69 |
| | 5 | 1.41 | | 5 | 0.55 | | 5 | 1.78 | | 5 | 0.93 |
| | 6 | 1.25 | | 6 | 0.35 | | 6 | 1.49 | | 6 | 0.66 |
| | 7 | 1.23 | | 7 | 0.63 | | 7 | 1.27 | | 7 | 1.23 |
| | 8 | 1.17 | | 8 | 0.17 | | 8 | 1.01 | | 8 | 1.23 |
| | 9 | 1.21 | | 9 | 0.79 | | 9 | 0.65 | | 9 | 1.34 |
| | 10 | 0.79 | | 10 | 0.26 | | 10 | 0.61 | | 10 | 0.91 |
| | 11 | 1.04 | | 11 | 0.41 | | 11 | 0.79 | | 11 | 1.20 |
| | 12 | 1.62 | | 12 | 0.19 | | 12 | 0.67 | | 12 | 0.58 |
| | 13 | 0.94 | | 13 | 0.27 | | 13 | 0.80 | | 13 | 0.53 |
| | 14 | 0.93 | | 14 | 0.10 | | 14 | 0.66 | | 14 | 0.85 |
| | 15 | 1.16 | | 15 | 0.10 | | 15 | 0.64 | | 15 | 1.14 |
| | 16 | 1.62 | | 16 | 0.16 | | 16 | 0.53 | | 16 | 0.56 |
| | 17 | 0.72 | | 17 | 0.53 | | 17 | 0.69 | | 17 | 0.89 |
| | 18 | 1.50 | | 18 | 0.45 | | 18 | 0.68 | | 18 | 0.37 |
| | 19 | 0.80 | | 19 | 0.11 | | 19 | 0.45 | | 19 | 0.71 |
| | 20 | 0.98 | | 20 | 0.14 | | 20 | 0.53 | | 20 | 0.48 |
| | 21 | 0.78 | | 21 | 0.17 | | 21 | 0.90 | | 21 | 0.72 |
| | 22 | 1.47 | | 22 | 1.18 | | 22 | 0.79 | | 22 | 0.70 |
| | 23 | 1.24 | | 23 | 1.09 | | 23 | 1.11 | | 23 | 0.89 |
| | 24 | 1.04 | | 24 | 0.58 | | 24 | 0.99 | | 24 | 0.44 |
| | 25 | 0.95 | | 25 | 0.85 | | 25 | 1.03 | | 25 | 0.72 |
| | 26 | 0.71 | | 26 | 0.26 | | 26 | 1.00 | | 26 | 1.01 |
| | 27 | 0.78 | | 27 | 1.87 | | 27 | 1.65 | | 27 | 0.67 |
| | 28 | 1.62 | | 28 | 2.60 | | 28 | 1.45 | | 28 | 0.82 |
| | 29 | 1.62 | | 29 | 1.34 | | 29 | 1.90 | | 29 | 1.24 |
| | 30 | 1.57 | | 30 | 1.03 | | 30 | 1.56 | | 30 | 1.34 |
| 5 | 1 | 2.15 | 6 | 1 | 1.19 | 7 | 1 | 1.32 | 8 | 1 | 1.48 |
| | 2 | 1.74 | | 2 | 1.48 | | 2 | 1.16 | | 2 | 1.44 |
| | 3 | 2.60 | | 3 | 1.30 | | 3 | 0.70 | | 3 | 1.64 |
| | 4 | 2.22 | | 4 | 1.34 | | 4 | 0.89 | | 4 | 1.06 |
| | 5 | 2.47 | | 5 | 1.23 | | 5 | 0.85 | | 5 | 1.11 |
| | 6 | 2.51 | | 6 | 1.40 | | 6 | 0.65 | | 6 | 1.23 |
| | 7 | 1.63 | | 7 | 1.68 | | 7 | 1.60 | | 7 | 1.11 |

**Note:** Table is continued on the next page.

| 8mm, 3.5mm/s | | | | | | | | | | | |
|---|---|---|---|---|---|---|---|---|---|---|---|
| **Gel** | **Image** | **pERK** | **Gel** | **Image** | **pERK** | **Gel** | **Image** | **pERK** | **Gel** | **Image** | **pERK** |
| | 8 | 1.98 | | 8 | 1.78 | | 8 | 1.45 | | 8 | 1.19 |
| | 9 | 1.97 | | 9 | 1.67 | | 9 | 1.32 | | 9 | 1.11 |
| | 10 | 1.75 | | 10 | 1.68 | | 10 | 1.23 | | 10 | 1.37 |
| | 11 | 1.75 | | 11 | 1.43 | | 11 | 1.38 | | 11 | 1.39 |
| | 12 | 1.95 | | 12 | 1.39 | | 12 | 0.70 | | 12 | 1.29 |
| | 13 | 1.86 | | 13 | 1.48 | | 13 | 0.48 | | 13 | 1.01 |
| | 14 | 1.78 | | 14 | 1.07 | | 14 | 0.54 | | 14 | 1.00 |
| | 15 | 1.35 | | 15 | 1.21 | | 15 | 0.48 | | 15 | 1.42 |
| | 16 | 1.52 | | 16 | 0.91 | | 16 | 1.17 | | 16 | 1.25 |
| | 17 | 1.29 | | 17 | 1.04 | | 17 | 1.23 | | 17 | 1.48 |
| | 18 | 0.92 | | 18 | 0.97 | | 18 | 0.95 | | 18 | 1.85 |
| 5 | 19 | 1.35 | 6 | 19 | 0.97 | 7 | 19 | 0.43 | 8 | 19 | 1.06 |
| | 20 | 0.53 | | 20 | 0.84 | | 20 | 0.44 | | 20 | 0.87 |
| | 21 | 0.97 | | 21 | 0.82 | | 21 | 0.49 | | 21 | 1.02 |
| | 22 | 2.46 | | 22 | 0.64 | | 22 | 0.99 | | 22 | 1.07 |
| | 23 | 2.23 | | 23 | 1.15 | | 23 | 0.99 | | 23 | 1.04 |
| | 24 | 2.15 | | 24 | 1.17 | | 24 | 1.13 | | 24 | 0.86 |
| | 25 | 1.71 | | 25 | 0.43 | | 25 | 0.84 | | 25 | 1.57 |
| | 26 | 1.88 | | 26 | 0.36 | | 26 | 0.81 | | 26 | 1.31 |
| | 27 | 2.10 | | 27 | 0.54 | | 27 | 1.07 | | 27 | 1.29 |
| | 28 | 2.72 | | 28 | 1.01 | | 28 | 0.91 | | 28 | 1.13 |
| | 29 | 2.97 | | 29 | 1.02 | | 29 | 0.75 | | 29 | 1.13 |
| | 30 | 3.10 | | 30 | 0.94 | | 30 | 1.18 | | 30 | 1.08 |
| | 1 | 1.58 | | | | | | | | | |
| | 2 | 1.13 | | | | | | | | | |
| | 3 | 1.52 | | | | | | | | | |
| | 4 | 0.91 | | | | | | | | | |
| | 5 | 1.29 | | | | | | | | | |
| | 6 | 1.83 | | | | | | | | | |
| | 7 | 1.98 | | | | | | | | | |
| | 8 | 1.41 | | | | | | | | | |
| | 9 | 1.56 | | | | | | | | | |
| | 10 | 1.46 | | | | | | | | | |
| | 11 | 1.29 | | | | | | | | | |
| | 12 | 0.82 | | | | | | | | | |
| | 13 | 1.90 | | | | | | | | | |
| | 14 | 2.21 | | | | | | | | | |
| | 15 | 1.45 | | | | | | | | | |
| 9 | 16 | 1.47 | – | – | | – | – | | – | – | |
| | 17 | 1.43 | | | | | | | | | |
| | 18 | 1.34 | | | | | | | | | |
| | 19 | 1.39 | | | | | | | | | |
| | 20 | 1.82 | | | | | | | | | |
| | 21 | 1.37 | | | | | | | | | |
| | 22 | 1.30 | | | | | | | | | |
| | 23 | 1.34 | | | | | | | | | |
| | 24 | 1.06 | | | | | | | | | |
| | 25 | 1.25 | | | | | | | | | |
| | 26 | 0.96 | | | | | | | | | |
| | 27 | 0.68 | | | | | | | | | |
| | 28 | 1.74 | | | | | | | | | |
| | 29 | 0.77 | | | | | | | | | |
| | 30 | 0.93 | | | | | | | | | |

**Figure C.5. Immunofluorescence images showing pERK expression in the cortical-collagen constructs stretched to 4mm or 8mm at 0.5mm/s or 3.5mm/s.**

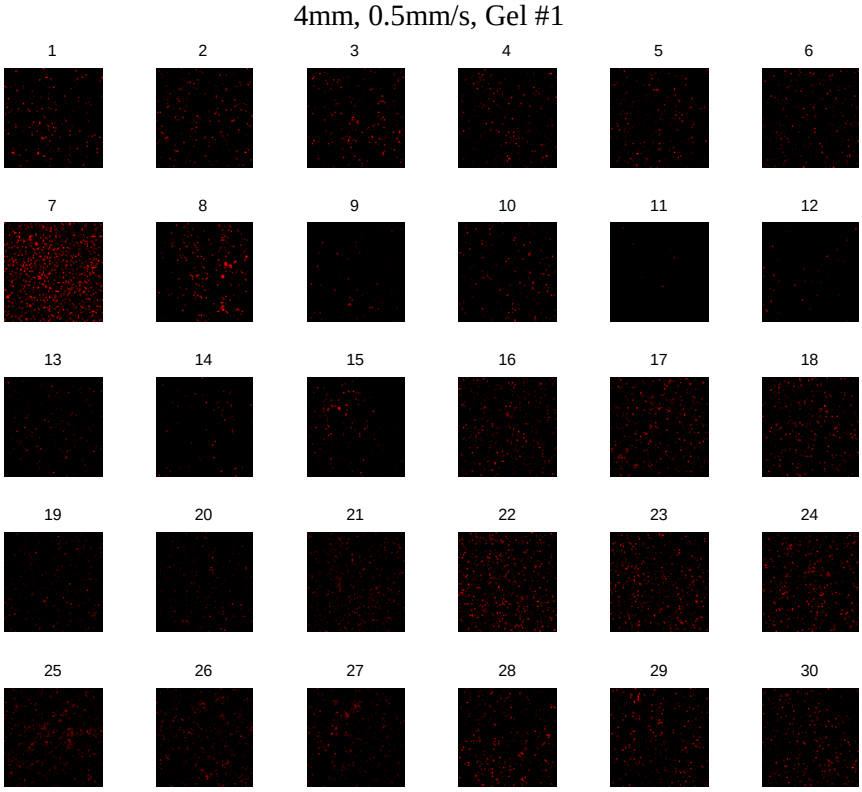


**Note:** Figure is continued on the next page.

4mm, 0.5mm/s, Gel #2

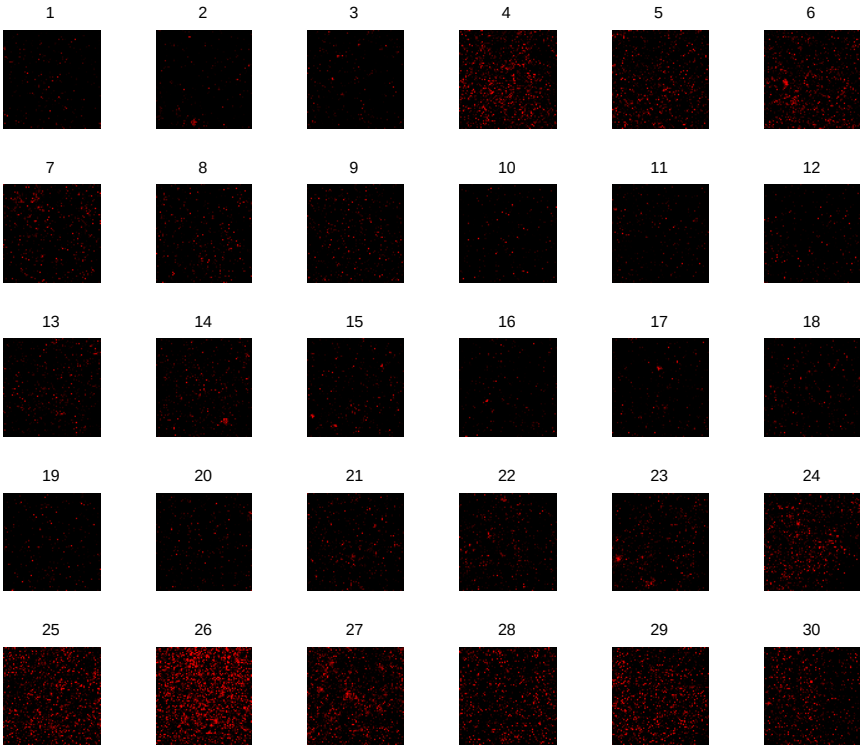


4mm, 0.5mm/s, Gel #3

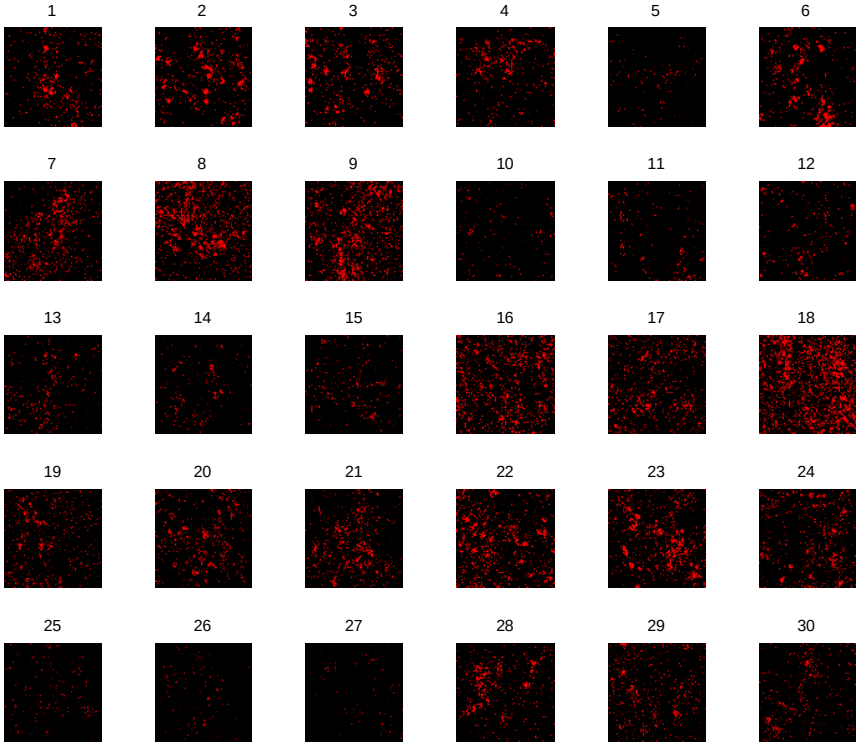


**Note:** Figure is continued on the next page.

4mm, 0.5mm/s, Gel #4

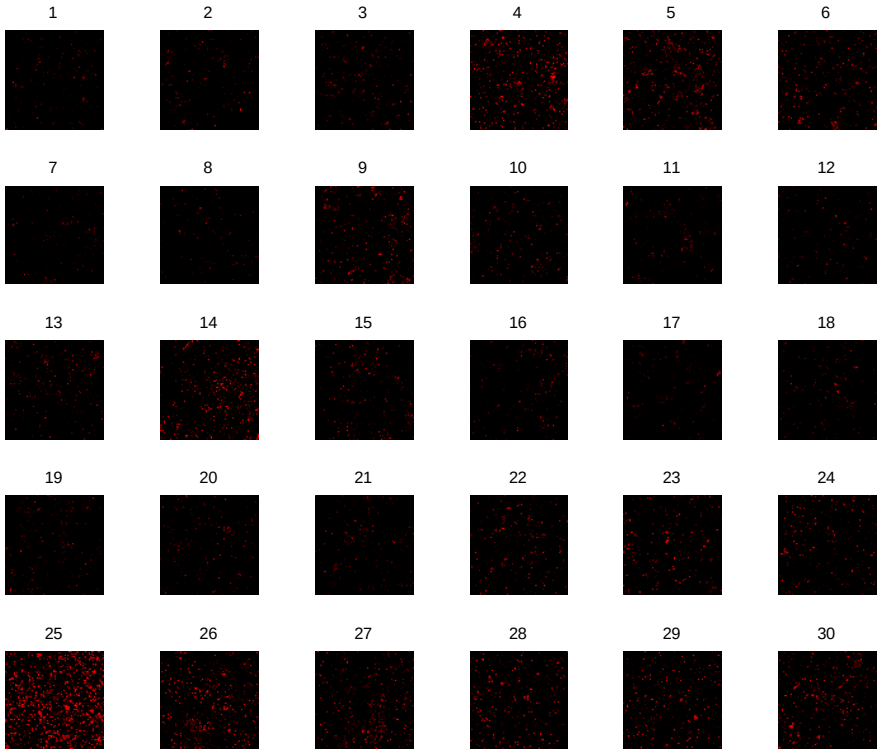


4mm, 0.5mm/s, Gel #5

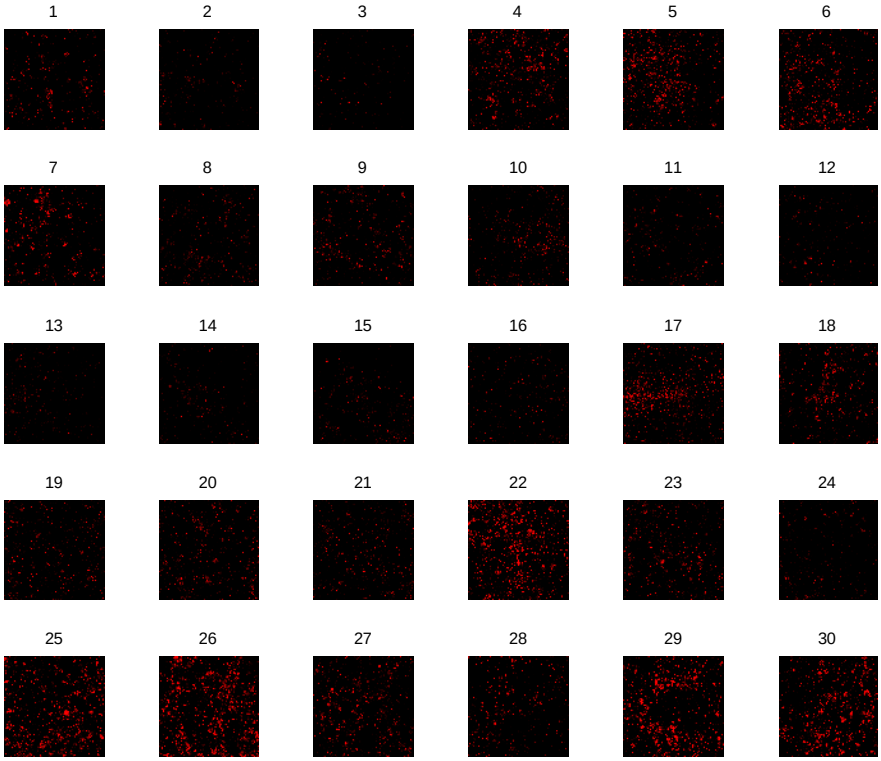


**Note:** Figure is continued on the next page.

4mm, 0.5mm/s, Gel #6

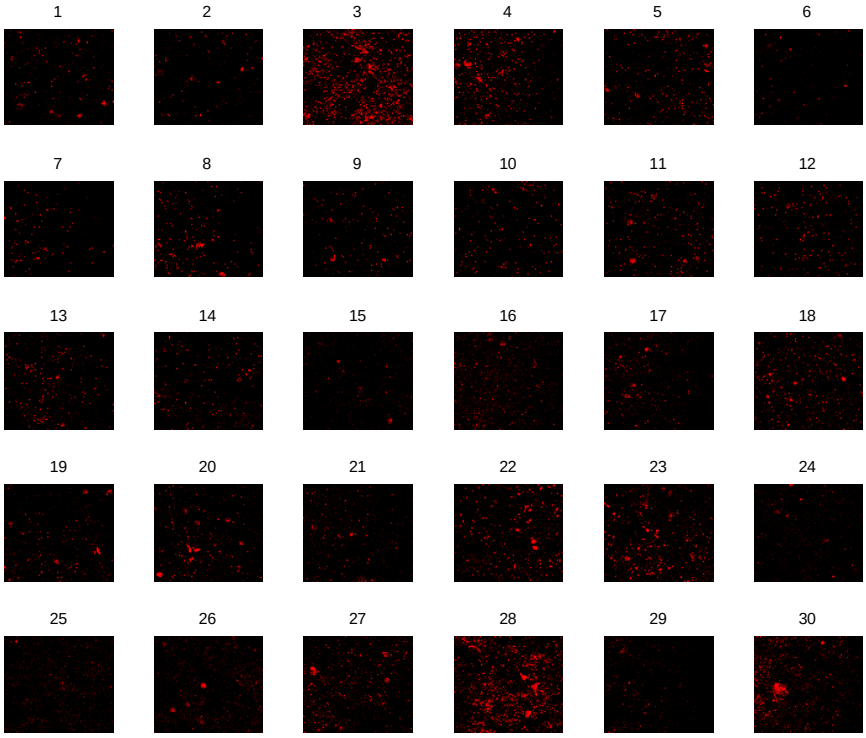


4mm, 0.5mm/s, Gel #7

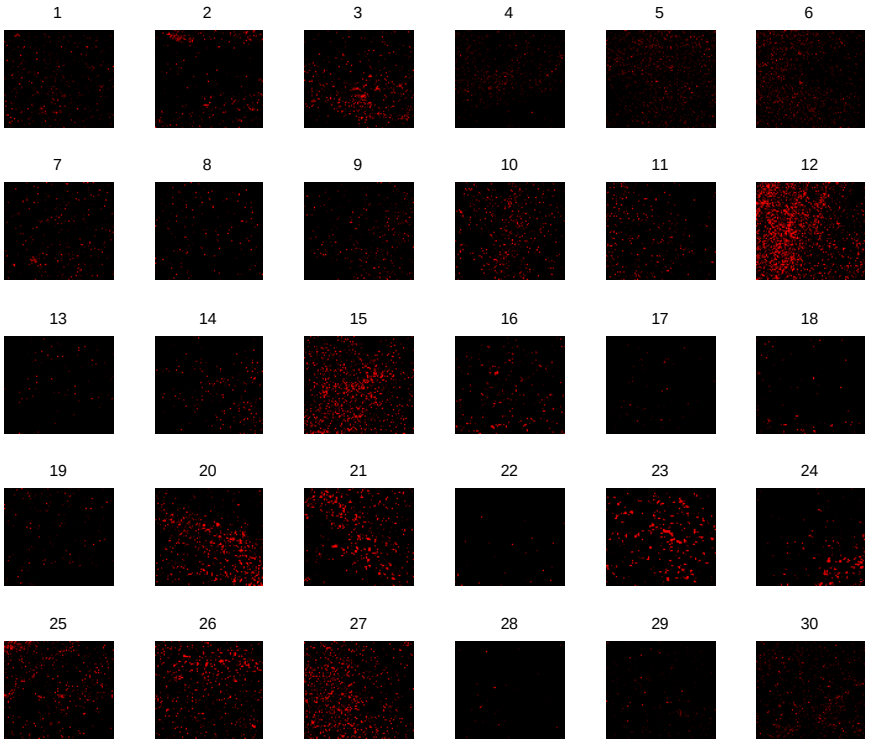


**Note:** Figure is continued on the next page.

4mm, 0.5mm/s, Gel #8

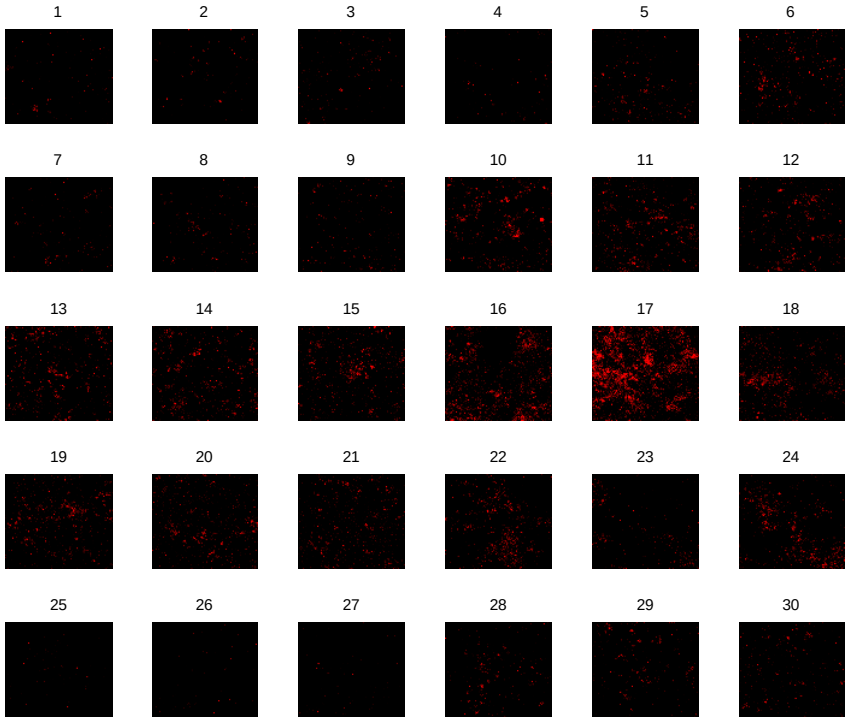


4mm, 3.5mm/s, Gel #1

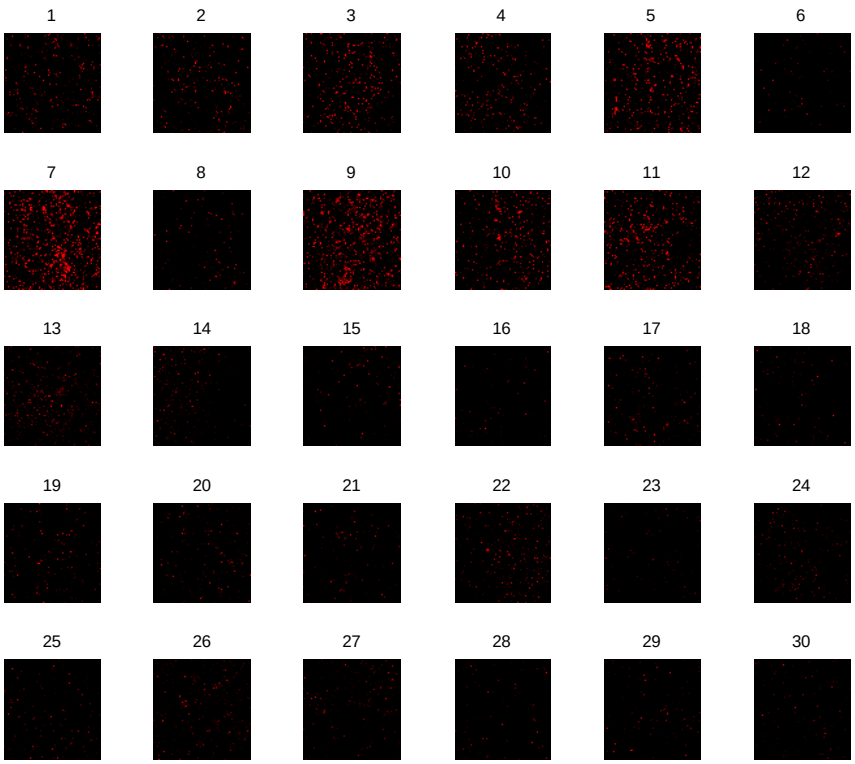


**Note:** Figure is continued on the next page.

4mm, 3.5mm/s, Gel #2

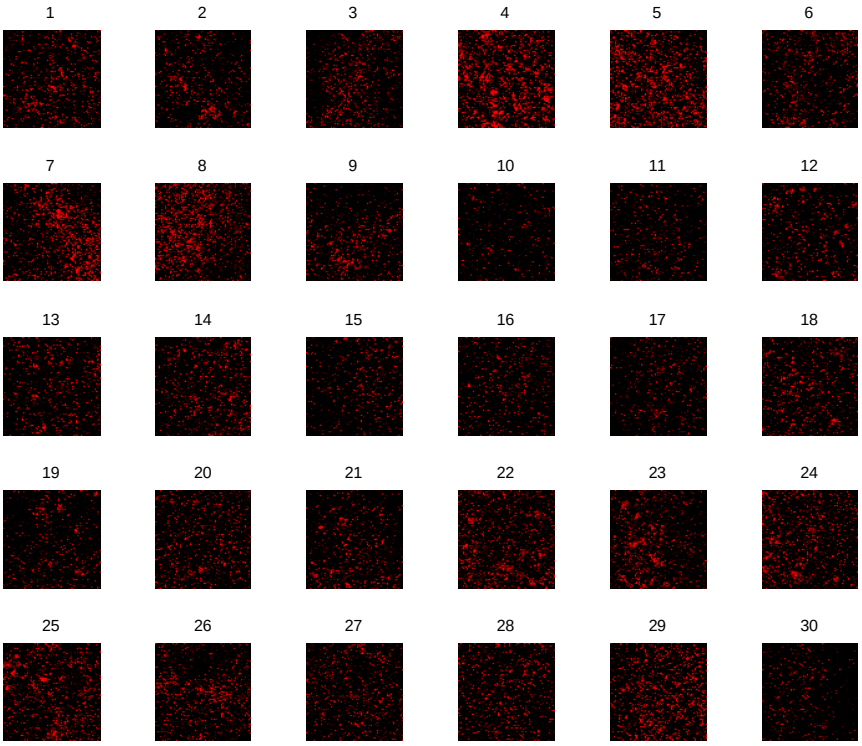


4mm, 3.5mm/s, Gel #3

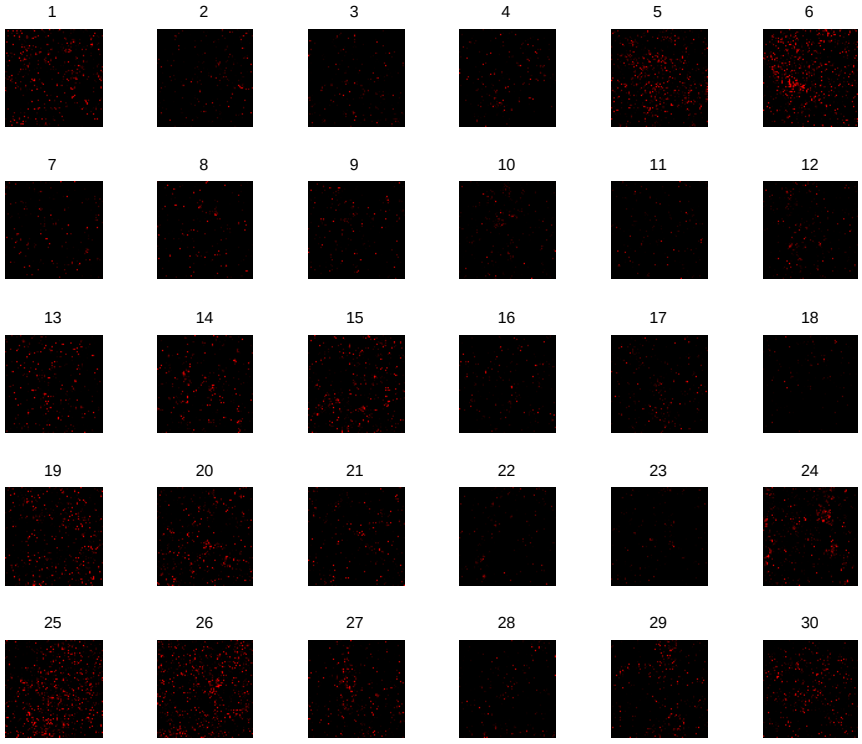


**Note:** Figure is continued on the next page.

4mm, 3.5mm/s, Gel #4

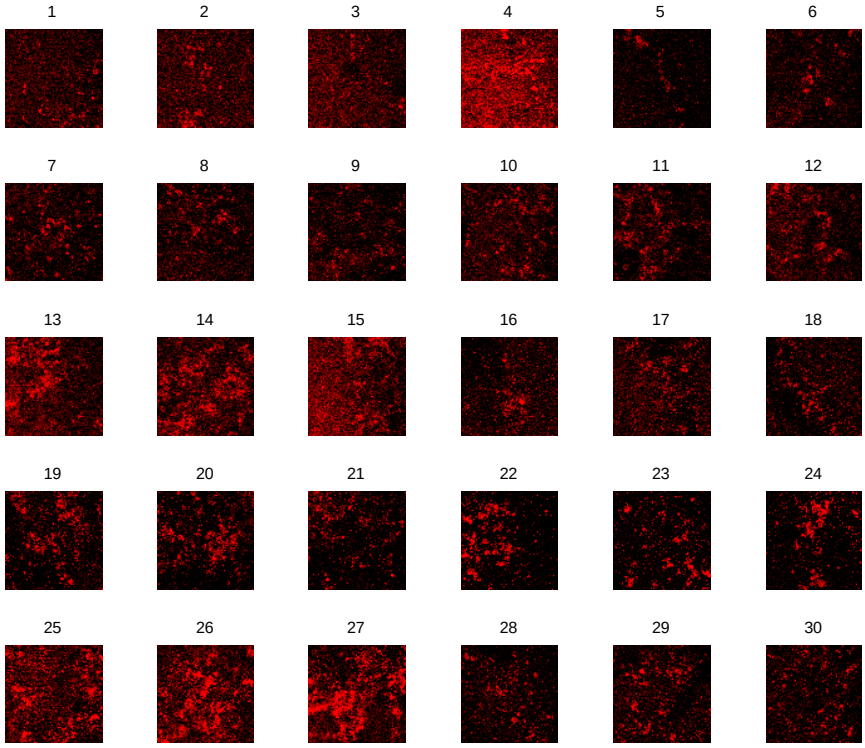


4mm, 3.5mm/s, Gel #5

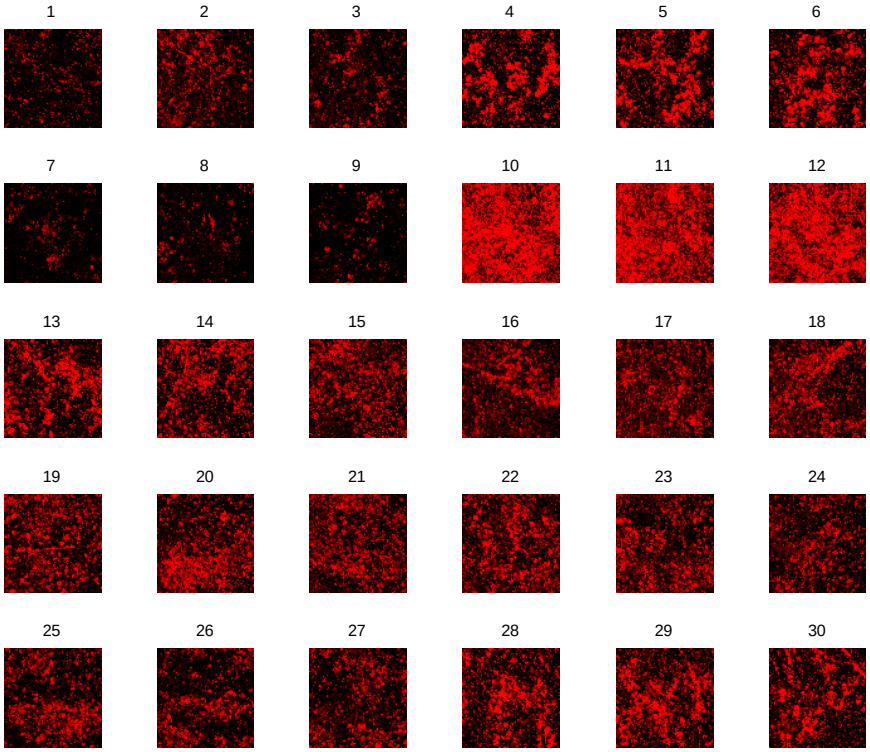


**Note:** Figure is continued on the next page.

4mm, 3.5mm/s, Gel #6

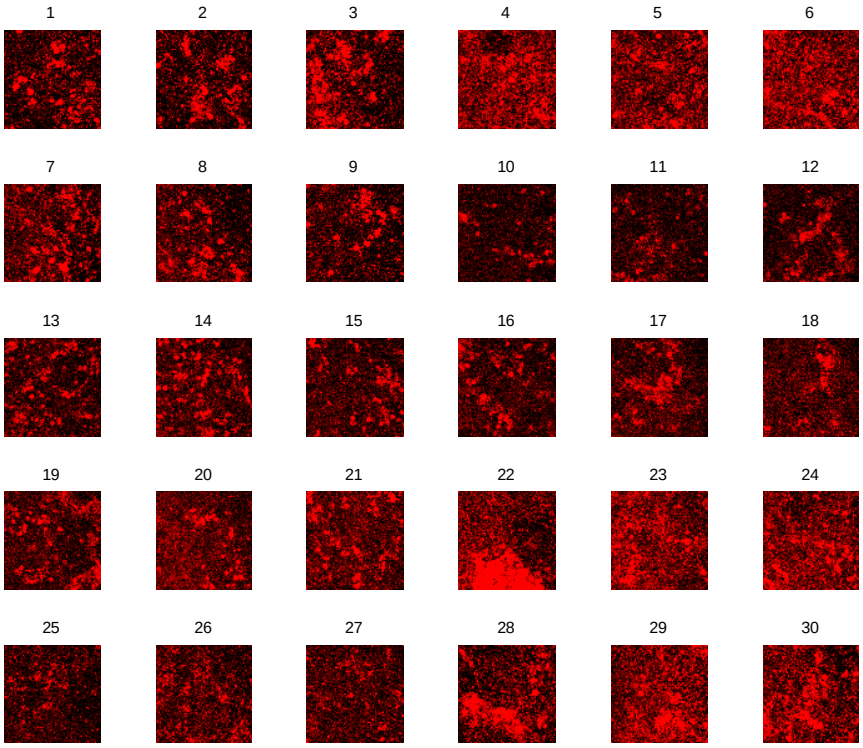


4mm, 3.5mm/s, Gel #7

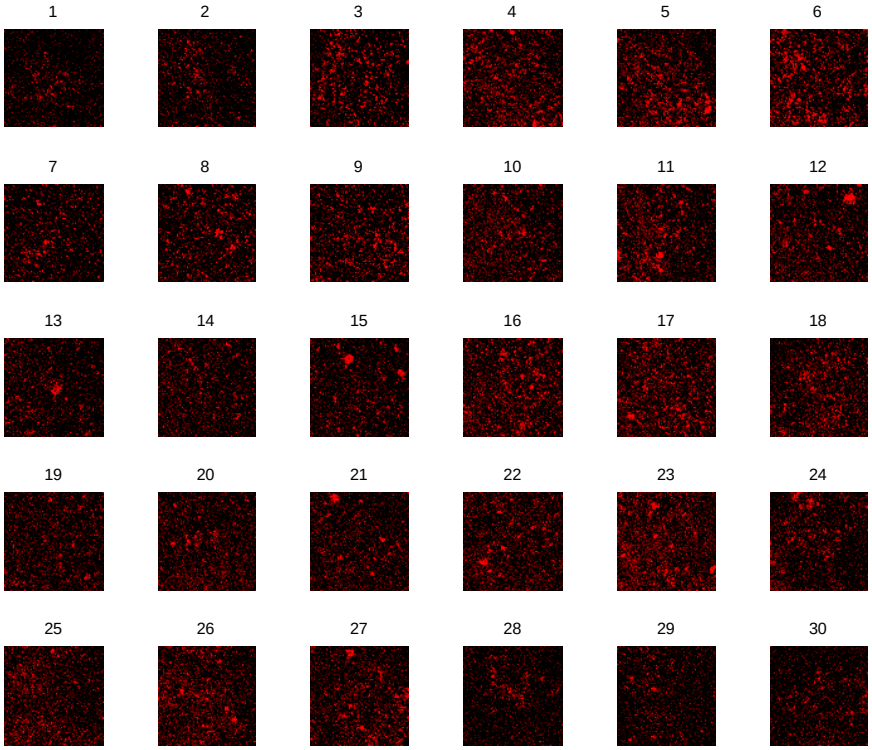


**Note:** Figure is continued on the next page.

8mm, 0.5mm/s, Gel #1

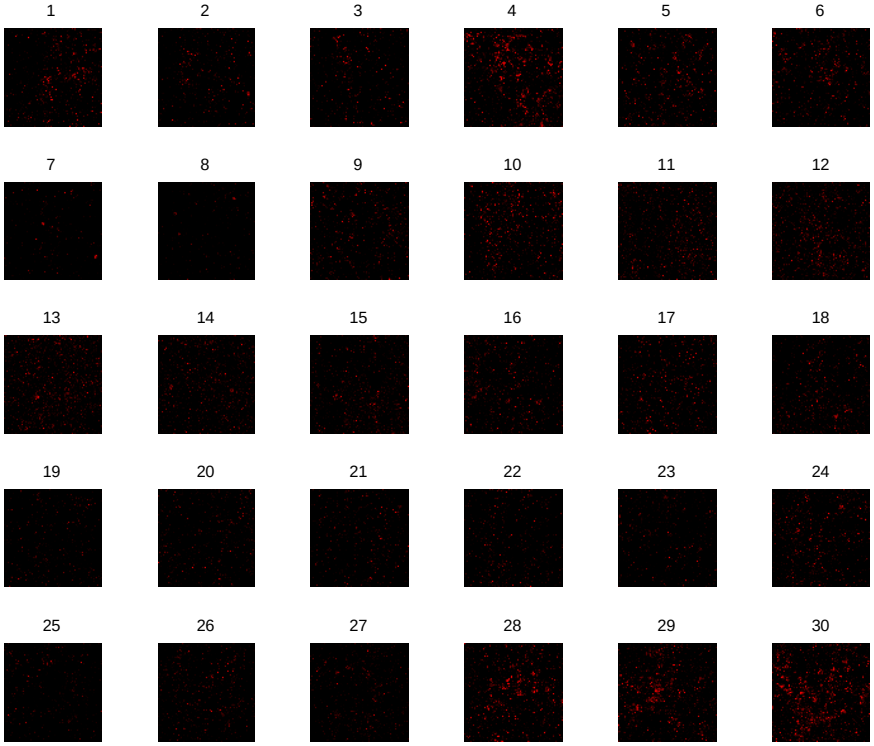


8mm, 0.5mm/s, Gel #2

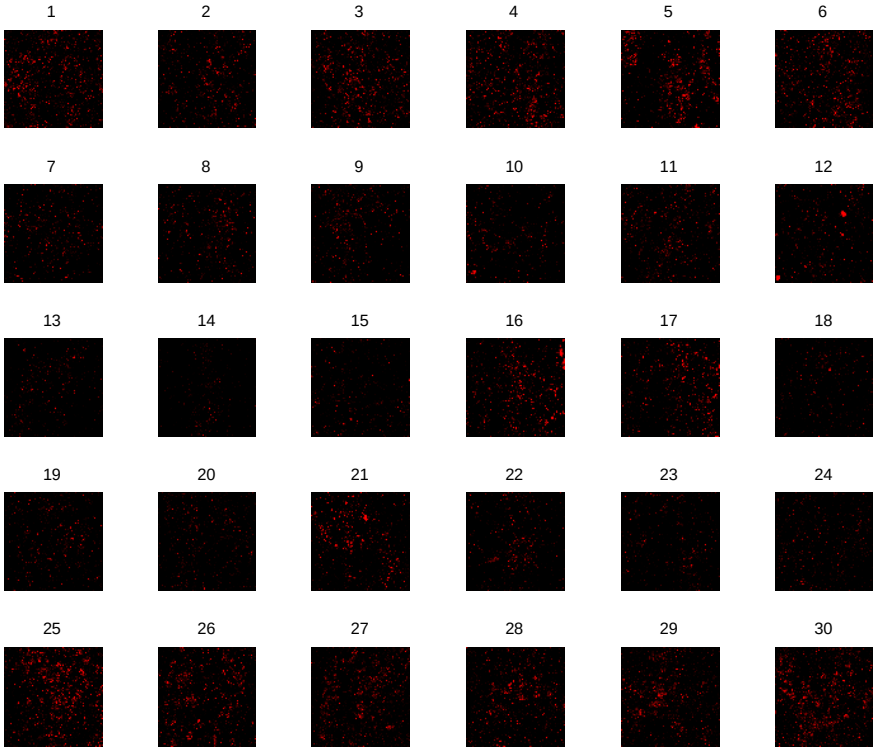


**Note:** Figure is continued on the next page.

8mm, 0.5mm/s, Gel #3

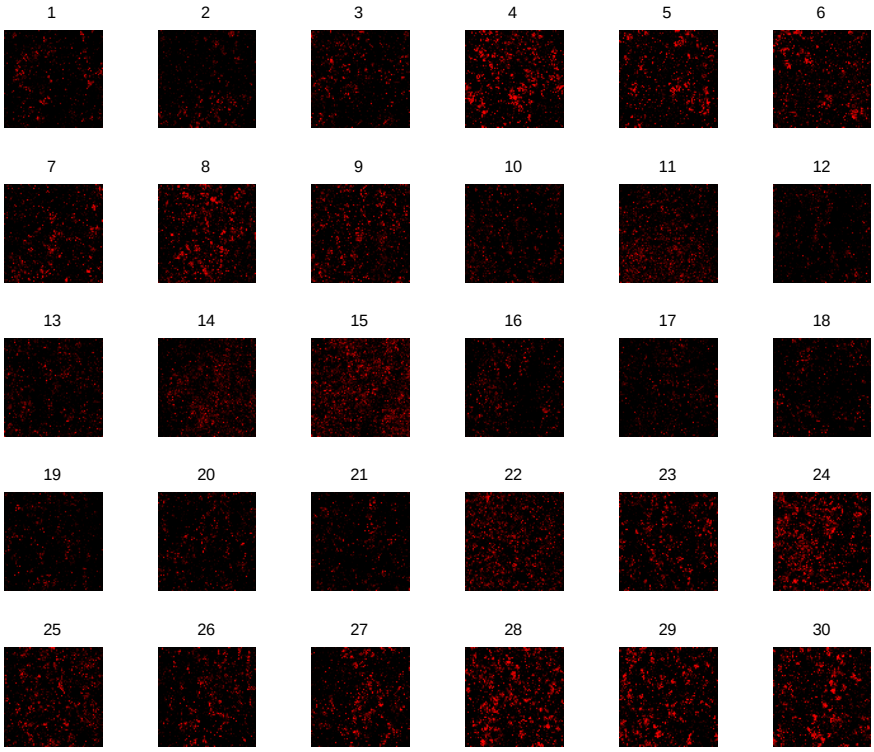


8mm, 0.5mm/s, Gel #4

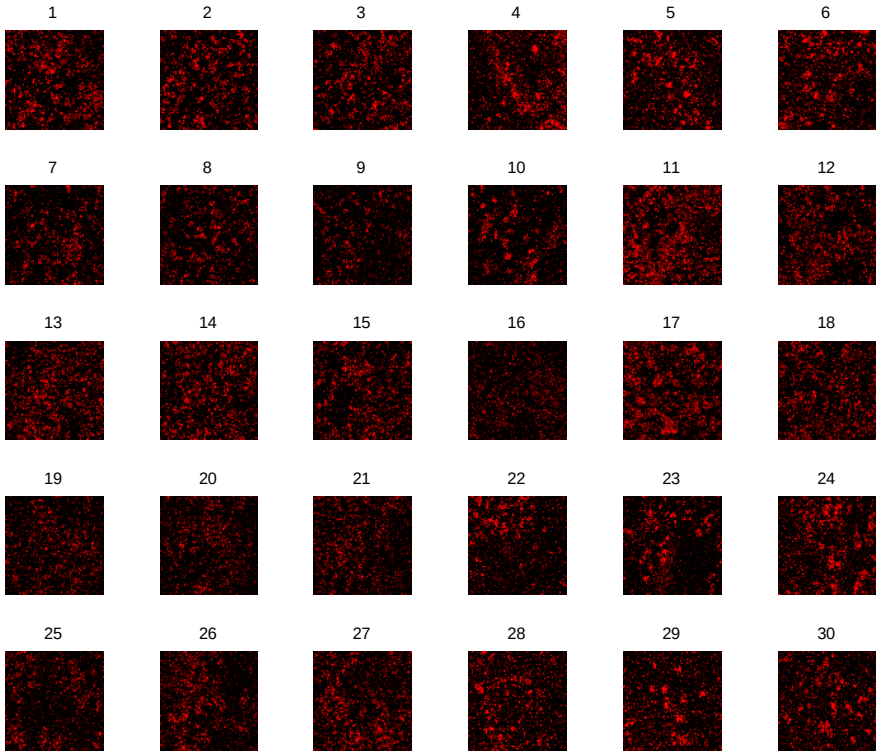


**Note:** Figure is continued on the next page.

8mm, 0.5mm/s, Gel #5

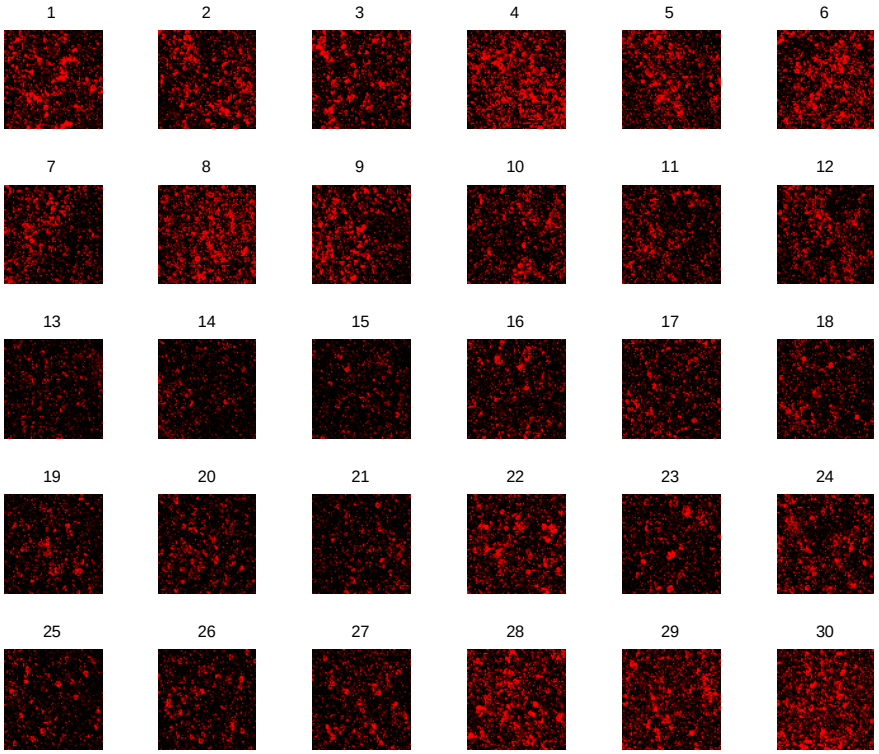


8mm, 0.5mm/s, Gel #6

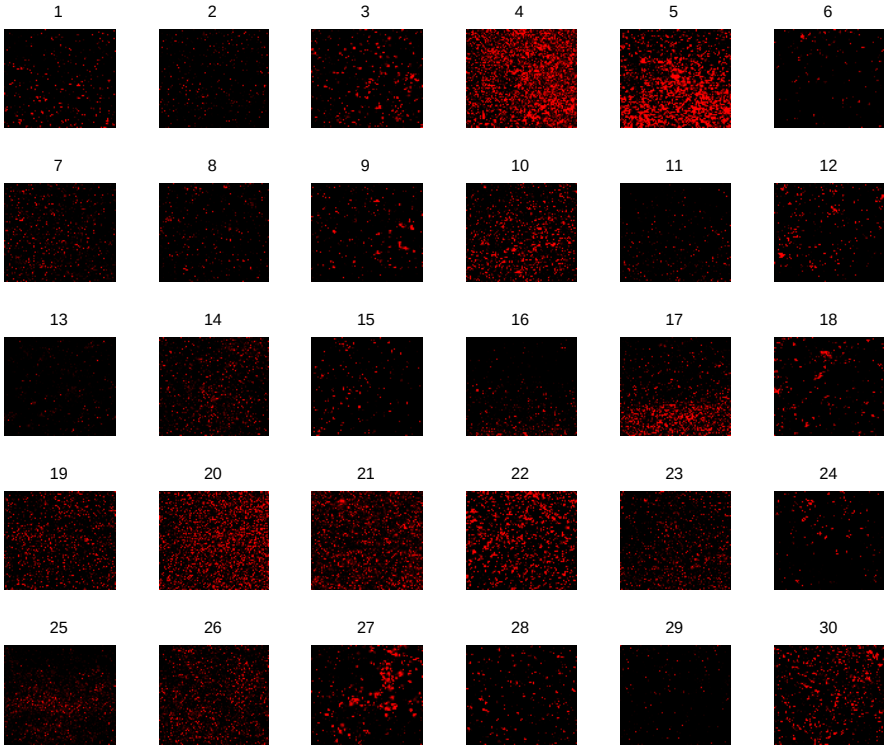


**Note:** Figure is continued on the next page.

8mm, 0.5mm/s, Gel #7

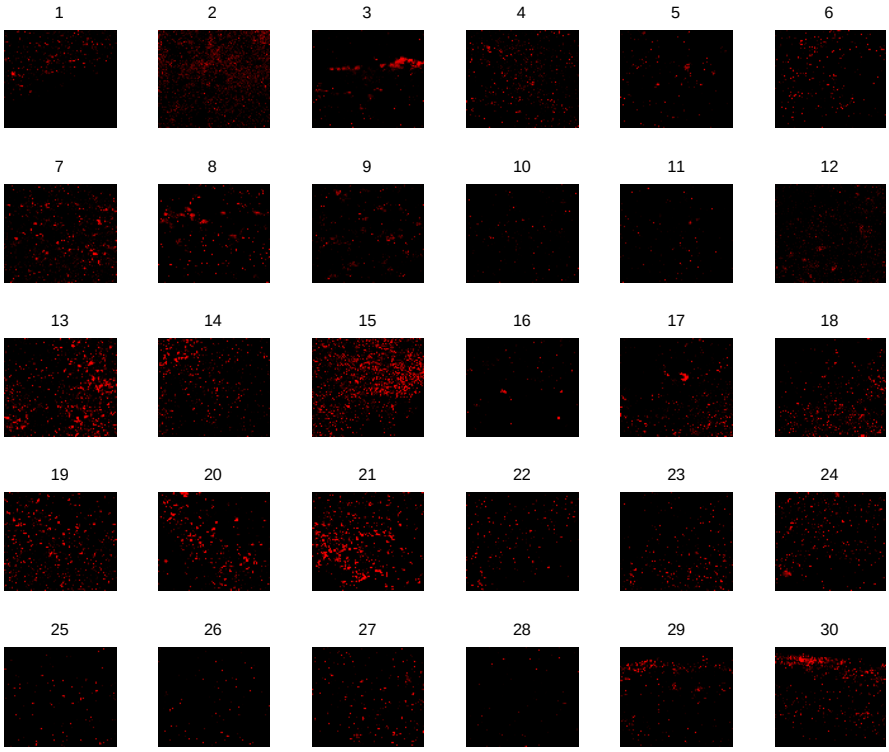


8mm, 0.5mm/s, Gel #8

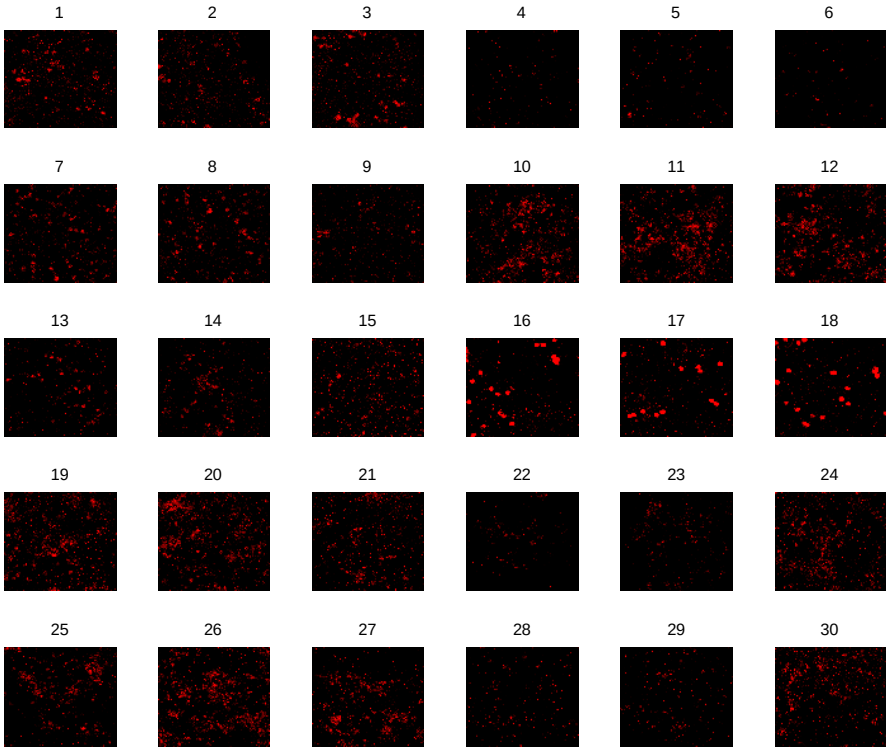


**Note:** Figure is continued on the next page.

8mm, 0.5mm/s, Gel #9

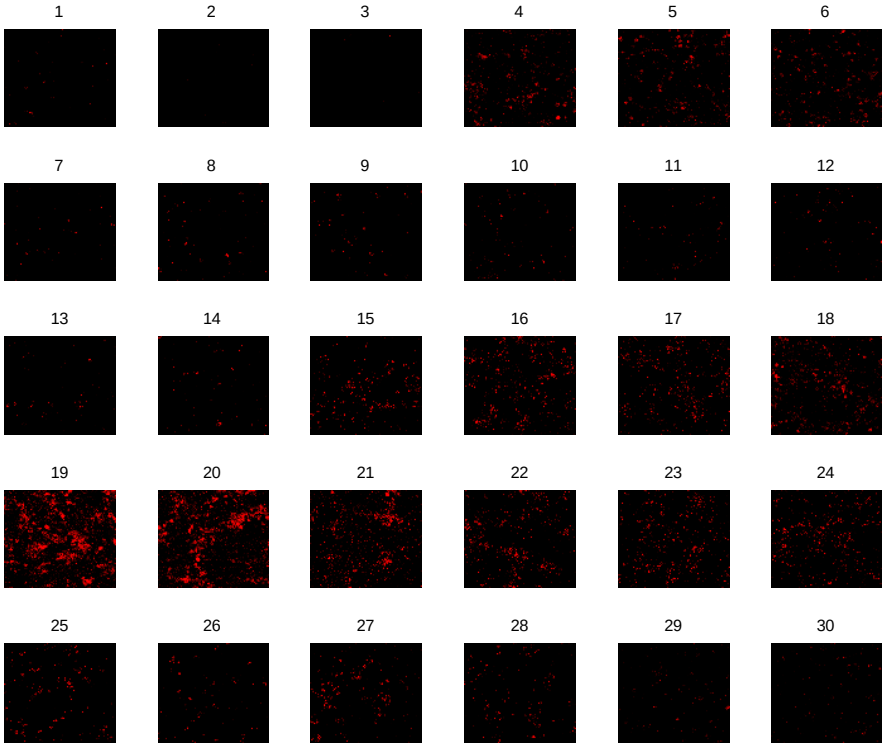


8mm, 3.5mm/s, Gel #1

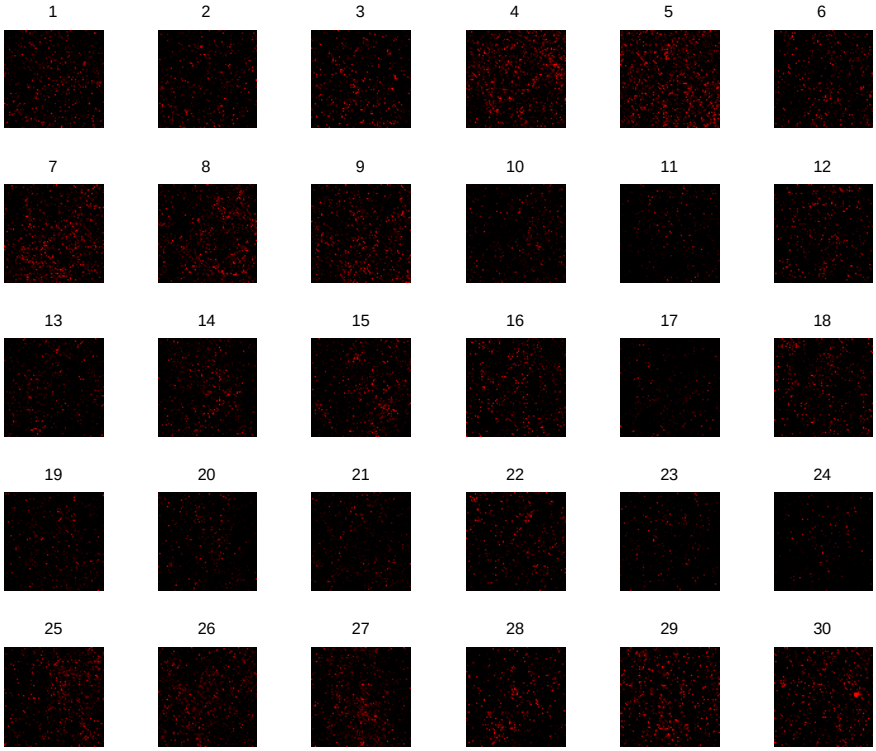


**Note:** Figure is continued on the next page.

8mm, 3.5mm/s, Gel #2

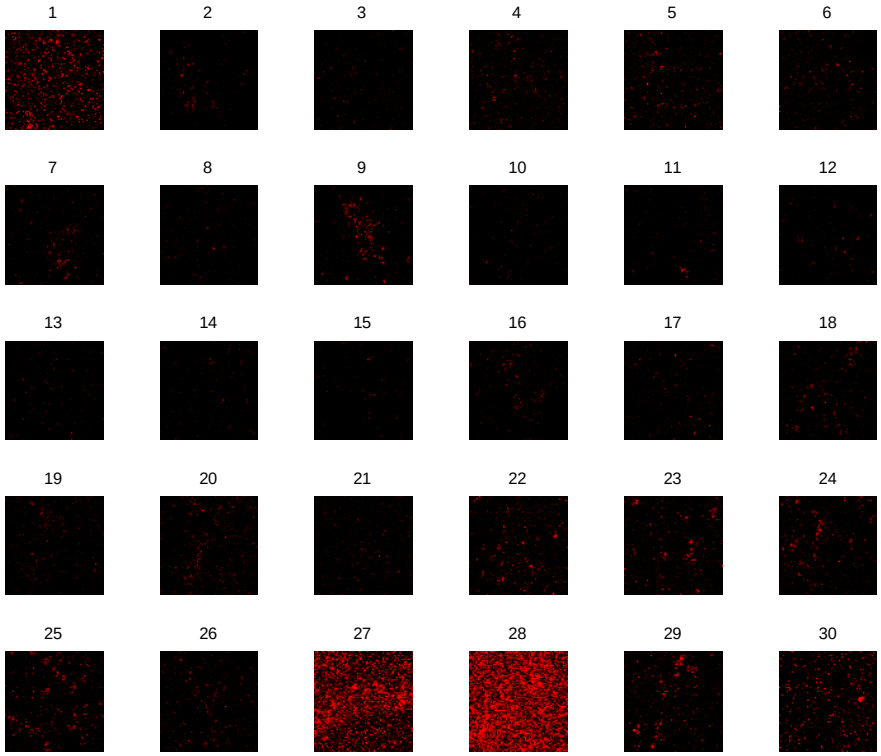


8mm, 3.5mm/s, Gel #3

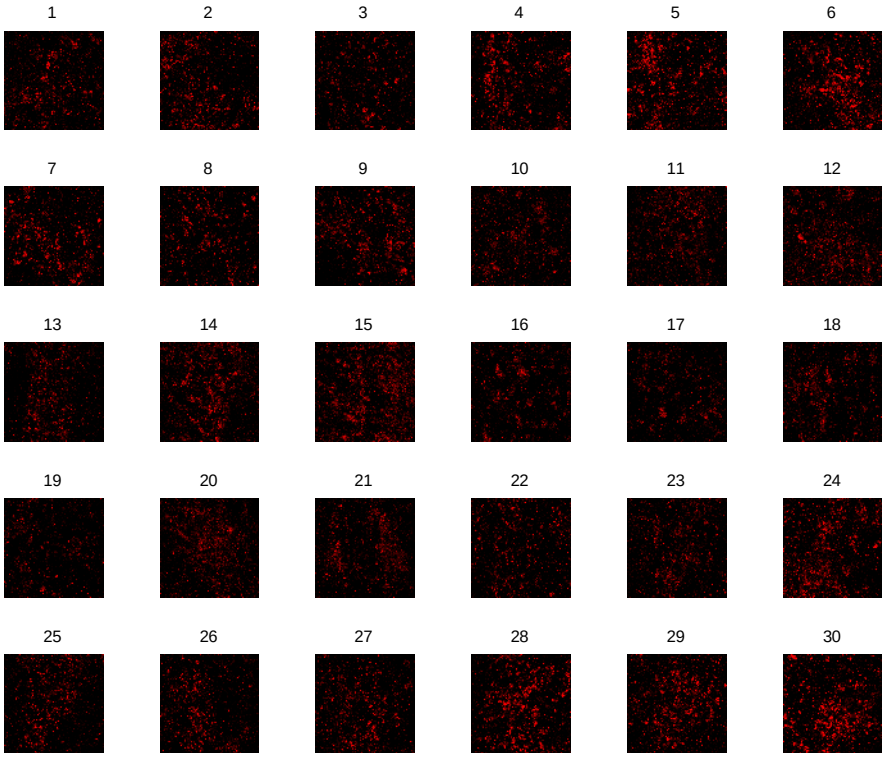


**Note:** Figure is continued on the next page.

8mm, 3.5mm/s, Gel #4

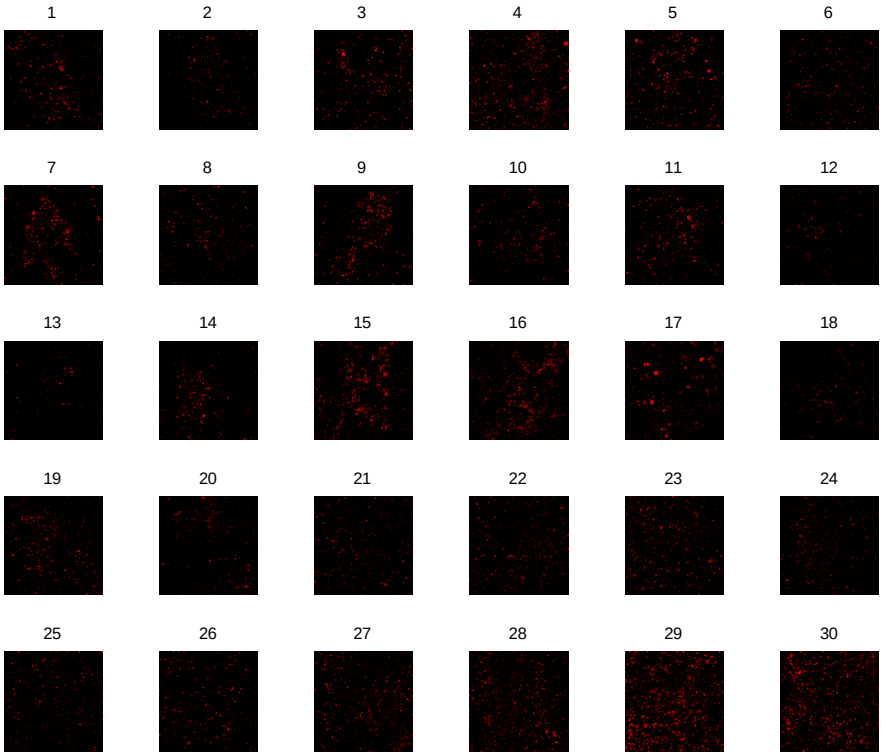


8mm, 3.5mm/s, Gel #5

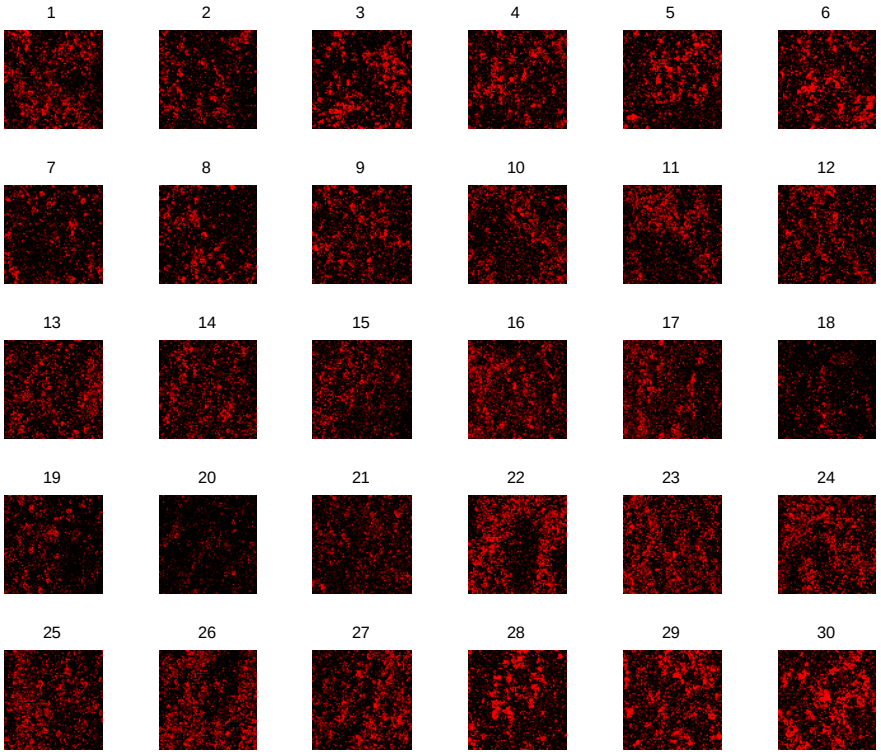


**Note:** Figure is continued on the next page.

8mm, 3.5mm/s, Gel #6

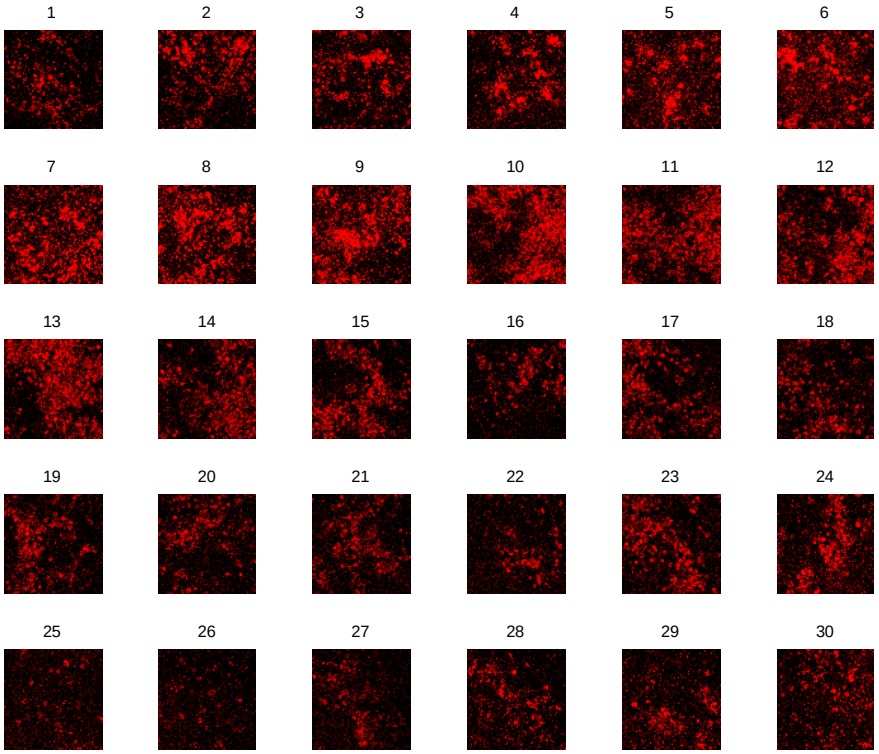


8mm, 3.5mm/s, Gel #7

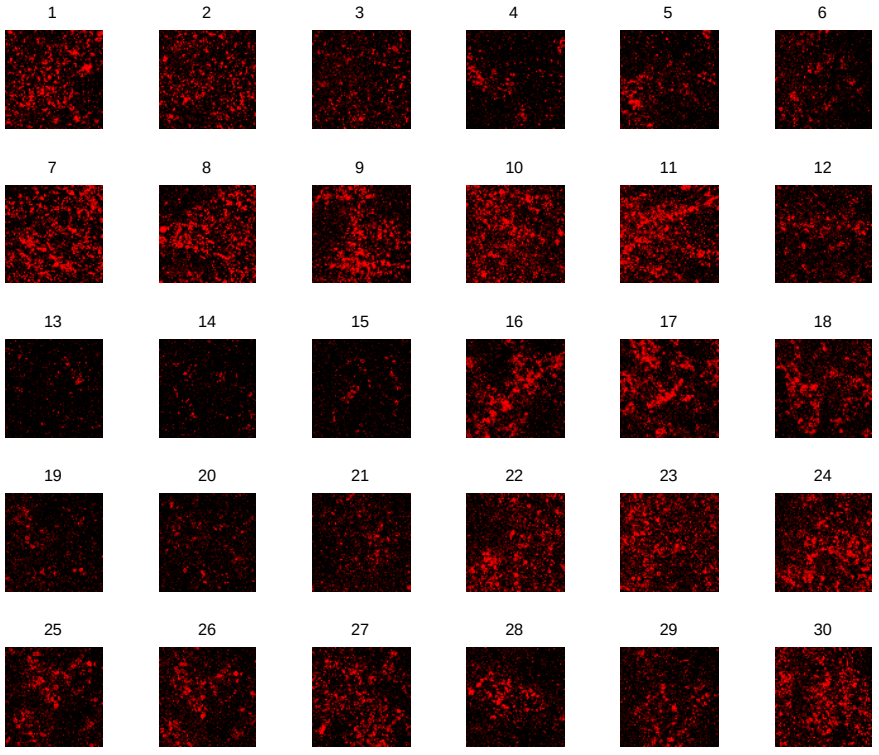


**Note:** Figure is continued on the next page.

8mm, 3.5mm/s, Gel #8

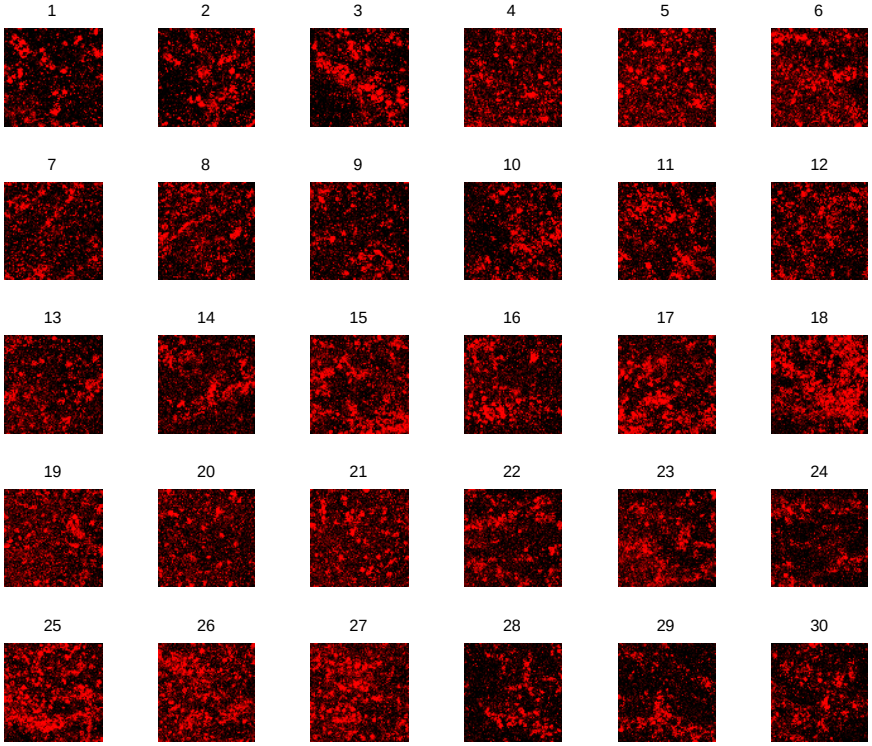


8mm, 3.5mm/s, Gel #9

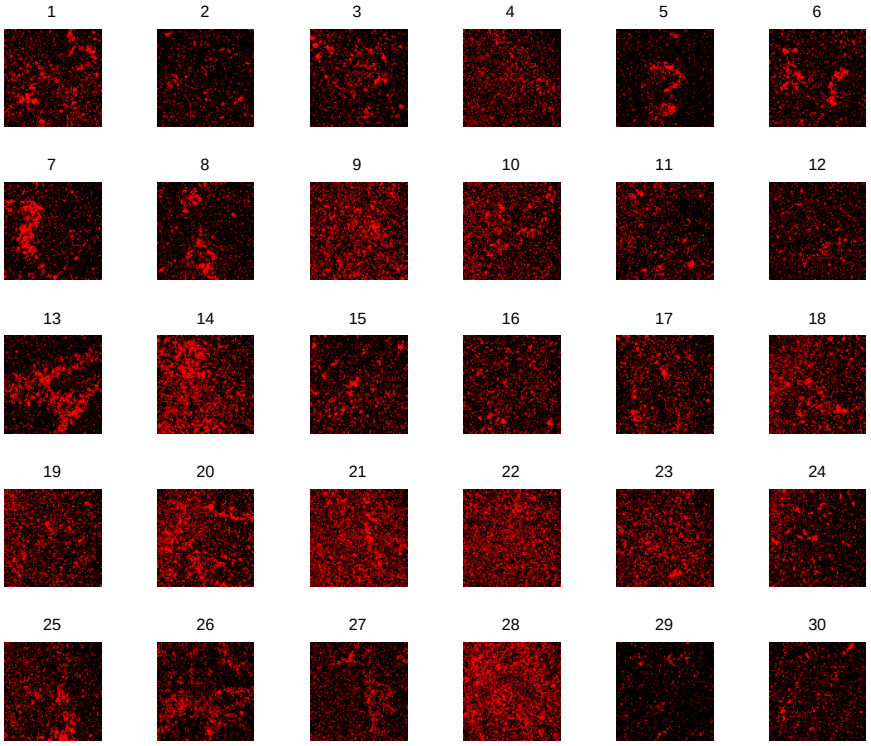

**Table C.5. Quantification of pERK in DRG-collagen constructs immediately after stretch to 4mm or 8mm at 0.5mm/s (Chapter 4).**

| Displacement | Gel | DRG | Normalized pERK in cell body | Normalized pERK in axons |
|---|---|---|---|---|
| 4mm | 1 | 1 | 0.95 | 1.21 |
| | | 2 | 1.07 | 0.99 |
| | | 3 | 0.74 | 0.67 |
| | | 4 | 1.00 | 1.08 |
| | | 5 | 0.80 | 1.20 |
| | | 6 | 0.85 | 0.72 |
| | | 7 | 0.55 | 0.93 |
| | | 8 | 1.00 | 1.23 |
| | 2 | 1 | 0.76 | 0.83 |
| | | 2 | 0.87 | 0.83 |
| | | 3 | 0.84 | 1.06 |
| | | 4 | 0.69 | 1.26 |
| | | 5 | 0.74 | 0.95 |
| | | 6 | 0.66 | 0.80 |
| | | 7 | 1.03 | 1.52 |
| | | 8 | 1.09 | 0.80 |
| | | 9 | 0.65 | 0.68 |
| | | 10 | 1.10 | 1.18 |
| | | 11 | 1.18 | 1.47 |
| | | 12 | 0.80 | 1.02 |
| | | 13 | 1.06 | 1.18 |
| | | 14 | 1.54 | 1.34 |
| 8mm | 1 | 1 | 2.70 | 1.94 |
| | | 2 | 2.36 | 1.96 |
| | | 3 | 4.07 | 2.43 |
| | | 4 | 3.16 | 2.21 |
| | 2 | 1 | 1.77 | 1.73 |
| | | 2 | 1.50 | 2.48 |
| | | 3 | 1.49 | 2.35 |
| | | 4 | 1.35 | 2.26 |
| | 3 | 1 | 0.92 | 1.01 |
| | | 2 | 0.87 | 0.87 |
| | | 3 | 0.97 | 1.11 |
| | | 4 | 1.10 | 1.00 |

**Figure C.6. Immunofluorescence images showing pERK expression (red) in DRG-collagen constructs immediately after stretch to 4mm or 8mm at 0.5mm/s. Collagen (green) was also immunolabeled in one NCC (8mm Gel #1) to show the shape of the gel.**

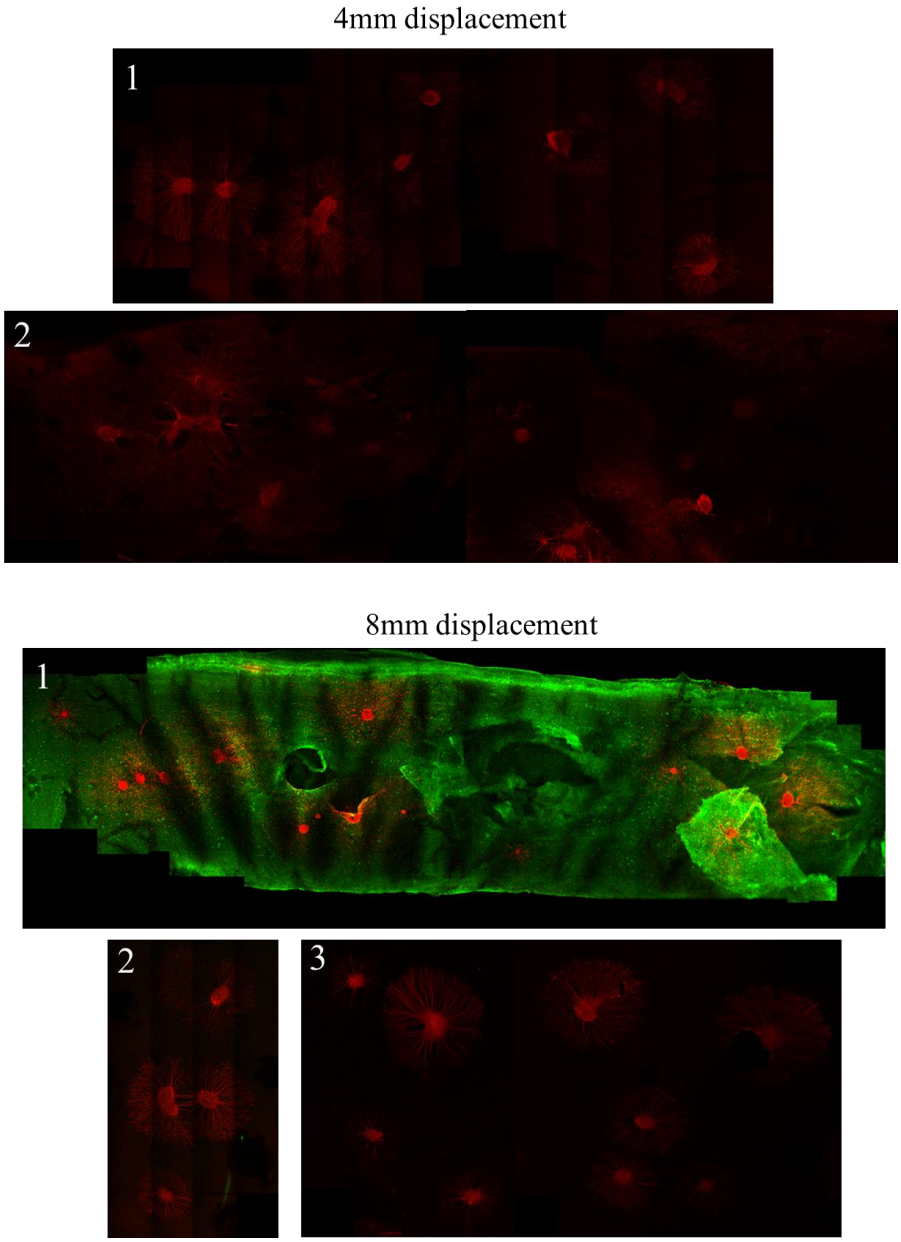

**Table C.6. Quantification of axonal FAK phosphorylation with & without RGD treatment in unloaded NCCs (Chapter 7).**

| Untreated | | | Treated | | |
|---|---|---|---|---|---|
| **Gel** | **DRG** | **Ratio of pFAK to total FAK** | **Gel** | **DRG** | **Ratio of pFAK to total FAK** |
| 1 | 1 | 0.82 | 1 | 1 | 0.61 |
| | 2 | 0.64 | | 2 | 0.73 |
| | 3 | 0.66 | | 3 | 0.60 |
| | 4 | 0.49 | | 4 | 0.75 |
| | 5 | 0.76 | | 6 | 0.81 |
| | 6 | 1.12 | 2 | 1 | 0.72 |
| 2 | 1 | 0.74 | | 2 | 0.90 |
| | 2 | 0.58 | | 3 | 0.51 |
| | 3 | 0.71 | | 4 | 0.49 |
| | 4 | 0.61 | | 5 | 0.52 |
| | 5 | 0.82 | 3 | 1 | 0.71 |
| | 6 | 0.76 | | 2 | 0.63 |
| 3 | 1 | 0.78 | | 3 | 0.58 |
| | 2 | 0.68 | | | |
| | 3 | 0.61 | | | |
| | 4 | 0.73 | | | |
| | 5 | 0.74 | | | |
| | 6 | 0.63 | | | |
| | 7 | 0.74 | | | |
| | 8 | 0.73 | | | |

**Figure C.7. Immunofluorescence images showing pFAK (red) & FAK (green) in unloaded NCCs with & without RGD treatment.**

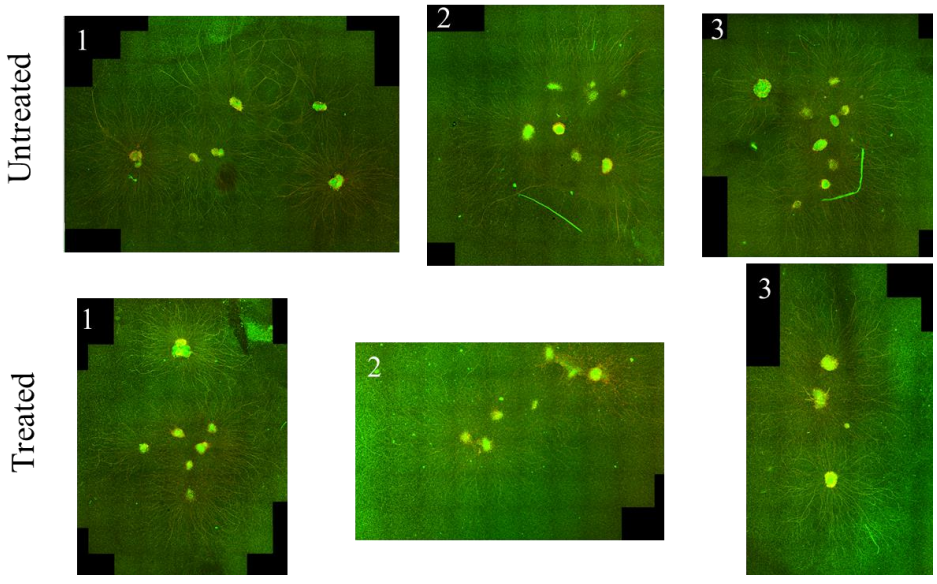

**Table C.7. Quantification of axonal SP expression normalized over unloaded control levels in unstretched & stretched NCC gels with & without RGD treatment (Chapter 7).**

| Unstretched | | | | | |
|---|---|---|---|---|---|
| Untreated | | | Treated | | |
| Gel | DRG | Normalized SP | Gel | DRG | Normalized SP |
| 1 | 1 | 0.87 | 1 | 1 | 0.88 |
| | 2 | 0.92 | | 2 | 0.86 |
| | 3 | 0.87 | | 3 | 0.94 |
| | 4 | 0.81 | | 4 | 0.86 |
| | 5 | 0.82 | | 5 | 1.10 |
| 2 | 1 | 1.32 | 2 | 1 | 0.86 |
| | 2 | 1.39 | | 2 | 0.91 |
| | | | | 3 | 0.89 |
| | | | | 4 | 1.38 |
| | | | | 5 | 1.33 |
| **Stretched** | | | | | |
| Untreated | | | Treated | | |
| Gel | DRG | Normalized SP | Gel | DRG | Normalized SP |
| 1 | 1 | 1.23 | 1 | 1 | 0.71 |
| | 2 | 1.22 | | 2 | 1.04 |
| | 3 | 0.84 | | 3 | 0.78 |
| 2 | 1 | 1.12 | | 4 | 0.81 |
| | 2 | 1.12 | | 5 | 0.86 |
| | 3 | 1.17 | | 6 | 0.94 |
| | 4 | 1.10 | | 7 | 0.64 |
| | 5 | 1.11 | | 8 | 0.68 |
| 3 | 1 | 1.13 | | 9 | 0.91 |
| | 2 | 0.77 | 2 | 1 | 1.25 |
| | 3 | 0.69 | | 2 | 1.33 |
| | | | | 3 | 1.15 |
| | | | | 4 | 1.04 |
| | | | | 5 | 0.83 |
| | | | 3 | 1 | 0.74 |
| | | | | 2 | 0.94 |
| | | | | 3 | 0.83 |
| | | | | 4 | 1.16 |
| | | | | 5 | 0.80 |
| | | | | 6 | 0.84 |

**Figure C.8. Immunofluorescence images showing SP (green) & βIII-tubulin (blue) expression in unstretched & stretched NCCs with & without RGD treatment.**

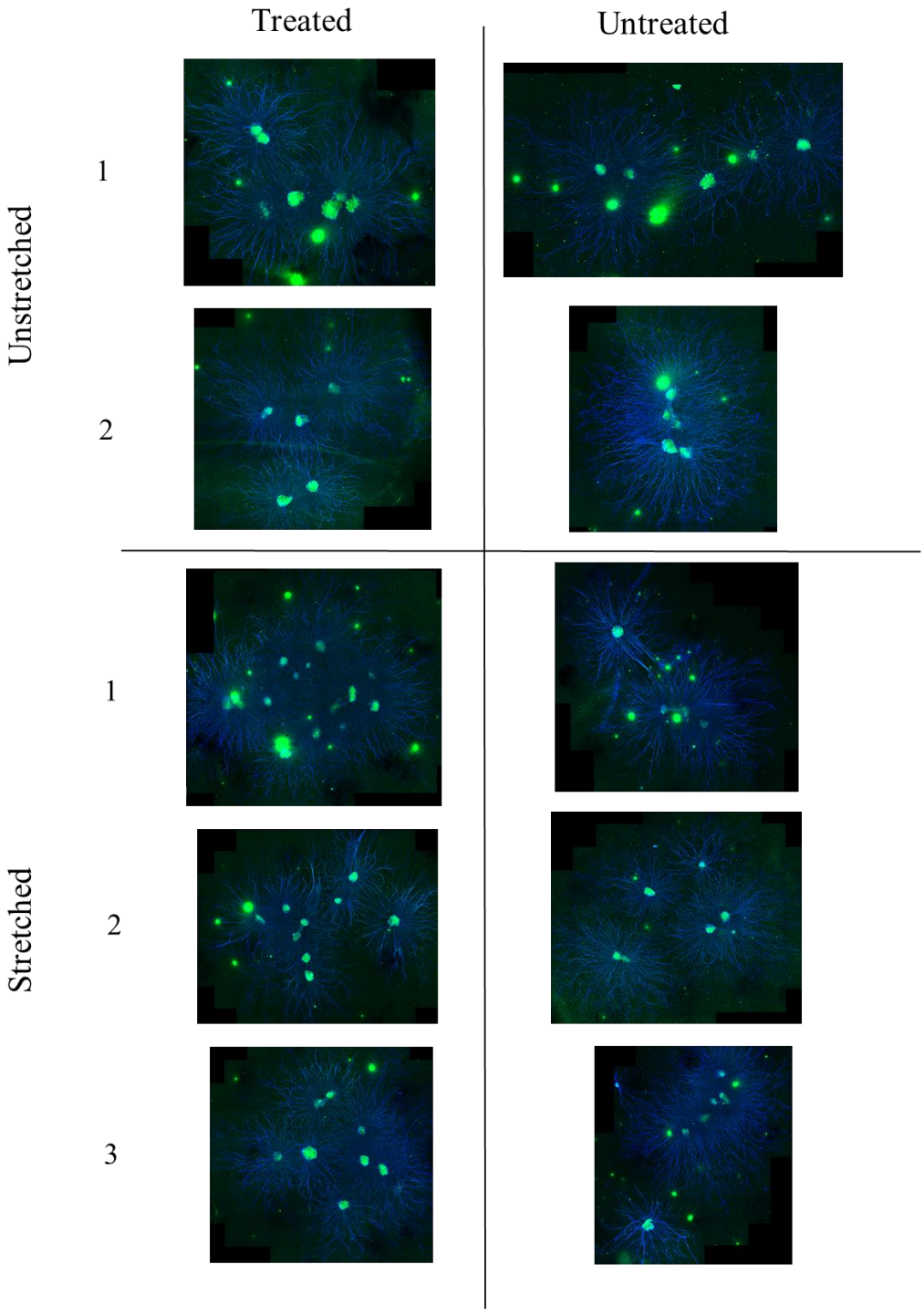

**Table C.8. Quantification of axonal SP expression in each region of interest (ROI) in unstretched & stretched NCCs, with TC-I15 treatment (0μM, 10μM, 100μM, 1000μM) (Chapter 7).**

| Normalized SP in unstretched NCCs | | | | | |
|---|---|---|---|---|---|
| **Gel** | **ROI** | **0mM** | **10mM** | **100mM** | **1000mM** |
| 1 | 1 | 0.90 | 0.83 | 0.92 | 1.12 |
| | 2 | 0.75 | 1.02 | 0.85 | 1.23 |
| | 3 | – | 1.39 | – | – |
| 2 | 1 | 0.99 | 0.88 | 1.10 | 0.88 |
| | 2 | 1.35 | 1.15 | 0.98 | 1.02 |
| 3 | 1 | 0.77 | 1.10 | 1.28 | 1.07 |
| | 2 | 1.28 | 1.23 | 1.15 | 0.90 |
| | 3 | 0.60 | – | – | – |
| 4 | 1 | 1.40 | | | |
| | 2 | 1.43 | | | |
| | 3 | 1.43 | | | |
| 5 | 1 | 0.67 | | | |
| | 2 | 0.79 | | | |
| | 3 | 0.93 | | | |
| 6 | 1 | 0.97 | | | |
| | 2 | 1.03 | | | |
| **Normalized SP in stretched NCCs** | | | | | |
| **Gel** | **ROI** | **0mM** | **10mM** | **100mM** | **1000mM** |
| 1 | 1 | 1.56 | 1.66 | 0.90 | 0.93 |
| | 2 | 1.59 | 1.64 | 1.04 | 0.74 |
| | 3 | 1.91 | 2.02 | 0.74 | -- |
| 2 | 1 | 1.83 | 1.70 | 1.06 | 0.91 |
| | 2 | 1.87 | 1.60 | 0.87 | 0.63 |
| | 3 | 1.98 | 1.23 | 0.97 | 1.09 |
| 3 | 1 | 1.27 | 1.77 | 1.48 | 0.79 |
| | 2 | 2.03 | 1.17 | 1.32 | 0.74 |
| | 3 | 2.71 | 1.34 | 1.56 | 1.12 |
| 4 | 1 | 1.78 | 1.31 | 0.89 | 1.53 |
| | 2 | 1.36 | 1.63 | 0.78 | 1.68 |
| | 3 | 1.22 | 3.02 | 0.66 | 1.23 |
| | 4 | – | 1.36 | 1.80 | 0.88 |
| 5 | 1 | 1.30 | | 0.85 | 0.61 |
| | 2 | 1.66 | | 1.58 | 0.98 |
| | 3 | – | | 0.70 | – |

**Note:** Missing values (–) are due to an unequal number of ROIs available for analysis.

**Figure C.9. Immunofluorescence images showing SP in unstretched & stretched NCCs, with TC-I15 treatment (0μM, 10μM, 100μM, 1000μM).**

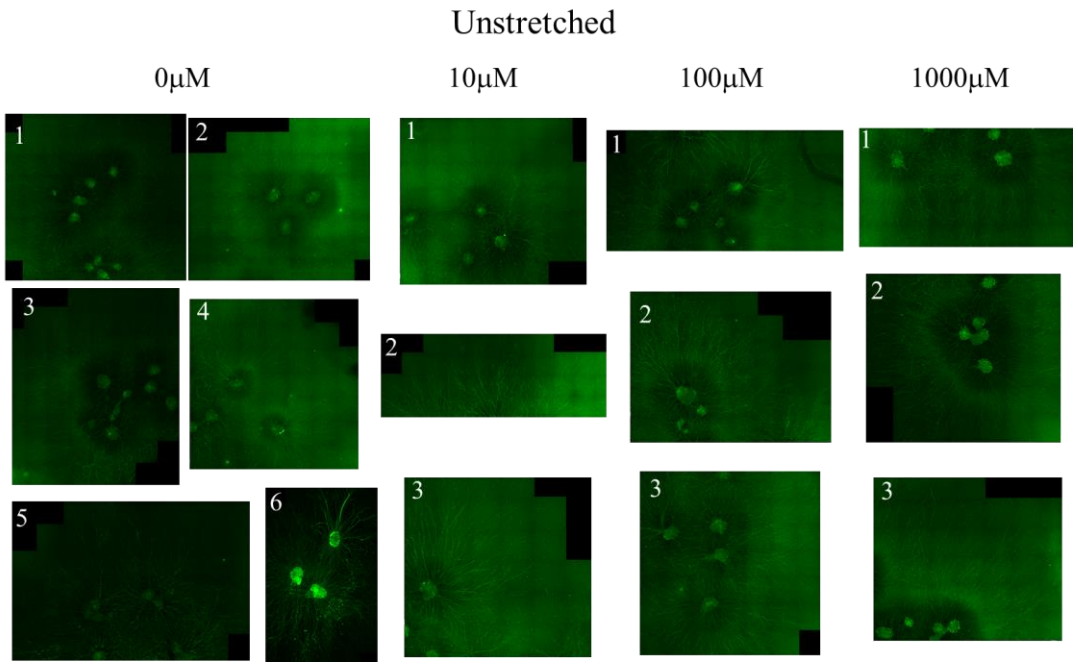


**Note:** Figure is continued on the next page.

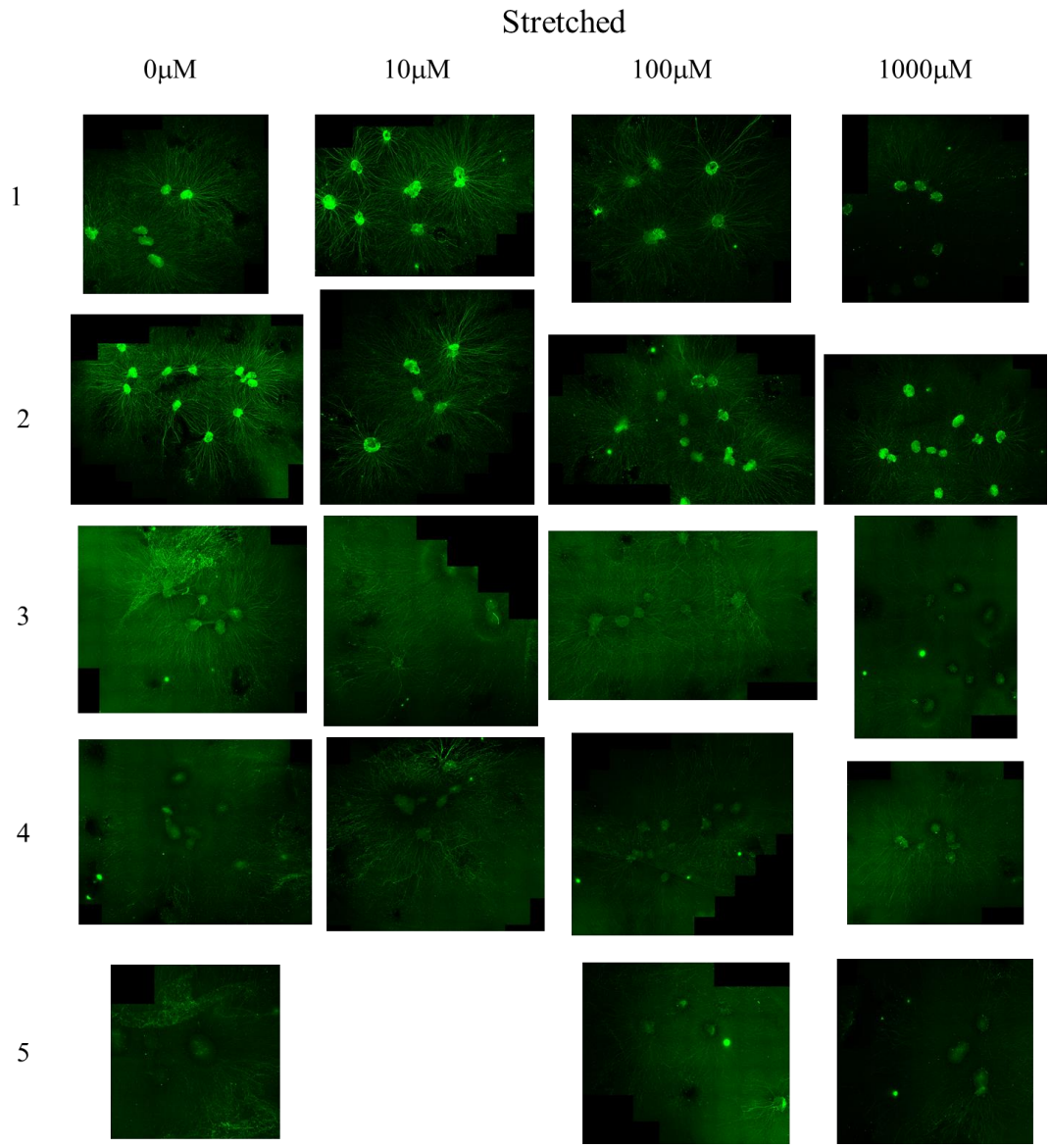
Stretched
0μM
10μM
100μM
1000μM
1
2
3
4
5

**Table C.9. Quantification of axonal SP expression in unstretched & stretched NCCs with & without Y27632 treatment (Chapter 8).**

| Unstretched | | | | | | Stretched | | | | | |
|---|---|---|---|---|---|---|---|---|---|---|---|
| Untreated | | | Treated | | | Untreated | | | Treated | | |
| Gel | DRG | SP | Gel | DRG | SP | Gel | DRG | SP | Gel | DRG | SP |
| 1 | 1 | 1.19 | 1 | 1 | 1.12 | 1 | 1 | 1.61 | 1 | 1 | 1.31 |
| | 2 | 1.03 | | 2 | 1.08 | | 2 | 1.68 | | 2 | 1.39 |
| | 3 | 1.10 | 2 | 1 | 1.46 | | 3 | 1.33 | | 3 | 1.30 |
| 2 | 1 | 0.87 | | 2 | 1.30 | | 4 | 1.27 | 2 | 1 | 1.27 |
| 3 | 1 | 1.04 | | 3 | 1.46 | | 5 | 1.21 | | 2 | 1.15 |
| | 2 | 0.86 | | 4 | 1.32 | 2 | 1 | 1.27 | | 3 | 1.36 |
| | 3 | 0.77 | 3 | 1 | 1.00 | | 2 | 1.14 | | 4 | 1.30 |
| 4 | 1 | 1.08 | | 2 | 1.29 | | 3 | 1.27 | | 5 | 1.29 |
| | 2 | 1.38 | | 3 | 1.01 | | 4 | 1.22 | | 6 | 1.23 |
| 5 | 1 | 1.00 | 4 | 1 | 1.09 | 3 | 1 | 1.32 | 3 | 1 | 0.91 |
| 6 | 1 | 1.02 | | 2 | 0.86 | | 2 | 1.37 | | 2 | 0.64 |
| | 2 | 1.08 | | 3 | 0.69 | | 3 | 1.44 | | 3 | 0.65 |
| | 3 | 0.77 | 5 | 1 | 1.11 | | 4 | 1.55 | | 4 | 0.61 |
| 7 | 1 | 1.19 | | 2 | 0.98 | 4 | 1 | 1.45 | | 5 | 0.70 |
| | 2 | 0.86 | | 3 | 0.84 | | 2 | 1.51 | | 6 | 0.65 |
| | 3 | 1.08 | 6 | 1 | 0.81 | | 3 | 1.15 | 4 | 1 | 0.54 |
| | | | | 2 | 0.95 | | 4 | 1.36 | | 2 | 0.42 |
| | | | | | | 5 | 1 | 1.57 | | 3 | 0.45 |
| | | | | | | | 2 | 1.05 | | 4 | 0.54 |
| | | | | | | | 3 | 1.11 | 5 | 1 | 0.63 |
| | | | | | | | 4 | 0.92 | | 2 | 0.73 |
| | | | | | | 6 | 1 | 1.26 | | 3 | 0.64 |
| | | | | | | | 2 | 1.50 | 6 | 1 | 0.72 |
| | | | | | | | 3 | 1.27 | | 2 | 0.88 |
| | | | | | | | 4 | 1.27 | | 3 | 1.03 |
| | | | | | | 7 | 1 | 1.19 | | | |
| | | | | | | | 2 | 1.17 | | | |
| | | | | | | | 3 | 1.22 | | | |
| | | | | | | | 4 | 1.08 | | | |
| | | | | | | | 5 | 1.33 | | | |
| | | | | | | 8 | 1 | 1.12 | | | |
| | | | | | | | 2 | 1.26 | | | |
| | | | | | | | 3 | 1.32 | | | |
| | | | | | | | 4 | 1.21 | | | |
| | | | | | | | 5 | 1.22 | | | |

**Figure C.10. Immunofluorescence images showing SP (green) & βIII-tubulin (blue) expression in unstretched & stretched NCCs with & without Y27632 treatment.**

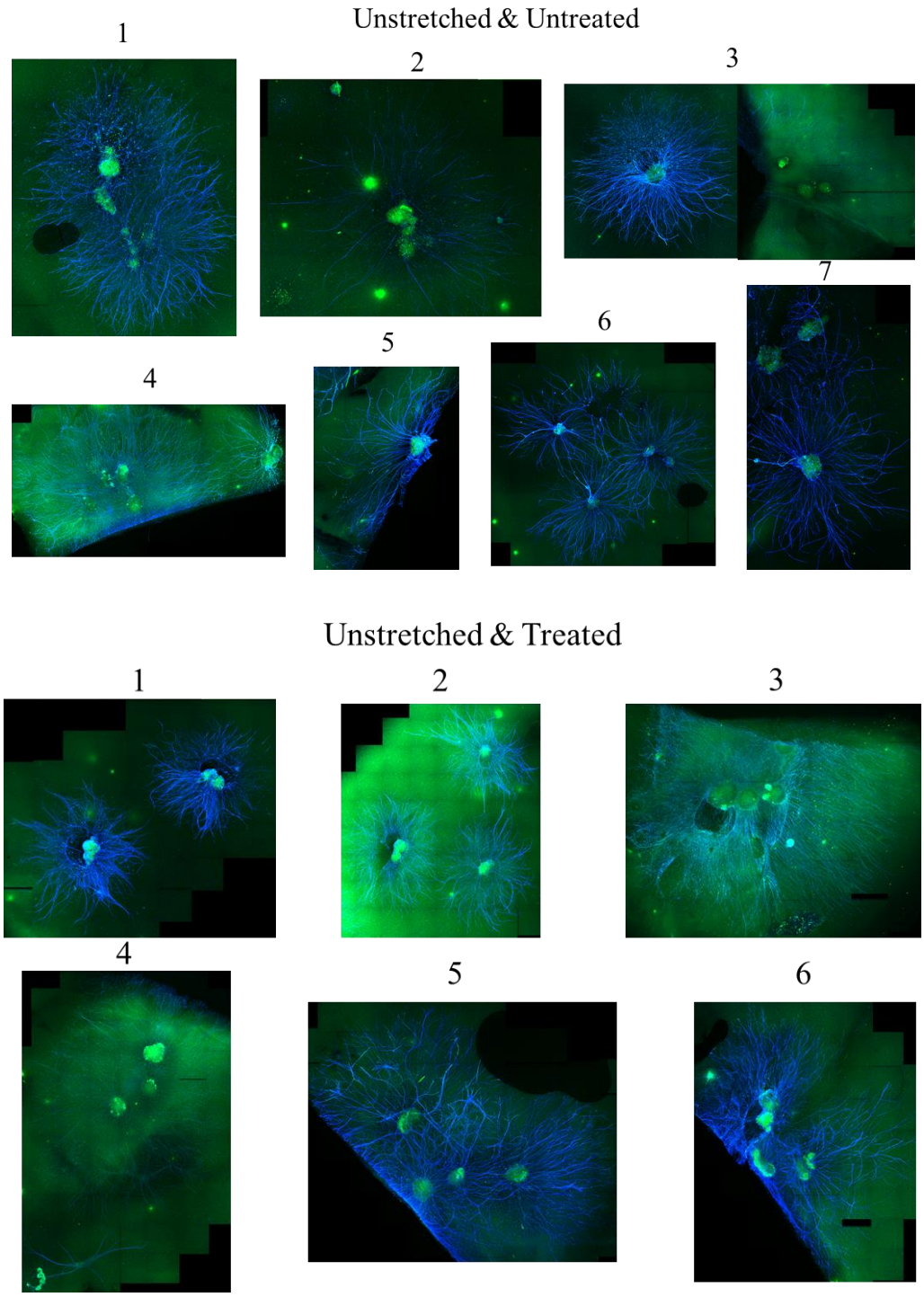


**Note:** Figure is continued on the next page.

Stretched & Untreated

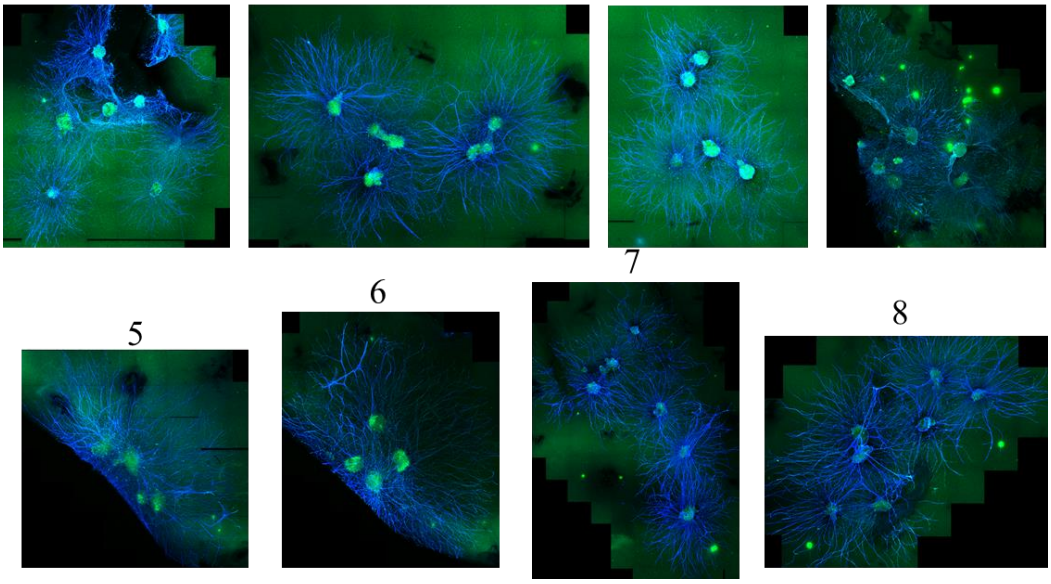


Stretched & Treated

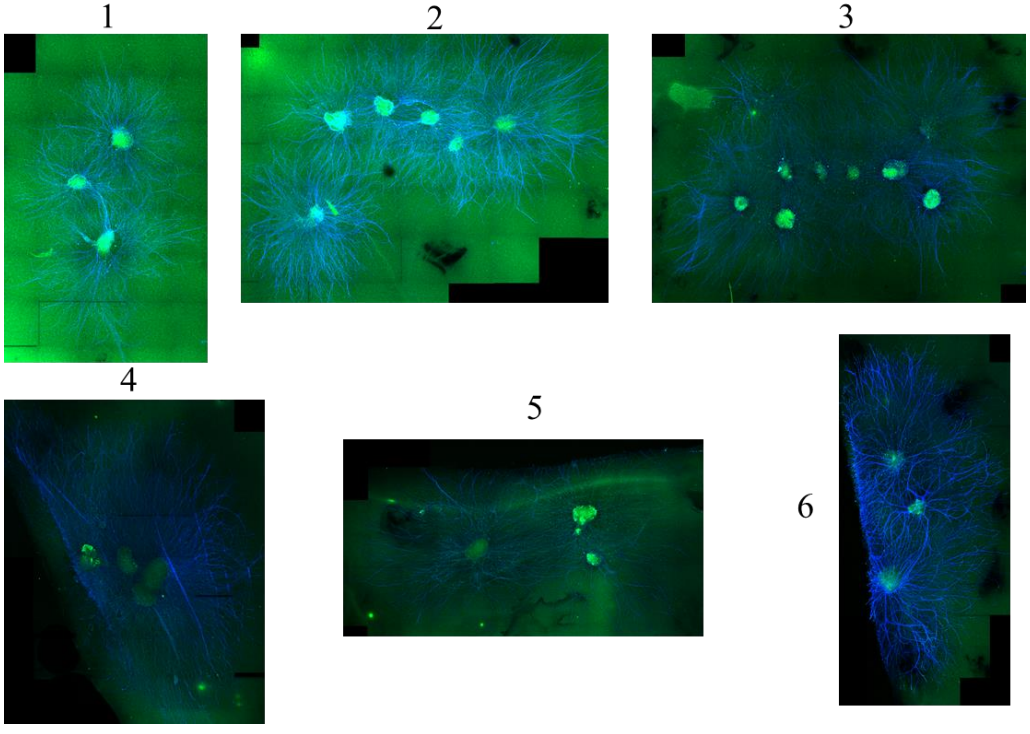

# APPENDIX D

# MATLAB Code for Automated Densitometry

This appendix contains the MATLAB code that performs automated densitometry on images of fluorescently labeled cortical-collagen cultures and rat spinal cord. In particular, it was used to analyze neuronal pERK expression in studies from Chapter 4 and spinal expression of substance P and Iba1 in studies summarized in Chapter 8. This MATLAB script (*densitometry_manual_threshold_fluor.m*) quantifies the percent positively labeled pixels in fluorescent images. The inputs of this script are RGB images or uniformly cropped ROIs, which must be saved in the same file directory as the MATLAB code. Prior to running the script, the user must specify which images to analyze by changing the file names in variable "D". The threshold (0-250) for positive pixels, denoted as "pos_thresh" in the code, is first defined based on baseline levels in the images from the unloaded control gels or un-operated normal rats, in the studies in this thesis. Once the script computes the percent positively labeled pixels for all images, the user needs to manually type variable names in the command window in order to obtain results. Entering "Iname" into the command window returns a list of the images that were processed; "percpos" returns the calculated percent positive pixels.

## densitometry_manual_threshold_fluor.m

```
%% This script was written to calculate and visualize percent positive
%% pixels per image.

%%To run the file, you want to create an excel file that has the detailed
%% information about the images to be analyzed, then number those images
%% with a common name that has an ordered numerical (1, 2...) ending.

%% NOTE: for the excel file, please have the following columns (in
%% order): rat #, tissue type, injury type, image no., threshold, raw
%% results, normalized results. Number normal controls last.

%% This code requires MATLAB 7.0 (or higher) and imaging toolbox.

%% Written by Ling Dong (modified from K. Quinn) on Feb 2, 2009.
%% Modified by Kristen Nicholson December 2009

clear all;
close all;

D = dir('*.tif'); % specify which images to analyze (* = wildcard character)

for k=1:length(D);

    file=D(k).name; % reads file in

    imag_orig = imread(file);  % load the image

    % imag = imag_orig(:,:,1); % grab the red labeled image
    imag = imag_orig(:,:,2); % grab the green labeled image
    intensity(k) = mean(mean(imag));
    invImag = 255-imag;
    imag = invImag;

    % calc number of pixels
    [a b]=size(imag);
    tsize=a*b;
    low=double(min(imag(:)));
    high=double(max(imag(:)));
    whiteSpace = 0.85*high;
    pos_thresh = 140; % input based on normal run
    % higher value corresponds to a higher +ive threshold.

    backg=sum(sum(imag>whiteSpace));
    posp=sum(sum(imag<pos_thresh));
    % calc percent of positive pixels in tissue
    percpos(k)=  posp/(tsize-backg);
    tpost(k) = posp;
    Iname(k) = {file};

    % map out pos and neg pixels
    pmap=(imag<pos_thresh);
```

```
    nmap=(imag>whiteSpace);

    %   make figure for each image, if you are processing a bunch of images,
    %   you may want to comment this part out
    % make positive pixels more green, and background pixels less blue
    imag1(:,:,1)=double(imag)/255;
    imag1(:,:,2)=(1-pmap).*double(imag)/255+pmap;
    imag1(:,:,3)=double(imag)/255.*(1-nmap);

    h = figure(1);
    subplot(3,1,3);
    subimage(imag);
    axis image
    axis off
    subplot(3,1,2);
    subimage(imag1);
    axis image
    axis off
    colormap gray
    subplot(3,1,1);
    subimage(imag_orig)
    axis image
    axis off
    drawnow

    % save the gray-scale, inverted, and pos/neg images as a new figure
    saveas(h, ['densitometry' D(k).name], 'jpg')

    clear imag imag1
    clf
end
```

# APPENDIX E

# Neuronal Shape & Orientation in Response to Neuron-Collagen Construct Stretch

Table E.1 summarizes the neuronal aspect ratio and orientation data collected after NCC stretch in studies presented in Chapter 4 (Figure 4.8). The aspect ratios and orientation angles of the neurons included are measured from NCCs that underwent loading: (1) at 0.5mm/s to 4mm displacement (n=5 NCC), (2) at 3.5mm/s to 4mm displacement (n=3 NCC), (3) at 0.5mm/s to 8mm displacement (n=5 NCC), or (4) at 3.5mm/s rate to 8mm displacement (n=5 NCC). The aspect ratio and orientation were assessed from 30 neurons in each NCC and was measured directly in the ImageJ software by tracing the outer boundary of the cell and setting *shape descriptors* as measurements. In contrast, to measure the orientation angle, an assessor who was blinded to the experimental groups was required to define the major axis of the neuron based on visual assessment. When the major axis was difficult to identify (i.e. an aspect ratio close to 1), the orientation angle was recorded as "round". Since fewer NCCs were stretched at 3.5mm/s to 4mm displacement as compared to the other loading conditions, an asterisk (*) in the table indicates that no data are available for the 3.5mm/s, 4mm displacement loading group.

**Table E.1. Summary of neuronal aspect ratio & orientation after NCC stretch.**

| Neuron | Aspect ratio | | | | Orientation (°) | | | |
|---|---|---|---|---|---|---|---|---|
| **Magnitude (mm)** | **4** | **4** | **8** | **8** | **4** | **4** | **8** | **8** |
| **Rate (mm/s)** | **0.5** | **3.5** | **0.5** | **3.5** | **0.5** | **3.5** | **0.5** | **3.5** |
| 1 | 1.2 | 1.2 | 1.4 | 1.3 | 56.3 | 83.7 | 85.1 | 18.3 |
| 2 | 1.8 | 1.2 | 1.1 | 1.2 | 78.3 | 87.5 | round | 51.2 |
| 3 | 1.5 | 1.4 | 1.6 | 1.3 | 72.5 | 50.9 | 36.0 | 83.6 |
| 4 | 1.1 | 1.2 | 1.4 | 1.4 | 52.7 | 67.5 | 47.3 | 47.2 |
| 5 | 1.5 | 1.5 | 1.4 | 1.4 | 90.0 | 85.2 | 88.0 | 82.1 |
| 6 | 1.9 | 1.3 | 1.4 | 1.4 | 39.7 | 54.1 | 79.5 | 88.3 |
| 7 | 1.6 | 1.4 | 1.3 | 1.4 | 74.3 | 43.0 | 77.5 | 47.8 |
| 8 | 1.7 | 1.6 | 1.5 | 1.4 | 72.6 | 15.0 | 66.9 | 36.1 |
| 9 | 1.7 | 1.4 | 1.3 | 1.2 | 87.5 | 29.7 | 87.3 | 51.4 |
| 10 | 1.5 | 1.7 | 1.3 | 1.4 | 81.9 | 22.5 | 69.4 | 20.6 |
| 11 | 1.8 | 1.3 | 1.4 | 1.4 | 87.8 | 33.0 | 88.1 | 58.3 |
| 12 | 1.2 | 1.3 | 1.4 | 1.4 | 69.0 | 21.3 | 85.3 | 56.9 |
| 13 | 1.6 | 1.3 | 1.2 | 1.3 | 70.8 | 58.4 | 34.2 | 26.1 |
| 14 | 1.6 | 1.3 | 1.4 | 1.5 | 45.0 | 31.4 | 57.8 | 52.5 |
| 15 | 1.4 | 1.6 | 1.4 | 1.7 | 80.0 | 30.4 | 51.0 | 63.4 |
| 16 | 1.4 | 1.2 | 1.4 | 1.1 | 79.6 | 63.9 | 74.3 | 51.5 |
| 17 | 1.4 | 1.1 | 1.2 | 1.4 | 31.6 | 85.1 | 56.3 | 66.0 |
| 18 | 1.7 | 1.1 | 1.2 | 1.3 | 45.0 | 75.3 | 65.8 | 45.0 |
| 19 | 1.2 | 1.5 | 1.2 | 1.4 | 51.3 | 88.6 | 69.6 | 82.4 |
| 20 | 1.3 | 1.3 | 1.3 | 1.2 | 85.5 | 71.0 | 77.9 | 55.9 |
| 21 | 1.2 | 1.2 | 1.3 | 1.3 | 55.5 | 56.9 | 45.0 | 60.0 |
| 22 | 1.4 | 1.5 | 1.3 | 1.3 | 41.6 | 36.4 | 81.6 | 56.7 |
| 23 | 2.0 | 1.7 | 1.3 | 1.2 | 82.9 | 42.2 | 66.9 | 86.1 |
| 24 | 1.5 | 1.2 | 1.2 | 1.4 | 35.3 | 58.9 | 51.7 | 70.4 |
| 25 | 1.2 | 1.2 | 1.2 | 1.3 | 80.4 | 40.4 | 81.0 | 63.8 |
| 26 | 1.3 | 1.5 | 1.3 | 1.3 | 43.8 | 29.2 | 74.6 | 52.0 |
| 27 | 1.6 | 1.2 | 1.3 | 1.2 | 77.0 | 88.8 | 78.7 | 49.4 |
| 28 | 1.3 | 1.5 | 1.6 | 1.4 | 40.6 | 43.2 | 47.7 | 40.8 |
| 29 | 1.1 | 1.3 | 1.3 | 1.4 | round | 80.9 | 88.2 | 67.2 |
| 30 | 1.2 | 1.3 | 1.3 | 1.2 | 80.0 | 88.1 | 67.7 | 29.5 |
| 31 | 1.6 | 1.7 | 1.3 | 1.6 | 12.7 | 45.7 | 45.5 | 47.4 |
| 32 | 1.3 | 1.2 | 1.4 | 1.3 | 50.9 | 45.0 | 65.9 | 45.9 |
| 33 | 1.5 | 1.3 | 1.3 | 1.4 | 33.3 | 42.0 | 39.6 | 79.1 |
| 34 | 1.0 | 1.2 | 1.4 | 1.4 | round | 48.4 | 32.7 | 69.7 |
| 35 | 1.7 | 1.6 | 1.4 | 1.4 | 61.0 | 86.2 | 83.3 | 77.7 |
| 36 | 1.3 | 1.6 | 1.6 | 1.4 | 46.5 | 90.0 | 58.1 | 78.1 |
| 37 | 1.3 | 1.3 | 1.3 | 1.1 | 30.1 | 60.3 | 86.9 | round |
| 38 | 1.5 | 1.1 | 1.4 | 1.8 | 78.1 | round | 47.2 | 82.9 |
| 39 | 1.3 | 1.5 | 1.2 | 1.6 | 58.0 | 78.7 | 59.2 | 64.5 |
| 40 | 1.2 | 1.3 | 1.6 | 1.6 | round | 76.0 | 66.9 | 86.8 |
| 41 | 1.2 | 1.2 | 1.3 | 2.0 | 70.0 | 83.7 | 33.7 | 78.2 |
| 42 | 1.7 | 1.4 | 1.3 | 2.0 | 51.5 | 29.9 | 76.6 | 66.9 |
| 43 | 1.5 | 1.5 | 1.3 | 1.5 | 64.8 | 35.4 | 37.4 | 50.8 |
| 44 | 1.3 | 1.4 | 1.3 | 1.3 | 74.8 | 79.3 | 76.5 | 20.3 |

**Note** – Table is continued on the next page.

| Neuron | Aspect ratio | | | | Orientation (°) | | | |
|---|---|---|---|---|---|---|---|---|
| **Magnitude (mm)** | **4** | **4** | **8** | **8** | **4** | **4** | **8** | **8** |
| **Rate (mm/s)** | **0.5** | **3.5** | **0.5** | **3.5** | **0.5** | **3.5** | **0.5** | **3.5** |
| 45 | 1.6 | 1.4 | 1.4 | 1.4 | 65.1 | 51.0 | 69.4 | 61.5 |
| 46 | 1.7 | 1.4 | 1.4 | 1.2 | 34.2 | 54.9 | 54.4 | 79.4 |
| 47 | 1.8 | 1.3 | 1.5 | 1.3 | 47.4 | 57.7 | 66.4 | 70.3 |
| 48 | 1.7 | 1.3 | 1.4 | 1.4 | 63.4 | 85.7 | 64.9 | 67.2 |
| 49 | 1.2 | 1.2 | 1.4 | 1.5 | 49.9 | 78.7 | 88.2 | 72.2 |
| 50 | 1.5 | 1.4 | 1.6 | 1.2 | 84.4 | 55.8 | 64.4 | 62.1 |
| 51 | 1.1 | 1.4 | 1.7 | 1.9 | round | 12.8 | 87.6 | 44.4 |
| 52 | 1.6 | 1.5 | 1.5 | 1.8 | 82.6 | 31.2 | 71.6 | 50.5 |
| 53 | 1.3 | 1.3 | 1.5 | 1.5 | 70.6 | 63.3 | 89.0 | 48.2 |
| 54 | 1.7 | 1.7 | 1.4 | 1.3 | 62.4 | 76.1 | 70.9 | 44.3 |
| 55 | 1.3 | 1.2 | 1.4 | 1.3 | 78.2 | 43.8 | 82.4 | 61.3 |
| 56 | 1.3 | 1.4 | 1.5 | 1.3 | 48.4 | 89.1 | 64.9 | 37.6 |
| 57 | 2.1 | 1.4 | 1.4 | 1.4 | 60.8 | 36.4 | 76.8 | 59.2 |
| 58 | 2.9 | 1.4 | 1.3 | 1.4 | 80.1 | 28.9 | 56.3 | 76.5 |
| 59 | 1.2 | 1.3 | 1.5 | 1.3 | 47.9 | 85.1 | 31.9 | 47.9 |
| 60 | 1.2 | 1.3 | 1.3 | 1.2 | 69.1 | 58.2 | 62.8 | 49.7 |
| 61 | 1.8 | 1.5 | 1.4 | 1.4 | 82.7 | 66.0 | 83.1 | 78.0 |
| 62 | 1.4 | 1.3 | 1.7 | 1.4 | 50.8 | 47.9 | 85.5 | 65.1 |
| 63 | 1.2 | 1.3 | 1.6 | 1.4 | 90.0 | 81.3 | 66.2 | 57.2 |
| 64 | 1.7 | 1.3 | 1.3 | 1.2 | 48.8 | 58.9 | 80.7 | 63.4 |
| 65 | 1.8 | 1.1 | 1.4 | 1.3 | 66.5 | round | 64.7 | 52.5 |
| 66 | 1.7 | 1.4 | 1.3 | 1.4 | 53.8 | 88.2 | 79.9 | 58.9 |
| 67 | 1.3 | 1.5 | 1.3 | 1.2 | 46.7 | 74.2 | 71.8 | 79.8 |
| 68 | 1.3 | 1.1 | 1.4 | 1.6 | 55.4 | round | 47.9 | 68.7 |
| 69 | 1.8 | 1.3 | 1.3 | 1.3 | 81.3 | 88.4 | 54.9 | 56.3 |
| 70 | 1.6 | 1.4 | 1.2 | 1.2 | 60.3 | 68.2 | 66.8 | 74.3 |
| 71 | 1.7 | 1.3 | 1.5 | 1.4 | 80.4 | 52.4 | 69.6 | 29.5 |
| 72 | 1.3 | 1.3 | 1.3 | 1.6 | 71.0 | 79.0 | 49.6 | 60.0 |
| 73 | 1.4 | 1.2 | 1.4 | 1.3 | 56.9 | 80.4 | 39.9 | 64.4 |
| 74 | 1.4 | 1.3 | 1.3 | 1.4 | 45.0 | 84.2 | 75.0 | 67.4 |
| 75 | 2.4 | 1.2 | 1.0 | 1.3 | 45.0 | 83.7 | round | 85.4 |
| 76 | 1.2 | 1.3 | 1.2 | 1.7 | 60.7 | 57.6 | 47.1 | 70.9 |
| 77 | 1.4 | 1.5 | 1.3 | 1.5 | 61.2 | 46.8 | 41.2 | 36.2 |
| 78 | 1.4 | 1.2 | 1.2 | 1.4 | 85.1 | 47.1 | 83.4 | 84.4 |
| 79 | 1.7 | 1.3 | 1.3 | 1.4 | 52.8 | 46.4 | 77.9 | 38.0 |
| 80 | 1.1 | 1.3 | 1.5 | 1.3 | 51.6 | 35.0 | 88.7 | 68.0 |
| 81 | 1.7 | 1.3 | 1.4 | 1.3 | 35.9 | 87.5 | 38.8 | 82.9 |
| 82 | 3.0 | 1.4 | 1.3 | 1.3 | 74.6 | 85.2 | 79.1 | 45.0 |
| 83 | 1.8 | 1.4 | 1.6 | 1.3 | 66.5 | 87.2 | 73.1 | 41.4 |
| 84 | 1.7 | 1.5 | 1.4 | 1.4 | 52.3 | 64.5 | 78.7 | 64.0 |
| 85 | 1.1 | 1.3 | 1.4 | 1.3 | round | 81.5 | 87.3 | 49.7 |
| 86 | 1.8 | 1.3 | 1.3 | 1.3 | 88.7 | 44.4 | 74.1 | 40.1 |
| 87 | 1.7 | 1.4 | 1.3 | 1.2 | 84.4 | 31.5 | 33.9 | 17.3 |
| 88 | 1.3 | 1.4 | 1.5 | 1.3 | 33.3 | 39.6 | 77.1 | 51.1 |
| 89 | 2.3 | 1.1 | 1.2 | 1.3 | 82.9 | round | 70.7 | 80.9 |
| 90 | 1.5 | 1.5 | 1.2 | 1.4 | 88.3 | 59.8 | 64.7 | 50.8 |

**Note** – Table is continued on the next page.

| Neuron | Aspect ratio | | | | Orientation (°) | | | |
|---|---|---|---|---|---|---|---|---|
| **Magnitude (mm)** | **4** | **4*** | **8** | **8** | **4** | **4** | **8** | **8** |
| **Rate (mm/s)** | **0.5** | **3.5*** | **0.5** | **3.5** | **0.5** | **3.5** | **0.5** | **3.5** |
| 91 | 1.0 | | 1.2 | 1.2 | round | | 54.9 | 55.5 |
| 92 | 1.1 | | 1.3 | 1.4 | round | | 59.6 | 84.9 |
| 93 | 1.1 | | 1.1 | 1.3 | round | | 41.2 | 48.5 |
| 94 | 1.2 | | 1.3 | 1.4 | 81.9 | | 56.5 | 45.0 |
| 95 | 1.1 | | 1.1 | 1.3 | round | | 61.5 | 75.5 |
| 96 | 1.1 | | 1.2 | 1.3 | round | | 38.7 | 64.8 |
| 97 | 1.0 | | 1.5 | 1.3 | round | | 87.8 | 65.9 |
| 98 | 1.0 | | 1.4 | 1.5 | round | | 52.3 | 72.0 |
| 99 | 1.1 | | 1.2 | 1.4 | round | | 88.2 | 43.2 |
| 100 | 1.0 | | 1.3 | 1.4 | round | | 88.8 | 69.7 |
| 101 | 1.1 | | 1.4 | 1.6 | round | | 79.0 | 29.2 |
| 102 | 1.1 | | 1.4 | 1.2 | round | | 50.4 | 61.3 |
| 103 | 1.0 | | 1.2 | 1.4 | round | | 89.1 | 77.8 |
| 104 | 1.0 | | 1.2 | 1.5 | round | | 59.6 | 38.8 |
| 105 | 1.3 | | 1.4 | 1.3 | 30.3 | | 78.2 | 55.2 |
| 106 | 1.2 | | 1.3 | 1.8 | round | | 73.5 | 40.8 |
| 107 | 1.4 | | 1.6 | 1.4 | 57.0 | | 81.3 | 87.9 |
| 108 | 1.2 | | 1.4 | 1.3 | 75.4 | | 54.6 | 20.8 |
| 109 | 1.4 | | 1.3 | 1.4 | 42.8 | | 86.1 | 73.7 |
| 110 | 1.2 | | 1.3 | 1.3 | 54.1 | | 75.7 | 59.9 |
| 111 | 1.0 | | 1.4 | 1.5 | round | | 89.2 | 51.1 |
| 112 | 1.2 | | 1.3 | 1.7 | 68.2 | | 64.3 | 40.0 |
| 113 | 1.1 | | 1.3 | 1.3 | round | | 80.7 | 59.5 |
| 114 | 1.2 | | 1.5 | 1.5 | round | | 80.8 | 60.6 |
| 115 | 1.1 | | 1.6 | 1.3 | round | | 83.9 | 42.1 |
| 116 | 1.1 | | 1.2 | 1.4 | 27.9 | | 25.4 | 77.5 |
| 117 | 1.2 | | 1.3 | 1.2 | 45.0 | | 70.4 | 67.9 |
| 118 | 1.2 | | 1.4 | 1.5 | 67.3 | | 46.1 | 48.4 |
| 119 | 1.1 | | 1.3 | 1.8 | round | | 47.1 | 52.3 |
| 120 | 1.1 | | 1.8 | 1.3 | round | | round | 33.7 |
| 121 | 1.4 | | 1.2 | 1.4 | 69.8 | | 50.0 | 45.0 |
| 122 | 1.2 | | 1.5 | 1.2 | 62.3 | | 60.0 | 73.4 |
| 123 | 1.2 | | 1.2 | 1.2 | 85.6 | | 66.5 | 72.2 |
| 124 | 1.2 | | 1.2 | 1.4 | 74.4 | | 72.8 | 76.0 |
| 125 | 1.5 | | 1.2 | 1.2 | 86.7 | | 51.0 | 41.8 |
| 126 | 1.4 | | 1.3 | 1.2 | 54.2 | | 9.2 | 66.2 |
| 127 | 1.2 | | 1.3 | 1.3 | 57.9 | | 51.0 | 66.6 |
| 128 | 1.3 | | 1.6 | 1.2 | 64.1 | | 59.1 | 68.6 |
| 129 | 1.2 | | 1.5 | 1.5 | 70.2 | | 53.1 | 35.2 |
| 130 | 1.2 | | 1.2 | 1.2 | round | | 34.6 | 50.9 |
| 131 | 1.2 | | 1.4 | 1.5 | 67.5 | | 58.5 | 73.4 |
| 132 | 1.0 | | 1.1 | 1.2 | round | | round | 43.4 |
| 133 | 1.3 | | 1.2 | 1.4 | 60.0 | | 84.1 | 76.4 |
| 134 | 1.1 | | 1.2 | 1.2 | round | | 52.0 | 82.5 |
| 135 | 1.3 | | 1.2 | 1.3 | 69.3 | | 70.9 | 87.3 |
| 136 | 1.1 | | 1.3 | 1.4 | 79.5 | | 32.9 | 78.0 |

**Note** – Table is continued on the next page.

* No data are available for the 3.5mm/s, 4mm loading group beyond Neuron #90.

| Neuron | Aspect ratio | | | | Orientation (°) | | | |
|---|---|---|---|---|---|---|---|---|
| **Magnitude (mm)** | **4** | **4*** | **8** | **8** | **4** | **4** | **8** | **8** |
| **Rate (mm/s)** | **0.5** | **3.5*** | **0.5** | **3.5** | **0.5** | **3.5** | **0.5** | **3.5** |
| 137 | 1.1 | | 1.4 | 1.2 | round | | 48.0 | 85.7 |
| 138 | 1.2 | | 1.3 | 1.6 | 54.3 | | 88.9 | 88.8 |
| 139 | 1.2 | | 1.4 | 1.3 | 88.6 | | 75.4 | 58.8 |
| 140 | 1.5 | | 1.2 | 1.3 | 77.7 | | 86.0 | 49.3 |
| 141 | 1.2 | | 1.3 | 1.2 | 66.2 | | 12.9 | 53.9 |
| 142 | 1.4 | | 1.3 | 1.3 | 72.0 | | 70.0 | 52.6 |
| 143 | 1.1 | | 1.1 | 1.6 | round | | 34.8 | 83.5 |
| 144 | 1.1 | | 1.4 | 1.2 | 77.5 | | 80.2 | 66.5 |
| 145 | 1.2 | | 1.4 | 1.2 | 68.6 | | 59.6 | 37.0 |
| 146 | 1.2 | | 1.2 | 1.2 | 88.6 | | 85.3 | 40.2 |
| 147 | 1.2 | | 1.3 | 1.2 | 76.4 | | 70.9 | 70.7 |
| 148 | 1.0 | | 1.2 | 1.5 | round | | 85.9 | 66.8 |
| 149 | 1.1 | | 1.2 | 1.2 | round | | 70.6 | 73.2 |
| 150 | 1.0 | | 1.2 | 1.3 | round | | 31.2 | 86.1 |

* No data are available for the 3.5mm/s, 4mm loading group beyond Neuron #90.

# APPENDIX F

# Neuron-Collagen Construct Strains

This appendix contains the applied macroscopic strains of the individual NCCs that are used throughout this thesis for studies in which the MPS values were not detailed in the associated chapters. The MPS values reported for each NCC here were measured by tracking fiducial markers on the gel surface and averaged within each NCC as detailed in Chapter 3. Five tables are summarized in this appendix corresponding to five separate NCC studies. Table F.1 details the MPS for the 3D DRG cultures that underwent 4mm (physiologic) or 8mm (non-physiologic) stretch in the studies presented in Chapter 4. Table F.2 and Table F.3 summarize the applied strains for the integrin inhibition studies presented in Chapter 7 using the RGD peptide and the small molecule inhibitor TC-I15, respectively. Strains for the studies presented in Chapter 8, including the MPS imposed on NCCs used for assessing RhoA activity and those for the in vitro ROCK inhibition study, are listed separately in Table F.4 and Table F.5. Strains were measured from non-overlapping four-node elements across the NCC surface; the average and standard deviations of all regional MPS values are reported for each NCC.

**Table F.1. Average strains applied to the 3D DRG cultures that underwent 4mm or 8mm stretch at 0.5mm/s in the studies presented in Chapter 4.**

| Sample | Group | MPS |
|---|---|---|
| 1 | 4mm stretch | 0.107±0.052 |
| 2 | 4mm stretch | 0.084±0.039 |
| 3 | 8mm stretch | 0.179±0.020 |
| 4 | 8mm stretch | 0.160±0.049 |
| 5 | 8mm stretch | 0.170±0.034 |

**Table F.2. Average strains applied to the NCCs that were treated with the RGD peptide and those that were untreated in studies presented in Chapter 7.**

| Sample | Group | MPS |
|---|---|---|
| 1 | RGD treated | 0.308±0.014 |
| 2 | RGD treated | 0.206±0.066 |
| 3 | RGD treated | 0.140±0.045 |
| 4 | untreated | 0.253±0.086 |
| 5 | untreated | 0.208±0.062 |
| 6 | untreated | 0.157±0.042 |

**Table F.3. Average strains applied to the NCCs that received α2β1 integrin inhibition by TC-I15 with various concentrations (10μM, 100μM, 1000μM) & those that were untreated in studies presented in Chapter 7.**

| Sample | Group | MPS |
|---|---|---|
| 1 | 10μM TC-I15 treated | 0.214±0.086 |
| 2 | 10μM TC-I15 treated | 0.197±0.075 |
| 3 | 10μM TC-I15 treated | 0.243±0.011 |
| 4 | 10μM TC-I15 treated | 0.174±0.067 |
| 5 | 100μM TC-I15 treated | 0.238±0.076 |
| 6 | 100μM TC-I15 treated | 0.183±0.069 |
| 7 | 100μM TC-I15 treated | 0.157±0.057 |
| 8 | 100μM TC-I15 treated | 0.265±0.148 |
| 9 | 100μM TC-I15 treated | 0.213±0.021 |
| 10 | 1000μM TC-I15 treated | 0.198±0.062 |
| 11 | 1000μM TC-I15 treated | 0.140±0.055 |
| 12 | 1000μM TC-I15 treated | 0.156±0.049 |
| 13 | 1000μM TC-I15 treated | 0.224±0.118 |
| 14 | 1000μM TC-I15 treated | 0.181±0.038 |
| 15 | untreated | 0.238±0.082 |
| 16 | untreated | 0.179±0.028 |
| 17 | untreated | 0.236±0.118 |
| 18 | untreated | 0.246±0.056 |
| 19 | untreated | 0.203±0.072 |

**Table F.4. Average strains applied to the NCCs that were used to assess RhoA activity at 30 minutes & 6 hours in studies presented in Chapter 8.**

| Sample | Group | MPS |
|---|---|---|
| 1 | 30 min | 0.143±0.033 |
| 2 | 30 min | 0.239±0.107 |
| 3 | 30 min | 0.132±0.048 |
| 4 | 6hrs | 0.183±0.074 |
| 5 | 6hrs | 0.172±0.093 |
| 6 | 6hrs | 0.113±0.025 |
| 7 | 6hrs | 0.163±0.067 |
| 8 | 6hrs | 0.138±0.040 |

**Table F.5. Average strains applied to the NCCs that received ROCK inhibition by Y27632 & those untreated in studies presented in Chapter 8.**

| Sample | Group | MPS |
|---|---|---|
| 1 | Y27632 treated | 0.236±0.081 |
| 2 | Y27632 treated | 0.203±0.073 |
| 3 | Y27632 treated | 0.208±0.089 |
| 4 | Y27632 treated | 0.175±0.084 |
| 5 | Y27632 treated | 0.163±0.163 |
| 6 | Y27632 treated | 0.142±0.029 |
| 7 | untreated | 0.244±0.081 |
| 8 | untreated | 0.161±0.034 |
| 9 | untreated | 0.191±0.045 |
| 10 | untreated | 0.173±0.037 |
| 11 | untreated | 0.184±0.026 |
| 12 | untreated | 0.179±0.019 |
| 13 | untreated | 0.208±0.062 |
| 14 | untreated | 0.157±0.042 |

# APPENDIX G

# Summary of Information for Human Cervical Facet Capsular Ligament Samples

This appendix details the donor information, specimen dimensions and the displacement at the onset of anomalous fiber alignment for the human cervical cadaveric facet capsular ligament samples used in this thesis. This set of human cervical capsule samples was used in the studies reported in Chapter 5 to reveal collagen reorganization patterns in the anomalous realignment (AR) and normal realignment (NR) regions and also were modeled in Chapter 6 to understand the multi-scale mechanics of this ligament. All facet joints were removed from fresh, unembalmed human cervical spines and the bone-ligament-bone specimens were isolated from the joint as described previously in great detail (Quinn and Winkelstein 2009; Quinn 2010). The width, length and thickness of each tissue specimen were measured using a digital caliper. All samples underwent uniaxial tensile loading to failure with collagen organization tracked by quantitative polarized light imaging during stretch, as detailed in prior work (Quinn and Winkelstein 2009). Table G.1 summarizes the donor information and Table G.2 summarizes the sample dimensions and the displacements at which the initial anomalous fiber realignment occurred in each specimen.

**Table G.1. Donor information for the human cervical facet capsule samples.**

| Specimen | Donor ID | Level | Side | Sex | Age (years) |
|---|---|---|---|---|---|
| 1 | C390 | C4/C5 | L | F | 74 |
| 2 | C846 | C4/C5 | L | M | 64 |
| 3 | C846 | C4/C5 | R | M | 64 |
| 4 | C457 | C4/C5 | L | F | 39 |
| 5 | C611 | C4/C5 | L | M | 79 |
| 6 | C446 | C4/C5 | L | M | 47 |
| 7 | C012 | C4/C5 | R | M | 75 |
| **Mean** | | | | | **63** |
| **SD** | | | | | **15** |

**Table G.2. Sample sizes & AR displacement for the human cadaver samples.**

| Specimen | Donor ID | Width (mm) | Length (mm) | Thickness (mm) | AR* displacement (mm) |
|---|---|---|---|---|---|
| 1 | C390 | 7.52 | 5.37 | 0.41 | 3.79 |
| 2 | C846 | 8.37 | 6.60 | 0.37 | 3.00 |
| 3 | C846 | 6.58 | 4.94 | 0.30 | 1.49 |
| 4 | C457 | 8.74 | 6.38 | 0.38 | 2.56 |
| 5 | C611 | 5.77 | 4.43 | 0.50 | 3.20 |
| 6 | C446 | 6.12 | 6.09 | 0.44 | 2.26 |
| 7 | C012 | 7.24 | 5.47 | 0.51 | 2.99 |
| **Mean** | | **7.19** | **5.61** | **0.42** | **2.76** |
| **SD** | | **1.11** | **0.79** | **0.08** | **0.74** |

*AR = anomalous realignment

# APPENDIX H

# Network Diagnostics: Equations & Measurements

This appendix details the mathematical definitions and measurements of network diagnostics that are used in the studies presented Chapter 5. The network diagnostics summarized here include the *modularity* and *number of modules*, which describe the modular structure of the network from static and dynamic community detection (Newman 2006; Mucha et al. 2010a). They also include *stationarity* and *flexibility*, both of which characterize the stability of module composition of the multilayer network (Bassett et al. 2011; Bassett et al. 2013). The mathematical definitions of modularity, stationarity and flexibility are provided in Section H.1. Those diagnostics were calculated for static and multilayer networks constructed using the collagen alignment data from seven human cervical facet capsular ligaments, as well as their corresponding benchmark random networks created by random rewiring. Information on those human cervical facet capsule samples is provided in Appendix G. In Donor IDs listed in this appendix, "L" and "R" indicate the left and right facet joints of a specimen, respectively.

Section H.2 summarizes the network diagnostic measurements in four tables. Table H.1 lists the static modularity and the number of modules for the anomalous realignment (AR) and normal realignment (NR) networks and their respective benchmark random networks before ligament loading; the corresponding measurements after

ligament stretch are summarized in Table H.2. Table H.3 details the modularity and the number of modules of multilayer AR and NR networks and their respective permuted benchmark networks. The stationarity and flexibility of the multilayer networks are summarized in Table H.4.

**H.1. Mathematical Definitions of Network Diagnostics**

*Modularity* is a quality function used to measure to what extent a given partition of a network compartmentalizes its communities (Porter et al. 2009; Fortunato 2010). Modularity of a weighted network is defined as:

$$Q_{\text{static}} = \frac{1}{2\omega}\sum_{ij}\left(A_{ij} - \frac{k_i k_j}{2\omega}\right)\delta(g_i, g_j),$$

where $A_{ij}$ is the adjacency tensor, $2\omega=\Sigma_{ij}\, A_{ij}$, $k_i$ is the strength of node $i$, $k_j$ is the strength of node $j$, $\delta$ is the Kronecker delta ($\delta$=1 for $i$ and $j$ in the same community), $g_i$ is the community to which node $i$ is assigned, and $g_j$ is the community to which node $j$ is assigned (Newman 2004; Newman 2006). Modularity is optimized using the Louvain locally greedy algorithm (Blondel et al. 2008).

For the case of temporal networks, the multilayer modularity is defined as:

$$Q_{\text{multilayer}} = \frac{1}{2\mu}\sum_{ijlr}\left[\left(A_{ijl} - \gamma_l \frac{k_{il}k_{jl}}{2\omega_l}\right)\delta_{lr} + \delta_{ij}C_{jlr}\right]\delta(g_{il}, g_{jr}),$$

where $A_{ijl}$ is the adjacency tensor between nodes $i$ and $j$ in network slice $l$, $\gamma_l$ is the structural resolution parameter that can be used to tune the size of modules of layer $l$, $k_{il}$ is the strength of node $i$ in layer $l$, $C_{jlr}$ is the connection strength of node $j$ between layer $r$ and layer $l$, $c_{jl}=\Sigma_r\, C_{jlr}$, $2\mu=\Sigma_{jr}\,(k_{jr}+c_{jr})$, $g_{il}$ is community $i$ in time slice $l$ and $g_{jr}$ is community $j$ in time slice $r$ (Mucha et al. 2010b). Modularity optimization is performed using a Louvain-like locally greedy algorithm (Blondel et al. 2008).

*Stationarity* is a measure of the mean similarity of module composition over time, calculated as the mean autocorrelation over consecutive time steps. The autocorrelation

function *U(t, t+m)* of two states of the same community *G(t)* at *m* time steps apart is computed using the following formula:

$$U(t, t+m) \equiv \frac{|G(t) \cap G(t+m)|}{|G(t) \cup G(t+m)|},$$

Where $|G(t) \cap G(t+m)|$ is the number of common nodes in both *G(t)* and *G(t+m)*, and $|G(t) \cup G(t+m)|$ is the total number of nodes in *G(t)* and *G(t+m)* (Palla et al. 2007). The stationarity is then defined as:

$$\zeta \equiv \frac{\sum_{t=t_0}^{t_f-1} U(t, t+1)}{t_f - t_0 - 1},$$

where $t_0$ is the time when a community emerges, and $t_f$ is the final time step before the given community is extinguished (Palla et al. 2007; Bassett et al. 2011).

*Flexibility* is a measure of change in the module composition in multilayer networks. Flexibility of node *i* is defined as:

$$f_i = \frac{m}{t_f - 1},$$

where *m* is the number of times the given node changes modular assignment. The flexibility of the entire network is defined as:

$$F = \frac{1}{N} \sum_{i=1}^{N} f_i,$$

where *N* is the total number of nodes in the network (Bassett et al. 2011).

## H.2. Measurements of Network Diagnostics for Studies in Chapter 5

**Table H.1. Modularity & the number of modules of the static collagen networks in AR & NR regions & the corresponding random networks before ligament stretch.**

| | AR | | | | NR | | | |
|---|---|---|---|---|---|---|---|---|
| | Modularity | | Number of modules | | Modularity | | Number of modules | |
| Donor ID | Real | Random | Real | Random | Real | Random | Real | Random |
| C390L | 0.4746 | 0.1109 | 2 | 4 | 0.3255 | 0.0989 | 2 | 4 |
| C846L | 0.2296 | 0.0695 | 3 | 4 | 0.1096 | 0.0715 | 2 | 2 |
| C846R | 0.3525 | 0.0816 | 2 | 4 | 0.2041 | 0.0801 | 2 | 3 |
| C457L | 0.2897 | 0.0779 | 3 | 4 | 0.0241 | 0.0240 | 2 | 2 |
| C611L | 0.4658 | 0.1033 | 2 | 5 | 0.0489 | 0.0489 | 2 | 2 |
| C446L | 0.1933 | 0.0735 | 3 | 4 | 0.2805 | 0.1053 | 2 | 2 |
| C012R | 0.0477 | 0.0303 | 3 | 3 | 0.1019 | 0.0469 | 3 | 3 |

**Table H.2. Modularity & the number of modules of the static collagen networks in AR & NR regions & the corresponding random networks after ligament stretch.**

| | AR | | | | NR | | | |
|---|---|---|---|---|---|---|---|---|
| | Modularity | | Number of modules | | Modularity | | Number of modules | |
| Donor ID | Real | Random | Real | Random | Real | Random | Real | Random |
| C390L | 0.0960 | 0.0960 | 2 | 2 | 0.0189 | 0.0189 | 2 | 2 |
| C846L | 0.3898 | 0.0989 | 2 | 4 | 0.2775 | 0.0699 | 2 | 4 |
| C846R | 0.0000 | 0.0000 | 1 | 1 | 0.1300 | 0.0387 | 3 | 4 |
| C457L | 0.1213 | 0.1042 | 2 | 2 | 0.0655 | 0.0643 | 2 | 2 |
| C611L | 0.1510 | 0.0668 | 2 | 4 | 0.2607 | 0.1491 | 2 | 2 |
| C446L | 0.1006 | 0.1006 | 2 | 2 | 0.1333 | 0.0551 | 2 | 4 |
| C012R | 0.0046 | 0.0046 | 3 | 4 | 0.1165 | 0.0515 | 3 | 3 |

**Table H.3. Modularity & the number of modules of the multilayer collagen networks in AR & NR regions & the respective random networks.**

| | AR | | | | NR | | | |
|---|---|---|---|---|---|---|---|---|
| | Modularity | | Number of modules | | Modularity | | Number of modules | |
| Donor ID | Real | Random | Real | Random | Real | Random | Real | Random |
| C390L | 0.2450 | 0.2439 | 4 | 3 | 0.2601 | 0.2588 | 2 | 2 |
| C846L | 0.2663 | 0.2657 | 4 | 4 | 0.1385 | 0.1376 | 4 | 4 |
| C846R | 0.2154 | 0.2151 | 2 | 2 | 0.0249 | 0.0247 | 2 | 2 |
| C457L | 0.1292 | 0.1286 | 3 | 3 | 0.1646 | 0.1638 | 4 | 4 |
| C611L | 0.1203 | 0.1195 | 4 | 4 | 0.1077 | 0.1042 | 2 | 3 |
| C446L | 0.0797 | 0.0785 | 3 | 3 | 0.2158 | 0.2143 | 2 | 2 |
| C012R | 0.0168 | 0.0165 | 4 | 3 | 0.0884 | 0.0870 | 3 | 3 |

**Table H.4. Stationarity & flexibility of the multilayer collagen networks in AR & NR regions & the respective random networks.**

| | AR | | | | NR | | | |
|---|---|---|---|---|---|---|---|---|
| | Stationarity | | Flexibility | | Stationarity | | Flexibility | |
| Donor ID | Real | Random | Real | Random | Real | Random | Real | Random |
| C390L | 0.770 | 0.410 | 0.385 | 0.540 | 0.528 | 0.389 | 0.381 | 0.503 |
| C846L | 0.527 | 0.442 | 0.487 | 0.566 | 0.548 | 0.340 | 0.428 | 0.585 |
| C846R | 0.824 | 0.689 | 0.382 | 0.439 | 0.992 | 0.904 | 0.295 | 0.318 |
| C457L | 0.546 | 0.409 | 0.413 | 0.523 | 0.554 | 0.347 | 0.425 | 0.590 |
| C611L | 0.628 | 0.403 | 0.481 | 0.571 | 0.874 | 0.490 | 0.161 | 0.479 |
| C446L | 0.715 | 0.443 | 0.328 | 0.514 | 0.970 | 0.497 | 0.158 | 0.459 |
| C012R | 0.529 | 0.449 | 0.447 | 0.483 | 0.756 | 0.435 | 0.370 | 0.532 |

# APPENDIX I

# Predicted Multi-Scale Tissue Mechanics of Human Cervical Facet Capsular Ligaments

This appendix details the tissue-level, network-level and fiber-level mechanics of the human cervical facet capsular ligament during stretch that were predicted from the finite element-based multi-scale models presented in Chapter 6, and in comparison to previously reported experimental measurements (Quinn and Winkelstein 2009; Quinn 2010). Figure I.1 presents the force-displacement curves for each sample that were generated from the model and the raw data from the experiment up to the onset of anomalous realignment (AR) of collagen fibers. Additionally, the predicted and experimentally measured maximum principal strains in sub-regions of the human cervical facet capsule at 50% of AR displacement and at the onset of AR are shown in Figure I.2 for each sample. The colormap in those figures represents the strain magnitude and the arrow indicates the principal strain direction.

Figure I.3 summarizes the spatial distribution of experimentally detected anomalous fiber realignment and heat maps of the fiber stretch ratios, maximum principal stresses and maximum principal strains that were predicted from model simulations for each sample. Different injury scores, including the mean fiber stretch ratio score, maximum principal stress score, maximum principal strain score, von Mises stress score

and von Mises strain score, for regions with and without AR of each sample are listed in Table I.1. Information on the human cervical facet capsule samples used to construct the image-based multi-scale models in the studies presented in Chapter 6 is provided in Appendix G. In Donor IDs listed in this appendix, “L” and “R” indicate the left and right facet joints of a specimen, respectively.

**Figure I.1. Force-displacement curves from the experiment & model for each specimen in Chapter 6.**

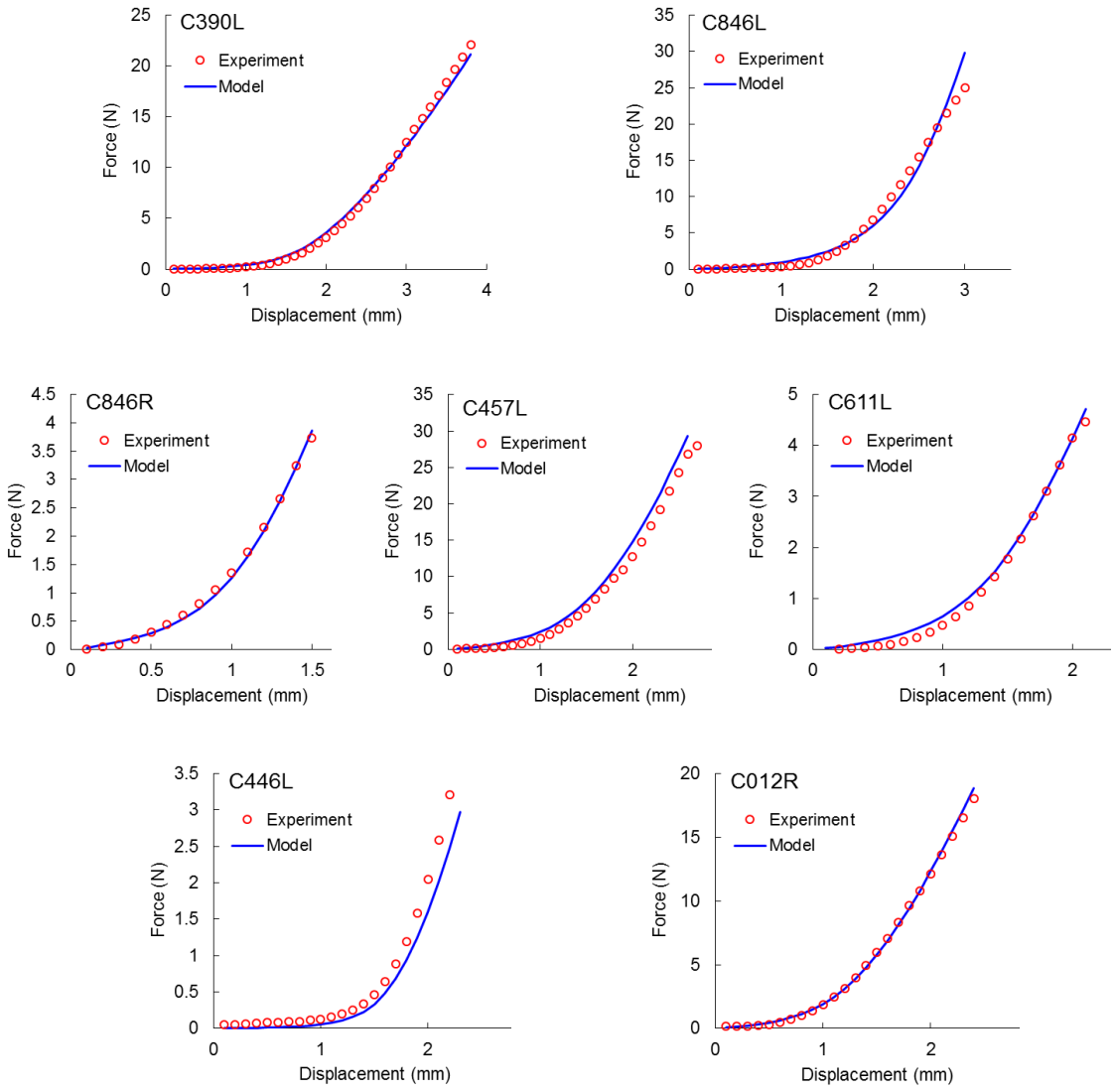

**Figure I.2. Regional maximum principal strain profiles of the experiment & model for each specimen in Chapter 6.**

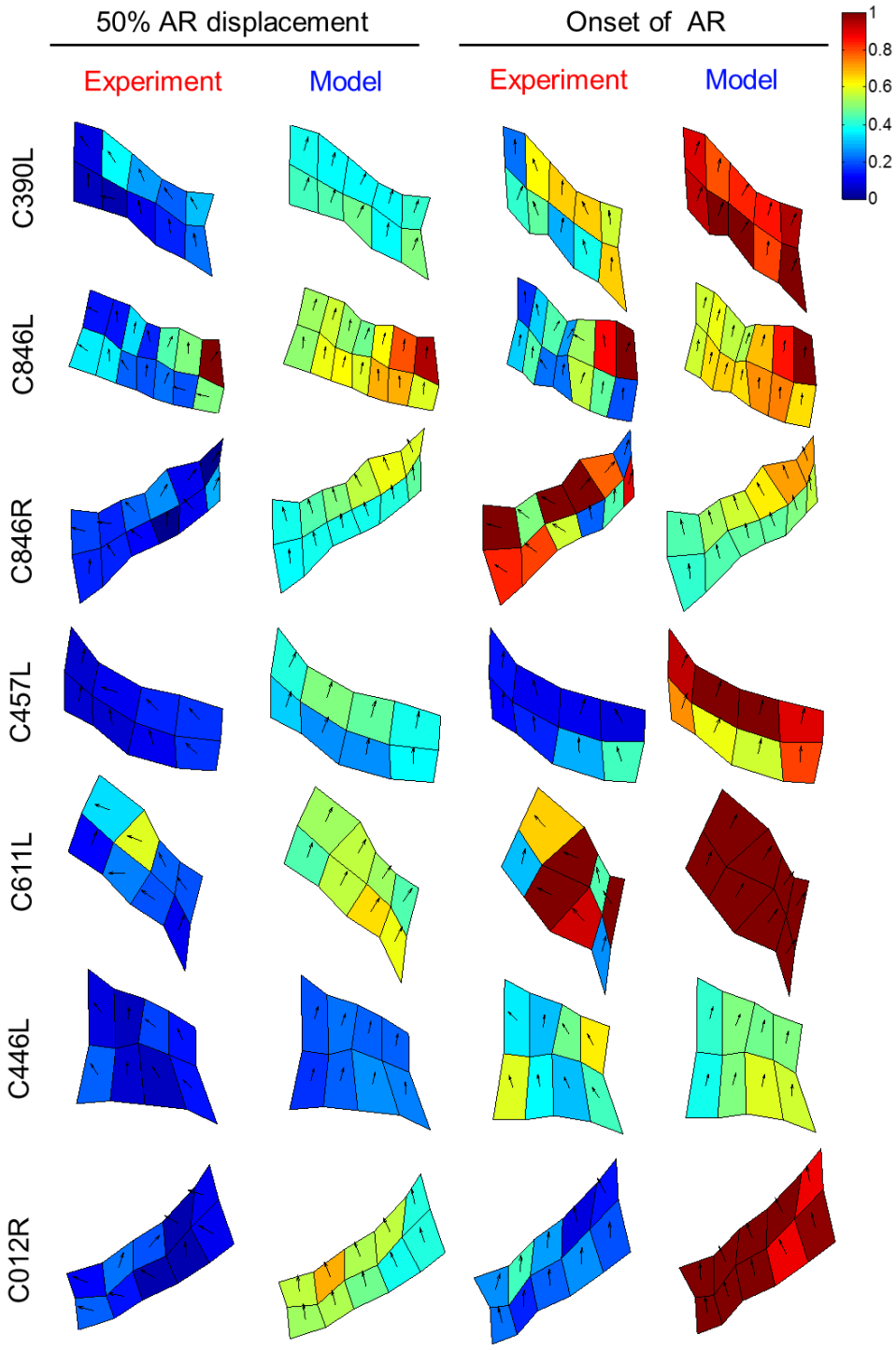

**Figure I.3. Spatial distribution of AR (red elements in plots in 1st column) & the predicted fiber & elemental mechanics for each specimen in Chapter 6.**

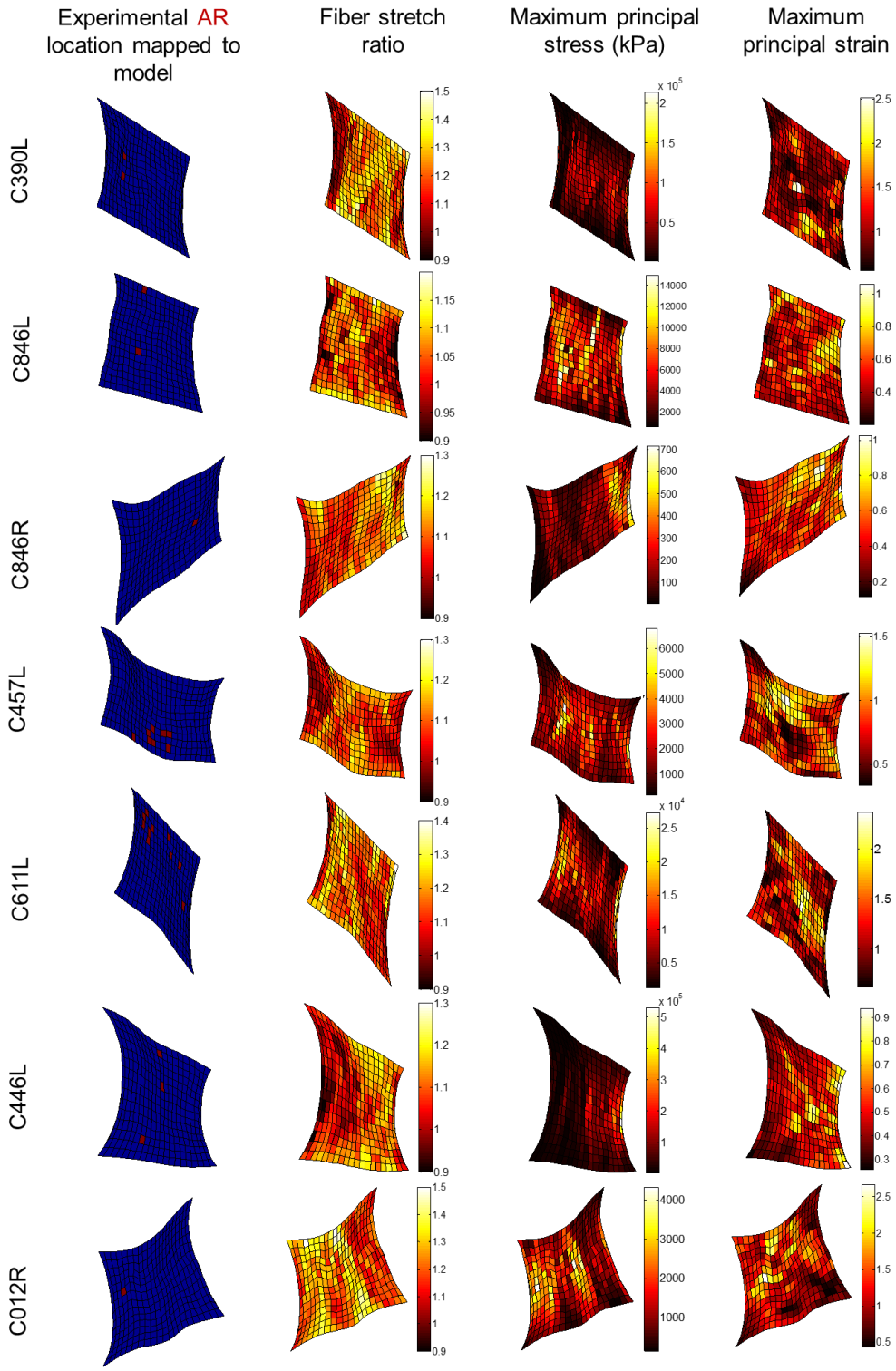

**Table I.1. Summary of the injury scores in regions with anomalous fiber realignment (AR) & regions with normal realignment (NR) based on model predictions of fiber stretch ratio & elemental stresses & strains for each specimen in Chapter 6.**

| Donor ID | Region | Stretch ratio score | Maximum principal stress score | Maximum principal strain score | von Mises stress score | von Mises strain score |
|---|---|---|---|---|---|---|
| C390L | AR | 0.61 | 0.51 | 0.25 | 0.51 | 0.36 |
| | NR | 0.53 | 0.29 | 0.39 | 0.28 | 0.45 |
| C846L | AR | 0.76 | 0.49 | 0.55 | 0.48 | 0.50 |
| | NR | 0.62 | 0.50 | 0.41 | 0.50 | 0.44 |
| C846R | AR | 0.50 | 0.53 | 0.68 | 0.52 | 0.78 |
| | NR | 0.44 | 0.32 | 0.55 | 0.32 | 0.60 |
| C457L | AR | 0.75 | 0.42 | 0.36 | 0.41 | 0.40 |
| | NR | 0.51 | 0.44 | 0.50 | 0.44 | 0.55 |
| C611L | AR | 0.62 | 0.34 | 0.47 | 0.34 | 0.44 |
| | NR | 0.47 | 0.33 | 0.39 | 0.33 | 0.37 |
| C446L | AR | 0.63 | 0.14 | 0.32 | 0.14 | 0.39 |
| | NR | 0.58 | 0.20 | 0.39 | 0.20 | 0.49 |
| C012R | AR | 0.57 | 0.90 | 0.60 | 0.89 | 0.69 |
| | NR | 0.42 | 0.40 | 0.40 | 0.40 | 0.45 |

# APPENDIX J

# Quantification of Immunolabeled Proteins in the DRG & Spinal Cord of Rats

This appendix summarizes the quantification of immunolabeled proteins in the DRG and spinal cord of rats used in the studies presented in Chapter 7 and Chapter 8. The facet joint mechanics and mechanical hyperalgesia of the corresponding rats listed here are provided in the following Appendix K. In each table and figure of this appendix, quantified protein expression and raw images are identified by the study group, rat number and corresponding image number.

Table J.1 details the quantification of the fraction of IB4-positive and susbstance P (SP)-positive DRG neurons that express the integrin subunit β1 in naïve un-operated rats, which represent assessment of the constitutive expression of the integrin subunit β1 in the studies presented in Chapter 7. The corresponding images, with IB4, SP and integrin subunit β1 co-labeled, are summarized in Figure J.1. Table J.2 details the average labeling intensity of the integrin subunit β1 in both small-diameter (4-21μm) and medium-diameter (21-40μm) DRG neurons separately at day 7 after sham procedures or a facet joint distraction, corresponding to data from the studies presented in Chapter 7. Images of the DRGs that were used for the measurements in Table J.2 are shown in Figure J.2.

Tables J.3 and J.4 and Figure J.3 through Figure J.6 summarize the protein quantification and immunofluorescence images obtained at day 1 after a painful facet joint injury or sham procedure followed by intra-articular injection of the ROCK inhibitor (Y27632) or saline vehicle (veh), in the studies reported in Chapter 8. Specifically, Table J.3 details the number of SP-positive neurons and the total number of small-diameter and medium-diameter neurons in the DRG of the *injury+veh, injury+Y27632* and *sham+veh* groups. The corresponding DRG images are provided in Figure J.3. Table J.4 summarizes the quantified protein expression of SP in the superficial dorsal horn and Iba1 in both the superficial and deep dorsal horns of the spinal cord of the *injury+veh, injury+Y27632* and *sham+veh* groups. Immunolabeling was quantified by densitometry using a custom MATLAB code provided in Appendix D; protein expression was quantified as the fraction of positively-labeled pixels in each image. Figures J.4, J.5 and J.6 provide the corresponding spinal cord images, with SP, Iba1 and nuclear DNA (by DAPI fluorescence stain) co-labeled, for the *injury+veh, injury+Y27632* and *sham+veh* groups, respectively.

**Table J.1. Constitutive expression of integrin subunit β1 in the IB4-positive & SP-positive DRG neurons of naïve rats (Chapter 7).**

| Rat | Image | Fraction of IB4-positive neurons expressing integrin subunit β1 | Fraction of SP-positive neurons expressing integrin subunit β1 |
|---|---|---|---|
| F14 | 1-1 | 0.64 | 1.00 |
| | 1-2 | 0.50 | 1.00 |
| | 2-1 | 0.48 | 0.75 |
| | 2-2 | 0.65 | 0.80 |
| | 3-1 | 0.50 | 0.80 |
| | 5-1 | 0.50 | 0.94 |
| | 5-2 | 0.33 | 1.00 |
| | 6-1 | 0.52 | 1.00 |
| | 6-2 | 0.80 | 1.00 |
| F15 | 1-2 | 0.73 | 0.80 |
| | 2-1 | 0.60 | 0.94 |
| | 2-2 | 0.48 | 1.00 |
| | 3-1 | 0.40 | 0.94 |
| | 3-2 | 0.30 | 0.89 |
| | 4-1 | 0.64 | 1.00 |
| | 4-2 | 0.56 | 1.00 |
| | 5-1 | 0.58 | 0.92 |
| N13 | 1-1 | 0.18 | 0.64 |
| | 1-2 | 0.35 | 0.84 |
| | 2-1 | 0.67 | 0.92 |
| | 2-2 | 0.64 | 0.80 |
| | 3-1 | 0.56 | 0.71 |
| | 3-2 | 0.27 | 0.73 |
| | 4-1 | 0.43 | 0.69 |
| | 5-1 | 0.61 | 0.77 |
| | 5-2 | 0.71 | 0.79 |
| | 6-1 | 0.50 | 0.77 |
| N14 | 1-1 | 0.47 | 0.62 |
| | 1-2 | 0.54 | 0.86 |
| | 2-1 | 0.33 | 0.60 |
| | 3-1 | 0.50 | 0.53 |
| | 3-2 | 0.30 | 0.38 |
| | 4-1 | 0.57 | 0.82 |
| | 4-2 | 0.38 | 0.70 |
| | 5-1 | 0.57 | 0.71 |
| | 5-2 | 0.44 | 0.46 |

**Note:** Rats F14 and F15 were generated by Christine Weisshaar and Rats N13 and N14 were generated by Martha Zeeman. The rat numbering scheme reflects their records.

**Figure J.1. Immunofluorescence images showing constitutive expression of the integrin subunit β1. The integrin subunit β1 (red), substance P (blue) & IB4 (green) are co-labeled in the DRG from un-operated normal rats. The image number is indicated in parentheses.**

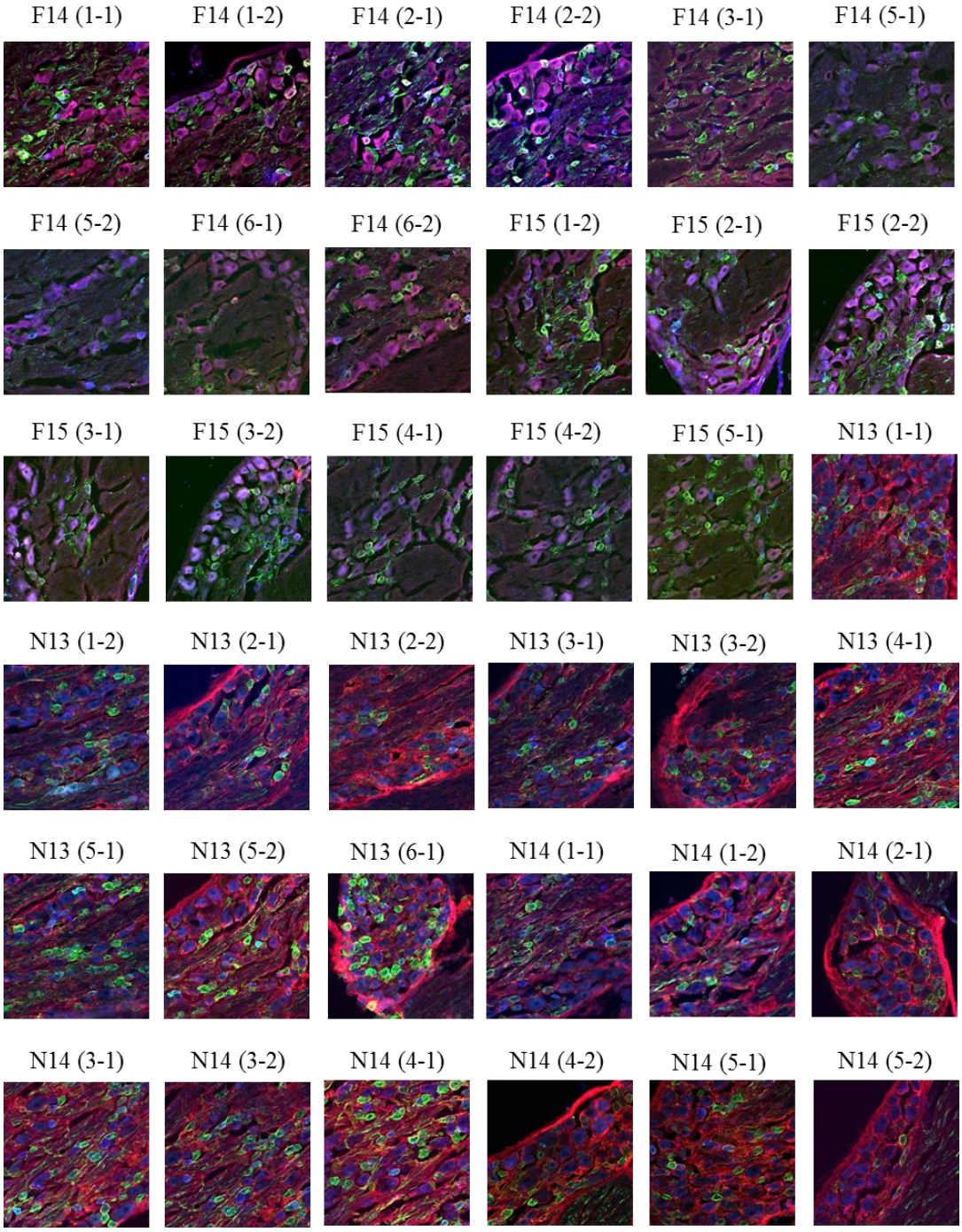

**Table J.2. Average intensity of integrin subunit β1 immunolabeling in small-sized & medium-sized DRG neurons at day 7 after sham procedures or facet joint distraction (FJD) (Chapter 7).**

| Sham | | | | FJD | | | |
|---|---|---|---|---|---|---|---|
| **Rat** | **Image** | **Small neuron** | **Medium neuron** | **Rat** | **Image** | **Small neuron** | **Medium neuron** |
| 132 | 1 | 0.75 | 0.94 | 134 | 1 | 0.94 | 0.66 |
| | 2 | 0.71 | 0.66 | | 2 | 0.83 | 0.57 |
| | 3 | 0.59 | 0.76 | | 3 | NA | 0.74 |
| | 4 | 0.72 | 0.60 | | 4 | 0.79 | 1.01 |
| | 5 | 0.97 | 0.92 | | 5 | 0.88 | 0.77 |
| | 6 | 0.76 | 0.71 | | 6 | 1.11 | 1.22 |
| 141 | 1 | 0.73 | 0.65 | 143 | 1 | 0.61 | 0.76 |
| | 2 | 0.53 | 0.61 | | 2 | 0.87 | 0.98 |
| | 3 | 0.67 | 0.64 | | 3 | 0.84 | 1.00 |
| | 4 | 0.49 | 0.63 | | 4 | 0.71 | 0.77 |
| | 5 | 0.58 | 0.71 | | 5 | 0.76 | 0.78 |
| | 6 | 0.55 | 0.63 | | 6 | 0.95 | 0.86 |
| 142 | 1 | 0.72 | 0.84 | 152 | 1 | 0.97 | 1.34 |
| | 2 | 0.79 | 0.85 | | 2 | 1.30 | 1.46 |
| | 3 | 0.48 | 0.59 | | 3 | 1.52 | 1.78 |
| | 4 | 0.61 | 0.58 | | 4 | 1.97 | 1.74 |
| | 5 | 0.42 | 0.41 | | 5 | 1.83 | 1.76 |
| | 6 | 0.47 | 0.57 | | 6 | 1.70 | 0.28 |
| 150 | 1 | 0.81 | 1.02 | 155 | 1 | 1.60 | 1.69 |
| | 2 | 1.37 | 1.46 | | 2 | 1.07 | 1.28 |
| | 3 | 0.91 | 1.12 | | 3 | 1.49 | 1.34 |
| | 4 | 0.80 | 0.73 | | 4 | 1.20 | 1.12 |
| | 5 | 1.12 | 1.30 | | 5 | 1.10 | 1.26 |
| | 6 | 1.02 | 1.23 | | 6 | 1.38 | 1.36 |
| 152 | 1 | 0.92 | 0.89 | | | | |
| | 2 | 1.08 | 0.98 | | | | |
| | 3 | 1.49 | 1.37 | | | | |
| | 4 | 1.07 | 0.95 | | | | |
| | 5 | 1.30 | 1.22 | | | | |
| | 6 | 1.07 | 1.11 | | | | |

**Note:** All rats listed in this table were generated by Jeffery Kras and the rat numbering scheme reflects his records.
NA: No small-diameter neurons were identified.

**Figure J.2. Immunofluorescence images showing the expression of the integrin subunit β1 in DRG neurons at day 7 in sham & FJD rats.**

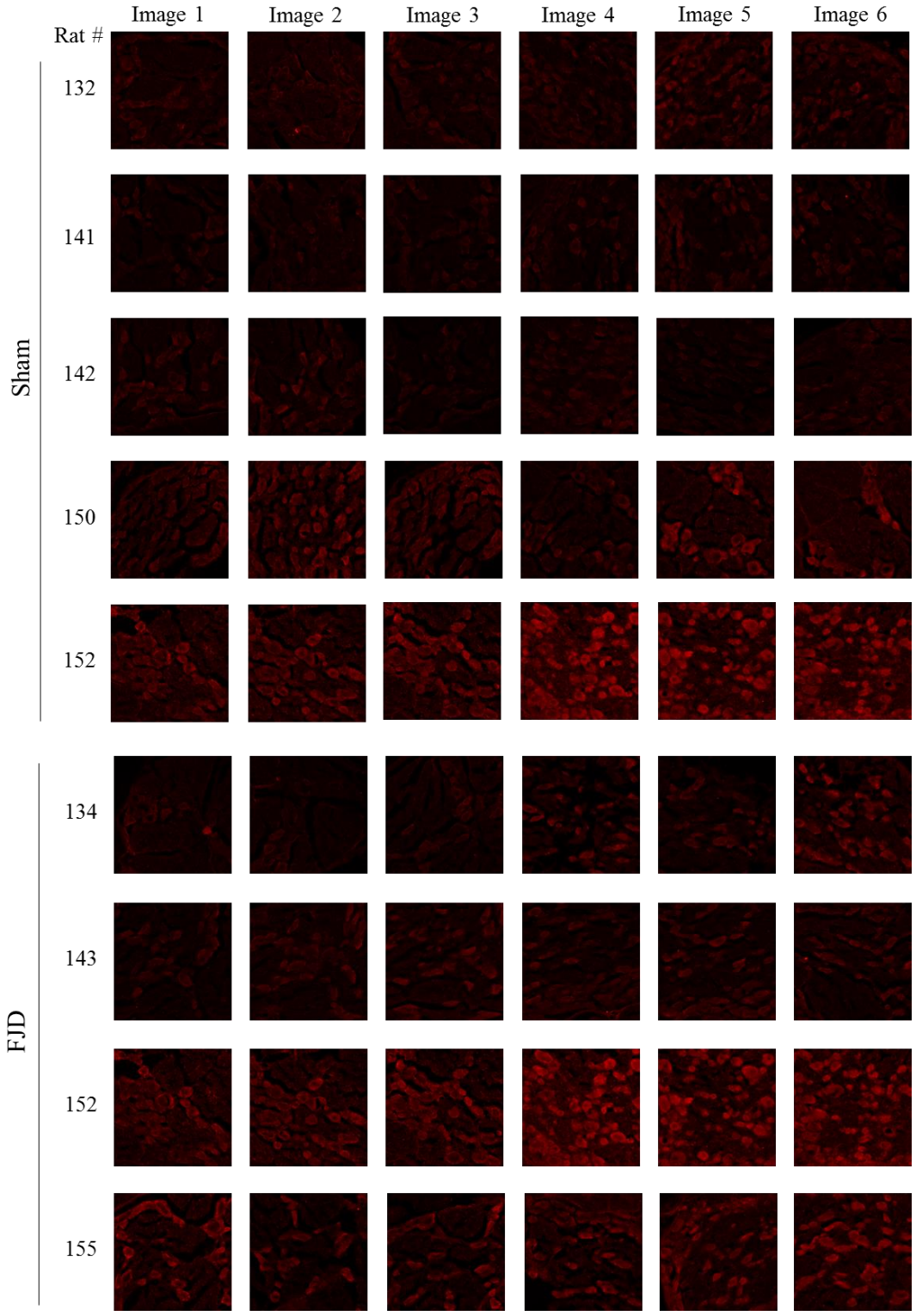

**Table J.3. Number of SP-positive neurons & total number of small-diameter & medium-diameter neurons in the DRG at day 1 in the *injury+veh*, *injury+Y27632* & *sham+veh* groups (Chapter 8).**

| Group | Rat | Image | Number of SP-positive neurons | Number of small- & medium-diameter neurons |
|---|---|---|---|---|
| injury+veh | 2 | 1 | 8 | 26 |
| | | 2 | 11 | 35 |
| | | 3 | 9 | 39 |
| | 4 | 1 | 4 | 29 |
| | | 2 | 8 | 30 |
| | | 3 | 6 | 22 |
| | 5 | 1 | 5 | 30 |
| | | 2 | 9 | 30 |
| | | 3 | 10 | 30 |
| | 8 | 1 | 10 | 25 |
| | | 2 | 4 | 24 |
| | | 3 | 11 | 31 |
| | 11 | 1 | 9 | 23 |
| | | 2 | 6 | 25 |
| | | 3 | 7 | 23 |
| | 21 | 1 | 4 | 24 |
| | | 2 | 5 | 15 |
| | | 3 | 9 | 21 |
| injury+Y27632 | 1 | 1 | 8 | 32 |
| | | 2 | 3 | 23 |
| | | 3 | 7 | 29 |
| | 3 | 1 | 4 | 31 |
| | | 2 | 6 | 25 |
| | | 3 | 7 | 32 |
| | 6 | 1 | 2 | 16 |
| | | 2 | 4 | 26 |
| | | 3 | 5 | 30 |
| | 9 | 1 | 6 | 27 |
| | | 2 | 6 | 23 |
| | | 3 | 7 | 21 |
| | 12 | 1 | 5 | 29 |
| | | 2 | 9 | 36 |
| | | 3 | 5 | 19 |
| | 23 | 1 | 7 | 16 |
| | | 2 | 4 | 21 |
| | | 3 | 5 | 24 |

**Note:** Table is continued on the next page.

| Group | Rat | Image | Number of SP-positive neurons | Number of small- & medium-diameter neurons |
|---|---|---|---|---|
| sham+Y27632 | 7 | 1 | 6 | 28 |
| | | 2 | 5 | 29 |
| | | 3 | 6 | 29 |
| | 10 | 1 | 4 | 19 |
| | | 2 | 5 | 20 |
| | | 3 | 5 | 28 |
| | 13 | 1 | 3 | 27 |
| | | 2 | 5 | 20 |
| | | 3 | 6 | 29 |
| | 14 | 1 | 6 | 20 |
| | | 2 | 4 | 19 |
| | | 3 | 5 | 24 |
| | 24 | 1 | 7 | 19 |
| | | 2 | 5 | 21 |
| | | 3 | 7 | 23 |

**Note:** Surgery for all rats listed in this table was performed by Christine Weisshaar.

**Figure J.3. Immunofluorescence images showing SP expression in DRG neurons at day 1 in *injury+veh*, *injury+Y27632* & *sham+veh* groups. Images are labeled by rat number & image number in parentheses.**

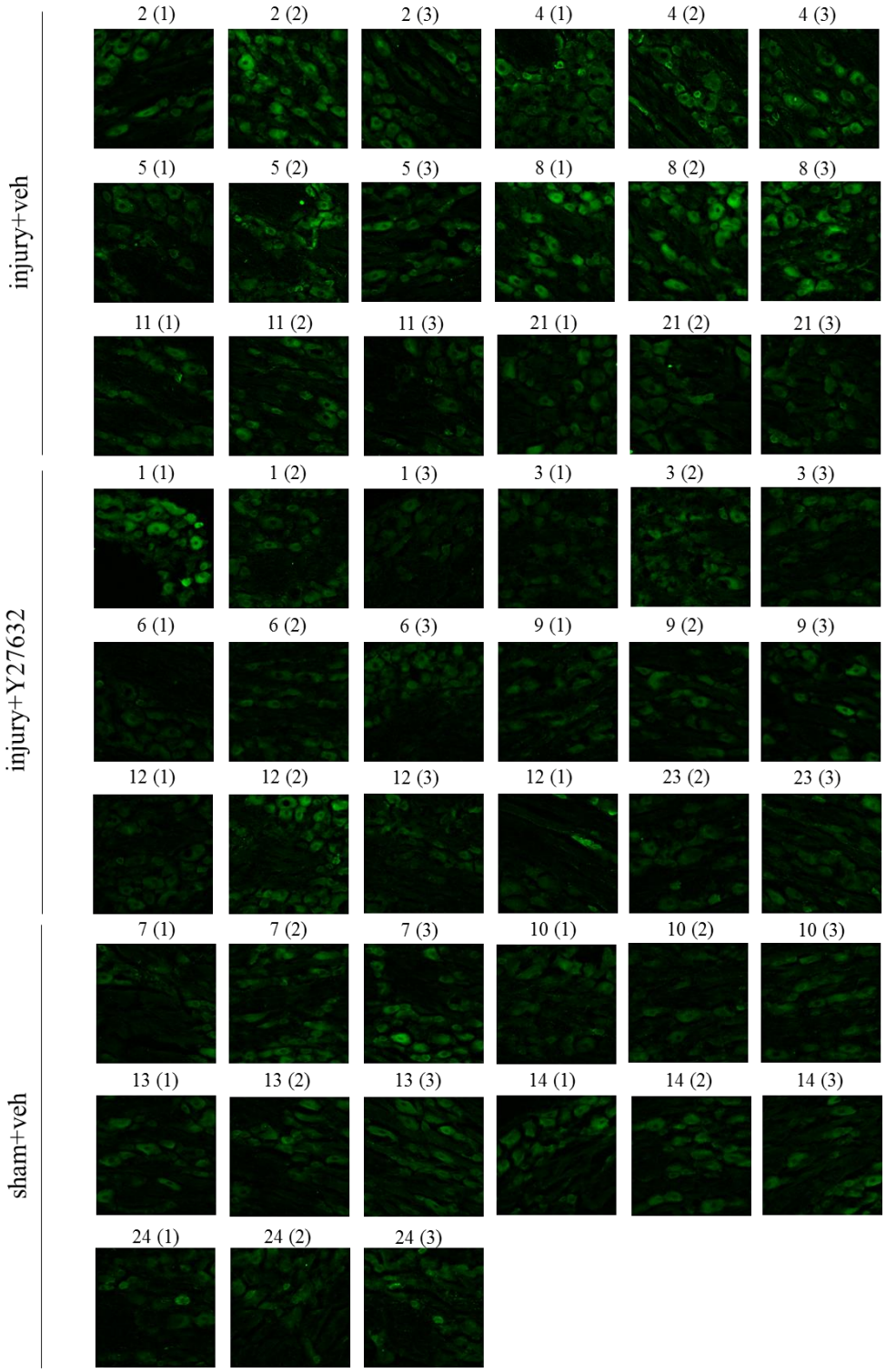

**Table J.4. Densitometric quantification of SP in superficial dorsal horn & Iba1 in superficial & deep dorsal horns at day 1 in *injury+veh*, *injury+Y27632* & *sham+veh* groups (Chapter 8).**

| Group | Rat # | Image | SP | Iba1 (superficial) | Iba1 (deep) |
|---|---|---|---|---|---|
| injury+veh | 2 | 1 | 1.28 | 3.80 | 2.22 |
| | | 2 | – | 3.04 | 1.00 |
| | | 3 | 3.14 | 2.49 | – |
| | | 4 | 2.63 | 1.55 | – |
| | | 5 | – | – | 0.57 |
| | | 6 | 5.34 | 2.98 | 0.73 |
| | | 7 | 3.19 | 2.06 | 1.45 |
| | | 8 | 1.53 | 1.80 | 1.32 |
| | | 9 | – | – | 2.24 |
| | 4 | 1 | | – | 0.73 |
| | | 2 | 1.02 | 1.55 | 1.74 |
| | | 3 | 0.81 | 3.08 | 0.28 |
| | | 4 | 1.18 | 2.48 | 2.19 |
| | | 5 | – | – | 2.01 |
| | | 6 | 0.73 | 1.68 | 0.93 |
| | | 7 | 1.33 | 1.73 | 0.60 |
| | | 8 | 1.01 | 1.28 | 1.38 |
| | | 9 | – | – | 0.96 |
| | 5 | 1 | 1.22 | 2.53 | – |
| | | 2 | 3.68 | 1.81 | 1.89 |
| | | 3 | 2.01 | 2.01 | – |
| | | 4 | 2.79 | 2.34 | – |
| | | 5 | 4.83 | 2.05 | 1.68 |
| | | 6 | – | 1.37 | 1.75 |
| | | 7 | 1.88 | 1.89 | 2.65 |
| | | 8 | 2.52 | 1.56 | 0.95 |
| | | 9 | – | 1.06 | 1.15 |
| | | 10 | 0.36 | 1.85 | 0.59 |
| | 8 | 1 | 3.35 | 2.91 | 1.85 |
| | | 2 | – | 2.38 | 1.19 |
| | | 3 | 1.61 | 2.06 | 0.88 |
| | | 4 | 3.31 | 3.15 | 1.53 |
| | | 5 | 1.86 | 1.84 | 1.40 |
| | | 6 | 1.69 | 1.62 | – |
| | | 7 | – | – | 0.67 |
| | 11 | 1 | 0.87 | 1.53 | 0.77 |
| | | 2 | 2.19 | 2.26 | 0.91 |
| | | 3 | 0.92 | 2.12 | 0.98 |
| | | 4 | 1.34 | 1.81 | 1.15 |
| | | 5 | 2.66 | 2.93 | 1.76 |
| | | 6 | 4.21 | 2.22 | 1.34 |
| | | 7 | – | – | 1.18 |
| | | 8 | 2.75 | 2.51 | 0.77 |
| | 21 | 1 | 0.78 | 2.65 | 1.94 |
| | | 2 | 2.81 | 2.51 | 2.05 |
| | | 3 | 3.13 | 2.23 | 1.49 |
| | | 4 | – | – | 1.35 |
| | | 5 | 2.85 | 2.13 | – |
| | | 6 | 2.60 | 2.55 | 2.30 |
| | | 7 | 1.52 | 1.56 | 2.11 |
| | | 8 | 2.12 | 1.89 | 1.03 |
| | | 9 | – | – | 1.71 |
| | | 10 | 0.80 | 1.51 | – |
| | | 11 | – | – | 2.57 |

**Note:** Table is continued on the next page.

Missing values (–) are due to a torn tissue section, poor labeling in part of the tissue section or an artifact in the image preventing accurate quantification of immunolabeling in the dorsal horn.

| Group | Rat | Image | SP | Iba1 (superficial) | Iba1 (deep) |
|---|---|---|---|---|---|
| injury+Y27632 | 1 | 1 | 0.49 | 0.39 | 0.61 |
| | | 2 | – | – | 0.49 |
| | | 3 | 0.56 | 0.57 | – |
| | | 4 | 0.70 | 0.56 | – |
| | | 5 | 1.97 | 0.68 | 0.29 |
| | | 6 | 0.80 | 0.62 | – |
| | | 7 | 0.98 | 1.09 | 0.90 |
| | | 8 | 0.35 | 0.97 | 0.81 |
| | 3 | 1 | – | 1.73 | – |
| | | 2 | 0.17 | 0.63 | – |
| | | 3 | 1.87 | 2.22 | 1.27 |
| | | 4 | 0.52 | 1.00 | 0.53 |
| | | 5 | 0.86 | 0.66 | 0.60 |
| | | 6 | – | 0.92 | 0.43 |
| | | 7 | 0.64 | 1.14 | 1.29 |
| | | 8 | 0.63 | – | 1.07 |
| | | 9 | 0.29 | 0.72 | – |
| | | 10 | 0.92 | 1.28 | – |
| | | 11 | 1.37 | 1.30 | – |
| | 6 | 1 | 1.64 | 0.92 | – |
| | | 2 | 3.13 | 2.10 | 0.87 |
| | | 3 | 1.88 | – | 1.60 |
| | | 4 | 0.55 | 1.13 | 0.24 |
| | | 5 | – | – | 0.23 |
| | | 6 | 0.80 | 0.61 | – |
| | | 7 | 1.14 | – | 0.65 |
| | | 8 | – | 0.44 | 0.30 |
| | | 9 | 0.63 | 0.55 | 0.21 |
| | | 10 | – | – | 0.07 |
| | 9 | 1 | 0.66 | 1.11 | 1.23 |
| | | 2 | 1.41 | – | 0.86 |
| | | 3 | 1.46 | 1.66 | 1.44 |
| | | 4 | 1.43 | 0.51 | 0.56 |
| | | 5 | 0.16 | 0.20 | 0.51 |
| | | 6 | 0.62 | 0.48 | 1.11 |
| | | 7 | 1.59 | 1.34 | 0.73 |
| | | 8 | 1.24 | 0.53 | – |
| | 12 | 1 | 1.22 | 1.19 | 1.18 |
| | | 2 | – | 0.95 | – |
| | | 3 | 0.27 | 1.37 | 1.30 |
| | | 4 | 0.70 | – | 1.31 |
| | | 5 | 0.56 | 0.97 | 0.89 |
| | | 6 | 0.61 | 0.87 | 0.95 |
| | | 7 | 1.09 | 1.72 | 0.70 |
| | 23 | 1 | 0.77 | 0.82 | 1.97 |
| | | 2 | 0.71 | 0.91 | 0.80 |
| | | 3 | 0.91 | 0.51 | 1.38 |
| | | 4 | 1.16 | 0.68 | 1.14 |
| | | 5 | – | 0.63 | 1.72 |
| | | 6 | 0.52 | 1.04 | 1.00 |
| | | 7 | 0.90 | 0.89 | 1.28 |
| | | 8 | 0.47 | 0.73 | 0.79 |

**Note:** Table is continued on the next page.

Missing values (–) are due to a torn tissue section, poor labeling in part of the tissue section or an artifact in the image preventing accurate quantification of immunolabeling in the dorsal horn.

| Group | Rat | Image | SP | Iba1 (superficial) | Iba1 (deep) |
|---|---|---|---|---|---|
| sham+veh | 7 | 1 | 1.52 | – | 0.91 |
| | | 2 | – | 2.05 | 1.14 |
| | | 3 | 2.11 | 1.54 | 0.85 |
| | | 4 | 2.78 | – | 0.59 |
| | | 5 | – | 1.62 | 0.71 |
| | | 6 | 4.04 | 2.22 | 0.89 |
| | | 7 | 2.95 | 1.71 | 0.79 |
| | | 8 | 5.21 | 1.75 | 0.65 |
| | | 9 | 3.96 | 2.01 | 1.39 |
| | | 10 | 3.68 | 1.28 | 1.00 |
| | | 11 | – | 1.89 | 1.04 |
| | | 12 | – | – | 0.76 |
| | 10 | 1 | 5.41 | 1.48 | 1.13 |
| | | 2 | 3.29 | 0.99 | 0.76 |
| | | 3 | – | – | 0.48 |
| | | 4 | – | – | 0.71 |
| | | 5 | – | – | 1.27 |
| | | 6 | 4.35 | 1.73 | 1.32 |
| | | 7 | 1.35 | 1.12 | 0.65 |
| | | 8 | 1.31 | 1.25 | 1.13 |
| | | 9 | 3.74 | 1.45 | 1.14 |
| | | 10 | 1.20 | 0.96 | 0.82 |
| | | 11 | 2.05 | 1.24 | 1.41 |
| | 13 | 1 | 0.19 | 0.98 | 1.19 |
| | | 2 | 0.50 | 1.07 | 0.62 |
| | | 3 | 0.60 | 2.38 | 2.17 |
| | | 4 | 0.41 | 1.14 | 2.27 |
| | | 5 | 0.69 | 1.21 | 1.35 |
| | | 6 | 0.32 | 0.56 | 1.14 |
| | 14 | 1 | 0.10 | 0.05 | – |
| | | 2 | 3.01 | 1.34 | 0.21 |
| | | 3 | 0.96 | 0.87 | 0.65 |
| | | 4 | 0.58 | 0.49 | 0.26 |
| | | 5 | 0.55 | 1.08 | 1.39 |
| | | 6 | 2.25 | 0.59 | 0.60 |
| | 24 | 1 | 0.77 | 1.07 | 0.80 |
| | | 2 | 5.87 | 2.85 | 2.75 |
| | | 3 | 3.21 | 1.10 | – |
| | | 4 | 2.93 | 1.80 | 1.10 |
| | | 5 | 0.73 | 1.17 | 1.40 |
| | | 6 | 1.77 | 1.59 | 1.90 |
| | | 7 | 0.58 | 0.89 | 1.48 |
| | | 8 | – | – | 0.85 |
| | | 9 | 6.00 | 2.31 | – |

**Note:** Missing values (–) are due to a torn tissue section, poor labeling in part of the tissue section or an artifact in the image preventing accurate quantification of immunolabeling in the dorsal horn. Surgery for all rats listed in this table was performed by Christine Weisshaar.

**Figure J.4. Immunofluorescence images showing expression of SP (green), Iba1 (red) and DAPI (blue) in the spinal dorsal horn at day 1 in the *injury+veh* group. Images are indicated by the rat number with the image number in parentheses.**

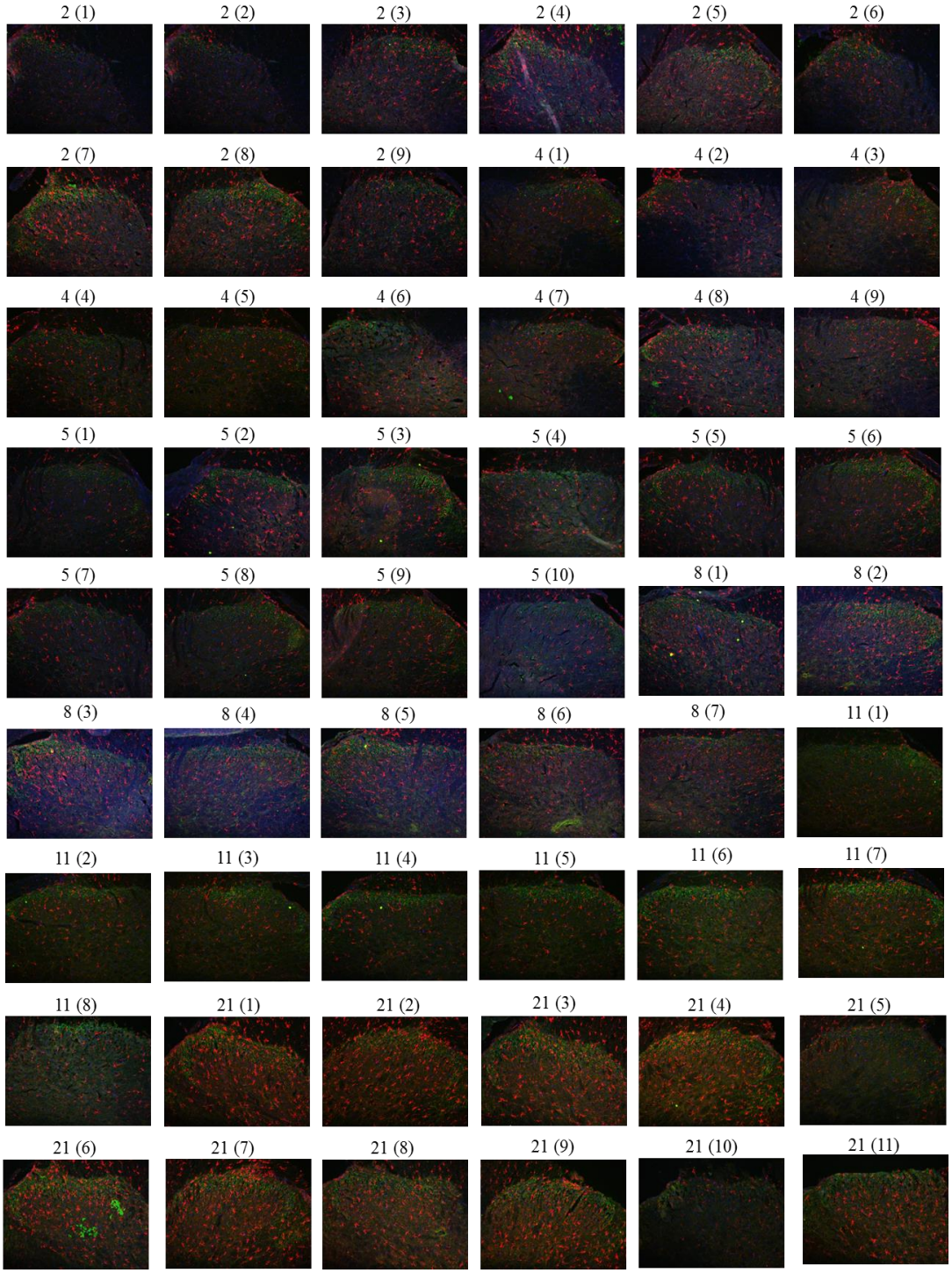

**Figure J.5. Immunofluorescence images showing expression of SP (green), Iba1 (red) and DAPI (blue) in the spinal dorsal horn at day 1 in the *injury+Y27632* group. Images are indicated by the rat number with the image number in parentheses.**

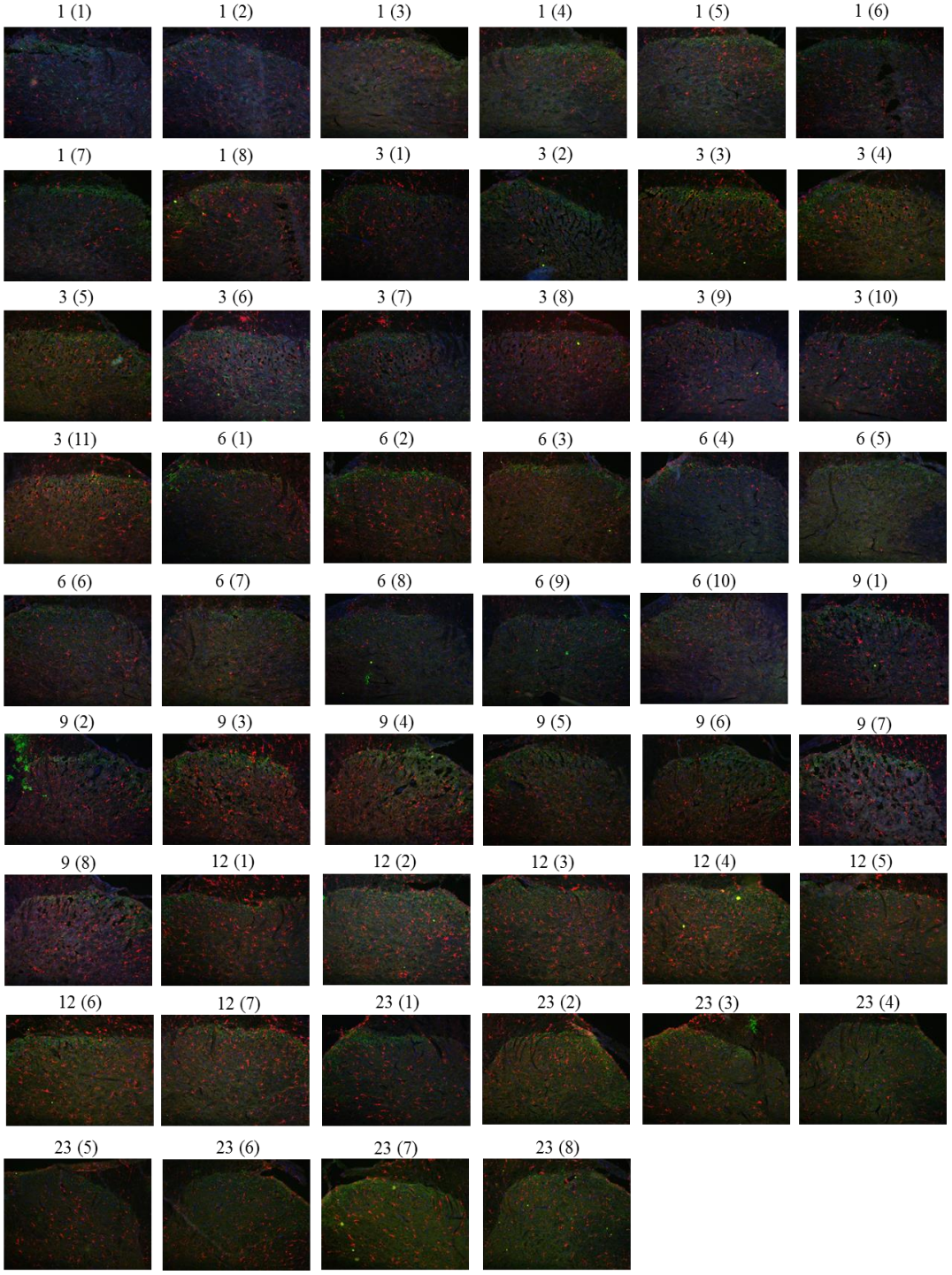

**Figure J.6. Immunofluorescence images showing expression of SP (green), Iba1 (red) and DAPI (blue) in the spinal dorsal horn at day 1 in the *sham+veh* group. Images are indicated by the rat number with the image number in parentheses.**

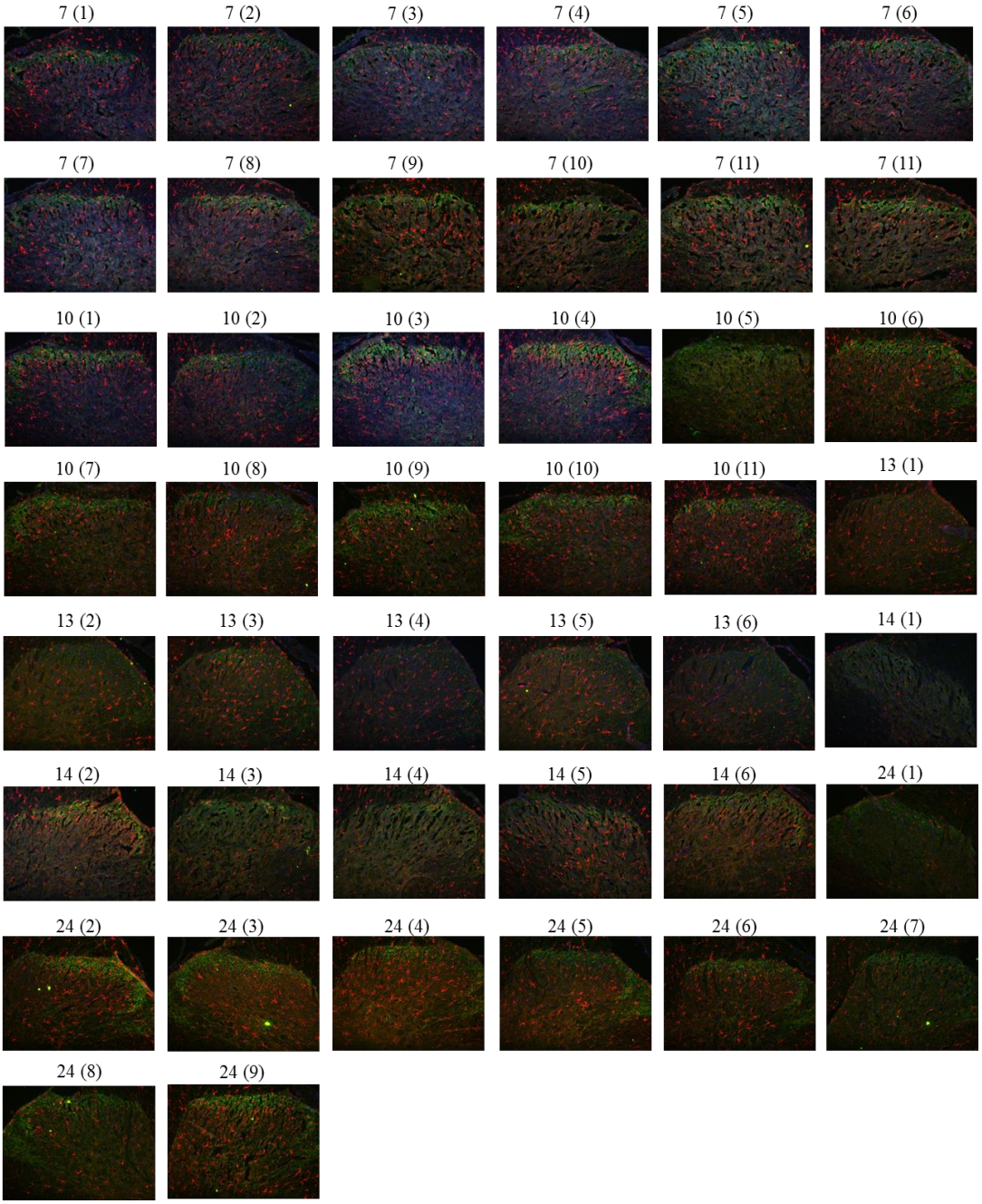

# APPENDIX K

# Facet Joint Distraction Mechanics & Mechanical Hyperalgesia

This appendix summarizes the mechanical injury and behavioral responses for each rat included in the studies presented in Chapters 7 and 8. As detailed in Chapter 7, the displacement and strains applied across the C6/C7 facet joint during distraction were calculated based on the displacements of bead markers that were placed on the laminae of the C6 and C7 vertebrae and the C6/C7 facet capsule. The mechanical outcomes summarized in this appendix include the vertebral displacement, capsular displacement and peak maximum principal strain (MPS) across the facet capsule. All values describing the joint mechanics for rats that underwent sham procedures but no distraction are reported as zeros.

Mechanical hyperalgesia was quantified by the withdrawal threshold of each rat's bilateral forepaws in response to von Frey filament stimulation and was measured at various time points before and after surgical procedures. Two subsets of studies presented in Chapter 7 and Chapter 8 used rats that were generated previously by other lab members. For those rats, the average withdrawal thresholds of the left and right forepaws over three rounds of testing at each time point are listed in Table K.1 and Table K.2 below. Table K.1. details the forepaw withdrawal thresholds on days 0, 1 and 7 and the

imposed facet joint distraction mechanics for the rats that underwent painful facet joint distraction (*FJD*) or sham procedures (*sham*) and whose DRG tissue was used to characterize stretch-induced integrin subunit β1 expression in neurons at day 7 in Chapter 7. Those rats were originally used in a prior study of anatomical characterization of afferents innervating the distracted C6/C7 facet joint performed by Jeffery Kras and their behavioral responses have been published previously (Kras et al. 2013). Table K.2 summarizes the forepaw withdrawal thresholds measured for *FJD* and *sham* rats prior to, and at 1 day after, surgery, as well as the applied joint displacements and strains. The DRG tissue from those rats was used to measure RhoA activity as detailed in Chapter 8. Those rats were originally used by Nate Crosby for electrophysiological recording from the spinal cord; their forepaw withdrawal thresholds also have been published (Crosby et al. 2013).

Table K.3 summarizes the withdrawal thresholds for rats that underwent painful facet joint distraction followed by intra-articular Y27632 injection (*FJD+Y27632*) or vehicle (*FJD+veh*) injection at the time of injury and for rats that underwent sham procedures followed by intra-articular vehicle injection (*sham+veh*), for the studies presented in Chapter 8. In that study inhibiting ROCK, the forepaw withdrawal thresholds were assessed at day 0 prior to surgery and at 8 hours and 1 day after surgery. The data are reported as separate values for the left and right paws at each time point. The corresponding facet joint mechanics for those rats undergoing facet joint distraction are detailed in Table K.4.

**Table K.1. Forepaw withdrawal thresholds & imposed facet joint mechanics for rats in which integrin subunit β1 expression was assessed in the DRG (Chapter 7).**

| | | Forepaw withdrawal threshold | | | Facet joint mechanics | | |
|---|---|---|---|---|---|---|---|
| **Rat #** | **Group** | **day 0** | **day 1** | **day 7** | **Vertebral distraction (mm)** | **Capsular distraction (mm)** | **Peak MPS** |
| 134 | FJD | 8.7 | 3.7 | 3.7 | 0.48 | 0.22 | 0.178 |
| 143 | FJD | 13.3 | 5.0 | 4.7 | 0.46 | 0.12 | 0.093 |
| 152 | FJD | 20.5 | 3.2 | 6.3 | 0.40 | 0.15 | 0.112 |
| 155 | FJD | 10.0 | 3.7 | 2.5 | 0.53 | 0.18 | 0.150 |
| 132 | sham | 18.7 | 11.5 | 22.3 | 0 | 0 | 0 |
| 141 | sham | 21.5 | 17.5 | 17.8 | 0 | 0 | 0 |
| 142 | sham | 17.0 | 18.7 | 16.8 | 0 | 0 | 0 |
| 150 | sham | 19.7 | 17.8 | 14.2 | 0 | 0 | 0 |
| 154 | sham | 14.0 | 12.2 | 13.7 | 0 | 0 | 0 |

**Note:** All rats listed in this table were generated by Jeffery Kras and the rat numbering scheme reflects his records.

**Table K.2. Forepaw withdrawal thresholds & imposed facet joint mechanics for rats in which RhoA activity was assessed in the DRG (Chapter 8).**

| | | Forepaw withdrawal threshold | | Facet joint mechanics | | |
|---|---|---|---|---|---|---|
| **Rat #** | **Group** | **day 0** | **day 1** | **Vertebral distraction (mm)** | **Capsular distraction (mm)** | **Peak MPS** |
| 20 | FJD | 4.5 | 2.2 | 0.54 | 0.28 | 0.375 |
| 21 | FJD | 7.6 | 8.8 | 0.47 | 0.29 | 0.265 |
| 25 | FJD | 13.1 | 5.7 | -- | -- | -- |
| 27 | FJD | 16.3 | 7.7 | 0.69 | 0.33 | 0.316 |
| 24 | sham | 6.2 | 3.3 | 0 | 0 | 0 |
| 26 | sham | 5.1 | 5.7 | 0 | 0 | 0 |

**Note:** All rats listed in this table were generated by Nate Crosby and the rat numbering scheme reflects his records. The mechanical data for Rat #25 in the FJD group are not available.

**Table K.3. Forepaw withdrawal thresholds for rats undergoing FJD & intra-articular injections (Chapter 8).**

| | | Forepaw withdrawal threshold | | | | | |
|---|---|---|---|---|---|---|---|
| | | day 0 | | 8hrs | | day 1 | |
| Rat # | Group | Right | Left | Right | Left | Right | Left |
| 2 | FJD+veh | 9.3 | 15.0 | 5.3 | 8.0 | 2.7 | 4.7 |
| 4 | FJD+veh | 11.7 | 15.0 | 9.3 | 8.0 | 4.7 | 6.7 |
| 5 | FJD+veh | 19.3 | 11.3 | 6.7 | 10.0 | 5.3 | 6.0 |
| 8 | FJD+veh | 11.7 | 9.3 | 8.0 | 8.0 | 5.3 | 4.7 |
| 11 | FJD+veh | 8.7 | 8.7 | 4.0 | 5.3 | 4.7 | 4.0 |
| 16 | FJD+veh | 18.7 | 13.3 | 9.3 | 8.0 | 7.3 | 6.0 |
| 17 | FJD+veh | 13.3 | 8.0 | 11.0 | 8.0 | 6.7 | 5.3 |
| 21 | FJD+veh | 10.0 | 11.0 | 3.3 | 8.7 | 4.0 | 6.7 |
| 22 | FJD+veh | 11.7 | 8.7 | 7.3 | 6.0 | 5.3 | 4.0 |
| 26 | FJD+veh | 8.0 | 8.7 | 5.3 | 6.0 | 3.3 | 4.7 |
| 32 | FJD+veh | 7.3 | 8.0 | 5.3 | 6.7 | 3.3 | 4.0 |
| 1 | FJD+Y27632 | 11.7 | 13.3 | 10.3 | 22.3 | 10.0 | 13.3 |
| 3 | FJD+Y27632 | 15.0 | 13.3 | 12.0 | 9.0 | 11.7 | 17.0 |
| 6 | FJD+Y27632 | 20.5 | 19.3 | 22.3 | 22.3 | 22.3 | 15.3 |
| 9 | FJD+Y27632 | 13.3 | 15.0 | 15.0 | 9.3 | 13.3 | 11.7 |
| 12 | FJD+Y27632 | 10.0 | 9.3 | 8.0 | 8.0 | 9.3 | 6.0 |
| 15 | FJD+Y27632 | 10.0 | 8.7 | 8.7 | 8.0 | 9.3 | 7.3 |
| 18 | FJD+Y27632 | 13.3 | 22.3 | 17.0 | 26.0 | 17.0 | 20.7 |
| 19 | FJD+Y27632 | 11.7 | 18.7 | 10.0 | 17.0 | 9.3 | 15.0 |
| 23 | FJD+Y27632 | -- | 11.7 | -- | 15.0 | -- | 13.3 |
| 27 | FJD+Y27632 | 13.3 | 11.0 | 11.7 | 13.3 | 10.0 | 13.3 |
| 28 | FJD+Y27632 | 11.0 | 10.3 | 10.0 | 11.0 | 11.7 | 17.0 |
| 30 | FJD+Y27632 | 8.7 | 10.0 | 8.0 | 8.7 | 22.3 | 15.3 |
| 7 | sham+veh | 8.7 | 10.0 | 6.7 | 13.3 | 8.0 | 9.3 |
| 10 | sham+veh | 13.3 | 13.3 | 11.7 | 13.3 | 8.7 | 11.7 |
| 13 | sham+veh | 11.0 | 15.0 | 7.3 | 11.7 | 7.3 | 11.7 |
| 14 | sham+veh | 11.7 | 13.3 | 9.3 | 15.0 | 7.3 | 15.0 |
| 20 | sham+veh | 9.3 | 10.0 | 11.0 | 13.3 | 8.0 | 9.3 |
| 24 | sham+veh | 8.7 | 17.0 | 6.7 | 17.0 | 8.0 | 15.0 |
| 25 | sham+veh | 12.7 | 13.3 | 8.7 | 13.3 | 7.3 | 15.0 |
| 29 | sham+veh | 11.7 | 13.3 | 11.7 | 13.3 | 15.0 | 11.7 |
| 31 | sham+veh | 8.0 | 9.3 | 8.0 | 9.3 | 8.0 | 8.7 |
| 33 | sham+veh | 15.0 | 13.3 | 15.0 | 22.3 | 13.3 | 13.3 |
| 35 | sham+veh | 22.3 | 18.7 | 26.0 | 18.7 | 15.0 | 22.3 |
| 36 | sham+veh | 8.7 | 10.0 | 9.3 | 8.0 | 10.0 | 7.3 |

**Note:** Surgeries for all rats in this table were performed by Christine Weisshaar. The mechanical hyperalgesia data for Rat #23's right paw are not available, since that rat had an injured toenail on his right paw that affected withdrawal measurements. Only the left withdrawal thresholds for Rat #23 were used.

**Table K.4. Imposed facet joint mechanics for rats that received FJD & intra-articular injections (Chapter 8).**

| | | Facet joint mechanics | | |
|---|---|---|---|---|
| **Rat #** | **Group** | **Vertebral distraction (mm)** | **Capsular distraction (mm)** | **Peak MPS** |
| 2 | FJD+veh | 0.48 | 0.23 | 0.139 |
| 4 | FJD+veh | 0.18 | 0.22 | 0.166 |
| 5 | FJD+veh | 0.59 | 0.36 | 0.226 |
| 8 | FJD+veh | 0.74 | 0.44 | 0.497 |
| 11 | FJD+veh | 0.91 | 0.50 | 0.378 |
| 16 | FJD+veh | 0.41 | 0.17 | 0.153 |
| 17 | FJD+veh | 0.60 | 0.23 | 0.133 |
| 21 | FJD+veh | 0.55 | 0.26 | 0.272 |
| 22 | FJD+veh | 0.28 | 0.19 | 0.134 |
| 26 | FJD+veh | 0.57 | 0.21 | 0.168 |
| 32 | FJD+veh | 0.37 | 0.16 | 0.106 |
| 1 | FJD+Y27632 | 0.43 | 0.27 | 0.107 |
| 3 | FJD+Y27632 | 0.30 | 0.21 | 0.083 |
| 6 | FJD+Y27632 | 0.38 | 0.15 | 0.256 |
| 9 | FJD+Y27632 | 0.65 | 0.41 | 0.399 |
| 12 | FJD+Y27632 | 0.39 | 0.29 | 0.159 |
| 15 | FJD+Y27632 | 0.48 | 0.36 | 0.252 |
| 18 | FJD+Y27632 | 0.64 | 0.39 | 0.318 |
| 19 | FJD+Y27632 | 0.70 | 0.35 | 0.359 |
| 23 | FJD+Y27632 | 0.44 | 0.25 | 0.167 |
| 27 | FJD+Y27632 | 0.52 | 0.19 | 0.147 |
| 28 | FJD+Y27632 | 0.64 | 0.42 | 0.344 |
| 30 | FJD+Y27632 | 0.51 | 0.30 | 0.211 |
| 7 | sham+veh | 0 | 0 | 0 |
| 10 | sham+veh | 0 | 0 | 0 |
| 13 | sham+veh | 0 | 0 | 0 |
| 14 | sham+veh | 0 | 0 | 0 |
| 20 | sham+veh | 0 | 0 | 0 |
| 24 | sham+veh | 0 | 0 | 0 |
| 25 | sham+veh | 0 | 0 | 0 |
| 29 | sham+veh | 0 | 0 | 0 |
| 31 | sham+veh | 0 | 0 | 0 |
| 33 | sham+veh | 0 | 0 | 0 |
| 35 | sham+veh | 0 | 0 | 0 |
| 36 | sham+veh | 0 | 0 | 0 |

**Note:** Surgeries for all rats in this table were performed by Christine Weisshaar.

# APPENDIX L

# RhoA Activity in DRGs & NCCs after Stretch

This appendix summarizes the RhoA activity measurements in the dorsal root ganglion (DRG) following in vivo facet joint distraction and in vitro neuron-collagen construct (NCC) stretch; studies are presented in Chapter 8. Tissue lysate was obtained from fresh DRGs at 1 day after a painful facet joint injury; mechanical hyperalgesia measurements taken before and after facet joint distraction are summarized in Appendix K. Lysate from the NCCs was collected at 30 minutes and 6 hours after their stretch, from separate groups of NCCs. Unloaded sham tissue and control NCCs were also included at each time point to control for the effects of the surgical procedures and NCC manipulations, respectively. Active GTP-bound RhoA and total RhoA were measured separately using ELISA-based techniques as detailed in Section 8.3.1. RhoA activity was calculated as the ratio of active-to-total RhoA for comparison of RhoA activity between samples. Table L.1 summarizes the fold change in RhoA activity over sham levels in the rats; Table L.2 lists the RhoA activity in the NCCs as fold change over unloaded control levels.

**Table L.1. RhoA activity in DRGs 1 day after facet joint distraction or sham operations in vivo (Chapter 8).**

| Rat # | Group | Time point | Relative RhoA activity (fold change over control*) |
|---|---|---|---|
| 20 | distraction | day 1 | 1.58 |
| 21 | distraction | day 1 | 1.85 |
| 25 | distraction | day 1 | 1.12 |
| 27 | distraction | day 1 | 1.96 |
| 24 | sham | day 1 | 1.07 |
| 26 | sham | day 1 | 0.93 |

* The control level was calculated as the average RhoA activity in sham rats.
**Note:** All rats listed in this table were generated by Nate Crosby and the rat numbering scheme reflects his records.

**Table L.2. RhoA activity in NCCs 30 minutes & 6 hours after NCC stretch or in unloaded controls (Chapter 8).**

| Sample | Group | Time point | Relative RhoA activity (fold change over control*) |
|---|---|---|---|
| 1 | stretch | 30 min | 2.08 |
| 2 | stretch | 30 min | 1.28 |
| 3 | stretch | 30 min | 2.84 |
| 4 | control | 30 min | 1.34 |
| 5 | control | 30 min | 0.88 |
| 6 | control | 30 min | 0.78 |
| 7 | stretch | 6 hrs | 1.54 |
| 8 | stretch | 6 hrs | 1.15 |
| 9 | stretch | 6 hrs | 1.95 |
| 10 | stretch | 6 hrs | 1.13 |
| 11 | stretch | 6 hrs | 3.18 |
| 12 | control | 6 hrs | 0.91 |
| 13 | control | 6 hrs | 0.91 |
| 14 | control | 6 hrs | 1.18 |
| 15 | control | 6 hrs | 1.12 |
| 16 | control | 6 hrs | 0.88 |

* The control level was calculated as the average RhoA activity in unloaded NCCs.

# APPENDIX M

# Quantification of Spinal Neuronal Firing

This appendix summarizes the neuronal firing data acquired by electrophysiological recordings from the rat's spinal dorsal horn in the studies presented in Chapter 8. The recording protocol and the analysis methods are detailed in Chapter 8 and reported in prior publications (Quinn et al. 2010; Crosby et al. 2013). Three tables are included detailing the neuronal spike counts evoked by the different mechanical stimulations that were applied to the forepaw of the different groups of rats used in the ROCK inhibition study. Each table lists the total number of evoked spike counts summed over all repetitions for each modality of mechanical stimulation strength: ten light brushing (Brush), stimulation of four different von Frey (vF) filaments (1.4g, 4g, 10g, and 26g) applied five times each, and one noxious pinch held for 10s (Pinch). The corresponding mechanical hyperalgesia measurements taken before and after the facet joint distraction and the joint mechanics during distraction for this group or rats are summarized in Appendix K

Table M.1 summarizes the neuronal firing measurements at day 1 in rats that received facet joint injury and vehicle treatment (*injury+veh* group). Table M.2 details the total neuronal spike counts at day 1 in rats that underwent facet joint injury and the ROCK inhibitor Y27632 treatment (*injury+Y27632* group). Table M.3 lists the number of

evoked spikes at 1 day in rats that experienced sham operations and vehicle injection (*sham+veh* group).

**Table M.1. Total spike counts of spinal neurons at day 1 in the *injury+veh* group (Chapter 8).**

| Rat # | Neuron ID | Brush | vF 1.4g | vF 4g | vF 10g | vF 26g | Pinch |
|---|---|---|---|---|---|---|---|
| 16 | 16-1 | 53 | 42 | 68 | 65 | 94 | 35 |
| 16 | 16-2 | 79 | 24 | 51 | 79 | 326 | 371 |
| 16 | 16-3 | 177 | 17 | 46 | 114 | 310 | 261 |
| 16 | 16-4 | 27 | 13 | 27 | 30 | 27 | 10 |
| 16 | 16-5 | 24 | 32 | 21 | 63 | 48 | 9 |
| 16 | 16-6 | 48 | 11 | 3 | 38 | 131 | 50 |
| 16 | 16-7 | 24 | 8 | 12 | 14 | 19 | 2 |
| 16 | 16-8 | 62 | 3 | 20 | 36 | 85 | 61 |
| 17 | 17-1 | 193 | 71 | 84 | 157 | 193 | 217 |
| 17 | 17-2 | 125 | 28 | 22 | 26 | 61 | 33 |
| 17 | 17-3 | 88 | 13 | 15 | 48 | 49 | 54 |
| 17 | 17-4 | 42 | 23 | 25 | 31 | 31 | 35 |
| 17 | 17-5 | 80 | 13 | 29 | 58 | 100 | 78 |
| 17 | 17-6 | 57 | 17 | 31 | 46 | 90 | 17 |
| 17 | 17-7 | 33 | 14 | 61 | 291 | 316 | 155 |
| 17 | 17-8 | 115 | 25 | 41 | 100 | 141 | 95 |
| 17 | 17-9 | 74 | 34 | 41 | 43 | 90 | 42 |
| 17 | 17-10 | 26 | 18 | 54 | 79 | 173 | 91 |
| 22 | 22-1 | 62 | 48 | 35 | 26 | 101 | 30 |
| 22 | 22-2 | 48 | 18 | 52 | 275 | 75 | 19 |
| 22 | 22-3 | 82 | 45 | 50 | 106 | 75 | 30 |
| 22 | 22-4 | 33 | 6 | 6 | 14 | 21 | 19 |
| 22 | 22-5 | 33 | 19 | 48 | 48 | 52 | 59 |
| 22 | 22-6 | 33 | 34 | 34 | 46 | 102 | 66 |
| 22 | 22-7 | 36 | 27 | 50 | 40 | 48 | 39 |
| 22 | 22-8 | 36 | 20 | 38 | 28 | 28 | 87 |
| 26 | 26-1 | 31 | 21 | 26 | 27 | 77 | 90 |
| 26 | 26-2 | 30 | 56 | 83 | 96 | 90 | 170 |
| 26 | 26-3 | 42 | 49 | 84 | 103 | 143 | 56 |
| 26 | 26-4 | 174 | 208 | 279 | 219 | 316 | 231 |
| 26 | 26-5 | 49 | 10 | 41 | 138 | 101 | 48 |
| 26 | 26-6 | 40 | 11 | 25 | 47 | 70 | 43 |
| 26 | 26-7 | 44 | 15 | 43 | 62 | 131 | 75 |
| 26 | 26-8 | 38 | 41 | 51 | 82 | 142 | 59 |
| 26 | 26-9 | 56 | 23 | 29 | 56 | 146 | 36 |
| 26 | 26-10 | 13 | 58 | 56 | 91 | 52 | 14 |
| 26 | 26-11 | 43 | 33 | 76 | 99 | 95 | 41 |
| 26 | 26-12 | 15 | 10 | 21 | 52 | 51 | 78 |
| 32 | 32-1 | 388 | 101 | 205 | 126 | 292 | 184 |
| 32 | 32-2 | 122 | 60 | 69 | 73 | 102 | 54 |
| 32 | 32-3 | 92 | 14 | 38 | 110 | 87 | 105 |
| 32 | 32-4 | 18 | 21 | 18 | 17 | 26 | 11 |
| 32 | 32-5 | 20 | 3 | 28 | 128 | 422 | 39 |
| 32 | 32-6 | 6 | 9 | 4 | 21 | 70 | 17 |
| 32 | 32-7 | 70 | 47 | 52 | 117 | 404 | 41 |
| 32 | 32-8 | 130 | 35 | 68 | 107 | 153 | 279 |
| 32 | 32-9 | 121 | 75 | 160 | 243 | 310 | 571 |
| 32 | 32-10 | 94 | 57 | 62 | 143 | 198 | 206 |
| 32 | 32-11 | 51 | 38 | 37 | 82 | 101 | 105 |

**Table M.2. Total spike counts of spinal neurons at day 1 in the *injury+Y27632* group (Chapter 8).**

| Rat # | Neuron ID | Brush | vF 1.4g | vF 4g | vF 10g | vF 26g | Pinch |
|---|---|---|---|---|---|---|---|
| 15 | 15-1 | 88 | 46 | 38 | 72 | 85 | 33 |
| 15 | 15-2 | 52 | 6 | 29 | 81 | 245 | 59 |
| 15 | 15-3 | 44 | 7 | 7 | 24 | 35 | 31 |
| 15 | 15-4 | 55 | 30 | 61 | 49 | 56 | 56 |
| 15 | 15-5 | 38 | 12 | 21 | 29 | 55 | 46 |
| 15 | 15-6 | 30 | 20 | 40 | 56 | 91 | 11 |
| 15 | 15-7 | 25 | 12 | 41 | 171 | 279 | 185 |
| 15 | 15-8 | 26 | 9 | 31 | 62 | 45 | 46 |
| 18 | 18-1 | 37 | 58 | 48 | 50 | 65 | 114 |
| 18 | 18-2 | 91 | 273 | 371 | 202 | 358 | 203 |
| 18 | 18-3 | 80 | 21 | 34 | 71 | 81 | 77 |
| 18 | 18-4 | 69 | 40 | 25 | 40 | 83 | 28 |
| 18 | 18-5 | 88 | 22 | 50 | 141 | 263 | 66 |
| 18 | 18-6 | 62 | 108 | 84 | 219 | 126 | 133 |
| 18 | 18-8 | 62 | 6 | 25 | 33 | 72 | 59 |
| 18 | 18-9 | 33 | 36 | 104 | 142 | 179 | 129 |
| 19 | 19-1 | 27 | 8 | 36 | 110 | 76 | 20 |
| 19 | 19-2 | 15 | 11 | 18 | 22 | 13 | 16 |
| 19 | 19-3 | 42 | 27 | 40 | 46 | 68 | 37 |
| 19 | 19-4 | 45 | 14 | 49 | 56 | 104 | 59 |
| 19 | 19-5 | 39 | 27 | 38 | 74 | 221 | 80 |
| 19 | 19-6 | 23 | 7 | 38 | 16 | 37 | 17 |
| 19 | 19-7 | 121 | 59 | 27 | 42 | 82 | 91 |
| 19 | 19-8 | 18 | 11 | 14 | 24 | 41 | 287 |
| 19 | 19-9 | 26 | 3 | 7 | 17 | 34 | 12 |
| 19 | 19-10 | 24 | 17 | 29 | 37 | 102 | 101 |
| 19 | 19-11 | 27 | 19 | 15 | 11 | 18 | 23 |
| 27 | 27-1 | 13 | 9 | 18 | 20 | 37 | 8 |
| 27 | 27-2 | 15 | 7 | 9 | 23 | 25 | 13 |
| 27 | 27-3 | 29 | 17 | 26 | 39 | 78 | 29 |
| 27 | 27-4 | 10 | 4 | 7 | 8 | 27 | 16 |
| 27 | 27-5 | 5 | 41 | 41 | 38 | 35 | 87 |
| 27 | 27-6 | 52 | 39 | 55 | 45 | 50 | 39 |
| 27 | 27-8 | 11 | 15 | 17 | 49 | 37 | 30 |
| 27 | 27-9 | 3 | 7 | 10 | 9 | 13 | 6 |
| 28 | 28-1 | 116 | 21 | 32 | 69 | 21 | 13 |
| 28 | 28-2 | 37 | 8 | 48 | 44 | 71 | 10 |
| 28 | 28-3 | 44 | 57 | 70 | 17 | 44 | 4 |
| 28 | 28-4 | 60 | 36 | 16 | 9 | 34 | 45 |
| 28 | 28-5 | 26 | 14 | 28 | 29 | 21 | 8 |
| 28 | 28-6 | 34 | 28 | 23 | 46 | 143 | 45 |
| 28 | 28-7 | 19 | 4 | 37 | 67 | 66 | 46 |
| 28 | 28-8 | 29 | 10 | 21 | 16 | 37 | 21 |
| 28 | 28-9 | 67 | 27 | 78 | 95 | 127 | 117 |
| 28 | 28-10 | 42 | 20 | 46 | 93 | 44 | 44 |
| 30 | 30-1 | 23 | 4 | 48 | 31 | 44 | 24 |
| 30 | 30-2 | 93 | 16 | 9 | 18 | 69 | 42 |
| 30 | 30-3 | 91 | 56 | 77 | 76 | 129 | 58 |
| 30 | 30-4 | 70 | 31 | 60 | 67 | 204 | 98 |
| 30 | 30-5 | 37 | 6 | 51 | 61 | 68 | 28 |
| 30 | 30-6 | 104 | 19 | 50 | 88 | 83 | 39 |
| 30 | 30-7 | 27 | 2 | 5 | 10 | 27 | 14 |

**Table M.3. Total spike counts of spinal neurons at day 1 in the *sham+veh* group (Chapter 8).**

| Rat # | Neuron ID | Brush | vF 1.4g | vF 4g | vF 10g | vF 26g | Pinch |
|---|---|---|---|---|---|---|---|
| 25 | 25-1 | 27 | 23 | 47 | 51 | 53 | 27 |
| 25 | 25-2 | 26 | 15 | 42 | 69 | 56 | 24 |
| 25 | 25-3 | 57 | 39 | 50 | 33 | 29 | 21 |
| 25 | 25-4 | 32 | 22 | 24 | 32 | 47 | 12 |
| 25 | 25-5 | 57 | 14 | 45 | 48 | 70 | 80 |
| 25 | 25-6 | 8 | 17 | 14 | 23 | 31 | 10 |
| 25 | 25-7 | 39 | 9 | 15 | 30 | 53 | 25 |
| 25 | 25-8 | 10 | 16 | 17 | 42 | 45 | 54 |
| 25 | 25-9 | 16 | 6 | 11 | 24 | 69 | 41 |
| 25 | 25-10 | 11 | 4 | 7 | 19 | 41 | 29 |
| 25 | 25-11 | 16 | 5 | 12 | 31 | 57 | 33 |
| 29 | 29-1 | 8 | 4 | 31 | 29 | 83 | 53 |
| 29 | 29-2 | 19 | 5 | 9 | 17 | 14 | 11 |
| 29 | 29-3 | 15 | 6 | 7 | 17 | 15 | 4 |
| 29 | 29-4 | 12 | 7 | 11 | 43 | 159 | 20 |
| 29 | 29-5 | 36 | 11 | 17 | 10 | 23 | 18 |
| 29 | 29-6 | 29 | 28 | 35 | 62 | 79 | 37 |
| 29 | 29-7 | 66 | 7 | 25 | 44 | 9 | 0 |
| 29 | 29-8 | 19 | 3 | 5 | 11 | 8 | 13 |
| 29 | 29-9 | 19 | 4 | 18 | 21 | 30 | 9 |
| 33 | 33-1 | 23 | 39 | 88 | 66 | 84 | 134 |
| 33 | 33-2 | 78 | 78 | 140 | 119 | 261 | 31 |
| 33 | 33-3 | 20 | 19 | 34 | 29 | 43 | 8 |
| 33 | 33-4 | 23 | 11 | 39 | 76 | 239 | 14 |
| 33 | 33-5 | 41 | 24 | 29 | 37 | 92 | 95 |
| 33 | 33-6 | 14 | 9 | 10 | 21 | 37 | 28 |
| 33 | 33-7 | 46 | 24 | 85 | 58 | 275 | 235 |
| 33 | 33-8 | 37 | 37 | 26 | 17 | 26 | 7 |
| 33 | 33-9 | 27 | 11 | 37 | 23 | 42 | 83 |
| 31 | 31-1 | 383 | 14 | 51 | 64 | 133 | 5 |
| 31 | 31-2 | 78 | 27 | 23 | 35 | 31 | 33 |
| 31 | 31-3 | 487 | 67 | 161 | 85 | 242 | 91 |
| 31 | 31-4 | 39 | 19 | 66 | 97 | 70 | 35 |
| 31 | 31-5 | 40 | 19 | 10 | 29 | 64 | 59 |
| 31 | 31-6 | 48 | 29 | 58 | 61 | 134 | 25 |
| 31 | 31-7 | 43 | 24 | 57 | 145 | 69 | 51 |
| 31 | 31-8 | 15 | 12 | 39 | 39 | 49 | 21 |
| 31 | 31-9 | 41 | 40 | 53 | 51 | 67 | 70 |
| 31 | 31-10 | 51 | 24 | 17 | 24 | 0 | 0 |
| 35 | 35-1 | 37 | 10 | 27 | 32 | 44 | 25 |
| 35 | 35-2 | 29 | 30 | 15 | 14 | 51 | 16 |
| 35 | 35-3 | 28 | 12 | 4 | 3 | 9 | 1 |
| 35 | 35-4 | 3 | 7 | 12 | 14 | 16 | 12 |
| 36 | 36-1 | 22 | 7 | 32 | 73 | 33 | 14 |
| 36 | 36-2 | 69 | 30 | 28 | 56 | 56 | 42 |
| 36 | 36-3 | 28 | 5 | 39 | 45 | 92 | 34 |
| 36 | 36-4 | 3 | 4 | 28 | 17 | 55 | 13 |
| 36 | 36-5 | 59 | 1 | 18 | 62 | 20 | 1 |
| 36 | 36-6 | 15 | 13 | 11 | 26 | 19 | 13 |
| 36 | 36-7 | 35 | 33 | 26 | 45 | 155 | 31 |
| 36 | 36-8 | 11 | 3 | 10 | 18 | 22 | 13 |
| 36 | 36-9 | 102 | 55 | 79 | 130 | 94 | 19 |

# REFERENCES


Abbadie, C., Brown, J. L., Mantyh, P. W., & Basbaum, A. I. (1996). Spinal cord substance P receptor immunoreactivity increases in both inflammatory and nerve injury models of persistent pain. *Neuroscience*, *70*(1), 201–9.

Afrah, A. W., Fiskå, A., Gjerstad, J., Gustafsson, H., Tjølsen, A., Olgart, L., Stiller, C.O., Hole, K., & Brodin, E. (2002). Spinal substance P release in vivo during the induction of long-term potentiation in dorsal horn neurons. *Pain*, *96*(1-2), 49–55.

Aghvami, M., Barocas, V. H., & Sander, E. A. (2013). Multiscale mechanical simulations of cell compacted collagen gels. *Journal of Biomechanical Engineering*, *135*(7), 71004.

Ahmed, A. M., Duncan, N. A., & Burke, D. L. (1990). The effect of facet geometry on the axial torque-rotation response of lumbar motion segments. *Spine*, *15*(5), 391–401.

Alavi, S. H., Ruiz, V., Krasieva, T., Botvinick, E. L., & Kheradvar, A. (2013). Characterizing the Collagen Fiber Orientation in Pericardial Leaflets Under Mechanical Loading Conditions. *Annals of Biomedical Engineering*, *41*(3), 547–561.

Alford, P. W., & Taber, L. A. (2008). Computational study of growth and remodelling in the aortic arch. *Computer Methods in Biomechanics and Biomedical Engineering*, *11*(5), 525–38.

Atanasov, D. (2010). Two-phase linear regression model. Retrieved from http://www.mathworks.com/matlabcentral/fileexchange/26804-two-phase-linear-regression-model

Ateshian, G. A., Maas, S., & Weiss, J. A. (2013). Multiphasic Finite Element Framework for Modeling Hydrated Mixtures With Multiple Neutral and Charged Solutes. *Journal of Biomechanical Engineering*, *135*(11), 111001.

Bain, A. C., Raghupathi, R., & Meaney, D. F. (2001). Dynamic stretch correlates to both morphological abnormalities and electrophysiological impairment in a model of traumatic axonal injury. *Journal of Neurotrauma*, *18*(5), 499–511.

Ban, E., Zhang, S., Zarei, V., Barocas, V. H., Winkelstein, B. A., & Picu, C. R. (2017). Collagen organization in facet capsular ligaments varies with spinal region and with ligament deformation. *Journal of Biomechanical Engineering*, *139*(7), 071009.

Baniassadi, M., Ahzi, S., Garmestani, H., Ruch, D., & Remond, Y. (2012). New approximate solution for N-point correlation functions for heterogeneous materials. *Journal of the Mechanics and Physics of Solids*, *60*(1), 104–119.

Barnsley, L., Lord, S., & Bogduk, N. (1994). Whiplash injury. *Pain*, *58*(3), 283–307.

Barros, C. S., Franco, S. J., & Müller, U. (2011). Extracellular matrix: functions in the nervous system. *Cold Spring Harbor Perspectives in Biology*, *3*(1), a005108. doi:10.1101/cshperspect.a005108

Basbaum, A. I., Bautista, D. M., Scherrer, G., & Julius, D. (2009). Cellular and molecular mechanisms of pain. *Cell*, *139*(2), 267–84.

Bassett, D. S., Owens, E. T., Daniels, K. E., & Porter, M. A. (2012). Influence of network topology on sound propagation in granular materials. *Physical Review E*, *86*(4), 041306.

Bassett, D. S., Owens, E. T., Porter, M. A., Manning, M. L., & Daniels, K. E. (2014). Extraction of force-chain network architecture in granular materials using community detection. *Soft Matter*, *11*(14), 2731–44.

Bassett, D. S., Porter, M. A., Wymbs, N. F., Grafton, S. T., Carlson, J. M., & Mucha, P. J. (2013a). Robust detection of dynamic community structure in networks. *Chaos*, *23*(1), 013142.

Bassett, D. S., Wymbs, N. F., Porter, M. A., Mucha, P. J., Carlson, J. M., & Grafton, S. T. (2011). Dynamic reconfiguration of human brain networks during learning. *Proceedings of the National Academy of Sciences of the United States of America*, *108*(18), 7641–6.

Bassett, D. S., Wymbs, N. F., Porter, M. A., Mucha, P. J., & Grafton, S. T. (2013b). Cross-linked structure of network evolution, *Chaos*, 24(1): 013112.

Bershadsky, A. D., Balaban, N. Q., & Geiger, B. (2003). Adhesion-dependent cell mechanosensitivity. *Annual Review of Cell and Developmental Biology*, *19*, 677–95.

Bhave, G., & Gereau, R. W. (2003). Growing pains: the cytoskeleton as a critical regulator of pain plasticity. *Neuron*, *39*(4), 577–9.

Billiar, K. L., & Sacks, M. S. (2000). Biaxial mechanical properties of the native and glutaraldehyde-treated aortic valve cusp: Part II--A structural constitutive model. *Journal of Biomechanical Engineering*, *122*(4), 327–35.

Blondel, V. D., Guillaume, J.-L., Lambiotte, R., & Lefebvre, E. (2008). Fast unfolding of communities in large networks. *Journal of Statistical Mechanics: Theory and Experiment*, *2008*(10), P10008.

Blouin, J.-S., Siegmund, G. P., Carpenter, M. G., & Inglis, J. T. (2007). Neural Control of Superficial and Deep Neck Muscles in Humans. *Journal of Neurophysiology*, *98*(2), 920–928. doi:10.1152/jn.00183.2007

Boccafoschi, F., Bosetti, M., Sandra, P. M., Leigheb, M., & Cannas, M. (2010). Effects of mechanical stress on cell adhesion: a possible mechanism for morphological changes. *Cell Adhesion & Migration*, *4*(1), 19–25.

Bogduk, N. (1982). The clinical anatomy of the cervical dorsal rami. *Spine*, *7*(4), 319–30.

Bogduk, N. (2011). On cervical zygapophysial joint pain after whiplash. *Spine*, *36*(25 Suppl), S194–9.

Bogduk, N., Wilson, A. S., & Tynan, W. (1982). The human lumbar dorsal rami. *Journal of Anatomy*, *134*(Pt 2), 383–97.

Bogduk, N., & Yoganandan, N. (2001). Biomechanics of the cervical spine Part 3: minor injuries. *Clinical Biomechanics*, *16*(4), 267–275.

Bonfoco, E., Chen, W., Paul, R., Cheresh, D. A., & Cooper, N. R. (2000). beta1 integrin antagonism on adherent, differentiated human neuroblastoma cells triggers an apoptotic signaling pathway. *Neuroscience*, *101*(4), 1145–52.

Bonner, T. J., Newell, N., Karunaratne, A., Pullen, A. D., Amis, A. A., M J Bull, A., & Masouros, S. D. (2015). Strain-rate sensitivity of the lateral collateral ligament of the knee. *Journal of the Mechanical Behavior of Biomedical Materials*, *41*, 261–70.

Borza, C. M., Su, Y., Chen, X., Yu, L., Mont, S., Chetyrkin, S., Voziyan, P., Hudson, B.G., Billings, P.C., Jo, H., Bennett, J.S., Degrado, W.F., Eckes, B., Zent, R., & Pozzi, A. (2012). Inhibition of integrin α2β1 ameliorates glomerular injury. *Journal of the American Society of Nephrology : JASN*, *23*(6), 1027–38.

Bráz, J. M., & Basbaum, A. I. (2010). Differential ATF3 expression in dorsal root ganglion neurons reveals the profile of primary afferents engaged by diverse noxious chemical stimuli. *Pain*, *150*(2), 290–301.

Braz, J. M., Nassar, M. A., Wood, J. N., & Basbaum, A. I. (2005). Parallel "pain" pathways arise from subpopulations of primary afferent nociceptor. *Neuron*, *47*(6), 787–93.

Breuls, R. G. M., Sengers, B. G., Oomens, C. W. J., Bouten, C. V. C., & Baaijens, F. P. T. (2002). Predicting local cell deformations in engineered tissue constructs: a multilevel finite element approach. *Journal of Biomechanical Engineering*, *124*(2), 198.

Cao, X., Lin, Y., Driscoll, T., Franco-Barraza, J., Cukierman, E., Mauck, R., & Shenoy, V. (2015). A chemomechanical model of matrix and nuclear rigidity regulation of focal adhesion size. *Biophysical Journal*, *109*(9), 1807–1817.

Cavanaugh, J. M., Lu, Y., Chen, C., & Kallakuri, S. (2006). Pain generation in lumbar and cervical facet joints. *The Journal of Bone and Joint Surgery. American Volume*, *88 Suppl 2*, 63–7.

Chandran, P. L., & Barocas, V. H. (2004). Microstructural mechanics of collagen gels in confined compression: poroelasticity, viscoelasticity, and collapse. *Journal of Biomechanical Engineering*, *126*(2), 152–66.

Chandran, P. L., & Barocas, V. H. (2006). Affine versus non-affine fibril kinematics in collagen networks: theoretical studies of network behavior. *Journal of Biomechanical Engineering*, *128*(2), 259–70.

Chandran, P. L., & Barocas, V. H. (2007). Deterministic material-based averaging theory model of collagen gel micromechanics. *Journal of Biomechanical Engineering*, *129*(2), 137.

Chang, Y.-W., & Winkelstein, B. A. (2011). Schwann cell proliferation and macrophage infiltration are evident at day 14 after painful cervical nerve root compression in the rat. *Journal of Neurotrauma*, *28*(12), 2429–38.

Chaplan, S. R., Bach, F. W., Pogrel, J. W., Chung, J. M., & Yaksh, T. L. (1994). Quantitative assessment of tactile allodynia in the rat paw. *Journal of Neuroscience Methods*, *53*(1), 55–63.

Chaturvedi, L. S., Gayer, C. P., Marsh, H. M., & Basson, M. D. (2008). Repetitive deformation activates Src-independent FAK-dependent ERK motogenic signals in human Caco-2 intestinal epithelial cells. *American Journal of Physiology. Cell Physiology*, *294*(6), C1350–61.

Chen, C., Lu, Y., Kallakuri, S., Patwardhan, A., & Cavanaugh, J. M. (2006). Distribution of A-delta and C-fiber receptors in the cervical facet joint capsule and their response to stretch. *The Journal of Bone and Joint Surgery. American Volume*, *88*(8), 1807–16.

Chen, P., & Shenoy, V. B., (2011). Strain stiffening induced by molecular motors in active crosslinked biopolymer networks. *Soft Matter*, *7*(2), 355–358.

Chen, X., Nadiarynkh, O., Plotnikov, S., & Campagnola, P. J. (2012). Second harmonic generation microscopy for quantitative analysis of collagen fibrillar structure. *Nature Protocols*, *7*(4), 654–69.

Cheng, C., Webber, C. A., Wang, J., Xu, Y., Martinez, J. A., Liu, W. Q., McDonald, D., Guo, G.F., Nguyen, M.D., & Zochodne, D.W. (2008). Activated RHOA and peripheral axon regeneration. *Experimental Neurology*, *212*(2), 358–69.

Cheng, J.K., & Ji, R.R. (2008). Intracellular signaling in primary sensory neurons and persistent pain. *Neurochemical Research*, *33*(10), 1970–8.

Chicurel, M. E., Chen, C. S., & Ingber, D. E. (1998). Cellular control lies in the balance of forces. *Current Opinion in Cell Biology*, *10*(2), 232–9.

Chieh, H.F., Sun, Y., Liao, J.D., Su, F.C., Zhao, C., Amadio, P. C., & An, K.N. (2010). Effects of cell concentration and collagen concentration on contraction kinetics and mechanical properties in a bone marrow stromal cell-collagen construct. *Journal of Biomedical Materials Research. Part A*, *93*(3), 1132–9.

Chua, W. H., & Bogduk, N. (1995). The surgical anatomy of thoracic facet denervation. *Acta Neurochirurgica*, *136*(3-4), 140–4.

Claeson, A. A., & Barocas, V. H. (2017). Planar biaxial extension of the lumbar facet capsular ligament reveals significant in-plane shear forces. *Journal of the Mechanical Behavior of Biomedical Materials*, *65*, 127–136.

Claeson, A. A., Yeh, Y.-J., Black, A. J., Akkin, T., & Barocas, V. H. (2015). Marker-free tracking of facet capsule motion using polarization-sensitive optical coherence tomography. *Annals of Biomedical Engineering*, *43*(12), 2953–66.

Coderre, T. J., Katz, J., Vaccarino, A. L., & Melzack, R. (1993). Contribution of central neuroplasticity to pathological pain: review of clinical and experimental evidence. *Pain*, *52*(3), 259–85.

Corder, G., Tawfik, V. L., Wang, D., Sypek, E. I., Low, S. A., Dickinson, J. R., Sotoudeh C., Clark J.D., Barres B.A., Bohlen C.J., & Scherrer, G. (2017). Loss of μ opioid receptor signaling in nociceptors, but not microglia, abrogates morphine tolerance without disrupting analgesia. *Nature Medicine*, *23*(2), 164–173.

Costigan, M., Scholz, J., & Woolf, C. J. (2009). Neuropathic pain: a maladaptive response of the nervous system to damage. *Annual Review of Neuroscience*, *32*, 1–32.

Côté, P., Cassidy, J. D., & Carroll, L. (1998). The Saskatchewan Health and Back Pain Survey. The prevalence of neck pain and related disability in Saskatchewan adults. *Spine*, *23*(15), 1689–98.

Côté, P., Cassidy, J. D., & Carroll, L. (2000). The factors associated with neck pain and its related disability in the Saskatchewan population. *Spine*, *25*(9), 1109–17.

Côté, P., Cassidy, J. D., Carroll, L. J., & Kristman, V. (2004). The annual incidence and course of neck pain in the general population: a population-based cohort study. *Pain*, *112*(3), 267–73.

Coull, J. A. M., Beggs, S., Boudreau, D., Boivin, D., Tsuda, M., Inoue, K., Gravel, C., Salter, M.W., & De Koninck, Y. (2005). BDNF from microglia causes the shift in neuronal anion gradient underlying neuropathic pain. *Nature*, *438*(7070), 1017–1021.

Crisco, J. J., Moore, D. C., & McGovern, R. D. (2002). Strain-rate sensitivity of the rabbit MCL diminishes at traumatic loading rates. *Journal of Biomechanics*, *35*(10), 1379–85.

Crosby, N. D., Gilliland, T. M., & Winkelstein, B. A. (2014). Early afferent activity from the facet joint after painful trauma to its capsule potentiates neuronal excitability and glutamate signaling in the spinal cord. *Pain*, *155*(9), 1878–87.

Crosby, N. D., Weisshaar, C. L., & Winkelstein, B. A. (2013). Spinal neuronal plasticity is evident within 1 day after a painful cervical facet joint injury. *Neuroscience Letters*, *542*, 102–6.

Crosby, N. D., & Winkelstein, B. A. (2016). Spinal Astrocytic Thrombospondin-4 Induced by Excitatory Neuronal Signaling Mediates Pain After Facet Capsule Injury. *Annals of Biomedical Engineering*, *44*(11), 3215–3224.

Cullen, D. K., Lessing, M. C., & LaPlaca, M. C. (2007a). Collagen-dependent neurite outgrowth and response to dynamic deformation in three-dimensional neuronal cultures. *Annals of Biomedical Engineering*, *35*(5), 835–46.

Cullen, D. K., Simon, C. M., & LaPlaca, M. C. (2007b). Strain rate-dependent induction of reactive astrogliosis and cell death in three-dimensional neuronal-astrocytic co-cultures. *Brain Research*, *1158*, 103–15.

Cullen, D. K., Tang-Schomer, M. D., Struzyna, L. A., Patel, A. R., Johnson, V. E., Wolf, J. A., & Smith, D. H. (2012). Microtissue engineered constructs with living axons for targeted nervous system reconstruction. *Tissue Engineering. Part A*, *18*(21-22), 2280–9.

Cullen, D. K., Vernekar, V. N., & LaPlaca, M. C. (2011). Trauma-induced plasmalemma disruptions in three-dimensional neural cultures are dependent on strain modality and rate. *Journal of Neurotrauma*, *28*(11), 2219–33.

Curatolo, M., Bogduk, N., Ivancic, P. C., McLean, S. A., Siegmund, G. P., & Winkelstein, B. A. (2011). The role of tissue damage in whiplash-associated disorders: discussion paper 1. *Spine*, *36*(25 Suppl), S309–15.

D'Mello, R., & Dickenson, A. H. (2008). Spinal cord mechanisms of pain. *British Journal of Anaesthesia*, *101*(1), 8–16.

De Vita, R., & Slaughter, W. S. (2006). A structural constitutive model for the strain rate-dependent behavior of anterior cruciate ligaments. *International Journal of Solids and Structures*, *43*(6), 1561–1570.

Delmas, P., Hao, J., & Rodat-Despoix, L. (2011). Molecular mechanisms of mechanotransduction in mammalian sensory neurons. *Nature Reviews. Neuroscience*, *12*(3), 139–53.

Deng, B., Begeman, P. C., Yang, K. H., Tashman, S., & King, A. I. (2000). Kinematics of human cadaver cervical spine during low speed rear-end impacts. *Stapp Car Crash Journal*, *44*, 171–88.

Devor, M., & Wall, P. D. (1990). Cross-excitation in dorsal root ganglia of nerve-injured and intact rats. *Journal of Neurophysiology*, *64*(6), 1733–46.

Dina, O. A., Hucho, T., Yeh, J., Malik-Hall, M., Reichling, D. B., & Levine, J. D. (2005). Primary afferent second messenger cascades interact with specific integrin subunits in producing inflammatory hyperalgesia. *Pain*, *115*(1-2), 191–203.

Dina, O. A., McCarter, G. C., de Coupade, C., & Levine, J. D. (2003). Role of the sensory neuron cytoskeleton in second messenger signaling for inflammatory pain. *Neuron*, *39*(4), 613–24.

Dina, O. A., Parada, C. A., Yeh, J., Chen, X., McCarter, G. C., & Levine, J. D. (2004). Integrin signaling in inflammatory and neuropathic pain in the rat. *European Journal of Neuroscience*, *19*(3), 634–642.

Diniz, C. A. R., & Brochi, L. C. (2005). Robustness of two-phase regression tests. *Revstat - Statistical Journal*, *3*(1), 1–18.

Domercq, M., Vázquez-Villoldo, N., & Matute, C. (2013). Neurotransmitter signaling in the pathophysiology of microglia. *Frontiers in Cellular Neuroscience*, *7*, 49.

Dong, L., Crosby, N. D., & Winkelstein, B. A. (2013a). Gabapentin alleviates facet-mediated pain in the rat through reduced neuronal hyperexcitability and astrocytic activation in the spinal cord. *The Journal of Pain : Official Journal of the American Pain Society*, *14*(12), 1564–72.

Dong, L., Guarino, B. B., Jordan-Sciutto, K. L., & Winkelstein, B. A. (2011). Activating transcription factor 4, a mediator of the integrated stress response, is increased in the dorsal root ganglia following painful facet joint distraction. *Neuroscience*, *193*, 377–86.

Dong, L., Odeleye, A. O., Jordan-Sciutto, K. L., & Winkelstein, B. A. (2008). Painful facet joint injury induces neuronal stress activation in the DRG: implications for cellular mechanisms of pain. *Neuroscience Letters*, *443*(2), 90–4.

Dong, L., Quindlen, J. C., Lipschutz, D. E., & Winkelstein, B. A. (2012). Whiplash-like facet joint loading initiates glutamatergic responses in the DRG and spinal cord associated with behavioral hypersensitivity. *Brain Research*, *1461*, 51–63.

Dong, L., Smith, J. R., & Winkelstein, B. A. (2013b). Ketorolac reduces spinal astrocytic activation and PAR1 expression associated with attenuation of pain after facet joint injury. *Journal of Neurotrauma*, *30*(10), 818–25.

Dong, L., & Winkelstein, B. A. (2010). Simulated whiplash modulates expression of the glutamatergic system in the spinal cord suggesting spinal plasticity is associated with painful dynamic cervical facet loading. *Journal of Neurotrauma*, *27*(1), 163–74.

Draper, N., & Smith, H. (2014). *Applied regression analysis* (3rd ed.). New York: John Wiley & Sons, Inc.

Dubin, A. E., & Patapoutian, A. (2010). Nociceptors: the sensors of the pain pathway. *The Journal of Clinical Investigation*, *120*(11), 3760–72.

Dubner, R., & Ruda, M. A. (1992). Activity-dependent neuronal plasticity following tissue injury and inflammation. *Trends in Neurosciences*, *15*(3), 96–103.

Dubový, P., Brázda, V., Klusáková, I., & Hradilová-Svíženská, I. (2013). Bilateral elevation of interleukin-6 protein and mRNA in both lumbar and cervical dorsal root ganglia following unilateral chronic compression injury of the sciatic nerve. *Journal of Neuroinflammation*, *10*(1), 824.

Dubreuil, C. I., Winton, M. J., & McKerracher, L. (2003). Rho activation patterns after spinal cord injury and the role of activated Rho in apoptosis in the central nervous system. *The Journal of Cell Biology*, *162*(2), 233–43.

Dwyer, A., Aprill, C., & Bogduk, N. (1990). Cervical zygapophyseal joint pain patterns. I: A study in normal volunteers. *Spine*, *15*(6), 453–7.

Eck, J. C., Hodges, S. D., & Humphreys, S. C. (2001). Whiplash: a review of a commonly misunderstood injury. *The American Journal of Medicine*, *110*(8), 651–6.

Erdemir, A., Bennetts, C., Davis, S., Reddy, A., & Sibole, S. (2015). Multiscale cartilage biomechanics: technical challenges in realizing a high-throughput modelling and simulation workflow. *Interface Focus*, *5*(2), 20140081.

Evans, M. C., & Barocas, V. H. (2009). The modulus of fibroblast-populated collagen gels is not determined by final collagen and cell concentration: Experiments and an inclusion-based model. *Journal of Biomechanical Engineering*, *131*(10), 101014.

Feng, Y., LoGrasso, P. V., Defert, O., & Li, R. (2016). Rho Kinase (ROCK) Inhibitors and Their Therapeutic Potential. *Journal of Medicinal Chemistry*, *59*(6), 2269–2300.

Ferrari, L. F., & Levine, J. D. (2015). Plasma membrane mechanisms in a preclinical rat model of chronic pain. *The Journal of Pain : Official Journal of the American Pain Society*, *16*(1), 60–6.

Fournier, A. E., Takizawa, B. T., & Strittmatter, S. M. (2003). Rho kinase inhibition enhances axonal regeneration in the injured CNS. *The Journal of Neuroscience : The Official Journal of the Society for Neuroscience*, *23*(4), 1416–23.

Franchi, M., Quaranta, M., Macciocca, M., Leonardi, L., Ottani, V., Bianchini, P., Diaspro, A., & Ruggeri, A. (2010). Collagen fibre arrangement and functional crimping pattern of the medial collateral ligament in the rat knee. *Knee Surgery, Sports Traumatology, Arthroscopy*, *18*(12), 1671–8.

Freedman, B. R., Bade, N. D., Riggin, C. N., Zhang, S., Haines, P. G., Ong, K. L., & Janmey, P.A. (2015). The (dys)functional extracellular matrix. *Biochimica et Biophysica Acta (BBA) - Molecular Cell Research*, *1853*(11), 3153–3164.

Freeman, M. D., Croft, A. C., Rossignol, A. M., Weaver, D. S., & Reiser, M. (1999). A review and methodologic critique of the literature refuting whiplash syndrome. *Spine*, *24*(1), 86–96.

Fruchterman, T. M. J., & Reingold, E. M. (1991). Graph drawing by force-directed placement. *Software: Practice and Experience*, *21*(11), 1129–1164.

Fujioka, H., Dairyo, Y., Yasunaga, K., & Emoto, K. (2012a). Neural Functions of Matrix Metalloproteinases: Plasticity, Neurogenesis, and Disease. *Biochemistry Research International*, *2012*, 1–8.

Fujioka, H., Dairyo, Y., Yasunaga, K. I., & Emoto, K. (2012b). Neural functions of matrix metalloproteinases: Plasticity, neurogenesis, and disease. *Biochemistry Research International*.

Ganguly, N., Deutsch, A., & Mukherjee, A. (Eds.). (2009). *Dynamics On and Of Complex Networks*. Boston, MA: Birkhäuser Boston.

Gao, Y.-J., & Ji, R.-R. (2009). c-Fos and pERK, which is a better marker for neuronal activation and central sensitization after noxious stimulation and tissue injury? *The Open Pain Journal, 2*, 11–17.

Geddes, D. M., Cargill, R. S., & LaPlaca, M. C. (2003). Mechanical stretch to neurons results in a strain rate and magnitude-dependent increase in plasma membrane permeability. *Journal of Neurotrauma*, *20*(10), 1039–49.

Gefen, A., van Nierop, B., Bader, D. L., & Oomens, C. W. (2008). Strain-time cell-death threshold for skeletal muscle in a tissue-engineered model system for deep tissue injury. *Journal of Biomechanics*, *41*(9), 2003–12.

Glazer, A. M., Lewis, J. G., & Kaminsky, W. (1996). An automatic optical imaging system for birefringent media. *Proceedings of the Royal Society of London A: Mathematical, Physical and Engineering Sciences*, *452*(1955).

Gold, M. S., & Gebhart, G. F. (2010). Nociceptor sensitization in pain pathogenesis. *Nature Medicine*, *16*(11), 1248–57.

González-Forero, D., Montero, F., García-Morales, V., Domínguez, G., Gómez-Pérez, L., García-Verdugo, J. M., & Moreno-López, B. (2012). Endogenous Rho-kinase signaling maintains synaptic strength by stabilizing the size of the readily releasable pool of synaptic vesicles. *The Journal of Neuroscience : The Official Journal of the Society for Neuroscience*, *32*(1), 68–84.

Good, B. H., de Montjoye, Y.-A., & Clauset, A. (2010). Performance of modularity maximization in practical contexts. *Physical Review E*, *81*(4), 046106.

Green, E. M., Mansfield, J. C., Bell, J. S., & Winlove, C. P. (2014). The structure and micromechanics of elastic tissue. *Interface Focus*, *4*(2), 20130058.

Grienberger, C., & Konnerth, A. (2012). Imaging Calcium in Neurons. *Neuron*, *73*(5), 862–885.

Guan, J.-L. (1997). Role of focal adhesion kinase in integrin signaling. *The International Journal of Biochemistry & Cell Biology*, *29*(8), 1085–1096.

Guan, Z., Kuhn, J. A., Wang, X., Colquitt, B., Solorzano, C., Vaman, S., … Basbaum, A. I. (2015). Injured sensory neuron–derived CSF1 induces microglial proliferation and DAP12-dependent pain. *Nature Neuroscience*, *19*(1), 94–101.

Guanche, C. A., Noble, J., Solomonow, M., & Wink, C. S. (1999). Periarticular neural elements in the shoulder joint. *Orthopedics*, *22*(6), 615–7.

Gudavalli, M. R., & Triano, J. J. (1999). An analytical model of lumbar motion segment in flexion. *Journal of Manipulative and Physiological Therapeutics*, *22*(4), 201–8.

Guilluy, C., Swaminathan, V., Garcia-Mata, R., O'Brien, E. T., Superfine, R., & Burridge, K. (2011). The Rho GEFs LARG and GEF-H1 regulate the mechanical response to force on integrins. *Nature Cell Biology*, *13*(6), 722–7.

Hadi, M. F., & Barocas, V. H. (2013). Microscale fiber network alignment affects macroscale failure behavior in simulated collagen tissue analogs. *Journal of Biomechanical Engineering*, *135*(2), 021026.

Hadi, M. F., Sander, E. A., & Barocas, V. H. (2012a). Multiscale model predicts tissue-level failure from collagen fiber-level damage. *Journal of Biomechanical Engineering*, *134*(9), 091005.

Hadi, M. F., Sander, E. A., Ruberti, J. W., & Barocas, V. H. (2012b). Simulated remodeling of loaded collagen networks via strain-dependent enzymatic degradation and constant-rate fiber growth. *Mechanics of Materials : An International Journal*, *44*, 72–82.

Halata, Z., Rettig, T., & Schulze, W. (1985). The ultrastructure of sensory nerve endings in the human knee joint capsule. *Anatomy and Embryology*, *172*(3), 265–75.

Hang, L. H., Shao, D. H., Chen, Z., & Sun, W. J. (2013). Spinal RhoA/Rho kinase signalling pathway may participate in the development of bone cancer pain. *Basic & Clinical Pharmacology & Toxicology*, *113*(2), 87–91.

Hauser, R. A., Steilen, D., & Gordin, K. (2015). The biology of prolotherapy and its application in clinical cervical spine instability and chronic neck pain: a retrospective study. *European Journal of Preventive Medicine*, *3*(4), 85. 1

Hayashi, K., Frank, J. D., Dubinsky, C., Zhengling, H., Markel, M. D., Manley, P. A., & Muir, P. (2003). Histologic changes in ruptured canine cranial cruciate ligament. *Veterinary Surgery : VS*, *32*(3), 269–77.

He, R., Yang, L., Chen, G., Guo, L., & Pei, Y. (2016). Substance-P in symptomatic mediopatellar plica as a predictor of patellofemoral pain. *Biomedical Reports*, *4*(1), 21–26.

Hemphill, M. A., Dabiri, B. E., Gabriele, S., Kerscher, L., Franck, C., Goss, J. A., Alford, P. W., & Parker, K. K. (2011). A possible role for integrin signaling in diffuse axonal injury. *PloS One*, *6*(7), e22899.

Henry, J. L. (1993). Substance P and inflammatory pain: potential of substance P antagonists as analgesics. *Agents and Actions. Supplements*, *41*, 75–87.

Hiraga, A., Kuwabara, S., Doya, H., Kanai, K., Fujitani, M., Taniguchi, J., Arai K., Mori M., Hattori T., & Yamashita, T. (2006). Rho-kinase inhibition enhances axonal

regeneration after peripheral nerve injury. *Journal of the Peripheral Nervous System : JPNS*, *11*(3), 217–24.

Hirata, A., Inatani, M., Inomata, Y., Yonemura, N., Kawaji, T., Honjo, M., & Tanihara, H. (2008). Y-27632, a Rho-associated protein kinase inhibitor, attenuates neuronal cell death after transient retinal ischemia. *Graefe's Archive for Clinical and Experimental Ophthalmology*, *246*(1), 51–9.

Hirata, H., Gupta, M., Vedula, S. R. K., Lim, C. T., Ladoux, B., & Sokabe, M. (2017). Quantifying tensile force and ERK phosphorylation on actin stress fibers (pp. 223–234).

Hodgson, R. J., O'Connor, P. J., & Grainger, A. J. (2012). Tendon and ligament imaging. *The British Journal of Radiology*, *85*(1016), 1157–72. doi:10.1259/bjr/34786470

Hoffman, B. D., Grashoff, C., & Schwartz, M. A. (2011). Dynamic molecular processes mediate cellular mechanotransduction. *Nature*, *475*(7356), 316–23.

Hogg-Johnson, S., van der Velde, G., Carroll, L. J., Holm, L. W., Cassidy, J. D., Guzman, J., Côté P., Haldeman, S., Ammendolia, C., Carragee, E., Hurwitz, E., Nordin, M., & Peloso, P. (2008). The burden and determinants of neck pain in the general population: results of the Bone and Joint Decade 2000-2010 Task Force on Neck Pain and Its Associated Disorders. *Spine*, *33*(Supplement), S39–S51.

Holsgrove, T. P., Jaumard, N. V., Zhu, N., Stiansen, N. S., Welch, W. C., & Winkelstein, B. A. (2016). Upper cervical spine loading simulating a dynamic low-speed collision significantly increases the risk of pain compared to quasi-static loading with equivalent neck kinematics. *Doi.org*, *138*(12), 121006.

Hoy, D. G., Protani, M., De, R., & Buchbinder, R. (2010). The epidemiology of neck pain. *Best Practice & Research Clinical Rheumatology*, *24*(6), 783–792.

Hubbard, R. D., Quinn, K. P., Martínez, J. J., & Winkelstein, B. A. (2008). The role of graded nerve root compression on axonal damage, neuropeptide changes, and pain-related behaviors. *Stapp Car Crash Journal*, *52*, 33–58.

Hubbard, R. D., & Winkelstein, B. A. (2008). Dorsal root compression produces myelinated axonal degeneration near the biomechanical thresholds for mechanical behavioral hypersensitivity. *Experimental Neurology*, *212*(2), 482–9.

Humphrey, J. D., Dufresne, E. R., & Schwartz, M. A. (2014). Mechanotransduction and extracellular matrix homeostasis. *Nature Reviews. Molecular Cell Biology*, *15*(12), 802–12.

Hunt, D., Raivich, G., & Anderson, P. N. (2012). Activating transcription factor 3 and the nervous system. *Frontiers in Molecular Neuroscience*, *5*, 7.

Hynes, R. O. (2002). Integrins: bidirectional, allosteric signaling machines. *Cell*, *110*(6), 673–687.

In ’t Veld, P. J., & Stevens, M. J. (2008). Simulation of the mechanical strength of a single collagen molecule. *Biophysical Journal*, *95*(1), 33–9.

Inoue, M., Rashid, M. H., Fujita, R., Contos, J. J. A., Chun, J., & Ueda, H. (2004). Initiation of neuropathic pain requires lysophosphatidic acid receptor signaling. *Nature Medicine*, *10*(7), 712–8.

Institute of Medicine Report from the Committee on Advancing Pain Research, Care, and Education. (2011). *Relieving Pain in America: A Blueprint for Transforming Prevention, Care, Education, and Research - Institute of Medicine*. The National Academies Press.

Iorio, J. A., Jakoi, A. M., & Singla, A. (2016). Biomechanics of degenerative spinal disorders. *Asian Spine Journal*, *10*(2), 377–84.

Irons, H. R., Cullen, D. K., Shapiro, N. P., Lambert, N. A., Lee, R. H., & LaPlaca, M. C. (2008). Three-dimensional neural constructs: a novel platform for neurophysiological investigation. *Journal of Neural Engineering*, *5*(3), 333–341.

Ita, M. E., Crosby, N. D., Bulka, B. A., & Winkelstein, B. A. (2017a). Painful cervical facet joint injury is accompanied by changes in the number of excitatory and inhibitory synapses in the superficial dorsal horn that differentially relate to local tissue injury severity. *Spine*, *42*(12), E695–E701.

Ita, M. E., Zhang, S., Holsgrove, T. P., Kartha, S., & Winkelstein, B. A. (2017b). The Physiological Basis of Cervical Facet-Mediated Persistent Pain: Basic Science & Clinical Challenges. *Journal of Orthopaedic & Sports Physical Therapy*, 47(7):450-461.

Janmey, P. A., & McCulloch, C. A. (2007). Cell mechanics: integrating cell responses to mechanical stimuli. *Annual Review of Biomedical Engineering*, *9*(1), 1–34.

Jaumard, N. V, Welch, W. C., & Winkelstein, B. A. (2011). Spinal facet joint biomechanics and mechanotransduction in normal, injury and degenerative conditions. *Journal of Biomechanical Engineering*, *133*(7), 071010.

Jenkins, G., Redwood, K. L., Meadows, L., & Green, M. R. (1999). Effect of gel re-organization and tensional forces on alpha2beta1 integrin levels in dermal fibroblasts. *European Journal of Biochemistry*, *263*(1), 93–104.

Ji, R. R., Baba, H., Brenner, G. J., & Woolf, C. J. (1999). Nociceptive-specific activation of ERK in spinal neurons contributes to pain hypersensitivity. *Nature Neuroscience*, *2*(12), 1114–9.

Jiao, Y., Stillinger, F. H., & Torquato, S. (2007). Modeling heterogeneous materials via two-point correlation functions: Basic principles. *Physical Review E*, *76*(3), 031110.

Jokinen, J., Dadu, E., Nykvist, P., Kapyla, J., White, D. J., Ivaska, J., Vehviläinen, P., Reunanen, H., Larjava, H., Häkkinen, L., &Heino, J. (2004). Integrin-mediated Cell

Adhesion to Type I Collagen Fibrils. *Journal of Biological Chemistry*, *279*(30), 31956–31963.

Jones, C. A. R., Liang, L., Lin, D., Jiao, Y., & Sun, B. (2014). The spatial-temporal characteristics of type I collagen-based extracellular matrix. *Soft Matter*, *10*(44), 8855–63.

Joshi, A. R., Bobylev, I., Zhang, G., Sheikh, K. A., & Lehmann, H. C. (2015). Inhibition of Rho-kinase differentially affects axon regeneration of peripheral motor and sensory nerves. *Experimental Neurology*, *263*, 28–38.

Julius, D., & Basbaum, A. I. (2001). Molecular mechanisms of nociception. *Nature*, *413*(6852), 203–210.

Jutla, I. S., Lucas, G. S. J., & Mucha, P. J. (2011). A generalized louvain method for community detection implemented in matlab.

Kaiser, M. (2011). A tutorial in connectome analysis: topological and spatial features of brain networks. *NeuroImage*, *57*(3), 892–907. Neurons and Cognition; Physics and Society.

Kallakuri, S., Li, Y., Chen, C., & Cavanaugh, J. M. (2012). Innervation of cervical ventral facet joint capsule: Histological evidence. *World Journal of Orthopedics*, *3*(2), 10–4.

Kallakuri, S., Singh, A., Lu, Y., Chen, C., Patwardhan, A., & Cavanaugh, J. M. (2008). Tensile stretching of cervical facet joint capsule and related axonal changes. *European Spine Journal*, *17*(4), 556–63.

Kamada, T., & Kawai, S. (1989). An algorithm for drawing general undirected graphs. *Information Processing Letters*, *31*(1), 7–15.

Kasch, H., Stengaard-Pedersen, K., Arendt-Nielsen, L., & Staehelin Jensen, T. (2001). Headache, neck pain, and neck mobility after acute whiplash injury: a prospective study. *Spine*, *26*(11), 1246–51.

Katsumi, A., Naoe, T., Matsushita, T., Kaibuchi, K., & Schwartz, M. A. (2005). Integrin activation and matrix binding mediate cellular responses to mechanical stretch. *The Journal of Biological Chemistry*, *280*(17), 16546–9.

Keely, P. J., Conklin, M. W., Gehler, S., Ponik, S. M., & Provenzano, P. P. (2007). Investigating integrin regulation and signaling events in three-dimensional systems. *Methods in Enzymology*, *426*, 27–45.

Khalsa, P. S., & Ge, W. (2004). Encoding of tensile stress and strain during stretch by muscle mechano-nociceptors. *Muscle & Nerve*, *30*(2), 216–24.

Khalsa, P. S., Ge, W., Uddin, M. Z., & Hadjiargyrou, M. (2004). Integrin alpha2beta1 affects mechano-transduction in slowly and rapidly adapting cutaneous mechanoreceptors in rat hairy skin. *Neuroscience*, *129*(2), 447–59.

Khalsa, P. S., Hoffman, A. H., & Grigg, P. (1996). Mechanical states encoded by stretch-sensitive neurons in feline joint capsule. *Journal of Neurophysiology*, *76*(1), 175–87.

Khalsa, P. S., LaMotte, R. H., & Grigg, P. (1997). Tensile and compressive responses of nociceptors in rat hairy skin. *Journal of Neurophysiology*, *78*(1), 492–505.

Khalsa, P. S., Zhang, C., Sommerfeldt, D., & Hadjiargyrou, M. (2000). Expression of integrin alpha2beta1 in axons and receptive endings of neurons in rat, hairy skin. *Neuroscience Letters*, *293*(1), 13–6.

Khasabov, S. G., Rogers, S. D., Ghilardi, J. R., Peters, C. M., Mantyh, P. W., & Simone, D. A. (2002). Spinal neurons that possess the substance P receptor are required for the development of central sensitization. *Journal of Neuroscience*, *22*(20).

Kim, E. K., & Choi, E.-J. (2010). Pathological roles of MAPK signaling pathways in human diseases. *Biochimica et Biophysica Acta (BBA) - Molecular Basis of Disease*, *1802*(4), 396–405.

Kiryu-Seo, S., Kato, R., Ogawa, T., Nakagomi, S., Nagata, K., & Kiyama, H. (2008). Neuronal Injury-inducible Gene Is Synergistically Regulated by ATF3, c-Jun, and STAT3 through the Interaction with Sp1 in Damaged Neurons. *Journal of Biological Chemistry*, *283*(11), 6988–6996.

Koeck, F. X., Schmitt, M., Baier, C., Stangl, H., Beckmann, J., Grifka, J., & Straub, R. H. (2016). Predominance of synovial sensory nerve fibers in arthrofibrosis following

total knee arthroplasty compared to osteoarthritis of the knee. *Journal of Orthopaedic Surgery and Research*, *11*, 25. doi:10.1186/s13018-016-0359-0

Kong, D., Ji, B., & Dai, L. (2010). Stabilizing to disruptive transition of focal adhesion response to mechanical forces. *Journal of Biomechanics*, *43*(13), 2524–9. doi:10.1016/j.jbiomech.2010.05.019

Kopp, M. A., Liebscher, T., Niedeggen, A., Laufer, S., Brommer, B., Jungehulsing, G. J., Strittmatter, S. M., Dirnagl, U., & Schwab, J. M. (2012). Small-molecule-induced Rho-inhibition: NSAIDs after spinal cord injury. *Cell and Tissue Research*, *349*(1), 119–32. doi:10.1007/s00441-012-1334-7

Korenczuk, C. E., Votava, L. E., Dhume, R. Y., Kizilski, S. B., Brown, G. E., Narain, R., & Barocas, V. H. (2017). Isotropic failure criteria are not appropriate for anisotropic fibrous biological tissues. *Journal of Biomechanical Engineering*.

Koul, H. L., Qian, L., & Surgailis, D. (2003). Asymptotics of M-estimators in two-phase linear regression models. *Stochastic Processes and Their Applications*, *103*(1), 123–154.

Kras, J. V, Dong, L., & Winkelstein, B. A. (2013a). The prostaglandin E2 receptor, EP2, is upregulated in the dorsal root ganglion after painful cervical facet joint injury in the rat. *Spine*, *38*(3), 217–22.

Kras, J. V, Dong, L., & Winkelstein, B. A. (2014). Increased interleukin-1α and prostaglandin E2 expression in the spinal cord at 1 day after painful facet joint injury: evidence of early spinal inflammation. *Spine*, *39*(3), 207–12.

Kras, J. V, Kartha, S., & Winkelstein, B. A. (2015a). Intra-articular nerve growth factor regulates development, but not maintenance, of injury-induced facet joint pain & spinal neuronal hypersensitivity. *Osteoarthritis Cartilage*, *23*(11), 1999–2008.

Kras, J. V, Tanaka, K., Gilliland, T. M., & Winkelstein, B. A. (2013b). An anatomical and immunohistochemical characterization of afferents innervating the C6-C7 facet joint after painful joint loading in the rat. *Spine*, *38*(6), E325–31.

Kras, J. V, Weisshaar, C. L., Quindlen, J., & Winkelstein, B. A. (2013c). Brain-derived neurotrophic factor is upregulated in the cervical dorsal root ganglia and spinal cord and contributes to the maintenance of pain from facet joint injury in the rat. *Journal of Neuroscience Research*, *91*(10), 1312–21.

Kras, J. V., Weisshaar, C. L., Pall, P. S., & Winkelstein, B. A. (2015b). Pain from intra-articular NGF or joint injury in the rat requires contributions from peptidergic joint afferents. *Neuroscience Letters*, *604*, 193–198. doi:10.1016/j.neulet.2015.07.043

Kwan, O., & Fiel, J. (2002). Critical appraisal of facet joints injections for chronic whiplash. *Medical Science Monitor : International Medical Journal of Experimental and Clinical Research*, *8*(8), RA191–5.

Lai, V. K., Hadi, M. F., Tranquillo, R. T., & Barocas, V. H. (2013). A multiscale approach to modeling the passive mechanical contribution of cells in tissues. *Journal of Biomechanical Engineering*, *135*(7), 71007.

Lake, S. P., & Barocas, V. H. (2011). Mechanical and structural contribution of non-fibrillar matrix in uniaxial tension: a collagen-agarose co-gel model. *Annals of Biomedical Engineering*, *39*(7), 1891–903.

Lake, S. P., & Barocas, V. H. (2012). Mechanics and kinematics of soft tissue under indentation are determined by the degree of initial collagen fiber alignment. *Journal of the Mechanical Behavior of Biomedical Materials*, *13*, 25–35.

Lake, S. P., Hadi, M. F., Lai, V. K., & Barocas, V. H. (2012). Mechanics of a fiber network within a non-fibrillar matrix: model and comparison with collagen-agarose co-gels. *Annals of Biomedical Engineering*, *40*(10), 2111–21.

Lake, S. P., Hald, E. S., & Barocas, V. H. (2011). Collagen-agarose co-gels as a model for collagen-matrix interaction in soft tissues subjected to indentation. *Journal of Biomedical Materials Research. Part A*, *99*(4), 507–15.

Lake, S. P., Miller, K. S., Elliott, D. M., & Soslowsky, L. J. (2009). Effect of fiber distribution and realignment on the nonlinear and inhomogeneous mechanical properties of human supraspinatus tendon under longitudinal tensile loading. *Journal of Orthopaedic Research* , *27*(12), 1596–602.

Laplaca, M. C., & Prado, G. R. (2010). Neural mechanobiology and neuronal vulnerability to traumatic loading. *Journal of Biomechanics*, *43*(1), 71–8.

LaPlaca, M. C., Simon, C. M., Prado, G. R., & Cullen, D. K. (2007). CNS injury biomechanics and experimental models. *Progress in Brain Research*, *161*, 13–26.

Latremoliere, A., & Woolf, C. J. (2009). Central sensitization: a generator of pain hypersensitivity by central neural plasticity. *The Journal of Pain*, *10*(9), 895–926.

Lee, D. J., & Winkelstein, B. A. (2012). The failure response of the human cervical facet capsular ligament during facet joint retraction. *Journal of Biomechanics*, *45*(14), 2325–9.

Lee, K. E., Davis, M. B., Mejilla, R. M., & Winkelstein, B. A. (2004a). In vivo cervical facet capsule distraction: mechanical implications for whiplash and neck pain. *Stapp Car Crash Journal*, *48*, 373–95.

Lee, K. E., Davis, M. B., & Winkelstein, B. A. (2008). Capsular ligament involvement in the development of mechanical hyperalgesia after facet joint loading: behavioral and inflammatory outcomes in a rodent model of pain. *Journal of Neurotrauma*, *25*(11), 1383–93.

Lee, K. E., Franklin, A. N., Davis, M. B., & Winkelstein, B. A. (2006). Tensile cervical facet capsule ligament mechanics: failure and subfailure responses in the rat. *Journal of Biomechanics*, *39*(7), 1256–64.

Lee, K. E., Thinnes, J. H., Gokhin, D. S., & Winkelstein, B. A. (2004b). A novel rodent neck pain model of facet-mediated behavioral hypersensitivity: implications for persistent pain and whiplash injury. *Journal of Neuroscience Methods*, *137*(2), 151–9. d

Lee, K. E., & Winkelstein, B. A. (2009). Joint distraction magnitude is associated with different behavioral outcomes and substance P levels for cervical facet joint loading in the rat. *The Journal of Pain*, *10*(4), 436–45.

Lei, S., Czerwinska, E., Czerwinski, W., Walsh, M. P., & MacDonald, J. F. (2001). Regulation of NMDA receptor activity by F-actin and myosin light chain kinase. *The Journal of Neuroscience* , *21*(21), 8464–72.

Lessey, E. C., Guilluy, C., & Burridge, K. (2012). From mechanical force to RhoA activation. *Biochemistry*, *51*(38), 7420–32.

Lian, X., Wang, X.-T., Wang, W.-T., Yang, X., Suo, Z.-W., & Hu, X.-D. (2015). Peripheral inflammation activated focal adhesion kinase signaling in spinal dorsal horn of mice. *Journal of Neuroscience Research*, *93*(6), 873–81.

Liao, H., & Belkoff, S. M. (1999). A failure model for ligaments. *Journal of Biomechanics*, *32*(2), 183–188.

Liao, J. K., Seto, M., & Noma, K. (2007). Rho kinase (ROCK) inhibitors. *Journal of Cardiovascular Pharmacology*, *50*(1), 17–24.

Lin, Y. W., Cheng, C. M., Leduc, P. R., & Chen, C. C. (2009). Understanding sensory nerve mechanotransduction through localized elastomeric matrix control. *PloS One, 4*(1), e4293.

Lindå, H., Sköld, M. K., & Ochsmann, T. (2011). Activating transcription factor 3, a useful marker for regenerative response after nerve root injury. *Frontiers in Neurology*, *2*, 30.

Lindner, D., Zietsch, C., Becher, P. M., Schulze, K., Schultheiss, H. P., Tschöpe, C., & Westermann, D. (2012). Differential expression of matrix metalloproteases in human fibroblasts with different origins. *Biochemistry Research International*, 2012: 875742.

Liu, H., Mantyh, P. W., & Basbaum, A. I. (1997). NMDA-receptor regulation of substance P release from primary afferent nociceptors. *Nature, 386*(6626), 721–724.

Lohse, C., Bassett, D. S., Lim, K. O., & Carlson, J. M. (2014). Resolving anatomical and functional structure in human brain organization: identifying mesoscale organization in weighted network representations. *PLoS Computational Biology*, *10*(10), e1003712.

Lopez-Garcia, M. D. C., Beebe, D. J., & Crone, W. C. (2010). Young's modulus of collagen at slow displacement rates. *Bio-Medical Materials and Engineering*, *20*(6), 361–9.

Lord, S. M., Barnsley, L., Wallis, B. J., & Bogduk, N. (1996). Chronic cervical zygapophysial joint pain after whiplash. A placebo-controlled prevalence study. *Spine*, *21*(15), 1737–44; discussion 1744–5.

Lu, Y., Chen, C., Kallakuri, S., Patwardhan, A., & Cavanaugh, J. M. (2005a). Neural response of cervical facet joint capsule to stretch: a study of whiplash pain mechanism. *Stapp Car Crash Journal*, *49*, 49–65.

Lu, Y., Chen, C., Kallakuri, S., Patwardhan, A., & Cavanaugh, J. M. (2005b). Neurophysiological and biomechanical characterization of goat cervical facet joint capsules. *Journal of Orthopaedic Research*, *23*(4), 779–87.

Lu, Y.-B., Franze, K., Seifert, G., Steinhäuser, C., Kirchhoff, F., Wolburg, H., Guck, J., Janmey, P., Wei, E-Q., & Reichenbach, A. (2006). Viscoelastic properties of individual glial cells and neurons in the CNS. *Proceedings of the National Academy of Sciences of the United States of America*, *103*(47), 17759–64.

Luo, L. (2000). Rho GTPases in neuronal morphogenesis. *Nature Reviews. Neuroscience*, *1*(3), 173–80.

Luscombe, N. M., Babu, M. M., Yu, H., Snyder, M., Teichmann, S. A., & Gerstein, M. (2004). Genomic analysis of regulatory network dynamics reveals large topological changes. *Nature*, *431*(7006), 308–12.

Ma, W., Zheng, W. H., Powell, K., Jhamandas, K., & Quirion, R. (2001). Chronic morphine exposure increases the phosphorylation of MAP kinases and the transcription factor CREB in dorsal root ganglion neurons: an in vitro and in vivo study. *The European Journal of Neuroscience*, *14*(7), 1091–104.

MacArthur, M. W., & Thornton, J. M. (1993). Conformational analysis of protein structures derived from NMR data. *Proteins*, *17*(3), 232–51.

MacVicar, J., Borowczyk, J. M., MacVicar, A. M., Loughnan, B. M., & Bogduk, N. (2012). Cervical medial branch radiofrequency neurotomy in new zealand. *pain medicine*, *13*(5), 647–654.

Magou, G. C., Pfister, B. J., & Berlin, J. R. (2015). Effect of acute stretch injury on action potential and network activity of rat neocortical neurons in culture. *Brain Research*.

Malik-Hall, M., Dina, O. A., & Levine, J. D. (2005). Primary afferent nociceptor mechanisms mediating NGF-induced mechanical hyperalgesia. *The European Journal of Neuroscience*, *21*(12), 3387–94.

Manchikanti, L., Boswell, M. V, Singh, V., Pampati, V., Damron, K. S., & Beyer, C. D. (2004). Prevalence of facet joint pain in chronic spinal pain of cervical, thoracic, and lumbar regions. *BMC Musculoskeletal Disorders*, *5*, 15.

Manchikanti, L., Pampati, V., Singh, V., & Falco, F. J. E. (2013). Assessment of the escalating growth of facet joint interventions in the medicare population in the United States from 2000 to 2011. *Pain Physician*, *16*(4), E365–78.

Manchikanti, L., Singh, V., Falco, F. J. E., Cash, K. M., & Fellows, B. (2008). Cervical Medial Branch Blocks for Chronic Cervical Facet Joint Pain. *Spine*, *33*(17), 1813–1820.

Mantyh, P. W., Rogers, S. D., Honore, P., Allen, B. J., Ghilardi, J. R., Li, J., & Randy S. (1997). Inhibition of Hyperalgesia by Ablation of Lamina I Spinal Neurons Expressing the Substance P Receptor. *Science*, *278*(5336).

Marjoram, R. J., Lessey, E. C., & Burridge, K. (2014). Regulation of RhoA activity by adhesion molecules and mechanotransduction. *Current Molecular Medicine*, *14*(2), 199–208.

Markenson, J. A. (1996). Mechanisms of chronic pain. *The American Journal of Medicine*, *101*(1A), 6S–18S.

Martin, B. I., Deyo, R. A., Mirza, S. K., Turner, J. A., Comstock, B. A., Hollingworth, W., & Sullivan, S. D. (2008). Expenditures and health status among adults with back and neck problems. *JAMA*, *299*(6), 656.

Martinac, B. (2004). Mechanosensitive ion channels: molecules of mechanotransduction. *Journal of Cell Science*, *117*(Pt 12), 2449–60.

Maxwell, W. L., & Graham, D. I. (1997). Loss of axonal microtubules and neurofilaments after stretch-injury to guinea pig optic nerve fibers. *Journal of Neurotrauma*, *14*(9), 603–14.

McDonald, J. H. (2014). *Handbook of Biological Statistics* (3rd ed.). Baltimore, Maryland, U.S.A: Sparkly House Publishing.

McLain, R. F. (1994). Mechanoreceptor endings in human cervical facet joints. *Spine*, *19*(5), 495–501.

McLain, R. F., & Pickar, J. G. (1998). Mechanoreceptor endings in human thoracic and lumbar facet joints. *Spine*, *23*(2), 168–73.

McMullan, R., Hiley, E., Morrison, P., & Nurrish, S. J. (2006). Rho is a presynaptic activator of neurotransmitter release at pre-existing synapses in C. elegans. *Genes & Development*, *20*(1), 65–76.

Meisel, H.-J., Seller, K., L Th, A., B Ttner-Janz, K., Stosberg, P., Moser, A., Miller L. E., Block, J. E., & Pimenta, L. (2014). Minimally invasive facet restoration implant for chronic lumbar zygapophysial pain: 1-year outcomes. *Annals of Surgical Innovation and Research*, 8:7.

Meunier, D., Achard, S., Morcom, A., & Bullmore, E. (2009). Age-related changes in modular organization of human brain functional networks. *NeuroImage*, *44*(3), 715–23.

Midwood, K. S., & Schwarzbauer, J. E. (2002). Elastic Fibers: Building Bridges Between Cells and Their Matrix. *Current Biology*, *12*(8), R279–R281.

Mietto, B. S., Mostacada, K., & Martinez, A. M. B. (2015a). Neurotrauma and inflammation: CNS and PNS responses. *Mediators of Inflammation*, *2015*, 251204.

Mietto, B. S., Mostacada, K., Martinez, A. M. B., Mietto, B. S., Mostacada, K., & Martinez, A. M. B. (2015b). Neurotrauma and Inflammation: CNS and PNS Responses. *Mediators of Inflammation*, *2015*, 1–14.

Miller, E. J., & Rhodes, R. K. (1982). Preparation and characterization of the different types of collagen. *Methods in Enzymology*, *82 Pt A*, 33–64.

Miller, K. S., Connizzo, B. K., Feeney, E., Tucker, J. J., & Soslowsky, L. J. (2012a). Examining differences in local collagen fiber crimp frequency throughout mechanical testing in a developmental mouse supraspinatus tendon model. *Journal of Biomechanical Engineering*, *134*(4), 041004.

Miller, K. S., Connizzo, B. K., & Soslowsky, L. J. (2012b). Collagen fiber re-alignment in a neonatal developmental mouse supraspinatus tendon model. *Annals of Biomedical Engineering*, *40*(5), 1102–10.

Miller, M. W., Basra, S., Kulp, D. W., Billings, P. C., Choi, S., Beavers, M. P., McCarty, O. J., Zou, Z., Kahn, M. L., Bennett, J. S., & DeGrado, W. F. (2009). Small-molecule inhibitors of integrin 2 1 that prevent pathological thrombus formation via an

allosteric mechanism. *Proceedings of the National Academy of Sciences*, *106*(3), 719–724.

Molander, C., Xu, Q., Rivero-Melian, C., & Grant, G. (1989). Cytoarchitectonic organization of the spinal cord in the rat: II. The cervical and upper thoracic cord. *The Journal of Comparative Neurology*, *289*(3), 375–85.

Moore, S. W., Roca-Cusachs, P., & Sheetz, M. P. (2010). Stretchy proteins on stretchy substrates: the important elements of integrin-mediated rigidity sensing. *Developmental Cell*, *19*(2), 194–206.

Morgan, F. R., & Mitton, R. G. (1960). Mechanical Properties of Raw Collagen Fibres. *J. Soc. Leather Trades' Chemists*, 44: 2–23.

Mucha, P. J., Richardson, T., Macon, K., Porter, M. A., & Onnela, J. P. (2010). Community structure in time-dependent, multiscale, and multiplex networks. *Science (New York, N.Y.)*, *328*(5980), 876–8.

Mueller, B. K., Mack, H., & Teusch, N. (2005). Rho kinase, a promising drug target for neurological disorders. *Nature Reviews Drug Discovery*, *4*(5), 387–398.

Münster, S., Jawerth, L. M., Leslie, B. A., Weitz, J. I., Fabry, B., & Weitz, D. A. (2013). Strain history dependence of the nonlinear stress response of fibrin and collagen networks. *Proceedings of the National Academy of Sciences of the United States of America*, *110*(30), 12197–202.

Myers, J. P., Santiago-Medina, M., & Gomez, T. M. (2011). Regulation of axonal outgrowth and pathfinding by integrin-ECM interactions. *Developmental Neurobiology*, *71*(11), 901–23.

Nahin, R. L. (2015). Estimates of Pain Prevalence and Severity in Adults: United States, 2012. *The Journal of Pain*, *16*(8), 769–780.

Nair, A., Baker, B. M., Trappmann, B., Chen, C. S., & Shenoy, V. B. (2014). Remodeling of fibrous extracellular matrices by contractile cells: predictions from discrete fiber network simulations. *Biophysical Journal*, 107(8):1829-1840.

Nascimento, D., Pozza, D. H., Castro-Lopes, J. M., & Neto, F. L. (2011). Neuronal injury marker atf-3 is induced in primary afferent neurons of monoarthritic rats. *Neurosignals*, *19*(4), 210–221.

Neary, J. T., Kang, Y., Willoughby, K. A., & Ellis, E. F. (2003). Activation of extracellular signal-regulated kinase by stretch-induced injury in astrocytes involves extracellular ATP and P2 purinergic receptors. *The Journal of Neuroscience*, *23*(6), 2348–56.

Negreiros, E. M. A., Leão, A. C. M., Santiago, M. F., & Mendez-Otero, R. (2003). Localization of ganglioside 9-O-acetyl GD3 in point contacts of neuronal growth cones. *Journal of Neurobiology*, *57*(1), 31–7.

Newman, M. (2010). *Networks: An Introduction*. OUP Oxford.

Newman, M. E. J. (2006). Modularity and community structure in networks. *Proceedings of the National Academy of Sciences of the United States of America*, *103*(23), 8577–82.

Nicholson, K. J., Quindlen, J. C., & Winkelstein, B. A. (2011). Development of a duration threshold for modulating evoked neuronal responses after nerve root compression injury. *Stapp Car Crash Journal*, *55*, 1–24.

Nicholson, K. J., Zhang, S., Gilliland, T. M., & Winkelstein, B. A. (2014). Riluzole effects on behavioral sensitivity and the development of axonal damage and spinal modifications that occur after painful nerve root compression. *Journal of Neurosurgery. Spine*, *20*(6), 751–62.

Nörenberg, W., Hofmann, F., Illes, P., Aktories, K., & Meyer, D. K. (1999). Rundown of somatodendritic N-methyl-D-aspartate (NMDA) receptor channels in rat hippocampal neurones: evidence for a role of the small GTPase RhoA. *British Journal of Pharmacology*, *127*(5), 1060–3.

Noyes, F. R., DeLucas, J. L., & Torvik, P. J. (1974). Biomechanics of anterior cruciate ligament failure: an analysis of strain-rate sensitivity and mechanisms of failure in primates. *The Journal of Bone and Joint Surgery. American Volume*, *56*(2), 236–53.

O'Brien, C., Woolf, C. J., Fitzgerald, M., Lindsay, R. M., & Molander, C. (1989). Differences in the chemical expression of rat primary afferent neurons which innervate skin, muscle or joint. *Neuroscience*, *32*(2), 493–502.

O'Toole, M., Lamoureux, P., & Miller, K. E. (2015). Measurement of Subcellular Force Generation in Neurons. *Biophysical Journal*, *108*(5), 1027–1037.

Oakes, P. W., & Gardel, M. L. (2014). Stressing the limits of focal adhesion mechanosensitivity. *Current Opinion in Cell Biology*, *30*, 68–73.

Ohsawa, M., & Kamei, J. (2010). RhoA/Rho kinase signaling in the spinal cord and diabetic painful neuropathy. *European Journal of Pharmacology*, *644*(1-3), 1–4.

Ono, K., & Kanno, M. (1996). Influences of the physical parameters on the risk to neck injuries in low impact speed rear-end collisions. *Accident; Analysis and Prevention*, *28*(4), 493–9.

Paiva-Lima, P., Bakhle, Y. S., & Francischi, J. N. (2014). Dual effects of Rho-kinase inhibitors on a rat model of inflammatory pain. *Pain Research & Management*, *19*(6), e172–8.

Panjabi, M. M., Cholewicki, J., Nibu, K., Grauer, J., & Vahldiek, M. (1998a). Capsular ligament stretches during in vitro whiplash simulations. *Journal of Spinal Disorders*, *11*(3), 227–32.

Panjabi, M. M., Cholewicki, J., Nibu, K., Grauer, J. N., Babat, L. B., & Dvorak, J. (1998b). Mechanism of whiplash injury. *Clinical Biomechanics (Bristol, Avon)*, *13*(4-5), 239–249.

Panjabi, M. M., Maak, T. G., Ivancic, P. C., & Ito, S. (2006). Dynamic intervertebral foramen narrowing during simulated rear impact. *Spine*, *31*(5), E128–34.

Park, B. H., & de Boer, J. F. (2008). Polarization-sensitive optical coherence tomography (pp. 653–695). Springer Berlin Heidelberg.

Patel, T. P., Man, K., Firestein, B. L., & Meaney, D. F. (2015). Automated quantification of neuronal networks and single-cell calcium dynamics using calcium imaging. *Journal of Neuroscience Methods*.

Pearson, A. M., Ivancic, P. C., Ito, S., & Panjabi, M. M. (2004). Facet joint kinematics and injury mechanisms during simulated whiplash. *Spine*, *29*(4), 390–7.

Petrenko, A. B., Yamakura, T., Baba, H., & Shimoji, K. (2003). The role of N-methyl-D-aspartate (NMDA) receptors in pain: a review. *Anesthesia and Analgesia*, *97*(4), 1108–16.

Petrie, S., Collins, J. G., Solomonow, M., Wink, C., Chuinard, R., & D'Ambrosia, R. (1998). Mechanoreceptors in the human elbow ligaments. *The Journal of Hand Surgery*, *23*(3), 512–8.

Petrie, S., Collins, J., Solomonow, M., Wink, C., & Chuinard, R. (1997). Mechanoreceptors in the palmar wrist ligaments. *The Journal of Bone and Joint Surgery. British Volume*, *79*(3), 494–6.

Pettersson, K., Hildingsson, C., Toolanen, G., Fagerlund, M., & Björnebrink, J. (1997). Disc pathology after whiplash injury. A prospective magnetic resonance imaging and clinical investigation. *Spine*, *22*(3), 283–7; discussion 288.

Pfister, B. J., Iwata, A., Taylor, A. G., Wolf, J. A., Meaney, D. F., & Smith, D. H. (2006). Development of transplantable nervous tissue constructs comprised of stretch-grown axons. *Journal of Neuroscience Methods*, *153*(1), 95–103.

Provenzano, P. P., & Vanderby, R. (2006). Collagen fibril morphology and organization: implications for force transmission in ligament and tendon. *Matrix Biology : Journal of the International Society for Matrix Biology*, *25*(2), 71–84.

Quinn, K. P. (2010). Integrating electrophysiological, mechanical, and optical methods to define the mechanisms of painful facet joint injury. *Dissertations Available from ProQuest*.

Quinn, K. P., Bauman, J. A., Crosby, N. D., & Winkelstein, B. A. (2010a). Anomalous fiber realignment during tensile loading of the rat facet capsular ligament identifies mechanically induced damage and physiological dysfunction. *Journal of Biomechanics*, *43*(10), 1870–5.

Quinn, K. P., Dong, L., Golder, F. J., & Winkelstein, B. A. (2010b). Neuronal hyperexcitability in the dorsal horn after painful facet joint injury. *Pain*, *151*(2), 414–21.

Quinn, K. P., Lee, K. E., Ahaghotu, C. C., & Winkelstein, B. A. (2007). Structural changes in the cervical facet capsular ligament: potential contributions to pain following subfailure loading. *Stapp Car Crash Journal*, *51*, 169–87.

Quinn, K. P., & Winkelstein, B. A. (2008). Altered collagen fiber kinematics define the onset of localized ligament damage during loading. *Journal of Applied Physiology (Bethesda, Md. : 1985)*, *105*(6), 1881–8.

Quinn, K. P., & Winkelstein, B. A. (2009). Vector correlation technique for pixel-wise detection of collagen fiber realignment during injurious tensile loading. *Journal of Biomedical Optics*, *14*(5), 054010.

Quinn, K. P., & Winkelstein, B. A. (2010). Full field strain measurements of collagenous tissue by tracking fiber alignment through vector correlation. *Journal of Biomechanics*, *43*(13), 2637–2640.

Quinn, K. P., & Winkelstein, B. A. (2011). Detection of altered collagen fiber alignment in the cervical facet capsule after whiplash-like joint retraction. *Annals of Biomedical Engineering*, *39*(8), 2163–73.

Raghupathy, R., Witzenburg, C., Lake, S. P., Sander, E. A., & Barocas, V. H. (2011). Identification of regional mechanical anisotropy in soft tissue analogs. *Journal of Biomechanical Engineering*, *133*(9), 091011.

Raoux, M., Rodat-Despoix, L., Azorin, N., Giamarchi, A., Hao, J., Maingret, F., Crest, M., Coste, B. &Delmas, P. (2007). Mechanosensor channels in mammalian somatosensory neurons. *sensors (Basel, Switzerland)*, 7(9):1667-1682.

Renaudin, A., Lehmann, M., Girault, J., & McKerracher, L. (1999). Organization of point contacts in neuronal growth cones. *Journal of Neuroscience Research*, *55*(4), 458–71.

Rexed, B. (1952). The cytoarchitectonic organization of the spinal cord in the cat. *The Journal of Comparative Neurology*, *96*(3), 414–95.

Ribeiro, A., Balasubramanian, S., Hughes, D., Vargo, S., Powell, E. M., & Leach, J. B. (2013). β1-Integrin cytoskeletal signaling regulates sensory neuron response to matrix dimensionality. *Neuroscience*, *248*, 67–78.

Robinson, P. S., & Tranquillo, R. T. (2009). Planar biaxial behavior of fibrin-based tissue-engineered heart valve leaflets. *Tissue Engineering Part A*, *15*(10), 2763–2772.

Roeder, B. A., Kokini, K., Sturgis, J. E., Robinson, J. P., & Voytik-Harbin, S. L. (2002). Tensile mechanical properties of three-dimensional type I collagen extracellular matrices with varied microstructure. *Journal of Biomechanical Engineering*, *124*(2), 214–22.

Ross, T. D., Coon, B. G., Yun, S., Baeyens, N., Tanaka, K., Ouyang, M., & Schwartz, M. A. (2013). Integrins in mechanotransduction. *Current Opinion in Cell Biology*, *25*(5), 613–8.

Rosso, F., Giordano, A., Barbarisi, M., & Barbarisi, A. (2004). From cell-ECM interactions to tissue engineering. *Journal of Cellular Physiology*, *199*(2), 174–80.

Rothman, S. M., Guarino, B. B., & Winkelstein, B. A. (2009). Spinal microglial proliferation is evident in a rat model of painful disc herniation both in the presence of behavioral hypersensitivity and following minocycline treatment sufficient to attenuate allodynia. *Journal of Neuroscience Research*, *87*(12), 2709–17.

Rubinov, M., & Sporns, O. (2010). Complex network measures of brain connectivity: uses and interpretations. *NeuroImage*, *52*(3), 1059–69.

Sacks, M. S. (2003). Incorporation of experimentally-derived fiber orientation into a structural constitutive model for planar collagenous tissues. *Journal of Biomechanical Engineering*, *125*(2), 280–7.

Saito, K., Hitomi, S., Suzuki, I., Masuda, Y., Kitagawa, J., Tsuboi, Y., Kondo, M., Sessle, B. J. & Iwata, K. (2008). Modulation of trigeminal spinal subnucleus caudalis neuronal activity following regeneration of transected inferior alveolar nerve in rats. *Journal of Neurophysiology*, *99*(5), 2251–2263.

Samarakoon, R., & Higgins, P. J. (2003). Pp60c-src mediates ERK activation/nuclear localization and PAI-1 gene expression in response to cellular deformation. *Journal of Cellular Physiology*, *195*(3), 411–20.

Sander, E. A., & Barocas, V. H. (2009). Comparison of 2D fiber network orientation measurement methods. *Journal of Biomedical Materials Research Part A*, *88A*(2), 322–331.

Sander, E. A., Barocas, V. H., & Tranquillo, R. T. (2011). Initial fiber alignment pattern alters extracellular matrix synthesis in fibroblast-populated fibrin gel cruciforms and correlates with predicted tension. *Annals of Biomedical Engineering*, *39*(2), 714–729.

Sander, E. A., Stylianopoulos, T., Tranquillo, R. T., & Barocas, V. H. (2009a). Image-based multiscale modeling predicts tissue-level and network-level fiber reorganization in stretched cell-compacted collagen gels. *Proceedings of the National Academy of Sciences of the United States of America*, *106*(42), 17675–80.

Sander, E. A., Tranquillo, R. T., & Barocas, V. H. (2009b). Image-based multiscale structural models of fibrous engineered tissues. *Conference Proceeding IEEE Engineering in Medicine and Biology Society*, *2009*, 4270–2.

Sato, S., Oguma, H., Murakami, G., & Noriyasu, S. (2002). Morphometrical study of the joint surface and capsule of the lumbar zygapophysial joint with special reference to their laterality. *Okajimas Folia Anatomica Japonica*, *79*(1), 43–53.

Schenck, R. C., Kovach, I. S., Agarwal, A., Brummett, R., Ward, R. A., Lanctot, D., & Athanasiou, K. A. (1999). Cruciate injury patterns in knee hyperextension: a cadaveric model. *Arthroscopy : The Journal of Arthroscopic & Related Surgery*, *15*(5), 489–95.

Schultz, R. A., Miller, D. C., Kerr, C. S., & Micheli, L. (1984). Mechanoreceptors in human cruciate ligaments. A histological study. *The Journal of Bone and Joint Surgery. American Volume*, *66*(7), 1072–6.

Schwartz, M. (2004). Rho signalling at a glance. *Journal of Cell Science*, *117*(Pt 23), 5457–8. doi:10.1242/jcs.01582

Schwartz, M. A. (2010). Integrins and extracellular matrix in mechanotransduction. *Cold Spring Harbor Perspectives in Biology*, *2*(12), a005066.

Scott, D., Jull, G., & Sterling, M. (2005). Widespread sensory hypersensitivity is a feature of chronic whiplash-associated disorder but not chronic idiopathic neck pain. *The Clinical Journal of Pain*, *21*(2), 175–81.

Seong, J., Ouyang, M., Kim, T., Sun, J., Wen, P. C., Lu, S., … Wang, Y. (2011). Detection of focal adhesion kinase activation at membrane microdomains by fluorescence resonance energy transfer. *Nat Commun*, *2*, 406.

Siddique, R., & Thakor, N. (2014). Investigation of nerve injury through microfluidic devices. *Journal of the Royal Society, Interface / the Royal Society*, *11*(90), 20130676.

Siddique, R., Vyas, A., Thakor, N., & Brushart, T. M. (2014). A two-compartment organotypic model of mammalian peripheral nerve repair. *Journal of Neuroscience Methods*, *232*, 84–92.

Siegmund, G. P., Davis, M. B., Quinn, K. P., Hines, E., Myers, B. S., Ejima, S., Ono, K., Kamiji, K., Yasuki, T. & Winkelstein, B. A. (2008). Head-turned postures increase the risk of cervical facet capsule injury during whiplash. *Spine*, *33*(15), 1643–1649.

Siegmund, G. P., Myers, B. S., Davis, M. B., Bohnet, H. F., & Winkelstein, B. A. (2000). Human cervical motion segment flexibility and facet capsular ligament strain under combined posterior shear, extension and axial compression. *Stapp Car Crash Journal*, *44*, 159–70.

Siegmund, G. P., Myers, B. S., Davis, M. B., Bohnet, H. F., & Winkelstein, B. A. (2001). Mechanical evidence of cervical facet capsule injury during whiplash: a cadaveric study using combined shear, compression, and extension loading. *Spine*, *26*(19), 2095–101.

Silver, F. H., Seehra, G. P., Freeman, J. W., & DeVore, D. (2002). Viscoelastic properties of young and old human dermis: A proposed molecular mechanism for elastic energy storage in collagen and elastin. *Journal of Applied Polymer Science*, *86*(8), 1978–1985.

Singh, A., Lu, Y., Chen, C., Kallakuri, S., & Cavanaugh, J. M. (2006). A new model of traumatic axonal injury to determine the effects of strain and displacement rates. *Stapp Car Crash Journal*, *50*, 601–23.

Smith, A. D., Jull, G., Schneider, G., Frizzell, B., Hooper, R. A., Dunne-Proctor, R., & Sterling, M. (2014). Cervical radiofrequency neurotomy reduces psychological

features in individuals with chronic whiplash symptoms. *Pain Physician*, *17*(3), 265–74.

Solomonow, M. (2004). Ligaments: a source of work-related musculoskeletal disorders. *Journal of Electromyography and Kinesiology*, *14*(1), 49–60.

Spanjaard, E., & de Rooij, J. (2013). Mechanotransduction: vinculin provides stability when tension rises. *Current Biology : CB*, *23*(4), R159–61.

Spedden, E., & Staii, C. (2013). Neuron biomechanics probed by atomic force microscopy. *International Journal of Molecular Sciences*, *14*(8), 16124–40.

Spedden, E., White, J. D., Naumova, E. N., Kaplan, D. L., & Staii, C. (2012). Elasticity maps of living neurons measured by combined fluorescence and atomic force microscopy. *Biophysical Journal*, *103*(5), 868–77.

Sperry, M. M., Ita, M. E., Kartha, S., Zhang, S., Yu, Y.-H., & Winkelstein, B. (2017). The Interface of mechanics and nociception in joint pathophysiology: insights from the facet and temporomandibular joints. *Journal of Biomechanical Engineering*, *139*(2), 021003.

Stamboulian, S., Choi, J. S., Ahn, H. S., Chang, Y. W., Tyrrell, L., Black, J. A., Waxman, S. G., Dib-Hajj, S. D. (2010). ERK1/2 mitogen-activated protein kinase phosphorylates sodium channel Na(v)1.7 and alters its gating properties. *The Journal of Neuroscience* , *30*(5), 1637–47.

Staniszewska, I., Sariyer, I. K., Lecht, S., Brown, M. C., Walsh, E. M., Tuszynski, G. P., Safak, M., Lazarovici, P. & Marcinkiewicz, C. (2008). Integrin alpha9 beta1 is a receptor for nerve growth factor and other neurotrophins. *Journal of Cell Science*, *121*(Pt 4), 504–13.

Steeds, C. E. (2009). The anatomy and physiology of pain. *Surgery (Oxford)*, *27*(12), 507–511.

Stein, A. M., Vader, D. A., Weitz, D. A., & Sander, L. M. (2011). The micromechanics of three-dimensional collagen-I gels. *Complexity*, *16*(4), 22–28.

Stemper, B. D., Yoganandan, N., & Pintar, F. A. (2005). Effects of abnormal posture on capsular ligament elongations in a computational model subjected to whiplash loading. *Journal of Biomechanics*, *38*(6), 1313–23.

Sterling, M., Hendrikz, J., Kenardy, J., Kristjansson, E., Dumas, J. P., Niere, K., Cote, J., Deserres, S., Rivest, K., & Jull, G. (2012). Assessment and validation of prognostic models for poor functional recovery 12 months after whiplash injury: A multicentre inception cohort study. *Pain*, *153*(8), 1727–1734.

Stevens, G. R., Zhang, C., Berg, M. M., Lambert, M. P., Barber, K., Cantallops, I., Routtenberg, A., & Klein, W. L. (1996). CNS neuronal focal adhesion kinase forms clusters that co-localize with vinculin. *Journal of Neuroscience Research*, *46*(4), 445–55.

Strine, T. W., & Hootman, J. M. (2007). US national prevalence and correlates of low back and neck pain among adults. *Arthritis and Rheumatism*, *57*(4), 656–65.

Susilo, M. E., Paten, J. A., Sander, E. A., Nguyen, T. D., & Ruberti, J. W. (2015). Collagen network strengthening following cyclic tensile loading. *Interface Focus*, *6*(1).

Suzuki, R., Morcuende, S., Webber, M., Hunt, S. P., & Dickenson, A. H. (2002). Superficial NK1-expressing neurons control spinal excitability through activation of descending pathways. *Nature Neuroscience*, *5*(12), 1319–1326.

Svensson, R. B., Mulder, H., Kovanen, V., & Magnusson, S. P. (2013). Fracture mechanics of collagen fibrils: influence of natural cross-links. *Biophysical Journal*, *104*(11), 2476–84.

Swingler, K. (1996). *Applying Neural Networks: A Practical Guide*. Morgan Kaufmann.

Tang, H.-B., Li, Y.-S., Arihiro, K., & Nakata, Y. (2007). Activation of the neurokinin-1 receptor by substance P triggers the release of substance P from cultured adult rat dorsal root ganglion neurons. *Molecular Pain*, *3*, 42.

Tang-Schomer, M. D., Patel, A. R., Baas, P. W., & Smith, D. H. (2010). Mechanical breaking of microtubules in axons during dynamic stretch injury underlies delayed elasticity, microtubule disassembly, and axon degeneration. *FASEB Journal*, *24*(5), 1401–10.

Tatsumi, S., Mabuchi, T., Katano, T., Matsumura, S., Abe, T., Hidaka, H., Suzuki, M., Sasaki, Y., Minami, T. & Ito, S. (2005). Involvement of Rho-kinase in inflammatory and neuropathic pain through phosphorylation of myristoylated alanine-rich C-kinase substrate (MARCKS). *Neuroscience*, *131*(2), 491–8.

Thunes, J. R., Pal, S., Fortunato, R. N., Phillippi, J. A., Gleason, T. G., Vorp, D. A., & Maiti, S. (2016). A structural finite element model for lamellar unit of aortic media indicates heterogeneous stress field after collagen recruitment. *Journal of Biomechanics*, *49*(9), 1562–9.

Tibrewal, S., Khan, O. H., & Tibrewal, S. B. (2007). Facet joint injection in lower back pain--is its continued use justified? *Journal of the Royal Society of Medicine*, *100*(7), 301–2.

Todd, A. J. (2002). Anatomy of primary afferents and projection neurones in the rat spinal dorsal horn with particular emphasis on substance p and the neurokinin 1 receptor. *Experimental Physiology*, *87*(2), 245–249.

Todd, A. J. (2010). Neuronal circuitry for pain processing in the dorsal horn. *Nature Reviews. Neuroscience*, *11*(12), 823–36.

Tomaselli, K. J., Doherty, P., Emmett, C. J., Damsky, C. H., Walsh, F. S., & Reichardt, L. F. (1993). Expression of beta 1 integrins in sensory neurons of the dorsal root ganglion and their functions in neurite outgrowth on two laminin isoforms. *The Journal of Neuroscience*, *13*(11), 4880–8.

Tominaga, Y., Ndu, A. B., Coe, M. P., Valenson, A. J., Ivancic, P. C., Ito, S., Rubin, W., & Panjabi, M. M. (2006). Neck ligament strength is decreased following whiplash trauma. *BMC Musculoskeletal Disorders*, *7*, 103.

Tönges, L., Koch, J.-C., Bähr, M., & Lingor, P. (2011). ROCKing Regeneration: Rho Kinase Inhibition as Molecular Target for Neurorestoration. *Frontiers in Molecular Neuroscience*, *4*, 39.

Topp, K. S., & Boyd, B. S. (2006). Structure and Biomechanics of Peripheral Nerves: Nerve Responses to Physical Stresses and Implications for Physical Therapist Practice. *Physical Therapy*, *86*(1), 92–109.

Tower, T. T., Neidert, M. R., & Tranquillo, R. T. (2002). Fiber alignment imaging during mechanical testing of soft tissues. *Annals of Biomedical Engineering*, *30*(10), 1221–33.

Tranquillo, R. T., Girton, T. S., Bromberek, B. A., Triebes, T. G., & Mooradian, D. L. (1996). Magnetically orientated tissue-equivalent tubes: application to a circumferentially orientated media-equivalent. *Biomaterials*, *17*(3), 349–57.

Traud, A. L., Frost, C., Mucha, P. J., & Porter, M. A. (2009). Visualization of communities in networks. *Chaos (Woodbury, N.Y.)*, *19*(4), 041104.

Tsuda, M., Shigemoto-Mogami, Y., Koizumi, S., Mizokoshi, A., Kohsaka, S., Salter, M. W., & Inoue, K. (2003). P2X4 receptors induced in spinal microglia gate tactile allodynia after nerve injury. *Nature*, *424*(6950), 778–783.

Tsujino, H., Kondo, E., Fukuoka, T., Dai, Y., Tokunaga, A., Miki, K., … Noguchi, K. (2000). Activating Transcription Factor 3 (ATF3) Induction by Axotomy in Sensory and Motoneurons: A Novel Neuronal Marker of Nerve Injury. *Molecular and Cellular Neuroscience*, *15*(2), 170–182.

Ulmann, L., Hatcher, J. P., Hughes, J. P., Chaumont, S., Green, P. J., Conquet, F., Buell, G. N., Reeve, A. J., Chessell, I. P., & Rassendren, F. (2008). Up-regulation of p2x4 receptors in spinal microglia after peripheral nerve injury mediates BDNF release and neuropathic pain. *Journal of Neuroscience*, *28*(44), 11263–11268.

Vader, D., Kabla, A., Weitz, D., & Mahadevan, L. (2009). Strain-induced alignment in collagen gels. *PloS One*, *4*(6), e5902.

Van Eerd, M., Patijn, J., Lataster, A., Rosenquist, R. W., van Kleef, M., Mekhail, N., & Van Zundert, J. (2010). 5. Cervical facet pain. *Pain Practice* , *10*(2), 113–23.

Van Wijk, B. C. M., Stam, C. J., & Daffertshofer, A. (2010). Comparing brain networks of different size and connectivity density using graph theory. *PloS One*, *5*(10), e13701.

Vanderheiden, S. M., Hadi, M. F., & Barocas, V. H. (2015). Crack propagation versus fiber alignment in collagen gels: experiments and multiscale simulation. *Journal of Biomechanical Engineering*, *137*(12), 121002.

Vasseur, P. B., Saunders, G., & Steinback, C. (1981). Anatomy and function of the ligaments of the lower cervical spine in the dog. *American Journal of Veterinary Research*, *42*(6), 1002–6.

Voycheck, C. A., Luu, K., McMahon, P. J., & Debski, R. E. (2014). Collagen fiber alignment and maximum principal strain in the glenohumeral capsule predict location of failure during uniaxial extension. *Biomechanics and Modeling in Mechanobiology*, *13*(2), 379–385.

Voyvodic, F., Dolinis, J., Moore, V. M., Ryan, G. A., Slavotinek, J. P., Whyte, A. M., Hoile, R. D., & Taylor, G. W. (1997). MRI of car occupants with whiplash injury. *Neuroradiology*, *39*(1), 35–40.

Walker, D. M., & Tordesillas, A. (2014). Examining overlapping community structures within grain property networks. In *2014 IEEE International Symposium on Circuits and Systems (ISCAS)* (pp. 1275–1278).

Wallquist, W., Zelano, J., Plantman, S., Kaufman, S. J., Cullheim, S., & Hammarberg, H. (2004). Dorsal root ganglion neurons up-regulate the expression of laminin-associated integrins after peripheral but not central axotomy. *The Journal of Comparative Neurology*, *480*(2), 162–169.

Wang, H., Nair, A., Chen, C. S., Wells, R. G., & Shenoy, V. B. (2014). Long range force transmission in fibrous matrices enabled by tension-driven alignment of fibers. *Biophysical Journal*, *107*(11), 2592–2603.

Wang, H.-G., Lu, F.-M., Jin, I., Udo, H., Kandel, E. R., de Vente, J., Walter, U., Lohmann, S. M., Hawkins, R. D., & Antonova, I. (2005). Presynaptic and postsynaptic roles of NO, cGK, and RhoA in long-lasting potentiation and aggregation of synaptic proteins. *Neuron*, *45*(3), 389–403.

Weinberg, E. J., Shahmirzadi, D., & Mofrad, M. R. K. (2010). On the multiscale modeling of heart valve biomechanics in health and disease. *Biomechanics and Modeling in Mechanobiology*, *9*(4), 373–87.

Weisshaar, C. L., Dong, L., Bowman, A. S., Perez, F. M., Guarino, B. B., Sweitzer, S. M., & Winkelstein, B. A. (2010). Metabotropic glutamate receptor-5 and protein kinase C-epsilon increase in dorsal root ganglion neurons and spinal glial activation in an adolescent rat model of painful neck injury. *Journal of Neurotrauma*, *27*(12), 2261–71.

Weisshaar, C. L., Kras, J. V., Pall, P. S., Kartha, S., & Winkelstein, B. A. (2017). Ablation of IB4 non-peptidergic afferents in the rat facet joint prevents injury-induced pain and thalamic hyperexcitability via supraspinal glutamate transporters. *Neuroscience Letters*, *655*, 82–89.

Weisshaar, C. L., & Winkelstein, B. A. (2014). Ablating spinal NK1-bearing neurons eliminates the development of pain and reduces spinal neuronal hyperexcitability and inflammation from mechanical joint injury in the rat. *The Journal of Pain*, *15*(4), 378–386.

Wenger, M. P. E., Bozec, L., Horton, M. A., & Mesquida, P. (2007). Mechanical properties of collagen fibrils. *Biophysical Journal*, *93*(4), 1255–63.

Winkelstein, B. a, Nightingale, R. W., Richardson, W. J., & Myers, B. S. (1999). Cervical facet joint mechanics: its application to whiplash injury. *Stapp Car Crash Journal*, *43*(724), 243–252.

Winkelstein, B. A. (2011). How can animal models inform on the transition to chronic symptoms in whiplash? *Spine*, *36*(25 Suppl), S218–25.

Winkelstein, B. A., Nightingale, R. W., Richardson, W. J., & Myers, B. S. (2000). The cervical facet capsule and its role in whiplash injury: a biomechanical investigation. *Spine*, *25*(10), 1238–46.

Witzenburg, C. M., Dhume, R. Y., Shah, S. B., Korenczuk, C. E., Wagner, H. P., Alford, P. W., & Barocas, V. H. (2017). Failure of the porcine ascending aorta: multidirectional experiments and a unifying microstructural model. *Journal of Biomechanical Engineering*, *139*(3), 031005.

Woolf, C. J. (2011). Central sensitization: implications for the diagnosis and treatment of pain. *Pain*, *152*(3 Suppl), S2–15.

Woolf, C. J., & Fitzgerald, M. (1983). The properties of neurones recorded in the superficial dorsal horn of the rat spinal cord. *The Journal of Comparative Neurology*, *221*(3), 313–28.

Woolf, C. J., & Salter, M. W. (2000). Neuronal Plasticity: Increasing the Gain in Pain. *Science*, *288*(5472).

Woolf, C. J., & Salter, M. W. (2000). Neuronal plasticity: increasing the gain in pain. *Science (New York, N.Y.)*, *288*(5472), 1765–9.

Wu, X., & Xu, X.-M. (2016). RhoA/Rho kinase in spinal cord injury. *Neural Regeneration Research*, *11*(1), 23–7.

Xu, B., Chow, M.-J., & Zhang, Y. (2011). Experimental and modeling study of collagen scaffolds with the effects of crosslinking and fiber alignment. *International Journal of Biomaterials*, *2011*, 172389.

Xu, B., Li, H., & Zhang, Y. (2013). Understanding the viscoelastic behavior of collagen matrices through relaxation time distribution spectrum. *Biomatter*, *3*(3).

Yahia, L. H., & Garzon, S. (1993). Structure on the capsular ligaments of the facet joints. *Annals of Anatomy - Anatomischer Anzeiger*, *175*(2), 185–188. d

Yahia, L. H., & Newman, N. (1991). Innervation of spinal ligaments of patients with disc herniation. An immunohistochemical study. *Pathology, Research and Practice*, *187*(8), 936–8.

Yamagishi, S., Fujitani, M., Hata, K., Kitajo, K., Mimura, F., Abe, H., & Yamashita, T. (2005). Wallerian Degeneration Involves Rho/Rho-kinase Signaling. *Journal of Biological Chemistry*, *280*(21), 20384–20388.

Yamamoto, E., Hayashi, K., & Yamamoto, N. (1999). Mechanical properties of collagen fascicles from the rabbit patellar tendon. *Journal of Biomechanical Engineering*, *121*(1), 124–31.

Yamashita, T., Minaki, Y., Ozaktay, A. C., Cavanaugh, J. M., & King, A. I. (1996). A morphological study of the fibrous capsule of the human lumbar facet joint. *Spine*, *21*(5), 538–43.

Yen, C.-T., & Lu, P.-L. (2013). Thalamus and pain. *Acta Anaesthesiologica Taiwanica*, *51*(2), 73–80.

Yoganandan, N., Knowles, S. A., Maiman, D. J., & Pintar, F. A. (2003). Anatomic Study of the Morphology of Human Cervical Facet Joint. *Spine*, *28*(20), 2317–2323.

Yoshimi, E., Kumakura, F., Hatori, C., Hamachi, E., Iwashita, A., Ishii, N., Terasawa, T., Shimizu, Y., & Takeshita, N. (2010a). Antinociceptive effects of AS1892802, a novel

rho kinase inhibitor, in rat models of inflammatory and noninflammatory arthritis. *Journal of Pharmacology and Experimental Therapeutics*, *334*(3).

Yoshimi, E., Yamamoto, H., Furuichi, Y., Shimizu, Y., & Takeshita, N. (2010b). Sustained analgesic effect of the Rho kinase inhibitor AS1892802 in rat models of chronic pain. *Journal of Pharmacological Sciences*, *114*(1), 119–22.

Zarei, V., Liu, C. J., Claeson, A. A., Akkin, T., & Barocas, V. H. (2017). Image-based multiscale mechanical modeling shows the importance of structural heterogeneity in the human lumbar facet capsular ligament. *Biomechanics and Modeling in Mechanobiology*, 16(4):1425-1438.

Zhang, S., Bassett, D. S., & Winkelstein, B. A. (2016a). Stretch-induced network reconfiguration of collagen fibres in the human facet capsular ligament. *Journal of the Royal Society Interface*, *13*(114), 20150883.

Zhang, S., Cao, X., Stablow, A. M., Shenoy, V. B., & Winkelstein, B. A. (2016b). Tissue strain reorganizes collagen with a switchlike response that regulates neuronal extracellular signal-regulated kinase phosphorylation in vitro: implications for ligamentous injury and mechanotransduction. *Journal of Biomechanical Engineering*, *138*(2), 021013.

Zhang, S., Kartha, S., Lee, J., & Winkelstein, B. A. (2017a). Techniques for Multiscale Neuronal Regulation via Therapeutic Materials and Drug Design. *ACS Biomaterials Science & Engineering*.

Zhang, S., Nicholson, K. J., Smith, J. R., Gilliland, T. M., Syré, P. P., & Winkelstein, B. A. (2013). The roles of mechanical compression and chemical irritation in regulating spinal neuronal signaling in painful cervical nerve root injury. *Stapp Car Crash Journal*, *57*, 219–42.

Zhang, S., Singh, S., & Winkelstein, B. A. (2017b). Collagen organization regulates stretch-initiated painrelated neuronal signals in vitro: Implications for structurefunction relationships in innervated ligaments. *Journal of Orthopaedic Research*.

Zhang, S., Zarei, V., Winkelstein, B., & Barocas, V. (2017c). Multiscale mechanics of the cervical facet capsular ligament: with particular emphasis on anomalous fiber realignment prior to tissue failure. *Biomechanics and Modeling in Mechanobiology*.

Zhang, S., Zhao, E., & Winkelstein, B. A. (2017d). A nociceptive role for integrin signaling in pain after mechanical injury to the spinal facet capsular ligament. *Annals of Biomedical Engineering*.

Zhu, X., Gerstein, M., & Snyder, M. (2007). Getting connected: analysis and principles of biological networks. *Genes & Development*, *21*(9), 1010–24.

Zimmermann, M. (1983). Ethical guidelines for investigations of experimental pain in conscious animals. *Pain*, *16*(2), 109–110.

Zylka, M. J. (2005). Nonpeptidergic circuits feel your pain. *Neuron*, *47*(6), 771–2.